Understanding Complex Systems

Springer : COMPLEXITY

Visarath In
Antonio Palacios
Patrick Longhini *Editors*

International Conference on Theory and Application in Nonlinear Dynamics (ICAND 2012)

Springer

Springer Complexity

Springer Complexity is an interdisciplinary program publishing the best research and academic-level teaching on both fundamental and applied aspects of complex systems—cutting across all traditional disciplines of the natural and life sciences, engineering, economics, medicine, neuroscience, social and computer science.

Complex Systems are systems that comprise many interacting parts with the ability to generate a new quality of macroscopic collective behavior the manifestations of which are the spontaneous formation of distinctive temporal, spatial or functional structures. Models of such systems can be successfully mapped onto quite diverse "real-life" situations like the climate, the coherent emission of light from lasers, chemical reaction–diffusion systems, biological cellular networks, the dynamics of stock markets and of the internet, earthquake statistics and prediction, freeway traffic, the human brain, or the formation of opinions in social systems, to name just some of the popular applications.

Although their scope and methodologies overlap somewhat, one can distinguish the following main concepts and tools: self-organization, nonlinear dynamics, synergetics, turbulence, dynamical systems, catastrophes, instabilities, stochastic processes, chaos, graphs and networks, cellular automata, adaptive systems, genetic algorithms and computational intelligence.

The three major book publication platforms of the Springer Complexity program are the monograph series "Understanding Complex Systems" focusing on the various applications of complexity, the "Springer Series in Synergetics", which is devoted to the quantitative theoretical and methodological foundations, and the "SpringerBriefs in Complexity" which are concise and topical working reports, case-studies, surveys, essays and lecture notes of relevance to the field. In addition to the books in these two core series, the program also incorporates individual titles ranging from textbooks to major reference works.

Understanding Complex Systems

Founding Editor: Scott Kelso

Future scientific and technological developments in many fields will necessarily depend upon coming to grips with complex systems. Such systems are complex in both their composition—typically many different kinds of components interacting simultaneously and nonlinearly with each other and their environments on multiple levels—and in the rich diversity of behavior of which they are capable.

The Springer Series in Understanding Complex Systems series (UCS) promotes new strategies and paradigms for understanding and realizing applications of complex systems research in a wide variety of fields and endeavors. UCS is explicitly transdisciplinary. It has three main goals: First, to elaborate the concepts, methods and tools of complex systems at all levels of description and in all scientific fields, especially newly emerging areas within the life, social, behavioral, economic, neuro- and cognitive sciences (and derivatives thereof); second, to encourage novel applications of these ideas in various fields of engineering and computation such as robotics, nano-technology and informatics; third, to provide a single forum within which commonalities and differences in the workings of complex systems may be discerned, hence leading to deeper insight and understanding.

UCS will publish monographs, lecture notes and selected edited contributions aimed at communicating new findings to a large multidisciplinary audience.

For further volumes:
http://www.springer.com/series/5394

Visarath In · Antonio Palacios
Patrick Longhini
Editors

International Conference on Theory and Application in Nonlinear Dynamics (ICAND 2012)

Springer

Editors
Visarath In
Patrick Longhini
Spawar Systems Center
San Diego
USA

Antonio Palacios
Department of Mathematics
San Diego State University
San Diego
USA

ISSN 1860-0832 ISSN 1860-0840 (electronic)
ISBN 978-3-319-02924-5 ISBN 978-3-319-02925-2 (eBook)
DOI 10.1007/978-3-319-02925-2
Springer Cham Heidelberg New York Dordrecht London

Library of Congress Control Number: 2013955130

Printed on acid-free paper

Springer is part of Springer Science+Business Media (www.springer.com)

Organizers

Adi Bulsara, SPAWAR, San Diego
Takashi Hikihara, Kyoto University, Japan
Visarath In, SPAWAR, San Diego
Ljupco Kocarev, Macedonain Acad.
Patrick Longhini, SPAWAR, San Diego
Antonio Palacios, San Diego State University
Michael F. Shlesinger, Office of Naval Research
Hiroyuki Torikai, Osaka University, Japan
Mark Spano, Arizona State University

Sponsor

Office of Naval Research (ONR)
875 N. Randolph St., Suite 1475
Arlington, VA 22217

Army Research Office
Engineering Sciences Directorate
Mechanical Sciences Division
2800 Powder Mill Road
Adelphi, MD 20783-1197

Preface

Over the past three decades, the field of Nonlinear Science has evolved from being a valuable theoretical tool to study physical systems with dynamic behavior in space and time to a critical component to model, design and fabricate actual devices that exploit the inherently nonlinear features of many natural phenomena. Yet, while there has been significant progress in developing theoretical ideas and methods to study nonlinear phenomena under an assortment of system boundary conditions and preparations, there exist comparatively fewer devices that actually take advantage of the rich behavior exhibited by theoretical models. Consider, for instance, the fact that a shark's sensitivity to electric fields is 400 times more powerful than the most sophisticated, currently available, electric field sensor. In fact, despite significant advances in material properties, in many cases it remains a daunting task to duplicate the superior signal processing capabilities of most animals.

Bridging the gap between theory and biologically inspired devices can only be accomplished by bringing together researchers working in theoretical methods in nonlinear science with those performing experimental works. Other areas of strong interest among the research community, where theoretical findings can one day lead to novel technologies that exploit nonlinear behavior, include: chaos gates, social networks, communication, sensors, lasers, molecular motors, biomedical anomalies and stochastic resonance. A common theme among these and many other related areas is the fact that nonlinear systems tend to be highly sensitive to perturbations when they occur near the onset of a bifurcation. This behavior is universal among many nonlinear phenomena and, if properly understood and manipulated, it can lead to significant enhancements in systems response. Representative examples have been observed in a large number of laboratory experiments on systems ranging from solid state lasers to superconducting loops, and such behavior has been hypothesized to account for some of the more striking information-processing properties of biological neurons. Furthermore, background noise can precipitate this behavior, thereby playing a significant role in the optimization of the response of these systems to small external perturbations.

Since 2005, we have held a series of meetings to bring together researchers across various disciplines working on theory and experiments in nonlinear science. The first meeting was 2005 Device Applications of Nonlinear Dynamics (DANOLD) meeting, held in Catania, Italy. Then in 2007 ICAND, the research

community met again in Poipu Beach, Koloa (Kauai), Hawaii, USA. More recently, the 2010 ICAND meeting was held in Alberta, Canada, at the luxurious Fairmont Chateau in Lake Louise. And, of course, 2012 ICAND was held in Seattle, Washington, USA. This last meeting brought together researchers from physics, engineering, and biology who were involved in the analysis and development of applications that incorporate and, indeed, exploit the nonlinear behavior of certain dynamical systems. The focus for 2012 ICAND was equally divided between theory and implementation of theoretical ideas into actual devices and systems. Contemporary topics on complex systems, such as social networks, were also featured among selected lecturers.

The organizers extend their sincerest thanks to the principle sponsors of the meeting: Army Research Office (Washington, DC), Office of Naval Research (Washington, DC), Office of Naval Research-Global (Tokyo), San Diego State University (College of Sciences), and SPAWAR Systems Center Pacific. A special mention to Dr. Samuel Stanton from the Army Research Office and to Dr. Michael Shlesinger from the Office of Naval Research for their support and insight to hold such a diverse meeting. In addition, we extend our appreciation to Tania Gomez at SDSU for their hardwork in preparation and financial duty, which enabled the conference to run smoothly. We would also like to thank our colleagues who chaired the session and to all the personal who spent many hours making this meeting a success. Finally, we thank Springer for their production of an elegant proceeding.

San Diego, USA, August 2013

Visarath In
Patrick Longhini
Antonio Palacios

Contents

Part I
Invited Speakers

Exploiting Chaos for Quantum Control

Ying-Cheng Lai

Abstract The field of *Quantum Chaos* is referred to as the study of quantum behaviors of systems whose corresponding classical dynamics are chaotic, or study of quantum manifestations of classical chaos. Equivalently, it means that quantum behaviors depend on the nature of the classical dynamics, implying that classical chaos can be used to control or manipulate quantum behaviors. We discuss two examples here: using transient chaos to control quantum transport in nanoscale systems and exploiting chaos to regularize relativistic quantum tunneling dynamics in Dirac fermion and graphene systems.

1 Introduction

Controlling chaos in dynamical systems has been studied for more than two decades since the seminal work of Ott, Grebogi, and Yorke [1]. The basic idea was that chaos, while signifying random or irregular behavior, should not be viewed as a nuisance in applications of nonlinear dynamical systems. In particular given a chaotic system, the fact that there are an infinite number of unstable periodic orbits embedded in the underlying chaotic invariant set means that there are an equally infinite number of choices for the operational state of the system depending on need, provided that any such state can be stabilized. Then, the intrinsically sensitive dependence on initial conditions, the hallmark of any chaotic system, implies that it is possible to apply small perturbations to stabilize the system about any desirable state. Controlling chaos has since been studied extensively and examples of successful experimental implementation abound in physical, chemical, biological, and engineering systems

Y.-C. Lai (✉)
School of Electrical, Computer and Energy Engineering, Arizona State University,
Tempe, Arizona 85287, USA
e-mail: Ying-Cheng.Lai@asu.edu

V. In et al. (eds.), *International Conference on Theory and Application in Nonlinear Dynamics (ICAND 2012)*, Understanding Complex Systems,
DOI: 10.1007/978-3-319-02925-2_1,

[2]. The vast literature on controlling chaos, however, has been limited to nonlinear dynamical systems in the classical domain.

Recently, it has been articulated that chaos can be exploited to control or manipulate quantum-mechanical behaviors [3, 4]. For example, in the context of quantum transport through nanostructures, a fundamental characteristic is conductance fluctuations. It has been demonstrated that chaos, more specifically transient chaos, can be effective in modulating the conductance-fluctuation patterns, and it has been suggested [4] that this can be realized experimentally by applying an external gate voltage in a device of suitable geometry to generate classically inaccessible potential barriers. Adjusting the gate voltage allows the characteristics of the dynamical invariant set responsible for transient chaos to be varied in a desirable manner which, in turn, can induce continuous changes in the statistical characteristics of the quantum conductance-fluctuation pattern. In another example, it has been shown that chaos can be utilized to suppress, significantly, the spread in the tunneling rate commonly seen in systems whose classical dynamics are regular, and this is called regularization of quantum tunneling dynamics by chaos [3]. More recently, it has been demonstrated that similar effects arise in relativistic quantum systems [5].

This Brief Review has two purposes: (1) to discuss the two aforementioned examples of exploiting chaos for quantum control, and (2) to argue that the principle of chaos-based quantum control is more general with potentially significant applications in nanoscience.

2 Controlling Quantum Transport by Transient Chaos

A fundamental quantity characterizing the transport of an electron through a nanostructure, such as a quantum dot or a quantum point contact, is quantum transmission probability, or simply quantum transmission. In general, quantum transmission is determined by many electronic and system parameters such as the Fermi energy, the strength of external magnetic field (if there is one), and the details of the geometry of the structure. If the structure is connected through electron waveguides (or leads) to electron reservoirs (i.e., contacts) to form a circuitry, the conductances defined with respect to various voltage biases among the contacts, together with the corresponding currents, will be determined by the quantum transmission [6]. This means that the conductances can also depend sensitively on electronic and geometrical parameters. For example, as the Fermi energy of the electron changes, the conductances can exhibit wild fluctuations and sharp resonances [7–13]. In applications such as the development of electronic circuits and nanoscale sensors, severe conductance fluctuations are undesirable and are to be eliminated so that stable device operation can be achieved. The outstanding question is then, can practical and experimentally feasible schemes be articulated to modulate quantum conductance fluctuations? It has been demonstrated recently and understood theoretically that classical *transient chaos* can be used to effectively modulate conductance-fluctuation patterns associated with quantum transport through nanostructures [4].

Intuitively, the basic principle underlying the transient-chaos based strategy for modulating quantum transport is quantum interference. It has been known that quantum pointer states, which are resonant states of finite but long lifetime formed inside the nanostructure [14–16], can cause sharp conductance fluctuations - a kind of Fano resonance [17, 18]. To give a specific example, consider quantum-dot systems, a paradigm for investigating all kinds of quantum transport phenomena through nanostructures. Such a system typically consists of a finite device region of certain geometrical shape, such as a square, a circle, or a stadium, and a number of leads connected with the device region. For a quantum-dot system whose classical dynamics is either regular or contains a significant regular component, there are stable periodic orbits in the classical limit. If the dot geometry is closed, highly localized states can form around the classically stable periodic orbits as a result of quantum interference. When electronic waveguides (leads) are attached to the quantum dot so that it is open, some periodic orbits can still survive, leading to resonant states, or quantum pointer states. Since the corresponding classical orbits are stable, the resonant states can have long lifetime, so their coupling to the leads is weak. As a result, narrow resonances can form around the energy values that are effectively the eigenenergies for the stable periodic orbits in the corresponding closed system. When the dot geometry is modified so that the underlying classical dynamics becomes fully chaotic, no stable periodic orbits can exist. Although scars can still form around classically unstable periodic orbits in a closed chaotic system [19], the corresponding resonant states in the open system generally will have much shorter lifetimes. This means that these resonant states do couple to the leads more strongly, broadening the narrow resonances in the conductance-fluctuation pattern. Here chaos is transient because the system is open. According to the theory of transient chaos [20], the dynamical invariant sets responsible for transient chaos are non-attracting chaotic sets in the phase space. If the properties of transient chaos can be adjusted experimentally by parameter tuning, the quantum conductance fluctuation-patterns can then be controlled in a desirable manner. For example, one can change the effective geometry of the dot structure continuously so as to enhance the escape rate, a basic quantity characterizing transient chaos, and this could lead to significantly smoother quantum-conductance fluctuations.

To realize quantum control by using chaos, we conceive generating a region about the center of the device or structure with high potential so that it is impenetrable to classical particles. For example, consider a square quantum dot, a prototypical model in semiconductor two-dimensional electron-gas (2DEG) systems. When the dot is closed, the corresponding classical dynamics is integrable so that extremely narrow resonances can arise in the quantum transport dynamics of the corresponding open-dot system. Now imagine applying a gate voltage perpendicular to the device plane to generate a circular, classically forbidden region about the center of the dot, as shown schematically in Fig. 1. In general, the potential profile will be smooth in space. However, qualitatively, the classical scattering behavior is similar to that from an infinite potential well. Thus it is reasonable to impose the infinite potential-well assumption for the central region, which defines a "forbidden" region. Varying the voltage V_0 can change the effective radius R of the forbidden region. Classically, the

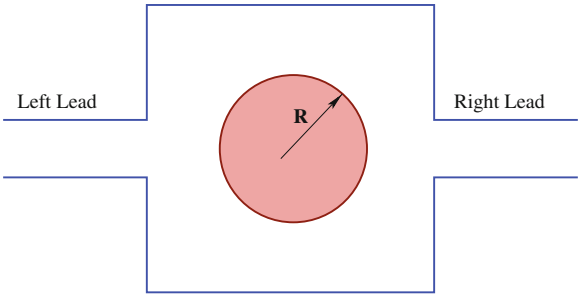

Fig. 1 Illustration of a possible scheme to control transport through a two-dimensional quantum-dot system. When semiconductor materials (e.g., silicon) are used, the system is the traditional two-dimensional electron-gas (2DEG) system described by the Schrödinger equation in non-relativistic quantum mechanics. If the material is graphene, in certain energy regime the system is described by the Dirac equation in relativistic quantum mechanics. By applying a suitable gate voltage perpendicular to the device plane to generate a *circular forbidden region* at the center of the device, the resulting closed system is a Sinai billiard, whose classical dynamics is fully chaotic. Open quantum-dot system can be formed by attaching two leads to the billiard system, one on the *left* and another on the *right side*. The classical dynamics of the device can thus be characterized as chaotic scattering

closed system is thus a Sinai billiard [21], which is fully chaotic, insofar as the radius of the central potential region R is not zero. When leads are connected to the device region so as to open the system, chaos becomes transient. The dynamical characteristics of the underlying chaotic invariant set can be adjusted in a continuous manner by increasing the radius R [22]. Quantum mechanically we thus expect to observe increasingly smooth variations in the conductance with, e.g., the Fermi energy, which has been demonstrated [4] using both semiconductor 2DEG and graphene [23–26] systems.

Insights into why classical chaos can smooth out quantum conductance fluctuations can also be gained from the semiclassical theory of quantum chaotic scattering [27–29]. In particular, in the semiclassical regime, it was established by Blümel and Smilansky that the energy autocorrelation function of the quantum transmission fluctuation is proportional to the Fourier transform of the particle-decay law in the classical limit [27]. For fully developed chaotic transport through a quantum dot, the decay law is exponential with the rate κ. As a result, the quantum energy correlation function decays as a Lorentzian function with the width given by $\hbar\kappa$, where $\hbar$ is the Planck's contant. In the theory of transient chaos [20], κ is the escape rate associated with the underlying non-attracting chaotic set. As the radius of the central potential region is increased, κ also increases. The energy autocorrelation function then decays more slowly, signifying less fluctuations, i.e., less number of *sharp resonances* in the quantum transmission. This semiclassical argument suggests that the degree of quantum transmission fluctuations can be controlled by classical chaos.

Extensive numerical support for the principle of transient-chaos based control of quantum transport and a detailed theoretical analysis can be found in Ref. [4, 30].

3 Effect of Chaos on Quantum Tunneling

The principle of regularization of quantum tunneling by chaos can be understood by considering the prototypical system in Fig. 2, which consists of two symmetrical cavities connected by a one-dimensional potential barrier along the line of symmetry. When the classical dynamics in each cavity is integrable, for sufficiently large energy the tunneling rate can have many values in a wide interval. Choosing the geometry of the cavity such that the classical dynamics become chaotic can greatly enhance and regularize quantum tunneling. Heuristically, this can be understood, as follows. When the potential barrier is infinite, each cavity is a closed system with an infinite set of eigenenergies and eigenstates. Many eigenstates are concentrated on classical periodic orbits, forming quantum scars [19]. For a classically integrable cavity, some stable or marginally stable periodic orbits can persist when the potential barrier becomes finite so that each cavity system is effectively an open quantum system. Many surviving eigenstates correspond to classical periodic orbits whose trajectories do not encounter the potential barrier, generating extremely low tunneling rate even when the energy is comparable with or larger than the height of the potential barrier. The eigenstates corresponding to classical orbits that interact with the potential barrier, however, can lead to relatively strong tunneling. In a small energy interval the quantum tunneling rate can thus spread over a wide range. However, when the classical dynamics is chaotic, isolated orbits that do not interact with the potential barrier are far less likely and, consequently, the states associated with low tunneling rates disappear, effectively suppressing the spread in the tunneling rate.

The idea of using chaos to regularize quantum tunneling dynamics was first conceived and demonstrated in non-relativistic quantum systems governed by the Schrödinger equation [3]. Recently, the question of whether chaos can regularize tunneling in relativistic quantum systems has been addressed [5], where the motion of massless Dirac fermions in the setting of resonant tunneling was investigated to facilitate comparison with the non-relativistic quantum case. In general, it is a chal-

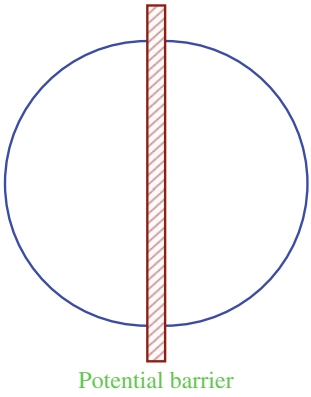

Fig. 2 A closed quantum system of arbitrary shape in two dimensions

lenging task to solve the Dirac equation in a confined geometry, due to the difficulties to incorporate zero-flux boundary conditions and to remove artificial, non-physical effects such as fermion doubling as a result of spatial discretization. A numerical scheme has then been developed [31] to overcome these difficulties, which is based on constructing a physically meaningful, Hermitian Hamiltonian. Extensive computations have revealed unequivocally the existence of surviving eigenstates that lead to extremely low tunneling rates. As for the non-relativistic quantum case, making the cavities classically chaotic can greatly regularize the quantum tunneling dynamics. To explore the practical implications, resonant tunneling devices made entirely of graphene [23] have been studied [5], where the tunneling rates for different energy values have been calculated. Qualitatively similar results have been obtained to those for massless Dirac fermions. One unique feature for both the Dirac fermion and graphene systems, which finds no counterpart in non-relativistic quantum tunneling devices, is the high tunneling rate in the regime where the particle energy is smaller than the height of the potential barrier. This is a manifestation of the Klein-tunneling phenomenon [32–34]. A theory has been developed [5] to explain the numerical findings, which is based on the concept of self energies and the complex energy spectrum of the non-Hermitian Hamiltonian for the "open" cavity.

4 General Thoughts on Chaos-Based Quantum Control

The general principle of chaos-based control of quantum behaviors is motivated by the term *quantum chaos*, which does not mean that there can actually be chaos in quantum mechanical systems but is referred to as the study of *quantum manifestations* of systems whose dynamics in the classical limit exhibit chaos [35, 36]. The basic reason that chaos may be ruled out in quantum systems is that the fundamental governing equations, the Schrödinger equation or the Dirac equation, are linear. At the present, there is tremendous literature on quantum chaos, where various quantum manifestations of classically chaotic systems have been studied. The general result is that distinct classical dynamics, integrable or chaotic, can lead to characteristically different quantum behaviors. Furthermore, different types of chaotic behaviors can generate distinct quantum manifestations. From the point of view of control, all these suggest that quantum behaviors can be manipulated or harnessed for desirable applications by choosing distinct classical dynamical behaviors, in particular chaotic dynamics.

The two examples discussed in this Brief Review, control of quantum transport and quantum tunneling, are based on building chaos into the system. In the transport problem that involves the Sinai billiard type of device structure, the properties of the underlying chaotic set can be modified, for example, by an externally adjustable gate voltage. In the tunneling problem, the geometry of the cavities are deliberately designed to yield chaotic dynamics in the classical limit. Once the structure is fixed, experimentally it may be difficult to change the characteristics of chaos. It is thus nec-

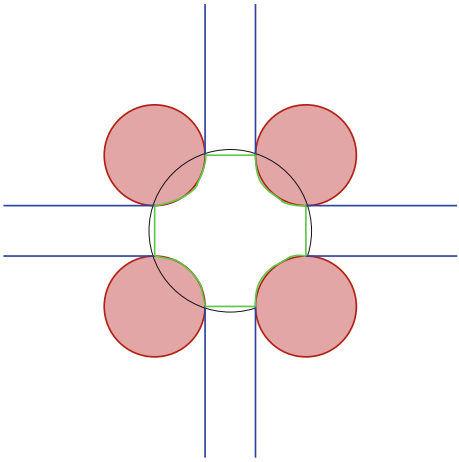

Fig. 3 A four terminal device in the presence of magnetic field. The area enclosed by the *green lines* indicates the region in the physical space where transient chaos can occur. The *black circle marks* the region in which the magnetic field is applied

essary to search for experimentally feasible schemes to modulate the characteristics of the underlying chaotic invariant sets in a continuous fashion.

Figure 3 presents a possible scheme where a single external parameter can be varied to realize chaos-based control of quantum transport. It is a four-terminal device, where four idealized leads join smoothly to form a quantum-dot structure, which has been used widely in the study of, for example, quantum Hall effect [6]. The structure typically exhibits chaotic scattering (transient chaos) in the classical limit. A perpendicular magnetic field can be applied. An earlier work [37] demonstrated that the dynamical invariants of the underlying non-attracting chaotic set can be modified continuously by changing the strength of the magnetic field. It is thus possible to modulate the quantum conductance-fluctuation patterns by simply adjusting the magnetic-field strength [38].

Acknowledgments The main idea of using chaos to manipulate quantum behaviors was generated through extensive discussions with Dr. L. Pecora from Naval Research Laboratory in January 2011 at Dr. M. Shlesinger's ONR Program Review Meeting at UCSD. The computations and theoretical analyses reported in the references [4, 5, 30, 31] on which this Review is based were mainly carried out by Dr. R. Yang, Dr. X. Ni, and Dr. L. Huang, all formerly affiliated with ASU.

References

1. E. Ott, C. Grebogi, J.A. Yorke, Phys. Rev. Lett. **64**, 1196 (1990)
2. S. Boccaletti, C. Grebogi, Y.-C. Lai, H. Mancini, D. Maza, Phys. Rep. **329**, 103 (2000)
3. L.M. Pecora, H. Lee, D.-H. Wu, T. Antonsen, M.-J. Lee, E. Ott, Phys. Rev. E **83**, 065201 (2011)
4. R. Yang, L. Huang, Y.-C. Lai, L.M. Pecora, Appl. Phys. Lett. **100**, 093105 (2012)
5. X. Ni, L. Huang, Y.-C. Lai, L.M. Pecora, EPL **98**, 50007 (2012)

6. S. Datta, *Electronic Transport in Mesoscopic Systems* (Cambridge University Press, Cambridge, 1995)
7. See, for example, R. A. Jalabert, H. U. Baranger, and A. D. Stone, Phys. Rev. Lett. **65**, 2442 (1990)
8. R. Ketzmerick, Phys. Rev. B **54**, 10841 (1996)
9. R.P. Taylor, R. Newbury, A.S. Sachrajda, Y. Feng, P.T. Coleridge, C. Dettmann, N. Zhu, H. Guo, A. Delage, P. J. Kelly, Z. Wasilewski. Phys. Rev. Lett. **78**, 1952 (1997)
10. A.S. Sachrajda, R. Ketzmerick, C. Gould, Y. Feng, P.J. Kelly, A. Delage, Z. Wasilewski, Phys. Rev. Lett. **80**, 1948 (1998)
11. B. Huckestein, R. Ketzmerick, C.H. Lewenkopf, Phys. Rev. Lett. **84**, 5504 (2000)
12. G. Casati, I. Guarneri, G. Maspero, Phys. Rev. Lett. **84**, 63 (2000)
13. R. Crook, C.G. Smith, A.C. Graham, I. Farrer, H.E. Beere, D.A. Ritchie, Phys. Rev. Lett. **91**, 246803 (2003)
14. W.H. Zurek, Rev. Mod. Phys. **75**, 715 (2003)
15. R. Akis, J.P. Bird, D.K. Ferry, Appl. Phys. Lett. **81**, 129 (2002)
16. D.K. Ferry, R. Akis, J.P. Bird, Phys. Rev. Lett. **93**, 026803 (2004)
17. U. Fano, Phys. Rev. **124**, 1866 (1961)
18. H. Ishio, Phys. Rev. E **62**, R3035 (2000)
19. Given a closed Hamiltonian system that exhibits fully developed chaos in the classical limit, one might expect the quantum wavefunctions associated with various eigenstates to be more or less uniform in the physical space. However, in the seminal work of McDonald and Kaufman [Phys. Rev. Lett. **42**, 1189 (1979) and Phys. Rev. A **37**, 3067 (1988)], it was observed that quantum eigen-wavefunctions can be highly non-uniform in the chaotic stadium billiard. A systematic study was subsequently carried out by Heller [Phys. Rev. Lett. **53**, 1515 (1984)], who established the striking tendency for wavefunctions to concentrate about classical unstable periodic orbits, which he named quantum scars. Semiclassical theory was then developed by Bogomolny [Physica D **31**, 169 (1988)] and Berry [Proc. Roy. Soc. (London) **A 423**, 219 (1989)], providing a general understanding of the physical mechanism of quantum scars. The phenomenon of quantum scarring was deemed counterintuitive and surprising but only for chaotic systems, as the phase space of an integrable system is not ergodic so that the quantum wavefunctions are generally not expected to be uniform. Relativistic quantum scars in chaotic graphene systems have also been reported [L. Huang, Y.-C. Lai, D. K. Ferry, S. M. Goodnick, and R. Akis, Phys. Rev. Lett. **103**, 054101 (2009)].
20. Y.-C. Lai, T. Tél, *Transient Chaos* (Springer, New York, 2011)
21. Y. Sinai, Russ. Math. Surv. **25**, 137 (1970)
22. See, for example, Chapter 18 in J. R. Dorfman, *An Introduction to Chaos in Nonequilibrium Statistical Mechanics* (Cambridge University Press, Cambridge 1999)
23. K.S. Novoselov et al., Science **306**, 666 (2004)
24. C. Berger et al., J. Phys. Chem. B **108**, 19912 (2004)
25. C.W.J. Beenakker, Rev. Mod. Phys. **80**, 1337 (2008)
26. A.H. Castro Neto et al., Rev. Mod. Phys. **81**, 109 (2009)
27. R. Blümel, U. Smilansky, Phys. Rev. Lett. **60**, 477 (1988)
28. R. Blümel, U. Smilansky, Physica D **36**, 111 (1989)
29. Y.-C. Lai, R. Blümel, E. Ott, C. Grebogi, Phys. Rev. Lett. **68**, 3491 (1992)
30. R. Yang, L. Huang, Y.-C. Lai, C. Grebogi, and L. M. Pecora, Chaos **2**3, 013125 (2013)
31. X. Ni, L. Huang, Y.-C. Lai, C. Grebogi, Phys. Rev. E **86**, 015702 (2012)
32. P. Strange, *Relativistic Quantum Mechanics with Applications in Condensed Matter Physics and Atomic Physics* (Cambridge University Press, Cambridge, 1998)
33. M.I. Katsnelson, K.S. Novoselov, A.K. Geim, Nat. Phys. **2**, 620 (2006)
34. C.W.J. Beenakker, Colloquium: andreev reflection and Klein tunneling in graphene. Rev. Mod. Phys. **80**, 1337 (2008)
35. F. Haake, *Quantum Signatures of Chaos*, 2nd edn. (Springer, Berlin, 2001)
36. H.J. Stöckmann, *Quantum Chaos: An Introduction* (Cambridge University Press, Cambridge, 1999)
37. W. Breymann, Z. Kov'acs, T. Tél, Phys. Rev. E **50**, 1994 (1994)
38. G.-L. Wang, L. Ying, Y.-C. Lai, and C. Grebogi, Phys. Rev. E **87**, 052908 (2013)

Random Vibration of a Nonlinear Autoparametric System

Kristjan Onu, Nishanth Lingala and N. Sri Namachchivaya

Abstract We examine a stochastically forced autoparametric system for its stationary motion and stability. The deterministic form of this system is nearly Hamiltonian (with small dissipation) and exhibits 1:2 resonance and phase-locking. We develop a stochastic averaging technique to achieve a lower dimensional description of the dynamics of this system. Stochastic averaging is possible due to three time scales involved in this problem. Each time scale is fully exploited while averaging. The dimensional reduction techniques developed here consist of a sequence of averaging procedures that are uniquely adapted to study stochastic autoparametric systems. What motivates our analysis is that classical averaging methods fail when the original Hamiltonian system has resonances, because, at these resonances, singularities arise in the lower-dimensional description. At these singularities we introduce *gluing conditions*; these complete the specification of the dynamics of the reduced model. Examination of the reduced Markov process (which takes values on a nonstandard space) yields important results for probability density functions.

1 Introduction

We investigate the random vibrations of a nonlinear autoparametric system of the form

$$\begin{aligned} &\ddot{q}_1(t) + \zeta_1 \dot{q}_1(t) + f_1(q_1(t), q_2(t)) = \xi(t) \\ &\ddot{q}_2(t) + \zeta_2 \dot{q}_2(t) + f_2(q_1(t), q_2(t)) = 0 \end{aligned} \qquad t \geq 0, \tag{1}$$

K. Onu (✉)
Department of Mechanical Engineering, McGill University, 817 Sherbrooke Street West, Montreal, QCH3A 2K6, Canada
e-mail: kristjan.onu@mcgill.ca

N. Lingala · N. Sri Namachchivaya
Department of Aerospace Engineering, University of Illinois at Urbana-Champaign, Urbana, Illinois 61801, USA
e-mail: lingala1@illinois.edu

N. Sri Namachchivaya
e-mail: navam@illinois.edu

V. In et al. (eds.), *International Conference on Theory and Application in Nonlinear Dynamics (ICAND 2012)*, Understanding Complex Systems,
DOI: 10.1007/978-3-319-02925-2_2, © Springer International Publishing Switzerland 2014

where for each time $t > 0$, $(q_1(t), q_2(t))$ represents the generalized coordinates of the system, the constants ζ_1 and ζ_2 are damping coefficients, and $\xi(t)$ is a stationary random process. We are interested in questions of stability of the stochastic system (1), and in the transfer of energy from the forced mode q_1 to the unforced mode q_2. It is well known that, in the presence of $1:2$ resonance and periodic excitation, as the intensity of excitation is increased, the excited mode reaches a certain value of amplitude at which saturation takes place and then the energy is transferred to the unforced mode. This may be undesirable, because disturbances affecting one mode may cause unwanted instability in another mode. Our effort is to answer whether the saturation and energy transfer occurs in the presence of noisy input. Towards this goal, we achieve a lower dimensional description of the above system.

The dissipation and random perturbations are assumed to be small. This means that their effect will be visible only over a long time horizon. When the nonlinearities are also assumed small, the dominant part of the dynamics is that of two uncoupled oscillators. In particular, the dynamics of the unperturbed system identify a reduced phase space (the orbit space) on which to carry out stochastic averaging. While the classical theory of stochastic averaging is a natural framework for such a program, the equations of interest contain resonances and bifurcations, which precludes a simple application of classical techniques. In particular, the resonance gives rise to an intermediate scale, and the bifurcations give rise to some non-standard singularities in the orbit space.

The equations of motion considered (1) can model the dynamics of a number of mechanical systems, namely a random excitation of a initially deformed shallow arch, a suspended elastic cable driven by planar excitation, or a water vessel subject to longitudinal wave action. To keep things as simple as possible, we shall consider a very simple system, namely a pendulum hanged from a mass which is attached by a spring to a support (Fig. 1). The mass is randomly excited. For clarity, we use *mass* to refer to the object at the free end of the spring, while the object at the end of the pendulum is referred to as the *bob*. The quantity φ is the angle of the pendulum (with respect to the vertical axis) and the quantity y represents the height of the mass (relative to a rest position defined by the position of the pendulum). The mass is forced according to a stochastic signal $\Xi(t)$. The subscripts here refer to the fact that this is our original physical model. The equations for such a system can be written as

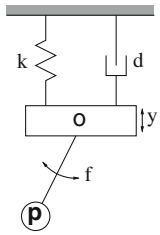

Fig. 1 Schematic of autoparametric system

$$(m_o + m_p)\ddot{y} + d_o\dot{y} + ky + m_p l(\ddot{\varphi}\sin\varphi + \dot{\varphi}^2\cos\varphi) = \Xi,$$
$$m_p l^2\ddot{\varphi} + d_p\dot{\varphi} + m_p l(g + \ddot{y})\sin\varphi = 0, \tag{2}$$

where m_o, d_o and k are the mass, damping and the spring constant of the spring-mass system and m_p, d_p and l are the mass, damping and the length of the pendulum. The kinetic and the potential energies of the system are given by

$$T = \frac{1}{2}(m_o + m_p)\dot{y}^2 + \frac{1}{2}m_p l^2\dot{\varphi}^2 + m_p l\dot{y}\dot{\varphi}\sin\varphi,$$
$$U = m_p gl(1 - \cos\varphi) + \frac{1}{2}ky^2.$$

It is clear that the nonlinearities in the equations of motion arise due to the gravitational restoring force and due to the dependence of kinetic energy on the angle φ which leads to inertial coupling between the the two coordinates. It also turns out (we shall use this later) that in the absence of noise and damping, this system is Hamiltonian, so the dynamics of y and φ are governed by the geometry of this Hamiltonian.

The above equations in dimensionless coordinates are

$$\ddot{\hat{\eta}} + 2\hat{\zeta}_o\dot{\hat{\eta}} + \hat{\eta} + R(\ddot{\hat{\theta}}\sin\hat{\theta} + \dot{\hat{\theta}}^2\cos\hat{\theta}) = \hat{\xi}(t),$$
$$R\ddot{\hat{\theta}} + 2R\hat{\zeta}_p\dot{\hat{\theta}} + R(q^2\sin\hat{\theta} + \ddot{\hat{\eta}}\sin\hat{\theta}) = 0.$$

where

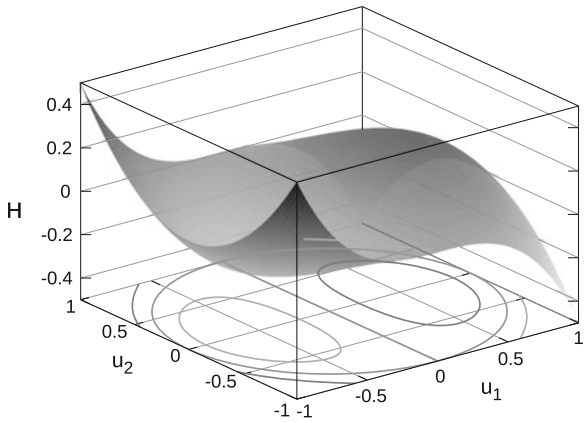

Fig. 2 Surface and contour plots of $K(u_1, u_2)$. $I = 1$

Fig. 3 State space $\mathfrak{M}$ for Y_t^ε

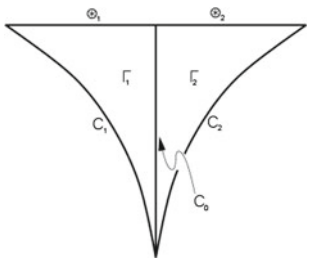

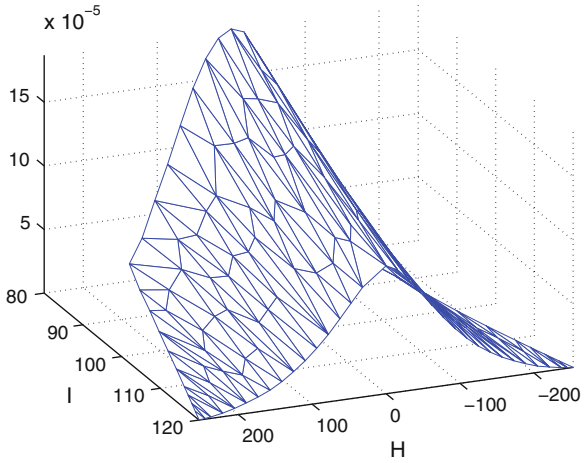

Fig. 4 Probability density by FEM

$$\omega^2 \stackrel{\text{def}}{=} \frac{g}{l}, \quad \omega_o^2 \stackrel{\text{def}}{=} \frac{k}{m_o + m_p}, \quad q \stackrel{\text{def}}{=} \frac{\omega}{\omega_o},$$

$$R \stackrel{\text{def}}{=} \frac{m_p}{m_o + m_p}, \quad \hat{\zeta}_o \stackrel{\text{def}}{=} \frac{d_o}{2\sqrt{k(m_o + m_p)}}, \quad \hat{\zeta}_p \stackrel{\text{def}}{=} \frac{d_p\sqrt{(m_o + m_p)}}{2l^2\sqrt{k}} = \frac{d_p}{2l^2\omega_o}.$$

and where

$$\hat{\xi}(t) = \frac{\hat{\xi}(t/\omega_o)}{kl}, \quad \hat{\eta}(t) = \frac{y(t/\omega_o)}{l}, \quad \hat{\theta}(t) = \varphi(t/\omega_o)$$

for all $t > 0$.

Our interest here is a refined stability analysis near the fixed point $(\hat{\eta}, \hat{\theta}) \equiv 0$ of the unperturbed system. In particular, we are interested in the effect of small random perturbations, so we will let $\hat{\xi}$ be of the form $\hat{\xi} = \varepsilon^2 \nu \xi$, where ξ is a noise process of "unit" variance and ν is some empirical parameter. Our dynamics are most interesting when they are not over-damped, so let $\hat{\zeta}_o$ and $\hat{\zeta}_p$ be of the form $\hat{\zeta}_o = \varepsilon^2 \zeta_o$ and $\zeta_p = \varepsilon^2 \zeta_p$, where ζ_o and ζ_p are some positive constants (this corresponds to letting d_o and d_p be of size ε). Guided by the corresponding analysis for periodic

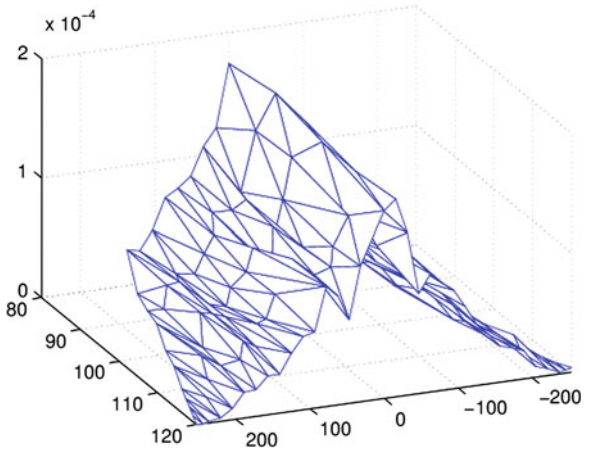

Fig. 5 Probability density by numerical simulation

forcing, we are interested in the behavior when q^2 is very close to $q_o^2 \equiv 1/4$. Let's replace q by $q_o + \varepsilon^2\mu$, where μ is an unfolding parameter. Since we are interested in $\hat{\eta}$ and $\hat{\theta}$ near the fixed point 0, we should look at these quantities on a finer resolution. Namely, let η and θ be defined by

$$\hat{\eta}(t) = \varepsilon\eta(t), \qquad \hat{\theta}(t) = \varepsilon\theta(t)$$

then the dynamics of the system yields

$$\begin{aligned} &\ddot{\eta} + 2\varepsilon^2\zeta_o\dot{\eta} + \eta + R(\ddot{\theta}\sin(\varepsilon\theta) + \varepsilon\dot{\theta}^2\cos(\varepsilon\theta)) = \varepsilon\nu\xi(t), \\ &R\ddot{\theta} + 2\varepsilon^2 R\zeta_p\dot{\theta} + R\left(\left(q_\circ + \varepsilon^2\mu\right)\frac{\sin(\varepsilon\theta)}{\varepsilon} + \ddot{\eta}\sin(\varepsilon\theta)\right) = 0, \end{aligned} \tag{3}$$

where ε is a small scaling parameter, $q_0 = 1/2$ signifying $1:2$ resonance, μ is the parameter representing unfolding from the resonance, R is the ratio of mass of the unforced mode to the total mass.

2 Single Mode Solutions

To clarify some general qualitative effects of noise, let's consider a simple stability analysis using some spectral methods and the first-order linearization. The mass on the spring can move only in the vertical (η) direction and is excited by $\nu\xi$. Assume that the pendulum is locked vertically, i.e. $\theta(t) \equiv 0$. We get the equation

$$\ddot{\eta} + 2\varepsilon^2\zeta_o\dot{\eta} + \eta = \varepsilon\nu\xi.$$

If ξ is white noise we can solve for η explicitly. Its power spectral density is

$$S_\eta(\omega) = \frac{\varepsilon^2 \nu^2 S_0}{(1-\omega^2)^2 + 4\varepsilon^4 \zeta_o^2 \omega^2},$$

where S_0 is the power spectral density of ξ. The peak intensity and the carrying frequency of η are determined by the filter parameter ζ_o.

The stability of the locked mass steady-state oscillation is now obtained by using the first-order approximation of sine and cosine in the dynamics for θ. We get

$$\ddot{\theta} + 2\varepsilon^2 \zeta_p \dot{\theta} + ((q_0 + \varepsilon^2 \mu)^2 + \varepsilon \ddot{\eta})\theta = 0,$$

and the power spectral density of $\ddot{\eta}$ is given by

$$S_{\ddot{\eta}}(\omega) = \frac{\omega^4 \varepsilon^2 \nu^2 S_0}{(1-\omega^2)^2 + 4\varepsilon^4 \zeta_o^2 \omega^2}.$$

The maximal Lyapunov exponent can now be easily calculated and the stability boundary can be obtained in terms of excitation intensity ν and the dissipation coefficients ζ_p. An explicit expression for the maximal Lyapunov exponents of the single mode solution is given by expanding it in ε, we have

$$\lambda_1 \approx \varepsilon^2 \left(-\zeta_p + \frac{1}{8\, q_o^2} S_{\ddot{\eta}}(2\,(q_o + \varepsilon^2 \mu)) \right) \quad \text{and} \quad \lambda_2 = \varepsilon^2 \left(-\zeta_p - \frac{1}{8\, q_o^2} S_{\ddot{\eta}}(2\,(q_o + \varepsilon^2 \mu)) \right).$$

The noise has no effect on the other two exponents; i.e., $\lambda_3 = \lambda_4 = -\varepsilon^2 \zeta_o$.

Since the point $\theta \equiv 0$ is a stable point for the hanging pendulum, the pendulum undergoes small random motion near $\theta \equiv 0$, and all four Lyapunov exponents are negative. However, as we further increase the noise intensity, the top exponent becomes positive when $\nu^2 S_0 = 8\zeta_o^2 \zeta_p$. The system then becomes unstable, and the following question arises.

- Do both the mass spring oscillator and the pendulum undergo random vibrations when the top exponent becomes positive (i.e., $\nu^2\, S_0 > 8\, \zeta_o^2\, \zeta_p$), i.e., does a new coupled-mode "stationary solution" or "stationary density function" appear?

3 Coupled Mode Solutions

Making use of a time-varying symplectic transformation (see [1] for details), we arrive at

$$\dot{x}_t^\varepsilon = \varepsilon b^1(x_t^\varepsilon, t) + \varepsilon^2 b^2(x_t^\varepsilon, t : \zeta, \mu) + \varepsilon \sigma(x_t^\varepsilon, t : \nu)\xi(t), \tag{4}$$

where (x_1, x_2) and (x_3, x_4) are conjugate pairs and can be thought of as the amplitudes of periodic orbits of the dominant dynamics.

The coefficients b^1, b^2, σ are periodic in time. Standard deterministic averaging can be used to average out the effects of rapidly-oscillating periodic coefficients. Let $\mathbb{M}$ be this averaging operator.

Definition 1 *(Time averaging operator)* For a function $\varphi \in C^\infty(\mathbb{R}^4 \times \mathbb{R})$ which is 2π periodic in its last argument, define the time averaging operator $\mathbb{M}$ by

$$(\mathbb{M}\varphi)(x) \equiv \frac{1}{2\pi}\int_0^{2\pi} \varphi(x,t)dt.$$

From the explicit formulas (see [1]) for b^1 (where $q = 1/2$), we see that for $x = (x_1, x_2, x_3, x_4) \in \mathbb{R}^4$,

$$(\mathbb{M}b^1)(x) = \left(-\tfrac{1}{2}x_2x_4,\ \ \tfrac{1}{2}(x_1x_4 - x_2x_3),\ \ \tfrac{1}{4}(x_2^2 - x_4^2),\ \ \tfrac{1}{2}(x_1x_2 + x_3x_4)\right).$$

Then the averaged system $\dot{x}_t = (\mathbb{M}b^1)(x)$ is a 4-dimensional Hamiltonian system with two first integrals K and I in involution.

The Hamiltonian associated with these dynamics is

$$K(x) = \frac{1}{4}x_1(x_4^2 - x_2^2) - \frac{1}{2}x_2x_3x_4. \tag{5}$$

The unperturbed four-dimensional Hamiltonian system

$$\dot{z} = \bar{\nabla}K(z) \tag{6}$$

has *two first integrals in involution*, namely, the Hamiltonian itself (5) and a second constant of motion (momentum variable)

$$I(x) = (x_1^2 + x_3^2) + \frac{1}{2}(x_2^2 + x_4^2). \tag{7}$$

The invariant I is functionally independent of K, exists globally and is single valued. Note that the Hamiltonian system's equations remain unchanged when $t \to -t$, $x_1 \to -x_1$ and $x_3 \to -x_3$.

3.1 Dimensional Reduction

Our main analytical tool is a certain method of dimensional reduction of nonlinear systems with symmetries and small noise. As the noise becomes asymptotically small, one can exploit symmetries and a separation of scales to use well-known methods (viz. stochastic averaging) to find an appropriate lower-dimensional description of the system.

In the flow given by (4), the quantities $(K(x), I(x))$ are slow-varying. The variation of $y_t^\varepsilon := (K(x_t^\varepsilon), I(x_t^\varepsilon))$ is given by the following set of equations

$$\dot{y}_t^\varepsilon = \varepsilon F^1(x_t^\varepsilon, t) + \varepsilon^2 F^2(x_t^\varepsilon, t : \zeta, \mu) + \varepsilon G(x_t^\varepsilon, t : \nu)\xi(t), \tag{8}$$

where $F_j^i(x,t) = (b^i(x,t).\nabla)y_j$ and $G_j(x,t) = (g(x,t).\nabla)y_j$.

Since K and I are integrals of motion for $\dot{x}_t = (\mathbb{M}b^1)(x)$, it is clear that $\mathbb{M}F^1(X) = 0$. Thus, to see the fluctuations of K and I, we need to look on a time scale of order $1/\varepsilon^2$. Thus, we make a time rescaling, setting $X_t^\varepsilon \stackrel{\text{def}}{=} x^\varepsilon_{t/\varepsilon^2}$ and $Y^\varepsilon \stackrel{\text{def}}{=} y^\varepsilon_{t/\varepsilon^2}$. Then we have

$$\begin{aligned}
\dot{X}_t^\varepsilon &= \frac{1}{\varepsilon} b^1(X_t^\varepsilon, t/\varepsilon^2) + b^2(X_t^\varepsilon, t/\varepsilon^2) + g(X_t^\varepsilon, t/\varepsilon^2)\,\frac{1}{\varepsilon}\xi(t/\varepsilon^2),\\
\dot{Y}_t^\varepsilon &= \frac{1}{\varepsilon} F^1(X_t^\varepsilon, t/\varepsilon^2) + F^2(X_t^\varepsilon, t/\varepsilon^2) + G(X_t^\varepsilon, t/\varepsilon^2)\,\frac{1}{\varepsilon}\xi(t/\varepsilon^2).
\end{aligned} \tag{9}$$

Roughly, our goal is to study (9) and show that as ε tends to zero, the dynamics of $Y^\varepsilon(X_t^\varepsilon)$ tends to a lower-dimensional Markov process and to identify the infinitesimal generator of the limiting law.

There are three time scales. The periodic fluctuations of the coefficients occur over time scales of order ε^2. The effects of drift due to b^1 can be seen on time scales of order ε. The drift and diffusion coefficients of Y_t^ε are of order 1. We perform two averaging steps, one to average ($\mathbb{M}$) the periodic behavior of the coefficients, and one to average (**A**) along the orbits of the Hamiltonian system $\dot{x}_t = (\mathbb{M}b^1)(x)$.

To understand the state space of the slow variable Y_t^ε, we consider the following symplectic transformation (it would also be useful later for simplifying calculations).

3.1.1 Structure of the Unperturbed System: Hamiltonian Structure

$$\begin{aligned}
x_1 &= u_1\cos(2\psi) + u_2\sin(2\psi), \quad & x_3 &= -u_1\sin(2\psi) + u_2\cos(2\psi),\\
x_2 &= \sqrt{2(I - u_1^2 - u_2^2)}\sin\psi, & x_4 &= \sqrt{2(I - u_1^2 - u_2^2)}\cos\psi.
\end{aligned} \tag{10}$$

The conjugate pairs are (u_1, u_2) and (ψ, I). This transformation yields

$$\dot{u}_{1t} = -u_{1t}u_{2t}, \qquad \dot{u}_{2t} = \frac{1}{2}(3u_{1t}^2 + u_{2t}^2 - I_t), \qquad \dot{\psi}_t = \frac{1}{2}u_{1t}, \quad \dot{I}_t = 0 \tag{11}$$

and the corresponding Hamiltonian is

$$K = \frac{1}{2}u_1\left(I - (u_1^2 + u_2^2)\right). \tag{12}$$

The relation between K, u_1, u_2, and I is illustrated in Fig. 2. Note that this system's equations remain unchanged when $t \to -t, u_2 \to -u_2$ and $\psi \to -\psi$. System (11) has four fixed points. They are $(u_1, u_2) = (0, \pm\sqrt{I})$ and $(u_1, u_2) = (\pm\frac{\sqrt{3I}}{3}, 0)$.

The points on the u_1 axis are saddle points and those on the u_2 axis are center fixed points.

3.1.2 State Space of Y_t^ε

The slow variable Y_t^ε evolves on an arrowhead. Let $\mathbf{S} \stackrel{\text{def}}{=} \{x \in \mathbb{R}^4 : K_* < K(x) < K^*,\ 0 < I(x) < I^*\}$. Then define an equivalence relation $\sim$ on $\mathbb{R}^4$ by identifying $x \sim y$ if x and y are on the same orbit of the hamiltonian flow $\dot{x}_t = (\mathbb{M}b^1)(x)$. Define $\mathfrak{M} \stackrel{\text{def}}{=} \bar{\mathbf{S}}/\sim$, and endow $\mathfrak{M}$ with the quotient topology defined by $\sim$. If $x \in \bar{\mathbf{S}}$, we let $[x] := \{y \in \bar{\mathbf{S}} :\ y \sim x\}$ be the equivalence class of x. $\pi(x) := [x]$. The slow variable Y_t^ε evolves on $\mathfrak{M} = \bigcup_{i=1}^2 \Gamma_i \cup \bigcup_{i=0}^2 [\mathfrak{c}_i] \cup \bigcup_{i=1}^2 \circledast_i$ where $\mathfrak{c}_i$ are the fixed points, the $\circledast_i$ are closed orbits whose union is $\partial\bar{\mathbf{S}}$, and each Γ_i is the π-image of a maximal open subset of $\mathbb{R}^4$ which does not intersect any of the $[\mathfrak{c}_i]$ or $\circledast_i$. The state space is illustrated in Fig. 3.

3.1.3 $\mathbb{M}$ & A Averaging

If the external noise $\xi(\tau)$ represents mean zero, stationary, independent stochastic processes with the strong mixing property, then roughly, as $\varepsilon \to 0$, $\frac{1}{\varepsilon}\xi(t/\varepsilon^2)$ approaches a white noise process. Khasminskii [2] gave a rigorous proof that a family of processes X_t^ε converges to a diffusion process. The aim here is to make use of this and derive a reduced graph-valued process for the integrals of motion, Y^ε.

We have pointed out that that there are three time-scales involved in our averaging problems. The first step is to average the periodic fluctuations of the coefficients and obtain $\mathbb{M}$-averaged quantities as the precursors to the stochastically averaged drift and diffusion coefficients. Somewhat laborious calculations yield the $\mathbb{M}$-averaged quantities

$$m_i(x) \equiv \left(\mathbb{M}\left(F_1^2 + \mathfrak{f}_1 + \mathfrak{g}_1\right)\right)(x) \qquad \text{and} \qquad a_{ij}(x) \equiv \left(\mathbb{M}\left(\sigma\sigma^T\right)_{ij}\right)(x). \quad (13)$$

These calculations can be simplified by considering the symplectic transformation (10) which provides a convenient geometric structure of the unperturbed integrable Hamiltonian problem. In (K, I, u) coordinates, the drift and diffusion (13) coefficients are

$$\begin{aligned} m_1(K, I, u) &= -(\zeta_o + 2\zeta_p)K - \frac{1}{4}(8\mu + 3I)\,K\frac{u_2}{u_1} + \frac{1}{2}\left(3 + \frac{1}{R}\right)K^2\frac{u_2}{u_1^2}, \\ m_2(K, I, u) &= 2[\sigma^2 S_{\xi\xi}(1) - \zeta_o I + 2(\zeta_o - \zeta_p)K/u_1], \end{aligned} \quad (14)$$

$$a_{11}(K,I,u) = \frac{1}{2}\sigma^2 S_{\xi\xi}(1)K^2\frac{1}{u_1^2}, \quad a_{12}(K,I,u) = \sigma^2 S_{\xi\xi}(1)K,$$
$$a_{22}(K,I,u) = 2\sigma^2 S_{\xi\xi}(1)(I - 2K/u_1). \tag{15}$$

To obtain a limiting generator for the martingale problem, we need an averaging operator where the averaging is done with respect to the invariant measure concentrated on the closed trajectories. Using (14) in the **A**-averaging operator yields on each leaf Γ_i, for $z = (K, I) \in \Gamma_i$,

$$\mathfrak{b}_j^i(z) = \frac{1}{T_i(z)}\int_0^{T_i(z)} m_j\,(z, u(t))\,dt, \qquad \mathfrak{a}_{jk}^i(z) = \frac{1}{T_i(z)}\int_0^{T_i(z)} a_{jk}(u(t), K, I)dt,$$
$$\mathfrak{b}_1^i(z) = -(\zeta_o + 2\zeta_p)K, \qquad \mathfrak{b}_2^i(z) = 2[\sigma^2 S_{\xi\xi}(1) - \zeta_o I] + 4(\zeta_o - \zeta_p)K\frac{\mathscr{I}_i^1}{T_i},$$
$$\mathfrak{a}_{11}^i(z) = \frac{1}{2}\,\sigma^2 S_{\xi\xi}(1)K^2\,\frac{\mathscr{I}_i^2}{T_i}, \quad \mathfrak{a}_{12}^i(z) = \sigma^2 S_{\xi\xi}(1)K, \quad \mathfrak{a}_{22}^i(z) = 2\sigma^2 S_{\xi\xi}(1)(I - 2K\frac{\mathscr{I}_i^1}{T_i}).$$

Here, $T_i(z)$ is the time period of the Hamiltonian orbit on leaf i with value of K and I given by z and $\mathscr{I}_i^1 = \int_0^{T_i}\frac{1}{u_1(t)}dt$ and $\mathscr{I}_i^2 = \int_0^{T_i}\frac{1}{u_1^2(t)}dt$.

3.1.4 Generator of the Reduced Markov Process

We want to put these $\mathscr{L}_i$'s together to get a Markov process on $\mathfrak{M}$ with generator $\mathscr{L}_{\mathfrak{M}}^{\dagger}$ with domain $\mathscr{D}_{\mathfrak{M}}^{\dagger}$, where $\mathfrak{M}$ has a shape of an arrowhead.

Let us define the drift and diffusion coefficients

$$\mathfrak{b}_i(z) \equiv \left(\mathbf{A}\left(\mathbb{M}\left(F_i^2 + \mathfrak{f}_i + \mathfrak{g}_i\right)\right)\right)(z), \qquad \mathfrak{a}_{ij}(z) \equiv \left(\mathbf{A}\left(\mathbb{M}\left(\sigma\sigma^T\right)_{ij}\right)\right)(z) \tag{16}$$

for $i, j = 1, 2$ and for all $z \in \mathfrak{M}$, where

$$\mathfrak{f}_i(x,t) \equiv \sum_{j=1}^{4}\frac{\partial F_i^1}{\partial x_j}(x,t)\tilde{f}_j^1(x,t), \qquad \tilde{f}_i^1(x,t) \equiv \int_0^t\left\{b_i^1(x,s) - \mathbb{M}_s(b_i^1(x,s))\right\}ds,$$
$$\mathfrak{g}_i(x,t) \equiv \int_{-\infty}^{0}\mathbb{E}\left[\frac{\partial G_i}{\partial x_j}(x,t,\xi_t)g_j(x,t+\tau,\xi_{t+\tau})\right]d\tau,$$
$$\left(\sigma\sigma^T\right)_{jk}(x,t) \equiv \int_{-\infty}^{\infty}\mathbb{E}\left[G_j(x,t,\xi_t)G_k(x,t+\tau,\xi_{t+\tau})\right]d\tau.$$

exists uniformly in $x \in \mathbb{R}^4$.

For notational convenience, we also define $f_i \equiv f\big|_{\Gamma_i}$ for all $1 \le i \le 2$. From the results of [3] , it is clear the gluing conditions, which we need to specify at the interior edges, solely depend on the diffusion coefficients $\mathfrak{a}_{jk}^i$. To this end, we define $\mathring{\mathfrak{a}}_{jk}^i(z) \equiv \mathfrak{a}_{jk}^i(z)\,T(z)$. The limiting domain for the graph valued process is

$$\mathscr{D}^{\dagger}_{\mathfrak{M}} = \left\{ f \in C(\mathfrak{M}) \cap C^2(\cup_{i=1}^{2} \Gamma_i) : \lim_{z \to (K(\mathfrak{c}_i), I(\mathfrak{c}_i))} (\mathscr{L}_i f_i)(h) \text{ exists } \forall i, \right.$$
$$\left. \lim_{I \to I^*} (\mathscr{L}_i f_i)(z) = 0 \quad \forall i, \quad \text{and} \quad \sum_{i=1}^{2} \{\pm\} \, (\mathring{\mathfrak{a}}^i_{11} \frac{\partial f_i}{\partial z_1})(\mathfrak{c}_0) = 0 \right\}, \tag{17}$$

where the '+' sign is taken if the coordinate h on the leg Γ_i is greater than 0 (the value of $z_1 (= h)$ at the vertex $\mathfrak{c}_0$) and the '−' sign is taken otherwise. Then for $f \in \mathscr{D}^{\dagger}_{\mathfrak{M}}$, the generator is

$$(\mathscr{L}^{\dagger}_{\mathfrak{M}} f)(z) = \lim_{\substack{z' \to z \\ z \in \bar{\Gamma}_i}} (\mathscr{L}_i f_i)(z') = \sum_{j=1}^{2} \mathfrak{b}^i_j(z) \frac{\partial f_i}{\partial z_j}(z) + \frac{1}{2} \sum_{j,k=1}^{2} \mathfrak{a}^i_{jk}(z) \frac{\partial^2 f_i}{\partial z_j \partial z_k}(z) \tag{18}$$

for all $z \in \bar{\Gamma}_i$.

The gluing conditions can be derived by determining the asymptotic values of the drift and diffusion coefficients as $K \to 0$. The period is asymptotically equivalent to $T(z) \sim \ln |K|$ as $K \to 0$. This yields $\lim_{K \to 0} \mathring{\mathfrak{b}}^i_1 = 0$. Furthermore,

$$\lim_{K \to 0} \mathring{\mathfrak{a}}^i_{11}(\mathfrak{c}_0) \equiv \lim_{K \to 0} \left(\mathfrak{a}^i_{11}(z) \, T_i(z) \right) = \sigma^2 S_{\xi\xi}(1) \frac{I \sqrt{I}}{3} \geq 0.$$

The values of $\mathring{\mathfrak{b}}^i_2$, $\mathring{\mathfrak{a}}^i_{12}$ and $\mathring{\mathfrak{a}}^i_{22}$ in the limit $K \to 0$ all approach infinity. Hence $-\frac{\partial f_1}{\partial z_1} + \frac{\partial f_2}{\partial z_1} = 0$.

3.2 *Fokker–Planck Equation and Stationary Probability Density Function*

We turn our attention to producing solutions with the results of stochastic averaging theory presented in the previous section. Specifically, stationary probability density functions are produced. First, the Fokker–Planck equation is derived by taking the adjoint of the reduced generator (18). Then the solutions for the the autoparametric oscillator are obtained by a finite element formulation of the Fokker–Planck problem. Finally, the finite element results are validated with a sample path method.

Finite-element triangulations of the $K - I$ domains are produced using *TRIANGLE*. The domains of the Fokker–Planck equation have boundaries defined by polynomial functions. *TRIANGLE* does not allow specifying such boundaries directly, rather a certain number of points on the boundary must be given. In order to create elements of a specified area, *TRIANGLE* may place additional nodes between points given to it as input. Experience with *TRIANGLE* shows that these problems can be avoided by specifying the number of input points in (inverse) proportion to

the requested element area. Specifically, input points are placed by calculating the arc length along the boundary and the spacing between the points is made equal to the length of the side of an equilateral triangle with an area equal to the requested element area. As long as the domain triangulated does not include cusps, this procedure seems to produce triangulation that have none, or few, Steiner points.

Across the gluing edge, the finite element method is formulated carefully so that the solution does not exhibit any singularities. The solutions appear to be continuous across the gluing edge, as expected based on analytic calculations.

As the amplitude of stochastic forcing is varied, the peak of the probability distribution moves to larger values of I while remaining symmetric about the I axis. The latter fact is worth contemplating. Recalling the structure of the Hamiltonian, the outer edge of the domain in the left hand plane corresponds to a sink and the outer edge of the domain in the right hand plane is a valley. As such it seems reasonable to think that as forcing amplitude increases, the peak of the PDF will shift from the left hand plane to the right hand plane, but this is not observed in Figs. 4 or 5. In fact, simply by looking at the form of $\mathfrak{b}_1$ one notices that along the K axis, the drift coefficient tends to center the probability density on the I axis. It is curious that $\mathfrak{b}_1$ does not contain any stochastic effects; whether this is a generic feature for systems in 1:2 resonance remains to be determined.

4 Conclusions

A two degree-of-freedom nonlinear autoparametric vibration absorber with weak quadratic nonlinearities is considered. The averaged nonlinear response of the system in the absence of disspative and random effects is Hamiltonian. A nonstandard method of stochastic averaging is developed to reduce the dimension of a randomly-perturbed four-dimensional integrable Hamiltonian systems with one-to-two resonance. The reduction to a graph valued process was possible due to three time-scales involved in this problem.

The interest of this paper is when the original Hamiltonian system has one-to-two resonances. Hence the averaged nonlinear Hamiltonian system is integrable with both homoclinic and heteroclinic orbits in the phase-space. This gives rise to singularities in the lower-dimensional description. At these singularities, *gluing conditions* were derived, these gluing conditions completing the specification of the dynamics of the reduced model by examining the boundary-layer behavior close to homoclinic and heteroclinic orbits.

In this context it is also important to point to the work in [4] and [5] where they considered fast oscillating random perturbations of dynamical systems with first integrals. Then under suitable regularity and ergodicity conditions it was shown that the evolution of first integrals in an appropriate time scale is given by a diffusion process. The main emphasis in these papers is the mixing properties of fast oscillating random perturbations. The method used in this paper and the assumptions on the noise

terms are different, and the presence of one-to-two resonance leads to an interesting limiting generator.

Acknowledgments The authors would like to acknowledge the support of the National Science Foundation under grant numbers CMMI 07-58569 and CMMI-1030144. Any opinions, findings, and conclusions or recommendations expressed in this paper are those of the authors and do not necessarily reflect the views of the National Science Foundation.

References

1. K. Onu, Stochastic averaging for mechanical systems. PhD thesis, University of Illinois at Urbana-Champaign, 2010
2. R.Z. Khasminskii, A limit theorem for solutions of differential equations with random right-hand side. Theor. Probab. Appl. **11**, 390–406 (1966)
3. M.I. Friedlin, A.D. Wentzell, Diffusion processes on an open book and the averaging principle. Stoch. Proc. Appl. **113**(1), 101–126 (2004)
4. A.N. Borodin, M.I. Freidlin, Fast oscillating random perturbations of dynamical systems with conservation laws. Ann. Inst. H. Poincar Probab. Statist. **31**(3), 485–525 (1995)
5. R. Cogburn, J.A. Ellison, A stochastic theory of adiabatic invariance. Commun. Math. Phys. **149**(1), 97–126 (1992)

Nonlinear Dynamics of an Array of Nano Spin Transfer Oscillators

B. Subash, V. K. Chandrasekar and M. Lakshmanan

Abstract The dynamics of a macrospin variable representing homogeneous magnetization of the free layer of a nanospin transfer oscillator (STNO) can be represented by the Landau–Lifshitz–Gilbert–Slonczewski (LLGS) equation. This is a generalization of the evolution equation of a ferromagnetic spin system represented by the Heisenberg interaction. STNO is a fascinating nonlinear system exhibiting an interesting bifurcation-chaos scenario depending up on the nature of the applied external magnetic field and the spin current. In order to enhance the microwave power generated by STNOs, recently it has been suggested to consider series and parallel arrays of STNOs with appropriate couplings so that the oscillators get synchronized. We show here the interesting possibility of obtaining synchronization with a common external periodically varying applied magnetic field. We also study the mass synchronization in arrays of STNOs represented by phase oscillators and study the underlying properties.

1 Introduction

From a phenomenological point of view, the Landau-Lifshitz-Gilbert(LLG) equation is considered to be the basic dynamical equation for describing magnetization/magnetic moment or simply spin $\mathbf{S}(\mathbf{r}, t)$, including the damping effects [1–3], for bulk materials in applied magnetism. The Landau–Lifshitz (LL)

B. Subash · V. K. Chandrasekar · M. Lakshmanan (✉)
Centre for Nonlinear Dynamics, Department of Physics, Bharathidasan University, Tiruchirapalli 620 024, India
e-mail: subash.udt@gmail.com

V. K. Chandrasekar
e-mail: chandru25nld@gmail.com

M. Lakshmanan
e-mail: lakshman@cnld.bdu.ac.in

V. In et al. (eds.), *International Conference on Theory and Application in Nonlinear Dynamics (ICAND 2012)*, Understanding Complex Systems,
DOI: 10.1007/978-3-319-02925-2_3,

equation can also be deduced in a systematic manner by starting with a lattice spin Hamiltonian with Heisenberg type nearest neighbour interactions, by postulating appropriate spin Poisson brackets, and writing down the Hamilton's equation of motion for the spins and then taking the classical limit ($\hbar \to 0$) of the quantum spin dynamical equation and then the continuum limit to obtain the LL equation [4, 5]. Then the Gilbert damping term can be introduced phenomenologically [6]. The LLG equation is an extremely interesting nonlinear evolution equation, because of its length constraint, normalized as $|\mathbf{S}|^2 = 1$. Correspondingly it admits a large variety of dynamical structures including spin waves, elliptic function waves, solitary waves, solitons, lumps, dromions, vortices, bifurcations and chaos, spatio-temporal patterns, etc. [5].

In recent times the study of nonlinear dynamics of spin systems has received renewed interest due to the work of Slonczewski [7] and Berger [8] on the macrospin behaviour of spins of the free layer of a nanospin valve pillar of Fe/Cu/Fe type trilayers due to spin torque effect under the injection of a horizontal spin current in the presence of applied magnetic fields. In the semiclassical representation the corresponding nonlinear evolution is represented by a Landau–Lifshitz–Gilbert–Slonczewski (LLGS) equation [9] which includes an additional term to represent the effect of spin current on the magnetization spin vector. In the case of homogeneous magnetization, the dynamics of the macrospin of the free layer of the nano-valve pillar, the so called spin transfer nano-oscillator (STNO), is effectively a nonlinear oscillator equation exhibiting interesting bifurcation and chaos scenario.

Since the power generated by a single STNO is rather low for microwave generation, it has been recently suggested that the property of synchronization of nonlinear oscillators [10] can be profitably utilized for increased power generation by appropriate coupling of STNOs in series or parallel arrays [11, 12], with or without delay [13, 14]. Even a suitable addition of white noise to the injected current has been shown to lead to in-phase and anti-phase synchronizations of limit cycle oscillations of STNOs [15]. In this article, we investigate the interesting possibility of synchronizing limit cycle oscillations due to the action of a common applied periodically driven external magnetic field leading to synchronization of both in-phase and anti-phase limit cycle oscillations. We also consider the possibility of mass synchronization of coupled phase oscillators of different groups through appropriate coupling as a means of high quality synchronization of STNOs.

2 Heisenberg Ferromagnetic Spin Equation and Extension to STNO

It is well known that the expectation value of the spin angular momentum operator of an electron or equivalently magnetization per unit volume, after normalization, represented as a classical unit vector in three dimensions evolves [16] under the action of a time dependent external magnetic field $\mathbf{H}(t)$ as

$$\frac{d\mathbf{S}(t)}{dt} = -\gamma_0[\mathbf{S}(t) \times \mathbf{H}(t)], \quad \mathbf{H} = (H^x, H^y, H^z), \tag{1}$$

where $\mathbf{S}^2 = 1, \quad \mathbf{S} = (S^x, S^y, S^z)$. Here γ_0 is the gyromagnetic factor. From a knowledge of the hysteresis curves of ferromagnetic substances where the magnetization saturates, becomes uniform and aligns parallel to the magnetic field, Gilbert [6] introduced the phenomenological damping term to modify Eq. (1) (after suitable rescaling) as

$$\frac{d\mathbf{S}}{dt} = (\mathbf{S} \times \mathbf{H}(t)) + \lambda \mathbf{S} \times [\mathbf{S} \times \mathbf{H}(t)], \tag{2}$$

where λ is the phenomenological Gilbert damping coefficient. Extending the above phenomenological form of the evolution equation for a single spin to a lattice of spins representing a ferromagnetic material, for example a cubic lattice of N spins with nearest neighbour interactions, onsite anisotropy, demagnetizing field, applied external magnetic field and so on, the evolution equation for the spins can be written [5] as

$$\frac{d\mathbf{S}_i}{dt} = \mathbf{S}_i \times \mathbf{H}_{eff} + \lambda \mathbf{S}_i \times [\mathbf{S}_i \times \mathbf{H}_{eff}], \quad i = 1, 2, \ldots, N, \tag{3}$$

where

$$\mathbf{H}_{eff} = (\mathbf{S}_{i+1} + \mathbf{S}_{i-1} + AS_i^x \mathbf{n}_x + BS_i^y \mathbf{n}_y + CS_i^z \mathbf{n}_z + \mathbf{H}(t) + \cdots). \tag{4}$$

Here A, B and C are anisotropy parameters and $\mathbf{n}_x$, $\mathbf{n}_y$ and $\mathbf{n}_z$ are unit vectors. Going over to a continuum limit such that $\mathbf{S}_i(t) = \mathbf{S}(\mathbf{r}, t)$, $\mathbf{r} = (x, y, z)$ and $\mathbf{S}_{i+1} + \mathbf{S}_{i-1} = \mathbf{S}(\mathbf{r}, t) + \mathbf{a}.\nabla\mathbf{S} + \frac{a^2}{2}\nabla^2\mathbf{S} +$ higher order (here $\mathbf{a}$ is the lattice vector), the Landau–Lifshitz–Gilbert (LLG) equation for the spin vector in the form of a vector nonlinear partial differential equation can be written down as

$$\frac{\partial \mathbf{S}(\mathbf{r}, t)}{\partial t} = \mathbf{S} \times \mathbf{H}_{eff}(\mathbf{r}, t) + \mathbf{S} \times (\mathbf{S} \times \mathbf{H}_{eff}(\mathbf{r}, t)), \tag{5}$$

$$\mathbf{S}(\mathbf{r}, t) = (S^x(\mathbf{r}, t), S^y(\mathbf{r}, t), S^z(\mathbf{r}, t)), \quad \mathbf{S}^2 = 1, \tag{6}$$

and the effective field is given by

$$\begin{aligned} \mathbf{H}_{eff} &= \mathbf{H}_{\text{exchange}} + \mathbf{H}_{\text{anisotropy}} + \mathbf{H}_{\text{demag}} + \mathbf{H}_{\text{appl}}, \\ &= (\nabla\mathbf{S})^2 + AS^x \mathbf{n}_x + BS^y \mathbf{n}_y + CS^z \mathbf{n}_z + H_{\text{demag}} + \mathbf{H}(t). \end{aligned} \tag{7}$$

In the above, $\mathbf{H}_{\text{demag}}$ is the demagnetizing field of the material and $\mathbf{H}_{app}$ is the applied magnetic field. Equation (5) is a complicated vector nonlinear partial differential equation. Depending upon the nature of the interactions present in the system and the form of $\mathbf{H}_{eff}$, Eq. (5) can admit several kinds of interesting nonlinear

dynamical structures. These include spin waves, elliptic function waves, solitary waves, solitons, drominons, vortices, instability induced spatio-temporal patterns, etc. [5]

3 LLGS Equation and the Dynamics of a STNO

The LLG equation has attracted renewed interest in recent times due to intense study of magnetization dynamics in devices such as nanospin valves/pillars in connection with spin torque transfer effect. Slonczewski [7] and Berger [8] have independently shown in 1996 that when a polarized spin current passes through a trilayer of ferromagnetic/nonferromagnetic (conducting)/ferromagnetic materials of size 100 nm or so, a spin torque transfer effect occurs. Slonczewski [7] further showed semiclassically that the influence of spin current can be effectively analysed with the addition of a simple term to the LLG equation as

$$\frac{\partial \mathbf{S}}{\partial t} = \mathbf{S} \times [\mathbf{H}_{eff} + \lambda(\mathbf{S} \times \frac{\partial \mathbf{S}}{\partial t}) + \mathbf{S} \times \mathbf{j}], \quad \mathbf{S} = (S^x, S^y, S^z), \quad \mathbf{S}^2 = 1, \tag{8}$$

where the spin current term can be given in the form

$$\mathbf{j} = \frac{a.\mathbf{S}_P}{f(P)(3 + \mathbf{S}.\mathbf{S}_P)}, \qquad f(P) = \frac{(1 + P^3)}{4P^{\frac{3}{2}}}. \tag{9}$$

Here $\mathbf{S}_p$ is the pinned or fixed direction of the polarized spin current that is normally taken as perpendicular to the direction of flow of current, a is related to the strength of the spin current and $f(P)$ is a polarization factor. A simple approximation can be made to the above form of the spin current as

$$\mathbf{j} \; = \; a\mathbf{S}_p. \tag{10}$$

Then the spin torque transfer effect can be represented by the Landau–Lifshitz–Gilbert–Slonczewski (LLGS) equation

$$\frac{\partial \mathbf{S}}{\partial t} = \mathbf{S} \times \mathbf{H}_{eff} + \lambda \mathbf{S} \times \left[\mathbf{S} \times \frac{\partial \mathbf{S}}{\partial t}\right] + a\mathbf{S} \times [\mathbf{S} \times \mathbf{S}_p], \tag{11}$$

where $\mathbf{H}_{eff}$ is as given in Eq. (4).

The LLGS equation can also be written in a more transparent form by projecting the unit spin vector on a stereographic plane [17]

$$\omega \; = \; \frac{S^x + iS^y}{(1 + S^z)} \tag{12}$$

so that Eq. (8) becomes

$$i(1-i\lambda)\omega_t + \nabla^2\omega - \frac{2\omega^*(\nabla\omega)^2}{(1+\omega\omega^*)} + \frac{A}{2}\frac{(1-\omega^2)(\omega+\omega^*)}{(1+\omega\omega^*)} + \frac{B}{2}\frac{(1+\omega^2)(\omega-\omega^*)}{(1+\omega\omega^*)} - C(\frac{1-\omega\omega^*}{1+\omega\omega^*})\omega + \frac{1}{2}(H^x - ij^x)(1-\omega^2) + \frac{1}{2}i(H^y + ij^y)(1+\omega^2) - (H^z + ij^z)\omega = 0, \tag{13}$$

where $\mathbf{j} = a\mathbf{S}_p$, $\omega_t = (\frac{\partial\omega}{\partial t})$. From the form of Eq. (14) it is clear that the effect of the spin current term $\mathbf{j}$ simply is to change the magnetic field

$$\mathbf{H} = (H^x, H^y, H^z) \rightarrow (H^x - ij^x, H^y + ij^y, H^z + ij^z). \tag{14}$$

Thus one may realize that the effect of spin current and magnetic field complement each other.

Finally, when the free layer of the spin valve is homogeneous, the effect of exchange term in Eq. (11) or (14) can be neglected. The resultant LLGS equation is effectively that of a nonlinear oscillator (after rescaling),

$$\frac{d\mathbf{S}}{dt} = -\gamma\mathbf{S}\times\mathbf{H}_{eff} + \lambda\mathbf{S}\times\frac{d\mathbf{S}}{dt} - \gamma a\mathbf{S}\times(\mathbf{S}\times\hat{\mathbf{S}_p}), \tag{15}$$

where now

$$\mathbf{S} = \mathbf{S}(t) \tag{16}$$

only. Taking $\mathbf{H}_{eff} = -4\pi S_0 S_x\mathbf{i} + \kappa S_z\mathbf{k} + h_{a3}\mathbf{k}$, where the saturation magnetization $4\pi S_0 = 8400$ Oe for permalloy film, we can rewrite Eq. (15) equivalently in terms of the stereographic variable $\omega(t)$ as

$$(1-i\lambda)\dot{\omega} = -\gamma(a - ih_{a3})\omega + i\kappa\gamma\frac{(1-|\omega|^2)}{(1+|\omega|^2)}\omega + \frac{i\gamma 2\pi S_0}{1+|\omega|^2}[(1-\omega^2-|\omega|^2)\omega + \omega^*], \quad (\dot{\omega} = \frac{d\omega}{dt}). \tag{17}$$

Here γ is the gyromagnetic ratio. Eq. (15) or (17) may be considered as the LLGS equation describing the dynamics of the macrospin variable of a single STNO. Depending upon the type of interactions, a STNO can exhibit the standard bifurction-chaos scenario of a nonlinear oscillator [18, 19]. In Fig. 1, we represent the phase diagrams in the $(h_{dc} - a)$ plane indicating periodic regimes, including limit cycles and chaotic behaviour both for isotropic and anisotropic cases with oscillating mag-

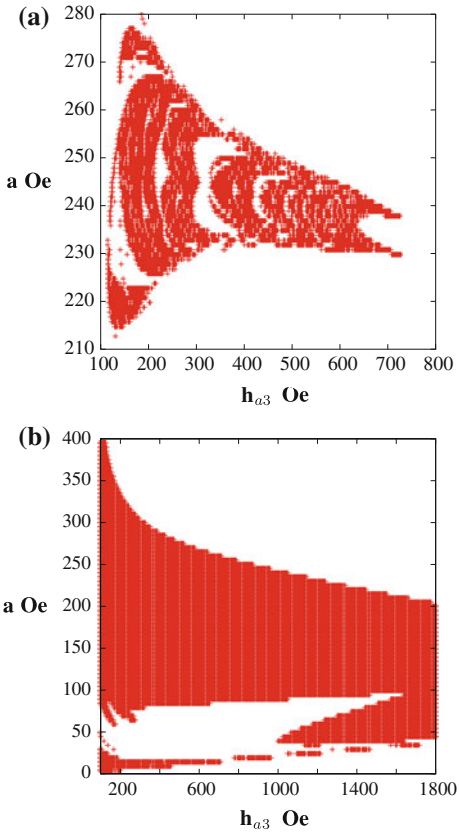

Fig. 1 Regions of chaos in the $a - h_{a3}$ space, for an applied alternating magnetic field along the z direction for isotropic **a** and anisotropic **b** cases. The *dark regions* indicate values for which the dynamics is chaotic, i.e, regions where the largest Lyapunov exponent is positive [19]. The *white regions* are the periodic regimes or limit cycles. Here h_{a3} is the applied dc magnetic field

netic field. Here $\mathbf{H} = (h_{dc} + h_{ac}\cos\omega t)\mathbf{i}$. Note that periodic oscillations of different types, chaos, period doubling transitions, etc. occur [19].

4 Dynamics of Arrays of STNOs

We next consider an array of two STNOs in the presence of a common applied magnetic field (Fig. 2)

$$\mathbf{H}_{app} = \mathbf{H}(t) = (h_{dc} + h_{ac}\cos\omega t, 0, 0), \tag{18}$$

by the system of LLGS equations of the magnetizations of two STNOs

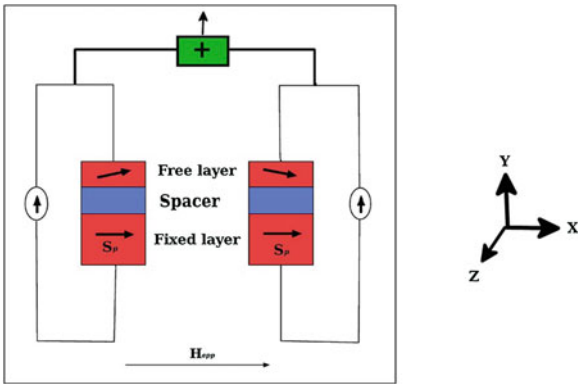

Fig. 2 The schematic representation of an array of two STNOs placed in the oscillatory external magnetic field

$$\frac{d\mathbf{S_1}}{dt} = -\gamma \mathbf{S_1} \times \mathbf{H_{1}}_{eff} + \lambda \mathbf{S_1} \times \frac{d\mathbf{S_1}}{dt} - \gamma a \mathbf{S_1} \times (\mathbf{S_1} \times \mathbf{S_p}), \tag{19}$$
$$\frac{d\mathbf{S_2}}{dt} = -\gamma \mathbf{S_2} \times \mathbf{H_{2}}_{eff} + \lambda \mathbf{S_2} \times \frac{d\mathbf{S_2}}{dt} - \gamma a \mathbf{S_2} \times (\mathbf{S_2} \times \mathbf{S_p}),$$

where $|\mathbf{S_1}|^2 = S_{1x}^2 + S_{1y}^2 + S_{1z}^2 = 1$, $|\mathbf{S_2}|^2 = S_{2x}^2 + S_{2y}^2 + S_{2z}^2 = 1$ or equivalently one can write down the corresponding evolution equation for the stereographic variables $\omega_1(t)$ and $\omega_2(t)$. Here we take $\mathbf{H_{1}}_{eff} = \mathbf{H_{2}}_{eff} = \mathbf{H}_{eff}$ with appropriate spin number.

We have numerically integrated the above set of equations and found that both in-phase and anti-phase synchronizations occur in the presence of oscillating magnetic field and spin current. For example, in Fig. 3a, b, we plot the **z** component of the spin vectors of the two oscillators for the anisotropic field strength $\kappa = 45$ Oe, external magnetic field strength $h_{dc} = 500$ Oe and external current $a = 220$ Oe, both time series and phase space plot. The figure clearly shows the existence of anti-phase synchronization.

In Fig. 3c, d, we present similar results for a different external magnetic field strength $h_{dc} = 500$ Oe and external current $a = 221$ Oe with all the other parameters unchanged. It clearly shows the existence of in-phase synchronization of limit cycle oscillations.

In order to confirm that the above synchronization aspects are robust, we present the results of our numerical analysis for the case in which there is a slight mismatch in the system parameters of the two STNOs with the choice of anisotropy strength $\kappa_1 = 45.0$ for the first oscillator and $\kappa_2 = 45.1$ for the second oscillator. In Fig. 3e–h we show the in-phase and anti-phase synchronizations for this case.

In Fig. 4 we show the occurrence of synchronization for 100 STNOs for external magnetic field strength $h_{dc} = 500$ Oe, external current $a = 220$ Oe and anisotropy strength κ_i, $i = 1, 2, \ldots 100$ distributed randomly between 45 and 46. In the phase space plot, Fig. 4 (right), we show that the 61th STNO is in in-phase with the 17th

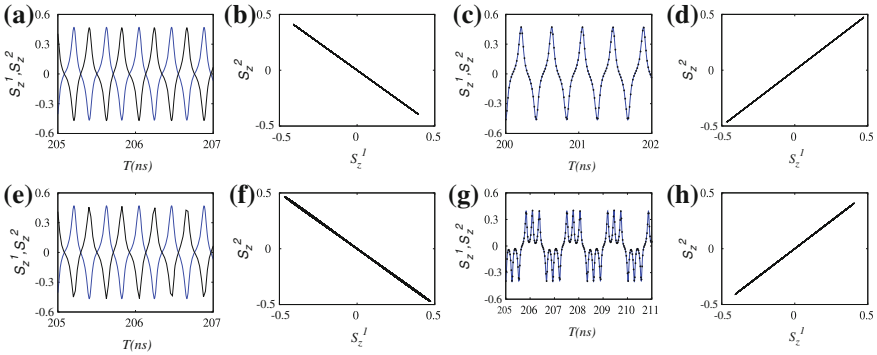

Fig. 3 The time series (**a**, **c**, **e**, **f**) and phase space plots (**b**, **d**, **f**, **h**) of an array of two STNOs with same anisotropy field $\kappa = 45.0$ (**a**–**d**) and with different anisotropy fields $\kappa_1 = 45.0$ Oe, $\kappa_2 = 45.1$ (**e**–**h**) placed in the oscillating external magnetic field of strength $h_{ac} = 10$ Oe of frequency $\omega = 15\, ns^{-1}$, exhibiting anti-phase (**a**, **b**, **e**, **f**) and in-phase (**c**, **d**, **g**, **h**) synchronizations. Other parameters are (**a**, **b**) $h_{dc} = 500$ Oe and $a = 220$ Oe, (**c**, **d**) $h_{dc} = 500$ Oe and $a = 221$ Oe, (**e**, **f**) $h_{dc} = 350$ Oe and $a = 245$ Oe and (**g**, **h**) $h_{dc} = 500$ Oe and $a = 220$ Oe

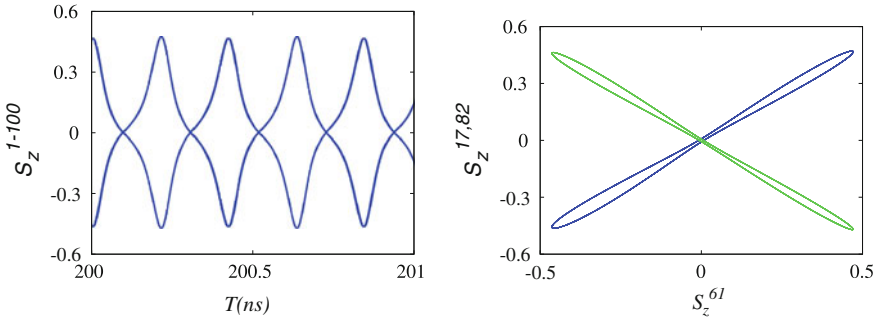

Fig. 4 The time series (*left*) and phase space (*right*) plots of an array of 100 nonidentical STNOs shows the anti-phase synchronization. In the right panel we show that the 61th STNO is in in-phase synchronization with the 17th STNO and in anti-phase synchronization with the 82nd STNO

STNO and in anti-phase synchronization with the 82nd STNO. So we confirm the phenomenon of synchronization in the presence of the external driven magnetic field even for large number of STNOs. For further details on synchronization of STNOs, see Ref. [20].

5 Mass Synchronization in an Array of STNOs

The dynamics of an array of STNOs can also be represented using models of coupled phase oscillators. For instance, if we consider the synchronization of coupled STNOs via external ac field, we assume that all the STNOs have the same output frequency.

According to Ref. [21] the energy injected from the external ac field H_{ac} to the ith STNO is given as

$$E_i = -\mu_0 M_S V_0 \oint \mathbf{H_{ac}}.d\mathbf{m}_i, \tag{20}$$

where $\mathbf{m}_i$ is the orbit of the small amplitude in-plane oscillation, μ_0 is the vacuum permeability and V_0 is the volume of the free layer. This energy injected by the ac current is much lesser compared to that injected by the dc current and hence the former can be treated as a perturbation. Thus one can represent the phase dynamics of the ith STNO as

$$\dot{\theta}_i = \omega_i - \frac{\sigma}{N}\sum_{j=1}^{N} \sin(\theta_i - \theta_j + \alpha), i = 1, 2, \ldots, N, \tag{21}$$

where α is the phase shift. Georges et al. [11] found that in the case of series or parallel arrays, there occurs a problem of impedance-matching where the output power does not increase with the number of oscillators for large values of N if $NR >> Z_0$ in the case of series arrays and the STNOs shunt each other with the output power increasing as N^2 only if $NZ_0 << R$; here Z_0 is the load. Hence the authors of [11] proposed hybrid arrays (a combination of series and parallel configuration). In this configuration, the phase of the oscillator (n, m) in the hybrid array can be described by the following equation

$$\dot{\theta}_i^{(\eta)} = \omega_i^{(\eta)} - \sum_{\eta'=1}^{N'} \frac{\sigma_{\eta\eta'}}{N} \sum_{j=1}^{N} \sin(\theta_i^{(\eta)} - \theta_j^{(\eta')} + \alpha_{\eta\eta'}) + \zeta_i^{(\eta)}(t), \tag{22}$$
$$i = 1, 2, \ldots, N,$$

where N' parallel branches have each N STNOs connected in series. $\sigma_{\eta\eta'}$ is the strength of the coupling between the STNOs in η' and those in η. Here $\omega_k^{(\eta)}$ is the natural frequency of the kth STNO in the branch η and $\zeta_i^{(1,2)}$ are independent Gaussian white noises with $\langle \zeta_i^{(\eta)}(t) \rangle = 0$ and $\langle \zeta_i^{(\eta)}(t)\ \zeta_j^{(\eta)'}(t) \rangle = 2D^{(\eta)}\delta(t - t')\delta_{ij}$ and $D^{(\eta)}$ are the noise intensities.

Now, a maximum output power can be harvested if all the STNOs are synchronized; let us call this phenomenon as mass synchronization. In this section let us discuss a method to induce mass synchronization in the system of STNOs that are in hybrid configuration by inducing synchronization in any one of the series or parallel arrays. That is, by inducing synchronization within the STNOs of any one of the series or parallel arrays, mass synchronization can be achieved. For a better understanding of the system configuration, let us refer to the following schematic diagram (Fig. 5).

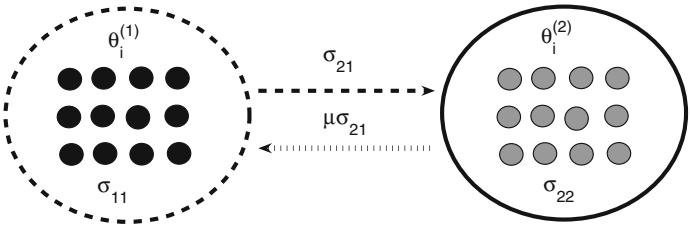

Fig. 5 Schematic representation of system (22) for $N' = 2$. $\theta_i^{(1)}$ is the source branch and $\theta_i^{(2)}$ is the target branch. The coupling strengths within the branches are quantified by the parameters σ_{11} and σ_{22}. The coupling strengths from the source to the target and the target to the source are quantified by the parameters $\sigma_{12} = \mu\sigma_{21}$ and σ_{21}, respectively [22]

In order to acheive mass synchronization, we plan to induce synchronization in any one of the arrays. For the same, we need to quantify the strength of the synchronization within each of the arrays.

We use Kuramoto's complex order parameter to measure the strength of synchronization within an array. The order parameter can be given as

$$z_\eta = r_\eta e^{i\psi^{(\eta)}} = \frac{1}{N}\sum_{j=1}^{N} e^{i\theta_j^{(\eta)}}. \tag{23}$$

When $r_\eta = 1$ there is complete synchronization within the ηth array and when $r_\eta = 0$ there is complete desynchronization in the ηth array. When r_η takes a value between 0 and 1, there is a partial synchronization in the ηth array. We shall use the time average of r_η in order to characterize the occurrence of strong synchronization within the corresponding array. Numerically, for $T = 10^5$ units, the occurrence of synchronization within an array can be characterized by $R_\eta > 0.8$. Here R_η is the time average of r_η, that is,

$$R_\eta =< r_\eta >= \frac{1}{T}\int_0^T r_\eta dt. \tag{24}$$

In order to find out the dynamical factors that cause the occurrence of mass synchronization, we numerically simulate system (22) using Runge–Kutta fourth order routine. We use a time step of 0.01.

We have fixed $N = 1000$ and have assumed a Lorentzian distribution for the oscillator frequencies given by $g(\omega^{(\eta)}) = \frac{\gamma_\eta}{\pi}\left[(\omega^{(\eta)} - \omega_\eta)^2 + \gamma_\eta\right]^{-1}$, where γ is the half width at half maximum and ω_η is the central frequency. We consider a random distributon for the initial phases of the STNOs, distributed between 0 and 2π.

Let us now discuss how the occurrence of synchronization in the source branch induces mass synchronization in the other branches as well, leading to an increase in the synchronized output power.

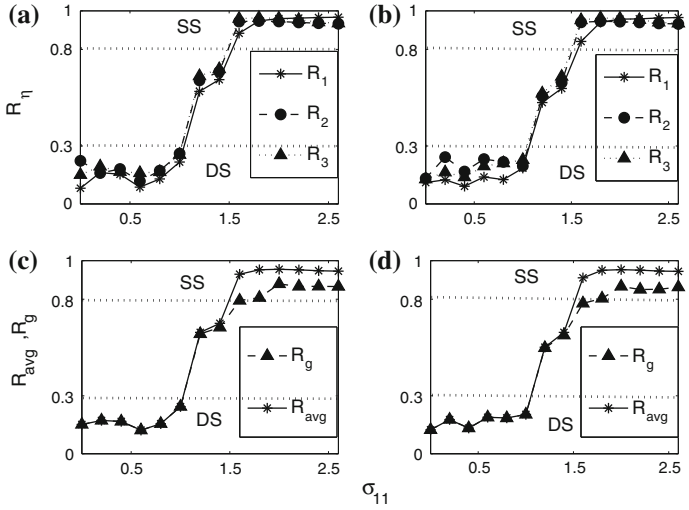

Fig. 6 The time average of r_η (**a** and **b**) and the time average local and global order parameters, R_{avg} and R_g, (**c** and **d**) for increasing σ_{11} is plotted for two different noise strengths $D^\eta = 0.1$ (**a** and **c**) and $D^\eta = 0.5$ ((b) and (d)) for $N' = 3$, $\eta = 1, 2, 3$. Here $\sigma_{\eta\eta} = 0.01$, $\sigma_{\eta 1} = 1.5$, $\sigma_{1\eta} = \mu\sigma_{\eta 1}$, for $\eta = 2, 3$, $\mu = 0.1$, $\alpha_{ij} = \pi/2 - 0.3$, $i, j = 1, 2, 3$, $\gamma_{1,2,3} = 0.05$, $\omega_1 = 1.5$, $\omega_{2,3} = 0.5$, and $\sigma_{23} = \sigma_{32} = 0.01$. The regions DS and SS denote the desynchronization and strong synchronization states characterized by the numerical thresholds of $R = 0.3$ and $R = 0.8$, respectively

For the case $N' = 3$ we consider three branches of coupled STNOs each having 1,000 oscillators. We set the values of the coupling parameters as follows: $\sigma_{\eta\eta} = 0.01$, $\sigma_{\eta 1} = 1.5$, $\sigma_{1\eta} = \mu\sigma_{\eta 1}$, for $\eta = 2, 3$, $\mu = 0.1$, $\alpha_{ij} = \pi/2 - 0.3$, $i, j = 1, 2, 3$, $\gamma_{1,2,3} = 0.05$, $\omega_1 = 1.5$, $\omega_{2,3} = 0.5$, and $\sigma_{23} = \sigma_{32} = 0.01$.

One of the three branches is the source in which synchronization is first established. The other two branches are target branches on to which synchronization will be induced by the synchronized source branch. In Fig. 6a, b we have plotted the time-averaged order parameter of the three branches R_1, R_2 and R_3 against the coupling strength of the source branch, for two different values of noise strengths, namely $D^\eta = 0.1$ and $D^\eta = 0.5$, respectively. For both the values of noise strengths, we see that when the synchronization of the source branch increases (R_1), the synchronization in the target branches also increases (R_2 and R_3). The synchronization in the target branch is purely induced by the synchronization in the source branch since the coupling strength of the oscillators within the target branches are $\sigma_{22} = \sigma_{33} = 0.01$.

In Fig. 6c, d we have plotted the local and global order parameters, R_{avg} and R_g, for $D^\eta = 0.1$ and $D^\eta = 0.5$, respectively. The local and global order parameters are given by the following expressions:

$$R_{avg} = < \frac{1}{N'} \sum_{\eta'=1}^{N'} r_{\eta'} >, \qquad R_g = < | \frac{1}{N'} \sum_{\eta'=1}^{N'} r_{\eta'} e^{i\psi_{\eta'}} | > . \tag{25}$$

The local order parameter measures the occurrence of synchronization within a branch, while the global order parameter quantifies the occurrence of synchronization in all the branches, globally in the system. Thus if $R_g = 1$, all the branches in the system are synchronized to a one and the same state.

The occurrence of synchronization in the source and the target branches are not influenced by changes in the strength of the noise in the system. This is evident from Fig. 6 panels (a) and (b), where for both the noise strengths the phenomenon of mass synchronization occurs in a similar manner.

Likewise, the local and the global order parameters also behave in a very similar manner for increasing σ_{11} for two different noise strengths. Thus we conclude that the phenomenon of occurrence of mass synchronization is not affected by the strength of the noise in the system.

6 Analytical Explanation

In order to analytically explain the occurrence of mass synchronization, we analyze system (22) in the continuum limit $N \to \infty$. In this limit, the evolution equation for the order parameter for Lorentzian distribution becomes (in the absence of noise)

$$\dot{z}_\eta + (\gamma_\eta - i\omega_\eta) z_\eta = \sum_{\eta'=1}^{N'} \frac{\sigma_{\eta\eta'}}{2} \left(e^{-i\alpha_{\eta\eta'}} z_{\eta'} - e^{i\alpha_{\eta\eta'}} z_{\eta'}^* z_\eta^2 \right), \tag{26}$$
$$\eta = 1, 2, \ldots, N'.$$

Here we use Ott and Antonsen [23] ansatz to derive the amplitude equation (26). From Fig. 6 one can note that the dynamics of the order parameter for all the target branches are similar. Thus one can consider the sate $r_\eta \simeq r_t$ and $\psi_\eta \simeq \psi_t$, $\eta = 2, ..., N'$ and the amplitude equation (26) becomes (for $\alpha_{\eta\eta'} = \alpha$)

$$\dot{r}_1 = -\gamma_1 r_1 + \left(\frac{1 - r_1^2}{2}\right)(\sigma_{11} r_1 \cos(\alpha) + \mu\sigma_{t1} r_t \cos(\psi_1 - \psi_t + \alpha)), \tag{27}$$

$$\dot{\psi}_1 = \omega_1 - \left(\frac{1 + r_1^2}{2r_1}\right)(\sigma_{11} r_1 \sin(\alpha) + \mu\sigma_{t1} r_t \sin(\psi_1 - \psi_t + \alpha)),$$

$$\dot{r}_t = -\gamma_t r_t + \left(\frac{1 - r_t^2}{2}\right)(\sigma_{tt} r_t \cos(\alpha) + \sigma_{t1} r_1 \cos(\psi_t - \psi_1 + \alpha)), \tag{28}$$

$$\dot{\psi}_t = \omega_t - \left(\frac{1 + r_t^2}{2r_t}\right)(\sigma_{tt} r_t \sin(\alpha) + \sigma_{t1} r_1 \sin(\psi_t - \psi_1 + \alpha)),$$

where $\gamma_t = \gamma_\eta$, $\omega_t = \omega_\eta$, $\sigma_{1t} = \sum_{\eta'=2}^{N'} \sigma_{\eta\eta'}$ and $\sigma_{tt} = \sum_{\eta'=2}^{N'} \sigma_{\eta\eta'}$, $\eta = 2, ..., N'$. One can assume $\mu = 0$ so that the source strongly (completely) drives the target branches. We have taken $\mu = 0$ for analytical convenience to start with. However, in general one can observe the occurrence of mass synchronization for $\mu < 1$ also as in the case of numerical simulations where μ =0.1. Thus when the strength of the synchronization increases in the source it induces synchronization in the targets.

From Eq. (27), for $\mu = 0$, the synchronization of the source is characterized by the stability of the fixed point $r_1^s = \sqrt{1 - 2\gamma_1/\bar{\sigma}_{11}}$, where $\bar{\sigma} = \sigma \cos(\alpha)$. On the other hand, the desynchronization state is characterized by the stability of the fixed point $r_1^d = 0$. When $\bar{\sigma}_{11} < 2\gamma_1$, the fixed point r_1^d becomes stable and there is no synchronization in the source. In this state the equation for the target branch is given as

$$\dot{r}_t = -\gamma_t r_2 + (\frac{1 - r_t^2}{2})(\sigma_{tt} r_t \cos(\alpha), \;\; \dot{\psi}_t = \omega_t - (\frac{1 + r_t^2}{2r_t})\sigma_{tt} r_t \sin(\alpha). \quad (29)$$

Again one can check that for $\bar{\sigma}_{tt} < 2\gamma_t$ the fixed point $r_t = 0$ is stable and the target branch is desynchronized. Thus when the source is desynchronized, the target branch is also desynchronized.

On the other hand, when the coupling strength in the source $\bar{\sigma}_{11}$ increases so that $\bar{\sigma}_{11} > 2\gamma_1$ the fixed point r_1^d becomes unstable and r_1^s becomes stable thus establishing synchronization in the source. The synchronization strength of the source increases as $\sqrt{1 - 2\gamma_1/\bar{\sigma}_{11}}$. After synchronization in the source is established, Eq. (29) reduces to

$$\dot{r}_t = -\gamma_t r_t + (\frac{1 - r_t^2}{2})(\sigma_{tt} r_t \cos(\alpha) + \sigma_{t1}\sqrt{1 - 2\gamma_1/\bar{\sigma}_{11}} \cos(\psi + \alpha)), \quad (30)$$

$$\dot{\psi} = \bar{\omega} - (\frac{1 + r_t^2}{2r_t})(\sigma_{tt} r_t \sin(\alpha) + \sigma_{t1}\sqrt{1 - 2\gamma_1/\bar{\sigma}_{11}} \sin(\psi + \alpha)),$$

where $\psi = \psi_t - \psi_1$ and $\bar{\omega} = \omega_t - \omega_1 + (\sigma_{11} - \gamma_1)\tan(\alpha_{11})$. This equation does not admit the fixed point $r_t = 0$. This means that when synchronization emerges in the source, the target branches also begin to get synchronized. The strength of the synchronization in the target increases according to $\sigma_{t1}\sqrt{1 - 2\gamma_1/\bar{\sigma}_{11}}$, eventually leading to synchronization with the target. This result holds good for $\mu < 1$ also as is evident from our numerical findings as depicted in panels (a) and (b) of Fig. 6 for $\mu = 0.1$. Here we can establish that when the source is completely synchronized the target is also completely synchronized. This means that the increase in σ_{11} to a sufficiently high value induces synchronization in the target also apart from inducing synchronization in the source.

7 Summary and Conclusion

We have presented a systematic study of synchronization of STNOs coupled through the external driven periodically varying magnetic field. We have studied in-phase and anti-phase synchronization scenario of two STNOs and extended it to more number of oscillators in the presence of a common oscillating magnetic field. We find that the synchronization is induced though the oscillating magnetic medium. Further, in order to check the practical possibility of this scenario we also find the same phenomenon in the case of two different anisotropic STNOs. We also made a detailed analysis of synchronization in terms of coupled phase models and brought out the phenomenon of mass synchronization.

Acknowledgments The work forms part of a Department of Science and Technology(DST), Government of India, IRHPA project and is also supported by a DST Ramanna Fellowship of M. L. He has also been financially supported by a DAE Raja Ramanna Fellowship.

References

1. D.C. Mattis, *Theory of Magnetism I: Statics and Dynamics* (Springer, Berlin, 1988)
2. M.D. Stiles, J. Miltat, Top. Appl Phys. **101**, 225 (2006)
3. G. Bertotti, I. Mayergoyz, C. Serpico, *Nonlinear Magnetization Dynamics in Nanosystems* (Elsevier, Amsterdam, 2009)
4. L.D. Landau, L.M. Lifshitz, Physik. Zeits. Sowjetunion **8**, 153–169 (1935)
5. M. Lakshmanan, Phil. Trans. R. Soc. A **369**, 1280–1300 (2011)
6. T.L. Gilbert, IEEE Trans. Magn. **40**, 3443–49 (2004)
7. J.C. Slonczewski, J. Magn. Magn. Mater. **159**, L261–L268 (1996)
8. L. Berger, Phys. Rev. B **54**, 9353–9358 (1996)
9. Y.B. Bazaliy, B.A. Jones, S.-C. Zhang, Phys. Rev. B **57**, R3213–R3216 (1998)
10. A. Pikovsky, M. Rosenblum, J. Kurths, *Synchronization—A Universal Concept in Nonlinear Sciences* (Cambridge University Press, Cambridge, 2001)
11. B. Georges, J. Grollier, V. Cros, A. Fert, Appl. Phys. Lett. **92**, 232504 (2008)
12. B. Georges, J. Grollier, M. Darques, V. Cros, C. Deranlot, B. Marcilhac, G. Faini, A. Fert, Phys. Rev. Lett. **101**, 017201 (2008)
13. J. Persson, Y. Zhou, J. Akerman, J. Appl. Phys. **101**, 09A503 (2007)
14. B. Georges, V. Cros, A. Fert, Phys. Rev. B **73**, 0604(R)–0609(R) (2006)
15. K. Nakada, S. Yakata, T. Kimura, J. Appl. Phys. **111**, 07C9920 (2012)
16. B. Hillebrands, K. Ounadjela, *Spin Dynamics in Confined Magnetic Structures* (Springer, Berlin, 2002)
17. M. Lakshmanan, K. Nakumara, Phys. Rev. Lett. **53**, 2497–2499 (1984)
18. Z. Yang, S. Zhang, Y.C. Li, Phys. Rev. Lett. **99**, 134101 (2007)
19. S. Murugesh, M. Lakshmanan, Chaos **19**, 043111(1–7) (2009)
20. B. Subash, V. K. Chandrasekar, M. Lakshmanan, Europhys. Lett. **102**, 17010 (2013)
21. J. Xu, G. Jin, J. Appl. Phys. **111**, 066101 (2012)
22. V.K. Chandrasekar, J.H. Sheeba, M. Lakshmanan, Chaos **20**, 045106 (2010)
23. E. Ott, T.M. Antonsen, Chaos **18**, 037113 (2008)

Interactive Ensembles of Imperfect Models: Lorenz 96 System

Lasko Basnarkov and Ljupčo Kocarev

Abstract Contemporary numerical weather prediction schemes are based on ensemble forecasting. Ensemble members are obtained by taking different (perturbed) models started with different initial conditions. We introduce one type of improved model that represents interactive ensemble of individual models. The improved model's performance is tested with the Lorenz 96 toy model. One complex model is considered as reality, while its imperfect models are taken to be structurally simpler and with lower resolution. The improved model is defined as one with tendency that is weighted average of the tendencies of individual models. The weights are calculated from past observations by minimizing the average difference between the improved model's tendency and that of the reality. It is numerically verified that the improved model has better ability for short term prediction than any of the individual models.

1 Introduction

Weather prediction and climate projection are among the fields whose progress strongly depends on the development of the nonlinear dynamics [14]. Even the interest in nonlinear dynamics has greatly increased after the seminal work of Lorenz in 1963 with an atmospheric model [7]. The reason for such interconnectedness is simple due to the fact that the models that are used in meteorology are described with nonlinear differential equations. The Lorenz 63 model is simple nonlinear system

L. Basnarkov (✉)
Faculty of Computer Science and Engineering, Saints Cyril and Methodius University, P.O. Box 393, Skopje, Macedonia
e-mail: lasko.basnarkov@finki.ukim.mk

L. Kocarev
Macedonian Academy of Sciences and Arts, Skopje, Macedonia
e-mail: lkocarev@ucsd.edu

V. In et al. (eds.), *International Conference on Theory and Application in Nonlinear Dynamics (ICAND 2012)*, Understanding Complex Systems,
DOI: 10.1007/978-3-319-02925-2_4,

of three ordinary differential equations. However, the weather prediction (short term forecasting) and the climate projection (long term prediction of averages or fluctuations) have a great impact on the life of humans. They demand elaborate models for obtaining more reliable predictions and operational models for numerical weather forecasting today have millions of degrees of freedom [14]. All atmospheric models are built upon the same basic physics laws and are mathematically represented with nonlinear partial differential equations. The number of the degrees of freedom generally depends on three factors: the number of the dynamical variables used in the model; the number of layers representing the atmosphere; and the number of the components used in the decomposition of the fields of variables in spherical functions—largest factor. Due to the growth of power of computing facilities, the dimensionality of the models permanently grows mainly through increase in the resolution—the number of the spherical components. Another possibility to use the available computer power is considering combinations of models. Today, weather forecast is based on ensemble predictions—multiple runs of simulations with perturbed initial conditions [6, 18]. More interesting and more promising application could be making interactive ensembles – simulations of models that dynamically exchange information [4]. In this work we present a simple case of a model with velocity vector that is weighted average of the vectors of the members of the ensemble. This results in improved model that extends the short term prediction range. The models and the truth are different versions of the Lorenz 96 system [8, 9]. The truth is the more complex version (and with more degrees of freedom) because the reality is always complex more than any model of it. In the following sections first we discuss some basic facts related to the atmospheric models. Then we introduce the Lorenz 96 model and the interactive ensemble. Next follow the results from numerical simulations. We finish with the conclusions and directions for future work.

2 Atmospheric Models

Current understanding of the main sources of errors in weather forecasting was pioneered by Bjerknes a century ago [3]. There are two types of errors: one is the limitation of the estimate of the state of the atmosphere—initial condition or analysis error and the other is imperfection of the models in duplicating the evolution of the state—model error. Both are based on the fact that the model is always simpler than the reality and that their comparison is performed in the state space of the model. The analysis error is the mismatch between the projection of the state of reality into the model's space and the estimate of that projection based on the model—a point from its attractor. The techniques used for decreasing this error are summarized as data assimilation. The model error can be understood as the difference between the equations of the model and the truth. It is closely related to the tendency error which is the difference between the velocity vectors (or tendency in meteorological community) of the model and of the trajectory consisting of the projections [5, 11].

We would like to stress that usually the model error is disregarded in analysis. In most of the works it is considered that one has the proper physical (and mathematical) model of the system that is under consideration. This means that the equations of motion are known and possibly the parameter values should be adjusted to be represent the reality. For this purpose very powerful techniques based on synchronization were developed to determine the parameters [15]. Since the correct values of the parameters are found the emergence of full synchronization means possibility of prediction because both the truth and the model are governed with the same equations. However, the atmosphere is a system that hardly admits perfect reproduction with models. Thus one should know that any of its models is imperfect.

The atmospheric models are based on the same fundamental laws of fluid mechanics. Depending on the level of complexity they belong to one or another class of partial differential equations that incorporate the basic processes involved in transport of fluids. However there are a plentiful unresolved processes that are not captured within this framework like the cloud formation or dissipation [14]. The influence of these processes on the dynamical variables of the atmosphere is parameterized. Mathematically, these processes are modeled with some parameters appearing in the equations. The values of those parameters are adjusted with fitting of the model's outputs with the observations. The difference between the models developed at different meteorological centers around the world generally appears in the choice of the parameterized processes and the values of the parameters.

In last years there was a change in the operational numerical weather prediction and climate projection as well from deterministic to probabilistic approach [14]. Instead of basing the predictions on a single run of a model, the probability of occurrence of particular event is calculated from ensemble of simulations. The ensemble consists of multiple runs of a single model started from different initial conditions. This kind of perturbation of initial conditions aims at capturing the uncertainty in knowledge of the state of the atmosphere—the analysis error. The uncertainties in the model (its parameters) are handled with making perturbations of the parameters, or with considering ensemble of models—grand ensemble [6, 18]. It is naturally to assume that taking models from different meteorological centers as members of the prediction ensemble should do even better. At the end of this line of reasoning comes the interactive ensemble of models. Here, instead of combining only the outputs of the models, they can exchange information on the fly, which means that the future state of some model depends on the current states of the others. However, the issue of designing the connection between the individual models represents a real challenge. First ideas for that task can be borrowed from the synchronization theory where the systems are diffusively coupled in order to nudge the states of one to the other. To clarify this let us denote the state of the model identified with the set of parameters μ as $\mathbf{x}_\mu$. If one considers that model isolated, its evolution is described with a differential equation (for simplicity ordinary differential equation)

$$\mathbf{x}_\mu = \mathbf{f}_\mu(\mathbf{x}_\mu). \tag{1}$$

Within the last equation the tendency $\mathbf{f}$ is a function of the parameters μ as well, but the dependence is expressed through subscript which also can serve to identify particular model. We can further assume that all models have the same state variables and just different values are assigned to them. Then the diffusive coupling or nudging will make the model μ evolve according to

$$\mathbf{x}_\mu = \mathbf{f}_\mu(\mathbf{x}_\mu) + \sum_\nu \mathbf{C}(\mathbf{x}_\nu - \mathbf{x}_\mu) \tag{2}$$

where the model identifier ν runs through the set of all models, and the coupling matrix $\mathbf{C}$ determines the strength of nudging between the individual models. This kind of connected ensemble was used to test the idea of interactive ensembles for the Lorenz 63 model [10, 19]. In that work as reality was considered one Lorenz 63 system, while as its models three other systems with different parameter values. For proper choice of the connection coefficients the interactive ensemble can even perfectly trace the truth, although the individual models do not. It was also found that if the connection coefficients have infinite values, the interactive ensemble is equivalent to a model with velocity vector that is weighted combination of the velocity vectors of the individual models—weighted ensemble [20]. The weighted ensemble is a good candidate for weather prediction models for decreasing the model error. In the next section an example of weighted ensemble is analyzed in more details.

3 Interactive Ensemble of Lorenz 1996 Models

Edward Lorenz published very nice paper that explained how one can progressively make more realistic models [9] based on a previous work [8]. He introduced a hierarchy of three models that mimic the behavior of some scalar atmospheric variable over one latitude circle. The models incorporated the basic processes present in the fluid dynamics—damping and advection and also the influence of external forces. For properly adjusted parameter values the solution of any of the three models has chaotic nature with traveling waves corresponding to, for example, the west to east wind jets. The models are systems of ordinary differential equations whose structure resembles spatially discretized version of a partial differential equation. The relevance of the model was proven by numerous works based on it (for example the Refs. [9, 12, 13]). The simplest version—model I describes the evolution of the scalar variable X at N equally spaced points around the circle according to the following cyclically symmetric system of equations

$$\dot{X}_n = -X_{n-2}X_{n-1} + X_{n-1}X_{n+1} - X_n + F_n. \tag{3}$$

The nonlinear terms correspond to the advection, the linear one models the damping, while F_n is the spatially dependent external forcing. The system has chaotic dynamics but the solution profile is not a smooth function and thus this model is used as a

starting point. The medium complexity Lorenz 96 model II is a smoothed version of the model I and is a good candidate for the role of a model in this work. Its definition is similar to the previous one

$$\dot{X_n} = [X, X]_{K,n} - X_n + F_n, \tag{4}$$

where the term in the brackets is short hand notation of the sum

$$[X, Y]_{K,n} = \sum_{j=-J}^{J}{}' \sum_{i=-J}^{J}{}' (-X_{n-2K-i} Y_{n-K-j} + X_{n-K+j-i} Y_{n+K+j})/K^2, \tag{5}$$

The number K in the last equation determines the range of the influence, and $J = K/2$ if K is even and $J = (K-1)/2$ if K is odd. The sign prime at the sum is used to note that in the case when K is even the first and last terms should be divided by 2 and when K is odd one has ordinary sum. As a truth, or real atmosphere, we use the most complex model of the hierarchy—version III. It is characterized with small-scale activity Y_n combined with the large-scale one X_n. The dynamical variable of the model III, Z_n, evolves as

$$\dot{Z_n} = [X, X]_{K,n} + b^2 [Y, Y]_{1,n} + c[Y, X]_{1,n} - X_n - bY_n + F_n, \tag{6}$$

where b and c are parameters and the large and small scale variables are given by

$$\begin{aligned} X_n &= \sum_{i=-I}^{I}{}' (\alpha - \beta |i|) Z_{n+i} \\ Y_n &= Z_n - X_n. \end{aligned} \tag{7}$$

The integer I and parameters α and β in the last equation are adjusted to make a low-pass filter such that X_n will be smoothed version of Z_n, and Y_n will represent the local weather. Again, the same short-hand notation is used with the brackets and the sign prime denotes the modified sum. The aim of Lorenz was to construct a model with traveling wave solution and chaotic dynamics and with large and small scale features. In most of the works the number of gridpoints is chosen to be $N = 960$ while the range of the interaction and the filter are $K = 32$ and $I = 12$. The parameters are taken to have values $b = 10$, $c = 2.5$ and

$$\begin{aligned} \alpha &= (3I^2 + 3)/(2I^3 + 4I), \\ \beta &= (2I^2 + 1)/(I^4 + 2I^2). \end{aligned} \tag{8}$$

The forcing term in the original formulation was taken constant $F_n = F$. However a more realistic choice is to consider it as spatially dependent. Because Lorenz 96 model is artificial we have taken random values of the forcing. In order to have a smoothly varying forcing function along the circle one can take a periodic function

with randomly selected Fourier components. For the model III—the truth—in this work we have decided to take as non-zero the 10 lowest Fourier components. For the average of the forcing the standard value was taken $f_0 = F = 15$. Thus the forcing term is given by the sum

$$F_n = f_0 \left[1 + \sum_{m=1}^{10} f_m^c \cos\left(\frac{2\pi mn}{N}\right) + f_m^s \sin\left(\frac{2\pi mn}{N}\right) \right], \tag{9}$$

where the spectral components f_m^c and f_m^s have random values from the interval $[-0.5, 0.5]$. As we have stated previously the models of the reality are assumed to be more simple and also, due to the imperfection, the forcing terms of the models have slightly perturbed values. The perturbation is performed in the same way by adding a function with randomly selected Fourier components to the forcing function of the truth. The number of harmonics is taken to be 10 again but with smaller amplitude. Because any representation of the atmosphere is its coarse image we have taken the number of the gridpoints of the models to be $M < N$. Thus, we have now models of one truth different from each other and from the truth as well. The difference is in the structure of equations and also in the only parameter—forcing term—which mimics different parameterizations of the unresolved physical processes.

As was stated previously one source of errors in short term prediction is the mismatch between the velocity vectors of the truth and its model—tendency error. A proper linear combination, or weighting of the velocities of different models could decrease that mismatch. The combination should be applied at every gridpoint generally with different weights at different positions. Denote with T_n^μ the tendency of the model μ at gridpoint n

$$\dot{X_n^\mu} = T_n^\mu = [X^\mu, X^\mu]_{K,n} - X_n^\mu + F_n^\mu. \tag{10}$$

Then the tendency of weighted ensemble as linear combination of the tendencies is given by

$$\dot{X_n^{IE}} = T_n^{IE} = \sum_\mu w_n^\mu T_n^\mu. \tag{11}$$

In operational weather prediction one is allowed to adjust the parameter values of the models to optimize it. For this case that would mean optimizing the forcing terms F_n. We assume that the optimization is done and the models are best solutions obtained at different meteorological centers. Then the quality of the interactive ensemble will depend only on the weights w_n^μ. One possible solution for determination of optimal weights is based on minimizing the average mismatch between the tendency of the ensemble and the truth. This is identified as average tendency error

$$D = \langle \sum_{n=0}^{M-1} |T_n^t - T_n^{IE}|^2 \rangle = \sum_{n=0}^{M-1} \langle \left| T_n^t - \sum_\mu w_n^\mu T_n^\mu \right|^2 \rangle, \tag{12}$$

where the tendency of the truth T_n^t is given by the RHS of Eq. (6) and angle brackets denote time average. As is usually done with the operational atmospheric models the optimization is based on the measurements data. In this case it is assumed that the tendency of the truth is observed, or calculated. For real models the tendency is not an observational quantity but should be estimated with interpolation and thus is prone to errors. This error as well as the presence of measurement noise can be modeled by adding noise to the tendency of the truth. Using all the observation data the optimal weights are obtained with differentiation of the average tendency error with respect to the weights

$$\frac{\partial D}{\partial w_n^\mu} = \frac{\partial \langle \left| T_n^t - \sum_\nu w_n^\nu T_n^\nu \right|^2 \rangle}{\partial w_n^\mu} = 2\langle T_n^\mu \left(T_n^t - \sum_\nu w_n^\nu T_n^\nu \right) \rangle = 0. \tag{13}$$

One could introduce the covariances between the models' tendencies $C_n^{\mu,\nu} = \langle T_n^\nu T_n^\mu \rangle$ and between the truth and the models $C_n^{\mu,t} = \langle T_n^t T_n^\mu \rangle$. The tendency covariances between the models can be organized in a matrix $\mathbf{C}_n$ and tendency covariances with the truth in a vector $\mathbf{c}_n$. Then the vector of weights $\mathbf{w}_n$ at gridpoint n is obtained from the following linear algebra problem

$$\mathbf{C}_n \mathbf{w}_n = \mathbf{c}_n. \tag{14}$$

The procedure that we have presented is a linear regression and is prone to over-fitting of the parameters—weights in this case [2]. The standard remedy of this problem is minimization od slightly modified error function

$$D + \lambda \sum_{n,\nu} (w_n^\nu)^2, \tag{15}$$

where λ is the regularization coefficient. Repeating the procedure with the derivatives one obtains the following equation for the weights

$$\sum_\nu \left(C_n^{\mu,\nu} - \lambda \right) w_n^\nu - C_n^{\mu,t} = 0. \tag{16}$$

or in matrix form

$$\left(\mathbf{C}_n - \lambda \mathbf{I} \right) \mathbf{w}_n = \mathbf{c}_n, \tag{17}$$

The solution of the matrix is obtained straightforwardly and reads

$$\mathbf{w}_n = \left(\mathbf{C}_n - \lambda \mathbf{I} \right)^{-1} \mathbf{c}_n. \tag{18}$$

In summary, for this toy case from the simulations are obtained the tendencies at every moment and every gridpoint and from them are calculated the covariances, and finally the weights.

4 Numerical Experiments

The numerical integration of the systems was performed with the fourth order Runge–Kutta algorithm with time step 0.001. The truth was considered to have $N = 960$ gridpoints—standard value in the literature, while to have simpler models of the reality one should choose smaller resolution for them. The weighted ensemble outperforms the individual models when the difference in resolution is larger, but too small number of points for the models will make them completely deviate from the truth. We have used in this study $M = 60$ points. The comparison of the models with the truth is done in the state space of the model—at its 60 gridpoints. Because in numerical weather forecasting the models are constantly fed with data from new measurements, the models are started form the state of the truth (at the models' gridpoints) with small perturbations to include the observational error. For technical reasons we have taken that this resetting is performed at some prescribed interval—2,000 time units in this case. First test is the visual comparison of the solution profiles at certain moment. In Fig. 1 are shown the solutions at two particular moments $t = 0.2$ and 1. It is evident that for small period the model's profile resembles to that of the truth—one has a good prediction. Clearly, as time goes on the prediction ability of the model fades away.

More precise estimate of the deviation of the prediction from the real trajectory is done by observing the evolution of Euclidean distance between the states of the model μ and the truth—prediction error

$$e^{\mu}(t) = \sqrt{\sum_{m=0}^{M-1} |Z_m(t) - X_m^{\mu}(t)|^2}. \tag{19}$$

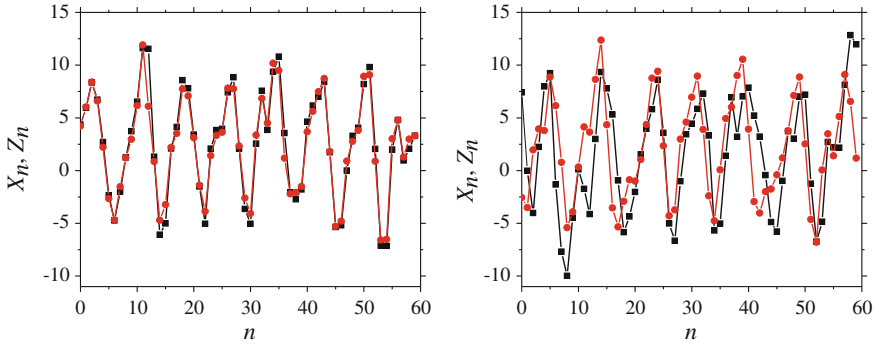

Fig. 1 Comparison of solution profiles of the truth—Lorenz 96 model III (in *black*) and its simpler representation—Lorenz 96 model II (in *red*) in the state space of the model. At *left* are shown the solutions at moment 0.2 after start at close initial condition, while in the *right* panel the moment when the solutions are taken is $t = 1$

The trajectories from identical nonlinear dynamical systems originating from close starting points initially separate with exponential rate on average [7, 17]. But if the dynamical systems are different the divergence should not be exponential [16]. This is particularly relevant for the meteorology because the atmosphere and any of its models are far from identical. In this study the exponential divergence is verified only when one takes the model to be the same class of functions as is the truth—model III. This is shown in left panel of the Fig. 2. If the model is different (or simpler) from the truth—class II, the separation is linear [11]. This happens regardless of whether the model has equal or smaller number of gridpoints. To explain this result one should remind that the state of the truth and its tendency are represented in the state space of the model. For small periods the evolutions of both states are governed by nearly constant tendencies. But it is almost impossible for the tendencies to coincide at every moment. This can be modeled with two particles moving along intersecting lines with constant velocities and starting from the intersection point at the same moment. With elementary kinematics it can be easily shown that the distance between the particles will grow linearly. In the case of perturbation of the initial condition, the lines do not intersect and then the separation is linear asymptotically. In the right panel are shown the prediction errors for three different models (class II) of the truth. Also are shown the prediction errors of the average of the outputs of the models $X_m^{\mathrm{av}} = (\sum_\mu X_m^\mu)/3$ and of the improved model. The improvement with the interactive ensemble is obtained for longer periods. The amount of improvement depends on the value of the regularization parameter λ which is obtained by trying different values. For this case its value was obtained $\lambda = 1{,}000$.

A more convenient measure for determination of the predictability range of a model is the anomaly correlation—AC [1]. It is cross correlation between two time series at the same moment—one obtained from the observations and the other from

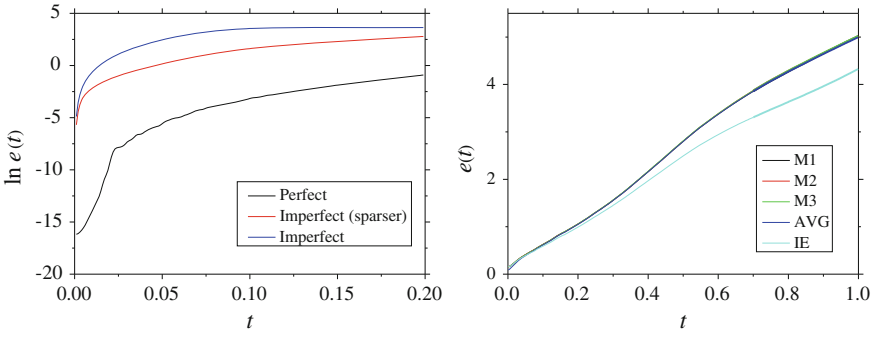

Fig. 2 If the model is identical with the truth (Lorenz 96 model III), the average initial error growth is exponential—verification at *left panel*. When the model and the truth are different the separation is linear—verification at *right panel*. *Lowest curve* in that plot corresponds to the weighted ensemble, while the others correspond to the individual models or the average of their output. To the observations of the state of the truth, as well as its tendency was added uniform noise with maximal value 5 % of the observed values

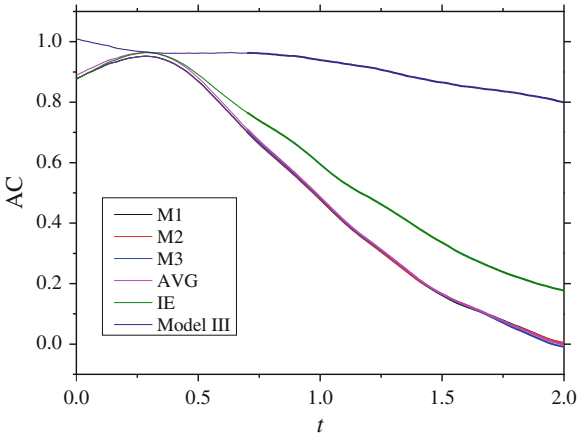

Fig. 3 Anomaly correlation AC between the truth and the models. The *top curve* (in *blue*) corresponds to the perfect model, the *middle* (in *green*) is for the improved model, and *lower curves* (almost *indistinguishable*) are for the individual models and average output of them

the model. For the model μ it is

$$\mathrm{AC}^{\mu} = \frac{\sum_{m=0}^{M-1} \langle (Z_m - \langle Z_m \rangle)(X_m^{\mu} - \langle X_m^{\mu} \rangle) \rangle}{\sqrt{\sum_{m=0}^{M-1} (Z_m - \langle Z_m \rangle)^2} \sqrt{\sum_{m=0}^{M-1} (X_m^{\mu} - \langle X_m^{\mu} \rangle)^2}}, \tag{20}$$

where the angular brackets denote time average for the testing period. As a predictability boundary is considered the time when AC falls below value 0.6 [1]. The AC curves for three individual models, their average output and the improved model are compared in Fig. 3. This confirms that the weighted ensemble is better model—17 % in this particular example. The top curve in the figure corresponds to the AC between a model that is identical with the truth (perfect model) started from perturbed initial condition. This shows that the imperfect models are weaker for prediction. The AC curves for the imperfect models have atypical behavior—increasing for short time and then decreasing instead of only decreasing. Maybe this is result of the structural difference between them and the truth.

5 Discussion

We have presented a procedure for combining systems with aim to make an improved model of some structurally more complex reality. As the truth was considered the most complex version of the Lorenz 96 model, while as models were taken the simpler versions. The models were assumed to have less degrees of freedom as well. The improved model was defined to be an interactive ensemble with velocity vector, or

tendency, that is a weighted combination of the tendencies of the individual models. The weights are obtained from past observations of the tendency of the truth such that the time average of the difference between the tendency of the improved model and the truth is minimal. For some choice of the parameters the weighted ensemble outperforms the individual models for 17 % according to the anomaly correlation as a predictability metric.

The traditional physical modeling of dynamical systems rests upon constructing the functions of velocity vectors from first principles. With machine learning and artificial intelligence tools those functions are determined from some prescribed set. This approach is using both—finding a good combination of different physical models. The meteorology is the area that is particularly relevant for this way of modeling because of existence of dozens of different atmospheric models. Other fields can use these ideas as well.

There is lot of work left to be done. First, the concept could be verified for models that are structurally different from each other—at least in presence (or absence) of some small magnitude terms. Another interaction combinations should be studied as well. One of them is the diffusive coupling, or nudging of the state variables of coupled models which is implemented in synchronization theory. This may be necessary for making interactive ensembles for climate projection—estimate of the averages, or fluctuations of the variables. In this work we have checked whether the weighted ensemble is better for predicting the climate than the individual models. As climatological variables were considered the time averages of the field at certain gridpoints—$\langle Z_n \rangle$ and $\langle X_n^\mu \rangle$. After calculating average mismatch $(\langle Z_n \rangle - \langle X_n^\mu \rangle)^2$ for whole space we found that it is not smaller for the improved model than the individual models. In that case the average output of the models X_n^{av} has best performance. This happens probably because the improvement is based on optimization of the tendency which is a short-term property. Maybe training the ensemble directly for the climatological variables will lead to the desired improvement. How to try this is an open question.

Acknowledgments This work was partially supported by project ERC Grant # 266722 (SUMO project).

References

1. N.A. Allgaier, K.D. Harris, C.M. Danforth, Phys. Rev. E **85**, 026201 (2012)
2. C.M. Bishop, *Pattern Recognition and Machine Learning*, 2nd edn. (Springer, Heidelberg, 2007)
3. V. Bjerknes, *Dynamic Meteorology and Hydrography, Part II. Kinematics* (Carnegie Institute, Gibson Bros, New York, 1911)
4. P. Bougeault et al., Bull. Am. Meteorol. Soc. **91**, 1059 (2010)
5. K. Judd, C.A. Reynolds, T.E. Rosmond, L.E. Smith, J. Atmos. Sci. **65**, 1749 (2008)
6. J.M. Lewis, Mon. Wea. Rev. **133**, 1865 (2005)
7. E.N. Lorenz, J. Atmos. Sci. **20**, 130 (1963)

8. E.N. Lorenz, in *Proceedings of Seminar on Predictability*, Reading, Berkshire, UK, ECMWF, 1996, p. 1
9. E.N. Lorenz, J. Atmos. Sci. **62**, 1574 (2004)
10. M. Mirchev, G. Duane, W. Tang, L. Kocarev, Commun. Nonlinear Sci. Numer. Simul. **17**, 2741–2751 (2012)
11. D. Orrell, L. Smith, J. Barkmeijer, T.N. Palmer, Nolinear Proc. Geoph. **8**(6), 357 (2001)
12. D. Orrell, J. Atmos. Sci. **60**, 2219 (2003)
13. E. Ott et al., Tellus A **56**, 415 (2004)
14. T. Palmer, Rep. Prog. Phys. **63**, 71 (2000)
15. A. Pikovsky, M. Rosenblum, J. Kurths, *Synchronization: A Universal Concept in Nonlinear Sciences* (Cambridge University Press, Cambridge, 2003)
16. L.A. Smith, Past and present variability in the solar-terrestial system: measurement, data analysis and theoretical models, in *International School of Physics "Enrico Fermi"*, ed. by C.G. Castagnoli, A. Provenzale (Il Nuovo Cimento, Bologna, 1997), p. 177
17. L.A. Smith, C. Ziehmann, K. Fraedrich, Q.J.R. Meteorol. Soc. **125**, 2855 (1999)
18. D.A. Stainforth et al., Nature **433**, 403 (2005)
19. L.A. van den Berge, F.M. Selten, W. Wiegerinck, G.S. Duane, Earth Syst. Dyn. **2**, 161 (2011)
20. W. Wiegerinck, W. Burgers, F.M. Selten, *SUMO—Supermodeling by Imperfect Models*. Technical Report, Workpackage 2 (2011)

Synthetic Computation: Chaos Computing, Logical Stochastic Resonance, and Adaptive Computing

Behnam Kia, K. Murali, Mohammad-Reza Jahed Motlagh, Sudeshna Sinha and William L. Ditto

Abstract Nonlinearity and chaos can illustrate numerous behaviors and patterns, and one can select different patterns from this rich library of patterns. In this paper we focus on synthetic computing, a field that engineers and synthesizes nonlinear systems to obtain computation. We explain the importance of nonlinearity, and describe how nonlinear systems can be engineered to perform computation. More specifically, we provide an overview of chaos computing, a field that manually programs chaotic systems to build different types of digital functions. Also we briefly describe logical stochastic resonance (LSR), and then extend the approach of LSR to realize combinational digital logic systems via suitable concatenation of existing logical stochastic resonance blocks. Finally we demonstrate how a chaotic system can be engineered and mated with different machine learning techniques, such as artificial neural networks, random searching, and genetic algorithm, to design different autonomous systems that can adapt and respond to environmental conditions.

B. Kia (✉) · W. L. Ditto
Department of Physics and Astronomy, University of Hawaii at Manoa, Honolulu, HI 96822, USA
e-mail: behnam@hawaii.edu

K. Murali
Department of Physics, Anna University, Chennai 600025, India

M-R. Jahed Motlagh
Department of Computer Engineering, Iran University of Science and Technology, 16846 Tehran, Iran

S. Sinha
Indian Institute of Science Education and Research (IISER), Mohali, Knowledge City, Sector 81, SAS Nagar, P.O. Manauli, Mohali, Punjab 140306, India

V. In et al. (eds.), *International Conference on Theory and Application in Nonlinear Dynamics (ICAND 2012)*, Understanding Complex Systems,
DOI: 10.1007/978-3-319-02925-2_5,

1 Introduction

Nonlinearity and chaos have been known and recognized as one of the main sources of variety, diversity, and adaption in nature and living systems [1, 2]. Nonlinearity and chaos provide a system with different types of solutions and behaviors to cope with different conditions, while preserving the determinism of the system. In this paper we provide an overview, discuss, and demonstrate how this nonlinearity and chaos can be engineered to perform different types of computations in a manual or adaptive fashion, and we name this field synthetic computing.

Chaos computing explains how a chaotic system can be engineered to implement different types of computations using different intrinsic patterns available in the system, and how by perturbing the chaotic system we can switch from one function to another [3–6]. In this approach we manually perform the function switching using the perturbation as a "knob" mechanism to program the computing. Here, manual switching means that we ourselves control and program the chaos-based system in order to obtain the desired functionality from it.

As another approach to synthetic computing, logical stochastic resonance has been introduced [7, 8]. It describes how by tuning parameters of a bistable nonlinear system in a noisy environment, we can build different types of computations. Bistability is widely observed in nature and living organisms. Logical stochastic resonance explains how a nonlinear, bistable system can be synthesized and engineered so that input and control data deepen and widen the potential well that corresponds to the state that represents the correct answer to the computation. In this process, the second well, which represents the wrong well, can be totally removed, making the system monostable. But in some natural bistable systems of interest, such as genetic regulatory networks, it is hard, if not impossible, to totally remove the wrong well. In such conditions the best we can do is to make the wrong well as shallow as possible, and use background noise to virtually cancel out the effects of its presence. Using noise to enhance the performance of a bistable system has been named stochastic resonance [9, 10]. Following this terminology, plus the fact that here noise is used to improve the logical performance of the system, the field is named logical stochastic resonance, or simply LSR [7].

In this paper, we have extended the approach of LSR to realize, systematically (i.e., directly implementing conventional higher level logic architecture or typical digital electronic structures), the combinational digital logic systems via suitable concatenation of bistable logic elements that follow the LSR paradigm through carefully crafted coupling schemes.

Taking a very different approach, we then introduce and demonstrate how a chaos-based system can learn to automatically select intrinsic patterns and behaviors as a solution or response to different input conditions. In other words, we present an adaptive version of chaos computing, where the chaos-based system evolves and learns to select the correct response, instead of being programmed or commanded to do so. In this approach, we combine different machine learning techniques, such as genetic algorithm, random search, and artificial neural network, with chaos theory

to enable the system to learn to select correct patterns and behaviors without need for explicit programming.

The organization of the paper is as follows: in Sect. 2, we explain the concept of synthetic computing, why it is important, and why we have named it synthetic computing. In Sect. 3, we overview and explain the first approach to synthetic computing, where chaotic systems are programmed to build different digital functions. Then in Sect. 4, we briefly overview LSR, and then we extend the approach of LSR to realize combinational digital logic systems via suitable concatenation of exisitng LSR blocks. In Sect. 5, we demonstrate how chaos theory and conventional machine learning techniques can be collected together so that an engineered system adaptively selects an optimal intrinsic solution or action. Finally in Sect. 6, the paper is concluded.

2 Synthetic Computing

Nonlinearity, especially when it leads to chaos, is a very unique condition. It combines the main advantage of random systems, namely rich behavior, with the determinism of a periodic system [11].

Unlike in linear systems, in a nonlinear system by changing parameters the system may undergo qualitative as well as quantitative changes in its behavior. As an example, consider the bifurcation diagram of the logistic map, $x_{n+1} = r x_n(1 - x_n)$, where r is the bifurcation parameter as depicted in Fig. 1.

A bifurcation diagram represents the steady state solutions of a chaotic system versus a given parameter, called the *bifurcation parameter* [12]. As is illustrated in Fig. 1, by changing one parameter, the system exhibits completely different behaviors. At some parameter values the system is periodic, and at some others it is chaotic (periodic with periodicity of infinity). Even more, at parameter values where there is chaos, the system is composed of an infinite number of unstable periodic orbits [12].

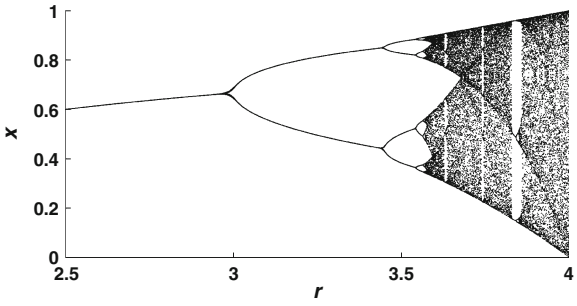

Fig. 1 Bifurcation diagram of a very simple map, Logistic map, is depicted. Despite the simplicity of the map, it exhibits a very rich dynamics

Furthermore, since the dynamics is deterministic, these patterns or behaviors are distinct and can be selected or stabilized [13]. For example, as explained earlier in Fig. 1, by tuning the bifurcation parameter, one can get very different periodic and orbits from the system. Also by using different chaos control techniques, such as OGY, one can stabilize one of the preexisting unstable periodic orbits (UPO) of the chaotic attractor [13]. Or using some other control techniques such as threshold controlling mechanism, one can stabilize a new UPO [14]. In another approach, very different orbits and behaviors can be selected by perturbing a chaotic system [4]. Or two identical or topologically conjugate chaotic systems can be synchronized to evolve identically or similarly in time [15].

All the techniques mentioned above for manipulating a nonlinear system can be observed and considered as a "knob" mechanism, which can be used to tune or program the nonlinear system. Different applications for nonlinear systems have been introduced based on this "knob" mechanism. The main motivation is that a nonlinear or a chaotic system contains all, or at least the majority of, behaviors or solutions of desire, and each of these solutions can be selected and extracted. The main proposed advantage of synthesizing and engineering nonlinear systems to build different applications is that since all solutions and behaviors are packed in one system, it will require less power and energy, area, time, and speed than in the case that all individual behaviors have to be implemented separately and then gathered together to achieve the same amount of performance and functionality. Chaos computing [3–6], data transmission using symbolic representation of chaotic orbits [16], or chaos based speech coding and synthesizing [17] are good examples of synthesizing chaotic systems to build practical applications.

After introducing the advantages of nonlinear systems, it is worthwhile to take a look back at linear systems and compare them with nonlinear systems. A linear system lacks the broad range of patterns and behaviors that a nonlinear system exhibits. Changing a parameter of a linear system results in changes of amplitude and/or frequency of the system solution. Linearity is a very positive attribute when it comes to analytical study of a system. But the truth is that a linear system has very little to contribute to building sophisticated engineering systems. A linear system has a very linear and restricted behavior. To obtain needed complex behavior, one would have to gather and combine a large group of such linear systems and organize them together to obtain the required functionality from them. This is in sharp contrast to nonlinearity where different behaviors coexist in one single, nonlinear system.

In this paper, we engineer and synthesize nonlinear systems to use the intrinsic rich behavior of nonlinear systems in computations and we call it synthetic computing. We have borrowed the term "synthetic" from synthetic biology and call our field synthetic computing, because, similar to synthetic biology where existing biological systems are re-designed and engineered to obtain something new, here we re-design and engineer nonlinear systems to obtain computations.

3 Chaos Computing

The main idea behind chaos computing is to harness the library of orbits/patterns inherent in chaotic systems in order to select out logic operations and then to utilize the sensitivity to initial conditions of those systems to perform rapid switching (morphing) between all of these logic functions [3, 4, 6]. These features are sufficient to perform reconfigurable logic operations using a chaotic system.

Data and control inputs to a chaotic system may be encoded as either the initial conditions or the parameters of the chaotic system. Here the focus is on the former (initial condition selection) technique. After applying the inputs, the system is allowed to evolve for a predefined time, after which the "final state" of the chaotic system is decoded as the computation's output.

To be more precise, consider the m digital data inputs, $X^1_{Data}, X^2_{Data}, \ldots, X^m_{Data}$, to a computing engine, and the n digital control inputs, $X^1_{Control}, X^2_{Control}, \ldots, X^n_{Control}$. Computation using this system consists of three steps:

Step 1: Each set of data and control inputs is mapped to a point on the unstable manifold of the chaotic system. This point is used as the initial condition for the chaotic system. Let T map (encode) the m data and n control inputs onto the space of the initial conditions. If L is a binary set {0,1}, then $L^{(n+m)}$ represents the domain of T, which consists of all the possible combinations of digital data and control inputs. Let β be the unstable manifold of the chaotic system, R^s the general state space of the chaotic system, and Y the output of the encoding map on the unstable manifold. In this case the general form of the encoding map, T, is as follows:

$$T : L^{(n+m)} \rightarrow \beta,\ \beta \subset R^s,\ L = \{0, 1\}$$
$$Y = T\left(X^1_{Data}, X^2_{Data}, \ldots, X^m_{Data}, X^1_{Control}, X^2_{Control}, \ldots, X^n_{Control}\right) \quad (1)$$

Step 2: Starting from the initial conditions produced by the encoding map, the chaotic system evolves for a fixed time (or for a fixed iteration number, if the chaotic system is discrete).

Step 3: After the evolution time, the system stops working and its state at the end of the evolution time is sampled and decoded to the outputs using a decoding map.

The encoding map maps different sets of the inputs to different points on the unstable manifold of the chaotic system, and these points are used as initial conditions for the chaotic system. Since the system is on the unstable manifold, the orbits of the chaotic system are very sensitive to the inputs, and the orbits dramatically change with just a one-bit change in the control input. Thus control inputs can select a chaotic logic function. To evaluate which digital function is selected with a particular control input, the association of a control input with a logic function are noted and then all possible combinations of data inputs are enumerated to construct the truth table of the function.

By changing the control input, and repeating this procedure (of constructing the truth table of the digital function), a second digital function different (with high

probability) from the first one is observed. This is the meaning of the reconfigurability of chaos computing. By using all possible control inputs and finding the type of function that the chaotic system implements, the full instruction set of the chaotic system is obtained [3].

Recently it was demonstrated how unstable periodic orbits, and a model based on them, both explains and predicts how, and how well, a chaotic system can do computations [4]. Furthermore, since unstable periodic orbits and their stability measures in terms of eigenvalues are extractable from experimental times series, time series technique for modeling and predicting chaos computing from a given time series of a chaotic system has been developed [3].

4 Logical Stochastic Resonance

Over the last few years, it has become increasingly obvious that understanding how noise and nonlinearity cooperate in a dynamical system to produce novel effects, is critical in understanding how complex systems behave and evolve. Stochastic resonance (SR) provides one such example wherein the cooperative behavior between noise and dynamics produces interesting, often counter intuitive, physical phenomena. SR has received much attention over the past few decades [9, 10] and consists of the enhancement of weak input signals through a delicate interplay between the signal, noise, and nonlinearity (threshold). Recently, it has been shown that a noisy bistable system, subjected to two square waves as inputs, produces a logical response in some optimal range of noise [7, 8]. The probability of getting such response increases to unity with increasing noise intensity, and then decreases for noise strengths exceeding the optimal window; this effect has been named "logical stochastic resonance" (LSR). To date, the relevance of LSR has been experimentally tested and used in assorted applications in fields including electrical, nanomechanical, optical, chemical and biological systems [8, 18–21].

In this section, we elucidate the implementation details of certain representative combinational logic systems using a concatenation of LSR elements. First we consider a simple combinational logic operation namely a half-adder. A typical half-adder can be realized with a XOR and an AND logic gates. As a standard practice, one can realize the XOR operation with a set of NOR or NAND gates [22]. Now we configure the single LSR element to emulate the NAND logic operation by fixing its nonlinearity or by fixing the constant bias value C; by using such a set of elements, the XOR logic operation is realized first. Then AND and OR logic operations with LSR elements are realized, easily, by inverting the logic output from NAND and NOR operations. The XOR logic circuit implementation using LSR modules is depicted in Fig. 2. Here the XOR logic operation is realized with five NAND gate LSR modules. The model equations with proper coupling for realizing the XOR logic operation are given as

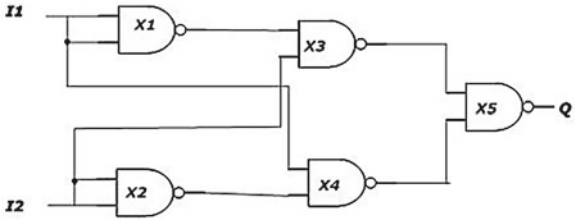

Fig. 2 Schematic diagram for realizing conventional XOR logic gate using LSR based NAND gates

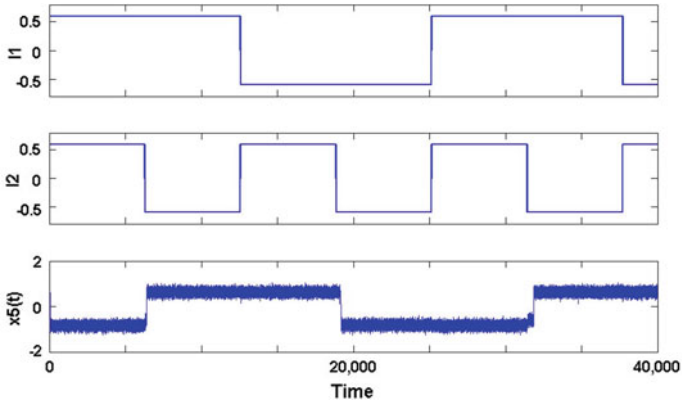

Fig. 3 Timing sequences from *top* to *bottom* for XOR logic gate implementation with individual LSR elements emulating NAND gate

$$\begin{aligned}
\dot{x}_1 &= -\alpha x_1 + \beta g(x_1) + D\eta(t) + 2I_1 + C,\\
\dot{x}_2 &= -\alpha x_2 + \beta g(x_2) + D\eta(t) + 2I_2 + C,\\
\dot{x}_3 &= -\alpha x_3 + \beta g(x_3) + D\eta(t) - \varepsilon x_1 + I_2 + C,\\
\dot{x}_4 &= -\alpha x_4 + \beta g(x_4) + D\eta(t) - \varepsilon x_2 + I_1 + C,\\
\dot{x}_5 &= -\alpha x_5 + \beta g(x_5) + D\eta(t) - \varepsilon x_3 - \varepsilon x_4 + C,
\end{aligned} \tag{2}$$

where the parameters α, β and C are fixed as 1.8, 3.0 and -0.8 respectively, ε (the coupling parameter) is fixed at 0.3, and the nonlinear function g(x) is given by:

$$\begin{aligned}
g(x) &= x \quad \text{when } x_l^* < x < x_u^*\\
g(x) &= x_l^* \quad \text{when } x < x_l^*\\
g(x) &= x_u^* \quad \text{when } x_u^* < x
\end{aligned} \tag{3}$$

Depending upon the parameter $C = -0.8$ or 0.0, the individual system emulates NAND or NOR logic respectively. MATLAB–SIMULINK simulation for the XOR logic results for noise intensity $D = 2.3$, $\mathbf{x_u^*} = 1.5$ and $\mathbf{x_l^*} = -1.0$ has been carried out. For the given logic inputs *I1* and *I2*, the corresponding simulated waveforms are presented in Fig. 3.

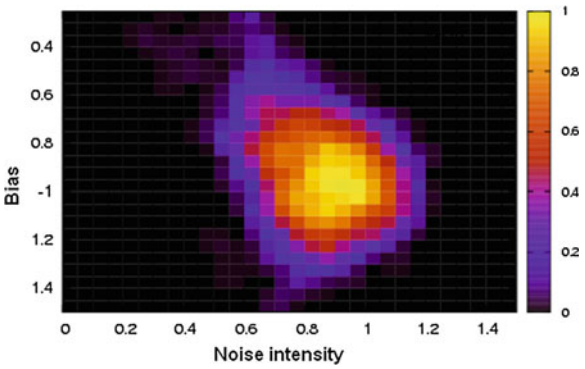

Fig. 4 Density map of $P(logic)$ (see text) for the *XOR* logic operation by using Eq. (2)

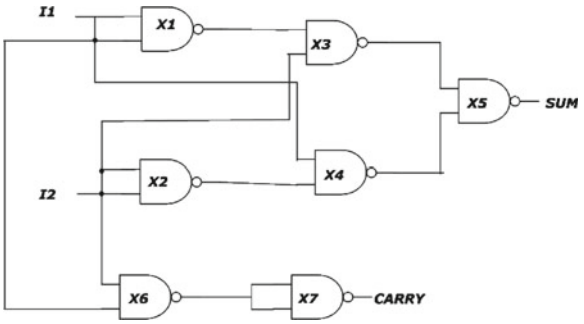

Fig. 5 Schematic diagram for realizing conventional half-adder circuit using LSR based NAND gates. A set of five LSR based NAND gates are used for realizing XOR logic gate to generate SUM output and two LSR based NAND gates are used to realize AND gate to generate CARRY output

Figure 4 depicts the probability P (logic) obtained from extensive numerical simulations for different bias and noise intensities. It is evident that the logic operation XOR is realized, consistently, in an optimal band of moderate noise using Eq. (2).

Then to realize a typical half-adder logic operation, we need a XOR logic gate and an AND logic gate. To realize AND logic, we need two NAND logic gates. The schematic diagram depicting the half-adder implementation using LSR elements is given in Fig. 5. The corresponding model equations are

$$\begin{aligned}
\dot{x}_1 &= -\alpha x_1 + \beta g(x_1) + D\eta(t) + 2I_1 + C,\\
\dot{x}_2 &= -\alpha x_2 + \beta g(x_2) + D\eta(t) + 2I_2 + C,\\
\dot{x}_3 &= -\alpha x_3 + \beta g(x_3) + D\eta(t) - \varepsilon x_1 + I_2 + C,\\
\dot{x}_4 &= -\alpha x_4 + \beta g(x_4) + D\eta(t) - \varepsilon x_2 + I_1 + C,\\
\dot{x}_5 &= -\alpha x_5 + \beta g(x_5) + D\eta(t) - \varepsilon x_3 - \varepsilon x_4 + C,\\
\dot{x}_6 &= -\alpha x_6 + \beta g(x_6) + D\eta(t) + I_1 + I_2 + C,\\
\dot{x}_7 &= -\alpha x_7 + \beta g(x_7) + D\eta(t) - 2\varepsilon x_6 + C,
\end{aligned} \tag{4}$$

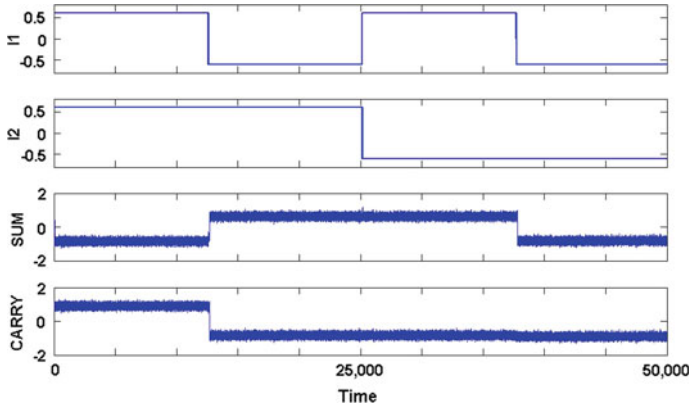

Fig. 6 Timing sequences from *top* to *bottom* for half adder implementation with individual LSR elements emulating NAND gate with $C = -0.8$. **a** Input I_1, **b** Input I_2, **c** Output $-x_5(t)$ corresponding to SUM, **d** Output $-x7(t)$ corresponding to CARRY. Here the noise intensity $D = 2.3$, thresholds $(\mathbf{x}_\mathbf{l}^*, \mathbf{x}_\mathbf{u}^*) = (-1.0, 1.5)$ are used

where, the parameter values are fixed as in Eq. 2. The simulated waveforms are shown in Fig. 6.

5 Adaptive Computing

The logic blocks and operations introduced in previous sections have no degree of freedom in choosing the type of computation they perform, rather they follow instructions received from a control unit. In this section we demonstrate how we can design a new generation of chaos computing systems that work autonomously to perform computations as they adapt to their environment *with no need for external programming*. Here we show how such chaos-based systems evolve to communicate with the environment in a meaningful manner to accomplish tasks and computations.

The aim is to extend the scope of chaos computing from chaos-based digital logic design and implementation to achieving artificial intelligence. Here by "intelligence" we mean the capability of the system to perceive its environment and take actions that maximize its fitness in that environment [23]. We introduce new models of chaos computing in which a chaos-based creature autonomously reconfigures itself to adapt to the environment. In this new scenario there are no external instructions and the system itself learns/evolves/adapts to external inputs. We call these synthesized intelligent systems "*chaos based creature*s."

Nonlinear and chaotic systems provide us with a library of different solutions and actions that coexist inside a system. We examined this fact in detail in Sect. 2. It is believed that the flexibility of natural and living systems and their ability for adaptation and coping with different conditions originates from nonlinearity as well [24]. We can safely assume that intelligence arises from a nonlinear system. So we

choose a chaotic system as the source of different solutions and actions and we use it as the main body of the model for intelligent creatures.

The next question is how a chaotic creature can know which intrinsic pattern and behavior is the optimal solution or reaction? In previous models of chaos computing we, or the control unit, explicitly control the chaos based logic block and select the demanded function. Instead, here we mate the chaos-based system with different machine learning techniques so that the creature itself learns to select appropriate actions.

For simplicity, assume the dynamics of the creature is modeled with a 1-D discrete logistic chaotic map:

$$x_{(n+1)} = r x_n (1 - x_n) \tag{5}$$

where r is the bifurcation parameter.

Here as an example we assume the creature responds to the environment by adjusting its oscillation periodicity.

We use two different techniques to extract different behaviors from the logistic map. First we use the bifurcation parameter as a "knob" and let the machine learning techniques to adjust this parameter to extract different periods as a response to the environment. Later we will use a chaos control technique to stabilize a periodic orbit as a response to the environment.

We have developed an artificial life environment, and then simulate the behavior of the creatures in this environment. This artificial life environment itself knows the appropriate and optimal solution to any environmental condition, and rewards or punishes the creatures based on how well (or badly) they respond to it. This is a supervised learning technique, where the optimal solutions are known and creatures are rewarded or punished accordingly.

5.1 Chaotic Creature with Random Searching (Learning)

We equip the chaotic creature with a random searching mechanism to adjust the bifurcation parameter to find the optimal response to the environment.

A random searching (learning) technique is a very simple search mechanism that takes random steps in the parameter domain to find the optimal solution [25]. We can formulate the random search as:

$$\begin{aligned} x_{n+1} &= r_j x_n (1 - x_n) \\ r_{e+1} &= r_e + \lambda, \quad \lambda \approx N(0, 0.065) \end{aligned} \tag{6}$$

where the bifurcation parameter, r, is updated based on a random search method. The random changes of the bifurcation parameter have a Gaussian distribution with zero mean and 0.01 variance. This very simple mechanism enables the creature to adjust its bifurcation parameter and choose different periods.

In a constant artificial life environment, where the environmental condition does not change, the creature is expected to adapt and adjust its oscillation periodicity to a fixed value, which is demanded and enforced by the artificial life environment, and stays there. This demanded period by the artificial life environment could be any period. In simulation, we observed periods that have small-sized intervals in the bifurcation diagram require longer training time than periods with larger intervals in the bifurcation diagram.

The creature can be improved to survive in a variable artificial life environment by addition of a simple perception artificial neural network (ANN) to the design. A variable artificial life environment is an environment that changes, and as a result a creature needs to change accordingly to survive. Here for simplicity we assume the variable environment has four different states, and each state demands the creature to oscillate at a specific period.

This artificial neural network is a very simple perception ANN, composed of two layers. The first layer is the input layer and the second layer is the output layer. The input layer is composed of two neurons, and a two bit state condition (00, 01, 10, or 11) is fed to this layer of neurons. The output layer has a single neuron, and the output of this neuron is the bifurcation parameter of the chaotic system. The activation function of these neurons is a sigmoidal function. This neuron maps the state condition of the artificial life environment to the bifurcation parameter of the chaotic system. One can consider this simple ANN as a classifier also. Its job is similar to the operation of the brain of a living system, although this perception network is very much simpler. This ANN drives the chaotic body based on the inputs.

The ANN needs to be trained first. Random searching is used here again to train the ANN through adjusting the synaptic weights between neurons. At each step of training, four different sets of inputs (00, 01, 10, and 11) are fed to the ANN, and the periods that the chaotic system oscillates at are measured and used to compute the fitness measure.

Using this model, a chaotic creature learns to respond appropriately to variable environmental conditions through adjusting its period. The number of iterations required to train the ANN greatly depends on the size of the intervals of the solution parameters in the bifurcation diagram of the chaotic system. Periods that have small-sized intervals in the bifurcation diagram require longer training time than periods with larger intervals in the bifurcation diagram.

5.2 Evolution of Chaotic Creatures

Now we introduce and study another model of creatures, in which they evolve to respond appropriately to their environment. We start from a constant artificial life environment, where the environment is unchanging and the creatures need to evolve to oscillate at a fixed period. This new model of creature is composed of a chaotic system to represent the library of different actions, and a controller to select different

intrinsic patterns from the chaotic system. Here we use a threshold mechanism for controlling chaos due to the simplicity of the controller.

Threshold mechanisms can be formulated as follows [14]: When the dynamics of the uncontrolled system is given by: $x_{n+1} = f(x_n)$ where f is a nonlinear function, the threshold mechanism is simply implemented as the following condition: if variable $x_{n+1} > x^*$ then the variable is adjusted back to x^*. The threshold control parameter x^* is the critical value that the state variable is not allowed to exceed, and control is triggered whenever the variable exceeds this threshold [14]. A chaotic system controlled by a threshold controller can yield periodic orbits of various orders under different threshold values [14].

This controlling methodology is implemented on the logistic map.

The important remaining question is how creatures know which period they need to choose, or to be more specific, which threshold value they need to use? We use a population of these creatures and apply genetic algorithm that let them evolve to find the appropriate periods.

Genetic algorithm is a branch of artificial intelligence that mimics the process of natural evolution [25]. Genetic algorithm operates on a population of individuals. Each individual represents one possible solution, which is encoded as the chromosome of the individual. The initial population is randomly crated, meaning that the initial chromosomes are randomly selected from the possible set of solutions. A fitness function is normally used to evaluate each individual to measure the effectiveness and performance of the solution that the individual represents.

The existing generation of individuals is then evolved to create a new generation. The key point is that the individuals with higher fitness value are more likely to reproduce the individuals of the second generation, and as a result they pass the good genes to the future generations. Based on a selection technique two parents are selected, and using crossover operator they reproduce a new individual for the new generation. But the new individual is normally is not a combination of its parents, rather in involves some random mutation as well.

The loop of creation of a new generation from the old generation continues until a termination condition has been reached. This termination condition can be convergence of the whole population to an optimal solution, production of an individual that meets the requirement for an optimal solution, or a fixed number of generations reached [25].

In the genetic algorithm we used here, the threshold value of the controller is used as the chromosome of the creature, and our creatures evolve to converge to suitable chromosomes (threshold value) that direct the system to oscillate at demanded periodicity by the artificial life environment.

We create an initial population of 100 chaos-based creatures with chromosomes randomly chosen from [0.9, 1]. Then based on the genetic algorithm, the creatures evolve. The fitness function that we use is: If the frequency of oscillation of the ith individual with ζ as chromosome (threshold value) is the demanded period, then set its fitness value to a positive constant value, otherwise set its fitness value to 0. For selecting a pair of parents for mating we have applied a tournament method [26]. We set the tournament size to four and selection probability to 0.9.

These selected parents can be mutated and copied to the new generation (cloning) with a probability of 0.1, or mated and mutated with a probability of 0.9. Here 0.9 is the probability of mating.

The crossover operator to compute the chromosomes of the offspring from the chromosomes of the parents is:

$$o_i = p_i' + r(p_i'' - p_i') \tag{7}$$

where $p_i{}'$ and p_i'' are the chromosomes of parents, o_i is the chromosome of the offspring, and r is a random number in the interval [0, 1].

The mutation operator used here is:

$$s = s \times (1 - c + 2cr) \tag{8}$$

where s is the chromosome of the individual, c is creep rate, which represent how much mutation can change individuals and is set it to 0.0001, and r is a random number in the interval [0, 1].

The genetic algorithm halts when all individuals of the population oscillate at the desired periodicity.

The required evolution time for convergence depends on the size of the solution interval. Genetic algorithm can find periods with large solution intervals in 10 iterations or so, but periods with smaller interval size require longer evolution time.

Similar to the creatures introduced in the previous section, these new creatures can be improved to survive in a variable artificial life environment by addition of a simple perception artificial neural network (ANN). The artificial life environment in this example is just like the environment introduced in previous part; it has four states, and 00, 01, 10, and 11, represent those states.

Here the ANN is very similar to the ANN used in the previous part. It is a simple perception ANN, composed of two layers. The first layer is the input layer and the second layer is the output layer. The input layer is composed of two neurons, and a two bit state condition (00, 01, 10, or 11) is fed to these two neurons. The output layer has a single neuron and the output of this neuron is the threshold value. The activation function of these neurons is a sigmoidal function. This neuron maps the state condition of the artificial life environment to the threshold value, which will be used by the chaos controller.

This ANN needs to be trained also, so a genetic algorithm is used to evolve a population of these creatures to one that responds to the variable environmental condition appropriately. The genetic algorithm we use here is very similar to the algorithm that is used for training the creatures in a constant environment, but with the difference that the weights of the ANN are now the chromosomes.

Using this model, the population of chaotic creatures evolves appropriately to respond to the variable environmental condition by adjusting their periods. The evolution time required to train the ANN largely depends on the size of the intervals of solution parameters. Periods that have small-sized intervals require a longer evolution time than periods with larger intervals.

6 Conclusions

In this paper we explained the importance of nonlinearity and chaos, and described how nonlinear and chaotic systems can be utilized as sources of different behaviors and patterns. We introduced the field of synthetic computing, where nonlinear and chaotic systems are engineered to perform computation, with the hope that utilizing the rich dynamics of nonlinear and chaotic systems can reduce the engineering effort required to build complex computing systems, and that it may result in efficiencies in terms of size, speed, energy, and power. Chaos computing was introduced as a field where we can manually program a chaotic system. In a different direction, we demonstrated how a chaotic system can be mated with machine learning techniques to build intelligent creatures that automatically select an optimal solution. With this new direction we proposed that nonlinearity and chaos provide a suitable framework for the evolution of order and intelligence. Different intrinsic patterns or behaviors of a chaotic system represent different possible solutions or reactions, and by using machine-learning techniques such as genetic algorithm or random searching, a creature is capable of selecting an optimal solution or reaction to an encountered problem or environmental conidia. This work introduces the possibility of new chaotic robots or intelligent systems, where solutions, reactions, and a portion of decision-making are embedded in a chaotic system.

We gave an overview of logical stochastic resonance (LSR), and then showed the intriguing possibility of concatenating nonlinear bistable oscillators with suitably chosen cross-coupling to realize different combinational digital logic circuit operations in the emergent dynamics of coupled LSR systems. Very recently, the feasibility of LSR in nano-mechanical oscillators, chemical systems, biological systems, and optical systems has been demonstrated. For example, it is demonstrated through simulation that LSR can work in a well-established dynamical model of bacteriophage-lambda, which could, in the presence of additive and/or multiplicative noise, form the basis of a biological computing element [20, 27–29]. Such results underscore the broad reach of the concept of LSR. Concatenating LSR elements with proper coupling to formulate coupled LSR modules can realize even higher-level logic architectures, which opens new vistas in noise-assisted computing devices.

Acknowledgments W. Ditto and B. Kia gratefully acknowledge support from the office of naval research under STTR grant and grant N00014-12-1-0026.

References

1. P. Collard, M. Clergue, Genetic algorithms: from hegemony to chaos. Complex Syst. **12**, 1–29 (2000)
2. C. Langton, Life at the edge of chaos, in *Artificial Life II*, ed. by C. Langton (Addison-Wesley Longman, Boston, 1991), pp. 41–91
3. B. Kia, A. Dari, W.L. Ditto, M. Spano, Unstable periodic orbits and noise in chaos computing. Chaos **21**, 047520–047528 (2011)

4. B. Kia, M. Spano, W. Ditto, Chaos computing in terms of periodic orbits. Phys. Rev. E. **84**, 036207–036214 (2011)
5. J.P. Crutchfield, W. Ditto, S. Sinha, Introduction to focus issue: intrinsic and designed computation: information processing in dynamical systems—beyond the digital hegemony. Chaos **20**, 037101–037106 (2010)
6. S. Sudeshn, W. Ditto, Dynamics based computation. Phys. Rev. Lett. **81**, 2156–2159 (1998)
7. K. Murali, S. Sinha, W. Ditto, A. Bulsara, Reliable logic circuit elements that exploit nonlinearity in the presence of a noise-floor. Phys. Rev. Lett. **102**, 0104101–0104104 (2009)
8. A. Bulsara, D. Dari, W. Ditto, K. Murali, S. Sinha, Logical stochastic resonance. Chem. Phys. **375**, 424–434 (2010)
9. L. Gammaitoni, P. Hanggi, P. Jung, F. Marchesoni, Stochastic resonance. Rev. Mod. Phys. **70**, 223–287 (1998)
10. A. Bulsara, L. Gammaitoni, Tuning it no noise. Phys. Today **49**, 39–45 (1996)
11. W. Ditto, T. Munakata, Principles and applications of chaotic systems. Commun. ACM **38**, 96–102 (1995)
12. A. Afraimovich, S. Hsu, *Lectures on Chaotic Dynamical Systems* (American Mathematical Society, Providence, 2003)
13. B. Andrievskii, A. Fradkov, Control of chaos: methods and applications II. Applications. Autom. Remote Control **65**, 505–533 (2004)
14. S. Sinha, Unidirecional adaptive dynamics. Phys. Rev. E. **49**, 4832–4842 (1994)
15. L. Pecora, T. Carroll, Synchronization in chaotic systems. Phys. Rev. Lett. **64**, 821–824 (1990)
16. E. Bollt, Review of chaos communication by feedback control of symbolic dynamics. IJBC **13**, 269–285 (2003)
17. B. Kia, W. Ditto, M. Spano, Chaos for speech coding and production. Lect. Notes Comput. Sci. **7015**, 270–278 (2011)
18. D. Guerra, A. Bulsara, W. Ditto, S. Sinha, K. Murali, P. Mohanty, A noise-assisted reprogrammable nanomechanical logic gate. Nano Lett. **10**, 1168–1171 (2010)
19. H. Ando, S. Sinha, R. Storni, K. Aihara, Synthetic gene networks as potential flexible parallel logic gates. Europhys. Lett. **93**, 50001 (2011)
20. A. Dari, B. Kia, A. Bulsara, X. Wang, W. Ditto, Noise-aided computation within a synthetic gene network through morphable and robust logic gates. Phys. Rev. E **83**, 041909–041920 (2011)
21. K. Murali, R. Mohamed, S. Sinha, W. Ditto, A. Bulsara, Realization of reliable and flexible logic gates using noisy nonlinear circuits. Appl. Phys. Lett. **95**, 194102–194105 (2009)
22. M. Mano, *Computer System Architecture* (Prentice-Hall, Englewood cliffs, 1993)
23. J. Russell, P. Norvig, *Artificial Intelligence: A Modern Approach* (Prentice Hall, Upper Saddle River, 2010)
24. M. Conrad, What is the use of chaos?, in *Chaos*, ed. by A. Holden (Manchester University Press, Manchester, 1986)
25. S. Sumathi, P. Surekha, *Computational Intelligence Paradigms, Theory and Applications Using MATLAB* (CRC Press, Boca Raton, 2010)
26. H. Stern, Y. Chassidim, M. Zo, Multiagent visual area coverage using a new genetic algorithm selection scheme. Eur. J. Oper. Res. **175**, 1890–1907 (2006)
27. A. Dari, B. Kia, A. Bulsara, A. Ditto, Creating morphable logic gates using logical stochastic resonance in an engineered gene network. Europhys. Lett. **93**, 18001 (2011)
28. A. Dari, B. Kia, A. Bulsara, W. Ditto, Logical stochastic resonance with correlated internal and external noise in a synthetic biological logic block. Chaos **21**, 047521 (2011)
29. A. Dari, A. Bulsara, W. Ditto, X. Wang, Reprogrammable biological logic gate that exploits noise, in *Biomedical Circuits and Systems Conference (BioCAS), IEEE conference*, pp. 337–340, 2011

Delay Differential Equation Models of Normal and Diseased Electrocardiograms

Claudia Lainscsek and Terrence J. Sejnowski

Abstract Time series analysis with nonlinear delay differential equations (DDEs) is a powerful tool since it reveals spectral as well as nonlinear properties of the underlying dynamical system. Here global DDE models are used to analyze electrocardiography recordings (ECGs) in order to capture distinguishing features for different heart conditions such as normal heart beat, congestive heart failure, and atrial fibrillation. To capture distinguishing features of the different data types the number of terms and delays in the model as well as the order of nonlinearity of the DDE model have to be selected. The DDE structure selection is done in a supervised way by selecting the DDE that best separates different data types. We analyzed 24 h of data from 15 young healthy subjects in normal sinus rhythm (NSR) of 15 congestive heart failure (CHF) patients as well as of 15 subjects suffering from atrial fibrillation (AF) selected from the Physionet database. For the analysis presented here we used 5 min non-overlapping data windows on the raw data without any artifact removal. For classification performance we used the Cohen Kappa coefficient computed directly from the confusion matrix. The overall classification performance of the three groups was around 72–99 % on the 5 min windows for the different approaches. For 2 h data windows the classification for all three groups was above 95 %.

C. Lainscsek (✉) · T. J. Sejnowski
Howard Hughes Medical Institute, Computational Neurobiology Laboratory, The Salk Institute for Biological Studies, 10010 North Torrey Pines Road, La Jolla, CA 92037, USA
e-mail: claudia@salk.edu

T. J. Sejnowski
Institute for Neural Computation, University of California at San Diego, La Jolla, CA 92093, USA
e-mail: terry@salk.edu

V. In et al. (eds.), *International Conference on Theory and Application in Nonlinear Dynamics (ICAND 2012)*, Understanding Complex Systems,
DOI: 10.1007/978-3-319-02925-2_6,

1 Introduction

In many physical and biological processes, DDEs have been used to describe the underlying dynamics. Such processes are typically characterized by a delayed reaction on some physical process (see Driver [1] for a list of examples). Delays play an important role in ECG data [2].

We do not try to find DDEs that model the data for the purpose of prediction but rather seek for global DDE models that capture distinguishing features of data for different heart conditions such as normal heart beat, congestive heart failure, and atrial fibrillation that could be used to discriminate between the three conditions.

A motivation for DDE analysis of nonlinear data comes from embedding theory in nonlinear time series analysis. An embedding converts a single time series into a multidimensional object in an embedding space (Whitney [3], Packard et al. [4], Takens [5], and Sauer et al. [6]). The reconstructed attractor reveals basic properties (dimension, Lyapunov spectrum, entropy) of the true attractor of the system. Thus, we can obtain valuable information about the dynamics of the system, even if we dont have direct access to all the systems variables. There are two basic ways of embeddings, the delay and the derivative embedding. For a delay embedding the time series itself and its delayed versions are used to construct the embedding, but the derivative embedding uses the time series and its successive derivatives. Judd and Mees [7] introduced the idea of non-uniform embeddings for time series with components of multiple timescales. DDE analysis utilizes all those ideas in a novel way for detection and classification.

DDE data analysis can also be seen as a novel way of combining Fourier analysis and higher order statistics in a time domain framework. The linear terms of a DDE correspond to the main frequencies or time-scales in the signal while the nonlinear terms in the DDE are related to nonlinear couplings between the harmonic signal parts.

Global vector field reconstruction [6, 8–10] uses the recorded data to generate a model whose integration provides a dynamical behavior equivalent to the behavior generated by the original system. Such a severe demand of equivalence, requiring a strong closeness between the original and the reconstructed vector fields, is not required for our data analysis method. However, as in global vector field reconstruction, the identification technique provides a global model which captures some essential features of the underlying dynamics.

This paper is organized as follows. Section 2 introduces the data used. In Sect. 3 good classifiers for ECG data are found via DDE analysis. Section 4 is the conclusion.

2 Data

We analyze 24 h data of 15 young healthy persons in normal sinus rhythm (NSR) (ECG sample frequency: 128 Hz) of 15 congestive heart failure (CHF) patients (ECG sample frequency: 250 Hz) as well as of 15 subjects suffering from atrial fibrillation

Table 1 ECG data used. The three conditions are normal sinus rhythm (NSR), congestive heart failure (CHF), and atrial fibrillation (AF). The data were downloaded from the Physionet database [11]

	NSR	CHF	AF
Subj.	http://physionet.org/physiobank/database/		
#	nsrdb/	chfdb/	itadb/
1	16265m.dat	chf01m.dat	11m.dat
2	16272m.dat	chf03m.dat	12m.dat
3	16788m.dat	chf07m.dat	15m.dat
4	16795m.dat	chf08m.dat	17m.dat
5	19090m.dat	chf12m.dat	18m.dat
6	16273m.dat	chf02m.dat	03m.dat
7	16420m.dat	chf04m.dat	05m.dat
8	16483m.dat	chf05m.dat	06m.dat
9	16539m.dat	chf06m.dat	07m.dat
10	16773m.dat	chf09m.dat	08m.dat
11	17052m.dat	chf10m.dat	10m.dat
12	17453m.dat	chf11m.dat	00m.dat
13	18177m.dat	chf13m.dat	01m.dat
14	18184m.dat	chf14m.dat	13m.dat
15	19088m.dat	chf15m.dat	16m.dat

(AF) (ECG sample frequency: 128 Hz) selected from the Physionet database [11]. Table 1 lists the files used. The first five subjects of each group are those of the CHAOS Controversial Topics in Nonlinear Dynamics "Is the Normal Heart Rate Chaotic? Data for study (http://physionet.org/challenge/chaos/)." The other ten subjects from each group are randomly selected records from the same databases.

3 DDE Analysis

Typically, a nonlinear delay differential equation has the form

$$\begin{aligned}\dot{x} &= f(a_i, x_{\tau j}) \\ &= a_1 x_{\tau_1} + a_2 x_{\tau_2} + a_3 x_{\tau_3} + \cdots + a_{i-1} x_{\tau_n} \\ &\quad + a_i x_{\tau_1}^2 + a_{i+1} x_{\tau_1} x_{\tau_2} + a_{i+2} x_{\tau_1} x_{\tau_3} + \cdots \\ &\quad + a_{j-1} x_{\tau_n}^2 + a_j x_{\tau_1}^3 + a_{j+1} x_{\tau_1} 2 x_{\tau_2} + \cdots \\ &\quad \vdots \\ &\quad \cdots + a_l x_{\tau_n}^m \end{aligned} \tag{1}$$

where $x = x(t)$ and $x_{\tau_j} = x(t-\tau_j)$. In the form (1), a DDE has n delays, l monomials with coefficients $a_1, a_2, \ldots, a_l$, and a degree m of nonlinearity. By a k-term DDE, we mean a DDE with k monomials selected from the right-hand side of Eq. (1). Although quite flexible, as for any global modeling technique there is a significant gain in accuracy by carefully selecting the structure of the model [12–14]. By structure selection or model learning, we mean retaining only those monomials that make the most significant contribution to the data dynamics. An equally important task is to select the right time-delays, since they are directly related to the primary time-scales and nonlinear couplings between them of the dynamics under study.

Lainscsek et al. [14] used a genetic algorithm to find a single DDE model for the classification of Parkinson movement data. Here we want to do an exhaustive search of models and delays to find the terms in Eq.(1) that best separate classes of data. To do so we look at all possible polynomial DDE models up to third order

$$\begin{aligned}\dot{x} = {} & a_1 x_{\tau_1} + a_2 x_{\tau_2} \\ & + a_3 x_{\tau_1}^2 + a_4 x_{\tau_1} x_{\tau_2} + a_5 x_{\tau_2}^2 \\ & + a_6 x_{\tau_1}^3 + a_7 x_{\tau_1}^2 x_{\tau_2} + a_8 x_{\tau_1} x_{\tau_2}^2 + a_9 x_{\tau 2}^3 \end{aligned} \tag{2}$$

with some of the a_i equal to zero. Only models with up to three terms are considered. If the analysis did not give any satisfactory results additional delays, increase the order of nonlinearity and/or use DDEs with more than three terms would be needed. There are 5 one-term models, 18 two-term models, and 32 three-term models.

Tables 2 and 3 list all these models. Note that e.g. the DDE models $\dot{x} = a_1 x_{\tau_1} + a_2 x_{\tau_1} x_{\tau_2}$ and $\dot{x} = a_1 x_{\tau_2} + a_2 x_{\tau_1} x_{\tau_2}$ are the same with exchanged delays τ_1 and τ_2. Therefore only the first of these two models was used. All such redundant DDE models were omitted. There are two linear DDEs (model 1 and 5) while all others are nonlinear. Seven of the DDEs have only one delay (models 1, 2, 4, 7, 9, 17, and 30) and nine models are symmetric (models 3, 6, 16, 22, 23, 25, 43, 52, 53) with two interchangeable delays.

The data were analyzed without filtering or artifact removal from the data. The NSR and AF data were sampled at 128 Hz, while the CHF data were sampled at 250 Hz. To use the same DDE with the same delays for all data, the NSR and AF data were upsampled using the MATLAB function resample [15] with the default options. Throughout this paper we use 5 min non-overlapping data windows for our analysis. Each window was renormalized to zero mean and unit variance to be able to compare data of different origin. The derivatives were computed numerically with an center difference algorithm [16].

For our supervised model selection task, we have to choose a classifier, select training data, select a classification tool, and cross-validate to take the small number of subjects into account. Here we chose seven different classifiers and tested the performance of each separately. Those classifiers are: (1) NSR versus AF versus CHF, (2) NSR versus AF, (3) NSR versus CHF, (4) AF versus CHF, (5) NSR versus (AF and CHF), (6) AF versus (NSR and CHF), and (7) CHF versus (NSR and AF). As training data we selected one 5 min data window every 20 min (e.g. for a 20 h

Table 2 One- and two-term DDE models. An 'x' denotes that the term a is nonzero. The different types of models are: L - linear, S - symmetric, 1 - single delay DDE. All other DDEs are nonlinear and have two non-interchangeable delays

Model #	a1 x_1	a2 x_2	a3 x_1^2	a4 x_1x_2	a5 x_2^2	a6 x_1^3	a7 $x_1^2x_2$	a8 $x_1x_2^2$	a9 x_2^3	Model type
1	×									1, L
2			×							1
3				×						S
4						×				1
5							×			
6	×	×								S, L
7	×		×							1
8	×			×						
9	×					×				1
10	×						×			
11		×	×							
12		×		×						
13		×				×				
14		×					×			
15			×	×						
16			×		×					S
17			×			×				1
18			×				×			
19				×		×				
20				×			×			
21						×	×			
22						×				S
23								×	×	S

recording of one subject 65 min data windows were used). We used repeated random sub-sampling validation [17] where we trained on 10 subjects of each group and tested on the remaining 5 subjects of each group. This was repeated 300 times with each subject equally often used as training and testing subject. As classifier we used singular value decomposition (SVD) [18]. The measure of performance was Cohens kappa κ [19–22] which can be computed directly from the confusion matrix [23]. A confusion matrix (also known as matching matrix, contingency table, or error matrix) is a specific table layout that allows visualization of the performance. Each column of the matrix represents the instances in a predicted class, while each row represents the instances in an actual class. A kappa value of one indicates perfect separation while a kappa value of zero indicates no separation of the 2 classes.

The best models and delays for the seven classification tasks can be selected in two different ways: Given the 55 different DDE models (see Tables 2 and 3) and all possible delays ranging from 1 to 100 time-steps (1 time-step is $\frac{1}{250}$ seconds since the sampling rate is 250 Hz) we have 431,350 different model/delay combinations. For each of those model/delay combinations the repeated random sub-sampling vali-

Table 3 Three term DDE models. An x denotes that the term a is nonzero. The different types of models are: L - linear, S - symmetric, 1 - single delay DDE. All other DDEs are nonlinear and have two non-interchangeable delays

Model #	a1 x_1	a2 x_2	a3 x_1^2	a4 x_1x_2	a5 x_2^2	a6 x_1^3	a7 $x_1^2x_2$	a8 $x_1x_2^2$	a9 x_2^3	Model type
24	×	×	×							
25	×	×		×						S
26	×	×				×				
27	×	×					×			
28	×		×	×						
29	×		×		×					
30	×		×			×				1
31	×		×				×			
32	×			×		×				
33	×			×				×		
34	×					×	×			
35	×					×			×	
36	×						×	×		
37		×	×	×						
38		×	×			×				
39		×	×				×			
40		×		×		×				
41		×		×			×			
42		×				×	×			
43			×	×	×					S
44			×	×		×				
45			×	×			×			
46			×		×					
47			×		×		×			
48			×			×	×			
49			×			×			×	
50			×				×	×		
51				×		×	×			
52				×		×			×	S
53				×			×	×		S
54						×	×	×		
55						×	×		×	

dation yields 300 different Cohen kappa values. We could take the mean over the 300 kappa values for each candidate model and select the model with the highest mean. We otherwise could look for the best worst case scenario: search the highest minimal value for each of the 300 kappa values and then report the mean of this model. For either strategy we would get a different model. In [24] we chose to pursue the second strategy while we here go for the first. Figure 1 illustrates for distinguishing between NSR and AF that the two approaches are highly correlated. In the case of

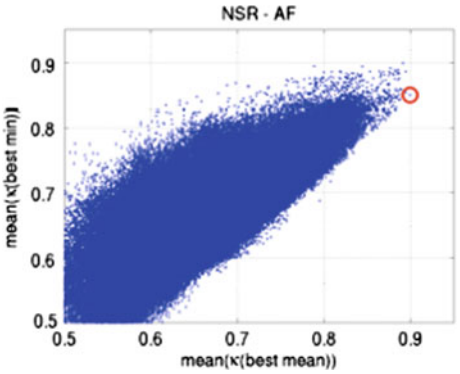

Fig. 1 Good model selection strategies: highest mean method versus best worst case scenario method. The selected value for both strategies is marked with a circle

Table 4 Best DDE models selected for the seven classification tasks. The 5th column lists the mean kappa value from the sub-sampling validation for the listed model and delays. The last column lists the kappa for all data using the mean weights from the sub-sampling validation. The delays are reported in time steps, where 1 time step is $\frac{1}{250}$ second giving a sampling rate of 250 Hz

Classifier	Model #	Delays		Mean (κ)	κ_{all}
NSR-AF-CHF	46	14	1	0.78 ± 0.07	0.83
NSR-AF	32	12	18	0.90 ± 0.07	0.96
NSR-CHF	39	15	8	0.99 ± 0.02	0.99
AF-CHF	51	5	49	0.81 ± 0.10	0.85
NSR-(AF, CHF)	32	12	18	0.93 ± 0.05	0.97
AF-(NSR, CHF)	38	16	3	0.64 ± 0.10	0.72
CHF-(NSR, AF)	25	1	5	0.84 ± 0.09	0.88

Table 5 List of SVD target values for the sub-sampling validation

Classifier	Classification	Target		
#	task	NSR	AF	CHF
1	NSR-AF-CHF	−1	0	1
2	NSR-AF	−1	1	
3	NSR-CHF	−1		1
4	AF-CHF		−1	1
5	NSR-(AF,CHF)	−1	1	1
6	AF-(NSR,CHF)	1	−1	1
7	CHF-(NSR,AF)	1	1	−1

choosing the best mean model we would get a mean kappa value of 0.90 while for the best worst case scenario choice the mean kappa value would be 0.85. Also the selected models are quite different: For the best mean a 3 term model with 1 linear and 2 nonlinear terms was selected while for the second approach a 2 term model with 2 nonlinear terms was selected. For this classifier the difference is big, while for most of the others (except AF CHF) the difference is neglectable. Table 4 lists the so selected best models and delays using the first approach. The mean of the 300 SVD weights from the sub-sampling validation for the selected model is then used

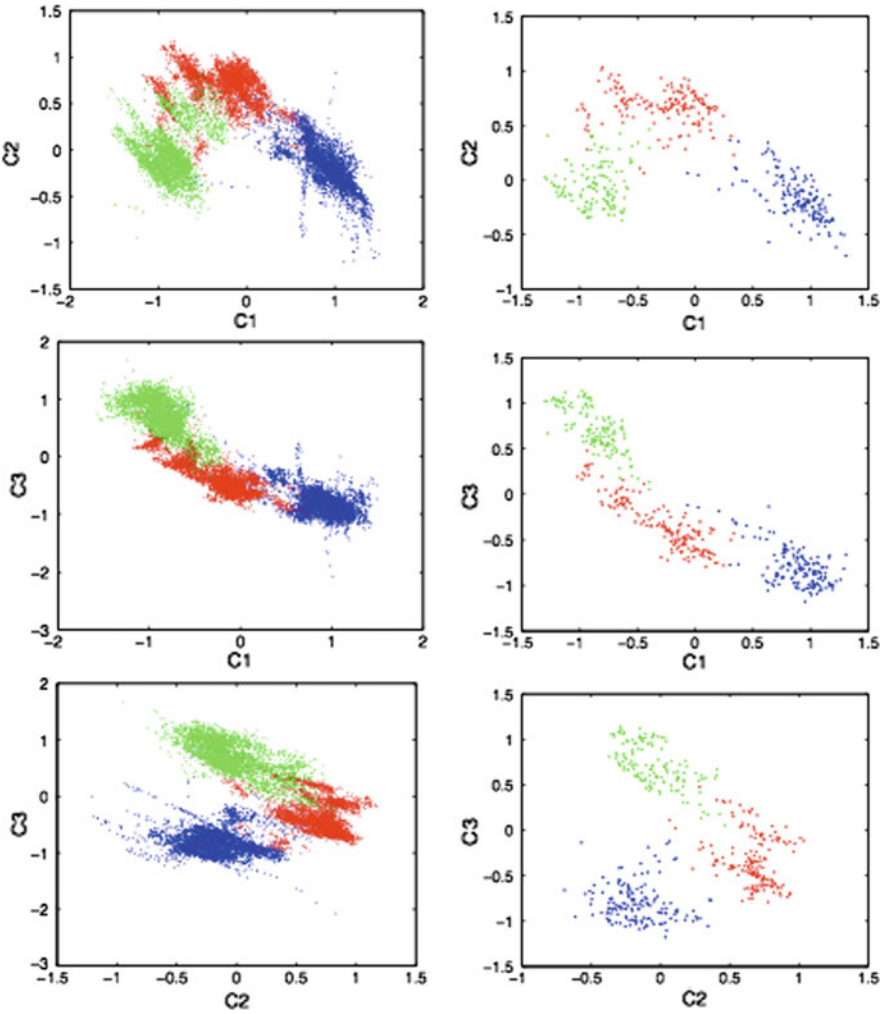

Fig. 2 Combined classifier outputs from Eq. (3). The left column shows the features for all 5 min data windows and the right column shows the outputs for 2 h data segments

to compute the kappa value on all data (all 5 min data windows). These values are listed in the last column in Table 4.

Table 5 lists the SVD target values for each data class. We combined all seven classifiers of Table 4 in the following way: C1 is the mean of all targets when NSR is $+1$ and others are -1, C2 is the mean of all targets when AF is $+1$ and others are -1, and C3 is the mean of all targets when CHF is $+1$ and others are -1:

Table 6 Classification performance of all 2 h data windows for all 15 subjects of each condition computed by combining all 7 classifiers in Table 4

	NSR			AF			CHF		
	% classified as								
	NSR	AF	CHF	NSR	AF	CHF	NSR	AF	CHF
1	100.0	0.0	0.0	0.0	100.0	0.0	0.0	0.0	100.0
2	99.9	9.1	0.0	0.0	100.0	0.0	0.0	0.0	100.0
3	100.0	0.0	0.0	0.0	100.0	0.0	0.0	0.0	100.0
4	100.0	0.0	0.0	0.0	100.0	0.0	0.0	0.0	100.0
5	100.0	0.0	0.0	0.0	100.0	0.0	0.0	0.0	100.0
6	100.0	0.0	0.0	0.0	100.0	0.0	0.0	0.0	100.0
7	100.0	0.0	0.0	0.0	100.0	0.0	0.0	11.1	88.9
8	100.0	0.0	0.0	0.0	100.0	0.0	0.0	0.0	100.0
9	100.0	0.0	0.0	0.0	100.0	0.0	0.0	33.3	66.7
10	100.0	0.0	0.0	0.0	100.0	0.0	0.0	11.1	88.9
11	100.0	0.0	0.0	0.0	100.0	0.0	0.0	11.1	88.9
12	100.0	0.0	0.0	0.0	100.0	0.0	0.0	0.0	100.0
13	100.0	0.0	0.0	0.0	100.0	0.0	0.0	0.0	100.0
14	100.0	0.0	0.0	0.0	100.0	0.0	0.0	0.0	100.0
15	100.0	0.0	0.0	0.0	90.9	9.1	0.0	0.0	100.0
Mean	99.4	0.6	0.0	0.0	99.4	0.0	0.0	4.4	95.6

$$
\begin{aligned}
C1 &= mean(2round(-C_1) - 0.5, -C_2, -C_3, -C_5, C_6, C_7) \\
C2 &= mean(1 - 2|round(C_1)|, C_2, -C_4, C_5, -C_6, C_7) \\
C3 &= mean(round(C_1) - 0.5, C_3, C_4, C_5, C_6, -C_7)
\end{aligned} \tag{3}
$$

where C_i denotes the features (distances from the SVD hyperplane) for the 7 ($i = 1, 2, \ldots, 7$) classifiers. Figure 2 shows the combined classifier outputs from Eq. (3) for 5 min data windows (left column) as well as for 2 h data segments (right column). The three classes are fairly well separated. Table 6 then lists the classification performance of all 2 h windows for each of the 15 subjects and 3 data classes using Eq. (3). NSR and AF can be detected with 99 % accuracy and CHF were detected with 96 % accuracy (Fig. 2).

4 Conclusion

We analyzed 24 h ECG data from healthy subjects and patients with either atrial fibrillation or congestive heart failure downloaded from the the Physionet database. While most published papers on this data set use the heart rate variability (HRV), the time interval between heart beats, we used the waveforms themselves. HRV analysis needs sophisticated pre-processing to automatically annotate that the time intervals

between the heart beats. HRV analysis is highly sensitive to artifact and errors and it is critical to manage artifact and time-interval detection errors appropriately prior to performing any HRV analyses. Using the data waveforms themselves, this is not an issue.

We analyzed the data using DDEs. The data were sampled at different sampling rates and we therefore upsampled the NSR and AF data to the same sampling rate as the CHF data. No other pre-processing of the data was done. We segmented the data into 5 min non-overlapping independent data windows and selected a subset of the data to select the best DDE models. This was done in a supervised way using repeated random sub-sampling validation. We searched for models that separated the different classes best. The so obtained models were then tested on the whole data set using 5 min and 2 h data segments. For the 5 min data windows we could separate the different data classes with a 72 % to 99 % accuracy. The models were also tested on 2 h data windows and achieved a 95 % to 99 % accuracy on all classes, NSR, AF and CHF.

References

1. R. Driver, Ordinary and Delay Differential Equations, Applied Mathematical Sciences, vol. 20 (Springer-Verlag, 1977)
2. G. Clifford, F (Azuaje, P McSharry, Advanced methods and tools for ECG data analysis (Artech House, 2006)
3. Ann Whitney, Math. **37**, 645 (1936)
4. N.H. Packard, J.P. Crutchfield, J.D. Farmer, R.S. Shaw, Phys. Rev. Lett. **45**, 712 (1980)
5. F. Takens, In dynamical systems and turbulence, Warwick 1980, Lecture Notes in Mathematics, ed. by D.A. Rand, L.S. Young (Springer, Berlin/Heidelberg 1981. Lecture Notes in Mathematics **898**, 366381 (1980)
6. T. Sauer, J.A. Yorke, M. Casdagli, J. Stat. Phys. **65**, 579 (1991)
7. K. Judd, A. Mees, Physica D **120**, 273 (1998)
8. G. Gouesbet, Phys. Rev. A **43**(10), 5321 (1991)
9. B. Bezruchko, D. Smirnov, Phys. Rev. E **63**, 016207 (2000)
10. C. Lainscsek, Phys. Rev. E **84**, 046205 (2011)
11. A. Goldberger, L. Amaral, L. Glass, J. Hausdorff, P. Ivanov, R. Mark, J. Mietus, G. Moody, C. Peng, H. Stanley, Circ. **101**, E215 (2000)
12. L.A. Aguirre, S.A. Billings, Int. J. Control **62**(3), 569 (1995)
13. C. Lainscsek, C. Letellier, I. Gorodnitsky, Phys. Lett. A **314**, 409 (2003)
14. C. Lainscsek, P. Rowat, L. Schettino, D. Lee, D. Song, C. Letellier, H. Poizner, Chaos **22**, 013119 (2012)
15. URL http://www.mathworks.com/help/toolbox/ident/ref/resample.html
16. E. Miletics, G. Moln arka, Comput. Math. Appl. **50**(7), 1167 (2005)
17. R. Kohavi, (Morgan Kaufmann, 1995), pp. 11371143.
18. W. Press, B. Flannery, S. Teukolsky, *W* (Numerical recipes in C, Cambridge University Press, Vetterling, 1990)
19. G. Cardillo (2009).URL http://www.mathworks.com/matlabcentral/fileexchange/15365-cohens-kappa/content/kappa.m
20. W. Scott, Public Opinion Quarterly (1955).
21. J. Cohen, Educ. Psychol. Measur. **20**(1), 37 (1960)
22. J. Fleiss, J. Cohen, Educ. Psychol. Measur. **33**, 613 (1973)
23. R. Kohavi, F. Provost, Machine Learning **30**(2/3), 271 (1998)
24. C. Lainscsek, T.J. Sejnowski, Chaos **23**(2), 023132 (2013)

Voltage Response of Non-Uniform Arrays of Bi-SQUIDs

Patrick Longhini, Susan Berggren, Anna Leese de Escobar, Antonio Palacios, Sarah Rice, Benjamin Taylor, Visarath In, Oleg A. Mukhanov, Georgy Prokopenko, Martin Nisenoff, Edmond Wong and Marcio C. De Andrade

Abstract Multi-loop arrays of Josephson Junctions (JJ) with non-uniform area distributions, which are known as Superconducting Quantum Interference Filters (SQIF), are the most highly sensitive sensors of changes in applied magnetic field as well as the absolute magnitude of magnetic fields. The non-uniformity of the loop sizes allows the array to produce a unique collective voltage response that has a pronounced single peak with a large voltage swing around zero magnetic field. To obtain high linear dynamic range, which is critical for a wide variety of applications, the linearity of the slope of the anti-peak response must be improved. We propose a novel scheme for enhancing linearity—a new configuration combining the SQIF array concept with the recently introduced bi-SQUID configuration, in which each individual SQUID loop is made up of three JJs as oppose to using two JJs per loop in standard DC SQUIDs. We show, computationally, that the additional junction offers a viable linearization method for optimizing the voltage response and dynamic range of SQIF arrays. We have realized SQIF arrays based on bi-SQUID cells and present first experimental results.

P. Longhini (✉) · A. L. de Escobar · S. Rice · B. Taylor · V. In · E. Wong · M. C. De Andrade
Space and Naval Warfare Systems Center, 53560 Hull Street, San Diego, CA 92152-5001, USA
e-mail: patrick.longhini@navy.mil

S. Berggren · A. Palacios
Nonlinear Dynamical Systems Group, Department of Mathematics, San Diego State University, San Diego, CA 92182, USA

O. A. Mukhanov · G. Prokopenko
HYPRES, Inc., 175 Clearbrook Road, Elmsford, NY 10523, USA

M. Nisenoff
M. Nisenoff Associates, 1201 Yale Place, Suite 1004, Minneapolis, MN 55403, USA

V. In et al. (eds.), *International Conference on Theory and Application in Nonlinear Dynamics (ICAND 2012)*, Understanding Complex Systems,
DOI: 10.1007/978-3-319-02925-2_7,

1 Introduction

The Superconductive Quantum Interference Device (SQUID) is one of the most sensitive magnetic field devices, and is used for wide range of applications including biology, medicine, geology, systems for semiconductor circuit diagnostics, security MRI and even cosmology research [1, 2]. In recent years, arrays of coupled oscillators have been considered as a general mechanism for improving signal detection and amplification [3]. Indeed, theoretical [4, 5] and experimental studies [6] have shown that arrays of SQUIDs can yield comparable improvements in signal output, relative to background noise, over those of a single device. A peculiar configuration that has gained considerable attention among the physics and engineering community is that of multi-loop arrays of JJs with non-uniformly distributed loop areas. Typically, each loop contains two JJs, i.e., a standard DC SQUID, but their size vary from loop to loop. These types of unconventional geometric structures of JJs are known to exhibit a magnetic flux dependent voltage response $V(\varphi_e)$, where φ_e denotes an external magnetic flux normalized by the quantum flux, that has a pronounced single peak with a large voltage swing at zero magnetic field. The potential high dynamic range and linearity of the anti-peak voltage response render the array an ideal detector of absolute strength of external magnetic fields, so these arrays are also commonly known as Superconducting Quantum Interference Filters (SQIFs). Since it was theoretically proposed [7, 8] and experimentally demonstrated for the first time [9] the SQIF concept is investigated and exploited by a continuously growing number of groups with respect to its basic properties [10, 11] and its suitability in various fields of application like magnetometry and RF electronics.

In this paper, we investigate numerically and experimentally a different approach, one that involves a change in the configuration of the array. Mainly, each individual array cell will now contain three JJs as oppose to the standard practice of two JJs per loop. These new type of SQUIDs are also known as bi-SQUIDs because the additional junction and main inductance form an additional single-junction SQUID. Since its invention in 2009 [12], theoretical works have shown that the voltage response of individual bi-SQUIDs can lead to achieving a response linearity close to 120 dB [12, 13]. The uniform arrays of bi-SQUIDs were also investigated and showed significant improvement in the response linearity in comparison with arrays of conventional dc SQUIDs. However, the linearity improvement was also quite sensitive to the fabrication spread in JJ critical currents resulting in some degradation of the array transfer function [14–16]. We consider serial and parallel multi-loop arrays of non-uniform bi-SQUIDs and examine in great detail their voltage response as a function of controlled parameters, including: inductive coupling between loops, number of loops, bias current, and distribution of loop areas.

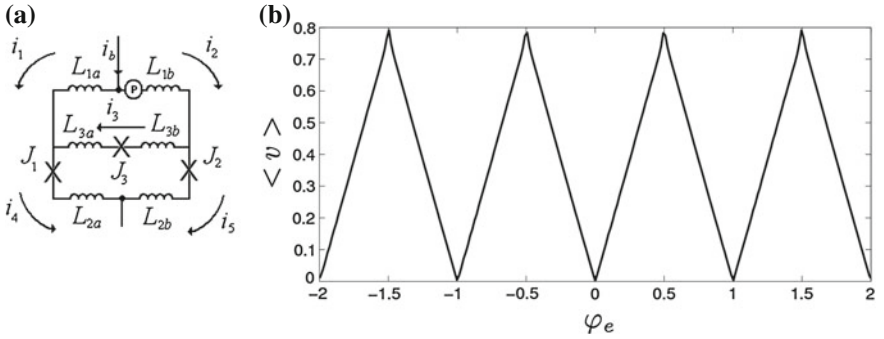

Fig. 1 **a** Circuit representation of a DC bi-SQUID device. 'P' is a phase source that accounts for the phase shift due to the external magnetic flux φ_e. **b** its time-averaged voltage response between the two junctions, as a function of the normalized external magnetic flux φ_e

2 Background

2.1 The DC Bi-SQUID

The DC bi-SQUID was originally introduced by Kornev et al. [12, 13] as a modified version of a conventional SQUID device but with the ability to produce a highly linear voltage response. Figure 1 shows a schematic diagram of the proposed bi-SQUID device. The main modification is the addition of a nonlinear inductance, in the form of a third Josephson Junction. This third junction, when combined with the main inductance in the loop, acts as a single-junction SQUID thus leading to a combined bi-SQUID system. More importantly, the works in Refs. [12, 13] demonstrate that tuning of the nonlinear inductance, through the critical current of the junctions, can lead to significant improvements in the linearity of the $V(\varphi_e)$ curve.

Figure 1a shows a circuit design of a bi-SQUID device in which the individual inductances, L_{ja} and L_{jb}, where $j = 1, 2, 3$, were added to resemble as close as possible the actual fabricated bi-SQUID thin-film structure.

Assuming identical junctions, direct calculations lead to the following governing equations for the phase dynamics:

$$\begin{aligned}
(L_1 + L_{2a})\,\dot{\varphi}_1 - L_{2b}\dot{\varphi}_2 - L_1\dot{\varphi}_3 &= L_{1b}i_b + \varphi_2 - \varphi_1 + 2\,\pi\varphi_e a_n + L_1 i_{c3}\sin\varphi_3 \\
&\quad + L_{2b}\sin\varphi_2 - (L_1 + L_{2a})\sin\varphi_1 \\
L_{2a}\dot{\varphi}_1 - (L_1 + L_{2b})\dot{\varphi}_2 - L_1\dot{\varphi}_3 &= -L_{1a}i_b + \varphi_2 - \varphi_1 + 2\pi\varphi_e a_n + L_1 i_{c3}\sin\varphi_3 \\
&\quad - L_{2a}\sin\varphi_1 + (L_1 + L_{2b})\sin\varphi_2 \qquad (1) \\
L_{2a}\dot{\varphi}_1 - L_{2b}\dot{\varphi}_2 - (L_{3a} + L_{3b})\dot{\varphi}_3 &= \varphi_2 - \varphi_3 + \varphi_1 - (L_{3a} + L_{3b})\,i_{c3}\sin\varphi_3 \\
&\quad - L_{2a}\sin\varphi_1 + L_{2b}\sin\varphi_2,
\end{aligned}$$

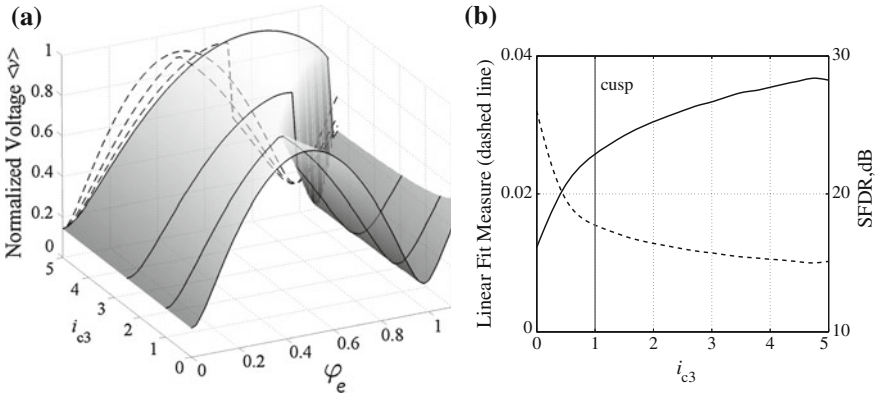

Fig. 2 **a** Numerical simulations of the voltage response of a single bi-SQUID as a function of the critical current i_{c3}. Parameters are: $i_b = 2$, $a_n = 1$, $L_{1a} = L_{1b} = 0.27$, $L_{2a} = L_{2b} = 0.24$, and $L_{3a} = L_{3b} = 0.3$. **b** Linearity test via linear fitting error and through calculations of Spur Free Dynamic Range (SFDR). Observe that best linear response is directly correlated with highest SFDR. Development of cusp for $i_{c3} > 1$

where φ_i are the phases on each of the junctions J_n, $n = 1, 2, 3$, $L_1 = (L_{1a} + L_{1b})$, $i_{c3} = I_{c3}/I_c$, is the normalized critical current across the third junction J_3, $I_{c1} = I_{c2} = I_c$, a_n is a nonlinearity parameter related to the loop size between J_1 and J_2, and $(\dot{})$ denotes differentiation with respect to the normalized time $\tau = \omega_c t$, $\omega_c = 2\pi V_c/\Phi_0$, $V_c = I_c R_N$. Figure 1(bottom) illustrates the average voltage response of a bi-SQUID device obtained numerically by integrating Eq. (1) and then calculating $< v >$ through

$$< v >= \frac{1}{T}\int_0^T \left(\frac{\dot{\varphi_1} + \dot{\varphi_2}}{2}\right) \tag{2}$$

with the following parameters: $i_b = 2$, $a_n = 1$, $L_{1a} = L_{1b} = 0.27$, $L_{2a} = L_{2b} = 0.24$, $L_{3a} = L_{3b} = 0.3$. The voltage response of the bi-SQUID is significantly more linear than that of the conventional SQUID. In fact, a linear fitting (not shown for brevity) of the $V(\varphi_e)$ curve confirms an almost perfect match with a straight line.

In Fig. 2 we now explore the effects of changing the nonlinear inductance on the linearity of the average voltage response curve $V(\varphi_e)$. Parameter values are the same as in Fig. 1(bottom) except that now the critical current i_{c3} is varied. The dashed lines in Fig. 2 are the projections of the individual voltage response curves (solid curves) for the particular values of $i_{c3} = 0$, 1, and 2.5. At small magnitudes of the critical current i_{c3}, the shape of the voltage response curve closely resembles that of a conventional SQUID. As the parameter i_{c3} increases, the transfer function linearity increases while the voltage response approaches a triangular shape. For larger values of the $i_{c3} > 1.0$ parameter, the voltage response curve develops a cusp which results in a hysteresis loop and a decrease in linearity. Thus, there appears to

be an optimal value of the critical current i_{c3}, located at intermediate magnitudes, where a bi-SQUID device can generate the most linear voltage response. To find that optimal value using SFDR, we compute the linearity of the voltage response as in Ref. [12], i.e., by biasing a single tone sinusoidal flux input at $\Phi_0/4$ with amplitude A, were $A/A_{max} = 0.3$ given that A_{max} corresponds to the flux amplitude $\Phi_0/4$ and then measuring the total harmonic distortion. Another approach for computing linearity is to calculate the slope of the voltage response and then fit a line using the nonlinear least squares method. Thus, our linear fit measure is computed by using the error from the linear fit and then dividing by the square of the slope of $V(\varphi_e)$ at the individual working point for each individual value of i_{c3}. Again we bias the sinusoidal flux input at $\Phi_0/4$ with an amplitude of $A/A_{max} = 0.3$. Note that the fitting of the line corresponds to the same amplitude as used in the SFDR. In Fig. 2b there is no loss in linearity because we never exceed the according branch of the hysteresis loop during the calculation of the fit error and SFDR. The linear fit measure can then be used as a test for linearity, i.e., small values would be indicative of high linearity. Likewise, large SFDR would indicate high linearity. In this work we adopted the nonlinear least squares approach and the results are shown in Fig. 2b.

Experiments with non-uniform multi-loop serial arrays of conventional SQUIDs have shown that the voltage swing of the response curve $V(\varphi_e)$ increases proportionally to the number of SQUIDs in the array. This critical observation should extend in a natural way to arrays of bi-SQUIDs with the potential for increasing SFDR and linearity beyond the values shown in Fig. 2. We explore this hypothesis next with two types of bi-SQUID arrays, one where the loops are connected serially and one where they are connected in parallel.

3 Serial Bi-SQUID Array

Generically, a serial array of N SQUIDs is able to yield a significantly higher output power than a single SQUID. In particular, dynamic range is known to increase as $N^{1/2}$ in the presence of thermal noise [11]. Furthermore, as suggested in Refs. [12, 13], a serial bi-SQUID array can be designed to produce a voltage output with a unique "anti-peak" at the zero applied magnetic flux. Thus, in principle, serial arrays of bi-SQUIDs can be implemented to produce a voltage anti-peak response with increased dynamic range and improved voltage linearity. Indeed, the motivation of this work is to build a (serial) SQIF [7, 8] array consisting of bi-SQUIDs. To pursue this goal, we consider in this section a serial array of N bi-SQUIDs, designed as is shown in Fig. 3. The phase dynamics of the serial array shown in Fig. 3 is described by the following system of differential equations.

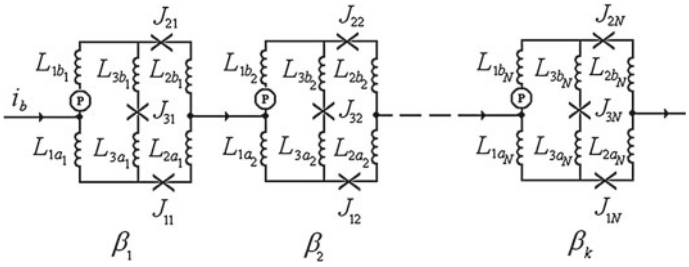

Fig. 3 Circuit representation of an array of bi-SQUID devices connected in series. 'P' is a phase source that accounts for the phase shift due to the external magnetic flux φ_e

$$
\begin{aligned}
(L_{1,i}+L_{2a,i})\,\dot{\varphi}_{i,1} - L_{2b,i}\dot{\varphi}_{i,2} - L_{1,i}\dot{\varphi}_{i,3} &= L_{1b,i}i_b + \varphi_{i,2} - \varphi_{i,1} + 2\pi\varphi_e a_{n,i} + M\Phi_i \\
&\quad + L_{1,i}i_{c3,i}\sin\varphi_{i,3} + L_{2b,i}\sin\varphi_{i,2} \\
&\quad - (L_{1,i}+L_{2a,i})\sin\varphi_{i,1} \\
L_{2a,i}\dot{\varphi}_{i,1} - (L_{1,i}+L_{2b,i})\dot{\varphi}_{i,2} - L_{1,i}\dot{\varphi}_{i,3} &= -L_{1a,i}i_b + \varphi_{i,2} - \varphi_{i,1} + 2\pi\varphi_e a_{n,i} + M\Phi_i \\
&\quad + L_{1,i}i_{c3,i}\sin\varphi_{i,3} - L_{2a,i}\sin\varphi_{i,1} \\
&\quad + (L_{1,i}+L_{2b,i})\sin\varphi_{i,2} \qquad (3) \\
L_{2a,i}\dot{\varphi}_{i,1} - L_{2b,i}\dot{\varphi}_{i,2} - (L_{3a,i}+L_{3b,i})\dot{\varphi}_{i,3} &= \varphi_{i,2} - \varphi_{i,3} + \varphi_{i,1} + M\Phi_i \\
&\quad - \left(L_{3a,i}+L_{3b,i}\right)i_{c3,i}\sin\varphi_{i,3} \\
&\quad - L_{2a,i}\sin\varphi_{i,1} + L_{2b,i}\sin\varphi_{i,2},
\end{aligned}
$$

where $\varphi_{i,j}$ are the phases on each of the junctions $J_{i,j}$, $i = 1,\ldots,N$, $j = 1,2,3$, $L_{1,i} = (L_{1a,i} + L_{1b,i})$, $a_{n,i}$ is a parameter related to the loop size between $J_{i,1}$ and $J_{i,2}$, and M is the coupling strength for the phase interaction Φ_i between nearest neighbors—one neighbor for the edge elements, two for the inner elements—according to

$$
\Phi_i = \begin{cases}
\dfrac{1}{a_{n,2}}(\varphi_{2,1} - \varphi_{2,2} - 2\pi\varphi_e a_{n,2}), & \text{for } i = 1 \\
\dfrac{1}{a_{n,i+1}}(\varphi_{i+1,1} - \varphi_{i+1,2} - 2\pi\varphi_e a_{n,i+1}) & \\
\quad + \dfrac{1}{a_{n,i-1}}(\varphi_{i-1,1} - \varphi_{i-1,2} - 2\pi\varphi_e a_{n,i-1}), & \text{for } i = 2,\ldots,N-1 \\
\dfrac{1}{a_{n,N-1}}(\varphi_{N-1,1} - \varphi_{N-1,2} - 2\pi\varphi_e a_{n,N-1}), & \text{for } i = N
\end{cases} \qquad (4)
$$

where, i_b is the bias current, $i_{c3} = I_{c3}/I_c$ is the normalized critical current of the third junction J_3 in each bi-SQUID cell, $a_{n,i}$ is the nonlinearity parameter related to the ith bi-SQUID loop. For simplicity, in this work we assume all inductances to be identical throughout the array. However, the computer code that was written to simulate the voltage response of the array can easily handle the case of non-identical inductances.

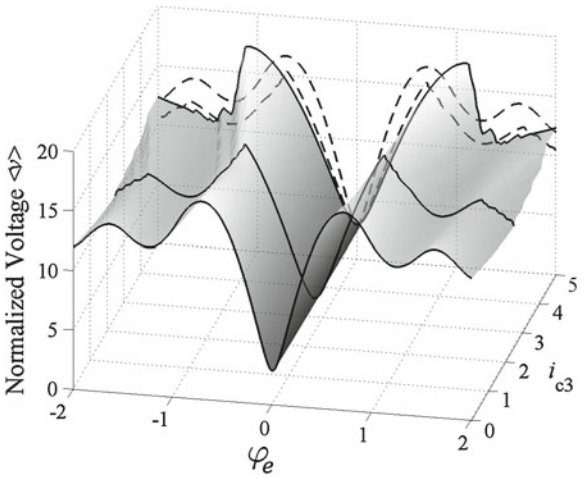

Fig. 4 Numerical simulations of the voltage response of a non-uniform serial bi-SQUID array ($N = 20$) as a function of the critical current i_{c_3} and external flux φ_e. Loop sizes are selected according to a Gaussian distribution. $L_{1a} = L_{1b} = 0.27$, $L_{2a} = L_{2b} = 0.24$, $L_{3a} = L_{3b} = 0.3$, $M = 0.005$

The main differences from the single bi-SQUID are the mutual inductances between elements.

Numerical simulations of Eq. (3) were carried out to explore, computationally, the voltage response of the serial array as a function of the external field φ_e and the critical current i_{c3}. Different distributions of loop sizes were investigated for each array, including: linear, Gaussian, exponential, logarithmic, and equal size. Among them, the Gaussian distribution in a serial array produced the highest linear response around the anti-peak. Note that other distributions excluding the equal sized were very similar to the Gaussian, however, the Gaussian was only slightly better and it would be redundant to display results on the other distributions. From now on in the article we are assuming that the distribution of loop sizes is Gaussian. Figure 4 shows the results of the simulations for a specific array with $N = 20$ bi-SQUID loops with loop sizes that vary according to a Gaussian distribution. As expected, the voltage output forms an anti-peak at $\varphi_e = 0$ magnetic flux and, more importantly, the linearity around the anti-peak appears to be changing as i_{c3} changes. For small magnitudes of that parameter the voltage response curve appears to mimic that of a conventional SQIF device made up of two-junctions per loop. But as the parameter increases the linearity of the anti-peak appears to increase and starts to resemble, near zero flux, the triangular shape of the voltage output of a single bi-SQUID. This numerical exploration suggests that careful adjustment of the critical current parameter can lead to significant improvements of linearity. As we did in Sect. 2 we can also use the least squares approximation method to fit a line to measure linearity. Figure 5 shows the results of the linear fitting and SFDR. Indeed, the error in the linear fitting decreases as i_{c3} increases thus indicating an increase in the linearity of the voltage output. The increase in linearity is similar to what was observed previously in a single bi-SQUID, see Fig. 2, except that now the voltage output does not develop a hysteresis loop so that the linearity does not decrease for larger values of the critical

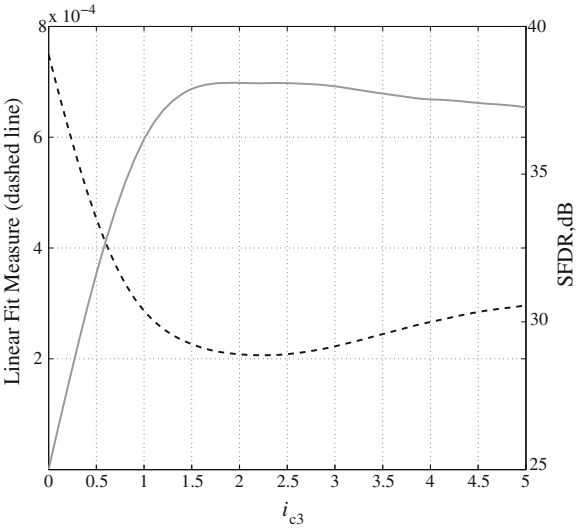

Fig. 5 Linearity test (*dashed line*) via linear fitting error of the voltage response of an array of $N = 20$ bi-SQUID devices connected in series as a function of the critical current i_{c3} and corresponding SFDR (*solid line*). The test shows that there exists a critical current where the error decreases significantly such that the linearity increases. It also shows an optimal value of the critical current where SFDR is optimum and beyond which only marginal improvements in linearity can be achieved

current. Instead, there appears to be a threshold value of the critical current i_{c3} beyond which the linearity remains unchanged as is shown in Fig. 5.

We wish to recall that in the special case of serial arrays the maximum voltage swing $V_{max}(\Phi)$ and transfer factor $\partial V/\partial \Phi$ increase directly proportional to the number of loops N in the array [17, 18] while the thermal noise voltage V_F is proportional to the square root of N. These relations imply that the dynamic range increases as $N^{1/2}$. However, we emphasize that for parallel arrays the situation is different: $V_{max}(\Phi)$ remains constant while the transfer factor $\partial V/\partial \Phi$ still increases proportional to N. Thermal noise voltage V_F scales as $N^{-1/2}$ [6, 9]. Therefore, the dynamic range is given by $V_{max}(\Phi)/V_F = N^{1/2}$.

In the next section we focus on the design of a parallel array of bi-SQUIDs which could also lead to additional benefits in the linearity of the voltage output, specially when the critical current i_c is no longer uniform [20].

4 Parallel Bi-SQUID Array

We now consider a one-dimensional array of N bi-SQUIDs connected in parallel as is shown schematically in Fig. 6. The coupling topology is based on designs discussed in Refs. [20–22]. Observe that now in the parallel array the junctions are

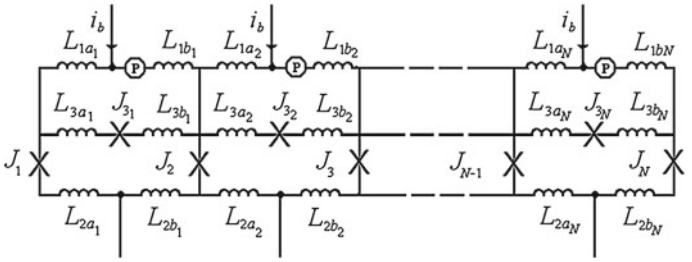

Fig. 6 Circuit representation of an array of bi-SQUID devices connected in parallel. '*P*' is a phase source that accounts for the phase shift due to the external magnetic flux φ_e

shared among neighboring loops, so that the indices of the phase differences ϕ_n of the "classical" SQUID junctions count the junctions and not the loops. This is in direct contrast to the phase differences $\phi_{3,n}$ of the third (bi-SQUID specific) junctions and to the serial arrays where the junctions from one loop to the next are different. As we did in the case of serial arrays, the derivation of the modeling equations was carried out based on conservation of current across the loops.

for $n = 1$:

$$B_1\dot{\varphi}_1 - \left(\frac{L_{2b,1}}{2A_1}\right)\dot{\varphi}_2 - \dot{\varphi}_{3,1} = \left(\frac{1}{A_1}\right)\left(L_{1b,1}i_b + \varphi_2 - \varphi_1 + 2\pi\varphi_e a_{n,1}\right)$$

$$- \left(\frac{L_{2a,1}}{A_1} + 1\right)\sin\varphi_1 + \left(\frac{L_{2b,1}}{2A_1}\right)\sin\varphi_2 + i_{c3,1}\sin\varphi_{3,1},$$

$$L_{2a,1}\dot{\varphi}_1 - \frac{L_{2b,1}}{2}\dot{\varphi}_2 + C_1\dot{\varphi}_{3,1} = \varphi_2 - \varphi_1 - \varphi_{3,1} - L_{2a,1}\sin\varphi_1 + \frac{L_{2b,1}}{2}\sin\varphi_2$$

$$- C_1 i_{c3,1}\sin\varphi_{3,1},$$

for $n = 2 \ldots N$:

$$\left(\frac{L_{2a,n-1}}{2A_{n-1}}\right)\dot{\varphi}_{n-1} - \frac{B_n}{2}\dot{\varphi}_n$$

$$\left(\frac{L_{2b,n}}{2A_n}\right)\dot{\varphi}_{n+1} + \dot{\varphi}_{3,n} - \dot{\varphi}_{3,n-1} = \left(\left(\frac{L_{1b,n-1}}{A_{n-1}}\right) - \left(\frac{L_{1b,n}}{A_n}\right) - 1\right)i_b$$

$$- \left(\frac{1}{A_n}\right)\left(\varphi_{n+1} - \varphi_n + 2\pi\varphi_e a_{n,n}\right)$$

$$+ \left(\frac{1}{A_{n-1}}\right)\left(\varphi_n - \varphi_{n-1} + 2\pi\varphi_e a_{n,n-1}\right)$$

$$- \left(\frac{L_{2a,n-1}}{2A_{n-1}}\right)\sin\varphi_{n-1} + \frac{B_n}{2}\sin\varphi_n$$

$$- \left(\frac{L_{2b,n}}{2A_n}\right)\sin\varphi_{n+1} - i_{c3,n}\sin\varphi_{3,n} + i_{c3,n-1}\sin\varphi_{3,n-1},$$

$$\frac{L_{2a,n}}{2}\dot{\varphi}_n - \frac{L_{2b}}{2}\dot{\varphi}_{n+1} + C_n\dot{\varphi}_{3,n} = \varphi_{n+1} - \varphi_n - \varphi_{3,n} - \frac{L_{2a,n}}{2}\sin\varphi_n + \frac{L_{2b}}{2}\sin\varphi_{n+1}$$

$$- C_n i_{c3,n}\sin\varphi_{3,n},$$

for $n = N + 1$:

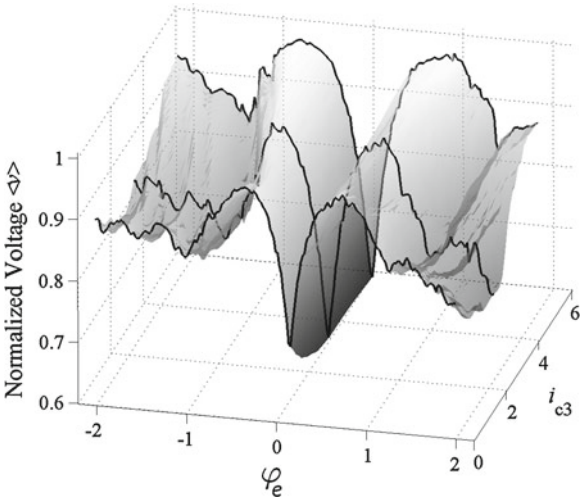

Fig. 7 Numerical simulations of the voltage response of a non-uniform parallel bi-SQUID array as a function of the critical current i_{c_3} and external flux φ_e. Loop sizes are selected according to a Gaussian distribution. Other parameters are the same as in Fig. 4

$$\left(\frac{L_{2a,N}}{2A_N}\right)\dot{\varphi}_N - B_{N+1}\dot{\varphi}_{N+1} - \dot{\varphi}_{3,N} = \left(\frac{1}{A_N}\right)\left(-L_{1b,N}i_b + \varphi_{N+1} - \varphi_N + 2\pi\varphi_e a_{n,N}\right)$$
$$-\left(\frac{L_{2a,N}}{2A_N}\right)\sin\varphi_N + \left(1 + \frac{L_{2b,N}}{A_N}\right)\sin\varphi_{N+1}$$
$$+ i_{c3,N}\sin\varphi_{3,N}, \tag{5}$$

where $A_n = L_{1a,n}+L_{1b,n}$ for $n = 1\ldots N$, $B_1 = \left(\frac{L_{2a,1}}{A_1} + 1\right)$, $B_n = \left(\frac{L_{2a,n}}{A_n} + \frac{L_{2b,n-1}}{A_{n-1}} + 2\right)$ for $n = 2, \ldots, N$, $B_{N+1} = \left(1 + \frac{L_{2b,N}}{A_N}\right)$, $C_n = (L_{3a,1} + L_{3b,1})$ for $n = 1\ldots N$, and φ_n is the phase difference for the nth junction (J_n), i_b is the normalized bias current, $i_{c3,n}$ is the normalized critical current for the third junction of the nth loop and it is assumed to be identical for each loop, Inductances are given by $\mathbf{L_n} = \left[L_{1a,n}, L_{1b,n}, L_{2a,n}, L_{2b,n}, L_{3a,n}, L_{3b,n}\right]$ for $n = 1, \ldots, N$. As we did in the serial case, we can simplify the inductances to $\mathbf{L_n} = a_{n,n}\mathbf{L_1}$, where $a_{n,n}$ corresponds to the n^{th} bi-SQUID loop dynamics. Computer simulations of Eq. (5) were performed to calculate the voltage response of the parallel array of bi-SQUIDs as function of the external field and the critical current i_{c3}. Figure 7 shows a representative example of these simulations for an array of $N = 20$ bi-SQUID loops. All other parameter values are the same as those used to generate Fig. 4. As expected, the parallel array can also produce an anti-peak voltage response centered around zero flux but the linearity appears to be not as good as in the case of a serial array.

5 Experimental Evaluation

We have designed various configurations of bi-SQUID SQIF arrays using HYPRES thin-film fabrication process [23] in order to study various different layout configurations, junction damping, and coupling schemes. Figure 8 shows fabricated chips microphotographs of representative chips, e.g., a set of 256 bi-SQUID-cell arrays connected in series and a set of four different designs of a parallel array with 10 bi-SQUID cells.

Figure 9 shows the measured flux-voltage characteristics of serial and parallel bi-SQUID SQIF arrays (Fig. 8). The measurements were done in liquid Helium using HYPRES cryogenic immersion probe. A DC current bias source was used to set an

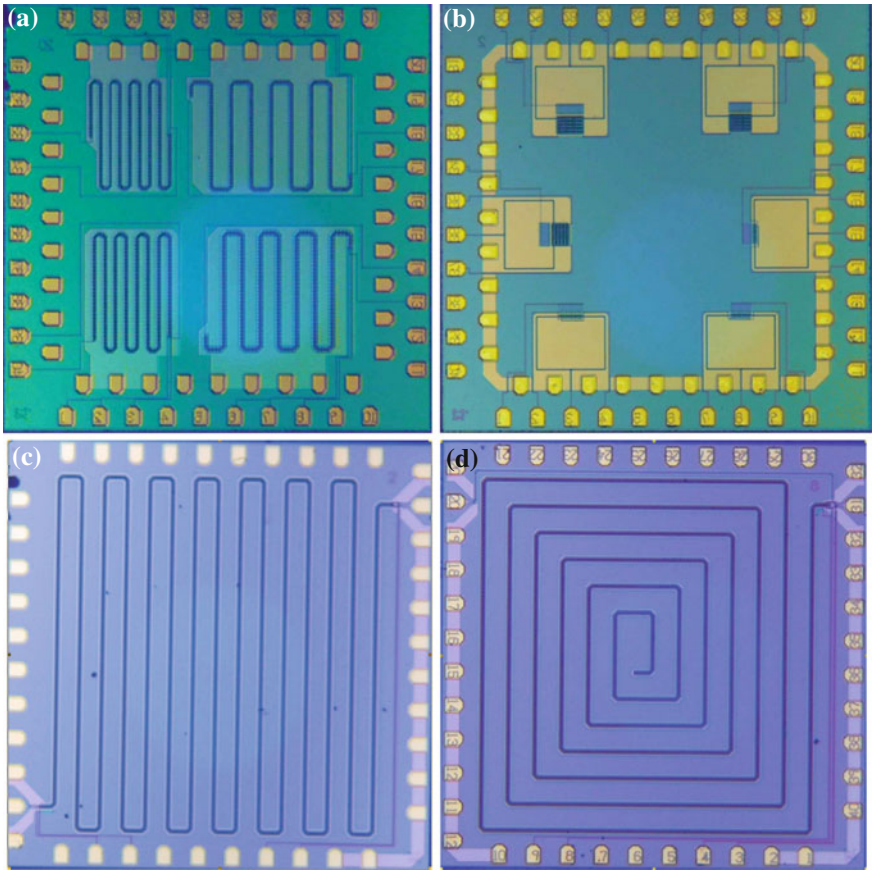

Fig. 8 Microphotographs of the fabricated bi-SQUID-SQIFs integrated on 5 mm × 5 mm chips **a** serial meander arrays consisting of 256 bi-SQUID cells. **b** a set of parallel 10 bi-SQUID cell arrays. **c** Serial meander SQIF array with 1,445 bi-SQUID cells. **d** Serial spiral SQIF array with 1,315 biSQUID cells

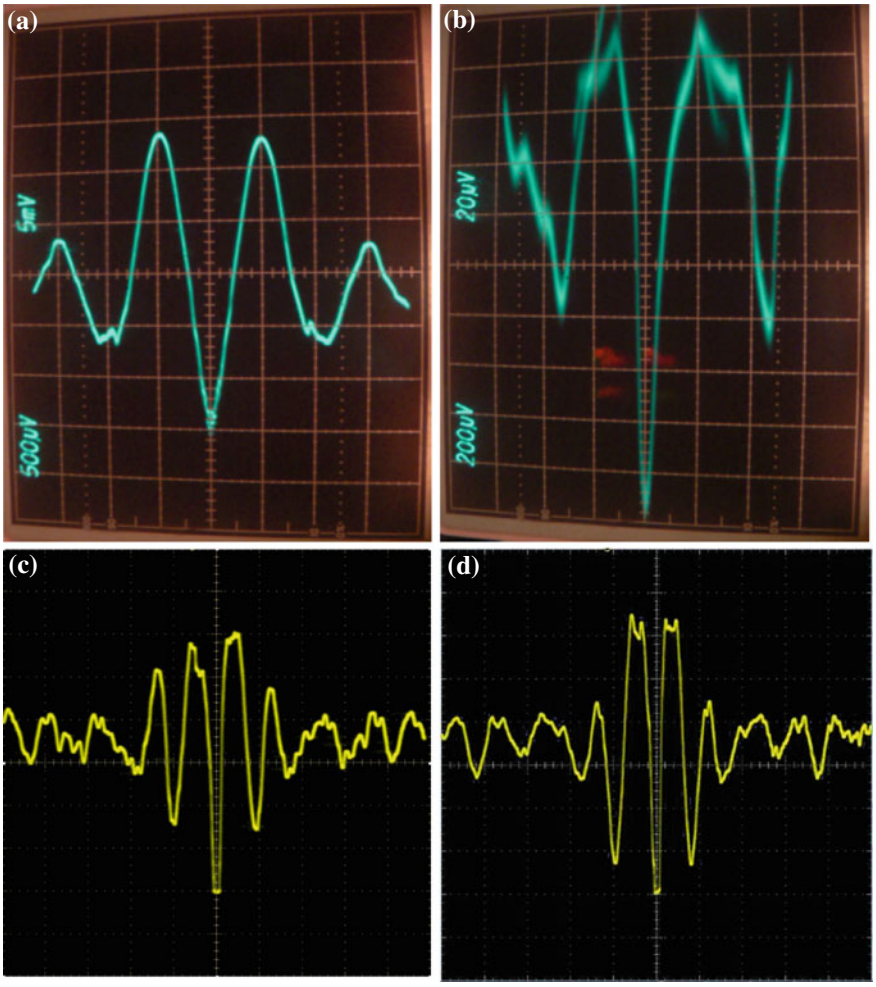

Fig. 9 Measured flux-voltage characteristics of bi-SQUID SQIF arrays: **a** a serial 256 bi-SQUID array. Voltage–Flux (V–F) response with 500 μA/div, 5 mV/div, maximum voltage ∼27 mV, coefficient of transformation is 68.75 mV/mA for $\Phi_0/2$ (Φ_0 is flux quantum); **b** a parallel 10 bi-SQUID array with 200 μA/div, 20 μV/div, maximum voltage ∼0.19 mV, coefficient of transformation is 3.75 mV/mA for $\Phi_0/2$; **c** Serial meander 1,445-cell array with 2 mA/div, 50 mV/div; maximum voltage 295 mV, coefficient of transformation 735 mV/mA for $\Phi_0/2$. **d** Serial spiral 1,315-cell array with 0.5 mA/div, 50 mV/div; maximum voltage 320 mV, coefficient of transformation 3200 mV/mA for $\Phi_0/2$

appropriate bias point for the arrays. A function generator supplied a sweep signal to applied variable flux bias to the arrays via the integrated magnetically coupled control lines.

Experimental measurements shown in Fig. 9 confirm that the collective voltage output of both serial and parallel types of arrays exhibits a pronounced single peak with a large voltage swing about zero magnetic flux. It also shows that bi-SQUIDs can be integrated into SQIF arrays and exhibit a linear response as predicted by results of modeling and simulations.

6 Conclusion

We have studied, analytically, computationally, and experimentally, the behavior of non-uniformarea in multi-loop arrays of Josephson Junctions, also known as Superconducting Quantum Interference Filters. Analytically, we used basic circuit laws to derivemodel equations for the phase across each of the junction. Two types of arrays were considered. One where the multi-loops are connected in series and one where the connections are in parallel. Numerical simulations of the model equations revealed that the collective voltage output of both arrays exhibits a pronounced single peak with a large voltage swing about zero magnetic flux. The shape of the anti-peak is due, mainly, to the non-uniformity of the multi-loop structure while its linearity appears to be directly correlated to parameter i_{c3}. The Gaussian distribution of loop sizes were used in a serial array which produced a clear linear response around the anti-peak. Various configurations of serial and parallel arrays of bi-SQUIDs were designed, fabricated, and tested. The test results validated the theoretical findings: a serial array of bi-SQUIDs with loop sizes spread according to a Gaussian distribution produces a highly linear anti-peak voltage response. The linearity and size of the anti-peak in the serial bi-SQUID array can be optimized by changing the critical current through the third junction of each bi-SQUID element and by changing the number of loops. We anticipate that both serial and parallel bi-SQUID SQIF arrays can be integrated into a two-dimensional (2D) array structure to deliver superior linearity at appropriate impedance. Interweaving the ideas of bi-SQUID and SQIF devices we produced a new devices that can be used as an absolute measurement devices that has improved dynamic range and linearity. Again the linearity is directly related to the spur free dynamic range. For practical application of this device a cross between a parallel series array of bi-SQUID should take advantage of each of the strengths of series and parallel arrays.

Acknowledgments We gratefully acknowledge support from the Tactical SIGINT Technology Program N66001-08-D-0154. We also wish to acknowledge support from the Office of Naval Research (ONR), Code 30, ONR NREIP Internship Program, the SPAWAR internal research funding (S&T) program, SPAWAR SBIR contracts N00039-08-C-0024 and N66001-09-R-0073. O. M. and G. P. thank V. Kornev, I. Soloviev, N. Klenov, A. Sharafiev for useful discussion related to bi-SQUID designs, D. Kirichenko for useful design and test advices, S. Tolpygo, R. Hunt, J. Vivalda, D. Yohannes, D. Amparo for chips fabrication, V. Dotsenko for cryoprobe design and fabrication.

References

1. R.L. Fagaly, Superconducting quantum interference device instruments and applications. Rev. Sci. Instrum. **77**, 101101 (2006)
2. L.E. Fong, J.R. Holzer, K.K. McBride, E.A. Lima, F. Baudenbacher, M. Radparvar, High resolution room-temperature sample scanning superconducting quantum interference device microscope configurable for geological and biomagnetic applications. Rev. Sci. Instrum. **76**, 053703 (2005)
3. M. Inchiosa, A. Bulsara, K. Wiesenfeld, L. Gammaitoni, Phys. Rev. Lett. **A252**, 20 (1999)
4. J.A. Acebron, A.R. Bulsara, M.E. Inchiosa, W.J. Rappel, Europhys. Lett. **56**, 354 (2001)
5. A. Palacios, J. Aven, P. Longhini, V. In, A. Bulsara, Cooperative dynamics in coupled noisy dynamical systems near a critical point: the DC SQUID as a case study. Phys. Rev. E **74**, 021122 (2006)
6. K.G. Stawiasz, M.B. Ketchen, Noise measurements of series SQUID arrays. IEEE Trans. Appl. Supercond. **3**, 1808 (1993)
7. J. Oppenlander, C. Haussler, N. Schopohl, Non-Phi(0)-periodic macroscopic quantum interference in one-dimensional parallel Josephson junction arrays with unconventional grating structure. Phys. Rev. B **63**, 024511 (2001)
8. C. Haussler, J. Oppenlander, N. Schopohl, Nonperiodic flux to voltage conversion of series arrays of DC superconducting quantum interference devices. J. Appl. Phys. **89**, 1875 (2001)
9. J. Oppenlander, C. Haussler, N. Schopohl, Superconducting multiple loop quantum interferometers. IEEE Trans. Appl. Supercond. **11**, 1271 (2001)
10. V.K. Kornev, I.I. Soloviev, J. Oppenlaender, C. Haeussler, N. Schopohl, The oscillation linewidth and noise characteristics of a parallel superconducting quantum interference filter. Supercond. Sci. Technol. **17**, S406 (2004)
11. J. Oppenlander, C. Haussler, A. Friesch, J. Tomes, P. Caputo, T. Trauble, N. Schopohl, Superconducting quantum interference filters operated in commercial miniature cryocoolers. IEEE Trans. Appl. Supercond. **15**, 936 (2005)
12. V.K. Kornev, I.I. Soloviev, N.V. Klenov, O.A. Mukhanov, Bi-SQUID: a novel linearization method for DC squid voltage response. Supercond. Sci. Technol. **22**, 114011 (2009)
13. V. Kornev, I. Soloviev, N. Klenov, O. Mukhanov, Progress in high-linearity multi-element Josephson structures. Phys. C Supercond. **470**, 886 (2010)
14. V.K. Kornev, I.I. Soloviev, N.V. Klenov, A.V. Sharafiev, O.A. Mukhanov, Linear bi-SQUID arrays for electrically small antennas. IEEE Trans. Appl. Supercond. **21**, 713 (2011)
15. V. Kornev, I. Soloviev, N. Klenov, A. Sharafiev, O. Mukhanov, Array designs for active electrically small superconductive antennas. Phys. C **479**, 119–122 (2012)
16. I.I. Soloviev, V.K. Kornev, N.V. Klenov, O.A. Mukhanov, Superconducting Josephson structures with high linearity of transformation of magnetic signal into voltage. Phys. Solid State **52**, 2252 (2010)
17. S.-G. Lee, Y. Huh, G.-S. Park, I.-S. Kim, Y.K. Park, J.-C. Park, Serial array high Tc SQUID magnetometer. IEEE Trans. Appl. Supercond. **7**, 3347 (1997)
18. R.P. Welty, J.M. Martinis, A series array of DC SQUIDs. IEEE Trans. Magn. **27**, 2924 (1991)
19. M. Matsuda, K. Nakamura, H. Mikami, S. Kuriki, Fabrication of magnetometers with multiple-SQUID arrays. IEEE Trans. Appl. Supercond. **15**, 817 (2005)
20. M. Horibe, Y. Tarutani, K. Tanabe, High-speed operation of SQUID array-type interface circuits using a cryocooler. Phys. C Supercond. **412–414**, 1533 (2004)
21. W.-T. Tsang, T. van Duzer, DC analysis of parallel arrays of two and three Josephson junctions. J. Appl. Phys. **46**, 4573 (1975)
22. R. Gerdemann, L. Alff, A. Beck, O.M. Froehlich, B. Mayer, R. Gross, Josephson vortex flow transistors based on parallel arrays of $YBa_2Cu_3O_7$-δ: bicrystal grain boundary junctions. IEEE Trans. Appl. Supercond. **5**, 3292 (1995)
23. HYPRES Design Rules. http://www.hypres.com

A Bistable Microelectronic Circuit for Sensing Extremely Low Electric Field

Andy Kho, Visarath In, Patrick Longhini, Daniel Leung, Norman Liu, Antonio Palacios, Joseph Neff and Adi Bulsara

Abstract Bistable systems are prevalently found in many sensor systems. Recently, we have explored unidirectionally coupled overdamped bistable systems that admit self-sustained oscillations when the coupling parameter is swept through the critical points of bifurcations. Complex behaviors emerge, in addition, from these relatively simple coupled systems when an external signal ac or dc is applied uniformly to all the elements in the array. In particular, we have demonstrated this emergent behavior for a coupled system comprised of mean-field hysteretic elements describing a single-domain ferromagnetic sample. The results are being used to develop extremely sensitive magnetic sensors capable of resolving field changes as low as 150 pT by observing the changes in the oscillation characteristics of the coupled sensors. In this paper, we explore the underlying dynamics of a coupled bistable system realized by coupling microelectronic circuits, which belong to the same class of dynamics as the aforementioned ferromagnetic system, with the nonlinear features and coupling terms modeled by hyperbolic tangent nonlinearities; these nonlinearities stem from the operational transconductance amplifiers used in constructing the microcircuits. The emergent behavior is being applied to develop an extremely sensitive electric-field sensor.

A. Kho (✉) · V. In · P. Longhini · D. Leung · N. Liu · J. Neff · A. Bulsara
Space and Naval Warfare Systems Center Pacific, 53560 Hull St, San Diego, CA 92152-5001, USA
e-mail: andy.kho@navy.mil

A. Palacios
Department of Mathematics and Statistics, Nonlinear Dynamics Group, San Diego State University, San Diego, CA 92182, USA

V. In et al. (eds.), *International Conference on Theory and Application in Nonlinear Dynamics (ICAND 2012)*, Understanding Complex Systems,
DOI: 10.1007/978-3-319-02925-2_8,

1 Introduction

In our previous work we have shown that an overdamped bistable system can self oscillate with a carefully chosen coupling topology [1–3]. The number of elements has to be odd with three or more elements, and they should be unidirectionally coupled with cyclic boundary conditions. When the coupling strength is set beyond the critical coupling, the system will spontaneously generate self oscillations.

This technique has already been employed with the coupled-core fluxgate magnetometer where three ferromagnetic cores were coupled together. Typically, a periodic signal is used to drive the ferromagnetic cores between its stable states; however, with the coupling technique, the drive signal was not necessary due to the system self oscillating. With this technique and the residence time detection (RTD) readout, a room temperature magnetometer with a resolution as low as 150 pT was realized.

A similar approach is what was used to develop an electric field sensor which is the subject of this paper. Instead of coupling ferromagnetic cores, however, an electronic chip was developed which uses the coupling technique to sense small currents. This chip, along with a conductive plate and the same RTD readout was used to build an extremely sensitive electric field sensor (see Fig. 1). The current system was designed to detect low frequency electric fields less than a few hundred hertz.

2 Dynamical Equations

The dynamical equations for the electric field sensor that were designed in hardware are given in Eq. (1) [4]. Each of the equations represents an element in the system. The number of elements must be odd and greater than two in order to generate self oscillations. Because three elements is the smallest and simplest to implement, this is the number that will be used for the rest of the paper.

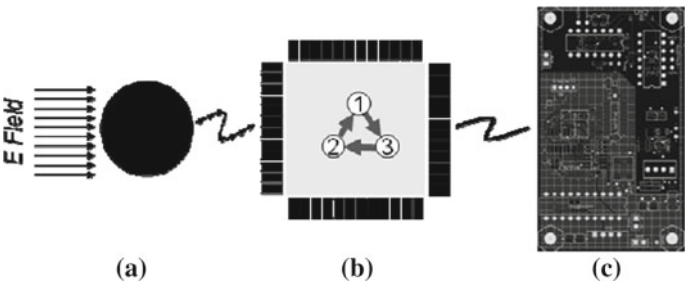

Fig. 1 The electric field sensor consists of a **a** conductive plate, **b** coupled bistable nonlinear chip, and **c** residence time difference (RTD) readout circuitry

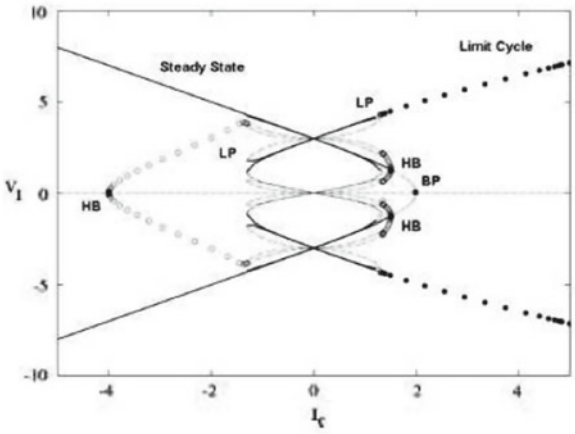

Fig. 2 Bifurcation diagram showing the system's voltage output in response to changes in coupling parameter I_c. The filled-in circles represent globally, asymptotically, stable limitcycle oscillations created at the onset, LP, of a heteroclinic bifurcation. The *solid lines* depict the local branches of stable steady-state solutions. The *empty circles* correspond to unstable branches of periodic oscillations that emerge via Hopf bifurcations. The parameters are $C_L = 1,\ g = 1,\ c = 1,\ I_s = 2$ and $I_c = 1$

$$\begin{aligned} C_L\dot{V}_1 &= -gV_1 + I_s tanh(c_s V_1) - I_c tanh(c_c V_2) - \varepsilon \\ C_L\dot{V}_2 &= -gV_2 + I_s tanh(c_s V_2) - I_c tanh(c_c V_3) - \varepsilon \\ C_L\dot{V}_3 &= -gV_3 + I_s tanh(c_s V_3) - I_c tanh(c_c V_1) - \varepsilon \end{aligned} \tag{1}$$

In this system the coupling is unidirectional with cyclic boundary conditions. V_1 receives a coupling term from V_2. V_2 receives a coupling term from V_3, and finally V_3 receives a coupling term from V_1. The coupling strength is set by adjusting I_c which is identical for all three elements. I_s, which is also identical for all three elements, controls the bistability of the system. It can be tuned so that the system is monostable when $I_s < g/c_s$ or bistable when $I_s \geq g/c_s$. In this paper, the bistable case is used. C_L sets the time constant for the system and ε is the signal being detected.

Figure 2 shows the bifurcation diagram of the dynamical system in Eq. (1) [4]. Part of the diagram shows the steady state (solid lines) and unstable regions (open circles), but the region being used for the electric field sensor is the stable limit-cycle created at the onset of a heteroclinic bifurcation (solid circles). The bifurcation diagram for N odd larger than 3 has more bifurcation points, however, they are all unstable and the same limit-cycle is still responsible for the oscillations. In the case where N is even, the limit cycle is replaced with a steady state, and it is not possible to generate oscillations with this topology. In order for the system to spontaneously generate oscillations, the coupling term, I_c, needs to be tuned past its critical value. If the system is tuned below this point, it will remain in steady state. The equation for the critical point has been worked out and is shown in Eq. (2) [4].

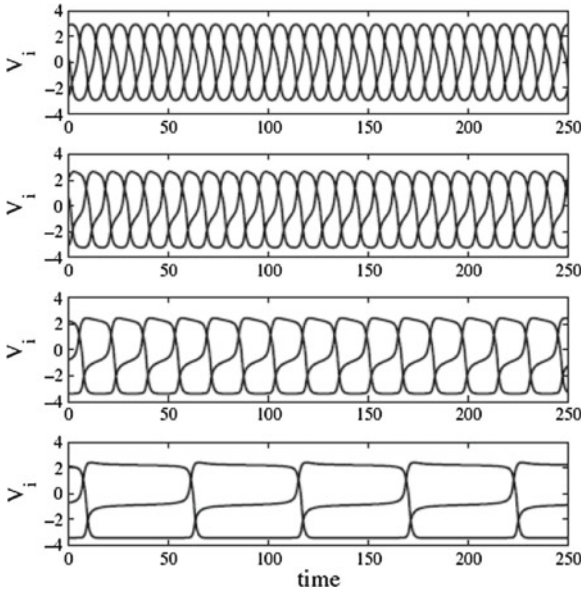

Fig. 3 Time series simulations of the coupled electric field system. e is set to 0, 0.025, 0.4, and 0.46 from top to bottom

$$I_{c,critical} = \varepsilon - \frac{g}{c} sech^{-1}\left(\sqrt{\frac{g}{I_s c}}\right) + I_s tanh\left[sech^{-1}\left(\sqrt{\frac{g}{I_s c}}\right)\right] \quad (2)$$

Figure 3 shows the time series of the electric field system when the coupling strength is set beyond the critical coupling so that the system oscillates a priori. The top figure shows what the signal looks like when there is no target signal present. The elements oscillate in a traveling wave pattern phase shifted by $360°/N$, where N is the number of elements. Moving down in the series of plots in Fig. 3, the target signal ε is set to 0, 0.25, 0.4, and 0.46. As ε is increased, the oscillation frequency (see Fig. 4) decreases and the duty cycle shifts. This duty cycle shift is what is measured to quantify the target signal.

3 Readout Strategy

The readout for the electric field sensor is the residence time difference (RTD) [5]. T+ is the time when it crosses the upper threshold until it reaches the lower threshold as shown in Fig. 5. T− is the time when it crosses the lower threshold until it reaches the upper threshold. The RTD is calculated by subtracting T− from T+. When there is no target signal present, T+ and T− are the same so the RTD equals zero (see Fig. 5a). When a target signal is present, the RTD is a non-zero number and can be related back to the input target signal (see Fig. 5b). In practice, the threshold crossings

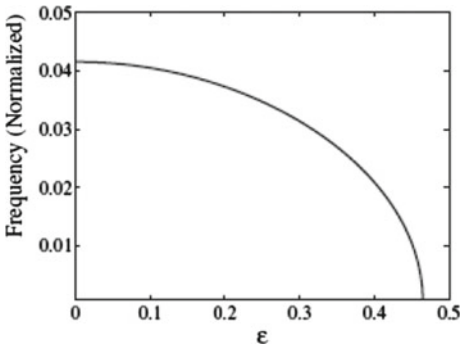

Fig. 4 Frequency response to an input target signal ε

are accumulated and kept track of at the input capture port of a PIC microcontroller. The PIC calculates T+, T−, and the RTD. It can also average the RTD as well as do some signal processing. The RTD is transmitted to the computer via the serial port.

The response to a DC input signal is shown in Fig. 6. When the signal is small, the response is linear. As the input signal approaches the bifurcation point, there is a sharp rise in the response. This allows the user to tune the circuit to operate in different regions of the response curve depending on the target signal characteristics.

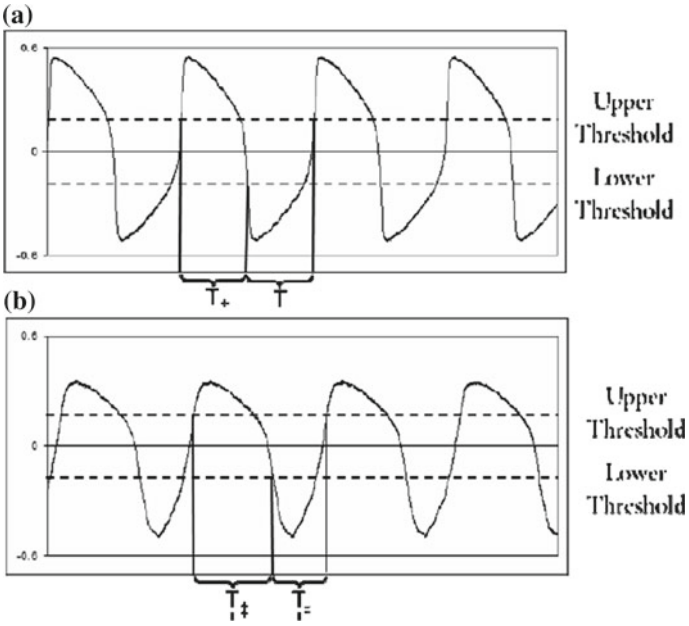

Fig. 5 Residence time detection readout is done by counting times spent in the upper and lower residence times. The difference in the upper and lower residence times can be related back to the input target signal. **a** No target signal. **b** Target signal present

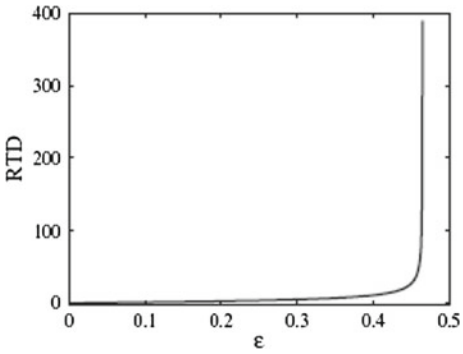

Fig. 6 RTD response curve of the electric field sensor. The responsivity greatly increases as the signal approaches the bifurcation point

4 Circuit

The basic circuit design based on the nonlinear equations was built out of operational transconductance amplifiers (OTAs). An OTA was used for both the Is and Ic term (see Fig. 7). C_L, which sets the time constant of the system, was set by the load capacitance including any parasitics. g is the linear conductance, and cc and cs are intrinsic transistor parameters. Figure 7 shows the basic building block for each of the elements in the system. The actual transistor layout is shown in Fig. 8. Putting all of these things together builds the entire system shown in Fig. 9. The input current mirror is there to copy the same input current into each element of the electric field sensor.

SPICE simulations were done to verify that the design would behave similarly to the numeric simulations. Careful consideration had to be given on choosing the circuit parameters. Is was set so that the oscillator was operating in the bistable region. I_c was adjusted accordingly so that the system would self oscillate. C_L was also chosen so that it would operate in the desired frequency range of 1–2 kHz. The values used for this particular simulation were $C_L = 66\,\text{nF}$, $I_c = 200\,\mu\text{A}$, and $I_s = 300\,\mu\text{A}$. The resultant time series, RTD response, and frequency response were shown in Fig. 10.

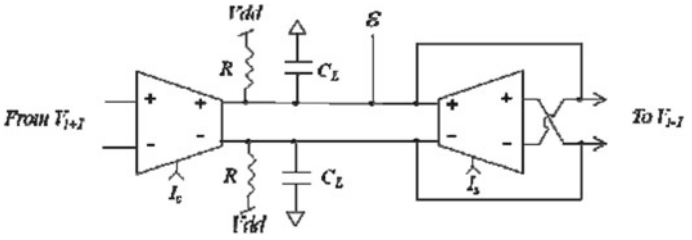

Fig. 7 The basic building block for each of the elements in the electric field sensor. g—linear conductance. c_c and c_s intrinsic transistor parameters. C_L output capacitance

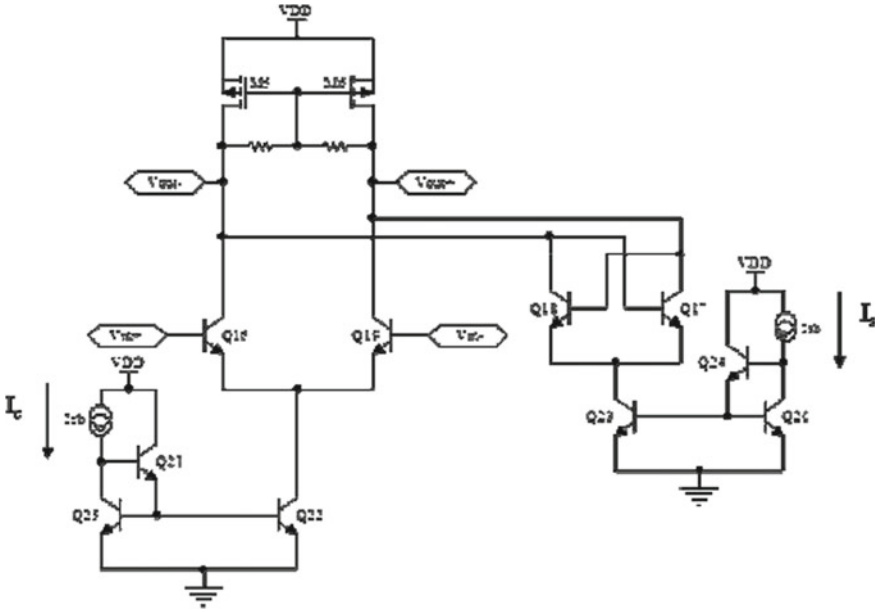

Fig. 8 The transistor layout for each of the elements in the electric field sensor. The OTAs are built with differential pair transistors

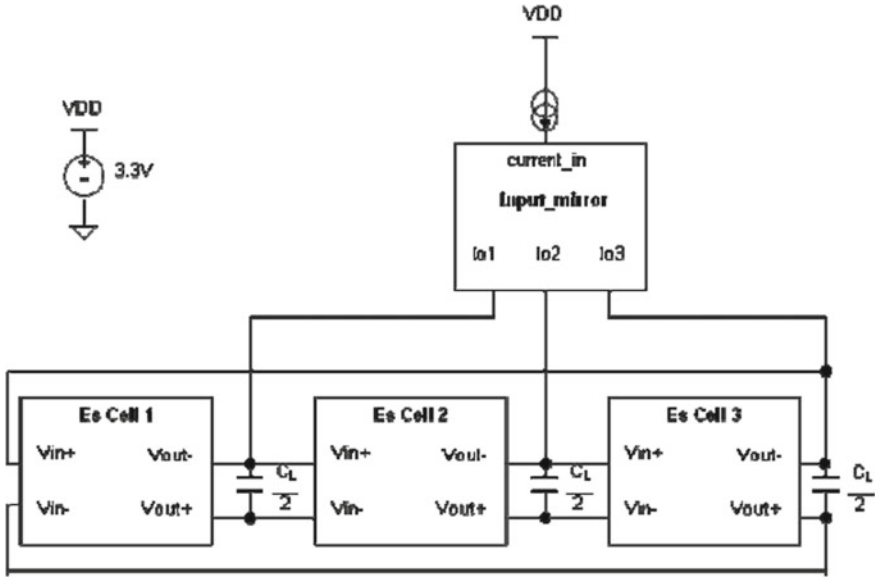

Fig. 9 The basic topology of the electric field sensor after putting all of the parts together

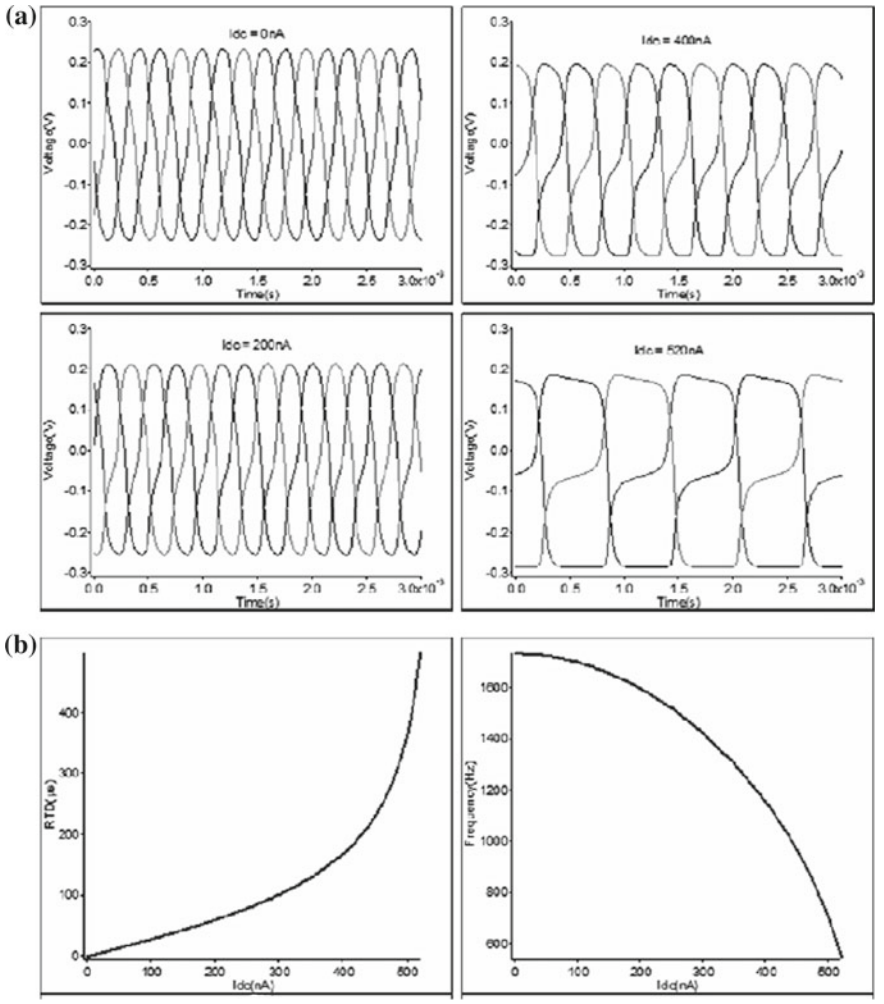

Fig. 10 **a** Time series SPICE simulation with increasing input signal. **b** RTD and Frequency response of the SPICE simulation. $I_c = 200\,\mu\text{A}$, $I_s = 300\,\mu\text{A}$, $C_L = 66\,\text{nF}$

After the chip was designed and the layout of the chip was done, it was sent out to be fabricated. A printed circuit board was also designed and fabricated so that the chip could be mounted and tested. Operational amplifier buffers had to be used at the output of the chip so that C_L could be set independent of the load. I_c and I_s were set with potentiometers so that these values could be carefully tuned. The time series and response curves were similar to the SPICE simulations. Taking noise into consideration, this chip was able to resolve current changes of 500 pA which resulted in an electric field resolution of about 56 Vm/(As) where A is the area of the plate and s is time in seconds.

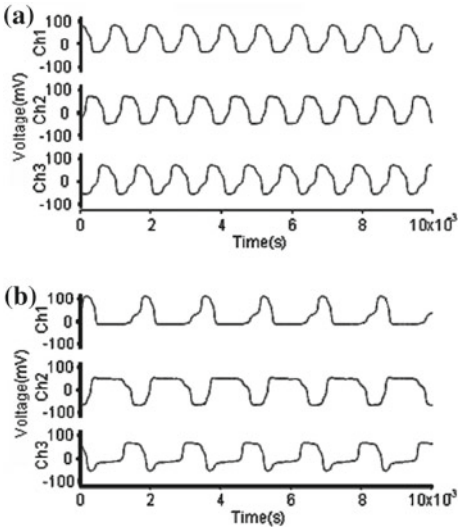

Fig. 11 The experimental time series of the electric field sensor chip that has one of its inputs reversed. **a** No input signal. **b** 30 nA input signal

A further enhancement that was done to the system was to alternate the inputs into the chip. In this case, the current mirror was replaced with a differential input so that every other element would get a reversed input signal. In the case where elements one and two got the straight input signal and element three got the reversed input signal, element one would have a much greater RTD response than the other two. In Fig. 11a where there was no input signal, the waveform looks symmetrical just like the non-alternating input case. When a 30 nA input signal was input into the system, however, it is clearly seen that channel one has a much greater RTD response than channels two and three as seen in Fig. 11b. This alternating input technique can also be employed on systems with more elements. In fact, simulations have shown that using this technique with more elements increases the RTD response even further.

5 Conclusion

A microelectronic realization of the coupled bistable system to detect small DC currents has been presented in this paper. With the proper coupling topology and coupling strength, the system will self oscillate. When a small signal enters the nonlinear chip, the duty cycle of the signal changes and the readout can be taken via the RTD method. Even though the presentation in this paper was to build an electric field sensor, the same chip can be interfaced with other transducers that produce a current output as well. In fact, the small size of the circuit affords the ability to place many of these circuits onto a single chip whereby a single chip (or small PCB) could host a series of different types of sensors.

References

1. V. In, A.R. Bulsara, A. Palacios, P. Longhini, A. Kho, J.D. Neff, Phys. Rev. E **68**, 045102(R) (2003)
2. V. In, A.R. Bulsara, A. Kho, P. Longhini, A. Palacios, Phys. Rev. E **72**, 045104(R) (2005)
3. V. In, A. Palacios, A.R. Bulsara, P. Longhini, A. Kho, J.D. Neff, S. Baglio, B. Ando, Phys. Rev. E **73**, 066121 (2006)
4. V. In, P. Longhini, N. Liu, A. Kho, J.D. Neff, A. Palacios, A.R. Bulsara, J Appl. Phys. **107**, 014506 (2010)
5. A.R. Bulsara, C. Seberino, L. Gammaitoni, M.F. Karlsson, B. Lundqvist, J.W.C. Robinson, Phys. Rev. E **67**, 016120 (2003)

Asynchronous Cellular Automaton Based Modeling of Nonlinear Dynamics of Neuron

Hiroyuki Torikai and Takashi Matsubara

Abstract A modeling approach of nonlinear dynamics of neurons by an asynchronous cellular automaton is introduced. It is shown that an asynchronous cellular automaton neuron model can realize not only typical nonlinear response characteristics of neurons but also their underlying occurrence mechanisms (i.e., bifurcation scenarios). The model can be implemented as an asynchronous sequential logic circuit, whose control parameter is the pattern of wires that can be dynamically updated in a dynamic reconfigurable FPGA. An on-FPGA learning algorithm (i.e., on-FPGA rewiring algorithm) is presented and is used to tune the model so that it reproduces nonlinear response characteristics of a neuron.

1 Introduction

The neuron is one of the most sophisticated nonlinear dynamical systems and its mathematical and hardware modelings have been investigated intensively [1–10]. Motivations for the hardware neuron include development of a neural prosthesis chip for clinical applications [9, 10] and development of an artificial neural network chip for engineering applications [1, 5–7]. Major classical approaches of hardware spiking neurons include: (i) implementation of a nonlinear *ordinary differential equation* (ab. ODE) by an analog circuit [1–4] and (ii) implementation of a numerical integration by a digital processor [5–8]. Recently, an alternative neuron modeling approach has been proposed, where the nonlinear dynamics of a neuron is modeled by an asynchronous cellular automaton that is implemented by an asynchronous sequential logic

H. Torikai (✉) · T. Matsubara
Graduate School of Engineering Science, Osaka University, 1-3 Machikaneyama-cho, Toyonaka, Osaka 560-8531, Japan
e-mail: hiroyuki.torikai@ieee.org

T. Matsubara
e-mail: matubara@hopf.sys.es.osaka-u.ac.jp

V. In et al. (eds.), *International Conference on Theory and Application in Nonlinear Dynamics (ICAND 2012)*, Understanding Complex Systems,
DOI: 10.1007/978-3-319-02925-2_9,

circuit [11–15]. The asynchronous sequential logic spiking neuron model (ab. ASN) consists of registers, logic gates, and reconfigurable wires, where the pattern of the wires among the registers and the gates is a control parameter that determines its nonlinear dynamics. Some types of ASNs (e.g., integrate-and-fire type and rotate-and-fire type) have been presented so far and their neuron-like properties have been analyzed intensively [11–15]. In this paper, it is shown that the ASN can realize typical nonlinear responses of neurons [11]. Also, some of our recent new results on learnings of the ASN are presented. Significances of the ASN include the following points. (a) The analog circuit neuron has a continuous time and a continuous state, and the digital processor neuron has a discrete time and a discrete state. On the other hand, the ASN has a discrete state and a continuous (state transition) time. Hence the ASN belongs to a different class of nonlinear dynamical systems from the major classical hardware spiking neuron models. We emphasize that investigation of such a new neuron modeling approach is an important fundamental nonlinear problem. (b) An important control parameter of the analog circuit neuron is a nonlinearity of a circuit element. Hence, its dynamic parameter adjustment is often troublesome. An important control parameter of the digital processor neuron is a coefficient of a nonlinear function. Hence, its dynamic parameter adjustment is possible but needs a numeric data processor. On the other hand, the control parameter of the ASN is the wiring pattern that can be dynamically adjusted based on a dynamic reconfigurable FPGA technology. (c) The ASN can be implemented with less hardware resources (i.e., smaller number of configuration logic blocks) than the digital processor neuron for some reasonable parameter cases. Such a low hardware cost property and the dynamic reconfiguration ability will be significantly useful to develop future applications of the ASN, e.g., a neural prosthesis chip whose area is small and whose parameters can be dynamically updated after implantation and an artificial neural network chip with an on-chip learning capability.

2 Asynchronous Sequential Logic Neuron Model

In this section, an *asynchronous sequential logic spiking neuron model* (ab. ASN), whose diagram is depicted in Fig. 1, is introduced [11–15]. The ASN has the following four registers whose bit lengths are denoted by positive integers N, M, K, and J, respectively.

(1) The *membrane register* is an N-bit bi-directional shift register having an integer state $V \in \mathbf{Z}_N \equiv \{0, \ldots, N-1\}$ encoded by the one-hot coding manner, where "$\equiv$" denotes "is defined by" hereafter. From a neuron model viewpoint, the state V can be regarded as a *membrane potential*.
(2) The *recovery register* is an M-bit bi-directional shift register having an integer state $U \in \mathbf{Z}_M \equiv \{0, \ldots, M-1\}$ encoded by the one-hot coding manner. From a neuron model viewpoint, the state U can be regarded as a *recovery variable*.

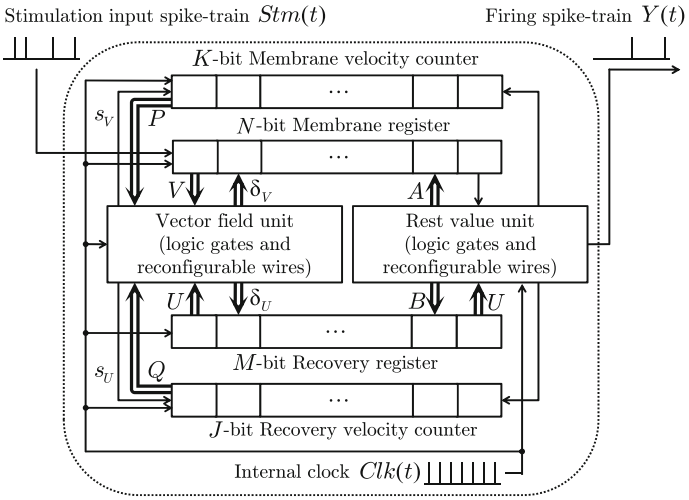

Fig. 1 Asynchronous sequential logic spiking neuron model (ab. ASN)

(3) The *membrane velocity counter* is a K-bit register having an integer state $P \in \mathbf{Z}_K \equiv \{0, \ldots, K-1\}$ encoded by the thermometer coding manner. The state P controls a velocity of the membrane potential V.
(4) The *recovery velocity counter* is a J-bit register having an integer state $Q \in \mathbf{Z}_J \equiv \{0, \ldots, J-1\}$ encoded by the thermometer coding manner.

The state Q controls a velocity of the recovery variable U. The states V, U, P, and Q are clamped to the ranges $[0, N-1]$, $[0, M-1]$, $[0, K-1]$, and $[0, J-1]$, respectively. As shown in Fig. 1, the registers and the velocity counters are connected to each other via the following two memoryless units. (i) The *vector field unit* consists of logic gates and reconfigurable wires. This unit determines the characteristics of a vector field of the states (V, U) as its name implies. (ii) The *reset value unit* consists of logic gates and reconfigurable wires. From a neuron model viewpoint, this unit determines values to which the states (V, U) are reset when the ASN fires, as its name implies. The ASN accepts a periodic *internal clock* $Clk(t)$ described by

$$Clk(t) = \begin{cases} 1 & \text{if } t \pmod 1 = 0, \\ 0 & \text{otherwise}, \end{cases}$$

where $t \in [0, \infty)$ is a continuous time. In the next subsection, autonomous behaviors of the ASN (i.e., behaviors when no stimulation input spike-train $Stm(t)$ is applied) are investigated. After that, in the next subsection, non-autonomous behaviors of the ASN (i.e., behaviors when a stimulation input spike-train $Stm(t)$ is applied) are investigated.

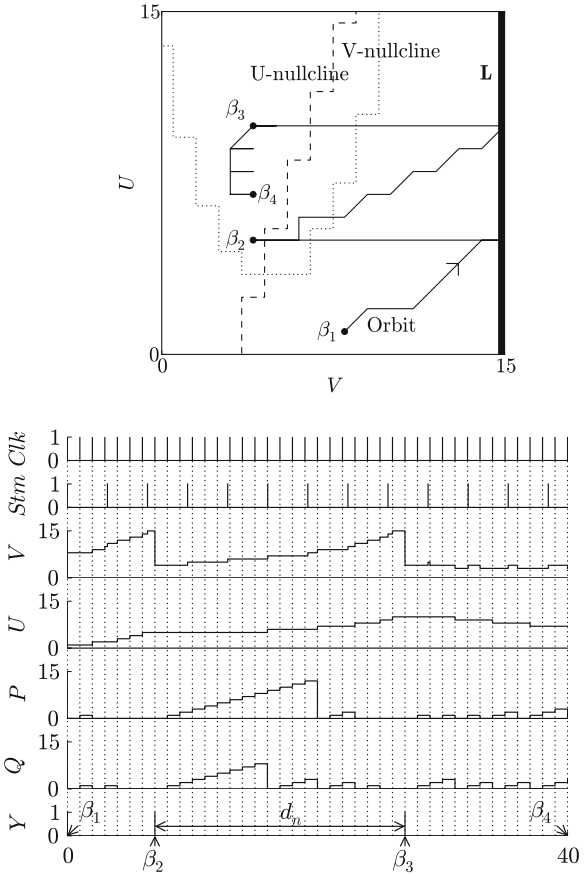

Fig. 2 A phase plane and state transitions. V-nullcline (U-nullcline) is a border between $D_V \in \{-1, 0\}$ and $D_V = 1$ ($D_U \in \{-1, 0\}$ and $D_U = 1$). The bit lengths of the ASN are $N = M = K = J = 16$. The parameters are $\boldsymbol{\Gamma} = (7, 0.3, 0.2, 3, 0.1, 16, 0.5, 0.3, 0)$ defined in (10). A periodic stimulation input spike-train $Stm(t)$ with a frequency 0.312 via the synaptic weight $W = 1$ is applied to the ASN

2.1 Autonomous Behaviors

Let us begin with defining the following subset $\mathbf{L}$ in the state space $\mathbf{Z}_N \times \mathbf{Z}_M$ (see also Fig. 2).

$$\mathbf{L} \equiv \{(V, U) | V = N - 1, U \in \mathbf{Z}_M\} \subset \mathbf{Z}_N \times \mathbf{Z}_M. \tag{1}$$

From a neuron model viewpoint, $\mathbf{L}$ can be regarded as a *firing threshold*. First, let us consider the case of $(V, U) \notin \boldsymbol{L}$. In this case, the vector field unit in Fig. 1 triggers the transition of the states (P, Q) of the velocity counters and the states (V, U) of the registers through signals $(s_V, s_U) \in \{0, 1\}^2$ and $(\delta_V, \delta_U) \in \{-1, 0, 1\}^2$ as follows.

$$
\begin{aligned}
P(t^+) &= \begin{cases} P(t)+1 & \text{if } s_V(t)=0, Clk(t)=1, \\ 0 & \text{if } s_V(t)=1, Clk(t)=1, \\ P(t) & \text{otherwise}, \end{cases} \\
Q(t^+) &= \begin{cases} Q(t)+1 & \text{if } s_U(t)=0, Clk(t)=1, \\ 0 & \text{if } s_U(t)=1, Clk(t)=1, \\ Q(t) & \text{otherwise}, \end{cases} \\
V(t^+) &= \begin{cases} V(t)+\delta_V & \text{if } Clk(t)=1, \\ V(t) & \text{otherwise}, \end{cases} \\
U(t^+) &= \begin{cases} V(t)+\delta_V & \text{if } Clk(t)=1, \\ V(t) & \text{otherwise}, \end{cases}
\end{aligned} \tag{2}
$$

where $t^+ = \lim_{\varepsilon \to +0} t + \varepsilon$, the velocity counters accept the internal clock $Clk(t)$ and the signals (s_V, s_U), and the registers accept the signals (δ_V, δ_U) from the vector field unit. The signals (s_V, s_U) and (δ_V, δ_U) are generated as follows.

$$
\begin{aligned}
s_V &= \begin{cases} 1 & \text{if } P \geq P_h(V,U), \\ 0 & \text{if otherwise}, \end{cases} \\
s_U &= \begin{cases} 1 & \text{if } Q \geq Q_h(V,U), \\ 0 & \text{if otherwise}, \end{cases} \\
\delta_V &= \begin{cases} D_V(V,U) & \text{if } P \geq P_h(V,U), \\ 0 & \text{otherwise}, \end{cases} \\
\delta_U &= \begin{cases} D_U(V,U) & \text{if } Q \geq Q_h(V,U), \\ 0 & \text{otherwise}, \end{cases} \\
&P_h : \mathbf{Z}_N \times \mathbf{Z}_M \to \mathbf{Z}_K, \ Q_h : \mathbf{Z}_N \times \mathbf{Z}_M \to \mathbf{Z}_J, \\
&D_V : \mathbf{Z}_N \times \mathbf{Z}_M \to \{-1, 0, 1\}, \ D_U : \mathbf{Z}_N \times \mathbf{Z}_M \to \{-1, 0, 1\},
\end{aligned} \tag{3}
$$

where the functions $P_h(V,U)$, $Q_h(V,U)$, $D_V(V,U)$, and $D_U(V,U)$ are discrete functions that are designed by the following rule.

$$
\begin{aligned}
&\mathscr{F}(V,U) = N(\gamma_1 (V/N - \gamma_2)^2 + \gamma_3 - U/M)/\lambda, \\
&\mathscr{G}(V,U) = \mu M(\gamma_4 (V/N - \gamma_2) + (\gamma_3 + \gamma_5) - U/M)/\lambda, \\
&P_h(V,U) = \lfloor |\mathscr{F}^{-1}(V,U)| \rfloor - 1, \ Q_h(V,U) = \lfloor |\mathscr{G}^{-1}(V,U)| \rfloor - 1, \\
&D_V(V,U) = \mathrm{sgn}(\mathscr{F}(V,U)), \ D_U(V,U) = \mathrm{sgn}(\mathscr{G}(V,U)),
\end{aligned} \tag{4}
$$

where $(\gamma_1, \gamma_2, \gamma_3, \gamma_4, \gamma_5)$ are parameters that characterize nullclines, (λ, μ) are parameters that work as time constants, the function $\lfloor x \rfloor$ gives the integer part of a real number x, $P_h(V,U)$ and $Q_h(V,U)$ are clamped to the ranges $[0, K-1]$ and

Table 1 Summary of the implementation and execution methods of Eqs. (1)–(9), and their orders of hardware costs

Equation	Implement or not	Hardware cost
Eq. (2)		$O(1)$
Eq. (3)	Implemented as	$O(N \times M)$
Eqs. (1) and (5)	logic gates and	$O(N + M)$
Eq. (6)	reconfigurable wires	$O(N + M)$
Eq. (8)		$O(1)$
Eq. (9)		$O(1)$
Eq. (4)	Wiring pattern setting rules	
Eq. (7)	(not implemented as a part of ASN)	

$[0, J-1]$, and the signum function $\mathrm{sgn}(x)$ gives the sign of a real number x, respectively.

Second, let us consider the case of $(V, U) \in \mathbf{L}$. In this case, the reset value unit in Fig. 1 triggers the reset of the states (P, Q) of the velocity counters and the states (V, U) of the registers through integer signals $(A, B) \in \mathbf{Z}_N \times \mathbf{Z}_M$ encoded by the one-hot coding manners as follows.

$$\begin{aligned}&(P(t^+), Q(t^+), V(t^+), U(t^+)) = \\ &\begin{cases}(0, 0, A, B) & \text{if } (V, U) \in \mathbf{L}, Clk(t) = 1, \\ (P(t), Q(t), V(t), U(t)) & \text{otherwise},\end{cases}\end{aligned} \tag{5}$$

where the signals (A, B) are generated as follows.

$$\begin{aligned}&(A, B) = (\mathscr{A}, \mathscr{B}(U)) \\ &\mathscr{A} \in \mathbf{Z}_N, \quad \mathscr{B}(U) : \mathbf{Z}_M \to \mathbf{Z}_M,\end{aligned} \tag{6}$$

where $\mathscr{A}$ is an integer and $\mathscr{B}(U)$ is a discrete function that are designed by the following rule.

$$\mathscr{A} = \lfloor \rho_1 N \rfloor, \quad \mathscr{B}(U) = U + \lfloor \rho_2 M \rfloor, \tag{7}$$

where (ρ_1, ρ_2) are parameters, and $\mathscr{A}$ and $\mathscr{B}(U)$ are clamped to the ranges $[0, N-1]$ and $[0, M-1]$, respectively. Repeating the resets, the ASN generates the following *firing spike-train* $Y(t)$.

$$Y(t) = \begin{cases}1 & \text{if } (V(t), U(t)) \in \mathbf{L}, Clk(t) = 1, \\ 0 & \text{otherwise}.\end{cases} \tag{8}$$

Note that Eqs. (2) and (5) represent the discrete state transitions triggered by the discrete signals, and Eqs. (3) and (6) represent the discrete functions. Also, Eq. (8) with Eq. (1) is the discrete function. Hence, they can be implemented by logic gates and reconfigurable wires, where the functional relations are determined by the wiring

patterns in the vector field unit and the reset value unit (see Table 1). On the other hand, Eqs. (4) and (7) represent the parameter (i.e., wiring pattern) setting rules and are not implemented as a part of the ASN (see Table 1).

2.2 Non-autonomous Behaviors

Let us now apply the following stimulation input spike-train $Stm(t)$ to the ASN.

$$Stm(t) = \begin{cases} 1 & \text{if } t = t_1, t_2, \ldots, \\ 0 & \text{otherwise,} \end{cases}$$

where $t = t_1, t_2, \ldots$ are input spike positions. From a neuron model viewpoint, the stimulation input spike-train $Stm(t)$ can be regarded as a *stimulation input*. A stimulation input spike $Stm = 1$ induces the transition of the membrane potential V as follows.

$$V(t^+) = V(t) + W \cdot Stm(t), \tag{9}$$

where $W \in \{1, -1\}$ is a parameter that can be regarded as a *synaptic weight* and $W = 1$ ($W = -1$) implies that the stimulation weight is excitatory (inhibitory). Note that the membrane register of the previous model [14] accepts the single signal $Stm(t)$ only and the model has the excitatory synaptic weight $W = 1$ only. In contrast, the membrane register of the ASN accepts the two signals W and $Stm(t)$ and the ASN has both the excitatory and the inhibitory synaptic weights $W \in \{1, -1\}$. Note also that Eq. (9) represents the discrete state transitions and thus is implemented by logic gates and reconfigurable wires (see Table 1). Figure 2 shows basic non-autonomous behaviors of the ASN, where the V-nullcline (U-nullcline) is a border between $D_V \in \{-1, 0\}$ and $D_V = 1$ ($D_U \in \{-1, 0\}$ and $D_U = 1$). As a result, the dynamics of the ASN is described by Eqs. (2)–(9), and is characterized by the following parameters.

$$N,\ M,\ K,\ J,\ \boldsymbol{\Gamma} = (\gamma_1, \gamma_2, \gamma_3, \gamma_4, \gamma_5, \lambda, \mu, \rho_1, \rho_2). \tag{10}$$

3 Reproduction of Inhibitory Dynamic Response Behaviors

For simplicity, we focus on the following periodic stimulation input spike-train $Stm(t)$.

$$Stm(t) = \begin{cases} 1 & \text{if } (t + \theta_0) \pmod{f_S^{-1}} = 0, \\ 0 & \text{otherwise,} \end{cases}$$

where f_S is an input frequency, $\theta_0 \in [0, f_S^{-1})$ is an initial input phase, and a *post-synaptic stimulation input* I to the ASN is defined as

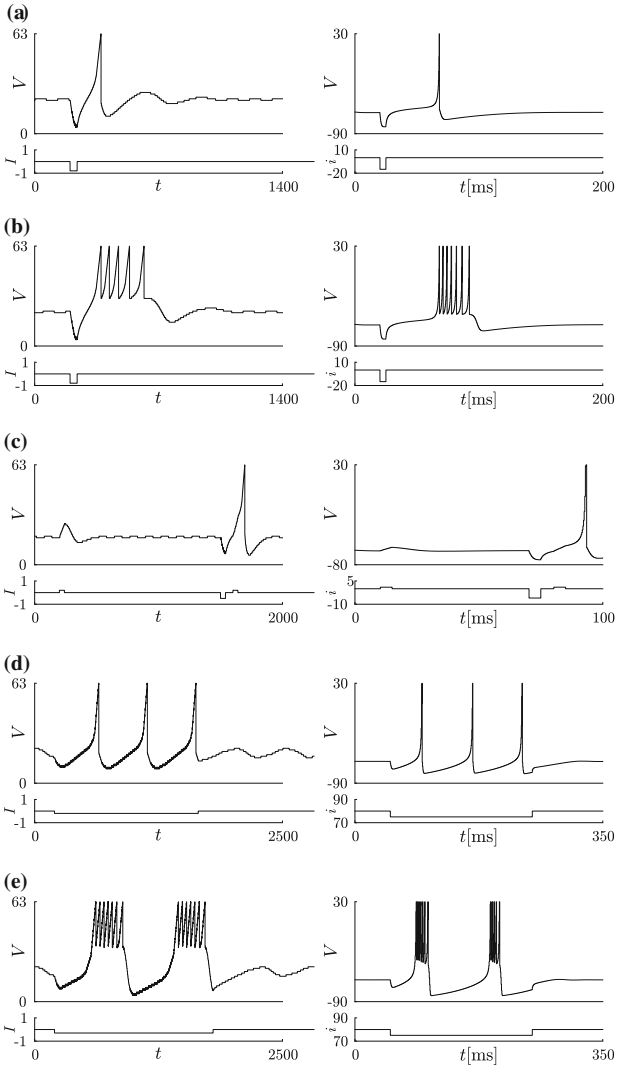

Fig. 3 Numerical simulation results of inhibitory dynamic response behaviors of the ASN (each *left* figure) and those of the Izhikevich simple model [16] (each *right* figure), where v denotes the membrane potential and i denotes the current input. **a**–**e** correspond to (**a**)–(*e*) in Table 2, respectively. The bit lengths of the ASN are $N = M = K = J = 64$. The parameters $\boldsymbol{\Gamma}$ of the ASN and the heights of the post-synaptic stimulation I are as the followings. **a** $\boldsymbol{\Gamma} = (7, 0.3, 0.2, 3, -0.1, 64, 0.5, 0.3, 0)$, $I = -0.8$. **b** $\boldsymbol{\Gamma} = (7, 0.3, 0.2, 3, -0.1, 64, 0.5, 0.48, -0.4)$, $I = -0.8$. **c** $\boldsymbol{\Gamma} = (7, 0.3, 0.2, 3, 0.1, 64, 0.5, 0.3, 0)$, $I = 0.2, -0.5$. **d** $\boldsymbol{\Gamma} = (7, 0.3, 0.5, -5, 0, 64, -0.2, 0.3, 0.1)$, $I = -0.2$. **e** $\boldsymbol{\Gamma} = (7, 0.3, 0.5, -5, 0, 64, -0.1, 0.55, -0.1)$, $I = -0.3$. The parameter values of the Izhikevich simple model can be found in [16]

$$I = f_S \cdot W.$$

According to [16, 17], biological and model neurons typically exhibit dynamic response behaviors (i.e., waveforms of the membrane potential in response to the stimulation input) that can be classified into fifteen excitatory types and five inhibitory types as shown in Table 2. It has been shown the ASN can reproduce all the twenty types of dynamic response behaviors. In this paper, we focus on the following inhibitory ones (a)–(e), which are shown in Table 2 [11]. (a) *A rebound spike* is a spike induced by an inhibitory stimulation input. (b) *A rebound burst* is a burst induced by an inhibitory stimulation input. (c) *Threshold variability* is a phenomenon that whether the stimulation input of the same strength induces a spike depends on the preceding inhibitory stimulation input. (d) *Inhibition-induced spiking* is persistent spike-train generation while an inhibitory stimulation input is applied. (e) *Inhibition-induced bursting* is persistent burst-train generation while an inhibitory stimulation input is applied. Numerical simulation results corresponding to the above behaviors (a)–(e) are shown in Fig. 3a–e, respectively.

4 Learning and Neural Responses

This section shows that the ASN can reproduce desired responses characteristics (i.e., relationships between the stimulation strength and the average firing frequency) obtained from a biological or model neuron, which is called a *teacher* neuron. As the teacher neuron, Izhikevich's resonator model [17] is used, whose stimulation strength is denoted by I. The control parameter, i.e., the wiring pattern, of the ASN is dynamically updated to reproduce the response characteristics of the teacher, where the distance between the responses of them is defined by using the metric-space analysis [18]. This procedure is called a *learning* hereafter. Figure 4 shows the responses characteristics of the teacher, the ASN before the learning, and the ASN after the learning. The response characteristics of the ASN before the learning is different from that of the teacher. The response characteristics of the ASN after the learning is similar to that of the teacher. This indicates that the learning enables the ASN to reproduce the responses characteristics of the teacher. More detailed investigations on the learning will be presented in our future works.

The ASN is implemented on Xilinx's FPGA Veitex-5 XUPV5-LX110T mounted on Digilent's OpenSPARC evaluation platform. The FPGA-implemented ASNN occupies 123 slices (each slice includes four 6-input LUTs and four FFs) of the FPGA device. For comparison, the teacher is also implemented on the same FPGA device using a forward Euler numerical integration with a time step 3 kHz. The implemented teacher occupies 532 slices, where the resolutions of the states are 16-bit binary fixed point numbers. These facts indicate that the ASN requires less hardware resources then a digital processor neuron. More detailed investigations on the hardware will be presented in our future works.

Table 2 The table summarizes reproduction abilities of dynamic response behaviors by typical neuron models and our models, where "+" denotes "reproducible", "−" denotes "not reproducible", and "·" denotes "partially reproducible". Each empty square denotes that sufficient parameter and initial value conditions are unknown but the model satisfies necessary conditions in principle [16]. Each dynamic response behavior is as follows. **a** Rebound spike. **b** Rebound bursting. **c** Threshold variability. **d** Inhibition-induced spiking. **e** Inhibition-induced bursting. **f** Tonic spiking. **g** Phasic spiking. **h** Tonic bursting. **i** Phasic bursting. **j** Mixed mode. **k** Spike frequency adaptation. **l** Class 1 excitable. **m** Class 2 excitable. **n** Spike latency. **o** Subthreshold oscillation. **p** Resonator. **q** Integrator. **r** Bistability. **s** Depolarizing after-potential. **t** Accommodation

	Inhibitory dynamic response behaviors					Excitatory dynamic response behaviors														
Neuron model	(a)	(b)	(c)	(d)	(e)	(f)	(g)	(h)	(i)	(j)	(k)	(l)	(m)	(n)	(o)	(p)	(q)	(r)	(s)	(t)
Izhikevich [17]	+	+	+	+	+	+	+	+	+	+	+	+	+	+	+	+	+	+	+	+
Hodgkin Huxley [19]	+	+	+	+		+	+	+			+	+	+	+	+	+	+	+	+	+
ASN [11–13, 15]	+	+	+	+	+	+	+	+	+	+	+	+	+	+	+	+	+	+	+	+

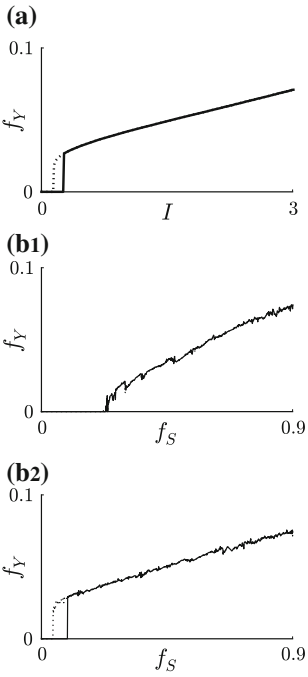

Fig. 4 Learning. **a** Teacher neuron = Izhikevich's resonator model. **b1** The ASN before learning. The sizes of registers are 32 and the internal clock frequency is $f_C = 3\,\text{kHz}$. **b2** The ASN after learning

5 Conclusions

The asynchronous sequential logic spiking neuron model (ab. ASN) was introduced. It was shown that the ASN can reproduce the typical twenty types of the dynamic response behaviors of neurons. Especially, in this paper, it was demonstrated that

the ASN can reproduce the five inhibitory dynamic response behaviors. Furthermore, it was shown that the learning algorithm enables the ASN to automatically reproduce the nonlinear response characteristics of an ODE-based neuron model. It was also confirmed that the ASN can be implemented with less hardware resources than a digital processor neuron for a reasonable parameter case. These reproduction abilities of neural dynamics and the low hardware cost property will be the keys to developing future applications of the ASN. Future problems include: (a) bifurcation analyses of the ASN, (b) clarification of relationships between the parameters of the ASN and experimentally measurable parameters of biological neurons, (c) development of a multi-compartment neuron model based on the ASN, including register-dynamics models of synaptic connections, and (d) development of a network of multi-compartment ASNs and its bio-inspired learning mechanisms such as the spike-timing dependent plasticity.

The authors would like to thank Professor Toshimitsu Ushio of Osaka University for valuable discussions. This work is partially supported by Toyota Riken Scholar and KAKENHI (24700225).

References

1. R. Vogelstein, U. Mallik, T. Vogelstein, G. Cauwenberghs, Dynamically reconfigurable silicon array of spiking neurons with conductance-based synapses. IEEE Trans. Neural Networks **18**(1), 253–265 (2007)
2. H. Chen, S. Saïandghi, L. Buhry, S. Renaud, Real-time simulation of biologically realistic stochastic neurons in vlsi. IEEE Trans. Neural Networks **21**(9), 1511–1517 (2010)
3. A. Basu, S. Ramakrishnan, C. Petre, S. Koziol, S. Brink, P.E. Hasler, Neural dynamics in reconfigurable silicon. IEEE Trans. Biomed. Circuits Syst. 4(5), 311–319 (2010)
4. J.V. Arthur, K.A. Boahen, Silicon-neuron design: a dynamical systems approach. IEEE Trans. Circuits Syst. I, **58**(5), 1034–1043 (2011)
5. E. Ros, E. Ortigosa, R. Agís, R. Carrillo, M. Arnold, Real-time computing platform for spiking neurons (RT-spike). IEEE Trans. Neural Networks **17**(4), 1050–1063 (2006)
6. R. Weinstein, M. Reid, R. Lee, Methodology and design flow for assisted neural-model implementations in FPGAs. IEEE Trans. Neural Syst. Rehabil. Eng. **15**(1), 83–93 (2007)
7. M. Pearson, G. Pipe, B. Mitchinson, K. Gurney, C. Melhuish, I. Gilhespy, M. Nibouche, Implementing spiking neural networks for real-time signal-processing and control applications: a model-validated FPGA approach. IEEE Trans. Neural Networks **18**(5), 1472–1487 (2007)
8. J.M. Nageswaran, N. Dutt, J.L. Krichmar, A. Nicolau, A.V. Veidenbaum, A configurable simulation environment for the efficient simulation of large-scale spiking neural networks on graphics processors. Neural Netw. **22**(5–6), 791–800 (2009)
9. T. Berger, D. Glanzman, *Toward Replacement Parts for the Brain: Implantable Biomimetic Electronics as Neural Prostheses* (The MIT Press, Cambridge, 2005)
10. Z. Zumsteg, C. Kemere, S. O'Driscoll, G. Santhanam, R. Ahmed, K. Shenoy, T. Meng, Power feasibility of implantable digital spike sorting circuits for neural prosthetic systems. IEEE Trans. Neural Syst. Rehabil. Eng. **13**(3), 272–279 (2005)
11. T. Matsubara, T. Torikai, Neuron-like responses and bifurcations of a generalized asynchronous sequential logic spiking neuron model. IEICE Trans. Fundam. **E95-A**(8), 1317–1328 (2012)
12. T. Hishiki, H. Torikai, A Novel Rotate-and-Fire Digital Spiking Neuron And its Neuron-like Bifurcations and Responses. IEEE Trans. Neural Networks **22**(5), 752–767 (2011)

13. T. Matsubara, H. Torikai, T. Hishiki, A generalized rotate-and-fire digital spiking neuron model and its on-FPGA learning. IEEE Trans. Circuits Syst. II Express Briefs **58**(10), 677–681 (2011)
14. T. Matsubara, H. Torikai, A novel asynchronous digital spiking neuron model and its various neuron-like bifurcations and responses, in *Proceedings of International Joint Conference on, Neural Networks*, 2011, pp. 741–748
15. S. Hashimoto, H. Torikai, A novel hybrid spiking neuron: bifurcations, responses, and on-chip learning. IEEE Trans. Circuits Syst. I **57**(8), 2168–2181 (2010)
16. E.M. Izhikevich, Which model to use for cortical spiking neurons? IEEE Trans. Neural Networks **15**(5), 1063–1070 (2004)
17. E.M. Izhikevich, *Dynamical Systems in Neuroscience: The Geometry of Excitability and Bursting* (The MIT Press, Cambridge, 2006)
18. J. Victor, K. Purpura, Metric-space analysis of spike trains: theory, algorithms and application. Netw. Comput. Neural Syst. **8**(2), 127–164 (May 1997)
19. A.L. Hodgkin, A.F. Huxley, A quantitative description of membrane current and its application to conduction and excitation in nerve. J. physiol. **117**(4), 500–544 (1952)

Nonlinear Behaviour of Vital Physiological Systems

Eugenijus Kaniusas

Abstract Nonlinearity is an intrinsic property of biological and physiological systems. Strictly speaking, almost all physiological processes are nonlinear. The linear behaviour seems to be rather an exception which is applicable only for small changes in physiological processes. Vital physiological systems such as heartbeat, respiration, blood circulation, oxygenation, and body temperature exhibit strong nonlinearities in order to fulfil their respective functions in time and space domains, and, on the other hand, to account for limiting environmental conditions. Nonlinearities ensure an effective use of body resources such as limited energy, available biological space for reactions, and finite time to provide a substantive output.

1 Introduction

Linearity describes the property of a system with, for instance, two quantities, namely, an input x and an output $f(x)$ which are directly proportional to each other. To be more precise, two properties of additivity (i.e., $f(x_1 + x_2) = f(x_1) + f(x_2)$) and homogeneity (i.e., $f(c \cdot x) = c \cdot f(x)$ with c as a scalar constant) are fulfilled by a linear system. From a physiological point of view, an increase of a stimulus, e.g., blood pressure, would yield a proportional increase in the response, e.g., vessel diameter, provided that the blood vessel can be approximated as a linear system. However, the distention of the vessel satiates for higher blood pressure, thereby indicating nonlinear behaviour of the vessel.

The linear behaviour seems to be rather an exception which is applicable only for small changes in physiological processes. The lack of this proportionality between input and output denotes a nonlinear system. In fact, nonlinearity is an intrin-

E. Kaniusas (✉)
Institute of Electrodynamics, Microwave and Circuit Engineering Vienna University of Technology, Gusshausstrasse 27-29/E354, Vienna, Austria
e-mail: kaniusas@tuwien.ac.at

V. In et al. (eds.), *International Conference on Theory and Application in Nonlinear Dynamics (ICAND 2012)*, Understanding Complex Systems,
DOI: 10.1007/978-3-319-02925-2_10,

sic property of biological and physiological systems and almost all physiological processes are nonlinear. Nonlinearity manifests not only as the aforementioned lack of the proportionality but also as a binary triggering (switching) of diverse electrochemical processes or even the blood flow, e.g., after a certain activation threshold has been reached or a specific substance is present in the vicinity of a molecular switch. Nonlinearity is necessary for these systems to comply with their (basic) function in the living body. Moreover, limited time (in terms of reaction time), limited space (compact structure of the body) and limited energy resources (efficient energy use) can be seen as ambient boundary conditions of biological systems. In fact, these conditions can be fulfilled only by nonlinear systems.

The present paper addresses structural nonlinearity in physiological systems, which is a prerequisite for functional nonlinearity. A few structural and functional nonlinearities are discussed from physiological and strategic perspective without nonlinear mathematics to facilitate their understanding. The justification of nonlinearities is presented in the performance of vital physiological systems, such as the biological information system, cardiorespiratory system, and hemodynamic system.

2 Structural Nonlinearity

Heterogenous structure of body tissues can be interpreted as structural nonlinearity which is needed to fulfil the corresponding nonlinear physiological function. Structures of different size will be exemplarily discussed from the molecular level to tissue structure up, and to organs.

2.1 Information System

Figure 1 illustrates special membrane proteins (with the size of about 10 nm) devoted to transport ions across the cell membrane and to maintain the resting membrane potential, namely, the membrane voltage u, across the cell membrane. Chemical energy is necessary to activate this pump. Such membrane proteins as well as gated channel proteins, e.g., voltage-gated channels for the inflow of Na^+ into the cell, act as nonlinear gate keepers (or switches) and selectively regulate the flow of ions through the membrane. This flow of ions, in turn, determines the temporal behaviour of u and releases action membrane potentials, the basic information carriers in biological systems.

Another important and highly-nonlinear structure on the molecular level is given by bonding of molecules in terms of the Lock and Key concept [1]. Here charge and shape complementarity, e.g., between an ion and a channel protein, determines if there is a binary match favourable from an energetic point of view. Provided this match, structural and functional changes can be initiated, e.g., favouring the ions passage through the channel.

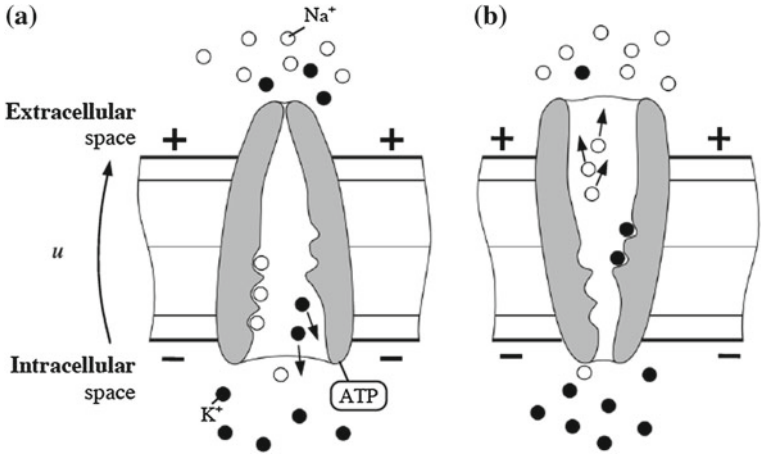

Fig. 1 Special membrane proteins for active and nonlinear transport of Na^+ and K^+ ions across the cell membrane, the so-called sodium-potassium pump. The ions are transported against their diffusion gradients, requiring hydrolysis of adenosine triphosphate (ATP) to provide the necessary energy. **a** Binding of three Na^+ ions and release of two K^+ ions inside the cell. **b** Subsequent release of the three Na^+ ions and binding of two new K^+ ions outside the cell. Image data partly taken from [1]

2.2 Cardiorespiratory System

Diverse nonlinear structures (with the size in the range of μm to mm) dominate in bodily tissues. One of the most important structures is given by the wall of arterial vessels (Fig. 2) in the cardiovascular system. The wall is composed of three layers (Fig. 2a) being responsible for passive and active changes in the vessels radius in response to the blood pressure. In particular, elastic fibers provide elasticity of the vessel, collagen fibers stabilize the vessel and prevent its overstretching with increasing blood pressure, whereas smooth muscles actively control the vessels radius. Interestingly, the relative amount of the latter three components varies strongly from central arteries (predominantly elastic) to peripheral arteries (predominantly muscular).

In consequence, there is a highly nonlinear relationship between the vessels radius and blood pressure inside the vessel (Fig. 2b). It can be observed that with increasing (absolute) pressure, the magnitude of the slope decreases nonlinearly, indicating that the artery wall becomes stiffer. For lower pressure values, (low) stiffness is maintained by elastic fibers, whereas for higher pressure the (stiffer) collagen fibers begin to be recruited and the artery stiffness increases.

In the respiratory system, numerous nonlinearities also dominate. For instance, the lung stiffness, i.e., the change in the transpulmonary pressure per change in lung volume, increases with increasing intrapulmonary (or intraalveolar) pressure. Other large structures subjected to mechanical stress, such as the skin or chest wall, exhibit nonlinear viscoelastic properties, which especially become dominant for relatively

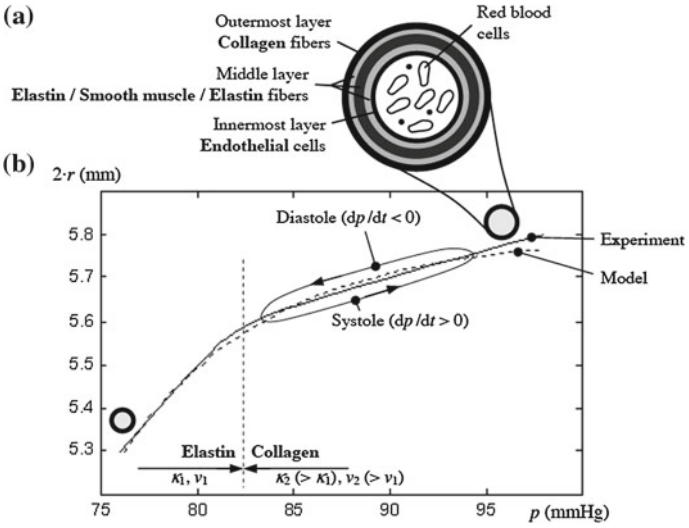

Fig. 2 **a** Qualitative structure of arterial vessel and its wall. **b** Nonlinear relationship of the inner vessel diameter $2 \cdot r$ and blood pressure p of the carotid artery with the experimental and modeled data taken from [1]. Relations of the module κ of volume elasticity (proportional to $\Delta p/\Delta r$) and the velocity ν (proportional to $\sqrt{\kappa}$) of propagating blood pressure waves are given for the regions dominated by elastin or collagen. The hysteretic behavior of r over the cardiac cycle is schematically indicated

high stress levels. Here the dynamic, nonlinear, and anisotropic behaviours are tightly interrelated with each other. For instance, the skin tissue requires a finite time to reach the state of deformation appropriate to the stress and a similar time to regain its unstressed shape [1].

Another prominent example of the structural nonlinearity is given by the heart, as illustrated in Fig. 3. The heart is a double pump with four chambers: right and left atria, right and left ventricles. The right and left sides of the heart are kept separate and comprise two pumps working in unison. The atria and ventricles are interconnected by one-way valves, the so-called atrioventricular valves. These valves ensure a unidirectional flow of blood from atria to ventricles on both sides of the heart. The blood flow out of the ventricles, i.e., out of the heart, is also governed by one-way valves, the so-called semilunar valves. The temporary activation of the heart muscles and the presence of valves yield highly pulsatile (nonlinear) blood flow and blood pressure in vessels.

3 Functional Nonlinearity

The discussed nonlinear structures yield nonlinear functionality over time. Examples of such functionalities will be discussed, which stem from the human information and hemodynamic systems.

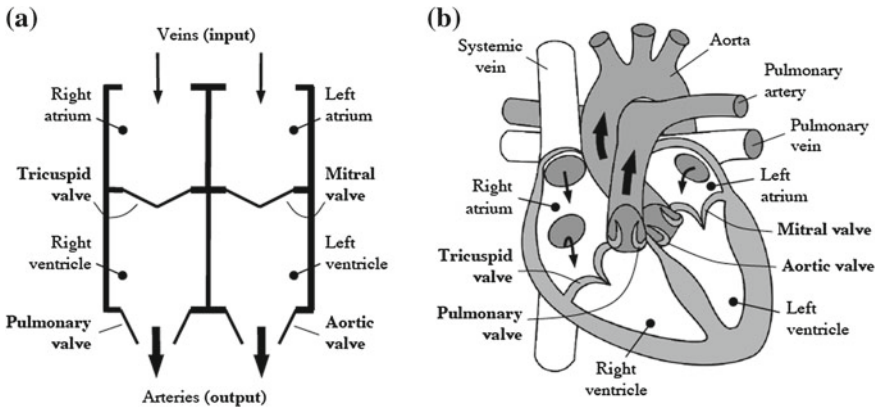

Fig. 3 The heart during blood ejection acting as a nonlinear pump. **a** Representation of the heart as four separate chambers with interconnecting valves. **b** A section through the heart, showing its basic structure. Image data partly taken from [1]

3.1 Information System

Even the basic information carrier in the body, i.e., the action membrane potential capable of fast propagation along nerves, has its origin in the nonlinear behaviour of the cell membrane. In fact, action potentials are the signals through which physiological information is conveyed within the body and processed in the central nervous system.

The nonlinear behaviour of the cell membrane in terms of its voltage u (Fig. 1) and its ionic conductance is depicted in Fig. 4. That is, the voltage u rapidly rises from its resting level to more positive values and then slowly recovers back to the resting level (Fig. 4a). The arising action impulse is known as the action membrane potential. The nonlinear conductivity changes of the membrane are responsible for this action impulse (Fig. 4b). The voltage-gated Na^+ channels, in principle similar to those depicted in Fig. 1, abruptly open for a short time period, after the membrane stimulation has reached a certain threshold. The ongoing change in u opens the voltage-gated K^+ channels, in the course of which u begins to recover. In short, gated (nonlinear) switching of ion channels is a fundamental mechanism behind the information system of the body.

3.2 Hemodynamic System

The discussed nonlinear relationship between the vessels radius and blood pressure (Fig. 2) causes not only the stiffness of the vessel but also its flow resistance to depend on the (absolute) blood pressure [2]. This nonlinear stress-strain relationship

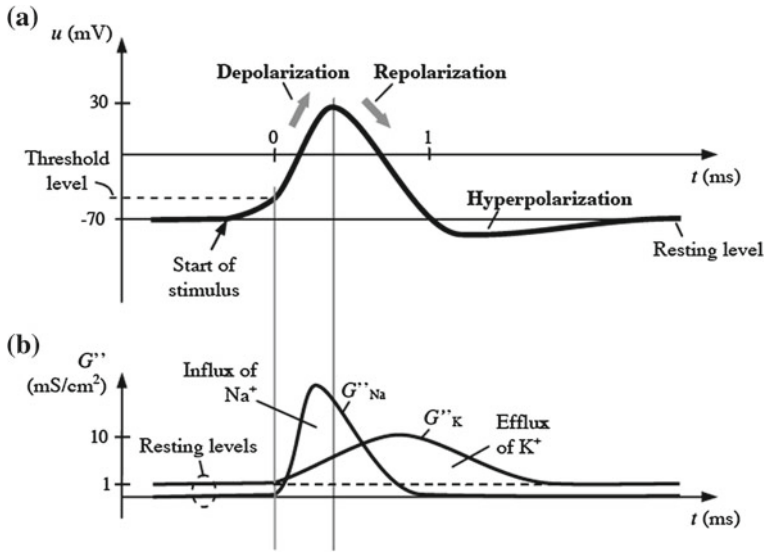

Fig. 4 Action membrane potential. **a** Voltage u across the cell membrane as an action impulse. **b** The corresponding highly nonlinear behavior of the area related membrane conductance $G"_K$ and $G"_{Na}$ for K^+ and Na^+ ions, respectively. Image data partly taken from [1]

is required for a stable vessel diameter under varying pressure conditions. On the other hand, the pulsatile action of the heart determines the pulsatile input into the arterial network. It means that the nonlinear input in combination with the nonlinear transmission properties of vessels governs important hemodynamic characteristics such as blood pressure and blood flow.

As illustrated in Fig. 5b, the resulting waveform of the blood pressure at the output of the heart is usually composed of two prominent peaks, compared to Fig. 6b. The first peak corresponds to the maximum ejection pressure of blood by the heart (ventricle) during systole. The second one appears after the dicrotic notch—the closure of semilunar valves—and corresponds mostly to the elastic recoil of central arteries during diastole.

In addition, any mechanical discontinuities along the vessel (i.e., nonlinearities along the blood flow), such as varying stiffness, tapering or branching of arteries, yield reflected waves of the blood pressure and blood flow. Fig. 5 shows the typical impact of the delayed reflected wave of the blood pressure, which superimposes the forward (incident) wave. In other words, mechanical discontinuities strongly affect diverse hemodynamic characteristics.

Another nonlinear phenomenon is shown in Fig. 2, namely, a hysteretic behaviour of the vessels radius over the cardiac cycle. Although almost linear range of this nonlinear relationship is occupied from systole to diastole (at rest), it is obvious that changes of the radius follow changes of the pressure with some delay. The width

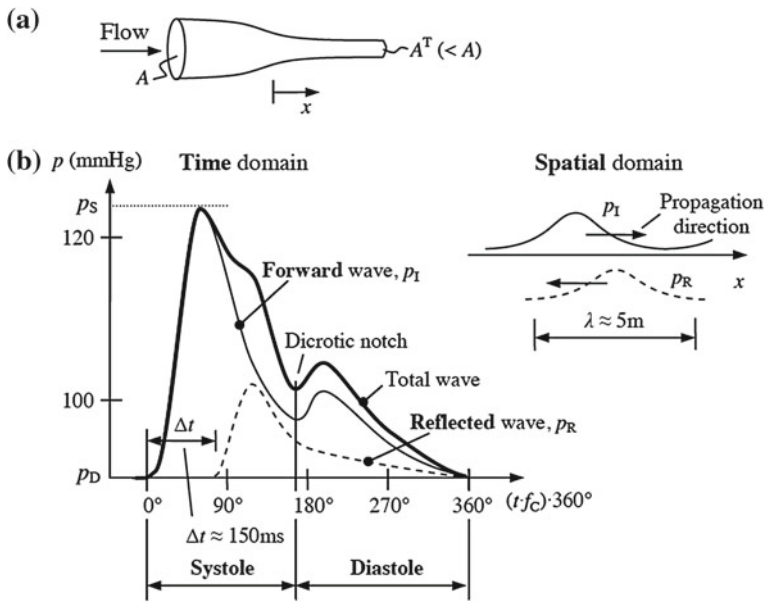

Fig. 5 **a** Narrowing of the arterial tree—a structural nonlinearity - represents the site of pulse wave reflections with A as the cross sectional area and f_C as heart rate. **b** Sketched positive reflection of blood pressure p waves with Δt as round-trip travel time from the aorta to the major reflecting site and back

of the hysteresis was observed to increase with increasing dominance of nonlinear viscoelastic properties of the vessels wall [3].

3.3 Biorhythms

Rhythmic behaviour in the information and hemodynamic systems arises in the course of nonlinear processes. It ensures an effective use of body resources, available biological space, and limited time to provide a substantive output [4].

These rhythms are ways to integrate and coordinate body functions and to anticipate environmental rhythms around the body. Tuning and synchronisation of rhythms reduce energy needs, especially during rest or sleep, or, in analogy, provide a special performance, especially during physical or mental stress. Provided limited biological space and limited time, a temporal compartmentalisation is needed to allow different environments to occur in the same space but at different times [5]. For instance, inspiration and expiration, systole and diastole, wakefulness and sleep cannot arise efficiently at the same time. A rhythmic stratification is needed, which is evident as biorhythm.

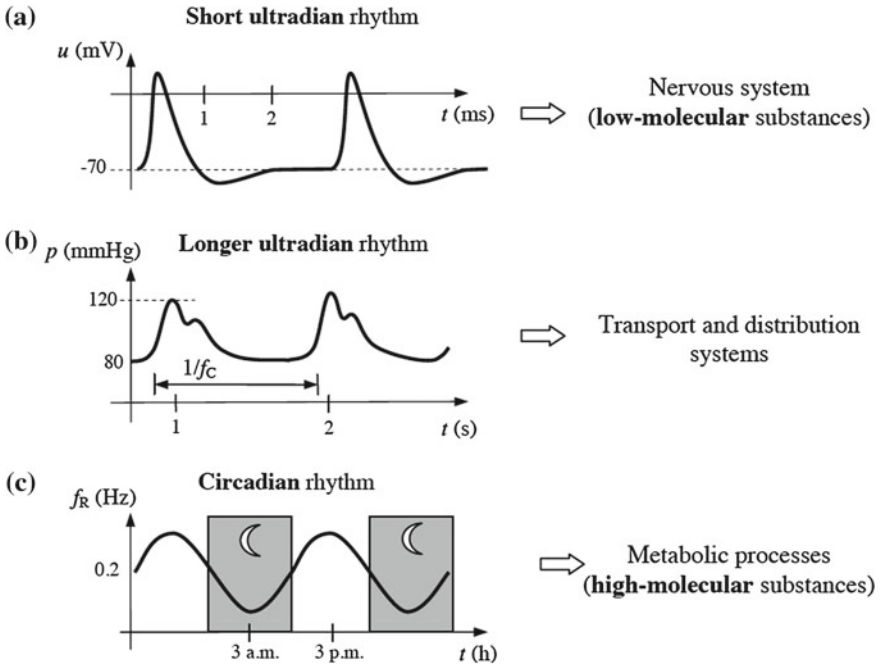

Fig. 6 Comparison of ultradian and circadian rhythms with respect to their nonlinear waveforms and origin. **a** Spiky action impulses of membrane voltage u. **b** Periodic variation of blood pressure p over cardiac cycles with heart rate f_C. **c** Sinusoidal changes of respiratory rate f_R over 24 h. Data given in accordance with [1, 4]

As illustrated in Fig. 6, these cyclic biological rhythms incorporate short-term cellular activity, the organs operation, mid-term distribution systems in the body, and long-term metabolic processes. Biological rhythms can be directly controlled (entrained) by the environment around the body (e.g., sleep-awake cycle) or can be driven by internal biological clocks (e.g., train of action impulses). In the time scale, rhythms extend from ultradian rhythms with the duration of less than 24 h (e.g., breathing cycle), to 24 h circadian rhythms (e.g., body temperature cycle), up to infradian rhythms with the duration of more than 24 h (e.g., menstruation cycle).

A continuous interplay occurs between vital physiological rhythms in terms of their phase and frequency. This interplay is intensified in resting states, whereas during stress the couplings seem to disappear.

4 Conclusions

Vital physiological systems related to heartbeat, respiration, blood circulation, oxygenation, and body temperature exhibit strong nonlinearities in order to fulfil their major functions in time and space domains. Intrinsic nonlinearities account for

limiting environmental conditions and insure an effective use of body resources, available biological space for reactions, and limited time to provide a substantial output. Consequently, numerous physiological parameters—such as heart rate variability registered by biomedical sensors—demonstrate nonlinear behaviour, which was only recently appreciated by the scientific community and started to be used for medical diagnosis.

Acknowledgments This work was supported by my research assistants Stefan Kampusch and Florian Thürk.

References

1. E. Kaniusas, *Biomedical Signals and Sensors I* (Springer, Heidelberg, 2012)
2. W.W. Nichols, M.F. ORourke, *McDonalds Blood Flow in Arteries: Theoretical, Experimental and Clinical principles*. (Hodder Arnold Publication Publisher, London, 2005)
3. Y.W. Shau, C.L. Wang, J.Y. Shieh, T.C. Hsu, Noninvasive assessment of the viscoelasticity of peripheral arteries. Ultrasound Med. Biol. **25**(9), 1377–1388 (1999)
4. G. Hildebrandt, M. Moser, M. Lehofer, *Chronobiology and Chronomedicine. Biological Rhythms and Medical Consequences* (Hippokrates Publisher, Stuttgart, 1998)
5. M. Moser, M. Fruhwirth, T. Kenner, The symphony of life. Importance, interaction, and visualization of biological rhythms. IEEE Eng. Med. Biol. Mag. **27**(1), 29–37 (2008)

Fabrication of Bistable MEMS Systems for Energy Harvesting

Teresa Emery

Abstract Non-linear devices are showing promise for responding to low frequency vibrations for energy harvesting applications [1–3]. Most MEMS scale energy harvesters take the form of cantilevers operating in their resonant frequency, but such operation is usually confined to the higher frequencies due to their small size [4–7]. Nonlinear energy harvesters do not operate at their resonant frequency and can harvest lower frequency vibration while still being MEMS scale [3]. One way to introduce non-linearity into a MEMS scale device is to make it bistable [8]. This bi-stability can be created in several ways including shape, magnet repulsion and attraction, and material stress. Each methods benefits and drawbacks will be discussed as it applies to energy harvesting and ease of fabrication.

1 Introduction

Powering micro-scale electronic devices through energy harvesting has been an active area of research for many years [8–11]. Vibration energy harvesting has been a main focus of much of this research due to the constant presence of mechanical vibrations from ambient sound and thermal noise. Ambient vibrations come from a variety of sources and are therefore have a wide spectrum of frequencies. Most of the energy from these vibrations is in low frequency components. Traditional energy harvesters are use linear resonant oscillators and convert the vibration into electricity using piezoelectric methods [8–11]. Resonant harvesters have very narrow bandwidth working only at or very near resonant frequency. Due to geometric constraints, the smaller the oscillator is the higher its resonant frequency creating a problem collecting energy from the lower frequency.

T. Emery (✉)
Nonlinear Dynamics, SSC Pacific, San Diego, CA 92152, USA
e-mail: teresa.emery@navy.mil

V. In et al. (eds.), *International Conference on Theory and Application in Nonlinear Dynamics (ICAND 2012)*, Understanding Complex Systems,
DOI: 10.1007/978-3-319-02925-2_11,

Nonlinear energy harvesting looks to overcome these problems by using stochastic nonlinear oscillators [1–5]. In the interest of looking at systems that can be fabricated at the MEMS scale, we are looking at bistable nonlinear oscillators. Oscillators with a bistable potential function do not operate at a particular frequency. The potential energy function of a bistable devices has a double well and energy harvested is collected from the device moving from one stable state to the other. This allows the device to collect energy from the lower frequency while still being small.

A macroscale device has been fabricated and tested by Gammaitonis group at the University of Perugia [1, 2]. In this case, the devices was an inverted pendulum with two magnets repelling each one on the tip of the cantilever and the other a distance Δ. From these experiments, the nonlinear oscillator out performs the linear oscillator at lower frequencies.

2 Methods

The first step to creating a nonlinear energy harvester on the MEMS scale is to recreate the bi-stability. The bi-stability in Gammaitonis macroscale device is the repelling magnets and the elastic restoring force of the brass lever. The magnets were glued to the end of the brass lever and the other to a moveable piece. The piezoelectric material used to transfer the vibration to electrical power was also adhere to the lever with adhesive like the magnets. At the macroscale, creating this device can be done with glue and a steady hand. At the MEMS scale, the whole process needs to be done with thin film processing and chemistry.

Standard microfabrication techniques are referred to as top down. Material is added or etched away from a carrier wafer vertically. The standard procedure for making a cantilever with silicon on insulator wafer is shown in Fig. 1. This standard procedure is important to remember for the placement of the piezoelectric material. To get the maximum voltage for each jump from one stable position to the other, the piezoelectric material needs to be placed at the position of highest stress. One would also like to deposit a thick layer of piezoelectric because the thicker the layer the more voltage that will be produced. These facts hinder bi-stable MEMS designs with motion in the plane of the wafer since the areas of highest stress are in the horizontal direction and the vertical surface is too narrow for a thick deposit.

The piezoelectric material creates challenges to the design as well. Most piezoelectric materials are ceramics that on a large scale are made in platinum crucibles from powered components and sintered at high temperatures. For thin film deposits, temperatures are still need to create the correct crystal for the piezoelectric effect [12]. The high temperature process complicate the fabrication process because it eliminates the use of plastics in the process. Thin plastic cantilevers would be very response to thermal vibrations but would burn at the high temperature needed for the piezoelectric layer.

Each process step has small amounts of error that could lead to a failed device. Standard MUMPS run give an error for each layer as $2\ /mu$m. This error need to be taken into consideration when designing the device. With more steps to create

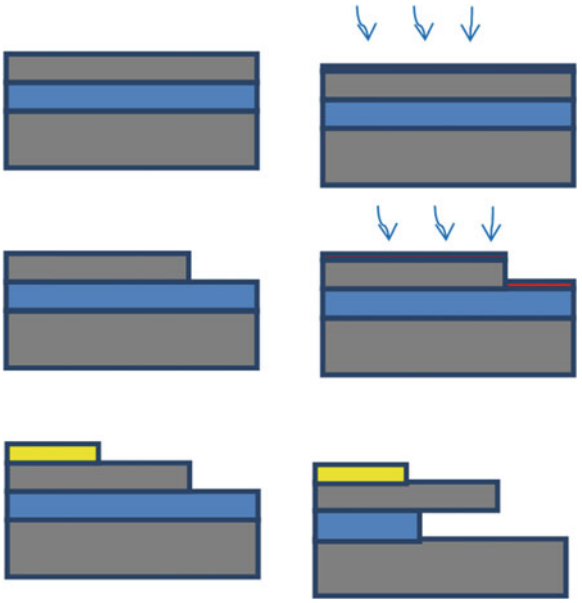

Fig. 1 Process for creating a silicon on insulator cantilever. Silicon oxide is the sacrificial layer releasing the cantilever for free motion

the device the more likely it will fail due to alignment errors. The final step to each device is the release. Most devices are released by dissolving a sacrificial layer. Because of the piezoelectric layer, this layer cannot be a plastic like photoresist. Silicon dioxide and silicon are the two most popular sacrificial layers. The reason is chemical. Silicon dioxide is usually etch in a strong acid hydrogen fluoride (HF). Silicon on the other hand is etched in a strong base potassium hydroxide (KOH). HF does not etch silicon and KOH does not etch silicon dioxide. This nice chemical compatibility is one of the main reasons that silicon remains the semiconductor of choice for the MEMS fabrication. The material system for the MEMS device can be reduce to the whether the piezoelectric material of choice is effected by acid or base. Once the device released, it cannot survive another deposition process.

Permanent magnets created the bi-stability in the initial macroscale device. For most applications, the magnetic field created by the magnets will not affect the sensor it is powering. Magnets have the benefit of creating the bistability without power and large number of magnetic materials to choose from. To recreate the macroscale device into the MEMS scale requires to deposition step be added to the standard cantilever fabrication. Most cantilevers are fabricated by starting with a silicon on insulator substrate (SOI). A SOI wafer has a carrier wafer of silicon with a buried silicon dioxed layer and single crystal silicon on top. The top layer of silicon is covered with photoresist and patterned to define the cantilever. The process of depositing and exposure are repeated twice to define the area for the piezoelectric material and its contacts.

To make the cantilever bi-stable, another mask layer is add to define the magnet at the tip of the cantilever. The magnet at the end of the cantilever and its opposing magnet need to be made of two different magnetic materials. If the two magnets were made of the same material and deposited at the same time it would be impossible two make them pole in opposite directions. To make the magnets repel each other, the first magnetic is deposited on the tip of the unreleased cantilever. The second magnetic material needs to have a higher coercivity. Coercivity is the needed applied magnetic field to flip a magnetic material. The two different materials are poled one direction to align all the domain and then poled in the opposite direction at a lower applied magnetic field. The lower field will flip only the magnet with the lower coercivity. After the magnets are defined and poled, a layer of polymide is deposited on the contacts and magnets to protect them from the HF for the cantilever release. The polymide layer is remove by an oxygen plasma.

For some sensors, an constantly moving magnetic field would be problematic for operation. For sensors like this, we were interested in developing other ways to create bi-stability. Materials deposited by thin film techniques are frequently stressed due to crystal lattice mismatch. When films are too stressed, they can delaminate and curl. Silicon nitride is a popular insulator that when deposited on silicon creates a stressed layer. By changing the ratio of silicon to nitrogen, the stress can be reduce. By using the same process, a film could be deposited with enough stress to create two stable states, concave and convex. Silicon nitride like silicon dioxide is not etch by KOH. A silicon carrier wafer would be deposited with the slightly stressed silicon nitride layer. The wafer would be pattern using photolithography and etch using dry etching in SF_6. The piezoelectric material and contact would be deposited using the same photolithography steps. After the top side is protected by polyimide layer, the backside of the wafer would be patterned and etch to open backside holes. The wafer would then go into a KOH bath for release. Other materials deposit stressed as well. Chrome is a known to deform wafers during thick deposits. Material like chrome could be added to the process to "correct" the level of stress.

The third method of creating bi-stability is structural. In macroscale devices, bi-stability has been produced by moving the supports of a double clamped beam closer together causing the beam to buckle. The beam has two stable positions: concave and convex. At the MEMS scale, we cannot nudge the supports to buckle the beam but deposit a curved beam. The deposition process for low stress nitride is low pressure chemical vapor deposition (LPCVD) and is done at 1000 °C. The depositing temperature makes using gray-scale lithography difficult due to the photoresist burning at these temperature. Gray-scale lithography combined with dry etching would create a curved hole for deposit but we want avoid gray-scale in an effort to keep the fabrication simple. Wet etching is not always anisotropic. KOH etches silicons close packed plane slower causing a 54.74° angle in the etch. Using a shallow etch, we can fabricate a curved hole to deposit the silicon nitride.

The process starts with a silicon wafer with either a silicon dioxide or silicon nitride layer. This process is showed in Fig. 2. The top-side surface is patterned with a holes for the size of the double clamped beam and the bottom-side is patterned with holes for the later release of the structure. Patterning the bottom surface at this stage

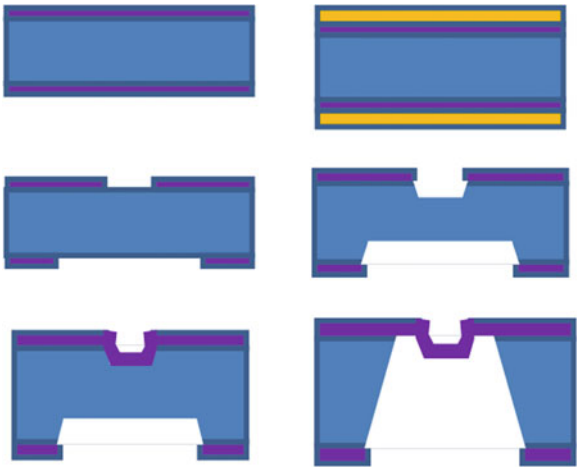

Fig. 2 Process for structural stressed bridge

prevents the topside from being scratch or damaged after the beams are etched. Both patterns are defined with photolithography and dry etch with SF6. Then the wafer is etched in KOH to create the curved holes and start the backside etch. LPCVD nitride is deposited over the shallow holes. LPCVD nitride process isconformal deposit on the whole surface for shallow etches on the $20/mu$m of less. The top-side is patterned and etch into beams followed by two more rounds of patterning to deposit and define the piezoelectric material and its contacts. The final beam can then be released using another KOH etch.

3 Conclusion

All designs presented here create a bistable MEMS device. These device need to be tested for failure modes and stress in order to determine the best design for energy harvesting. Since the response is not determined by the resonant frequency, the size of the device need to be look at for responding to the lower frequency and being MEMS scale. The best design might be determined by other factors including the supporting electronics. Although all devices are made using techniques developed for the semiconductor industry, some heat treatments will not work well with transistors. Each design might serve as an energy harvester for different device based on the fabrication parameters of the sensor they are designed to power. The next step in this research is to test these devices for power production and failure.

References

1. F. Cottone, L. Gammaitoni, H. Vocca, Nonlinear energy harvesting. Phys. Rev. Lett. **102**, 080601 (2009)
2. L. Gammaitoni, I. Neri, H. Vocca, Nonlinear oscillators for vibrational energy harvesting. Appl. Phys. Lett. **94**, 164102 (2009)
3. M. Ferrari, V. Ferrari, M. Guizzetti, Improved energy harvesting from wideband vibrations by nonlinear piezoelectric converters. Sens. Actuators A **192**, 425–431 (2010)
4. S. Anton, H. Sodano, A review of power harvesting using piezoelectric materials (2003–2006). Smart Mater. Struct. **16**(3), R1–R21 (2007)
5. S. Wang, K. Lam, C. Sun, Energy harvesting with piezoelectric drum transducer. Appl. Phys. Lett. **90**, 1–3 (2007)
6. S. Roundy, On the effectiveness of vibration-based energy harvesting. J. Intell. Mater. Struct. **16**(10), 809–823 (2005)
7. S. Beeby, M. Tudor, N. White, Energy harvesting vibration sources for microsystems applications. Meas. Sci. Technol. **17**, R175–R195 (2006)
8. A. Arrieta, P. Hagedorn, A. Erturk, A piezoelectric bistable plate for broadband energy harvesting. Appl. Phys. Lett. **97**, 104102 (2010)
9. J. Paradiso, T. Starner, Scavenging for mobile and wireless electronics. IEEE Pervasive Comput. **4**(1), 18–27 (2005)
10. S. Roundy, P. Wright, J. Rabaey, *Energy Scavenging For Wireless Sensor Networks* (Kluwer Academic Publishers, Boston, 2003)
11. R. Byrne, D. Diamond, Chemo/bio-sensor network. Nat. Mater. **5**, 421–424 (2006)
12. N. Ledermann, P. Muralt, J. Barborowski, 100 textured piezoelectric PbZrxTi1-xO3 thin films for MEMS: intergration, deposition, and properties. Sens. Actuators A **105**(2), 162–170 (2003)

Symbolic Toolkit for Chaos Explorations

Tingli Xing, Jeremy Wojcik, Roberto Barrio and Andrey Shilnikov

Abstract Computational technique based on the symbolic description utilizing kneading invariants is proposed for explorations of parametric chaos in a two exemplary systems with the Lorenz attractor: a normal model from mathematics, and a laser model from nonlinear optics. The technique allows for uncovering the stunning complexity and universality of the patterns discovered in the bi-parametric scans of the given models and detects their organizing centers—codimension-two T-points and separating saddles.

1 Introduction

Several analytic and experimental studies, including modeling simulations, have focused on the identification of key signatures to serve as structural invariants. Invariants would allow dynamically similar nonlinear systems with chaotic dynamics from diverse origins to be united into a single class [1–3]. Among these key structures are various homoclinic and heteroclinic bifurcations of low codimensions that are the heart of the understanding of complex behaviors because of their roles as organizing centers of dynamics in parameterized dynamical systems.

One computationally justified approach for studying complex dynamics capitalizes on the sensitivity of deterministic chaos. Sensitivity of chaotic trajectories can be quantified in terms of the divergence rate evaluated through the largest Lyapunov characteristic exponent. In several low-order dissipative systems, like the Rössler

T. Xing · J. Wojcik · A. Shilnikov (✉)
Neuroscience Institute and Department of Mathematics and Statistics, Georgia State University, Atlanta 30303, USA
e-mail: ashilnikov@gsu.edu

R. Barrio
Departamento de Matematica Aplicada and IUMA,University of Zaragoza, E-50009 Zaragoza, Spain

V. In et al. (eds.), *International Conference on Theory and Application in Nonlinear Dynamics (ICAND 2012)*, Understanding Complex Systems,
DOI: 10.1007/978-3-319-02925-2_12,

model, the computational technique based on the largest Lyapunov characteristic exponent reveals that they possess common, easily recognizable patterns involving spiral structures in bi-parametric planes [4, 5]. Such patterns have turned out to be ubiquitously in various discrete and continuous-time systems [6–9], and they are easily located, as spiral patterns have regular and chaotic spiral "arms" in the systems with the Shilnikov saddle-focus [10–14].

Application of the Lyapunov exponents technique fails, in general, to reveal fine structures embedded in the bi-parametric scans of Lorenz-like systems. This failure implies that the instability of the Lorenz attractors does not vary noticeably as control parameters of the system are varied. This holds true when one attempts to find the presence of characteristic spiral structures that are known to exist theoretically in Lorenz-like systems [4, 15], identified using accurate bifurcation continuation approaches [16, 17]. Such spirals in a bi-parametric parameter plane of a Lorenz-like system are organized around the T[erminal]-points; corresponding to codimension-two, closed heteroclinic connections involving two saddle-foci and a saddle at the origin, see Fig. 1. Such T-points have been located in various models of diverse origins including electronic oscillators [18, 19] and nonlinear optics [20].

Despite the overwhelming number of studies reporting the occurrence of various spiral structures, there is yet little known about construction details and generality of underlying bifurcation scenarios which gives rise to such spiral patterns. Additionally, little is known about how such patterns are embedded in the parameter space of the models with the Lorenz attractors. Here we present a computational toolkit capitalizing on the symbolic representation for the dynamics of Lorenz-like systems that employ kneading invariants [21]. We will then show how the toolkit detects various fractal structures in bi-parametric scans of two exemplary systems: a normal model from mathematics, and a laser model from nonlinear optics. For the further details we refer the reader to the original paper [22].

2 Kneading Invariants for a Lorenz Like System

Chaos can be quantified by several means. One customary way is through the evaluation of topological entropy. The greater the value of topological entropy, the more developed and unpredictable the chaotic dynamics become. Another practical approach for measuring chaos in simulations capitalizes on evaluations of the largest (positive) Lyapunov exponent of a long yet finite-time transient on the chaotic attractor.

A trademark of any Lorenz-like system is the strange attractor of the iconic butterfly shape, such as shown in Fig. 1 [23]. The "wings" of the butterfly are marked with two symmetric "eyes" containing equilibrium states, stable or not, isolated from the trajectories of the Lorenz attractor. This attractor is structurally unstable [24, 25] as it bifurcates constantly as the parameters are varied. The primary cause of structural and dynamic instability of chaos in the Lorenz equations and similar models is the singularity at the origin—a saddle with two one-dimensional outgoing separatrices. Both

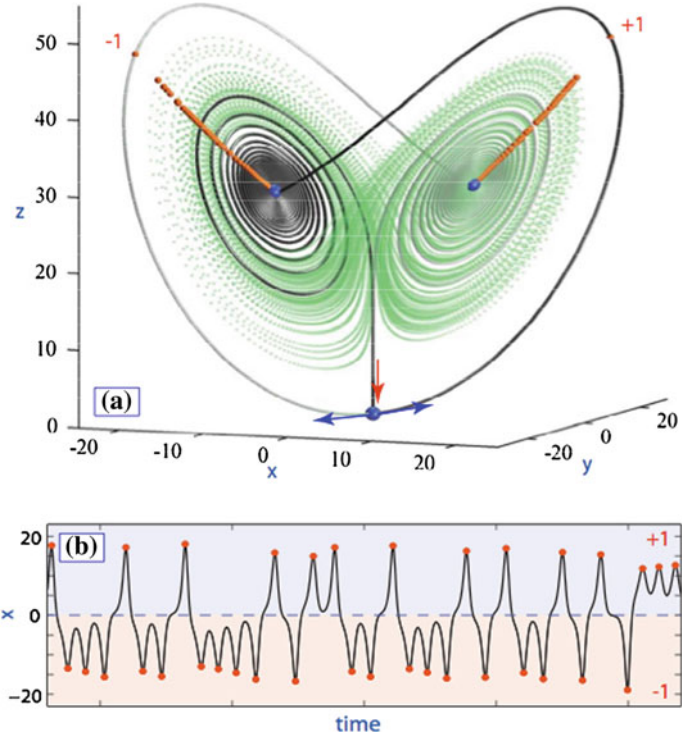

Fig. 1 (**a**) Heteroclinic connection (in *dark color*) between the saddle at the origin and two saddle-foci (*blue spheres*) being overlaid with the strange attractor (*green light color*) on the background at the primary T-point ($r = 30.38$, $\sigma = 10.2$) in the Lorenz model. Orange spheres on the butterfly wings indicating the turning points around the right and left saddle-foci define the kneading sequence entries, $\{\pm 1\}$, respectively. (**b**) A typical time evolution of either symmetric coordinate of the right separatrix of the saddle

separatrices densely fill the two spatially symmetric wings of the Lorenz attractor in the phase space [26]. The Lorenz attractor undergoes a homoclinic bifurcation when the separatrices of the saddle change the alternating pattern of switching between the butterfly wings centered around the saddle-foci. At such a change, the separatrices comes back to the saddle thereby causing a homoclinic explosions in phase space [27–30].

The time progression of the "right" (or symmetrical "left") separatrix of the origin can be described geometrically and categorized in terms of the number of alternations around the nonzero equilibrium states in the phase space of the Lorenz-like system (Fig. 1). Alternatively, the description can be reduced to the time-evolution of a coordinate of the separatrix, as shown in panel B of Fig. 1. The sign-alternation of the x-coordinate suggests the introduction of a $\{\pm 1\}$-based alphabet for the symbolic description of the separatrix. Namely, whenever the right separatrix turns around O_1 or O_2, we record $+1$ or 1, respectively. For example, the time

series shown in panel B generates the following kneading sequence starting with $\{+1, 1, 1, 1, +1, 1, 1, +1, 1, \ldots\}$.

We introduce and demonstrate a new computational toolkit for the analysis of chaos in the Lorenz-like models. The toolkit is inspired by the idea of kneading invariants introduced in [21]. A kneading invariant is a quantity that is intended to uniquely describe the complex dynamics of the system that admits a symbolic description using two symbols, here $+1$ and 1.

The kneading invariant for either separatrix of the saddle equilibrium state of the Lorenz attractor can be defined in the form of a formal power series:

$$P(q) = \sum_{n=0}^{\infty} \kappa_n q^n. \tag{1}$$

Letting $q \in (0, 1)$ guarantees the series is convergent. The smallest zero, q, if any, of the graph of (1) in the interval $q \in (0, 1)$ yields the topological entropy, $h(T) = \ln(1/q)$.

The kneading sequence $\{\kappa_n\}$ composed of only $+1$s corresponds to the "right" separatrix of the saddle converging to an ω-limit set with $x(t) > 0$, such as a stable focus or stable periodic orbit. The corresponding kneading invariant is maximized at $\{P_{\max}(q)\} = 1/(1-q)$. When the right separatrix converges to an attractor with $x(t) < 0$, then the kneading invariant is given by $\{P_{\min}(q)\} = 1/(1-q)$ because the first entry $+1$ in the kneading sequence is followed by infinite -1s. Thus, $[\{P_{min}(q)\}, \{P_{max}(q)\}]$ yield the range of the kneading invariant values; for instance $[\{P_{min}(1/2)\} = 0, \{P_{max}(1/2)\} = 2]$.

Two samples of the separatrix pathways shown in Fig. 2 generating the following kneading invariants illustrate the idea.

$$P_A(1/2) = +1 - 1/2 - 1/4 + 1/8 + 1/16 + 1/32 + 1/64 \ldots + 1/2^n \ldots = 1/2,$$
$$P_B(1/2) = +1 - 1/2 - 1/4 - 1/8 - 1/16 - 1/32 - 1/64 \ldots 1/2^n \ldots = 0,$$

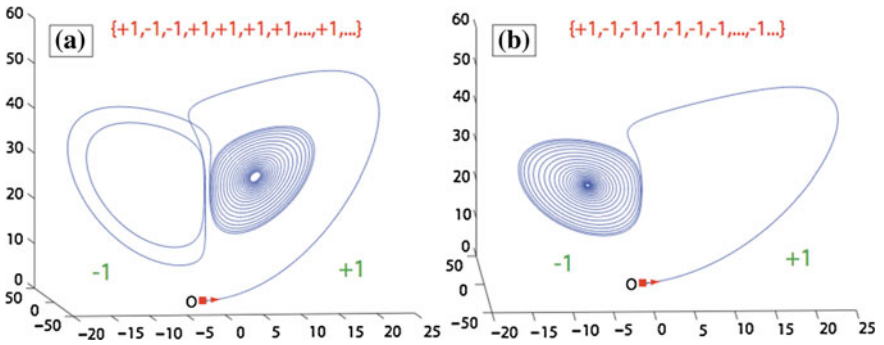

Fig. 2 Truncated kneading sequences generated by the right outgoing separatrix of the saddle at the origin in a typical Lorenz-like equation at two distinct values of the parameters

In computational studies of the models below, we will consider a partial kneading power series truncated to the first 20 entries: $P_{20}(q) = \sum_{n=0}^{20} \kappa_n q^n$. The choice of the number of entries is not motivated by numerical precision, but by simplicity, as well as by resolution of the bitmap mappings for the bi-parametric scans of the models. One has also to determine the proper value of q: setting it too small makes the convergence fast so that the tail of the series has a little significance and hence does not differentiate the fine dynamics of the Lorenz equation for longer kneading sequences.

At the first stage of the routine, we perform a bi-parametric scan of the model within a specific range in the parameter plane. The resolution of scans is set by using mesh grids of $[1000 \times 1000]$ equally distanced points. Next by integrating the same separatrix of the saddle point we identify and record the sequences $\{\kappa_n\}_0^{20}$ for each point of the grid in the parameter plane. Then we define the bi-parametric mapping: for the Shimizu-Morioka model below it is $(\alpha, \lambda) \rightarrow P_{20}(q)$ for some chosen q, the value of which determines the depth of the scan. The mapping is then colorized in Matlab by using various built-in functions ranging between to P_{20}^{min} and P_{20}^{max}, respectively. In the mapping, a particular color in the spectrum is associated with a persistent value of the kneading invariant on a level curve. Such level curves densely foliate the bi-parametric scans.

3 Kneading Scans of the Shimizu-Morioka Model

Here we will examine the kneading-based bi-parametric scanning of the Shimizu-Morioka model [16, 31]:

$$\dot{x} = y, \dot{y} = x - \lambda y - xz, \dot{z} = \alpha z + x^2; \tag{2}$$

with α and β being positive bifurcation parameters. The Z_2-symmetric model has three equilibrium states: a simple saddle, with one-dimensional separatrices, at the origin, and two symmetric stable-foci which can become saddle-foci through a super-critical Andronov-Hopf bifurcation.

This model was originally introduced to examine a pitch-fork bifurcation of the stable figure-8 periodic orbit that gives rise to multiple cascades of period doubling bifurcations in the Lorenz equation at large values of the Reynolds number. It was proved in [5] that the Eq. (2) would be a universal normal form for several codimension-three bifurcations of equilibria and periodic orbits on Z_2-central manifolds. The model turned out to be very rich dynamically: it exhibits various interesting global bifurcations [17] including T-points for heteroclinic connections.

In the case study of the Shimizu-Morioka model, we compare the proposed kneading scanning apparatus with the customary bi-parametric sweeping based on the evaluation of the Lyapunov exponent spectrum computed over a finite time interval. The latter is shown in Fig. 3 [32].

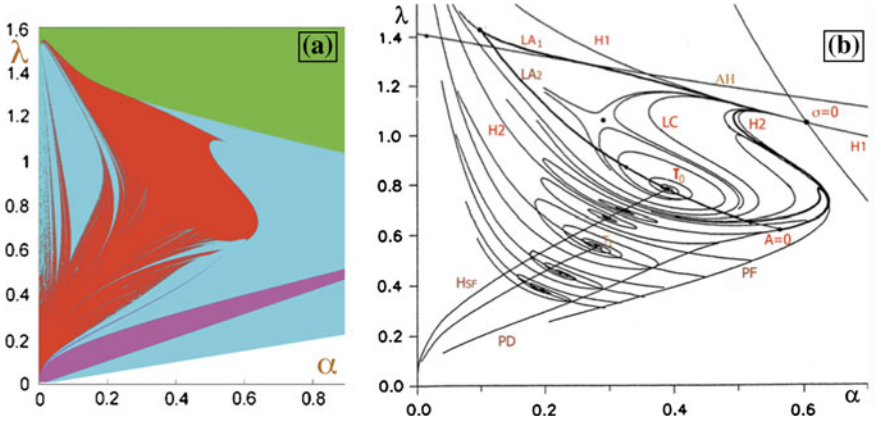

Fig. 3 (**a**) Existence regions of attractors of the Shimizu-Morioka model in (α, λ)-parameter plane being differentiated by the sign of the largest Lyapunov exponent, L_{max}. Color legend for the attractors of the model: *green–stable* equilibrium states, $L_{max} < 0$; *blue–stable* periodic orbits with a nodal normal behavior, $L_{max} = 0$; magenta - a periodic orbit with a focal normal behavior; *red* attractors with $L_{max} > 0$, with identified lacunae. Courtesy of [32]. (**b**) Detailed (α, λ)-parameter plane of the Shimizu-Morioka model obtained by the parameter continuation method (courtesy of [5]). Legend: AH stands for a supercritical Andronov-Hopf bifurcation, H_1 stands for the homoclinic butterfly made of two separatrix loops; the codimension-two points corresponding to the resonant saddle $\sigma = 0$ on H_1 organizes the bifurcation unfolding of the model; cod-2 point $A = 0$ stands for an orbit-flip bifurcation for the double-loop homoclinics on H_2. The thick line demarcates, with good precision, the existence region of the Lorenz attractor bounded by LA_1 and LA_2

The regions of the solid colors are associated with the sign of the largest Lyapunov exponent, L_{max}: $L_{max} < 0$ values correspond to steady state attractors in the green region; $L_{max} = 0$ corresponds to periodic attractors in the blue region; and $L_{max} > 0$ is associated with chaotic dynamics in the model in the region. Note the blue islands in the red-colored region that correspond to stability windows in chaos-land. Such windows in the Lorenz attractor have an emergent lacuna containing one more three periodic orbit. Other than lacunas, the diagram shows no sign of any structure in the red region corresponding to the chaotic dynamics.

Indeed, the structure of the bifurcation set of the Shimizu-Morioka model is very complex. The detailed bifurcation diagram is shown in the top panel of Fig. 4. It reveals several T-points, and multiples curves corresponding to an Andronov-Hopf (AH), pitch-fork (PF), period doubling (PD) and homoclinic (H) bifurcations that shape the existence region of the Lorenz attractor in the model. The detailed description of the bifurcation structure of the Shimizu-Morioka model is out of the scope of this paper. The reader can find a wealth of information on bifurcations of the Lorenz attractor in the original papers [5, 17]. We point out that those bifurcation curves were continued in the (α, λ)-parameter plane by following various bifurcating solutions, as periodic, homo- and heteroclinic orbits, in the phase space of the model.

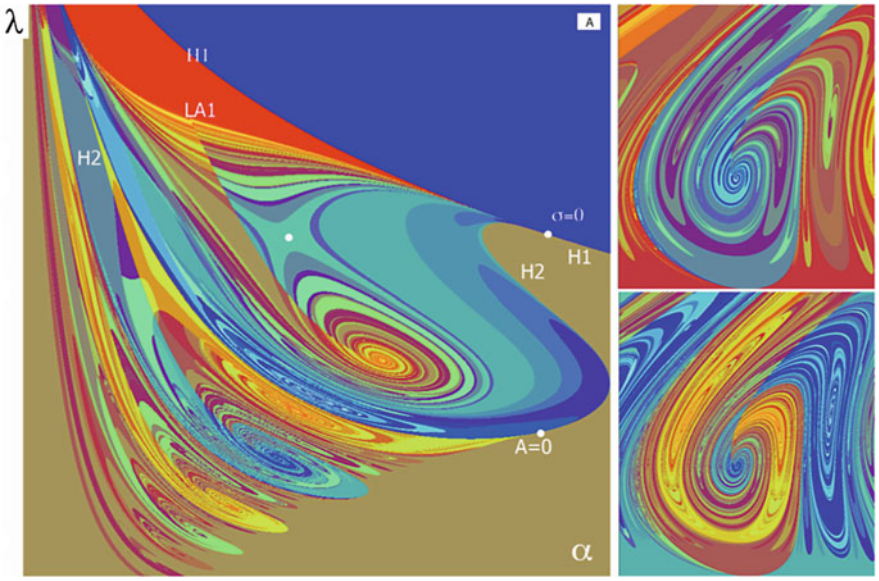

Fig. 4 (*left*) The scan revealing multiple T-points and saddles that globally organize complex chaotic dynamics of the Shimizu-Morioka model. Solid-color regions associated with constant values of the kneading invariant correspond to simple dynamics dominated by stable equilibria (*brown*) or stable periodic orbits (*blue*). The border between the *brown* and *blue* regions corresponds to the bifurcation curve of the homoclinic butterfly. The codimension-two point, $\sigma = 0$, gives rise to loci of bifurcation curves including LA_1 below which the Lorenz attractor exists. Bifurcation loci of the other codimension-two point, $A = 0$ (*yellow zone*) giving rise to subsidiary orbit-flip bifurcations on turns of spirals around T-points, are separated by saddles (two large scale ones) in the parameter plane.(*right*) Two zoom of distinct scanning depths of the (α, λ)-parametric mapping near the secondary T-point, T_1, revealing fine fractal structures embedding smaller-scale spirals around several visible descendant T-points

The panel A of Fig. 4 is a *de-facto* proof of the new kneading invariant mapping technique. The panel represents the color bi-parametric scan of the dynamics of the Shimizu-Morioka model that is based on the evaluation of the first 20 kneadings of the separatrix of the saddle on the grid of 1000×1000 points in the (α, λ)-parameter region. Getting the mapping took a few hours on a high-end workstation without any parallelization efforts. The color scan reveals a plethora of primary, large, and small scale T-points as well as the saddles separating spiral structures.

The solid-color zones in the mapping correspond to simple dynamics in the model. Such dynamics are due to either the separatrix converging to the stable equilibria or periodic orbits with the same kneading invariant (blue region), or to the symmetric and asymmetric stable figure-8 periodic orbits (brown region). The borderlines between the simple and complex dynamics in the Shimizu-Morioka model are clearly demarcated. On the top is the curve, LA_1, (see the top panel of Fig. 4). The transition from the stable 8-shaped periodic orbits to the Lorenz attractor (through the boundary, LA_2) is similar though more complicated as it involves a pitch-fork bifur-

cation and bifurcations of double-pulsed homoclinics, see [5, 17] for details. One can clearly see the evident resemblance between both diagrams found by using the bifurcationaly exact numerical methods and by scanning the dynamics of the model using the proposed kneading invariant technique. The latter reveals a richer structure providing finer details. The structure can be enhanced further by examining longer tails of the kneading sequences. This allows for the detection of smaller-scale spiral structures within scrolls of the primary T-vortices, as predicted by the theory.

4 6D Optically Pumped Laser Model

The coexistence of multiple T-points and accompanying fractal structures in the parameter plane is a signature for systems with the Lorenz attractor. The question remains whether the new computational technique will work for systems of dimensions higher than three. In fact, to apply the technique to a generic Lorenz-like system, only wave forms of a symmetric variable progressing in time, that consistently starts from the same initial condition near the saddle is required. Next is an example from nonlinear optics - a 6D model of the optically pumped, infrared red three-level molecular laser [33] Moloney, Forysiak, Uppal Harrison, [20] given by

$$\begin{aligned}
\dot{\beta} &= -\sigma\beta + g p_{23}, \\
\dot{p}_{21} &= p_{21} - \beta p_{31} + \alpha D_{21}, \\
\dot{p}_{23} &= -p_{23} + \beta D_{23} - \alpha p_{31}, \\
\dot{p}_{31} &= -p_{31} + \beta p_{21} + \alpha p_{23}, \\
\dot{D}_{21} &= -b(D_{21} - D_{21}^0) - 4\alpha p_{21} - 2\beta p_{23}, \\
\dot{D}_{23} &= -b(D_{23} - D_{23}^0) - 2\alpha p_{21} - 4\beta p_{23}.
\end{aligned} \tag{3}$$

Here, α and b are the Rabi flopping quantities representing the electric field amplitudes at pump and emission frequencies. The parameter α is a natural bifurcation parameter as it is easily varied experimentally. The second bifurcation parameter, b, can be varied to some degree at the laboratory by the addition of a buffer gas. This system presents, like the Lorenz equations, a symmetry $(\beta, p_{21}, p_{23}, p_{31}, D_{21}, D_{23}) \leftrightarrow (\beta, p_{21}, p_{23}, p_{31}, D_{21}, D_{23})$. The laser model has either a single central equilibrium state, O (with $\beta = 0$), or through a pitch-fork bifurcation, a pair of symmetric equilibrium states, $O_{1,2}$ (with $\beta \geq 0$); the stability of the equilibria depends on the parameter values.

Optically pumped, infrared lasers are known to demonstrate a variety of nonlinear dynamic behaviors, including Lorenz-like chaos [34]. An acclaimed example of the modeling studies of chaos in nonlinear optics is the two level laser Haken model [35] to which the Lorenz equation can be reduced. A validity that three level laser models would have the Lorenz dynamics was widely questioned at the time. It was comprehensively demonstrated [20] in 1991 that this plausible laser model possesses

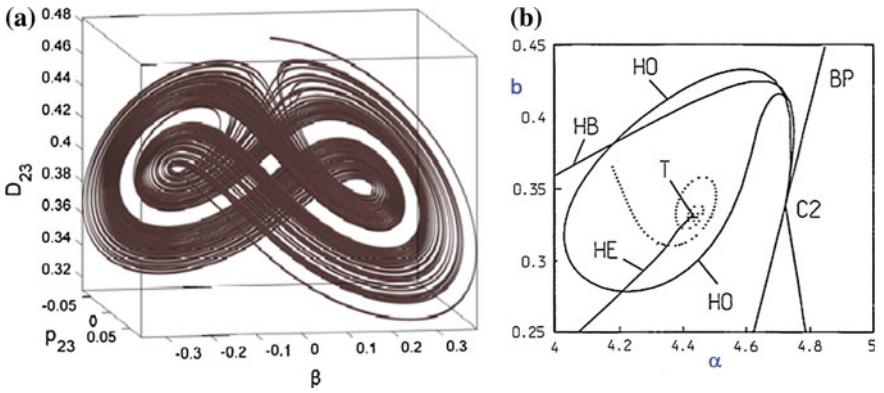

Fig. 5 (**a**) Lorenz attractor with a lacuna in the laser model at $a = 1.14$, $b = 0.2$, $q = 50$ and $\sigma = 10$. (**b**) (α, b)-bifurcation diagram of the model for $g = 52$ and $\sigma = 1.5$. BP and HB here denote the pitch-fork and Andronov-Hopf bifurcations, respectively. HO and HE denote the branches of the primary homoclinic (*of the saddle*) and heteroclinic orbits (*of the saddle-foci*). $C2$ is the codimension-two Khorozov-Taken point for the equilibrium state with double zero eigenvalues, and T is the primary terminal point. The spiraling curve connects the T-point with the homoclinic resonant saddle on HO, near which separatrix loops are double pulsed ones. Courtesy of [20]

a wealth of dynamical and structural features of Lorenz-like systems, including the Lorenz attractor *per se* (including lacunae), similar Andronov-Hopf, Z_2 pitchfork, and various homoclinic and heteroclinic bifurcations including codimension-two T-points, see Fig. 5. Similar structures were also discovered in another nonlinear optics model for a laser with a saturable absorber which can be reduced to the Shimizu-Morioka model near a steady state solution with triple zero exponents [36]

Likewise the Shimizu-Morioka model, the laser model (3) is rich in bifurcations. The list includes Andronov-Hopf bifurcations of equilibria, a pitch-fork bifurcation of periodic orbits, and various curious two homoclinic bifurcations of the saddle, as well as heteroclinic connections between the saddle and saddle-foci. Many of these bifurcations curves originate from a codimension-two Khorozov-Takens bifurcation of an equilibrium state with two zero Lyapunov exponents.

The panel in Fig. 6a represents the kneading scans of the dynamics of the laser model which is mapped onto the (α, b)-parameter plane with $g = 50$ and $\sigma = 1.5$. The scan is done using the same 50 kneading entries. It has regions of chaotic dynamics clearly demarcated from the solid color windows of persistent kneadings corresponding to trivial attractors such as stable equilibria and periodic orbits. The region of chaos has a vivid fractal spiral structure featuring a chain of T-points. Observe also a thin chaotic layer bounded away from the curve *Hom* by a curve of double-pulsed homoclinics with the kneading {1, 1, 0} connecting the codimension-two points: the resonant saddle and the orbit-flip both on *Hom*. One feature of these points is the occurrence of the Lorenz attractor with one or more lacunae [17, 25]. A strange attractor with a single lacuna containing a figure-8 periodic orbit in the phase space of the given laser model is shown in panel A of Fig. 5.

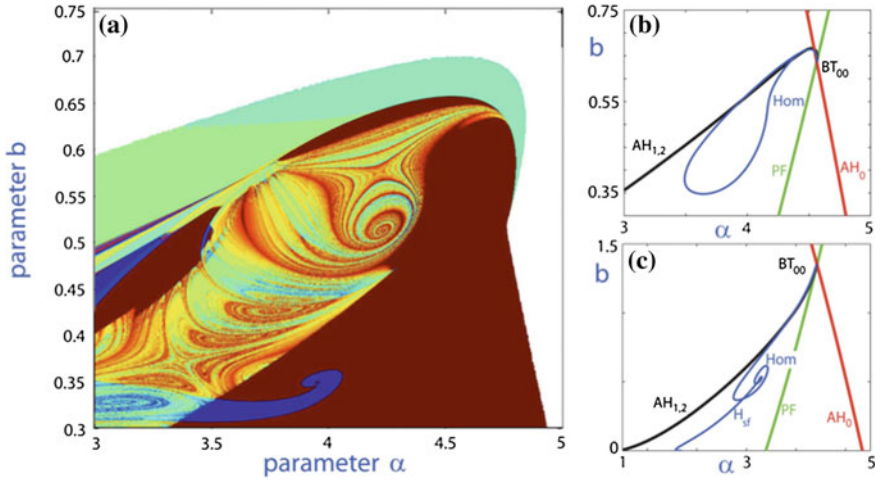

Fig. 6 (**a**) Bi-parametric scan of the laser model featuring the T-points and saddles typical for the Lorenz-like systems, mapping the dynamics of the 6D optically pumped infrared-red laser model onto the (electric-field-amplitude, omission-frequency)-diagram at $g = 50$ and $\sigma = 1.5$. Solid-color windows and fractal regions correspond to trivial and chaotic dynamics generated by the laser model. (**b**) Partial bifurcation diagram though the parameter continuation showing the curves for pitch-fork (PF) and Andronov-Hopf (AH_0) bifurcations for the equilibrium state, O, and another similar supercritical one for $O_{1,2}$. The homoclinic curve, *Hom* begins from the codimension-two point, BT for the Khorozov-Takens bifurcation and ends up at the resonant saddle point. (**c**) Elevating $\sigma = 2$ makes the *Hom* turned by a saddle point in the parameter plane and terminate at the primary T-point

5 Conclusions

We have demonstrated a new computational toolkit for thorough explorations of chaotic dynamics in three exemplary models with the Lorenz attractor. The algorithmically simple yet powerful toolkit is based on the scanning technique that maps the dynamics of the system onto the bi-parametric plane. The core of the approach is the evaluation of the kneading invariants for regularly or chaotically varying alternating patterns of a single trajectory - the separatrix of the saddle singularity in the system. In the theory, the approach allows two systems with structurally unstable Lorenz attractors to be conjugated with a single number - the kneading invariant. The kneading scans unambiguously reveal the key features in Lorenz-like systems such as a plethora of underlying spiral structures around T-points, separating saddles in intrinsically fractal regions corresponding to complex chaotic dynamics. We point out that no other techniques, including approaches based on the Lyapunov exponents, can reveal the discovered parametric chaos with such stunning clarity and beauty.

The kneading based methods shall be beneficial for detailed studies of other systems admitting reasonable symbolic descriptions, including symmetric and

asymmetric [16] systems of differential and difference equations that require two and more kneading invariants for the comprehensive symbolic description.

Acknowledgments This work is supported by the Spanish Research project MTM2012-31883 (to R.B.), and by NSF grant DMS-1009591, and MESRF project 14.740.11.0919 (to A.S). We thank Aaron Kelley, Sajiya Jalil and Justus Schwabedal for multi-hour fruitful discussions.

References

1. L.P. Shilnikov, A case of the existence of acountable number of periodic motions. Sov. Math. Dokl. **6**, 163 (1965)
2. L. Shilnikov, The theory of bifurcations and quasiattractors. Uspeh. Math. Nauk **36**(4), 240–242 (1981)
3. L. Shilnikov, Mathematical problems of nonlinear dynamics: a tutorial. Visions of nonlinear mechanics in the 21st century. J. Franklin Inst. **334**(5–6), 793–864 (1997)
4. V.V. Bykov, The bifurcations of separatrix contours and chaos. Phys. D **62**, 290–299 (1993)
5. A.L. Shilnikov, L.P. Shilnikov, D.V. Turaev, Normal forms and Lorenz attractors. Int. J. Bif. Chaos **3**, 1123–1139 (1993)
6. E.N. Lorenz, Compound windows of the Hénon-map. Phys. D **237**, 1689–1704 (2008)
7. P. Gaspard, R. Kapral, G. Nicolis, Bifurcation phenomena near homoclinic systems: a two-parameter analysis. J. Stat. Phys. **35**, 697–727 (1984)
8. R. Barrio, F. Blesa, S. Serrano, Qualitative analysis of the Ro ssler equations: bifurcations of limit cycles and chaotic attractors, Phys. D **238**, 1087–1100 (2009)
9. J.A.C. Gallas, The structure of infinite periodic and chaotic hub cascades in phase diagrams of simple autonomous flows. Int. J. Bif. Chaos **20**, 197–211 (2010)
10. L. Shilnikov, A. Shilnikov, Shilnikov bifurcation. Scholarpedia **2**(8), 1891 (2007)
11. R. Barrio, F. Blesa, S. Serrano, A. Shilnikov, Global organization of spiral structures in bi-parameter space of dissipative systems with Shilnikov saddle- foci. Phys. Rev. E **84**, 035201 (2011b)
12. A.L. Shilnikov, L.P. Shilnikov, R. Barrio, Symbolic dynamics and spiral structures due to the saddle-focus bifurcations, in Chaos, CNN, Memristors and Beyond eds. by A. Adamatzky, (2012)
13. L.P. Shilnikov, A.L. Shilnikov, D. Turaev, L.O. Chua, *Methods of Qualitative Theory in Nonlinear Dynamics*. Parta I and II (World Scientific Publishing Co. Inc., Singapore, 1998, 2001)
14. L. Shilnikov, The existence of a denumerable set of periodic motions in four-dimensional space in an extended neighborhood of a saddle-focus. Soviet Math. Dokl. **8**(1), 54–58 (1967)
15. P. Glendinning, C. Sparrow, T-points: a codimension two heteroclinic bifurcation. J. Stat. Phys. **43**, 479–488 (1986)
16. A. Shilnikov, Bifurcation and chaos in the Morioka-Shimizu system. Selecta Math. Soviet. **10**(2), 105–117 (1991)
17. A. Shilnikov, On bifurcations of the Lorenz attractor in the Shimizu-Morioka model. Phys. D **62**(1–4), 338–346 (1993)
18. V. Bykov, In bifurcations leasing to chaos in Chuas circuit. Int. J. Bif. Chaos **8**, 685–699 (1998)
19. F. Fernández-Sánchez, E. Freire, A.J. Rodrguez-Luis, T-points in a Z_2-symmetric electronic oscillator. I. Analysis. Nonlinear Dynam. **28**, 53–69 (2002)
20. W. Forysiak, J. Moloney, R. Harrison, Bifurcations of anoptically pumped three-level laser model, Physica D **53**, 162–186 (1991)
21. J. Milnor, W. Thurston, On iterated maps of the interval. Lecture Notes Math. **1342**, 465–563 (1988)
22. R. Barrio, A.L. Shilnikov, L.P. Shilnikov, Kneadings, symbolic dynamics and paining Lorenz chaos. A tutorial. Inter. J. Bif. Chaos **22**(4), 1230016–12330040 (2012)

23. E. Lorenz, Deterministic nonperiodic flow. J.AtmosphericSci. **20**, 130–141 (1963)
24. J. Guckenheimer, R.F. Williams, Structural stability of Lorenz attractors. Inst. Hautes E tudes Sci. Publ. Math. **50**, 59–72 (1979)
25. V. Afraimovich, V.V. Bykov, L.P. Shilnikov, On structurally unstable attracting limit sets of Lorenz attractor type. Trans. Moscow Math. Soc. **44**, 153–216 (1983)
26. A. Shilnikov, L. Shilnikov, On the nonsymmetric Lorenz model. Int. J. Bif. Chaos **1**, 773–776 (1991)
27. V. Afraimovich, V.V. Bykov, L.P. Shilnikov, The origin and structure of the Lorenz attractor. Sov. Phys. Dokl. **22**, 253–255 (1977)
28. J.L. Kaplan, J.A. Yorke, Preturbulence: a regime observed in a fluid flow model of Lorenz. Comm. Math. Phys. **67**, 93–108 (1979)
29. V.S. Afraimovich, L.P. Shilnikov, Strange attractors and quasiattractors, *Nonlinear Dynamics and Turbulence*, Interaction Mech. Math. Ser. (Pitman, Boston, 1983), pp. 1–34
30. L. Shilnikov, Bifurcations and strange attractors, in *Proceedings of International Congress of Mathematicians*, Beijing (China) (Invited Lectures). vol. 3, pp. 349–372 (2002)
31. T. Shimizu, N. Morioka, On the bifurcation of asymmetric limit cycle to an asymmetric one in a simple model. Phys. Lett. A **76**, 201–204 (1980)
32. S. Gonchenko, I. Ovsyannikov, C. Simo, D. Turaev, Three-dimensional Hénon-like maps and wild Lorenz-like attractors. Int. J. Bif. Chaos **15**(11), 3493–3508 (2005)
33. J. Moloney, W. Forysiak, T. Uppal, R. Harrison, Regular and chaotic dynamics of optically pumped molecular lasers. Phys. Rev. A **39**, 1277–1285 (1989)
34. U. Hubner, C. Weiss, N. Abraham, D. Tang, Lorenz-like chaos in nh3-fir lasers. Infrared Phys. Technol. **36**(1), 489–512 (1995)
35. H. Haken, Analogy between higher instabilities in fluids and lasers. Phys. Lett. A **53**, 77–78 (1975)
36. A. Vladimirov, D. Volkov, Low-intensity chaotic operations of a laser with a saturable absorber. Optics Commun. **100**(1–4), 351–360 (1993)

Enhancing Signal Resolution in a Noisy Nonlinear Sensor

Alexander P. Nikitin, Nigel G. Stocks and Adi R. Bulsara

Abstract It is well known that the resolution (defined as the smallest change in the signal being detected or quantified) of a sensor can be improved by increasing the observation time T of the measurement; typically, the resolution scales as $1/T^a$. Typically $a = 0.5$, or $a < 0.5$ if low frequency noise is present. We show that a neuronal system can display an enhanced scaling in the resolution, with the parameter $a = 1$; this occurs when the "inter spike intervals" are negatively correlated. We also show that, by introducing negative correlations into the time domain response of a nonlinear dynamical sensor, it is possible to replicate this enhanced scaling. This affords us the possibility of designing a novel class of biomimetic sensors that results in improved signal resolution by functionally utilizing negative correlations.

1 Introduction

In any measurement, one aspires to the highest possible accuracy. If the accuracy of a single measurement is not acceptable, usually due to unacceptable measurement errors e.g. stemming from a noise-floor, than the measurements are repeated N times and a statistical average (usually just the arithmetic mean) of the measurable is computed. For statistically independent errors, the total error of the measure-

A. P. Nikitin (✉)
School of Engineering and School of Life Sciences, University of Warwick, Coventry CV4 7AL, UK
e-mail: a.nikitin@warwick.ac.uk

N. G. Stocks
School of Engineering, University of Warwick, Coventry CV4 7AL, UK
e-mail: n.g.stocks@warwick.ac.uk

A. R. Bulsara
Space and Naval Warfare Systems Center Pacific, Code 71000,
San Diego, CA 92152-6147, USA
e-mail: bulsara@spawar.navy.mil

V. In et al. (eds.), *International Conference on Theory and Application in Nonlinear Dynamics (ICAND 2012)*, Understanding Complex Systems,
DOI: 10.1007/978-3-319-02925-2_13,

ment is reduced as $1/\sqrt{N}$, i.e. the accuracy of the measurement improves slowly in comparison to the rate of accumulation of the (statistical) data that are a part of the averaging operation. An improved scaling (improved rate of the reduction for measurement error with accumulating statistical data) is possible if the measurements are negatively correlated. This has been predicted to be a possibility in physiology [1]. Such living systems could, thus, improve their response to a weak target signal thereby benefitting from neagative correlations.

It is, of course, a very attractive undertaking to design engineering systems (or sensors) as analogs of a biological system which has (qualitative) matching dynamics. This is the aim of this paper. We show how the configuration and operation of a candidate nonlinear sensor having a temporal (in this case, event-based) readout, can be adapted to mimic the dynamics of an integrate-fire neuron with negatively correlated inter-spike intervals; these ideas were formulated by us in recent work [2]. We show that the sensor in this "biomimetic" mode yields a greatly reduced measurement error with the improved scaling $1/N$, when certain constraints (that will be quantified) are met.

In what follows, we start with the simplest neural dynamical model (perfect integrate-fire) and use it to explain the concept of "negative correlations"; we also introduce a definition of the neuron's resolution. The rest of the paper is concerned with a simple nonlinear dynamic sensor, a single-core fluxgate magnetometer, that operates in the time domain and whose dynamics can be mapped to the (integrate-fire) neural dynamics. Operating the magnetometer in this "biomimetic mode" is shown to lead to improved magnetic signal detection.

2 Perfect Integrate-Fire (PIF) Neuron Model

It has been shown [1] that electrosensory afferents of weakly electric fish have non-renewal statistics characterized by the fourth (or higher) Markov order. This means that a minimally correct model of neuronal spike trains for the electrosensory afferents should comprise four stochastic equations. It was also shown [1], that the observed significant improvement in the detectability of a weak signal by the electrosensory afferents, can be accounted for by a model of Markov order one. Such first Markov order models as the Perfect Integrate Fire (PIF) model with noisy threshold [3] are, in fact, known to describe a noise canceling mechanism that might, in fact, be realized in real neurons. We will see, later in this work, that the simple PIF model affords a prototype of the biomimetic magnetic field sensor. First, however, we discuss the effects of negative correlations in a simple PIF model.

The PIF model with noisy threshold can be described by the following equation,

$$\dot{v} = \beta + s, \tag{1}$$

where s is the (constant) signal to be estimated, β a constant bias current, and v the voltage across the nerve membrane. The threshold θ is a uniformly distributed

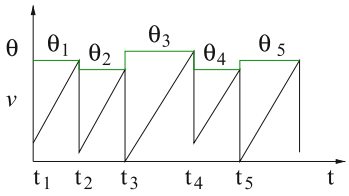

Fig. 1 The PIF model: dynamics of the membrane voltage v and the threshold θ

random variable, $\theta \in [\theta_a - D_u, \theta_a + D_u]$, that is independently defined for every inter-spike interval. D_u is the noise intensity, and θ_a the mean threshold, $\theta_a = \langle\theta\rangle$. The mode of operation is as follows: when the voltage v reaches the threshold θ, a spike is fired, a new threshold is chosen, and the voltage is reset to a new level $\eta = \theta - \theta_a$; this is schematized in Fig. 1. The ISIs generated by the model (1), with the above configuration of the threshold following each firing event, are strongly negatively correlated.

Denoting the times at which the level crossings occur as $t_0, t_1, \ldots, t_k$, the values of the threshold at crossing as $\theta_0, \theta_1, \ldots, \theta_k$, and the reset levels as $\eta_0 = \theta_0 - \theta_a, \ldots, \eta_k = \theta_k - \theta_a$ it is straightforward to show from (1) that the kth interspike interval (ISI) is given by,

$$T_k = (t_k - t_{k-1}) = \frac{\theta_k - \theta_{k-1} + \theta_a}{\beta + s}. \tag{2}$$

We decompose the inter-spike interval T_k into three quantities so that

$$T_k = \delta_k + \Delta - \delta_{k-1},$$

where we introduce the "jitters" δ_{k-1} and δ_k as

$$\delta_k = \theta_k/(\beta + s), \qquad \delta_{k-1} = \theta_{k-1}/(\beta + s),$$

and the mean inter-spike interval,

$$\Delta = \langle T_k\rangle = \theta_a/(\beta + s). \tag{3}$$

If the threshold is noiseless, and the signal $s = const$, then the process is exactly periodic because the spikes occur, precisely, at times $t_k = k\Delta + t_0$.

The serial correlation coefficient of the stochastic process can be calculated as,

$$\rho(m) = \frac{\langle (T_k - \langle T_k\rangle)(T_{k+m} - \langle T_{k+m}\rangle)\rangle}{\sigma_{T_k}\sigma_{T_{k+m}}} = \begin{cases} 1 : m = 0, \\ -\frac{1}{2} : m = 1, \\ 0 : m > 1. \end{cases} \tag{4}$$

It is easy to see the ISIs generated by the model (1) are strongly negatively correlated with $\rho(1) = -0.5$.

We now introduce the sum of N inter-spike intervals,

$$\tau_{ob,N} = \sum_{k=1}^{N} T_k = \delta_N - \delta_0 + N\Delta, \tag{5}$$

which is equivalent to an observation time in the measurement. The average of this sum is the mean observation time

$$T_{ob} = \langle \tau_{ob,N} \rangle = N\Delta, \tag{6}$$

and the variance,

$$\sigma^2_{\tau_{ob,N}} = 2\sigma^2_{\delta}, \tag{7}$$

is independent of N. This means that the noise in our measurement does not accumulate with an increasing number (N) of measurements. This is a direct result of the noise canceling mechanism that makes it attractive for practical applications to engineered systems .

To characterize the accuracy of the signal s estimation from the ISIs, we introduce the resolution R defined in [2, 4] as,

$$R = \left| \frac{\partial T_{ob,N}}{\partial s} \right|^{-1} \sigma_{\tau_{ob,N}}, \tag{8}$$

R is the smallest resolvable value of the measured quantity. The resolution is readily derived via a Taylor expansion of T_{ob} about $s = 0$: $T_{ob}(\delta s) = T_{ob}(0) + dT_{ob}/ds \times \delta s$. Noting that, physically, the resolution represents the signal value that results in $\sigma_{\tau_{ob,N}}$ being equal to the difference in T_{ob} with and without signal, we see that the resolution is given by $dT_{ob}/ds \times \delta s$ where the differential is evaluated at $s = 0$. Finally we set $\delta s = R$ when $\sigma_{\tau_{ob,N}} = T_{ob}(0) - T_{ob}(s)$. One can readily obtain the resolution R for the PIF model in the limit of very small target signal as:

$$R = \left| \frac{\partial}{\partial s} \frac{N\theta_a}{\beta + s} \right|^{-1}_{s=0} \sqrt{2}\sigma_{\delta} = \frac{\sqrt{2}\sigma_{\delta}\beta^2}{\theta_a} \frac{1}{N}, \tag{9}$$

which is seen to be proportional to $1/N$, an improvement over the $1/\sqrt{N}$ dependence for typical renewal processes (without negative correlations). We remind the reader that a smaller value for R implies better signal detection/quantification performance.

3 A Magnetic Field Sensor in the Biomimetic Mode

The PIF model, introduced above, can be characterized by (i) the dependence (i.e. rise) of the membrane voltage with external signal, and (ii) a comparator which imposes the threshold which, in turn, triggers (iii) the resetting mechanism. To operate in the "biomimetic mode", a sensor should mimic the oscillatory dynamics of the PIF model with negative correlations in its inter-spike intervals to exploit the noise canceling mechanism. We now consider the dynamics of a fluxgate magnetometer [4] that is operated in the temporal domain.

It is well known that the relaxation time of the magnetization variable in a ferromagnetic core depends on an applied external magnetic field. By altering the directions of the applied magnetic field, we can generate conditions for the ferromagnet under which its magnetization will periodically increase and decrease, i.e. it will oscillate (the oscillations are non-sinusoidal, of course). We can map the ferromagnetic core dynamics onto a PIF neuronal model by associating the increasing magnetization with the increasing membrane voltage of the cell membrane, and the decreasing magnetization with the reset in the membrane voltage.

As might be imagined, some engineering problems must be solved for a practical realization of the biomimetic mechanism. First, the magnetization is an internal parameter of the ferromagnet, and it is not easy to measure it directly. Therefore we replace, in our measurements, the magnetization with the B-field that is a linear combination of an unknown field B_0 (the target field that is to be measured), the known field B_+ that is used to induce the relaxation dynamics, and the magnetization M:

$$B = B_0 + B_+ + \mu_0 M, \tag{10}$$

where μ_0 is the magnetic constant. Since B_0 and B_+ are assumed to be constants during the relaxation process, the B field relaxes like the magnetization with rate

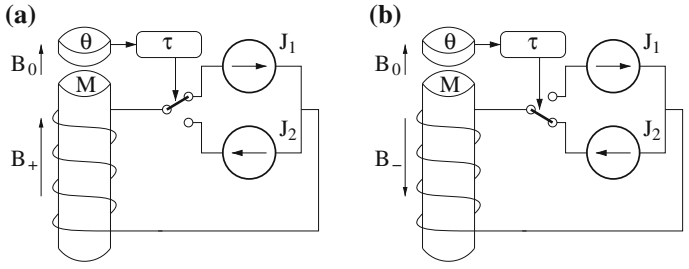

Fig. 2 The magnetic field sensor. **a** The magnetization M increases in the presence of the magnetic fields B_+ and B_0. The field B_+ is assumed to be $B_+ \gg |B_0|$ and corresponds to the current J_1 in the coil. **b** The resetting of the core magnetization occurs when the it reaches a threshold value θ in the magnetic comparator. At this point, the current J_1, in the coil, is replaced by the current J_2 for a time interval τ; this corresponds to a magnetic field switch from B_+ to B_- with an attendant coil current J_2

$dB/dt = \mu_0 dM/dt$. Having made the change in variables, we can use any B field sensor, with a very sharp sigmoidal characteristic, as a comparator of the B field with a threshold θ that will trigger the reset mechanism (see Fig. 2). The second engineering problem stems from the impossibility of, instantly, resetting the magnetization M in the ferromagnet. To reset the magnetization, we need to replace the magnetic field B_+ with B_- and this field is applied for a duration τ, to allow the magnetization to reach an acceptable level (this level is a 'design parameter' that is controlled via τ – careful selection is required for optimal performance); this is schematized in Fig. 2b.

The dynamics of the magnetization M of a single–domain ferromagnetic core in the one dimensional case can be described by the following differential Eq. (5) (see [4]),

$$\tau_a \frac{dM}{dt} = -M + M_s \tanh\left(\frac{CB}{\mu_0}\right), \tag{11}$$

where M_s is the saturation level of the magnetization, and τ_a its characteristic relaxation time. In Eq. (11), C is a non-linearity parameter that is proportional to the Curie temperature-to-temperature ratio. The parameter C characterizes the 'ferromagnet–paramagnet' phase transition: if $C > 1$ the core remains in its ferromagnetic phase; if $C < 1$ the core is in the paramagnetic phase. We now consider the magnetization in two operating scenarios.

3.1 The Noiseless Case

In the noiseless case, the magnetic sensor mimics a periodic oscillator. The phase plane of this oscillator is plotted in Fig. 3 wherein we show a working region of the parameters M and B bounded by the sections (branches) EF and GH. All the nonlinear dynamics occur on these branches. Switches between the branches occur

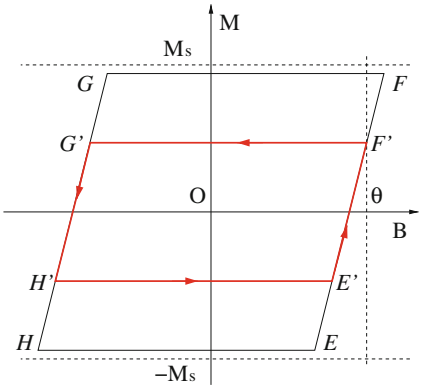

Fig. 3 The phase plane of the ferromagnetic oscillator in the variables M and B. The "limit cycle" $E'F'G'H'$ is shown in *red* with the *arrows* indicating the direction of motion on the phase plane. *Dashed lines* show the saturation levels $-M_s$ and M_s of the ferromagnet, and the threshold level θ

in two cases: when the B field crosses the threshold level θ; and when the system is forced to the branch GH for a duration τ.

The points in Fig. 3 have the following coordinates:

$$\begin{aligned} E &= \left[B_0 + B_+ + \mu_0 M_H, \quad M_H\right], \\ F &= \left[B_0 + B_+ + \mu_0 M_F, \quad M_F\right], \\ G &= \left[B_0 + B_- + \mu_0 M_F, \quad M_F\right], \\ H &= \left[B_0 + B_- + \mu_0 M_H, \quad M_H\right], \end{aligned} \tag{12}$$

where the parameters M_H and M_F can be found from the equation $dM/dt = 0$. This condition leads to the transcendental equations:

$$M_H = M_s \tanh\left(C\frac{B_0 + B_-}{\mu_0} + CM_H\right),$$

$$M_F = M_s \tanh\left(C\frac{B_0 + B_+}{\mu_0} + CM_F\right),$$

whose solutions M_H and M_F can be found numerically (here we assume that $-M_s < M_H < M_F < M_s$). We observe that the working region is less than the physically permitted states $[B, M]$ of the oscillator. The true region of acceptable values for the magnetization would, normally, be bounded by the saturation values $-M_s$ and M_s instead of M_H and M_F. However, we are concerned with the working region of the phase plane that is acceptable for the periodic oscillations, i.e. the region where an attractor can be located.

The role of a limit cycle (attractor) is played by the quadrilateral $E'F'G'H'$. Suppose a trajectory of the dynamical system starts at E' where, according to the equation $B = B_0 + B_+ + \mu_0 M$, the magnetization M is linearly dependent on the B field. Both M and B are non-linearly growing quantities due to Eq. (11). As the B field crosses the threshold θ (point F'), the trajectory is instantly switched to the point G'. Now the trajectory, according to Eq. (11), relaxes during the time interval τ to the point H'. Then, the trajectory instantly switches onto the branch EF (the point E'). It is easy to see from Fig. 3 that, for the existence of periodic oscillations, the threshold θ should satisfy the condition,

$$B_0 + B_+ + \mu_0 M_H < \theta < B_0 + B_+ + \mu_0 M_F.$$

If $\theta > B_0 + B_+ + \mu_0 M_F$ (the vertical dashed line does not cross the branch EF), then F is a stable point. We note that we are using a discrete two-state dynamical characterization i.e. for simplicity, we are using the instantaneous switches and the resetting time τ instead of a system of differential equations and their solutions. This means that a bifurcation (likely of saddle-node type) occurs at $\theta = B_0 + B_+ + \mu_0 M_F$ but cannot be correctly characterized unless we use the full differential equations to characterize the dynamical behavior (i.e. switching events and the resetting mecha-

nism). The above treatment (assuming the device to behave like a static nonlinearity) is valid as long as the characteristic time constant τ_a is the smallest time-scale in the system.

3.2 The Threshold Noise Case

Analogous with [3] we introduce noise in the threshold θ as a uniformly distributed variable in the interval $[\theta_a - D_u : \theta_a + D_u]$. According to our analysis of the magnetic sensor model in Sect. 3.1, the sensor output will retain its oscillatory properties if the parameters of the threshold noise satisfy the following inequalities, $\theta_a - D_u > M_H$ and $\theta_a + D_u < M_F$. It is important to note that, for modeling purposes, all noise sources are assumed to be internal to the sensor (the resolution is an intrinsic property of the sensor and cannot be defined in the presence of external noise); these are

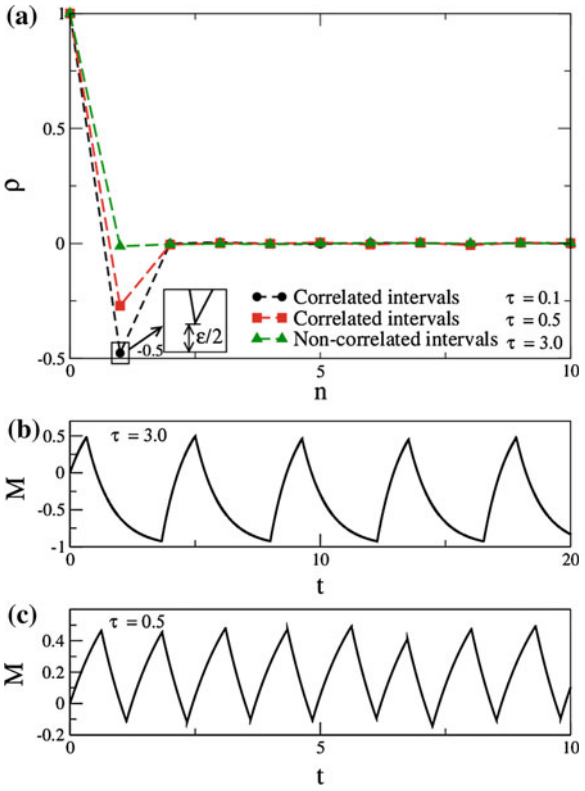

Fig. 4 **a** The correlation coefficient $\rho(n)$. **b** and **c** The magnetization M as a function of time t for the model described via (11). The time series corresponds to non-correlated intervals in **b** ($\tau = 3.0$) and negatively correlated intervals in **c** ($\tau = 0.5$). The parameters are $\theta_a = 2.5,\ D_u = 0.05,\ \mu_0 = 1,\ B_+ = -B_- = 2,\ C = 3$, and $B_0 = 0$

"consolidated" into an effective threshold noise. In our experiments (see e.g. [4] and references therein) we find that this is, in fact, a good assumption; the switching events are relatively clean with sensor noise appearing as a flucuating threshold.

Numerical simulations of Eq. (11) show that the level that the magnetization is reset to is strongly dependent on τ. For large τ (see Fig. 4b for $\tau = 3$) the magnetization approaches the saturation value and this reduces the negative correlation, as observed in the behavior of $\rho(1)$ (see Fig. 4a for $\tau = 3.0$). The reduction in negative correlation occurs because saturation of the magnetization results in a loss of memory in the magnetization variable when the threshold is crossed; for very strong saturation the magnetization is, effectively, reset to the same value every time with all memory effects being removed. In the opposite case, when τ is small, the level that the magnetization is reset to strongly depends on the value of the magnetization when the threshold was crossed and, hence, strong negative correlation is observed (see Fig. 4c for $\tau = 0.5$). The negative correlations can be characterized by the parameter ε, introduced as the half distance to $-1/2$ (see Fig. 4a),

$$\rho(1) = -\frac{1}{2} + \frac{\varepsilon}{2}.$$

The target magnetic field B_0 can be estimated from N time intervals, T_i, $i = 1, 2, ..., N$ as the total observation time $\tau_{ob} = \sum_{i=1}^{N} T_i$. The resolution, R, of the magnetic sensor is, then, defined via Eq. (8) with the replacement

$$\sigma_{\tau_{ob,N}} = \sigma_{\tau_{ob}} = \sqrt{\langle [\tau_{ob} - T_{ob}]^2 \rangle},$$

with the mean observation time identified as $T_{ob} = \langle \tau_{ob} \rangle$, and $s = B_0$ the target signal.

The (monotonic) dependence of the observation time T_{ob} on the external magnetic field B_0 is shown in Fig. 5a. This dependence can be used to estimate the target field. Fig. 5b shows that the resolution, R, has the scaling $T_{ob}^{-0.5}$ for the non-correlated intervals (e.g. for parameter value $\tau = 3.0$). However, when strong negative correlations exist (e.g. $\tau = 0.1$) the scaling is more complex. The scalings T_{ob}^{-1} and $T_{ob}^{-0.5}$ are shown as the black and red straight lines and these are seen to asymptote to the $\tau = 0.1$ data at small and large observation times respectively. This provides clear evidence that, at short observation times, the enhanced scaling T_{ob}^{-1} is observed; this scaling crosses over to $T_{ob}^{-0.5}$ at large observation time.

We have obtained theoretical results [6] that show that this dual scaling behavior appears to be a universal property in the sense that it occurs for linear and nonlinear reset mechanisms and in models of sensors and neural models. Moreover, our theory predicts the number of periods N^* at which the scaling crosses over from T_{ob}^{-1} to $T_{ob}^{-0.5}$; the result is $N^* \simeq 1/\varepsilon$ (see Fig. 5b) (note that the parameter ε can be estimated directly from the numerical results presented in Fig. 4a).

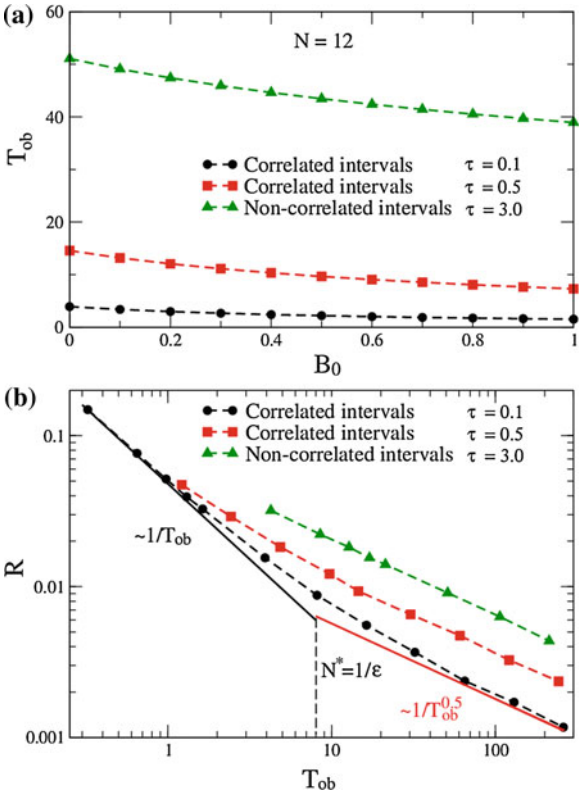

Fig. 5 **a** The observation time T_{ob} as a function of the external magnetic field B_0. **b** The resolution, R, versus the observation time, T_{ob}. The parameters are $\theta_a = 2.5$, $D_u = 0.05$, $\mu_0 = 1$, $B_+ = -B_- = 2$, $C = 3$

4 PIF Model with Deterministic Errors in the Reset

To explain the double scaling in the magnetometer model (see previous section), we introduce here the following solvable model with "deterministic errors" in the reset. The model is a modified PIF model (MPIF); it differs from the standard PIF model only through the different reset mechanism. In the PIF model, the resetting levels are $\eta_k = \theta_k - \theta_a$, i.e. the resetting level η_k is the result of a precisely shifted threshold θ_k. In the MPIF model, the shift of the threshold θ_k occurs with a "distortion" due to the transformation,

$$\eta_k = (\theta_k - \theta_a)(1 - c).$$

In Fig. 6, it is easy to see that the function $\eta(t)$ reproduces the dynamics of $\theta(t)$ with a compression on the v-axis. Thus, the parameter c is called the "compression". If $c = 0$, the MPIF model coincides with the PIF model; for $c = 1$, the resetting occurs

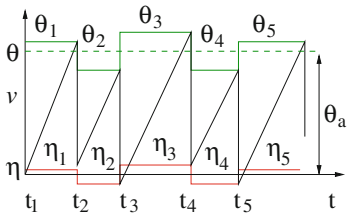

Fig. 6 Modified PIF (MPIF) model: typical dynamics of the membrane voltage v, the threshold θ and the resetting level η

at the constant level, $\eta_k = 0$. In this case, it should produce renewal oscillations. Hence, the compression c plays a role similar to the parameter τ in the magnetometer model.

Since the kth inter-spike interval produced by the MPIF model is

$$T_k = (t_k - t_{k-1}) = \frac{\theta_k - \theta_{k-1} + (1-c)\theta_a + c\theta_k}{\beta + s}, \tag{13}$$

we can decompose it into three random variables so that

$$T_k = \delta_k + \Delta_k - \delta_{k-1},$$

where we introduce the "jitter" terms $\delta_k = \theta_k/(\beta + s)$, $\delta_{k-1} = \theta_{k-1}/(\beta + s)$, and the noisy component of the ISI

$$\Delta_k = \frac{\theta_a}{\beta + s} + c\frac{\theta_{k-1} - \theta_a}{\beta + s}. \tag{14}$$

The variable Δ_k in Eq. (14) differs from Δ in Eq. (3) through a noisy component that is proportional to the parameter c. Therefore, the sum of N time intervals

$$\tau_{ob,N} = \sum_{k=1}^{N} T_k = \delta_N - \delta_0 + N\frac{\theta_a}{\beta + s} + \frac{c}{\beta + s}\sum_{k=0}^{N-1}(\theta_k - \theta_a) \tag{15}$$

includes the noisy term that is proportional to c and increasing with N.

The serial correlation coefficient differs from the one calculated for the PIF model; it has the additional term,

$$\rho(1) = -\frac{1}{2} + \frac{\varepsilon}{2}, \tag{16}$$

where the parameter ε is introduced as

$$\varepsilon = \frac{c^2}{2(1-c) + c^2}. \tag{17}$$

For very weak compression, $c \ll 1$, the last equation reduces to

$$\varepsilon \simeq \frac{c^2}{2}. \tag{18}$$

It is easy to show that the average observation times for both the PIF and the MPIF models are identical, $T_{ob} = \langle \tau_{ob,N} \rangle = N\theta_a/(\beta + s)$, but the variances are different. Moreover, in contrast to Eq. (7), the variance for the MPIF model,

$$\sigma^2_{\tau_{ob,N}} = 2\sigma^2_\delta \left(1 + c + N\frac{c^2}{2}\right), \tag{19}$$

increases with N. This dependence on N influences the resolution R. The resolution R for the MPIF model in the limit of an infinitesmially small target signal is

$$R = \frac{\sqrt{2}\sigma_\delta \beta^2}{\theta_a} \frac{1}{N} \sqrt{1 + c + N\frac{c^2}{2}}, \tag{20}$$

which, for a very weak compression $c \ll 1$, and using the approximation Eq. (18) becomes

$$R = \frac{\sqrt{2}\sigma_\delta \beta^2}{\theta_a} \frac{1}{N} \sqrt{1 + \varepsilon N}. \tag{21}$$

Now, it is easy to see that the resolution R has different scaling for different ranges of N. If $N \ll 1/\varepsilon$, the resolution is

$$R \simeq \frac{\sqrt{2}\sigma_\delta \beta^2}{\theta_a} \frac{1}{N};$$

If $N \gg 1/\varepsilon$, the resolution is

$$R \simeq \frac{c\sigma_\delta \beta^2}{\theta_a} \frac{1}{\sqrt{N}}.$$

Since the observation time T_{ob} is proportional to N, the resolution also has the double scaling in the terms of the observation times, $1/T_{ob}$ and $1/\sqrt{T_{ob}}$.

5 Conclusion

We conclude that operating a nonlinear sensor in the biomimetic mode can improve its performance, as quantified via the resolution. In particular, the analysis indicates that, absent the luxury of a long observation time, the above mode of operation might be particularly helpful. We reiterate that there is nothing special about the single core fluxgate magnetometer (used, here, as a test device); operating a generic nonlinear sensor in the correct working range should allow the benefits of negative correlations to be realized.

Acknowledgments The authors gratefully acknowledge support from the US Office of Naval Research and the US Office of Naval Research-Global.

References

1. R. Ratnam, M. Nelson, J. Neurosci. **20**(17), 6672–6683 (2000)
2. A. P. Nikitin, N. G. Stocks, A. R. Bulsara, Phys. Rev. Lett. **109**, 238103 (2012)
3. M. J. Chacron, B. Lindner, A. Longtin, Phys. Rev. Lett. **92**, 080601 (2004)
4. S. Baglio et al., IEEE Trans. Instr. Meas. **60**, 667 (2011)
5. H. E. Stanley, Introduction to Phase Transitions and Critical Phenomena (Oxford University Press, Oxford, 1971)
6. A. P. Nikitin, N. G. Stocks, A. R. Bulsara (to be published)

Distributed Bandpass Filtering and Signal Demodulation in Cortical Network Models

Mark D. McDonnell

Abstract Experimental recordings of cortical activity often exhibit narrowband oscillations, at various center frequencies ranging in the order of 1–200 Hz. Many neuronal mechanisms are known to give rise to oscillations, but here we focus on a population effect known as sparsely synchronised oscillations. In this effect, individual neurons in a cortical network fire irregularly at slow average spike rates (1–10 Hz), but the population spike rate oscillates at gamma frequencies (greater than 40 Hz) in response to spike bombardment from the thalamus. These cortical networks form recurrent (feedback) synapses. Here we describe a model of sparsely synchronized population oscillations using the language of feedback control engineering, where we treat spiking as noisy feedback. We show, using a biologically realistic model of synaptic current that includes a delayed response to inputs, that the collective behavior of the neurons in the network is like a distributed bandpass filter acting on the network inputs. Consequently, the population response has the character of narrowband random noise, and therefore has an envelope and instantaneous frequency with lowpass characteristics. Given that there exist biologically plausible neuronal mechanisms for demodulating the envelope and instantaneous frequency, we suggest there is potential for similar effects to be exploited in nanoscale electronics implementations of engineered communications receivers.

1 Introduction and Background

Neuronal information processing relies on the dynamical electrical properties of a neuron's membrane, such as its conductance, capacitance, and the various ionic currents that flow across it through ion channels, and which give rise to a time

M. D. McDonnell (✉)
Institute for Telecommunications Research, University of South Australia,
Mawson Lakes , SA 5087 , Australia
e-mail: Mark.McDonnell@unisa.edu.au

V. In et al. (eds.), *International Conference on Theory and Application in Nonlinear Dynamics (ICAND 2012)*, Understanding Complex Systems,
DOI: 10.1007/978-3-319-02925-2_14,

varying membrane potential. These currents are constantly changing over time, due to external input into a neuron at synaptic junctions. This external input occurs when an adjacent neuron 'spikes,' i.e. when its membrane potential reaches a large enough size to cause a short duration but large amplitude pulse, called an action potential, to propagate along cable-like structures called axons. When the action potential reaches the end of an axon it can cause chemical neurotransmitters to be released and then diffuse across a gap between neurons called a synapse. These neurotransmitters cause a change in conductance in the membrane of the neuron on the far side of the synapse, thus resulting in an ionic current flow across it [1].

Given that a neuron's membrane can be modelled in terms of currents, conductances and capacitance, it is no surprise that equivalent electrical circuits for them can be studied using frequency domain methods favoured in electronic engineering [2] or in the analysis of stochastic noise [3]. In particular, neuronal membranes can be studied as if they were electrical filters, and models of neuronal low, high and bandpass filters, have been discussed in terms of neuronal 'resonance' [4]. There are several biophysical mechanisms for achieving this, as reviewed by [5]. Examples of single cell mechanisms include slow potassium ion currents [6], synaptic short-term plasticity [7], and subthreshold membrane oscillations [1]. Mechanisms due to interactions between cells also can cause band-pass filtering [8], while the basilar membrane in the inner ear provides mechanical bandpass filtering of sounds prior to transduction by inner hair cells [9].

In this paper we focus on neurons in a population that each achieve a bandpass filtering characteristic solely through delayed distributed feedback, rather than their intrinsic properties. Such a network has previously been studied and understood using approaches favoured in nonlinear physics [10] in order to explain the phenomenon of 'sparsely synchronised population oscillations' [11, 12]. These oscillations are often observed in recordings of the overall electrical field produced in small volumes of cortical region V1 when an experimental animal is awake and has their visual field stimulated [13, 14]. The label 'sparse synchronisation' describes the fact that individual neurons in the region spike in an irregular fashion with an average rate much slower than the frequency of the population oscillation.

The novelty in the approach presented here is to recast the problem as one where it is assumed that the network's function is to act like a multivariate feedback system operating close to instability, thus producing a bandpass filter like response. This perspective leads us to posit that neuronal population spike rates, in the context of our assumption, can be treated as both a noisy version of a feedback control signal, as well as a compressed representation of the synaptic conductance or current.

Surprisingly, we find that the central assumption employed in electronic engineering design, namely that electrical dynamics is governed by *linear* differential equations, can also be employed for studying filtering in such a population of neurons, despite the obviously highly nonlinear behaviour that gives rise to the crucial aspect of 'spiking.'

The remainder of this paper articulates these ideas as follows.

- Section 2 describes how a single neuron with specified linear synaptic dynamics would *ideally* implement negative feedback, with gain, in order to produce a bandpass response.
- Section 3 introduces the concept of distributed feedback within a population of redundant neurons, as a means of implementing feedback gain without requiring active amplifiers. This Section also shows how distributed feedback can have the additional benefit of reducing additive noise on feedback signals via the averaging effects inherent in redundancy. The Section next extends the analysis of feedback noise by assuming that feedback is only possible via quantized signals. We study this, as quantization is highly analogous to spiking in the real cortical network. It is shown that performance close to the ideal bandpass filter response is readily achievable by a population of neurons with distributed quantized feedback, particularly in the presence of stochastic noise.
- Section 4 discusses the potential for exploiting effects like those discussed here in bio-inspired engineering, such as in frequency demodulation.

Unlike the model of [10], here we do not consider sparsely connected networks where neurons only rarely and asynchronously contribute feedback. This is an extension left for future work, as sparse connectivity has a significant impact on stability analysis. However, the work discussed here is expected to be readily extendible to the sparse connectivity scenario, as well as to randomly distributed delays.

2 Cortical Synapses as Filters: Open-Loop and Feedback Responses

2.1 Low Pass Filtering Due to Synaptic Current Dynamics

Our starting point is the so-called 'difference of two exponentials' model that describes how current flow across a neuron's membrane changes over time in response to a single synaptic event (i.e. a spike arrival). This model has been used many times in computational neuroscience. However, we study a variation of the model that includes a biophysically realistic delayed response, as in [10, 13], i.e. the neuron responds to the arrival of a presynaptic spike only after a delay of $\tau_l > 0$ ms.

The model for the change in current in response to a single incoming spike at time $t = 0$ is parameterised by two constants, the rise time τ_r and the fall time τ_d, where $\tau_r < \tau_d$, and is expressed as

$$i(t) = \frac{1}{\tau_d - \tau_r}\left(\exp\left(-\frac{(t-\tau_l)}{\tau_d}\right) - \exp\left(-\frac{(t-\tau_l)}{\tau_r}\right)\right)u(t-\tau_l), \qquad (1)$$

where $u(\cdot)$ is the Heaviside unit step function. It can easily be verified that Eq. (1) is the solution to a pair of first order differential equations, which can be rewritten compactly in state-space form as

$$\dot{\mathbf{z}} = A\mathbf{z} + \mathbf{u}, \tag{2}$$

where $\mathbf{u} = [0, \delta(t-\tau_l)/\tau_r]^T$ is the input vector, $\mathbf{z} = [z_1(t), z_2(t)]^T$ is the state vector, and $A = [-1/\tau_d, 1/\tau_d; 0, -1/\tau_r]$, and the synaptic current is $i(t) = z_1(t)$. We write the input as $\delta(t-\tau_l)$, which means we model the single input spike as a Dirac delta function, i.e. a single event (the spike arrival) occurs at time $t = 0$, buts its influence is seen only after delay $t = \tau_l$.

Equation (1) is also the solution to the following second order differential equation

$$\tau_r \tau_d \frac{d^2 i(t)}{dt^2} + (\tau_r + \tau_d)\frac{di(t)}{dt} + i(t) = x(t), \tag{3}$$

where $x(t) = \delta(t-\tau_l)$. Given that there is no feedback in this system, we can for the time being ignore τ_l in our analysis of the system itself, as it can be incorporated into the signal itself, by letting $x(t) = \delta(t-\tau_l)$. We thus can consider the response of the system to arbitrary inputs $x(t)$ into the dynamic of the systems. The fact that $0 < \tau_r < \tau_d$ ensures that the system only has damped solutions in response to bounded inputs, as expressed in Eq. (1).

Inspection of Eq. (3) when $x(t) = \delta(t-\tau_l)$ suggests that the current $i(t)$ can be interpreted as the impulse response of a linear time invariant filter, after a delay of τ_l. In the language of analog filtering or feedback control system design, the *transfer function* [15] of the system, $G(s)$, is given by the ratio of the Laplace transform of $i(t)$ to the Laplace transform of $x(t)$. For an arbitrary bounded input signal, $x(t)$, with Laplace transform $X(s)$, the Laplace transform of the response of the system can be written as $Y(s) = G(s)X(s)$, and in the time domain, the response $y(t)$ is the inverse Laplace transform of $Y(s)$.

For the system described by Eq. (3), the transfer function is

$$G(s) = \frac{I(s)}{X(s)} = \frac{1}{\tau_r \tau_d s^2 + (\tau_r + \tau_d)s + 1} = \frac{1}{\tau_d - \tau_r}\left(\frac{1}{\frac{1}{\tau_d} + s} - \frac{1}{\frac{1}{\tau_r} + s}\right), \tag{4}$$

which has the form of a typical 'two pole' analog low pass filter.

If $x(t)$ is a stationary stochastic process with a power spectral density $S_{xx}(\omega)$, the transfer function can also be expressed in terms of Fourier transforms by substitution of $s = i\omega$, and it can be shown that the power spectral density of the response is related to the power spectral density of $x(t)$ as $S_{yy}(\omega) = |G(i\omega)|^2 S_{xx}(\omega)$. From Eq. (4), we obtain

$$|G(i\omega)|^2 = \frac{1}{(1+\tau_r^2\omega^2)(1+\tau_d^2\omega^2)}, \tag{5}$$

and note that if $x(t)$ is white noise (i.e. its power spectral density is constant for all frequencies) then low frequencies $\omega \ll \frac{1}{\tau_d}$ will be reproduced at the output without attenuation, but frequencies $\omega \gg \frac{1}{\tau_d}$ will be heavily attenuated, i.e. filtered.

Inhibitory neurons in the cortex tend to have short rise times, $\tau_r \sim 0.5\,\text{ms}$, and decay times $\tau_d \sim 5\,\text{ms}$ [10], and thus the model expressed by Eq. (1) will, if isolated from feedback, enable the membrane current to encode unattenuated the frequency content of the input only up to about $f = 1/(2\pi\tau_d) \simeq 30\,\text{Hz}$.

2.2 The Impact of Negative Feedback due to Inhibition, With Delays

Introducing negative feedback into a system with a low pass filtering characteristic is well known to enable the possibility of inducing either a resonant response, or unstable oscillations. When a delay is included in the feedback path, such a negative feedback system is a simple model of an inhibitory neuron that connects to itself via an autapse. Inhibitory neurons provide negative feedback because the neurotransmitters they release after spiking have an inhibitory response on the neurons they synapse with. If a neuron forms a synapse with itself, then the synaptic connection is known as an autapse [16].

Consider for example, a system with an open loop transfer function given by $G(s)$ and negative feedback with gain K. When considering the model of Eq. (1), we must also explicitly take into account that the synaptic response to the feedback will be delayed relative to the response due to $x(t)$. The feedback system is shown in Fig. 1, and its closed loop transfer function is given by

$$H(s) = \frac{G(s)}{1 + K\exp(-\tau_l s)G(s)} = \frac{1}{\tau_r\tau_d s^2 + (\tau_r + \tau_d)s + 1 + K\exp(-\tau_l s)}. \quad (6)$$

Studying the transfer function with $s = i\omega$ enables analysis of the steady-state frequency response of the system when the input is either sinusoidal (or the sum of sinusoids) or random noise. For an input $x(t) = A\cos(\omega_x t + \phi(t))$, the steady state response of any linear time invariant system with transfer function $H(s)$ is given by $i(t) = A|H(i\omega)|\cos(\omega_x t + \phi(t) - \arg H(i\omega))$ [15].

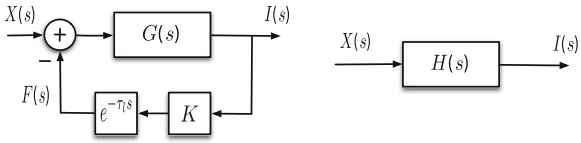

Fig. 1 Closed loop feedback system consisting of an external drive with Laplace transform $X(s)$, that is operated on by system $G(s)$, along with negative feedback. The output response has Laplace transform $I(s)$, and the feedback signal has Laplace transform $F(s)$. The feedback path consists of a delay relative to $X(s)$, a proportional gain K, and a subtraction from the input, $X(s)$. The overall closed loop transfer function, $H(s)$ is defined such that $I(s) = H(s)X(s)$

Moreover, the power spectral density (PSD) of the response, $S_{yy}(\omega)$ can be obtained for an input with arbitrary PSD, $S_{xx}(\omega)$ via the relationship $S_{yy}(\omega) = |H(i\omega)|^2 S_{xx}(\omega)$. From Eq. (6) we obtain

$$|H(i\omega)| = \frac{1}{\sqrt{(1 + K\cos(\tau_l\omega) - \tau_r\tau_d\omega^2)^2 + [(\tau_r + \tau_d)\omega + K\sin(\tau_l\omega)]^2}}. \quad (7)$$

Note that $|H(0)|^2 = 1/(K+1)^2$, and thus the DC value of the output is $y_{\mathrm{DC}}(t) = x_{\mathrm{DC}}/(K+1)$, so the feedback signal will have a DC component of $Kx_{\mathrm{DC}}/(K+1)$.

The frequency response, $|H(i\omega)^2|$ is shown in Fig. 2a for both $\tau_l = 0$ ms and $\tau_l = 1$ ms with $\tau_r = 0.5$ ms, $\tau_d = 5$ ms and various value of K. Clearly, for $\tau_l = 1$ ms, as K increases the closed loop system begins to show a bandpass filter characteristic,

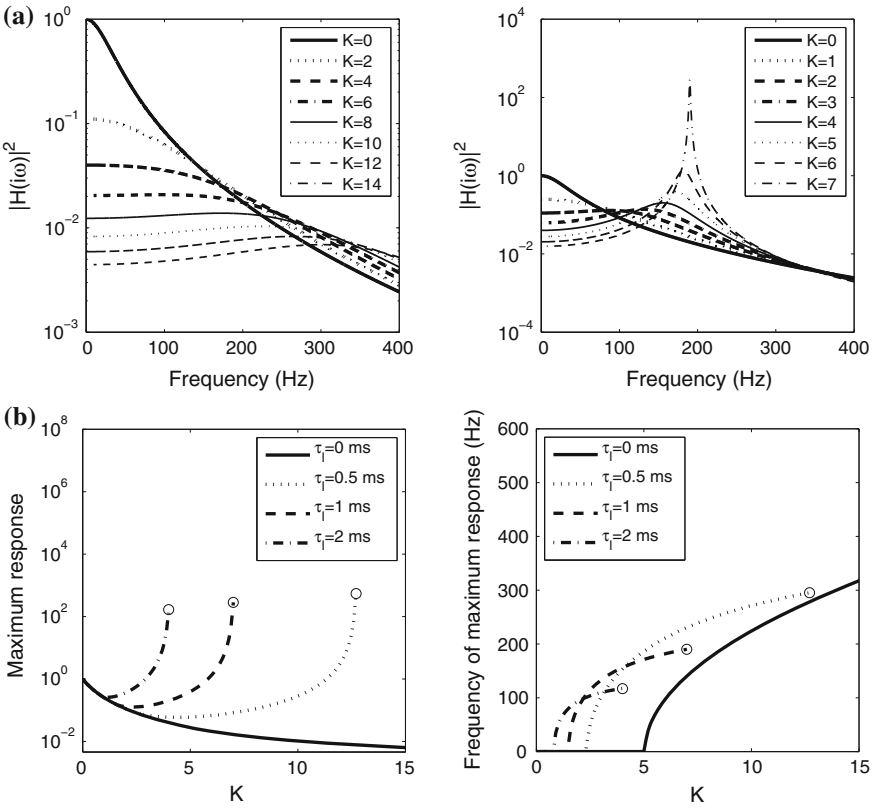

Fig. 2 **a** Frequency response of the closed loop negative feedback system, $H(s)$, for $\tau_l = 0$ ms (*left panel*) and $\tau_l = 1$ ms (*right panel*). **b** Illustration of resonant bandpass-filter like response, and stability, for the closed loop negative feedback system with delay. The maximum value of K that provides closed loop stability is shown with a circle for each value of τ_l. The time constants are $\tau_r = 0.5$ ms, and $\tau_d = 5$ ms.

with a resonant frequency near 200 Hz. The maximum response and the frequency of maximum response increase with K. However, there is a limit to how much K can be increased, because if it is too large, then the closed loop system becomes unstable. On the other hand, in the absence of a delay, although the system exhibits a bandpass characteristic for sufficiently large K, the resonant frequency is much higher than with the delay present. Moreover, the input is highly attenuated at all frequencies with respect to the open loop system ($K = 0$), which is not the case when $\tau_l = 1$ ms.

The closed loop system $H(s)$ has an unstable oscillatory mode if any root of its denominator has positive real part (it may also may have transient damped oscillatory modes even though $G(s)$ does not). Given that stability depends on the roots of the denominator, whether an unstable solution exists depends on the values of both K and τ_l. There is no closed form solution for the roots, but they can be obtained numerically as a function of K and τ_l.

Note that due to the physical constraint that the time constants τ_r and τ_d are both positive, the open loop system, $G(s)$ cannot have a bandpass characteristic. For the closed loop system without a delay (i.e. $\tau_l = 0$), the system will resonate and have a bandpass filtering characteristic if K is sufficiently large, and also be stable for all K. However, as suggested by Fig. 2a (left panel), the resonant frequency will be much larger than that of oscillations encountered in recordings of cortical activity, and moreover, the damping ratio, and therefore the peak response, grows very slowly with feedback gain.

These model deficiencies with respect to known biophysics are readily overcome by the inclusion of non-zero time delays. When these are included, as suggested by Fig. 2a (right panel), the closed loop transfer function can exhibit a bandpass filter characteristic with a resonant frequency at much lower (and therefore biophysically plausible) frequencies, and with a higher damping ratio.

However, non-zero delays make the closed loop system unstable when K is sufficiently large. Therefore, we will seek an appropriately small value of K, such that there is a large resonant (and therefore bandpass filter like) response, but a stable system.

To illustrate the resonant or bandpass filter-like behaviour of the closed loop system, Fig. 2b shows the maximum response of $|H(i\omega)|^2$, and the frequency of the maximum response (in hertz) as a function of K, up to the maximum stable K, for four values of delay, τ_l. The other time constants are $\tau_r = 0.5$ ms, and $\tau_d = 5$ ms. The figure shows that although the system is always stable for $\tau_l = 0$, it only shows a bandpass response at high frequencies, and with very large attenuation with respect to $K = 0$. As τ_l increases, however, the frequency of the maximum response also decreases, while still enabling a gain in amplitude response with respect to the system without delay or with respect to $K = 0$ with delay.

2.3 Example Simulations

We consider $\tau_r = 0.5$ ms, $\tau_d = 5$ ms and $\tau_l = 1$ ms. With these values, it can easily be shown numerically that the closed loop system is unstable for $k \gtrsim 7$, as illustrated in Fig. 2b. As shown in Fig. 2a, the system has a bandpass filter characteristic with a

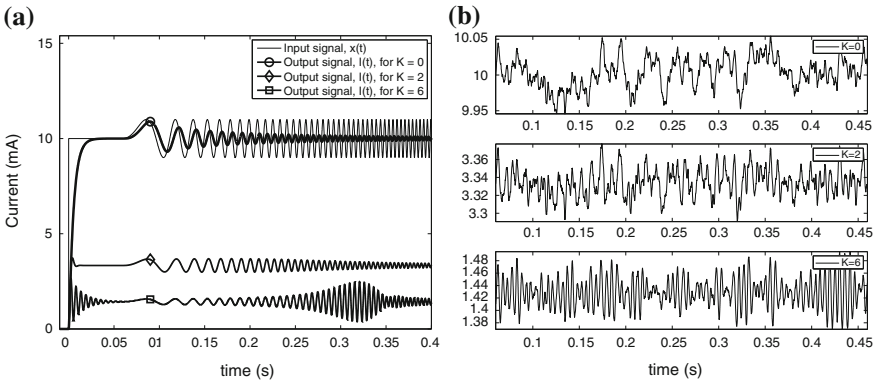

Fig. 3 **a** Simulated response of the closed loop system with feedback gain $K = 6$ and delay $\tau_l = 1$ ms, in response to a chirp input, for three values of K. **b** Simulated response of the closed loop system with feedback gain $K = 6$ and delay $\tau_l = 1$ ms, in response to white noise, for three values of K.

frequency of maximum response approaching 180 Hz as K approaches its maximum stable value, near $K = 7$. To illustrate the bandpass response for a non-random signal we use a swept chirp input of the form $x(t) = \sin(\pi k t^2)$, which is a signal with instantaneous frequency $f_{\mathrm{i}} = kt$ Hz that linearly increases with time.

Fig. 3a shows the input chirp when turned on after allowing transient response to a step DC input to die away. The figure also shows the results of simulations of system response, $i(t)$, for $K = 0$, $K = 2$ and $K = 6$. For $K = 6$, the closed loop gain exceeds unity in the neighbourhood of the resonant frequency, and therefore the feedback can be interpreted as amplifying frequencies within the passband. We also illustrate the bandpass response using white noise. Simulated closed loop responses are shown in Fig. 3b for three values of K. When the input is white noise, the power in the system response is many times smaller than that of the input, and its peak amplitude is much smaller than transient damped oscillations, and therefore we have not shown the input noise, or the transient responses. This example shows that narrowband oscillations are clearly observable in the case of $K = 6$.

A source of energy is required for the feedback amplification factor K, and in the biophysical system it is not clear how this amplification factor may be realised. In the following section we consider one biophysically plausible mechanism for enabling proportional gain, K. We then study the impact of feedback noise.

3 Feedback Amplification and Noise Reduction Via Redundancy

We now compare the 'autapse' model—a single neuron with ideal noiseless negative feedback (with gain)—with several scenarios where the feedback is noisy: (i) distributed feedback with stochastic additive noise; (ii) distributed feedback with quantization noise; (iii) distributed feedback with quantization and stochastic noise.

We find that when distributed feedback is quantized, stochastic noise significantly enhances overall performance compared with the absence of stochastic noise.

3.1 Ideal Distributed Feedback Equivalent to Feedback Gain of K

We consider now the case where feedback amplification is due to redundancy. The ideal scenario is that K parallel and identical systems receive the same input, but as well as self-feedback, each system receives feedback from all the other systems. To enable more general analysis below, we write the feedback signal from system i to system j as $F_{ij}(s) = f_{ij}[I_i(s)]$, where $f_{ij}(\cdot)$ is an arbitrary function, and also write the overall feedback to system j as $F_j(s)$—see Fig. 4.

Without any noise, we have $f_{ij}[I_i(s)] = I_i(s) \forall j$. Therefore if we set $N = K$, then $F_j(s) = \sum_{i=1}^{K} I_i(s) \forall j$. Given that each system receives the same input, it will also produce the same output and feedback signal, $I(s)$, and therefore all feedback signals are identical with $F_j(s) = KI(s) \exp(-\tau_l s)$. This illustrates that redundancy achieves feedback gain K in the overall system.

3.2 Distributed Feedback with Additive White Noise

Now we consider the same scenario but suppose each output signal, $I_i(s)$ acquires independent additive Gaussian white noise, $\eta_i(t)$ with mean zero, and variance σ^2, prior to being fed back. We write the Laplace transform of the noise as $N_i(s)$, and thus $F_{ij}(s) = f_{ij}[I_i(s)] = I_i(s) + N_i(s) \forall j$. Due to the independence of the noise from $x(t)$, and the linearity of the system, each feedback noise is equivalent to input noise that subtracts from $x(t)$. The subtraction is equivalent to an addition, due to the symmetry of Gaussian noise about its mean. Therefore, since there are K feedback signals, the total equivalent input noise for system j is $\xi_j(t)$, where $\xi(t)$ is white noise with zero mean and variance $K\sigma^2$. However, this compares very favourably

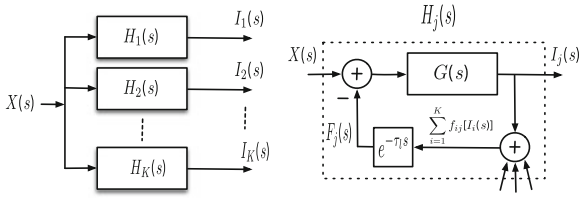

Fig. 4 Parallel redundant network of systems receiving the same input (*left panel*). The feedback signal paths to each system are shown in the *right panel*: system j receives feedback from all systems including itself, and as in the original stand-alone system, the feedback path is delayed with respect to the output of the system

with the situation in the ideal non redundant 'autapse' model. If there were feedback noise in that system, the feedback noise would be amplified, resulting in variance $K^2\sigma^2$. Therefore, the distributed feedback model will have a signal-to-noise ratio K times larger than the noisy autapse model, and is equivalent to the autapse model with additive input noise with variance $K\sigma^2$. We can write the feedback signal into each system j as $F_j(s) = KI(s) + \sum_{i=1}^{K} N_i(s)$, and thus the noise signal is identical in each output as well as the input.

Increasing redundancy (more parallel systems) whilst retaining only K feedback signals would potentially enable the noise at the output to be non-identical for each system, and thus allow noise reduction by averaging the outputs. However as soon as the feedback signals become sparse rather than dense, this introduces the possibility of instability, since some systems will impact on other systems after longer delays. Even in the case of $K+1$ systems with only autapses forbidden, this leads to positive feedback loops, and quite complex equivalent transfer functions. Therefore, we leave study of this for future work.

3.3 Distributed Quantized Feedback

In many engineered systems, feedback is only available in a digitized form. This means the feedback signal has been quantized in amplitude, and this quantization can be considered as a form of noise. Often quantization noise is modelled as additive white noise, but this is only an approximation that is more inaccurate as the number of quantization levels becomes small. We now consider a scenario similar to that of the previous subsection, except that instead of additive white feedback noise, each feedback signal is quantized. Like the additive white noise case, we can expect that each system j will have identical outputs, due to the redundancy. The overall output noise should decease as the number of quantization levels increases. However, unlike the additive stochastic noise case, the overall output variance will be of the order of K^2 rather than K, since the noise signals will not be independent, and redundancy does not provide a benefit in terms of noise reduction compared with the noisy autapse model.

3.4 Distributed Quantized Feedback with Independent Stochastic White Noise Prior to Quantisation

If the feedback signal is corrupted by white noise prior to quantization, then this can make the quantization noise largely independent for each feedback signal. This again enables the possibility of noise reduction due to averaging where the feedback signals enter each system. See [17, 18] for discussion.

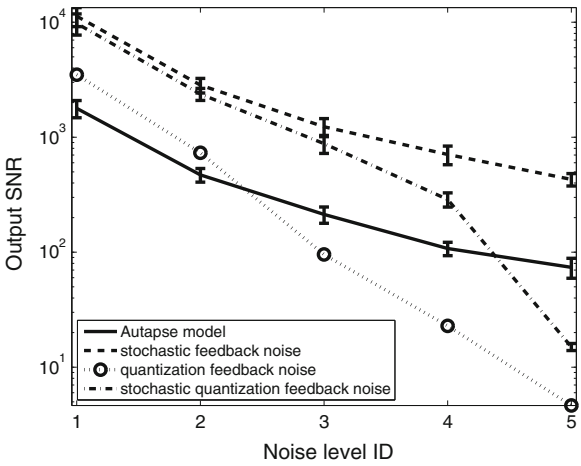

Fig. 5 Comparison of output signal-to-noise ratios for five different levels of feedback noise. For each model except the quantization feedback noise model, the feedback is corrupted by stochastic additive white Gaussian noise with variances 0.02, 0.04, 0.06, 0.08, 0.1, corresponding to Noise level ID $1-5$. For the two quantization models, the feedback is quantized to 8, 7, 6, 5, 4 bits, corresponding to Noise level ID $1-5$. Error bars indicated the standard deviation from 20 repeats, and the lines are the mean signal-to-noise ratio. No error bars are shown for the quantization feedback noise case, since in this case there is no stochastic noise, and therefore no variance

3.5 Example Results

Figure 5 shows how well the models described above perform in comparison with the ideal autapse model described in Sect. 2. In each case we simulate the system for a variety of noise levels, and then calculate the output signal-to-noise ratio in comparison with the ideal response.

These results show that the distributed feedback model with stochastic noise provides much improved performance than the autapse model with feedback noise, as expected. They also show that when the feedback is quantized, that stochastic noise significantly enhances performance over quantization alone. This is in line with theoretical work presented in [17], and implies that the stochastic and quantized feedback noise model can be described as a *stochastic pooling network* [18].

4 Possibilities for Bio-Inspired Engineering

We have discussed a model that plausibly explains why narrowband oscillations are often observed in recordings of cortical activity [10]. Models of this type have received much attention in neuroscience and computational neuroscience [10, 13, 14]. What is not known, however, is how cortical networks may utlize such

bandpass filter-like characteristics, if at all. From an engineering perspective, however, is it possible that a designed system may benefit from mimicking some aspect of how the cortical network achieves a resonant characteristic?

One common use for bandpass filters is in modulated communication. Their use enables frequency multiplexing, and they are also useful in demodulation of FM signals. Given that in the first case an ideal filter has a flat passband, its seems unlikely that one would wish to design a filter like the cortical network. However, there is more potential for demodulation of FM signals, since a filter with a linear increase in gain with frequency is required in a frequency discriminator.

We therefore propose in future work to compare performance achieved by each model described in Sect. 3, when the input is a linearly swept chirp, or other FM signal, and the output of the system is used to estimate instantaneous frequency as a function of time. We also propose that the distributed noisy feedback model may be adapted in designs of distributed communication systems consisting of small, cheap and redundant nodes, similar to models discussed in [18].

Acknowledgments M. D. McDonnell was supported by the Australian Research Council under ARC grant DP1093425 (including an Australian Research Fellowship), and an Endeavour Research Fellowship from the Australian Government.

References

1. E.M. Izhikevich, N.S. Desai, E.C. Walcott, F.C. Hoppensteadt, Trends Neurosci. **26**, 161 (2003)
2. W.J. Freeman, *Mass Action in the Nervous System* (Academic Press, New York, 1975)
3. A. Destexhe, M. Rudolph-Lilith, *Neuronal Noise* (Springer, New York, 2012)
4. G. Buzsáki, A. Draguhn, Science **304**, 1926 (2004)
5. B. Hutcheon, Y. Yarom, Trends Neurosci. **23**, 216 (2000)
6. Y. Gai, B. Doiron, J. Rinzel, PLoS Comp. Bio. **6**, e1000825 (2010)
7. B.P. Graham, C. Stricker, in Proceedings of the 2008 International Conference on Artificial Neural Networks (ICANN 2008), ed. by V. Kůrková, et. al (Lecture Notes in Computer Science LNCS 5164. Springer-Verlag, Berlin Heidelberg, Germany, 2008), pp. 268–276.
8. T. Sasaki, R. Kimura, M. Tsukamoto, N. Matsuki, Y. Ikegayan, J. Physiol. (London) **574**, 195 (2006)
9. C.D. Geisler, From Sound to Synapse (Oxford University Press, New York, 1998)
10. N. Brunel, X.J. Wang, J. Neurophysiol. **90**, 415 (2003)
11. N. Brunel, V. Hakim, Chaos **18**, 015113 (2008)
12. X.J. Wang, Physiol.l Rev. **90**, 1195 (2010)
13. A. Mazzoni, S. Panzeri, N.K. Logothetis, N. Brunel, PLoS Comp. Bio. **4**, e1000239 (2008)
14. K. Kang, M. Shelley, J.A. Henrie, R. Shapley, J. Comput. Neurosci. **29**, 495 (2010)
15. G.F. Franklin, J.D. Powell, A. Emami-Naeini, Feedback Control of Dynamic Systems, 5th edn. (Pearson Prentice Hall, New Jersey, 2006)
16. J.M. Bekkers, Current Biology **19**, R296 (2009)
17. M.D. McDonnell, N.G. Stocks, C.E.M. Pearce, D. Abbott, *Stochastic Resonance: From Suprathreshold Stochastic Resonance to Stochastic Signal Quantisation* (Cambridge University Press, Cambridge, 2008)
18. M.D. McDonnell, P.O. Amblard, N.G. Stocks, J. Stat. Mech: Theory Exp. **P0**, 1012 (2009)

Majority Rule in Nonlinear Opinion Dynamics

Michael Gabbay and Arindam K. Das

Abstract Using a nonlinear model of opinion dynamics on networks, we show the existence of asymmetric majority rule solutions for symmetric initial opinion distributions and symmetric network structure. We show that this occurs in triads as the result of a pitchfork bifurcation and arises in both chain and complete topologies with symmetric as well as asymmetric coupling. Analytical approximations for bifurcation boundaries are derived which closely match numerically-obtained boundaries. Bifurcation-induced symmetry breaking represents a novel mechanism for generating majority rule outcomes without built-in structural or dynamical asymmetries; however, the policy outcome is fundamentally unpredictable.

1 Introduction

Small group opinion change has long been a subject of intense study in social science with implications for decision making by a range of groups such as political leaders, judicial panels, corporate committees, and juries [4, 8]. Mathematical models of small group decision making have been proposed in social science disciplines such as psychology, sociology, political science, economics, and law [2, 5, 9]. In this paper, we put forth a novel mechanism for the generation of majority rule outcomes in small groups via a symmetry-breaking pitchfork bifurcation. This mechanism allows for asymmetric outcomes to appear for symmetric initial opinion distributions even when group members are symmetrically coupled. It occurs in the nonlinear opinion dynamics model of Refs. [6, 7] under conditions of high disagreement between the

M. Gabbay(✉)
Applied Physics Laboratory, University of Washington, Seattle, WA 98105, USA
e-mail: gabbay@uw.edu

A. K. Das
Department of Engineering and Design, Eastern Washington University, Cheney, WA 99004, USA
e-mail: arindam@uw.edu

V. In et al. (eds.), *International Conference on Theory and Application in Nonlinear Dynamics (ICAND 2012)*, Understanding Complex Systems,
DOI: 10.1007/978-3-319-02925-2_15,

ends of the distribution along a continuous opinion axis. For example, in a triad network consisting of a centrist bracketed by two opposed extremists, the centrist will form a majority pair with one of the extremists. This runs counter to intuition rooted in basic psychological mechanisms of attitude change which emphasize a convergence process of group member attitudes, and so would anticipate either deadlock or various degrees of compromise around the centrist's position, but not majority rule. In particular, it is not predicted by the most prominent network-based model of small group opinion dynamics, the Friedkin-Johnsen model, which is linear in the disagreement between group members [5]. The Friedkin-Johnsen and nonlinear opinion dynamics models are described in the next section. The majority rule outcome for a triad is demonstrated in simulation (Sect. 3) and via bifurcation analysis (Sect. 4). Majority rule in five-node networks is presented in Sect. 5.

2 Opinion Dynamics Models

Most recent work on opinion network dynamics in the physics community has focused on large networks motivated by an interest in population scale dynamics [1]. Consensus in small networks has been studied in the literature on distributed network control with sensor networks as a primary motivation [10, 11]. However, our nonlinear model is most closely related to that of Friedkin and Johnsen, which was explicitly developed for the social influence context and has been subjected to empirical investigation [5].

2.1 Friedkin-Johnsen Model

The Friedkin-Johnsen model describes the temporal evolution of a linear discrete time influence process in a group of N people (nodes) as a weighted average of their previous opinions and their initial opinions [5]:

$$x_i(k+1) = a_i \sum_{j=1}^{N} w_{ij} x_j(k) + (1 - a_i) x_i(0); \quad i = 1, 2, \ldots N, k \geq 0, \qquad (1)$$

where $x_i(k)$ is the opinion of node i at time k; $x_i(0)$ is the initial opinion; a_i is the susceptibility of node i; and w_{ij} is the coupling weight scaling node j's influence upon i. The w_{ij} are non-negative and satisfy $\sum_{j=1}^{N} w_{ij} = 1$. In addition, the susceptibility is given by $a_i = 1 - w_{ii}$.

Equation (1) can be cast as a difference equation by subtracting $x_i(k) = (1 + a_i - a_i)x_i(k)$ from both sides and rearranging to yield

$$x_i(k+1) - x_i(k) = a_i \sum_{j=1}^{N} w_{ij}(x_j(k) - x_i(k)) - (1 - a_i)(x_i(k) - x_i(0)). \quad (2)$$

If $a_i = 1 \forall i$ in Eq. (2), then the node opinions will all converge to exactly the same value for a (bidirectionally) connected network. The presence of $x_i(0)$ in the dynamics of the Friedkin-Johnsen model prevents such a collapse onto an exact consensus which would signify the unintuitive complete extinction of disagreement. However, because of the linear coupling in the Friedkin-Johnsen model, equilibria in which the member opinions are asymmetrically distributed around the mean must arise from pre-existing asymmetries; either skewed initial opinion distributions or lopsided coupling weights in favor of one extreme. This is not the case for the nonlinear model which we turn to next.

2.2 Nonlinear Model

We use the following model for the evolution of the opinion x_i [7]:

$$\frac{dx_i}{dt} = -\gamma_i(x_i - \mu_i) + \sum_{j=1}^{N} \kappa_{ij} h(x_j - x_i). \quad (3)$$

The first term on the right is a linear "self-bias force" which expresses the psychological tension that a person feels if her opinion is displaced from her natural bias μ_i and is proportional to her commitment γ_i. The second term is the "group influence force" on i where κ_{ij} is the coupling strength and $h(x_j - x_i)$ is the coupling function. The coupling strength, which we take to be non-negative, represents the components of influence of j upon i arising from their relationship; it depends on factors such as how often j communicates with i and the regard with which i holds j. The coupling function represents how the influence of j upon i depends on the difference between their opinions. We use a dependence motivated by social judgment theory [4] in which the force grows for $|x_j - x_i| < \lambda_i$, where λ_i is is latitude of acceptance, but wanes for differences in excess of λ_i:

$$h(x_j - x_i) = (x_j - x_i) exp\left[-\frac{1}{2}\frac{(x_j - x_i)^2}{\lambda_i^2}\right]. \quad (4)$$

For situations in which a group first starts discussing an issue it is appropriate to use natural bias initial conditions, $x_i(0) = \mu_i$.

In the linear limit, $\lambda_i \to \infty$, it can readily be seen that the (discretized) nonlinear model reduces to the form (2) of the Friedkin-Johnsen model, apart from parameter constraints. The natural bias μ_i plays the same role in preventing the collapse onto exact agreement in (3) as the initial opinion does in (1). When applied to group

decision-making, we assume that a common decision can be reached between group members if their final opinions $x_i(t_f)$ are sufficiently close. This is in accord with the intuition that people need not precisely agree in order to reach a compromise decision on a common course of action.

3 Triad Simulations

We simulate a triad network in which the natural biases are symmetrically distributed around zero: $\mu_1 = -\Delta\mu/2$, $\mu_2 = 0$, and $\mu_3 = \Delta\mu/2$. We use a chain topology whose ends, nodes 1 and 3, are not connected so that the symmetric, binary adjacency matrix elements are $A_{12} = A_{21} = A_{23} = A_{32} = 1$ and $A_{13} = A_{31} = 0$ (and also $A_{ii} = 0$). However, the complete network in which all members are connected, $A_{ij} = 1 - \delta_{ij}$ where δ_{ij} is Kroneckers delta, has similar behavior as will be seen in Sect. 4. We use the parameter v to allow for the possibility of asymmetric coupling between the center node 2 and the end nodes so that $\kappa_{12} = \kappa_{32} = \kappa + v$ and $\kappa_{21} = \kappa_{23} = \kappa - v$ where $|v| < \kappa$. A positive value of v signifies that the center node has greater influence on each of the end nodes than vice versa whereas negative v signifies that the ends have more influence. The equations of motion for the triad are then:

$$\begin{aligned}
\frac{dx_1}{dt} &= -\left(x_1 + \frac{\Delta\mu}{2}\right) + (\kappa + v)h(x_2 - x_1) + \kappa A_{31} h(x_3 - x_1), \\
\frac{dx_2}{dt} &= -x_2 + (\kappa - v)(h(x_1 - x_2) + h(x_3 - x_2)), \\
\frac{dx_3}{dt} &= -\left(x_3 - \frac{\Delta\mu}{2}\right) + (\kappa + v)h(x_2 - x_3) + \kappa A_{31} h(x_1 - x_3).
\end{aligned} \tag{5}$$

It will be useful to define the following pair of variables: the *discord* $r = x_3 - x_1$, the opinion difference between the outer nodes and the *asymmetry* $s = (x_3 - x_2) - (x_2 - x_1)$, the difference in distances from the outer nodes to the middle node.

Figure 1 shows simulations of the chain network for three values of the coupling strength κ and with symmetric coupling between all nodes. The difference in the natural biases of the end nodes is $\Delta\mu = 5$ and the initial opinions are set equal to the natural biases (except for a tiny displacement to the center node as an initial perturbation which always moves x_2 in the same direction for the asymmetric solutions). Three qualitatively distinct equilibria are observed. At low coupling, Fig. 1a shows a state of Symmetric High Discord (SHD) in which the end nodes barely move from their natural biases and the center node remains at zero. At intermediate coupling, Fig. 1b shows the Majority Rule (MR) state in which the center node moves toward one of the end nodes to form a majority rule pair. At high coupling, the outer nodes move considerably toward the center to form a Symmetric Low Discord (SLD) state as shown in Fig. 1c. The SHD state corresponds to a deadlock situation in which

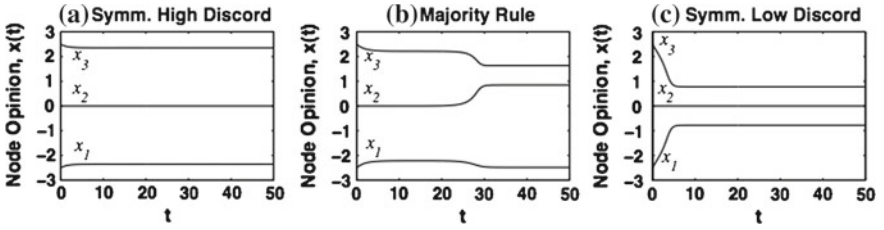

Fig. 1 Equilibrium outcomes in symmetrically-coupled ($v = 0$) triad chain network with high initial disagreement, $\Delta\mu = 5$, at different coupling strengths: **a** $\kappa = 1$, symmetric high discord; **b** $\kappa = 1.5$, majority rule; **c** $\kappa = 3$, symmetric low discord. Initial conditions: $x_1(0) = -2.5$, $x_2(0) = 10^{-6}$, $x_3(0) = 2.5$

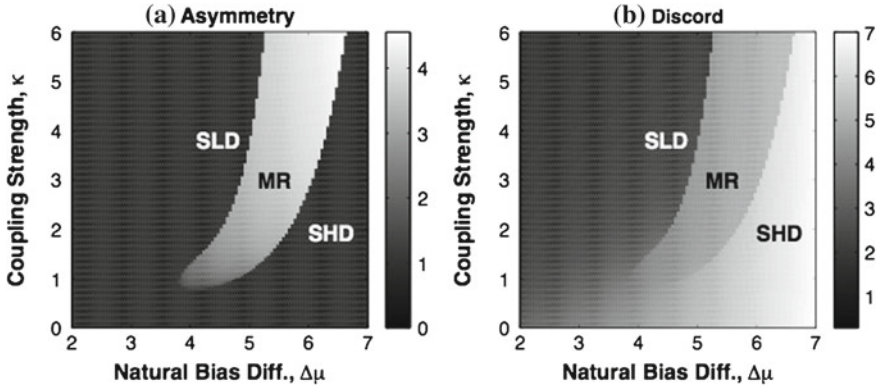

Fig. 2 Simulation of a symmetrically-coupled triad chain network over $\Delta\mu - \kappa$ parameter space showing final: **a** discord and **b** asymmetry (absolute value). Simulation duration is $t_f = 200$

all group members are far apart and no acceptable mutual decision can be made. In the MR state, the majority pair can likely agree on a common policy which will be the policy of the group if majority rule is sufficient for reaching a decision. In the SLD state, the distance between the outer nodes is much reduced and the basis for a compromise around the centrists position could be set. Simulations in which μ_1, μ_2, and μ_3 are randomly shifted by a small amount still display all three outcome types.

Figure 2 plots the asymmetry and discord of the symmetrically-coupled chain network with natural bias initial conditions. The emergence of the MR state only occurs past a critical value of the natural bias difference $\Delta\mu_c = 3.8$ which we call the *critical divergence*. Also, note the sharp discontinuities at the boundaries between the various outcome states. Below the critical divergence, asymmetric solutions do not exist and the discord is smoothly and symmetrically reduced as the coupling strength is raised as would occur in the equivalent case for the Friedkin-Johnsen model, for which the transition from deadlock to compromise to consensus is gradual with no possibility of an MR state.

4 Bifurcation Analysis for Triad

In this section, we show that the majority rule state is the result of spontaneous symmetry-breaking induced by a pitchfork bifurcation and we calculate bifurcation boundaries. We do this for the chain topology in which $A_{31} = 0$. We transform the system (5) into the discord and asymmetry variables, r and s, as well as the mean node opinion, $\bar{x} = \frac{1}{3}\sum_{i=1}^{3} x_i$. Using the fact that the coupling function is odd, $h(-x) = -h(x)$, results in the system:

$$\frac{dr}{dt} = -(r - \Delta\mu) - (\kappa + v)\left(h\left(\frac{r+s}{2}\right) + h\left(\frac{r-s}{2}\right)\right) \tag{6}$$

$$\frac{ds}{dt} = -s - (3\kappa - v)\left(h\left(\frac{r+s}{2}\right) - h\left(\frac{r-s}{2}\right)\right) \tag{7}$$

$$\frac{d\bar{x}}{dt} = -\bar{x} - \frac{2}{3}v\left(h\left(\frac{r+s}{2}\right) - h\left(\frac{r-s}{2}\right)\right) \tag{8}$$

For symmetric coupling, Eq. (8) implies that the mean equilibrium opinion is zero, the mean of the natural biases; this will not be the case for $v \neq 0$ in the MR state in which $s \neq 0$.

For the equilibrium SHD state, denoted by (r, s), the asymmetry is by definition $s = 0$. For large $\Delta\mu$ we take the discord to be $r \approx \Delta\mu + \theta$ where $\theta \ll 1$. Before showing the existence of the pitchfork bifurcation, it will be useful below to calculate θ . When $s = 0$, Eq. (6) becomes

$$\frac{dr}{dt} = -(r - \Delta\mu) - 2(\kappa + v)h\left(\frac{r}{2}\right), \tag{9}$$

which upon substituting the above form for r yields

$$0 = \theta + 2(\kappa + v)h\left(\frac{\Delta\mu + \theta}{2}\right). \tag{10}$$

Expanding the coupling function as $h(\frac{\Delta\mu+\theta}{2}) \approx h(\frac{\Delta\mu}{2}) + h'(\frac{\Delta\mu}{2})\frac{\theta}{2}$ and substituting into (10) enables us to solve for θ

$$\theta = -\frac{2(\kappa + v)h\left(\frac{\Delta\mu}{2}\right)}{1 + (\kappa + v)h'\left(\frac{\Delta\mu}{2}\right)} \tag{11}$$

where $h\left(\frac{\Delta\mu}{2}\right) = \frac{\Delta\mu}{2}e^{-\frac{\Delta\mu^2}{8}}$ and $h'\left(\frac{\Delta\mu}{2}\right) = \left(1 - \frac{\Delta\mu^2}{4}\right)e^{-\frac{\Delta\mu^2}{8}}$.

To show the bifurcation, we consider small perturbations s around $s = 0$ in Eq. (7). This results in the Taylor expansion,

$$\frac{ds}{dt} \approx -\left(1 + (3\kappa - v)h'\left(\frac{r}{2}\right)\right)s - \frac{1}{24}(3\kappa - v)h'''\left(\frac{r}{2}\right)s^3, \tag{12}$$

where only the odd power terms survive. When the coefficient of the linear term is positive, the symmetric state will be unstable. When $h'''(r/2) > 0$, we can rescale as follows:

$$\tau = \left[\frac{1}{24}(3\kappa - v)h'''\left(\frac{r}{2}\right)\right]t \tag{13}$$

$$R = -\frac{1 + (3\kappa - v)h'\left(\frac{r}{2}\right)}{\frac{1}{24}(3\kappa - v)h'''\left(\frac{r}{2}\right)} \tag{14}$$

which transforms (12) into the normal form of a supercritical pitchfork bifurcation, $ds/d\tau = Rs - s^3$, where the bifurcation occurs for $R = 0$, beyond which the symmetric $s = 0$ equilibrium is absolutely unstable and two stable asymmetric branches emerge [12].

When $h'''(r/2) < 0$, the pitchfork bifurcation is subcritical, exhibiting a hard loss of stability, multistability, and hysteresis. The relevant zero crossing of $h'''(x) = (-x^4 + 6x^2 - 3)e^{-\frac{1}{2}x^2}$ in marking the boundary between supercritical and subcritical bifurcations occurs at $x = (3 + \sqrt{6})^{1/2}$ corresponding to a discord of $r = 4.66$.

4.1 SHD Upper Boundary: κ_1

We now calculate the boundary in $\Delta\mu - \kappa$ parameter space given by the critical value of the coupling strength κ_1 at which the SHD state becomes absolutely unstable. Setting the coefficient of the first term on the righthand side of (12) equal to zero yields

$$\kappa = -\frac{1}{3h'(\frac{r}{2})} + \frac{v}{3}. \tag{15}$$

Substituting $r \approx \Delta\mu + \theta$, and expanding (15) to first order in θ gives

$$\kappa_1 \approx \frac{1}{3}\left\{\frac{1}{h'(\frac{\Delta\mu}{2})} - \frac{h''(\frac{\Delta\mu}{2})}{h'^2(\frac{\Delta\mu}{2})}\frac{\theta}{2}\right\} + \frac{v}{3} \tag{16}$$

The expression (11) for θ can be inserted into the above which, after rearranging, yields the characteristic equation

$$0 = 3h'(\frac{\Delta\mu}{2})\kappa_1^2 + \left(4 + M + 2vh'(\frac{\Delta\mu}{2})\right)\kappa_1 + \frac{1}{h'(\frac{\Delta\mu}{2})} + Mv - v^2h'(\frac{\Delta\mu}{2}), \tag{17}$$

where $M = \frac{\Delta\mu^4 - 12\Delta\mu^2}{(\Delta\mu^2-4)^2}$. This can be solved to give the following approximation for κ_1:

$$\kappa_1 \approx \frac{2}{3}\frac{e^{\frac{\Delta\mu^2}{8}}}{(\Delta\mu^2-4)}\left\{4 + M + 2vh'\left(\frac{\Delta\mu}{2}\right) - \left[4 + 8M + M^2 + 8vh'\left(\frac{\Delta\mu}{2}\right)\left(2 - M + 2vh'(\frac{\Delta\mu}{2})\right)\right]^{\frac{1}{2}}\right\}. \quad (18)$$

This increases rapidly as $\Delta\mu$ becomes very large. The appearance of v as a product with the very small $h'(\Delta\mu)$ implies that κ_1 will be nearly identical to the $v = 0$ case as $\Delta\mu$ gets large.

4.2 MR Lower Boundary in Subcritical Zone: κ_2

Turning now to the disappearance of the asymmetric solutions in the subcritical bifurcation regime, this corresponds to the transition between the multistable zone where the MR and SHD states coexist to the zone in which only the SHD state exists as the coupling strength is lowered. This transition occurs via a saddle-node bifurcation in which stable and unstable asymmetric equilibria collide. The associated bifurcation boundary κ_2 can be calculated by analyzing Eq. (7) around the MR equilibrium in which the minority node x_1 stays near its natural bias while the majority pair (x_2, x_3) is very nearly symmetrically positioned around the midpoint between their natural biases, $\Delta\mu/4$. Asymmetric coupling, $v \neq 0$, will shift the equilibrium mean of the majority rule pair by an amount given by $\varepsilon = (x_2 + x_3)/2 - \Delta\mu/4$. For large $\Delta\mu$, $x_2 - x_1 = (r - s)/2$ is large and we can neglect the term $h((r - s)/2)$ in Eq. (7). Accordingly, we make the approximations for the outer opinion coordinates: $x_1 \approx -\Delta\mu/2$ and $x_3 \approx \Delta\mu/2 + 2\varepsilon - x_2$. The asymmetry is then $s = x_3 - 2x_2 + x_3 = -3x_2 + 2\varepsilon$. Rearranging yields $x_2 = -s/3 + 2\varepsilon/3$ and then $x_3 = s/3 + \Delta\mu/2 + 4\varepsilon/3$ so that the discord can now be written in terms of s as $r = x_3 - x_1 = s/3 + \Delta\mu + 4\varepsilon/3$. The argument of the coupling function term retained from Eq. (7) is $(r + s)/2 = 2/3(s + 3/4\Delta\mu + \varepsilon)$. Finally, we transform to the variable $\tilde{s} = s + 3\Delta\mu/4 + \varepsilon$ and Eq. (7) becomes

$$\frac{d\tilde{s}}{dt} = -(\tilde{s} - \frac{3}{4}\Delta\mu - \varepsilon) - (3\kappa - v)h\left(\frac{2}{3}\tilde{s}\right). \quad (19)$$

Equation (8) can be used to calculate the shift ε in the mean of x_2 and x_3 (neglecting the $h((r - s)/2)$ term and using $x_1 = -\Delta\mu/2$) yielding $\varepsilon = -vh(\frac{r+s}{2}) = -vh(\frac{2}{3}\tilde{s})$. Taking $v \ll \kappa$, the first order contribution of v resulting from the last term in Eq. (19) is given by $vh(\frac{2}{3}\tilde{s})$ which cancels out the ε term. Thus, we get

$$\frac{d\tilde{s}}{dt} = -(\tilde{s} - \frac{3}{4}\Delta\mu) - 3\kappa h(\frac{2}{3}\tilde{s}), \tag{20}$$

and we see that the effect of asymmetric coupling between the center and the extremes disappears for small v and so will not impact the bifurcation boundary.

The equilibrium value for which the saddle-node bifurcation occurs is marked by the vanishing of the right-hand side of the above equation as well as its derivative, yielding upon rearrangement the conditions:

$$\tilde{s} - \frac{3}{4}\Delta\mu = -2\kappa_2\tilde{s}e^{-\frac{2}{9}\tilde{s}^2} \tag{21}$$

$$1 = -2\kappa_2(1 - \frac{4}{9}\tilde{s})e^{-\frac{2}{9}\tilde{s}^2}, \tag{22}$$

where κ_2 denotes the coupling strength at which the bifurcation occurs. Taking the ratio of (21) to (22) and rearranging yields the cubic equation

$$0 = \tilde{s}^3 - \frac{3}{4}\Delta\mu\tilde{s}^2 + \frac{27}{16}\Delta\mu. \tag{23}$$

For large $\Delta\mu$, it can be readily verified that to $O(\frac{1}{\Delta\mu})$, the solution to this equation is given by $\tilde{s} = 2(1 + \frac{1}{\Delta\mu})$. Employing (21) to solve for κ_2 and then substituting in this approximation for $\tilde{s}$ yields

$$\begin{aligned}\kappa_2 &= \frac{\frac{3}{4}\Delta\mu - \tilde{s}}{2\tilde{s}}^{\frac{2}{9}\tilde{s}^2} \\ &\approx \frac{1}{4}\frac{\Delta\mu^2 - 2\Delta\mu - 2}{\Delta\mu + 1}e^{\frac{1}{2}(1+\frac{1}{\Delta\mu})^2},\end{aligned} \tag{24}$$

which increases linearly to leading order in $\Delta\mu$. While the rapidly increasing κ_1 marks when the MR state will ensue from natural bias initial conditions, the linear dependence of κ_2 shows that the coupling strength for which a stable MR state is available does keep pace with $\Delta\mu$. This is significant because if a stochastic forcing is added to Eq. (3) to simulate random incoming external information for instance then transitions between states can occur in which the SHD state jumps to the MR state (and vice versa) as we have observed in simulations.

4.3 SLD Lower Boundary: κ_3

We now calculate the boundary κ_3 below which the SLD state given by $(r, s = 0)$ becomes absolutely unstable. The boundary can be calculated by using Eq. (9) and the coefficient of s in Eq. (12) to solve for r for which the system undergoes a pitchfork

bifurcation from the SLD equilibrium to the MR state. We obtain the conditions:

$$r - \Delta\mu = -(\kappa_3 + v) r e^{-r^2/8} \tag{25}$$

$$1 = -(3\kappa_3 - v)\left(1 - \frac{r^2}{4}\right) e^{-r^2/8}. \tag{26}$$

Neglecting small v, then taking the ratio of the above pair and rearranging gives

$$0 = r^3 - \Delta\mu r^2 - \frac{8}{3} r + 4\Delta\mu. \tag{27}$$

Near the bifurcation, the equilibrium discord for the SLD state is $r \approx 2$ and the solution to (27) to $O(1/\Delta\mu)$ is $r \approx 2 + 2/(3\Delta\mu)$. Using this in (25) enables us to calculate κ_3

$$\kappa_3 + v = -\frac{r - \Delta\mu}{r} e^{r^2/8} \tag{28}$$

$$\kappa_3 \approx \frac{\Delta\mu^2 - 2\Delta\mu + \frac{2}{3}}{2\Delta\mu + \frac{2}{3}} e^{\frac{1}{8}\left(2 + \frac{2}{3}\frac{1}{\Delta\mu}\right)^2} - v. \tag{29}$$

κ_3 shows a linear dependence for large $\Delta\mu$ as did κ_2 but, significantly, it also has a linear dependence upon small v.

4.4 Chain and Complete Stability Diagrams

Figure 3a displays the stability diagram of the chain network showing the regimes in $\Delta\mu - \kappa$ parameter space where the different outcomes are stable and the bound-

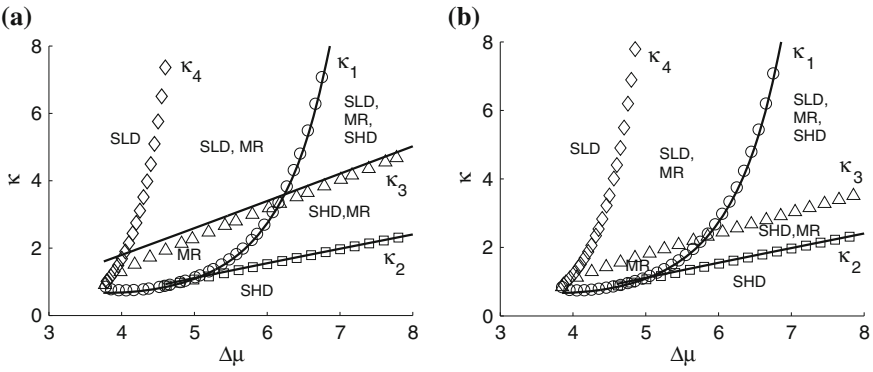

Fig. 3 Stability diagram of triad with symmetric coupling for: **a** chain network and **b** complete network. *Open markers* are numerically obtained boundaries. *Solid lines* are chain analytical approximations (18), (24), and (29) for κ_1, κ_2, and κ_3 respectively

aries between them. The open markers represent numerically-obtained bifurcation boundaries as found using the MATCONT software package for prediction-correction continuation [3]. The numerical curves agree very well with the analytical approximations (18), (24), and (29) for κ_1, κ_2, and κ_3 respectively, except in the immediate vicinity of the critical divergence. Also shown is the boundary κ_4 beyond which the MR state is no longer present. Note the presence of a substantial zone where only the MR state is stable. There are also multistable zones in which two or all three states are stable.

The stability diagram for the complete network is shown in Fig. 3b. For κ_1 and κ_2 the approximations derived for the chain network, (18) and (24), agree very well with the numerically-determined boundaries. This indicates that the coupling between the two outer nodes can be safely neglected due to their extremely disparate opinions in the SHD and MR states. However, the chain approximation for κ_3 is substantially higher than the complete network's κ_3. This is due to the significantly lower discord of the SLD state in the complete network, thereby making that state more robust. This reduces the size of the MR-only zone as compared with the chain. In addition, κ_4 shifts to the right in the complete network which has the effect of expanding the SLD-only zone.

For the asymmetric coupling case of $v < 0$, i.e., when the end nodes are more influential than the center node, κ_3 shifts upward as evident from (29) whereas κ_1 and κ_2 are nearly unchanged for large $\Delta\mu$. This decreases the size of the zone where the SLD state is stable and increases the size of the MR-only and MR-SHD zones as observed in simulations; in addition, the critical divergence shifts to lower values of $\Delta\mu$. For $v > 0$, κ_3 shifts downward and the critical divergence shifts to the right so that the MR-only and MR-SHD zones decrease in size. However, it is significant that skewed majority rule outcomes can arise even when the center node has greater influence than the end nodes.

5 Five-Node Networks

We have also observed majority rule outcomes in five node topologies as shown in Fig. 4. In the simulations, the natural biases are distributed uniformly over the range $\Delta\mu = 6$ and ordered so that $(\mu_1, \ldots, \mu_5) = (-3, -1.5, 0, 1.5, 3)$. Three different

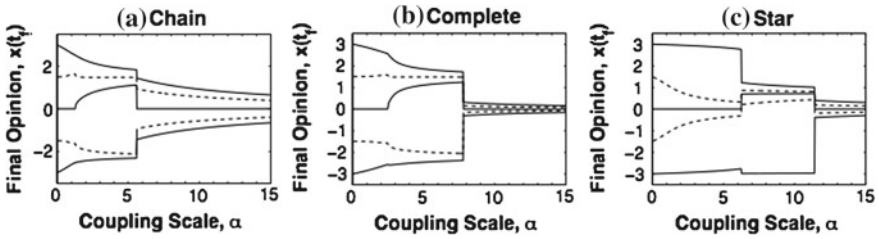

Fig. 4 Final node opinion versus coupling scale for five-node networks: **a** chain; **b** complete; **c** star. Simulation duration, $t_f = 200$

topologies are used: (1) the chain in which each node is connected only to its nearest neighbor along the opinion axis, $A_{ij} = \delta_{i,j\pm1}$; (2) the complete network where all nodes are connected to each other; and (3) the star in which the off-center nodes are only connected to the center node having $\mu_3 = 0$ so that $A_{i3} = A_{3i} = 1$ for $i \in 1, 2, 4, 5$ else $A_{ij} = 0$. The coupling strengths are identical for all ties, $\kappa_{ij} = \kappa A_{ij}$. But comparing the topologies for the same κ would allow topologies with more ties to have greater total coupling, thereby affording them a greater communication rate, for instance. Consequently, to compare topologies on a common basis, we relate the coupling strengths to the coupling scale α via the relationship $\kappa_{ij} = \alpha A_{ij}/\bar{d}$ where $\bar{d}$ is the mean degree, $\bar{d} = \sum_{i,j} A_{ij}/N$. From this form we see that α is equal to the average coupling strength, $\alpha = \sum_{i,j} \kappa_{ij}/N$. It is observed that in the MR state, the majority is 3-2 in the chain and complete networks whereas it is 4-1 in the star in which the intermediate negative node, x_2, is drawn upward into the positive x majority. We also note that the discontinuous transitions along the α axis occur first for the chain then the complete network and last for the star. The earlier transition to the SLD state for the chain network as compared with the star is striking since they both have the same number of directed edges, 12, and can be attributed to the fact that the couplings between the center and the outermost nodes present in the star are weaker compared with the only nearest-neighbor couplings in the chain; however, once achieved, the SLD state is much tighter in the star.

6 Conclusion

We have shown that an asymmetric outcome of majority rule arises from a symmetry-breaking pitchfork bifurcation using a model that is a nonlinear variant of the influential Friedkin-Johnsen model of opinion network dynamics. This symmetry-breaking route to majority rule only occurs for initial disagreements above the critical divergence. For lower disagreement, the more intuitive process of convergence toward the center applies as would be expected from the Friedkin-Johnsen model. This qualitative difference at low and high disagreement suggests that bifurcation-induced majority rule may be observable in laboratory experiments involving group discussion. Finally, we note that although there is a regime in which majority rule is predicted, the actual policy outcome in this regime is fundamentally unpredictable and may depend on relatively minor or random variables such as who speaks first.

Acknowledgments We acknowledge the support of the Defense Threat Reduction Agency and the Office of Naval Research under grant HDTRA1-10-1-0075.

References

1. C. Castellano, S. Fortunato, V. Loreto, Statistical physics of social dynamics. Rev. Mod. Phys. **81**, 591–646 (2009)
2. J.H. Davis, Group decision making and quantitative judgments: a consensus model, in *Understanding Group Behavior: Consensual Action by Small Groups*, ed. by E. Witte, J.H. Davis (Lawrence Erlbaum, Mahwah, 1996)
3. A. Dhooge, W. Govaerts, Y.A. Kuznetsov, Matcont: a MATLAB package for numerical bifurcation analysis of ODEs. ACM Trans. Math. Softw. **29**(2), 141–164 (2003)
4. A. Eagly, S. Chaiken, *The Psychology of Attitudes* (Harcourt, Fort Worth, 1993)
5. N.E. Friedkin, E.C. Johnsen, *Social Influence Network Theory: A Sociological Examination of Small Group Dynamics* (Cambridge University Press, Cambridge, 2011)
6. M. Gabbay, A dynamical systems model of small group decision making, in *Diplomacy Games*, ed. by R. Avenhaus, I.W. Zartman (Springer, Berlin, 2007)
7. M. Gabbay, The effects of nonlinear interactions and network structure in small group opinion dynamics. Phys. A Stat. Mech. Appl. **378**(1), 118–126 (2007)
8. J. Gastil, *The Group in Society* (Sage, Los Angeles, 2010)
9. M. Hinich, M. Munger, *Analytical Politics* (Cambridge University Press, Cambridge, 1997)
10. M. Mesbahi, M. Egerstedt, *Graph Theoretic Methods in Multiagent Networks* (Princeton University Press, Princeton, 2010)
11. V. Srivastava, J. Moehlis, F. Bullo, On bifurcations in nonlinear consensus networks. J. Nonlinear Sci. **21**, 875–895 (2011)
12. S.H. Strogatz, *Nonlinear Dynamics and Chaos* (Perseus Books, Reading, 1994)

Recent Advances on Information Transmission and Storage Assisted by Noise

P. I. Fierens, G. A. Patterson, A. A. García and D. F. Grosz

Abstract The interplay between nonlinear dynamic systems and noise has proved to be of great relevance in several application areas. In this presentation, we focus on the areas of information transmission and storage. We review some recent results on information transmission through nonlinear channels assisted by noise. We also present recent proposals of memory devices in which noise plays an essential role. Finally, we discuss new results on the influence of noise in memristors.

1 Introduction

In communication systems noise is usually regarded as a nuisance to cope with. However, it has been shown that in certain nonlinear channels information transmission is actually sustained by noise (see, e.g., [1–5]). In particular, dynamic systems comprised of a chain of bistable double-well potentials driven by a periodic signal have been extensively studied and were shown to be able to sustain noise-assisted fault-tolerant transmission [6, 7]. In Sect. 2 we review some recent progress on this topic.

In the last few years there has been an increased effort in the search of alternative technologies for computer memory devices. This effort is motivated by the perceived near future end of the ability of current technologies to provide support for the exponential increase of memory capacities as predicted by Moore's law. In this context, logic gates that work with the help of noise have been suggested (see, e.g.,

P. I. Fierens (✉) · D. F. Grosz
Instituto Tecnológico de Buenos Aires (ITBA) and Consejo Nacional de Investigaciones Científicas y Técnicas (CONICET), Buenos Aires, Argentina
e-mail: pfierens@itba.edu.ar

G. A. Patterson · A. A. García
Facultad de Ciencias Exactas y Naturales – Universidad de Buenos Aires (FCEN-UBA), Buenos Aires, Argentina

V. In et al. (eds.), *International Conference on Theory and Application in Nonlinear Dynamics (ICAND 2012)*, Understanding Complex Systems,
DOI: 10.1007/978-3-319-02925-2_16,

[8–16]). In a similar vein, it is possible to think of memories which can benefit from, and indeed work only in, the presence of noise. In Sect. 3, we review some recent advances in this area.

Resistive memories represent one of the most promising candidates for next generation computer memories, and are usually associated with a type of two-terminal passive circuit element known as a *memristor* [17, 18]. Recently, Stotland and Di Ventra [19] showed that noise may help increase the contrast ratio between low and high memory states. In Sect. 4, we present some new experimental results on the role played by noise in this type of system, extending those in Ref. [19].

2 Information Transmission

System performance in transmission lines can be characterized by means of several metrics commonly encountered in the area of communications, e.g., output Bit Error Rate (BER) and Signal-to-Noise Ratio (SNR) (see, e.g., [20, 21]). The BER of a communication system is a measure of the probability of receiving erroneous bits and represents one of the most important performance metrics used in digital communications. The SNR is also an important metric in analogue communications and its relevance in digital systems stems from the usual monotonic relation between BER and SNR. Specifically, for an additive Gaussian noise (AWGN) channel, increasing the SNR decreases the minimum allowable bit error rate [22]. However, this conclusion is not necessarily valid for a nonlinear communication channel. Several authors have studied bit error rate metrics for the case of a single double-well potential such as the one described in [6, 7, 23]. Barbay et al. [24, 25] developed theoretical expressions for the BER performance of a VCSEL which were experimentally validated. Duan et al. [26] also presented a theoretical calculation of the BER for a suprathreshold signal strength. Moreover, Godivier and Chapeau-Blondeau [27] studied the capacity of a channel comprised of a single double-well potential.

Ibáñez et al. [28] studied a double-well forward-coupled information transmission line. In this type of nonlinear channel, two different transmission regimes were identified, namely noise-supported and coupling-supported, corresponding to sub-critical and super-critical coupling strengths, respectively. While addition of noise to each potential well is required in order to sustain transmission in the sub-critical case, a super-critical coupling is strong enough to guarantee operation of the transmission line even in the absence of noise. In Ref. [28], it was shown that output BERs remain flat for a broad range of added noise, especially for a super-critical coupling strength.

Schmitt triggers (STs) are commonly used as ‘discrete’ models of double-well potentials (see, e.g., [23]). They also can be used as simple models of lasers with saturable absorbers, which are known to exhibit a stochastic resonant behavior [29]. As some schemes for optical pulse amplification and shaping (known as “2R regeneration”) mimic fast saturable-absorbers [30], STs may serve as experimental toy models for the analysis of some forms of optical regeneration in communication systems. A similar approach was followed, e.g., by Korman et al. [31] who mod-

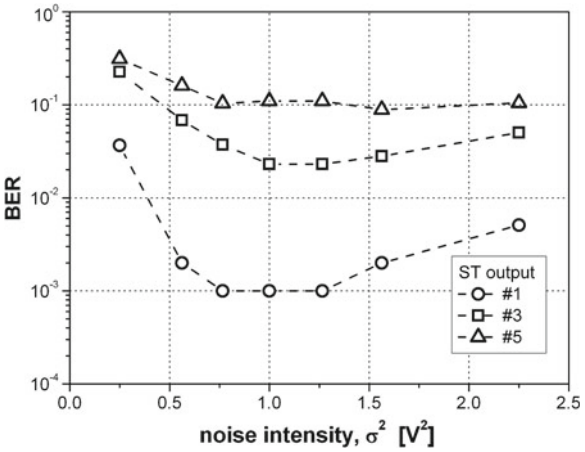

Fig. 1 Bit error rate as a function of noise intensity in a chain of five Schmitt triggers. BER is minimized for an optimal noise intensity. Figure taken from Ref. [32]

eled a mid-span repeater with a hysteresis-type nonlinearity of the same kind found in a Schmitt trigger. Patterson et al. [32] performed an experimental investigation of the transmission properties of a line comprised of five in-series Schmitt triggers from the point of view of a communication system, where each ST was fed with white Gaussian noise, and the first ST was driven by a pseudo-random sequence of bits. As shown in Fig. 1, an optimal noise intensity was found for which the BER

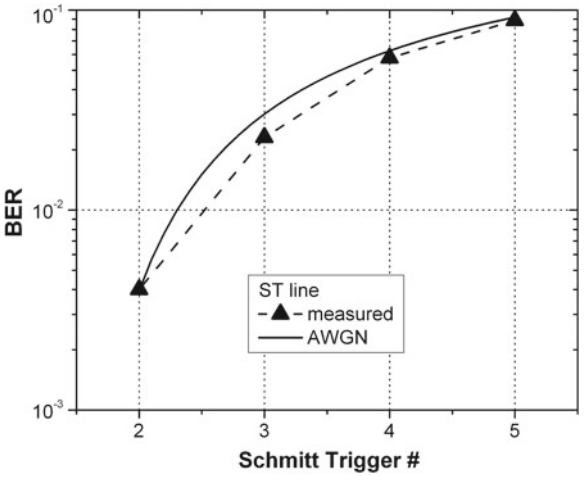

Fig. 2 Performance of a transmission line comprised of five in-line Schmitt triggers. The performance expected from an additive white Gaussian noise channel is also shown as a reference. Figure taken from Ref. [32]

is minimized. The rate of system performance degradation with distance (number of STs traversed by the information-carrying signal) was found to be similar to that observed in a linear AWGN communication channel (see Fig. 2).

A transmission line has an associated delay which depends on its physical characteristics. The time-delay properties of a double-well forward-coupled information transmission line were investigated in Ref. [33], showing that it can be regarded as a noise-tunable delay line for a broad range of noise and coupling-strength parameters. Such a tunable delay line may find applications, e.g., in the phase modulation of information-carrying signals.

3 Information Storage

Carusela et al. [34, 35] showed that a double-well forward-coupled transmission line, such as that described in Sect. 2, can work as a memory element when closed onto itself forming a loop. In particular, they showed that such a ring was able to sustain a traveling wave with the aid of noise long after the harmonic drive signal had been switched off. Building on the work in Refs. [34, 35], Ibáñez et al. [36, 37] showed that a ring of two bistable oscillators is capable of storing a single bit of information in the presence of noise. Figure 3 shows the probability of erroneous retrieval from the second oscillator. It can be observed that, for each retrieval time, there is an optimal noise intensity for which the probability of error is minimized. In Ref. [36] memory persistence time (T_m) was defined as the time elapsed until the first oscillator reaches a probability of error equal to that of the noiseless case. Figure 4 shows that there is an optimal noise intensity which maximizes memory

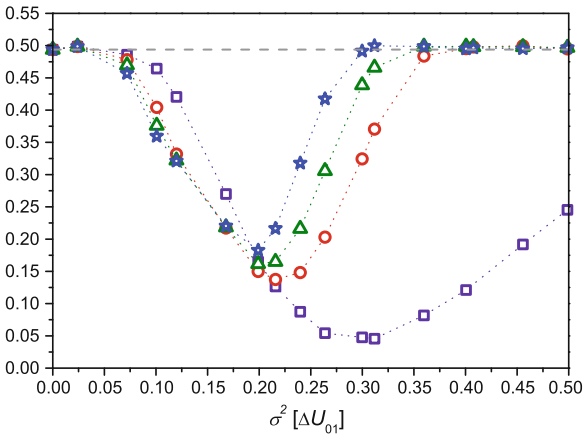

Fig. 3 Probability of erroneous information retrieval from the second oscillator as function of noise intensity for different observation times ($T = T_P$ *squares*, $10T_P$ *circles*, $20T_P$ *triangles*, $40T_P$ *stars*). T_P is an arbitrary time scale. Figure taken from Ref. [36]

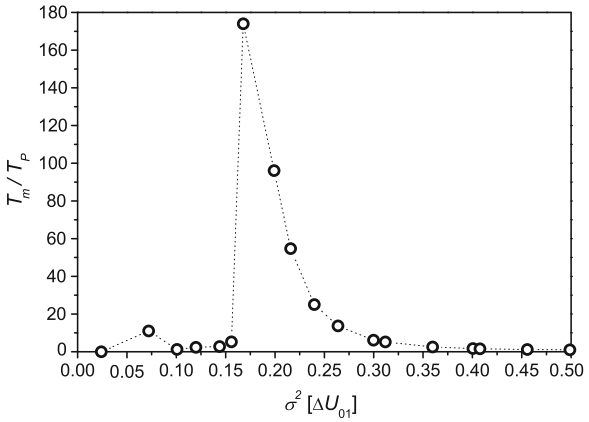

Fig. 4 Memory persistence as a function noise intensity. There is a noise intensity that maximizes persistence. Figure taken from Ref. [36]

persistence. Foreseeing a practical implementation of this type of memory device, its performance under varying physical parameters, such as noise bandwidth and time response of the bistable elements, was investigated in Ref. [38]. In particular, it was found that the device is more resilient to the action of noise when the noise and the bistable element bandwidths are of the same magnitude.

Bellomo et al. [39] proposed a multibit storage device consisting on a single Schmitt trigger (ST) and an element that introduces a finite delay in a loop configuration. The proposed device can be considered as a toy model of a long transmission link with in-line nonlinear elements such as saturable absorbers [29, 30]. Nonlinear delayed loops have been extensively studied (see, e.g., [40–46]). This type of systems usually presents a complex nonlinear behavior, including self-sustained oscillations and chaotic operation regimes. Memory devices that make use of regimes that show multistable behavior of delayed feedback loops have been proposed. Reference [40] presented a memory device that stores bits coded as particular oscillation modes of a delay feedback loop with an electro-optical modulator. Similarly, in Ref. [42] was shown that binary messages can be stored using controlled unstable periodic orbits of a particular class of delay-loop differential equations. However, memory devices proposed in Refs. [40, 42] were not assisted by noise. References [43, 45] studied the behavior of a delayed loop with a single threshold device and a bistable device, respectively, but focusing on the response of the system to a harmonic driving signal.

Experimental studies in Ref. [39] showed that the performance of the proposed multibit memory device is optimal for an intermediate value of noise intensity (see Fig. 5). It is interesting to note that, although performance was shown to deteriorate with time and with the number of stored bits, it also was found that the probability of error is independent of the number of bits when the elapsed time is normalized to the bit duration (see Fig. 6), a fact of relevance when considering practical implementations of the device.

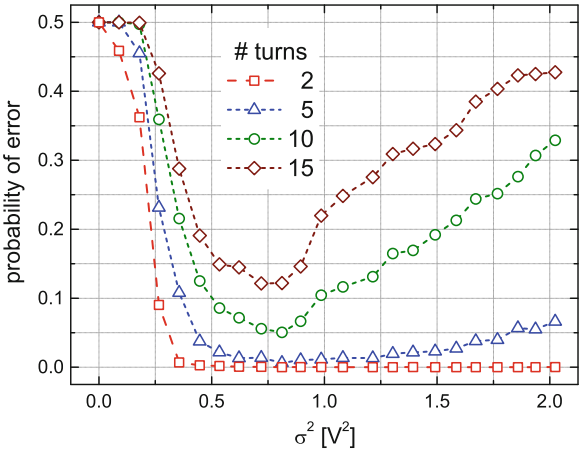

Fig. 5 Probability of erroneous retrieval as a function of noise intensity when 4 bits are stored. Different curves correspond to varying elapsed times. A turn corresponds to the mean time it takes the signal to travel through the loop elements. Figure taken from Ref. [39]

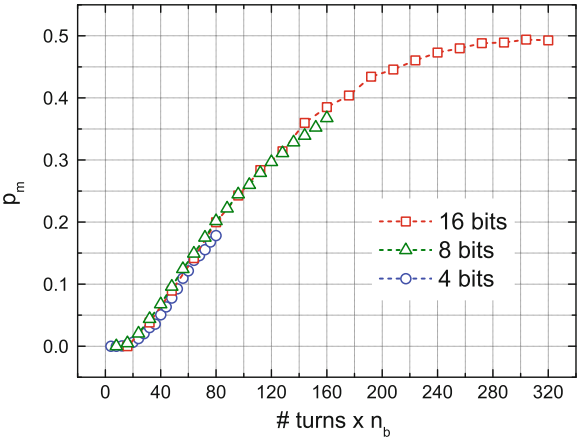

Fig. 6 Minimum probability of error as a function of elapsed time normalized to the bit duration. n_b: number of stored bits. Figure taken from Ref. [39]

4 Noise in Memristors

One of the proposed alternatives for succeeding current nonvolatile memory technologies is the so-called family of Resistive Random-Access Memories (ReRAMs) (see, e.g., [47]). ReRAMs are based in the resistive switching phenomenon observed in several materials, that is, the change of electrical resistance by the application of electrical pulses. Indeed, a high resistance may represent, say, a '0', and a low resistance may represent a '1' logic state.

Often, resistive switching devices are associated with a type of two-terminal passive circuit element known as a *memristor* [17, 18] which was originally proposed by Chua in Ref. [48]. There are different proposed mechanisms which try to explain the observed behavior of resistive switching materials (see, e.g., [17, 47, 49–53] and references therein). From a macroscopic point of view, one of the simplest models is that proposed in Ref. [17], described by

$$v(t) = R(s)i(t), \tag{1}$$

$$\frac{ds}{dt} = \alpha F(s, i)i(t), \tag{2}$$

where $v(t)$ is the applied voltage, $i(t)$ is the current, R is the device's resistance, $s \in [0, 1]$ is an internal state variable, α is a constant and $F(s, i)$ is a nonlinear function. Among the several suggested alternatives for $F(s, i)$ (see, e.g., [54]), one commonly used is

$$F(s, i) = 4s(1 - s). \tag{3}$$

Based on these equations, Stotland and Di Ventra [19] showed that noise may help increase the contrast ratio between low and high resistance values. This conclusion has important practical consequences as the contrast in resistance values can be associated with the probability of error in ReRAMs. Stotland and Di Ventra modified Eq. 2 by adding an internal noise term,

$$\frac{ds}{dt} = \alpha F(s, i)i(t) + \eta(t), \tag{4}$$

where $\eta(t)$ is white Gaussian noise. Patterson et al. [55] extend the results of Stotland and Di Ventra [19]. In particular, they show that external noise, that is, noise added to the externally applied voltage, does not help increase the contrast between low and high resistance states if Eqs. 1–3 are valid.

In order to explore the behavior of memristors under externally applied noise, we experimentally studied a sample of a manganite, $La_{0.35}Pr_{0.300}Ca_{0.375}MnO_3$. The behavior of this material has already been studied in, e.g., [52, 53, 56, 57]. Two silver contacts were placed on the sample and an externally controlled current was applied through them. The resistance between contacts was calculated by measuring the voltage drop across them when a small (± 1 mA) noiseless current was applied. Current pulses of 1 ms of duration were applied with varying amplitudes. Each current pulse was followed by 1 s of 'silent' (no current applied) 'setting' time and preceded by 20 ms of the small current used for resistance measurement (-1 mA applied during 10 ms and $+1$ mA during other 10 ms). Samples of zero mean white Gaussian current noise with 100 mA standard deviation were generated by software and added to the externally applied current. The actual noise bandwidth and detailed characteristics depend on several elements of the experimental setup such as, e.g., the bandwidth and the linearity of the digital-to-analog converter.

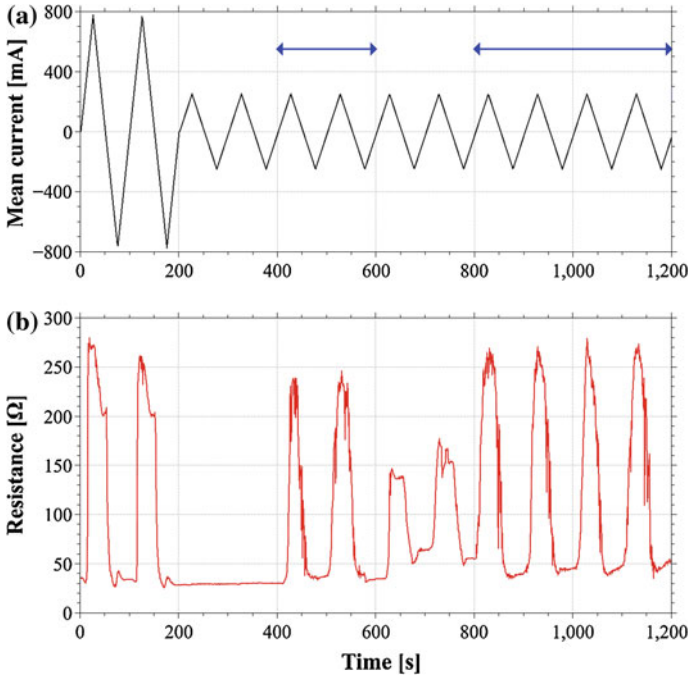

Fig. 7 Experimental results on the effect of noise on a memristor. **a** Measured mean pulse current as a function of time. **b** Measured memristor's resistance. Intervals where noise was added are indicated by (*blue*) *arrows* in (**a**)

Figure 7 shows the results of a typical experiment. For the first 200 s, noiseless high-current pulses (up to 800 mA) were applied and the memristor's resistance varied between ∼30 and ∼270Ω. During the following 200 s, the current amplitude was lowered (down to ∼200 mA) and no noticeable change on the resistance was observed. The low amplitude pulses were repeated for other 200 s, but now noise was added. Interestingly, the memristor responded to the added noise by varying its resistance in almost the same magnitude as it did when high-current pulses were applied. When noise is turned off, the memristor's resistance varies, but the change is not of the same magnitude as when noise is applied.

In summary, experimental data confirms that externally applied noise increases the contrast between low and high resistance states in a memristor, a fact of relevance in applications. Considering that Eqs. 1–3 disallow such an effect of noise (see [55]), our experimental results also point toward the need for more complex models.

5 Conclusions and Future Work

We have reviewed some recent advances on the field of information transmission and storage assisted by noise. Schemes of in-series hysteretic nonlinear elements, modeled by Schmitt triggers, were shown to enable transmission of subthreshold signals with low probability of errors for optimal noise intensities. Closed loops of such elements were also shown to sustain information storage only in the presence of moderate amounts of noise. Future work in these areas should address the influence of different types of noise. For example, 1/f-noise is found in several applications (see, e.g., [58]) and its eventual beneficial role in nonlinear systems as those described in this work has not been deeply investigated yet. It also remains to be explored the possibility of practical applications of noise-tunable delay lines as those described in Sect. 2.

We have also presented results on the effect of noise in memristors, where external noise helps commute resistive states in the presence of a small amplitude driving field. We believe these results are of significance since memristors are expected to operate in electronic circuits with a large scale of integration, and as such the effects of thermal noise will have to be coped with. Since simple models (see [55]) cannot account for the presented results, future work should focus on more complete models of memristors behavior.

Acknowledgments We gratefully acknowledge financial support from ANPCyT under project PICT-2010 #121. Memristor samples were provided by the Laboratory of Electrical and Magnetic Properties, Condensed Matter Group, CNEA (Argentina). We want to specially thank Fernando Gomez-Marlasca and Pablo Levy for their suggestions on the experiments.

References

1. F. Chapeau-Blondeau, Electron. Lett. **35**, 1055 (1999)
2. F. Chapeau-Blondeau, J. Rojas-Varela, Int. J. Bifurcat. Chaos **10**, 1951 (2000)
3. J.F. Lindner, S. Chandramouli, A.R. Bulsara, M. Löcher, W.L. Ditto, Phys. Rev. Lett. **81**(23), 5048 (1998)
4. M. Löcher, D. Cigna, E.R. Hunt, Phys. Rev. Lett. **80**(23), 5212 (1998)
5. J. García-Ojalvo, A.M. Lacasta, F. Sagués, J.M. Sancho, Europhys. Lett. **50**, 427 (2000)
6. R. Perazzo, L. Romanelli, R. Deza, Phys. Rev. E **61**(4), R3287 (2000)
7. Y. Zhang, G. Hu, L. Gammaitoni, Phys. Rev. E **58**(3), 2952 (1998)
8. K. Murali, S. Sinha, W.L. Ditto, A.R. Bulsara, Phys. Rev. Lett. **102**(10), 104101 (2009)
9. K. Murali, I. Rajamohamed, S. Sinha, W.L. Ditto, A.R. Bulsara, Appl. Phys. Lett. **95**(19), 194102 (2009)
10. K. Murali, S. Sinha, A. Bulsara, A. Dari, W. Ditto, in *International Conference on Applications of Nonlinear Dynamics (ICAND)*, ed. by V. In, A. Palacios, P. Longhini. AIP Conference Proceedings, vol. 1339 (2010), pp. 67–77
11. A.R. Bulsara, A. Dari, W.L. Ditto, K. Murali, S. Sinha, Chem. Phys. **375**(2–3), 424 (2010)
12. D. Guerra, A. Bulsara, W. Ditto, S. Sinha, K. Murali, P. Mohanty, Nano Lett. **10**(4), 1168 (2010)
13. K.P. Singh, S. Sinha, Phys. Rev. E **83**, 046219 (2011)
14. A. Dari, A. Bulsara, W. Ditto, X. Wang, in *2011 IEEE Biomedical Circuits and Systems Conference (BioCAS)* (2011), pp. 337–340

15. A. Dari, B. Kia, X. Wang, A.R. Bulsara, W. Ditto, Phys. Rev. E **83**, 041909 (2011)
16. A. Dari, B. Kia, A.R. Bulsara, W. Ditto, EPL (Europhys. Lett.) **93**(1), 18001 (2011)
17. D.B. Strukov, G.S. Snider, D.R. Stewart, R.S. Williams, Nature **453**, 80 (2008)
18. L. Chua, Proc. IEEE **100**(6), 1920 (2012)
19. A. Stotland, M. Di Ventra, Phys. Rev. E **85**, 011116 (2012)
20. B. Sklar, *Digital Communications: Fundamentals and Applications* (Prentice Hall, Upper Saddle River, 2001)
21. G.P. Agrawal, *Fiber-Optic Communication Systems*, 2nd edn. (Wiley, New York, 1997)
22. R. Blahut, *Principles and Practice of Information Theory*, vol. 1 (Addison-Wesley, Reading, 1987)
23. B. McNamara, K. Wiesenfeld, Phys. Rev. A **39**(9), 4854 (1989)
24. S. Barbay, G. Giacomelli, F. Marin, Phys. Rev. E **63**(5), 051110 (2001)
25. S. Barbay, G. Giacomelli, F. Marin, Phys. Rev. Lett. **85**, 4652 (2000)
26. F. Duan, D. Rousseau, F. Chapeau-Blondeau, Phys. Rev. E **69**(1), 011109 (2004)
27. X. Godivier, J. Rojas-Varela, F. Chapeau-Blondeau, Electron. Lett. **33**(20), 1666 (1997)
28. S.A. Ibáñez, P.I. Fierens, R.P.J. Perazzo, D.F. Grosz, Phys. D **238**(21), 2138 (2009)
29. L. Gammaitoni, P. Hänggi, P. Jung, F. Marchesoni, Rev. Mod. Phys. **70**(1), 223 (1998)
30. P.V. Mamyshev, in *24th European Conference on Optical, Communication, ECOC98*, vol. 1 (1998), pp. 475–476
31. C.E. Korman, R. Barry, U.C. Kozat, SIAM J. Appl. Math. **62**(5), 1794 (2002)
32. G.A. Patterson, A.F. Goya, P.I. Fierens, S.A. Ibáñez, D.F. Grosz, Phys. A **389**(9), 1965 (2010)
33. S.A. Ibáñez, P.I. Fierens, R.P.J. Perazzo, D.F. Grosz, Fluctuation Noise Lett. **8**(3–4), L315 (2008)
34. M.F. Carusela, R.P.J. Perazzo, L. Romanelli, Phys. Rev. E **64**, 031101 (2001)
35. M.F. Carusela, R.P.J. Perazzo, L. Romanelli, Phys. D, **168**177–183 (2002)
36. S.A. Ibáñez, P.I. Fierens, R.P.J. Perazzo, G.A. Patterson, D.F. Grosz, Eur. Phys. J. B **76**, 49 (2010)
37. P.I. Fierens, S. Ibáñez, R.P.J. Perazzo, G.A. Patterson, D.F. Grosz, Phys. Lett. A **374**(22), 2207 (2010)
38. P.I. Fierens, G. Bellomo, G.A. Patterson, D.F. Grosz, in *International Conference on Applications of Nonlinear Dynamics (ICAND)*, ed. by V. In, A. Palacios, P. Longhini. AIP Conference Proceedings, vol. 1339 (2010)
39. G. Bellomo, G. Patterson, P. Fierens, D. Grosz, Phys. Lett. A **375**(37), 3233 (2011)
40. T. Aida, P. Davis, IEEE J. Quantum. Electron. **28**(3), 686 (1992)
41. J. Losson, M.C. Mackey, A. Longtin, Chaos **3**, 167 (1993)
42. B. Mensour, A. Longtin, Phys. Lett. A **205**(1), 18 (1995)
43. B. Mensour, A. Longtin, Phys. Lett. A **244**(1–3), 59 (1998)
44. R. Morse, A. Longtin, Phys. Lett. A **359**(6), 640 (2006)
45. Y. Jin, H. Hu, Phys. A **382**(2), 423 (2007)
46. J.W. Middleton, E. Harvey-Girard, L. Maler, A. Longtin, Phys. Rev. E **75**(2), 021918 (2007)
47. A. Sawa, Mater. Today **11**(6), 28 (2008)
48. L. Chua, IEEE Trans. Circuit Theory **18**(5), 507 (1971)
49. M.D. Pickett, D.B. Strukov, J.L. Borghetti, J.J. Yang, G.S. Snider, D.R. Stewart, R.S. Williams, J. Appl. Phys. **106**(7), 074508 (2009)
50. M.J. Sánchez, M.J. Rozenberg, I.H. Inoue, Appl. Phys. Lett. **91**(25), 252101 (2007)
51. M.J. Rozenberg, M.J. Sánchez, R. Weht, C. Acha, F. Gomez-Marlasca, P. Levy, Phys. Rev. B **81**(11), 115101 (2010)
52. N. Ghenzi, M. Sánchez, F. Gomez-Marlasca, P. Levy, M. Rozenberg, J. Appl. Phys. **107**(9), 093719 (2010)
53. F. Gomez-Marlasca, N. Ghenzi, P. Stoliar, M.J. Sanchez, M.J. Rozenberg, G. Leyva, P. Levy, Appl. Phys. Lett. **98**(12), 123502 (2011)
54. Y.N. Joglekar, S.J. Wolf, Eur. J. Phys. **30**(4), 661 (2009)
55. G.A. Patterson, P.I. Fierens, D.F. Grosz, in *ICAND 2012*. doi:10.1007/978-3-319-02925-2_27

56. F. Gomez-Marlasca, P. Levy, in *Journal of Physics: Conference Series (IOP Publishing, 2009)*, vol. 167 (2009), p. 012036
57. N. Ghenzi, M. Sánchez, M. Rozenberg, P. Stoliar, F. Marlasca, D. Rubi, P. Levy, J. Appl. Phys. **111**(8), 084512 (2012)
58. P. Dutta, P.M. Horn, Rev. Mod. Phys. **53**, 497 (1981)

Transmission of Packets on a Hierarchical Network: Avalanches, Statistics and Explosive Percolation

Neelima Gupte and Ajay Deep Kachhvah

Abstract We discuss transport on load bearing branching hierarchical networks which can model diverse systems which can serve as models of river networks, computer networks, respiratory networks and granular media. We study avalanche transmissions and directed percolation on these networks, and on the V lattice, i.e., the strongest realization of the lattice. We find that typical realizations of the lattice show multimodal distributions for the avalanche transmissions, and a second order transition for directed percolation. On the other hand, the V lattice shows power-law behavior for avalanche transmissions, and a first order (explosive) transition to percolation. The V lattice is thus the critical case of hierarchical networks. We note that small perturbations to the V lattice destroy the power-law behavior of the distributions, and the first order nature of the percolation. We discuss the implications of our results.

1 Introduction

The study of transport processes on networks of varying types has attracted much recent interest [1, 2], and is important from the point of view of applications. Earlier studies of transport processes on networks has been carried out for important classes like scale free and random networks [3–5]. However, an important class of networks, viz., that of branching hierarchical networks [6, 7], has not yet been extensively

N. Gupte (✉)
Department of Physics, Indian Institute of Technology, Madras,
Chennai 600036, India
e-mail: gupte@physics.iitm.ac.in

A. D. Kachhvah
Nonlinear Physics Division, Institute for Plasma Research, Bhat,
Gandhinagar, Gujarat 382428, India
e-mail: ajaydeep@ipr.res.in

V. In et al. (eds.), *International Conference on Theory and Application in Nonlinear Dynamics (ICAND 2012)*, Understanding Complex Systems,
DOI: 10.1007/978-3-319-02925-2_17,

explored. Networks of the branching, hierarchical type are common in both real and engineering contexts. Examples of such networks include river networks [8], models of granular media [9], and voter models [10, 11], the Domany Kinzel cellular-automata model [12] and the branching hierarchical model of the lung inflation process [13, 14]. In this chapter, we explore transport processes such as avalanche dynamics, and percolation on typical branching hierarchical lattices, and on the V lattice, a special realization of such lattices. We show that the behavior of transport on the V lattice is very distinct from that on typical realizations, and the V lattice is thus the critical realization of the branching hierarchical lattices. We also show that this special behavior is soon lost when the lattice is perturbed, indicating its critical nature. We also discuss the implications of our results.

2 The Model

The base model for the load bearing hierarchical network [6, 15] discussed here is a regular $2D$ lattice of sites, where each site is connected at random to exactly one of its two neighbors in the layer below. The choice of the connection between the left and right neighbors to a given site i^D at any Dth layer is made with some probability p, where $(0 < p < 1)$, for a connection to the left neighbor i_l^{D-1}, and probability $(1 - p)$ to the right neighbor i_r^{D-1}. Each site has the capacity to bear unit weight if it is not connected to either of its neighbors in the layer above, and can bear weight $w + 1$ if it is connected to site(s) whose capacities add up to w, in the layer above. Thus, the capacity $w(i^D)$ of the ith site in the Dth layer is given by the equation

$$w(i^D) = l(i_l^{D-1}, i^D)w(i_l^{D-1}) + l(i_r^{D-1}, i^D)w(i_r^{D-1}) + 1 \tag{1}$$

The quantity $l(i_l^{D-1}, i^D) = 1$ if a connection exists between i_l^{D-1} and i^D, and 0 if otherwise. The network consists of clusters, where a cluster is a set of sites connected with each other. The trunk is defined as the set of connected sites in the largest cluster with the highest weight bearing capacity in each layer. The sum of the weight bearing capacities of the sites along the trunk is defined as the trunk capacity W_T of the given realization of the network. This model has similarity with the critical case $q(0, 1)$ of model of granular media [9], models of river networks [8], and the Takayasu model of the aggregation process with injection [16]. Other models analogous to our model are voter models [10, 11], the Domany-Kinzel cellular-automata model [12], and the branching hierarchical model of the lung inflation process [13, 14].

The base model has a very specific and unique realization which incorporates the largest possible V shaped cluster that the base model could have. The V-cluster includes all the sites in the topmost layer, and $(M - D + 1)$ sites in the Dth layer. One of the arms of the V constitutes the trunk, and all other connections run parallel to the arm of the V that is opposite to the trunk. The V-cluster is the largest possible cluster the base model could have. The trunk of this V-cluster bears the largest possible trunk

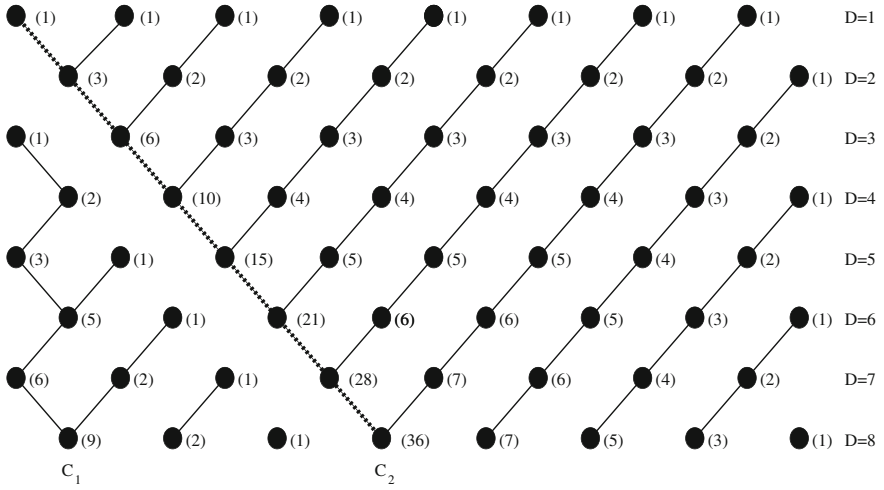

Fig. 1 The V lattice network of $D = 8$ layers with 8 sites per layers. The number in bracket beside each site denotes its weight bearing capacity. *Solid lines* show connection between the sites. The *beaded line* is the trunk of the V-cluster C_2

capacity of the base model. We call this special lattice the V lattice. Figure 1 shows the V lattice configuration. Structures similar to the V lattice can be seen in riverine deltas [17], in Martian gullies [18], and in granular flows [19], if the channels of maximal flow capacity are considered.[1]

3 The V lattice: The Critical Case for Transport

In this section we will discuss the critical nature of the V lattice, a special realization of the base lattice. The V lattice exhibits critical behavior for avalanche phenomena [20], site percolation phenomena [7], and capacity distribution and failure rate [6] quite distinct from the behavior seen for the base lattice model, manifesting its criticality. Here, we focus only on the avalanche and percolation properties of the V lattice.

3.1 Avalanche Times Distribution of the V Lattice

The behavior of avalanche processes for a given network topology provides an interesting example of the interplay between the nature of a transport process and the topology of the substrate. Here we aim to study the avalanche process of weight

[1] In the natural structures, the channels of high capacity can have some channels of lower capacity joining them, leading to an overall symmetry between left and right connections, however one direction is favored by the channels of high capacity, due to some feature like the nature of the geographic terrain, leading to variants of the V structure for the high capacity channels alone.

transmission on the V lattice. The avalanche is defined here in terms of weight transmission on the network.

To initiate the avalanche process on the network, some test weight W_{test} is deposited on a randomly chosen site in the first layer of the network. Since our base network is a directed network, the flow of weight transmission takes place in the downward direction. The site in the first layer absorbs weight equal to its capacity and transmits the excess weight to its neighboring site it is connected to in the layer below. This process of weight transmission continues till there is no excess weight left, and the transmission is successful. If the W_{test} is sufficiently large that it reaches the last layer without being fully absorbed, which completes one cycle of weight transmission, the excess weight is then deposited randomly on a site in the first layer and the second cycle of weight transmission starts here. If in the next cycle, the receiving site happens to be the one which has already saturated its capacity in the previous cycle, and now it does not have spare capacity to absorb any weight, the transmission is then said to be failed at that site. Otherwise the weight transmission continues till all excess weight is absorbed, and the transmission is said to be successful in this case. This process of the cycling of weight transmission through the lattice network is defined as an avalanche. The duration of an avalanche, or avalanche time, is defined to be the total number of layers traversed during all cycles of successful weight transmission by the test weight in the network.

We discuss the distribution of avalanche times of the V lattice. The avalanche times distribution $P(t)$ is, in fact, the distribution of the number of layers traversed during all cycles of successful avalanche transmissions by a test weight placed at a random site in the first layer for any lattice.

The avalanche times distribution $P(t)$ of the V lattice has been studied by Kachhvah and Gupte [20] for test weights which are fractions of the trunk capacity of the V lattice. It has been observed that for this lattice, the avalanche times distribution $P(t)$ displays a power law regime, i.e., $P(t) \sim t^{-\alpha}$, which gradually starts disappearing as the test weight starts approaching the trunk capacity of the V lattice. Figures 2, and 3 display the avalanche times distributions, corresponding to 1000 realizations, for the V lattice. The power law distribution is seen in the V lattice as weight transmissions on the V lattice can achieve success at any one of the layers. This behavior of the existence and subsequent disappearance of the power law regime in the distribution has been one of the indications that the V lattice is a critical case of the base lattice. It is to be noted that the avalanche times distribution averaged over many realizations of the base lattice shows Gaussian behavior Fig. 4 [20], and is quite distinct from the power-law behavior seen here.

3.2 Explosive Percolation on the V Lattice

The problem of site percolation has frequently been studied on networks due to its relevance for the problem of information transfer on the network. Therefore, it is important to study site percolation on the hierarchical networks. The site percolation

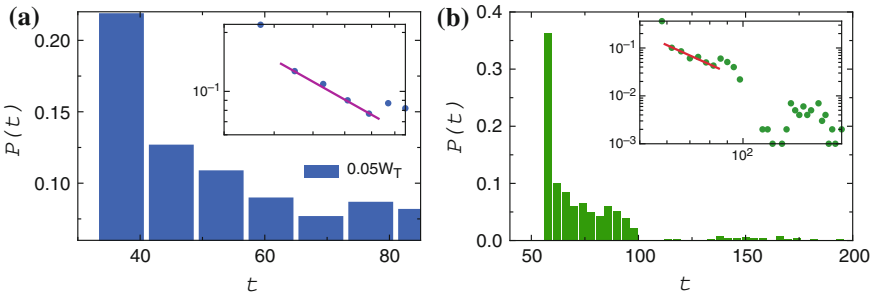

Fig. 2 The avalanche time distribution $P(t)$ corresponding to 1000 realizations for the V lattice network of side $M = 100$ when tested for weights equal to **a** $0.05W_T$, and **b** $0.2W_T$. Small regimes for $0.05W_T$ (as shown in *inset* of **a**) and $0.2W_T$ (as shown in *inset* of **b**) display power law i.e. $P(t) \sim t^{-\alpha}$ behavior with exponent $\alpha = 1.18$ and $\chi^2 = 0.0009$, and $\alpha = 2.96$ and $\chi^2 = 52.197$ respectively

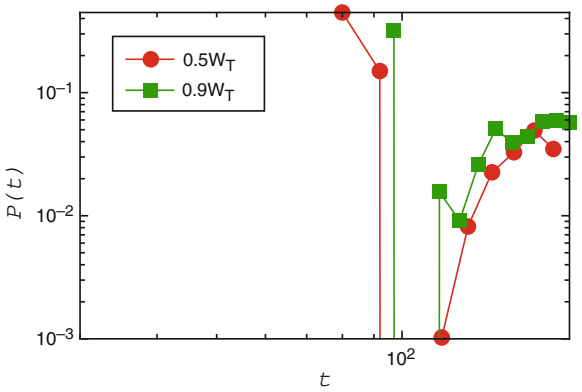

Fig. 3 The avalanche times distribution $P(t)$, corresponding to 1000 realizations, for the V lattice network of side $M = 100$ when tested for weights equal to **a** $0.5W_T$, and **b** $0.9W_T$. No power law regime is seen in the distributions corresponding to $0.5W_T$, and $0.9W_T$

problem is set up as follows: Typically, the transmission of information is modeled by packets of information hopping on the sites of the substrate networks. These packets could be the data packets of information in the Internet, which links computers of heterogeneous and high capacities capable of transmitting packets at high rates. For our hierarchical networks, the packets are deposited at a randomly chosen site on the topmost layer of the network. Each site retains the number of packets which saturates its capacity and the remaining packets are transmitted further. A packet at a given site sees the nearest neighbor sites linked to itself. If the targeted neighboring site is not fully occupied (i.e., it has not saturated its capacity), the packet moves there and looks for the next site that has spare capacity. If the target site is fully occupied, then the packet stops on the site which it occupies, and the transmission of the packet ends at that site. In this fashion, all packets hop from one site to another according

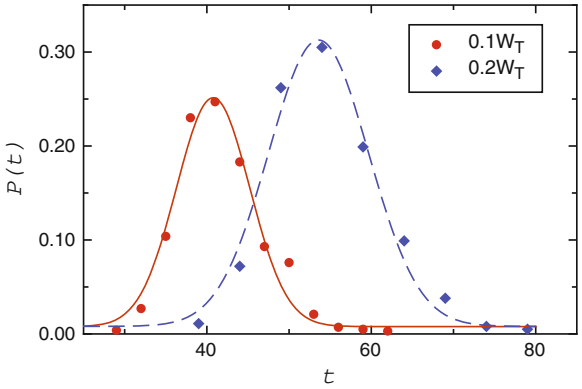

Fig. 4 The avalanche times distributions $P(t)$ for the base lattice, corresponding to 1000 realizations of networks of side $M = 100$, exhibits Gaussian behavior when tested for weights equal to $0.1W_T$ and $0.2W_T$, where W_T is the trunk capacity of base lattice

to the vacancy available on the neighboring sites, and this process continues till all the packets come to rest at some site. When the packet transmission has come to rest, at that time some of the sites would be occupied while the other would remain unoccupied or free. In this scenario, the network is composed of two sub-networks one of the unoccupied or free one and other of the occupied one, with the size of each network being a measure of the saturated or available capacity on the network. Hence, we study the transition to percolation in the occupied or unoccupied sub-networks. For the free sub-network, one anticipate a transition from the percolating to the non-percolating state when the packet density μ increases, where the packet density is the ratio of total number of packets to total number of sites in the network. In order to analyze the transition, we simulate the stochastic dynamics of packet transmission in the V lattice for different values of the packet density μ [7].

To study the percolation transition, the order parameter is defined to be the percolation strength $S = S_m/L$, where S_m indicates the number of sites belonging to the largest connected cluster of the unoccupied sub-network and L denotes the total number of sites in the network. The complement of the percolation strength S is defined as $S_1 = (1 - S)$, which is a measure of the fraction of occupied sites or of the size of the occupied sub-network. We note that S, the size of the connected cluster of unoccupied sites is a measure of the capacity available for transport for a given packet density. This goes to zero at the jamming transition where no more capacity is available, and its complement S_1 goes to the size of the lattice. Here S_1 is compared with the size of the percolating cluster which spans the size of the lattice at the percolation transition.

The numerical study by [7] shows that the percolation transition in the V lattice is a discontinuous or explosive one, which can be observed from the Fig. 5, and laws of the finite size scaling for continuous percolation transition does not hold for the V lattice. The percolation transition in the V lattice is contrary to second order continuous transition seen in the base lattice Fig. 6 [7], with associated second order percolation exponents. Here, again the V lattice shows critical behavior.

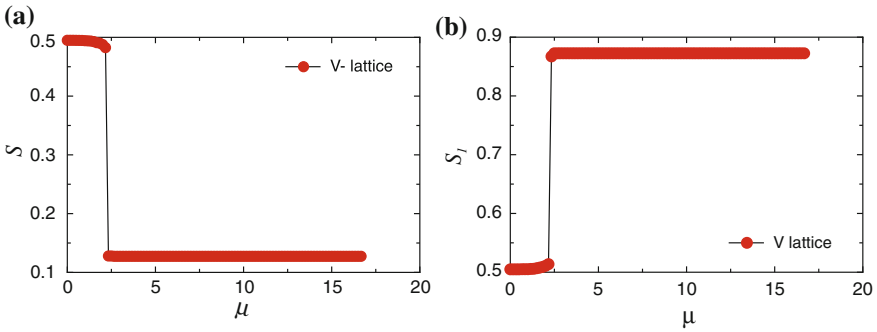

Fig. 5 **a** The order parameter S and **b** its complement S_1 as a function of packet density μ, averaged over 500 realizations, for the V lattice networks of (100 × 100) sites

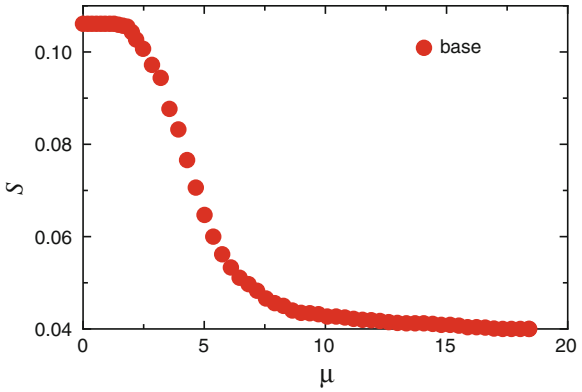

Fig. 6 The order parameter S as a function of packet density μ, averaged over 500 realizations, for the free sub-network in the base lattice network of (100 × 100) sites

4 Perturbed V Lattices: Annihilation of Criticality

We have seen that the V lattice is the critical case of the base model as it displays behaviors for the avalanche times distribution and site percolation quite distinct from those seen for the base lattice. Here we are interested in exploring whether a slight perturbation introduced in the structure of the V lattice destroys the critical nature of the V lattice for avalanche and site percolation phenomena. For this, perturbed V lattices are generated by switching the direction of the connections running parallel to arm opposite to the trunk in the V-cluster, with some probability $0 < p < 0.5$, but leaving the trunk or backbone untouched.

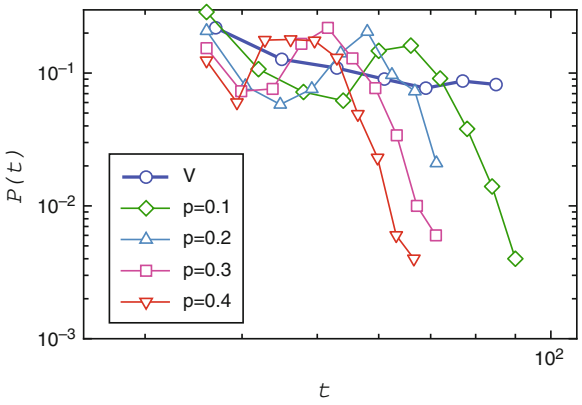

Fig. 7 The distributions of avalanche times of the V lattice and the perturbed V lattices obtained by switching connections with probability $p = 0.1, \ldots 0.4$, corresponding to 1000 realizations of a network of side $M = 100$ when tested for weights equal to $0.05 W_T$

4.1 Avalanche Time Distributions for the Perturbed V Lattice

To demonstrate that the V lattice is the only realization of the base lattice which displays power law behavior for the avalanche time distribution, we studied these distributions for the perturbed V lattices, for 1000 realizations and test weights equal to $0.05 W_T$ as shown in Fig. 7. It is observed that even a small perturbation ($p = 0.1$) in the topology of the V-cluster of the V lattice, destroys the power law behavior seen for the V lattice. Thus, the V lattice is found to be the only case of the base lattice which displays power law behavior.

4.2 The Percolation Transition for the Perturbed V Lattice

Again, in order to demonstrate that the V lattice is the only realization of the base lattice which displays explosive percolation transition, we explore the percolation transition on the perturbed V lattices. The order parameter S_1 is computed as a function of the packet density μ (see Fig. 8a) for the V lattice perturbed by different values of p, i.e., $0 < p < 0.5$. From Fig. 8a, one can notice that as the perturbation in the V lattice is increased (i.e., as p increases), the size of the jump ΔS_1 also reduces, where ΔS_1 is the difference between the values of S_1 before and after the transition. In Fig. 8b, the size of the largest jump ΔS_1 is plotted, corresponding to different p, for different lattice sizes L. It is apparent from Fig. 8b that the largest jump size ΔS_1, scales as a power law with system size L, defined as:

$$\Delta S_1 \sim L^{-\phi}. \tag{2}$$

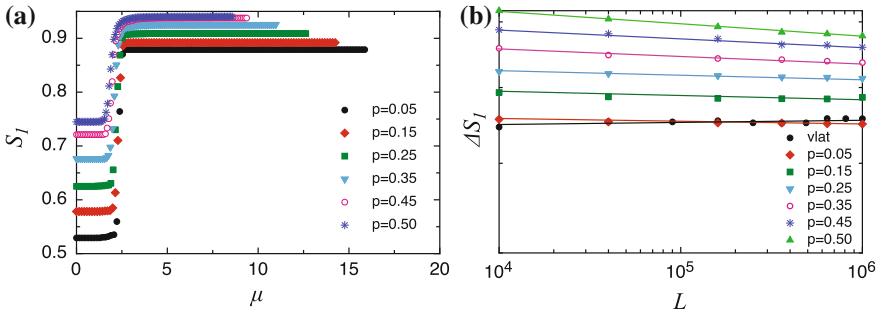

Fig. 8 Plot of **a** the order parameter S_1 of the occupied sub-lattice as a function of critical packet density μ for different values of $0 < p < 0.5$. **b** The largest jump size ΔS_1 of the V lattice, scales as a power law as function of the lattice size L i.e., $\Delta S_1 \sim L^{-\phi}$, where ϕ is 0.0019, 0.0023, 0.0029, 0.0059, 0.0079 and 0.011 for p equal to 0.05, 0.15, 0.25, 0.35, 0.45, 0.50, respectively

The above relation is similar to the relation between the largest jump size and the system size in [21] to show the discontinuity of the percolation transition. We find that $\phi > 0$ for all processes of the V lattice corresponding to different p. However, the values of ϕ are quite small. If, in the thermodynamic limit of infinite system size, we have

$$lim_{L\to\infty}\Delta S_1 = 0. \tag{3}$$

i.e. if, in the limit of infinite system size, the size of the largest jump ΔS_1 for the giant cluster goes to zero, then transitions are said to be weakly discontinuous. The percolation transitions in the perturbed V lattices are weakly discontinuous. We conclude that even a slight perturbation introduced in the V lattice destroys the nature of the percolation transition in the V lattice.

We thus conclude that the V lattice is indeed a critical case of the base lattice, as even a slight distortion in the structure of the V lattice destroys its critical nature.

5 Conclusions

To summarize, we have observed that in the case of branching hierarchical structure, the lattice with V-shaped clusters shows special behavior for transport processes which use this lattice as the substrate. Avalanche processes on this lattice show power law behavior, and percolation behavior on this lattice belongs to the explosive percolation class. This behavior sharply contrasts with the behavior seen for transport on typical realizations of the hierarchical networks, where avalanche transmissions are Gaussian, and the transition to percolation is of the usual second order type. Small perturbations to the V-cluster, rapidly destroy the special behavior, indicating the critical nature of the lattice. We note that this is one of the few examples where the nature of the substrate topology has led to the identification of a transition

of the explosive percolation class. We hope our results go some way towards the identification of special topologies where critical behavior is observed for transport properties. Such an identification maybe of utility in practical systems like power grids and computer and communication networks.

References

1. J. Duch, A. Arenas, Phys. Rev. Lett. **94**, 028701 (2005)
2. P. Holme, B.J. Kim, C.N. Yoon, S.K. Han, Phys. Rev. E **65**, 056109 (2002)
3. B. Tadić, G.J. Rodgers, Advs. Complex Syst. **05**, 445 (2002)
4. T. Ohira, R. Sawatari, Phys. Rev. E **58**, 193 (1998)
5. L. Zhao, Y.-C. Lai, K. Park, N. Ye, Phys. Rev. E **71**, 026125 (2005)
6. A.D. Kachhvah, N. Gupte, Phys. Rev. E **83**, 036107 (2011)
7. A.D. Kachhvah, N. Gupte, Phys. Rev. E **86**, 026104 (2012)
8. A.E. Scheidegger, Bull. Int. Acc. Sci. Hydrol. **12**, 15 (1967)
9. S.N. Coppersmith, C-h Liu, S. Majumdar, O. Narayan, T.A. Witten. Phys. Rev. E **53**, 4673 (1996)
10. D. Griffeath, in *Additive and Cancellative Interacting Particles Systems*. Lectures Notes in Mathematics, vol. 724 (Springer, Berlin, 1979)
11. T.M. Liggett, *Interacting Particles Systems* (Springer, Berlin, 1985)
12. E. Domany, W. Kinzel, Phys. Rev. Lett. **53**, 311 (1984)
13. B. Suki, A.-L. Barabasi, Z. Hantos, F. Petak, H.E. Stanley, Nature **368**, 615 (1994)
14. B. Suki, J.S. Andrade, M.F. Coughlin, D. Stamenovic, H.E. Stanley, M. Sujeer, S. Zapperi, Ann. Biomed. Eng. **26**, 608 (1998)
15. T.M. Janaki, N. Gupte, Phys. Rev. E **67**, 021503 (2003)
16. H. Takayasu, I. Nishikawa, H. Tasaki, Phys. Rev. A **37**, 3110 (1988)
17. H. Seybold, J.S. Andrade Jr, H.J. Herrmann, Proc. Natl. Acad. Sci. USA **104**, 16804 (2007)
18. D. Reiss, G. Erkeling, K.E. Bauch, H. Hiesinger, Geophys. Res. Lett. **37**, L06203 (2010)
19. T. Shinbrot, N.-H. Duong, L. Kwan, M.M. Alvarez, Proc. Natl. Acad. Sci. USA **101**, 8542 (2004)
20. A.D. Kachhvah, N. Gupte, Pramana J. Phys. **77**, 873 (2011)
21. J. Nagler, A. Levina, M. Timme, Nat. Phys. **7**, 265 (2011)

A Chaos MIMO-OFDM Scheme for Mobile Communication with Physical-Layer Security

Eiji Okamoto

Abstract Chaos communications enable a physical-layer security, which can enhance the transmission security in combining with upper-layer encryption techniques, or can omit the upper-layer secure protocol and enlarges the transmission efficiency. However, the chaos communication usually degrades the error rate performance compared to unencrypted digital modulations. To achieve both physical-layer security and channel coding gain, we have proposed a chaos multiple-input multiple-output (MIMO) scheme in which a rate-one chaos convolution is applied to MIMO multiplexing. However, in the conventional study only flat fading is considered. To apply this scheme to practical mobile environments, i.e., multipath fading channels, we propose a chaos MIMO-orthogonal frequency division multi-plexing (OFDM) scheme and show its effectiveness through computer simulations.

1 Introduction

In wireless communications, it is always needed to provide high-capacity transmission with a limited bandwidth, which is achieved by effective use of finite frequency resources. As one of the effective schemes, multiple-input multiple output (MIMO) transmission, in which the transmitter and the receiver use multiple antennas and simultaneously communicate each other [1], is drawing much attention. MIMO can increase the capacity in proportion to the minimum number of transmit and receive antennas with the same bandwidth.

On the other hand, wireless multihop and relay transmission has been widely used recently, in which the data are transmitted through a third person (terminal),

E. Okamoto (✉)
Department of Computer Science and Engineering, Graduate School of Engineering, Nagoya Institute of Technology, Gokiso-cho, Showa-ku, Nagoya 466-8555, Japan
e-mail: okamoto@nitech.ac.jp

V. In et al. (eds.), *International Conference on Theory and Application in Nonlinear Dynamics (ICAND 2012)*, Understanding Complex Systems,
DOI: 10.1007/978-3-319-02925-2_18,

and the security for the authorized transmission pair is becoming important. The data should not be decoded by unauthorized users. For those security enhancements, the upper-layer techniques such as public key encryption [2] or IPSec [3] scrambling are usually used and a physical-layer security is not considered. However, ensuring security is never exclusive at each transmission layer and adopting multiple secure protocols enhances the security. Or the physical-layer security can omit the upper-layer security and can simplify the system complexity. Chaos communications have been proposed in [4, 5] which achieve the physical-layer security. The chaotic deterministic and irregular properties can be utilized by applying the chaos into modulation and the transmit signals are scrambled. However, the objective of the conventional schemes in [4, 5] is focusing on the security enhancement and the bit error rate (BER) performance is degraded due to an extra power requirement of chaos signals. There are few studies on chaos transmission including channel coding function. In [6], the chaotic channel coding scheme is proposed with limiting the chaos states in decoding [7] for the practical decoding complexity, resulting in a lower security.

In MIMO multiplexing transmission, the multiplexed signals from each transmit antennas are received at each receive antenna and that signal becomes Gaussian. Also, various precoding schemes at the transmitter are proposed to improve the capacity or transmission quality. In this case the transmission signals also become Gaussian. Paying attention to these characteristics, we have proposed the chaos-MIMO transmission scheme in [8] as a precoding scheme, in which the rate-one chaotic random signal is used as second modulation at each MIMO transmit symbol for physical-layer encryption. The channel coding gain without lowering security is also obtained by correlating that random signal with the transmit bits. This coding gain is obtained in tradeoff with the decoding complexity increase. Similar MIMO transmission schemes using chaos stream have been proposed in [9, 10] and compared with those schemes, our scheme in [8] has an advantage of channel coding gain effect. However, the flat fading is assumed in [8] and it is needed to deal with multipath fading environments which occur in fast wireless transmission.

Therefore, in this chapter we apply orthogonal frequency division multiplexing (OFDM) [11] into chaos-MIMO scheme to enable a linear equalization of multi-path fading interference in the frequency domain, and propose a chaos-MIMO-OFDM scheme for mobile communications. We will show that the physical-layer security and improved transmission performance are obtained by the proposed scheme with a maximum likelihood sequence estimation (MLSE) in multipath fading environments compared with the conventional MIMO-OFDM scheme. In addition, it is shown that the error rate performance is improved by the subcarrier allocation adjustment of OFDM. In the following, the structure of chaos-MIMO-OFDM is introduced in Sect. 2, some numerical results are shown in Sect. 3, and the conclusion is drawn in Sect. 4.

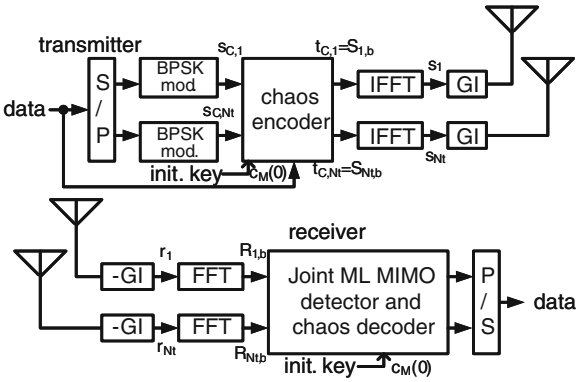

Fig. 1 Block diagram of chaos-MIMO-OFDM system

2 Chaos MIMO-OFDM System

The block diagram of the proposed chaos-MIMO-OFDM scheme is illustrated in Fig. 1. The MIMO-OFDM part is completely the same as the conventional schemes and in addition to that, the chaos signal correlated to the transmit bits is multiplied at the transmitter as the second modulation. By this chaos multiplication, the channel coding gain is obtained in addition to the encryption effect. In the following, MIMO-OFDM transmission, chaos-MIMO block, its allocation into OFDM subcarriers, and chaos symbol generation are introduced.

2.1 MIMO-OFDM Transmission

It is assumed that the numbers of MIMO transmit and receive antennas are N_t and N_r, respectively, and N is the number of OFDM subcarriers. Let $\mathbf{F}_N$ be (N, N) discrete Fourier transform matrix whose nth row and kth column is given by

$$W_N^{nk} = \frac{1}{\sqrt{N}} exp\left(-\frac{j2\pi nk}{N}\right)$$

The transmit n-th OFDM subcarrier from j-th antenna is denoted as $S_j(n)$ at $1 \leq j \leq N_t$ and $0 \leq n \leq N-1$ (introduced in detail in Sect. 2.4). When they are denoted as $\mathbf{S}_j = \{S_j(0), \ldots, S_j(N-1)\}$, the transmit time-domain sequence from jth antenna s_j is obtained by the inverse discrete Fourier transform as

$$\mathbf{s}_j = \{s_j(0), \ldots, s_j(N-1)\}, \ \mathbf{s}_j = \mathbf{F}_N^H \mathbf{S}_j$$

Here, H means the conjugate transpose of matrix. In practice, a part of s_j is duplicated at the top of the OFDM frame as a guard interval (GI). However, it is assumed that the signal processing of GI is perfectly done and is omitted in this study. When the received symbols at i-th receive antenna are denoted as $\mathbf{r}_i = \{r_i(0), \ldots, r_i(N-1)\}, 1 \leq i \leq N_r$, N-symbol impulse responseof L-path fading between jth transmit and ith receive antennas is $\mathbf{h}_{ij} = \{h_{0,ij}, h_{1,ij}, \ldots, h_{L-1,ij}, 0, \ldots, 0\}$, and the noise symbols at the receiver are $\mathbf{n}_i = \{n_i(0), \ldots, n_i(N-1)\}$, then, the receive symbol can be given by

$$r_j(k) = \sum_{j=1}^{N_t} \sum_{l=0}^{L-1} h_{l,\,ij} s_j(k) + n(k), \qquad 0 \leq k \leq N-1$$

Similarly in the frequency domain, when the channel coefficients of OFDM subcarriers are denoted as $\mathbf{H}_{ij} = \{H_{ij}(0), \ldots, H_{ij}(N-1)\}$, this is derived by $\mathbf{H}_{ij} = \mathbf{F}_N \mathbf{h}_{ij}$. After r_j reception, the received OFDM subcarriers are obtained by the discrete Fourier transform as

$$\mathbf{R}_i = \{R_i(0), \ldots, R_i(N-1)\}, \qquad \mathbf{R}_i = \mathbf{F}_N \mathbf{r_i}$$

2.2 Subcarrier Allocation of Chaos-MIMO Block to OFDM Frame

Let $B(\ll N)$ be the number of MIMO symbols per chaos-MIMO block. Then, NB chaos-MIMO blocks are transmitted in one OFDM frame of N subcarriers. One chaos-MIMO block consists of B subcarriers and $N_t B$ symbols. When b is the number of chaos-MIMO blocks in OFDM frame at $0 \leq b \leq N/B - 1$ and the corresponding numbers of subcarriers are $\{n_{bB}, \ldots, n_{(b+1)B-1}\}$, the block subcarrier allocation can be denoted as

$$n_{bB+n} = bB + n, \qquad 0 \leq n \leq B-1 \tag{1}$$

which is called as localized allocation in this study. Another distributed allocation can also be considered as

$$n_{bB+n} = nN/B + b \tag{2}$$

which is called as interleaved allocation. These two types are evaluated. The frequency allocation images are illustrated in Fig. 2.

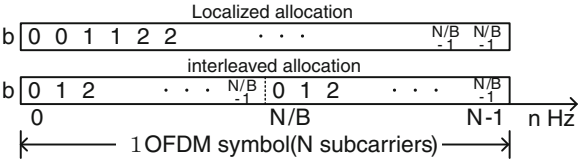

Fig. 2 Frequency allocation of chaos-MIMO into OFDM subcarriers (B = 2)

2.3 Maximum Likelihood Sequence Estimation of Chaos-MIMO Decoder

Let j-th transmit antenna B-column vector of b-th chaos-MIMO block be denoted as $\mathbf{S}_{j,b} = \{S_j(n_{bB}), \ldots, S_j(n_{(b+1)B-1})\}$ and similarly i-th receive B-column vector of that block is denoted as . Then, the corresponding frequency-domain channel matrix is given by $H_{ij,b} = diag[H_{ij}(n_{bB}), \ldots, H_{ij}(n_{(b+1)B-1})]$ and MLSE decoding can be conducted by

$$\hat{\mathbf{s}}_C = \arg\min_{\mathbf{s}_C} \sum_{j=1}^{N_t} \sum_{i=1}^{N_r} ||R_{i,b} - H_{ij,b} S_{j,b}||^2 \tag{3}$$

where the chaos decoding and MIMO detection are simultaneously done on every chaos MIMO block. Here, $\mathbf{s}_C$ is the information vector described in the next subsection and $\hat{\mathbf{s}}_C$ is the decoded information vector.

2.4 Chaos-MIMO Transmit Symbols in One Block

Let $N_t B$ transmit information symbol sequence be denoted as

$$\begin{aligned} \mathbf{s}_C &= \{s_{C,1}(0), \ldots, s_{C,1}(B-1), s_{C,2}(0), \ldots, s_{C,N_t}(B-1)\} \\ &= \{\mathbf{s}_{C,1}, \mathbf{s}_{C,2}, \ldots, \mathbf{s}_{C,N_t}\} \end{aligned} \tag{4}$$

where $s_{C,j}(k)$ means jth antenna and kth information symbol. MLSE in decod- ing is conducted on this sequence unit. In this study BPSK modulation is assumed as the first modulation (the second modulation is chaos multiplication) and one bit is assigned to each $s_{C,j}(k)$. Hence,the number of MLSE decoding search is $2^{N_t B}$. At this MLSE of B-symbol block, the chaos coded modulation has been applied for a longer sequence and the coding gain is obtained in addition to the physical-layer encryption compared with the conventional MIMO-maximum likelihood de-coding (MLD). However, as the tradeoff of the error rate improvement, the exponential increase of decoding search for the B-length block is needed in the MLSE decoding.

Let the chaos symbols for encryption and encoding be denoted as

$$\mathbf{c}_C = \{c(0), \ldots, c(N_t B - 1)\} \tag{5}$$

whose generation rule is described in Sect. 2.5. The chaos modulation is conducted as second modulation for s_C by the element multiplication (scalar product) of c_C as

$$\begin{aligned} \mathbf{t}_C = \mathbf{s}_C \circ \mathbf{c}_C &= \{s_{C,1}(0)c(0), s_{C,1}(1)c(1), \ldots, s_{C,N_t}(B-1)c(N_t B - 1)\} \\ &= \{t_{C,1}(0), \ldots, t_{C,1}(B-1), t_{C,2}(0), \ldots, t_{C,N_t}(B-1)\} \\ &= \{\mathbf{t}_{C,1}, \mathbf{t}_{C,2}, \ldots, \mathbf{t}_{C,N_t}\} \end{aligned} \tag{6}$$

by this modulation the transmit symbol is scrambled. Then, t_C is allocated into OFDM subcarriers by

$$\mathbf{S}_{j,b} = \mathbf{t}_{C,j} \tag{7}$$

as bth block as described in Sect. 2.3.

2.5 Generation of Chaos Sequence

In (6), the channel coding gain is obtained when the chaos symbol c_C correlated by the transmit bits is multiplied to s_C. Although the generation of c_C is arbitrary whenever it is correlated to source information, a chaos is used for simplicity in this study because the signal can be easily generated by nonlinear equation. Furthermore, c_C is made as a random unit vector not to change the transmit power. In particular, Bernoulli shift map [12] is used. Each chaos symbol $c(k)$ of c_C generated by

$$c(k) = \exp\{j2tan^{-1}\Im([s_k]/\Re[s_k])\}$$

where s_k is the pseudo Gaussian noise symbol of

$$s_k = 1/M \sum_{i=0}^{M-1} \{(\Re[c_{ki}] + \Im[c_{ki}]) \exp(j8\pi[\Re[c_{ki}] - \Im[c_{ki}])\}$$

here, k is $0 \leq k \leq N_t B - 1$ and c_{ki} is a chaos element signal of M independent chaos. To make s_k Gaussian noise, the number of chaos multiplexing M is set to relatively large number such as 10. Since $c(k)$ is a unit symbol, the encryption of $c(k)$ is conducted as a random phase shift and the transmission power is not changed. Let M-column chaos element vector be denoted as

$$\mathbf{c}_M(k) = [c_{k0} \ldots c_{k(M-1)}], c_{ki} \in C, 0 < \Re[c_{ki}], \Im[c_{ki}] < 1$$

the transmitter and receiver pair shares the initial chaos vector of

$$\mathbf{c}_M(0) = [c_{00} \ldots c_{0(M-1)}] \tag{8}$$

thus, this vector $\mathbf{c}_M(0)$ is the key signal of encryption and the proposed scheme is categorized as the common key encryption. Here, $\mathbf{c}_M(0)$ can be quantized to save the system memory. $\mathbf{c}_M(k)$ is iteratively modulated and processed in real and imaginary parts, respectively, as follows.

$$x_0 = \begin{cases} \Re[c_{k-1i}] & (b_k = 0) \\ 1 - \Re[c_{k-1i}] & (b_k = 1, \Re[c_{k-1i}]) > 1/2) \\ \Re[c_{k-1i}] + 1/2 & (b_k = 1, \Re[c_{k-1i}]) \leq 1/2) \end{cases} \tag{9}$$

$$y = \Im[c_{(k-1)i}]$$

$$x_{l+1} = 2x_l \mathrm{mod} 1, y_{l+1} = 2y_l \mathrm{mod} 1 \tag{10}$$

$$\Re[c_{ki}] = x_{Ite+b_k}, \Im[c_{ki}] = y_{Ite+b_k} \tag{11}$$

where b_k is the $\{(k + N_t B - 1)\mathrm{mod}N_t B\}$-th bit of corresponding transmit symbol of $\mathbf{s}_C$. By this cyclic shift modulation, the effect of convolutional coding is obtained even in rate-one coding. (9) is the chaos modulation and (10) is the chaos shift map equation. As (11), the chaos is processed *Ite* times to make a random signal and in this study Ite is set to 19 by heuristic search. The configuration of $c(k)$ may be widely changed and the configuration itself can also be a secret key component.

3 Numerical Results

The BER performances are evaluated through computer simulations using the simulation conditions listed in Table 1. It is assumed that the initial key is identical among the transmitter and the receiver, and the chaos synchronization is perfect. The channel is assumed as i.i.d. equivalent power 8-path quasi-static Rayleigh fading on every antenna and OFDM frame, which is perfectly known to the receiver. To obtain the average performance, the initial key vector of (8) is randomly changed at every OFDM frame in this simulation. Figure 3 shows the BER performance comparison with original MIMO-OFDM transmission where the subcarrier allocation is

Table 1 Block diagram of chaos-MIMO-OFDM system

Modulation	BPSK-OFDM
Num. of subcarriers	$N = 64$
Num. of antennas	$N_t = N_r = 2$
MIMO block length	$B = 2$
Chaos	Bernoulli shift map
Num. of chaos multiplexing	$M = 10$
Num. of chaos processing	$Ite = 19$
Initial chaos synchronization	Perfect
Channel	i.i.d. equivalent power 8-path quasi-static Rayleigh fading
Receive channel state inf. (CSI)	Perfect
Transmit CSI	N/A

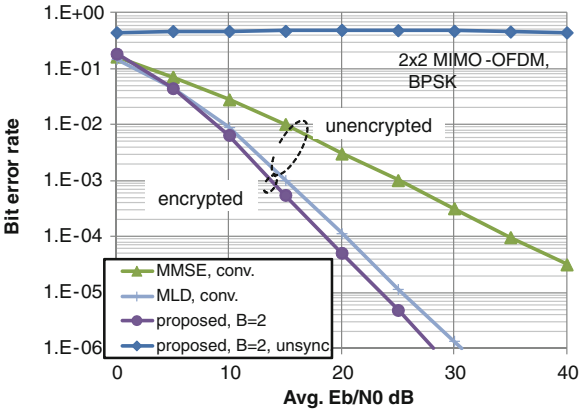

Fig. 3 Bit error rate performances in multipath fading channel

interleaved as (2) and $B = 2$ of one chaos-MIMO block consisting of two MIMO vectors. Here, the power degradation due to GI insertion is taken into account in the horizontal axis. It can be seen that the proposed scheme improved about 2 dB at BER $= 10^{-5}$ compared with the conventional unencrypted MIMO-MLD. It means that both the physical-layer security and channel coding gain can be obtained in the proposed scheme. The numbers of MLSE decoding search in the proposed and conventional schemes are $2^{N_t B}N/B = 512$ and $2^{N_t}N = 256$, respectively, and this calculation increase is the tradeoff of the proposed scheme. Figure 3 also shows that the BER of the proposed scheme with slightly different initial key, 10^{-3} different in the real part, becomes almost 0.5, which means the secrecy is achieved and the normal decoding cannot be done when the initial key of (8) is not shared.

Figure 4 shows the BER comparison for the different subcarrier allocations of Fig. 2. Both of the localized and interleaved allocations have the gain for the conventional MIMO transmission and a slight improvement is obtained in the distributed

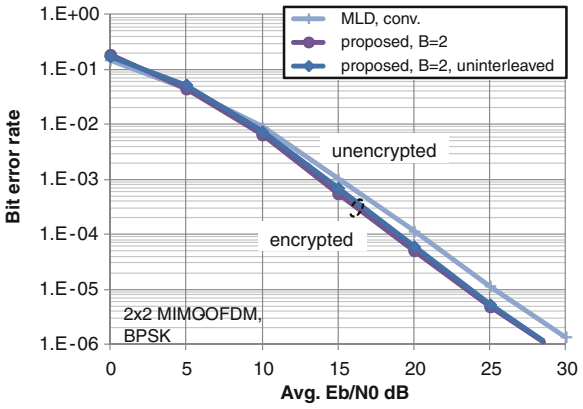

Fig. 4 BER comparison with different subcarrier allocation schemes

allocation. This is because the frequency-domain correlation of the channel coefficients is lower and more frequency-diversity effect can be obtained in the inter-leaved allocation. Hence, the interleaved allocation has better performance when the frequency selectivity of the channel is strong.

4 Conclusions

In this paper, we proposed a chaos-MIMO-OFDM transmission scheme and showed that the physical-layer security and channel coding gain were obtained in the multipath fading environments. Compared with the conventional MIMO-OFDM transmission, the coding gain is obtained in tradeoff with the increase of decoding calculation complexity. Furthermore, it was shown that the improved BER performance was obtained by the interleaved subcarrier allocation. The proposed scheme will be more effective in such as mobile multihop transmission where the upper-layer security protocols can be omitted and the simple and secure transmission can be achieved.

For future study, the complexity reduction of MLSE and the application to multihop cooperative communication scheme will be considered.

Acknowledgments This research was partially supported by KDDI foundation, A-STEP of JST, and Strategic Information and Communications R&D Promotion Programs (SCOPE) in Ministry of Internal Affairs and Communications. The author wishes to thank for their support.

References

1. G.J. Foschini, Layered spacetime architecture for wireless communication in a fading environment when using multiple antennas. Bell Labs Syst. Tech. J. **1**, 4159 (1996)
2. M.E. Hellman, An overview of public key cryptography. IEEE Commun. Mag. **16**(6), 24–32 (1978)
3. V. Manral, *Cryptographic Algorithm implementation requirements for Encapsulating Security Payload (ESP) and Authentication Header (AH), RFC 4835*
4. T.L. Carroll, L.M. Pecora, Synchronizing chaotic circuits. IEEE Trans. Cir. Sys. **38**(4), 453–456 (1991)
5. G. Kolumban, M.P. Kennedy, Recent results for chaotic modulation schemes, in *Proceedings Ieee International Symposium on Cir Systems* **3**, 141144 (May 2001)
6. B. Chen, G.W. Wornell, Analog error-correcting codes based on chaotic dynamical systems. IEEE Trans. Comm. **46**(7), 881–890 (1998)
7. F.J. Escribano, L. Lopez, M.A.F. Sanjuan, Iteratively decoding chaos encoded binary signals, in *Proceedings Eighth IEEE International Symposium on Signal Processing and Its Applications (ISSPA)*, Sydney, vol. 1, pp. 275–278, Aug 2005
8. E. Okamoto, A chaos MIMO transmission scheme for channel coding and physical-layer security. IEICE Trans. Commun. E **95-B**(4), 1384–1392 (2012)
9. G. Zheng, D. Boutat, T. Floquet, J.-P. Barbot, Secure communication based on multi-input multi-output. Chaotic System with Large Message Amplitude. Chaos Solitons Fractals **41**(3), 1510–1517 (2009)

10. S. Wang, X. Wang, M-DCSK-based chaotic communications in MIMO multipath channels with no channel state information. IEEE Trans. Circuits Syst. II Express Briefs **57**(12), 1001–1005 (2010)
11. J. G. Proakis, M. Salehi, *Digital Communications 5th edn*. (McGraw-Hill, Ney york 2008)
12. S. Kozic, T. Schimming, M. Hasler, Controlled one-and multidimensional modulations using chaotic maps. IEEE Trans. Circuits Syst. Fundam. Theory Appl. **53**(9), 2048–2059 (2006)

Acoustic Detection and Ranging Using Solvable Chaos

Ned J. Corron, Mark T. Stahl, Jonathan N. Blakely and Shawn D. Pethel

Abstract Acoustic experiments demonstrate a novel approach to ranging and detection that exploits the properties of a solvable chaotic oscillator. This nonlinear oscillator includes an ordinary differential equation and a discrete switching condition. The chaotic waveform generated by this hybrid system is used as the transmitted waveform. The oscillator admits an exact analytic solution that can be written as the linear convolution of binary symbols and a single basis function. This linear representation enables coherent reception using a simple analog matched filter and without need for digital sampling or signal processing. An audio frequency implementation of the transmitter and receiver is described. Successful acoustic ranging measurements are presented to demonstrate the viability of the approach.

1 Introduction

The wide bandwidth and aperiodic properties of chaos naturally suggest benefits for high-resolution, unambiguous ranging in radar, sonar, and ladar systems [1–14]. An obvious, conventional approach is to substitute chaos for the noise source in random-signal radar. In such a system, a segment of the transmitted waveform is sampled and stored, using a resolution defined by the signal bandwidth and the Nyquist sampling criterion. The stored signal is then used in a correlation receiver to detect a return signal and determine time of flight. The crosscorrelations are usually done digitally, using a digital signal processor (DSP) and fast-Fourier transforms (FFT). In this approach, the distinguishing properties of a chaotic waveform are not used: chaos is simply a replacement for a widebandwidth, random source. In contrast, we recently developed an alternative approach to detectionand ranging that truly exploits the

N. J. Corron · M. T. Stahl · J. N. Blakely · S. D. Pethel(✉)
U. S. Army RDECOM, Redstone Arsenal, Alabama 35898, USA
e-mail: shawn.pethel@us.army.mil

V. In et al. (eds.), *International Conference on Theory and Application in Nonlinear Dynamics (ICAND 2012)*, Understanding Complex Systems,
DOI: 10.1007/978-3-319-02925-2_19,

properties of a chaotic waveform to alleviate the most expensive parts of random-signal radar—i.e., sampling, digital memory, and digital signal processor—while still maintaining the performance of a correlation receiver [13, 14]

This new approach uses chaotic waveforms generated by an analytically solvable nonlinear oscillator comprising an ordinary differential equation and a discrete switching state [15, 16]. This hybrid oscillator admits an exact solution, which can be written as the linear convolution of binary symbols and a single, fixed basis function. This analytic representation is significant since it enables coherent reception using a simple analog matched filter and only a few stored binary symbols.

In this paper, we present recent acoustic experiments that demonstrate this new approach to ranging and detection. For these experiments, an amplified speaker emits an audio-frequency chaotic waveform generated by an electronic realization of the hybrid oscillator. The broadband, non-repeating, continuously transmitted waveform sounds like noise. A complementary receiver circuit incorporates a matched filter for the chaotic waveform. At repeated intervals, a sequence of symbols are detected and captured from the emitted waveform, thereby defining a transmitted reference signal for ranging. The captured symbol sequence is provided to the receiver, where it defines a matched filter for the reference waveform. Practically, the symbols define weights applied to elements of a microphone array, the outputs of which are summed and linearly filtered. The output of the matched filter is a continuous signal that is proportional to the cross-correlation of the transmitted and received signal at an evolving lag. In operation, a consistent peak in the output of the matched filter indicates a detected source, and a range estimate is derived by the time of flight for the consistent peak.

The entire experimental system is realized using simple analog and digital electronic circuit components. Importantly, the receiver does not require waveform sampling or digital signal processing for detection. Real-time measurements using only an oscilloscope provide visible evidence of detection and ranging with the system.

2 Solvable Chaotic Oscillator

The central element of the ranging demonstration system is the audio frequency oscillator shown schematically in Fig. 1. This electronic oscillator is a physical realization of a chaotic system previously considered by Saito and Fujita [15] and Corron et al. [16]. This circuit is a hybrid system, containing both an analog harmonic oscillator and digital logic circuits. The dynamics of the oscillator are equivalent to a dimensionless hybrid model including a continuous scalar state $v(t)$ and a discrete binary state $\nu_s(t)$. The continuous- time dynamics are described by the differential equation

$$\frac{d^2v}{dt^2} - 2\beta u\frac{dv}{dt} + (\omega^2 + \beta^2)\cdot(v - \nu_s) = 0 \tag{1}$$

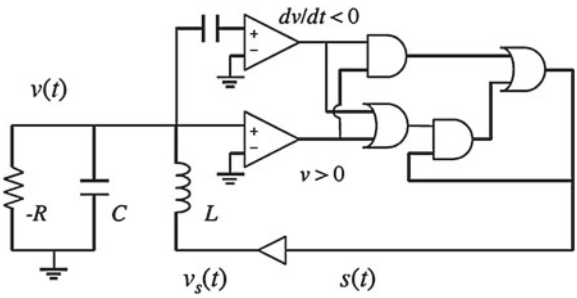

Fig. 1 Schematic representation of solvable chaotic oscillator used in the acoustic ranging experimental system

where $\omega = 2\pi$ and $0 < \beta \leq \ln 2$. Transitions in the discrete state are defined by the guard condition

$$\frac{dv}{dt}(t) = 0 \Rightarrow v_s(t) = \begin{cases} +1, & v \geq 0 \\ -1, & v < 0 \end{cases} \tag{2}$$

meaning $v_s(t)$ is set to the sign of $v(t)$ whenever its time derivative vanishes, and $v_s(t)$ maintains this value until the next critical point. In the circuit, $s(t)$ is the logic signal that determines $v_s(t)$. In this model, time is scaled by the natural frequency of the damped oscillator such that linear oscillations have unit period.

It is easily verified that this oscillator admits an exact, analytic solution

$$v(t) = \sum_{m=-\infty}^{\infty} s_m \cdot P(t-m) \tag{3}$$

$$v_s(t) = \sum_{m=-\infty}^{\infty} s_m \cdot \phi(t-m) \tag{4}$$

where each $s_m = \pm 1$ and $P(t)$ and $\phi(t)$ are fixed basis functions. In the solution, each symbol s_m modulates the fixed basis functions $P(t)$ and $\phi(t)$ centered at time $t = m$. Thus, it is correct to think of the symbol s_m as the information emitted by the oscillator at time $t = m$, and that the oscillator emits one symbol with each unit of time. The fixed basis functions are

$$P(t) = \begin{cases} (1-e^{-\beta})e^{-\beta}\left(\cos\omega t - \frac{\beta}{\omega}\sin\omega t\right), & t < 0 \\ 1 - e^{\beta(t-1)}\left(\cos\omega t - \frac{\beta}{\omega}\sin\omega t\right), & 0 \leq t < 1 \\ 0, & 1 \geq t \end{cases} \tag{5}$$

and

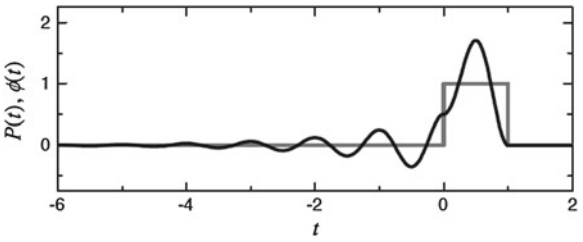

Fig. 2 Analytic basis functions $P(t)$ (*black*) and $\phi(t)$ (*gray*) for the solvable chaotic oscillator model with $\beta = \ln 2$

$$\phi(t) = \begin{cases} 0, & t < 0 \\ 1, & 0 \le t < 1 \\ 0, & 1 \ge t \end{cases} \tag{6}$$

which are shown in Fig. 2 for $\beta = \ln 2$.

For the acoustic system, we implemented the oscillator in an electronic circuit operating at roughly 10 kHz. The circuit is constructed using discrete analog and digital components on a solderless breadboard. The negative resistor and the inductor are realized using active circuits with operational amplifiers [17].

3 Acoustic Transmitter

The first advantage of using an exactly solvable chaotic oscillator is the availability of a compact symbolic representation for efficiently sampling the transmitted signal and storing a reference waveform. Here we show a transmitter design that achieves this important functionality.

The complete transmitter is shown in Fig. 3. At the center of the transmitter is the chaotic oscillator. The transmitted signal is the continuous state $v(t)$ of the free-running chaotic oscillator, which is amplified and emitted by a conventional speaker. The additional circuitry at the bottom of the transmitter schematic derives a clock signal from the regular return times of the oscillator. The clock signal drives a binary shift register, which uses the logic signal $s(t)$ for the data input. A divide-by-N counter circuit provides a signal to alternately enable and disable the shift register. For our experimental system, we typically use $N = 1024$.

In operation, the free-running oscillator generates a chaotic waveform that is continuously emitted from the speaker. While the shift register is enabled, the symbolic logic state $s(t)$ is sampled for each return and stored in the shift register. At any time, a fixed number M of the most recent values of the logic state $s(t)$ are stored, which correspond to a sequence of amplitudes s_m generated by the freerunning oscillator. Although the figure only shows an 8 bit shift register, for the acoustic system we use an 11 bit register.

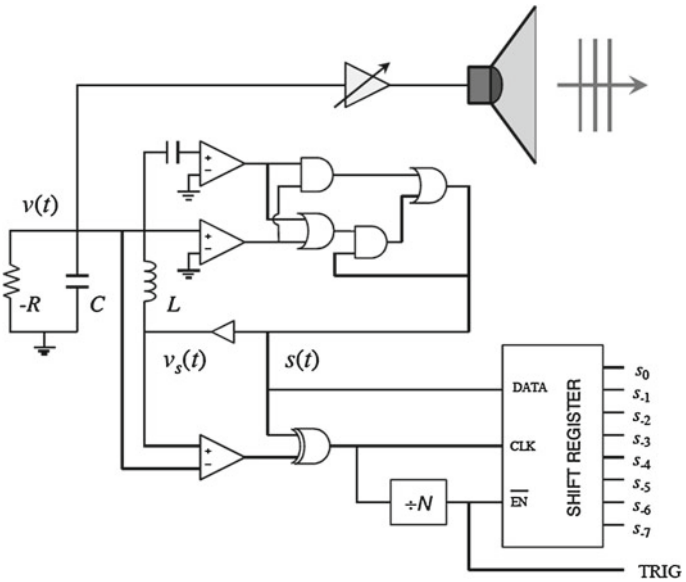

Fig. 3 Transmitter for acoustic ranging system incorporating the solvable chaotic oscillator and a shift register for storing symbols that define the reference waveform

After shifting N successive returns through the register, the shift register is disabled by the signal from the divide-by-N circuit. When disabled, the contents of the shift register are locked, thereby storing symbols that identify the signal transmitted just prior to the disabling transition. These stored symbols effectively define a reference waveform

$$v_{ref}(t) = \sum_{m=1-M}^{0} s_m \cdot P(t-m) \tag{7}$$

which can be used for detection and ranging in a correlation receiver. The number of stored symbols is M, which defines the length of the reference waveform. Compared to the usual Nyquist sampling criteria, this symbolic representation provides at least an order of magnitude reduction in the sampling and storage requirements for the reference waveform. The M symbols are provided to the receiver, along with the disable signal (TRIG) to mark an initial time for determining range for a reference waveform detected in the received signal.

A simulated oscillator waveform and shift register content is shown in Fig. 4. The top plot shows the oscillator waveforms $v(t)$ and $v_s(t)$. The continuous waveform $v(t)$ is the transmitted waveform emitted by the speaker. The middle plot shows the clock signal that is extracted from the oscillator waveforms and defines the symbol timing. The bottom waveform shows the trigger signal derived by the divide-by-N operation from the clock signal. The shift register is disabled by the low-to-high transition of the trigger signal. The arrows point to dots in the top plot that show the

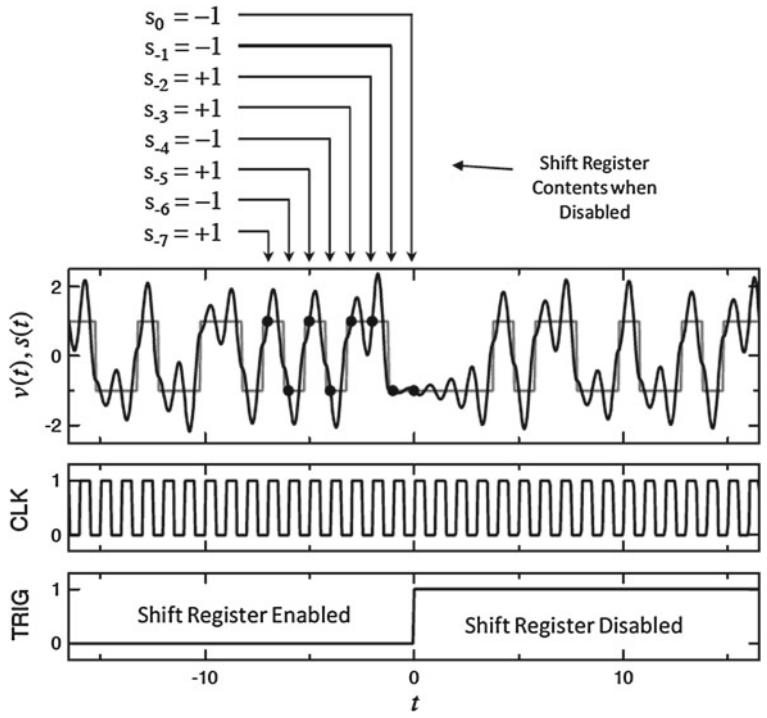

Fig. 4 Simulated transmitter waveforms, including the derived clock and trigger signals. *Arrows* point to dots on the switching waveform to indicate the most recent eight symbols stored in the shift register when disabled

most recent symbols captured and stored by the shift register when it is disabled. These symbols define the reference waveform for the correlation receiver.

4 Correlation Receiver

The second advantage of using an exactly solvable chaotic oscillator is the availability of a simple matched filter for the basis function [16]. This filter enables the construction of a simple correlation receiver for a chaotic waveform segment defined by truncated symbol sequence [13, 14]. For the acoustic system, we implement a receiver using discrete circuit components and without requirement for a DSP.

In the presence of additive white-Gaussian noise (AWGN) noise, a matched filter is the optimal linear receiver for detecting a given signal [18]. The matched filter for the reference waveform is mathematically equivalent to the correlation

$$\xi(t) = \int_{-\infty}^{\infty} \tilde{v}(\tau) \cdot v_{ref}(\tau - t) d\tau \tag{8}$$

where $\tilde{v}(\tau)$ is the filter input. A peak in the output of the matched filter indicates a strong correlation with the reference signal, indicating the strong likelihood that the reference signal was present in the input.

Using the analytic form of the reference waveform (7), the matched filter (8) can be written

$$\xi(t) = \int_{-\infty}^{\infty} \tilde{v}_M(\tau) \cdot P(\tau - t) d\tau \tag{9}$$

where

$$\tilde{v}_M(t) = \sum_{m=1-M}^{0} s_m \cdot \tilde{v}(\tau + m) \tag{10}$$

is the weighted sum of the filter input at M equally spaced delays. Equation (9) is a correlation of the summed signal $v_M(t)$ with the basis pulse $P(t)$. Hence, this equation can be implemented using a matched filter for the single basis pulse, which was previously shown to be

$$\frac{d\eta_p}{dt} = \tilde{v}_P(t+1) - \tilde{v}_P(t) \tag{11}$$

$$\frac{d\xi_p^2}{dt^2} + 2\beta \frac{d\xi_p}{dt} + \left(\omega^2 + \beta^2\right)(\xi_P - \eta_P) = 0 \tag{12}$$

where $\tilde{v}_P(t)$ is the filter input, $\tilde{\eta}_P(t)$ is an intermediate state, and $\tilde{\xi}_P(t)$ is the matched filter output [16]. Consequently, a matched filter for the reference waveform is

$$\frac{d\eta}{dt} = \sum_{m=1-M}^{0} s_m \cdot \{\tilde{v}(t+m+1) - \tilde{v}(t+m)\} \tag{13}$$

$$\frac{d\xi^2}{dt^2} + 2\beta \frac{d\xi}{dt} + \left(\omega^2 + \beta^2\right)(\xi - \eta) = 0 \tag{14}$$

where $\eta(t)$ is an intermediate state. Thus, the filter provided by Eqs. (13) and (14) is an exact matched filter for the reference waveform (7) defined by the M stored symbols, s_m.

Significantly, the matched filter for the reference waveform is sufficiently simple to enable analog implementation. That is, a DSP is not required to implement the matched filter receiver. Practical considerations require an additional signal delay on the filter input to make the matched filter causal.

Figure 5 shows a schematic analog implementation of the matched filter for the acoustic ranging system. The received waveform impinges on a microphone array, shown at top. The spacing of the microphones in the array is chosen to realize the

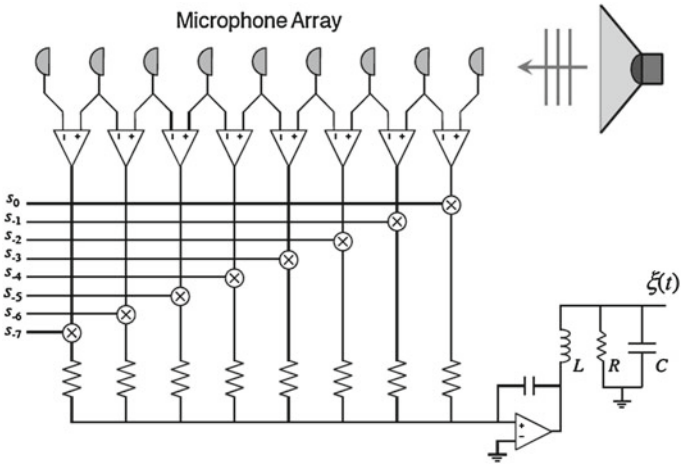

Fig. 5 Acoustic correlation receiver that realizes a matched filter for the solvable oscillator. The spacing of the microphones in the array is set to obtain the unit time delay specified in the matched filter equations

evenly spaced time delays required of the filter input in Eq. (13). Differential amplifiers between adjacent microphones provide the difference signal of successively lagged signals, which are multiplied by ± 1 according to the symbols defining the reference waveform. As a result, $M + 1$ microphones are required by the receiver. The summed differences are integrated and drive the harmonic filter to generate the matched filter output signal.

Fig. 6 Acoustic ranging system using solvable chaotic oscillator demonstrated in an anechoic test chamber

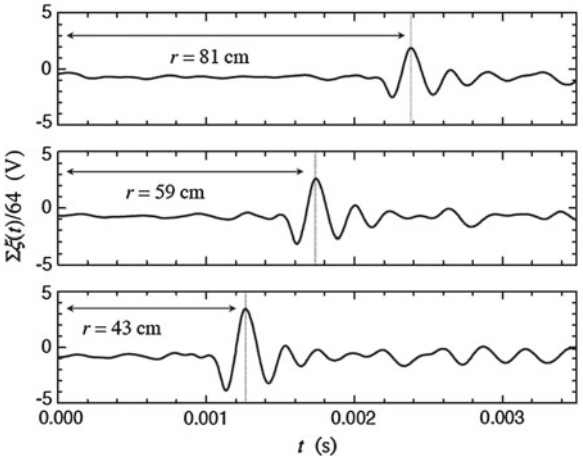

Fig. 7 Experimental acoustic detection and ranging observed in the receiver output using 64 averaged matched filter output signals for the source speaker positioned at three different ranges in front of the microphone array

5 Acoustic Detection and Ranging System

The transmitter and receiver were constructed and installed in an acoustically anechoic chamber for demonstration and test. The speaker was positioned at different ranges in front of the microphone array, as shown in Fig. 6. The microphone array contained twelve condenser microphones, so that the reference waveform was described using $M = 11$ bits. A handheld digital oscilloscope, triggered on the disable signal to the shift register, was used to monitor the receiver output.

Various transmitter and matched filter states were also connected to a computer for data acquisition purposes.

In operation, a consistent peak in the matched filter output was evident at a delay corresponding to the distance from speaker to microphone array. However, multiple received waveforms are required to unambiguously identify the peak corresponding to the signal path. From the matched filter output for a typical individual waveform, a return peak is comparable to and indistinguishable from background noise, intersymbol interference, or waveform sidelobes. In particular, using a relatively short reference waveform, the oscillator will naturally and randomly revisit each 11-bit symbol sequence fairly often. However, a consistent, unambiguous peak emerges when multiple receiver outputs are averaged, since the physical return provides the only consistent peak. In the experimental system, waveform averaging is easily and conveniently provided by the handheld oscilloscope. Typical outputs for 64 averaged matched filter output signals are shown in Fig. 7, which shows the detection and correctly estimated range for three different speaker positions (using the TRIG signal to define $t = 0$).

6 Conclusions

Using an acoustic system, we experimentally demonstrated a novel approach to ranging and detection that truly exploits the properties of chaos to simplify hardware and signal processing requirements. This approach uses waveforms generated by a solvable chaotic oscillator that includes both continuous and switching dynamics. This hybrid oscillator admits an exact analytic solution that offers two significant advantages. The first is a compact symbolic representation for efficiently sampling and storing a reference waveform. The second is the availability of a simple matched-filter receiver that can be constructed using low-cost, analog hardware. By exploiting these properties, we built and demonstrated an experimental acoustic ranging system that achieves comparable performance to the conventional random-signal approach while avoiding the costly digital sampling, storage and signal processor requirements. This successful demonstration proves the viability of this approach for ranging and detection, thereby enabling the development of new, low-cost sonar and radar technologies using chaotic waveforms.

References

1. K.M. Myneni, T.A. Barr, B.R. Reed, S.D. Pethel, N.J. Corron, High-precision ranging using a chaotic laser pulse train. Appl. Phys. Lett. **78**, 1496–1498 (2001)
2. B.C. Flores, E.A. Solis, G. Thomas, Assessment of chaos-based FM signals for range- Doppler imaging. IEE Proc.-Radar Sonar Navig. **150**, 313–322 (2003)
3. F.-Y. Lin, J.-M. Liu, Ambiguity functions of laser-based chaotic radar. IEEE J. Quantum Elec. **40**, 1732–1738 (2004)
4. F.-Y. Lin, J.-M. Liu, Chaotic radar using nonlinear laser dynamics. IEEE J. Quantum Elec. **40**, 815–820 (2004)
5. V. Venkatasubramanian, H. Leung, A novel chaos-based high-resolution imaging technique and its application to through-the-wall imaging. IEEE Signal Proc. Lett. **12**, 528–531 (2005)
6. T.L. Carroll, Chaotic system for self-synchronizing Doppler measurement. Chaos **15**, 013109 (2005)
7. T.L. Carroll, Optimizing chaos-based signals for complex targets. Chaos **17**, 033103 (2007)
8. Z. Liu, X. Zhu, W. Hu, F. Jiang, Principles of chaotic signal radar. Int. J. Bifurcation Chaos Appl. Sci. Eng. **17**, 1735–1739 (2007)
9. S. Qiao, Z.G. Shi, K.S. Chen, W.Z. Cui, W. Ma, T. Jiang, L.X. Ran, A new architecture of UWB radar utilizing microwave chaotic signals and chaos synchronization. Prog. Electromagn. Res. **75**, 225–237 (2007)
10. Z.G. Shi, S. Qiao, K.S. Chen, W.Z. Cui, W. Ma, T. Jiang, L.X. Ran, Ambiguity functions of direct chaotic radar employing microwave chaotic Colpitts oscillator. Prog. Electromagn. Res. **77**, 1–14 (2007)
11. T.L. Carroll, Adaptive chaotic maps for identification of complex targets. IET Radar Sonar Navig. **2**, 256–262 (2008)
12. T. Jiang, S. Qiao, Z. Shi, L. Peng, J. Huangfu, W.Z. Cui, W. Ma, L.X. Ran, Simulation and experimental evaluation of the radar signal performance of chaotic signals generated from a microwave Colpitts oscillator. Prog. Electromagn. Res. **90**, 15–30 (2009)
13. J.N. Blakely, N.J. Corron, Concept for low cost chaos radar using coherent reception. Proc. SPIE **8021**, 80211H (2011)

14. N. J. Corron, J. N. Blakely, Chaos for communication and radar. Proc. Int. Symp. Nonlinear Theory Appl. (NOLTA2011), 322–325 (2011)
15. T. Saito, H. Fujita, Chaos in a manifold piecewise linear system. Electron. Commun. Jpn. 1 **64**, 9–17 (1981)
16. N. J. Corron, J. N. Blakely, M. T. Stahl, A matched filter for chaos. Chaos **20**, 023123 (2010)
17. H. Zumbahlen (ed.), *Linear Circuit Design Handbook* (Elsevier/Newnes Press, USA, 2008)
18. G. L. Turin, An introduction to matched filters. IRE T. Inform. Theor. **6**, 311–329 (1960)

Using Phase Space Methods for Target Identification

Thomas L. Carroll and Frederic J. Rachford

Abstract The response of a radar or sonar target to a signal may be described by an impulse response function, which means that the target may be considered as a filter acting on a signal. It is known that filters are not exactly invertible, and this lack of invertibility may be used to identify the particular target that reflected a signal. We apply techniques from nonlinear dynamics to determine the probability that a function exists between 2 signals. If 2 identical signals are filtered by the same filter, then our statistic will indicate a high probability that a function exists between the 2 signals; if the 2 signals were filtered by different filters, then the statistic will show a low probability that the 2 signals are related by a function. We demonstrate target identification with both numerical simulations and acoustic experiments.

1 Introduction

Considering a radar (or sonar) target as more than a simple point scatterer brings up the possibility of identifying the target based on the reflected signal [1]. The response of a target to an incoming signal can be described by an impulse response function [2]

$$h(t,\,p) = \sum_{l=1}^{L} a_l\,(p)\delta\left[t - T_l\,(p)\right] + \sum_{m=1}^{M} b_m\,(p)\exp\left\{s_m\left[t - T_m\,(p)\right]\right\}\Theta\left[t - T_m\,(p)\right] \quad (1)$$

where p indicates that the quantity is dependent on the aspect angle. The index l is used for the specular reflections, while m is used for resonances. The coefficients

T. L. Carroll (✉) · F. J. Rachford
US Naval Research Lab, Code 6342, Washington, DC 20375, USA
e-mail: thomas.carroll@nrl.navy.mil

F. J. Rachford
e-mail: frederic.rachford@nrl.navy.mil

V. In et al. (eds.), *International Conference on Theory and Application in Nonlinear Dynamics (ICAND 2012)*, Understanding Complex Systems,
DOI: 10.1007/978-3-319-02925-2_20,

b_m and s_m are complex, and Θ is the step function. The T's are the delay times for each of the scatterers and resonances.

Based on Eq. (1), a target may be identified based on either the specular terms or on the resonant terms. To use the specular terms, a range-cross range profile is generated by matched filtering the signal reflected from the target and creating a pattern of points from the large peaks in the output of the matched filter [1]. Pattern recognition tools are then used to associate a particular pattern with a target. The patterns are highly dependent on aspect angle, so it may be necessary to compare many patterns for a particular target.

The resonant terms from Eq. 1 may also be used as identifiers [2–4]. The target is illuminated with a pulse of length T_g. After a time $t > T_g + T_m$ and $t > T_g + T_l$, only the complex exponentials remain in Eq. (1). These exponential terms are not aspect angle dependent, so measuring the decaying exponential response of the target allows one to identify the target for any aspect angle. The problem with identifying the target using this transient information is that the transient soon decays to a level below the noise background, so it's difficult to measure a long enough portion of the transient signal to identify the target. Other approaches to target identification use adaptive waveform design [5–8].

2 Filter ID Method

Because the target response may be described by an impulse response function (1), one may describe the target as a filter acting on a signal. Exact inversion of a filter is not possible, meaning that there is no function that can input a filtered signal and output the unfiltered signal. We are able to use this lack of invertibility as a means to identify a particular filter, and therefore a particular target. If a signal s is reflected from target A to give a reflected signal $s(A)$, and s is also reflected from target B to get $s(B)$, then the fact that there is no function from $s(A)$ to s, and no function from $s(B)$ to s implies that there is no function from $s(B)$ to $s(A)$ *unless* A and B are the same target (and the same signal s is used).

The impulse response function (Eq. 1) has both angle dependent and angle independent terms. The identification method described in this paper may be trained using target responses collected over a window of aspect angles, so that the angle dependent terms are averaged out, and identification is dominated by angle independent terms. Target ID methods that depend on resonances also use these angle independent terms [2–4], but unlike those methods that are based on short pulses, the method described in this paper uses a long modulated pulse, allowing us to signal average over a long pulse to improve the signal to noise ratio.

If the signals of interest are generated by deterministic dynamical systems, which is always the case for radar or sonar signals, then the signals may be analyzed using methods from the field of dynamical systems. There are algorithms from this field for determining the probability that 2 signals are related by a function [9]. These

algorithms depend on the concept of predictability ; if there is a function that inputs A and outputs $f(A)$, then one should be able to predict $f(A)$ if A is known.

A deterministic dynamical system has a finite number of variables and a set of rules that describes how these variables evolve over time. We may analyze the behavior of the dynamical system by plotting the trajectory of the system in a phase space (or state space), in which each axis corresponds to one of the variables from the system. If the dynamical system is dissipative, this trajectory forms a pattern in phase space called an attractor. Radar or sonar transmitters are examples of finite dimensional deterministic dynamical systems, so radar or sonar signals may be analyzed using dynamical systems methods.

Knowledge of the attractor for a system can be used to determine if one signal is predictable from another signal. A typical dynamical system based on ordinary differential equations , with a set of variables $\mathbf{x} = (x_1, x_2, \ldots x_d)$ may be described by

$$\frac{d\mathbf{x}}{dt} = h\,[\mathbf{x}] \tag{2}$$

We also have the set of variables $\mathbf{y} = (y_1, y_2, \ldots y_d)$, where

$$\mathbf{y} = \mathbf{f}\,(\mathbf{x}) \tag{3}$$

Consider a set of variables near $\mathbf{x}$, $\mathbf{x}_a = (x_1 + \delta_1, x_2 + \delta_2, \ldots x_d + \delta_d)$. If f is continuous and differentiable, then as

$$\delta \to 0,\ f\,(\mathbf{x}_a) \to f\,(\mathbf{x}) = \mathbf{y}. \tag{4}$$

If we have the signals $\mathbf{x}$ and $\mathbf{y}$, and would like to determine if $\mathbf{y} = \mathbf{f}\,(\mathbf{x})$, we apply the definition of Eqs. (2–4) by searching in the phase space of $\mathbf{y}$ for points that are within some distance ε of $\mathbf{y}$. We then locate the points with the corresponding time indices on $\mathbf{x}$, and measure the average distance δ between this set of points and $\mathbf{x}$. The size of this phase space radius δ is a measure of the probability that a function exists from $\mathbf{x}$ to $\mathbf{y}$. The smaller δ, the higher the probability there is a function. How to define "small" is a statistical question that we won't consider here, because we are only interested in relative measurements, i.e. given signals $\mathbf{y}$ and $\mathbf{z}$, which of these signals is more likely to be a function of $\mathbf{x}$.

2.1 Embedding

There is usually only one available signal from a radar or sonar, the signal that is transmitted and reflected, but an object that is equivalent in many ways to the signal vector $\mathbf{x}$ may be reconstructed from only one of the variables. It has been proven that it is possible to reconstruct an object that is topologically equivalent to the attractor for the dynamical system by using the method of delays [10, 11]. Using a digitized

version $s(i)$ of a continuous time signal $s(t)$. a a series of delay vectors is created from $s(i)$:

$$\mathbf{s}(i) = \left[s(i), s(i+\tau_1), \ldots s(i+\tau_{d-1})\right] \tag{5}$$

where the dimension d and delay times τ_j may be chosen by known methods [12, 13]. The set of these vectors over time form a reconstruction (also called an embedding) of the signal $s(i)$ in a phase space.

2.2 Function Statistic

When looking to see if a function exists between two signals embedded in phase space, we estimate the probability that there is a continuous function between the two signals by considering small neighborhoods in the phase space. If we want to know if there is a function that transforms signal Y into signal X, we locate a group of points on signal X that all fall within some small radius in phase space, and ask if the corresponding points on signal Y also fall within some small region. It is necessary to define what is meant by "small", but the general idea is that the smaller the region on signal Y, the more likely signal X is to be a function of Y. If signals Y and X are both produced by applying the same filter to signal Z, then the small region in Y will be at a minimum which is determined by the nearest neighbor distances on Y.

Our target ID algorithm treats a reflection from a radar target as a filter acting on signal Z. The first time we see the target, we transmit signal Z and record signal X. Later, we again transmit signal Z and receive signal Y. We then want to know if signals X and Y are reflections from the same target.

In order to detect a difference between signals, we first embed a digitized reflected signal x in a d dimensional phase space (or state space) by creating a series of delay vectors $\mathbf{x}(i) = \left[x(i), x(i+\tau_1), \ldots x(i+\tau_{d-1})\right]$. We then randomly pick some index i_1, $1 \le i_1 \le P - \tau_{d-1}$, where P is the number of points on the time series. The embedded delay vector corresponding to this index is $\mathbf{x}(i_1)$.

We then look for points that are nearby neighbors to $\mathbf{x}(i_1)$ in phase space. By neighbors, we mean the set of points for which the distance

$$d_{nni} = \sqrt{\sum_{j=0}^{d-1}\left[x\left(i_1+\tau_j\right) - x\left(i_{nni}+\tau_j\right)\right]^2} \tag{6}$$

is smallest. We find a group of M nearby phase space neighbors $\{\mathbf{x}(i_{nn1}), \mathbf{x}(i_{nn2}), \ldots \mathbf{x}(i_{nnM})\}$ and record the indices of all points: $R(i_1) = \{i_1, i_{nn1}, i_{nn2} \ldots i_{nnM}\}$. We then choose a new index point and find a new set of M neighbors, continuing until we have examined some number N of index points. The recorded sets of indices $\{R(i_1) \ldots R(i_N)\}$ form a reference which may later be used to identify this particular target.

To apply this reference, we then take a signal y which has been reflected from an unknown target and embed it in a d dimensional phase space. To make sure that the signal y is properly aligned in time with the reference x, we find the cross correlation between x and y to find out τ_y, the amount by which y leads or lags x. We then translate y by this amount so that it is aligned in time with x.

Next, from our previously recorded reference $\{R(i_1) \ldots R(i_N)\}$, we retrieve the indices of an index point and a set of neighbors. We examine the points $\{\mathbf{y}(i_1), \mathbf{y}(i_{nn1}), \mathbf{y}(i_{nn2}), \ldots \mathbf{y}(i_{nnM})\}$ on the unknown signal corresponding to these indices. If the unknown target is the same as the target used to create the reference, these points will be neighbors, and will be close together in phase space. If the unknown target is different from the reference target, the points on the unknown signal will not be neighbors, and they will be far apart in phase space. We define the phase space radius as

$$\varepsilon = \frac{1}{M} \sum_{j=1}^{M} \left| \mathbf{y}\left(i_{nnj}\right) - \mathbf{y}(i_1) \right| \tag{7}$$

where the differences are Euclidean distances. The average of the phase space radius over the entire signal as $\langle \varepsilon \rangle$.

2.3 Aspect Angle Dependence

As described in Eq. (1), part of the signal reflected from a target may be independent of the aspect angle Θ. It is possible to create a composite reference for a target that combines data from a window of angles to produce a reference that works for any angle within that window.

To produce a composite reference for a target, we follow roughly the same set of steps as above, but we use reflected signals $x(\Theta_j, t)$ from N_{ang} different angles Θ_j. We choose an index point i_1 and find the embedded points $\mathbf{x}\left(\theta_j, i_1\right)$, $j = 1, 2 \ldots N_{ang}$ on each of the signals corresponding to this index. We then search for a group of indices $\{i_{nn1}, i_{nn2} \ldots i_{nnM}\}$ whose corresponding points $\{\mathbf{x}\left(\theta_j, i_{nn1}\right), \mathbf{x}\left(\theta_j, i_{nn2}\right), \ldots \mathbf{x}\left(\theta_j, i_{nnM}\right)\}$, $j = 1, 2 \ldots N_{ang}$ fall within some minimum radius of the center point for all the signals, or for every angle,

$$\max_k \left(\left| \mathbf{x}\left(\theta_j, i_{nnk}\right) - \mathbf{x}\left(\theta_j, i_1\right) \right| \right) \leq \delta \quad j = 1, 2 \ldots N_{ang} \tag{8}$$

where k is the index of a nearest phase space neighbor. These points may have different locations on different signals The distance δ is then the smallest distance for which we can find M points that satisfy Eq. (8) for every angle (every value of j). For an individual signal, this set of indices probably does not give the closest M points to the center point.

As previously, these point indices are recorded and then a new index is chosen for a new set of center points. The set of recorded indices then forms a composite reference for the particular shape. When an unknown signal y is received, this composite reference is used to calculate $\langle \varepsilon \rangle$.

2.4 Phase Space Strands for Noise Mitigation

The effect of noise on the phase space distance $\langle \varepsilon \rangle$ was discussed in [14]. In [15], instead of searching for nearby points in phase space, a search was made for continuous portions of phase space trajectories called phase space strands. Phase space strands may also be used with the target identification algorithm to aid in distinguishing targets in noisy situations. The strand method is essentially the same as our phase space target identification algorithm, except that we compare distances between continuous sets of points in phase space, rather than just single points.

Phase space strands were first used for dimension estimation [16]. A strand is a group of consecutive points on a trajectory in phase space, rather than just one point. In order to create a reference from the reflected signal x, we first choose an index point on x. The strand of length n_s starting with $\mathbf{x}(i_0)$ is defined as

$$\mathbf{s}\left[\mathbf{x}\left(i_0\right)\right] = \left[\mathbf{x}\left(i_0\right), \mathbf{x}\left(i_0+1\right), \ldots \mathbf{x}\left(i_0+n_s-1\right)\right] \tag{9}$$

We then search for a number of strands $\mathbf{s}\left[\mathbf{x}\left(j\right)\right]$ on the signal x which have the smallest Euclidean distance from $\mathbf{s}\left[\mathbf{x}\left(i_0\right)\right]$. For a reference, we store the indices of the starting points on these strands. When we want to compare to an unknown signal y, we construct the strands $\mathbf{y}(i_0)$ and $\mathbf{y}(j)$ and find the radius

$$\varepsilon = \frac{1}{N_s}\sum_{j=1}^{N_s}\sqrt{\sum_{k=1}^{d}\left[y\left(j+\tau_d\right)-y\left(i_0+\tau_d\right)\right]^2} \tag{10}$$

which is then averaged over all the indices in the reference to get $\langle \varepsilon \rangle$. As with the single point method, a composite reference for multiple angles may be produced by finding the set of strands that minimize the distance for the signals from all the angles used to produce the reference (Eq. 8).

3 Finite Difference Time Domain Simulations

We tested the target ID algorithm with finite difference time domain (FDTD) [17] simulations of several simple radar targets. In the FDTD code, we defined a target shape, including types of materials used (all conductors for these simulations), and an incident RF signal. The FDTD code then simulated the electromagnetic scattering

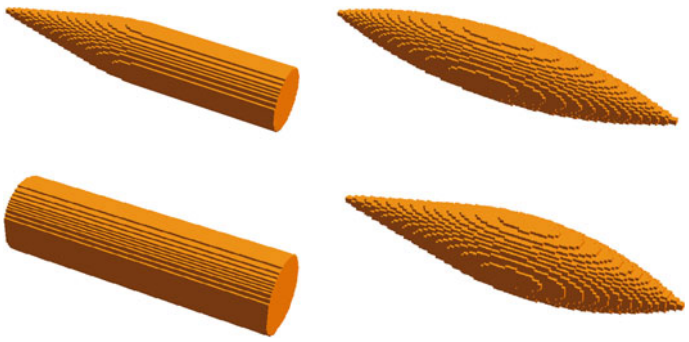

Fig. 1 (*Color online*) Shell (*top*), cylinder (*bottom*), double ogive (*top*) and cone ogive (*bottom*) models used in the FDTD simulations. All objects are 13 cm in diameter and 67 cm long

problem for the target and output a reflected signal. We began with two similar shapes, a shape that approximated a 130 mm artillery shell, and a cylinder of the same size. These two shapes are shown in Fig. 1 Both objects were 13 cm in diameter and 67 cm long . We created a frequency modulated signal based on the chaotic map

$$z\,(n+1) = 2.1z\,(n) \qquad \mathrm{mod}\ \ 1 \tag{11}$$

The frequency modulated signal was created from a series of concatenated sinusoids, with the frequency of the $n'th$ sinusoid determined by $\zeta\,(n) = 1.0 + \beta\,(z\,(n) + 0.5)$, where β was used to vary the modulation bandwidth. The sinusoids were matched in phase when one sinusoid ended and the other began. Mathematically, the nth sinusoid of s was given by

$$s\,(i) = \sin\left(2\pi t / \left[20\zeta\,(n)\right]\right)\left[i = 0, 1, 2 \ldots, i < 20\zeta\,(n)\right] \tag{12}$$

If $\zeta(n) = 1$, then the period of the sinusoid was 20 points.

The signal used with the FDTD simulations had a center frequency of 2 GHz and a bandwidth of approximately 400 MHz. The length of one pulse was 5.97×10^{-7} s, or 1200 sinusoids (just over 63,000 points). The range resolution of the pulse, estimated from its autocorrelation, was about 37.5 cm. We are not actually imaging the target, but matching it to a reference, which is why we can use a low resolution signal. The FDTD code transmitted each pulse as linearly polarized electromagnetic wave with the electric field polarization in the plane of the target. The wave was transmitted at 0° elevation and azimuthal angles from 0 to 20°. The mono-static back scattered pulse was collected in each instance and employed in this analysis. The grid size used to model the missiles was 5 mm.

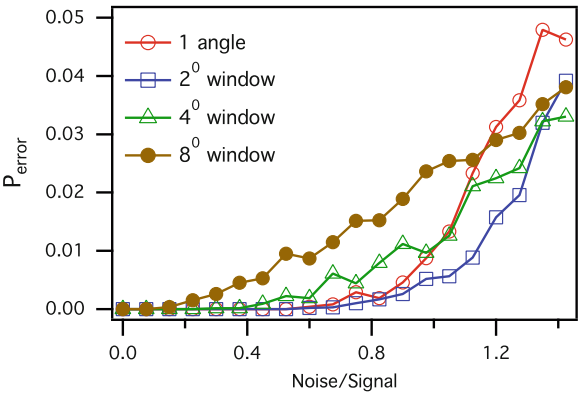

Fig. 2 (*Color online*) Fraction of errors in determining which of 4 shapes is present, as a function of added noise level. References for each shape were fitted for one angle or an angular window

3.1 Identification

We attempted to identify the different shapes when noise was present. For identification in the presence of noise, we used four different shapes, a cylinder, a shell, a shape consisting of two ogives back to back (the double ogive), and a shape containing a cone and an ogive back to back (the cone ogive).

For the noise studies, bandpass filtered noise was added to all signals. The noise was filtered to have the same bandwidth as the signals. We fitted composite references to signals covering angular windows of widths from 1 to 8°. We then compared unknown signals recorded for individual angles within the same windows to these composite references. For a given reference, if an unknown signal other than the correct unknown signal (the signal reflected from the same shape used to create the reference) gave a smaller phase space distance $\langle \varepsilon \rangle$, we counted the result as an error. We then divide the number of errors by the number of comparisons; there are four targets, and each is compared to the other three possible targets, so there are 12 chances to make an error. We also use 100 different realizations of the noise for each angle comparison. The results are shown in Fig. 2.

In Fig. 2, the largest error fraction sometimes occurs when a reference is generated from only a single angle. The errors are smaller for larger windows because when a reference is fit over a range of angles, the noise for each individual angle is averaged out, leading to a better reference. We confirmed this observation by repeating the noise simulations when no noise was added to the signals used to create the references, in which case the single angle reference gave the smallest error.

For all of these signals, the fraction of errors is only about 4 % for windows up to 8° wide, even when the noise level is larger than the signal. The 4 shapes used are very similar to each other, so distinguishing them is difficult, but the phase space radius method is able to tell the difference even in the presence of noise.

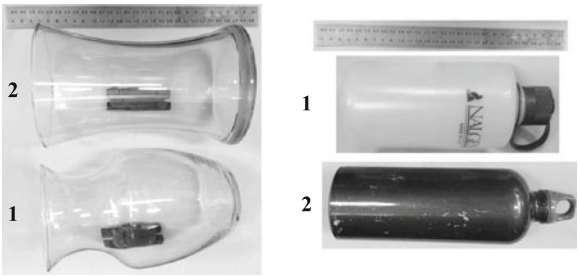

Fig. 3 The 2 glass vases (1 and 2) and the 2 bottles (1 and 2) that were used as targets. The ruler at the top of the picture was 30 cm long. The dark objects under the vases are mounting posts used to mount the vases.

4 Experiments

We used acoustic experiments as an inexpensive substitute for radar experiments. The target ID method was tested in acoustic experiments using objects with similar shapes and sizes. The targets were 2 glass vases and 2 bottles, shown in Fig. 3.

A speaker was driven with a frequency modulated signal based on a chaotic map. The map was described by

$$z(n+1) = 2.1z(n) \quad \mod 1 \tag{13}$$

The frequency modulated signal was created from a series of concatenated sinusoids, with the frequency of the $n'th$ sinusoid determined by $\zeta(n) = 1.0 + \beta(z(n) + 0.5)$, where β was used to vary the modulation bandwidth. The sinusoids were matched in phase when one sinusoid ended and the other began. Mathematically, the $n-th$ sinusoid of s was given by

$$s(i) = \sin(2\pi t / [40\zeta(n)])\,[i = 0, 1, 2 \ldots, i < 40\zeta(n)] \tag{14}$$

If $\zeta(n) = 1$, then the period of the sinusoid was 40 points.

The center frequency of the signal driving the speaker was 10 KHz, and the bandwidth was 2 KHz. The targets were mounted on a rotator that was approximately 2 m from the speaker. The reflected signal was recorded by a microphone placed just below the speaker. Because of the short distance from speaker to target, the transmitted signal was divided into 15 different pulses of 4 ms each. Each reflected pulse was digitized at a rate of 500 KHz. The pulses were combined after digitization by embedding all of them in the same phase space. Because of the large background noise, each set of 15 pulses was transmitted 10 times, and the reflections were coherently averaged in time to reduce noise. We used sound absorbing materials to lessen the acoustic clutter in the experiment, but we did not use an anechoic chamber, so clutter and noise were still present.

For each target, a set of references was created by reflecting signals from the target for each target rotation angle from 0 to 360°. Each target was then dismounted from the rotator. Unknown signals were then created by once again mounting each target on the rotator and again reflecting signals from the target for angles from 0 to 360°. Creating separate reference and unknown signals allowed us to test if the target ID method was robust to errors in target alignment and the different noise signals present at different times. The signal to noise plus clutter ratio for the reflected signals varied from $+3$ to $-10\,dB$, depending on the target rotation angle.

As described in above, additive noise increases the phase space distances between points or strands for an embedded signal. The changing signal to noise ratio for different aspect angles of the targets will therefore affect the measurements of phase space radius, altering the results of target identification. In order to minimize this effect, filtered noise was added to the signals to equalize the signal to noise ratios. The distance between closest strands in an embedded signal is proportional to the noise level [15], so the distances to nearest neighbor strands for all signals were used as an indicator of the signal to noise ratio; the smaller the distance, the smaller the signal to noise ratio. A Gaussian random noise signal was filtered to match the bandwidth of the reflected signals, and was added to each signal with an amplitude proportional to the difference between the nearest strand distance for that signal and the largest value of the nearest strand distance for all signals.

We reflected signals from each of the four targets as before, creating separate reference and unknown signals. For a given unknown signal, we calculated the average phase space radius for each of the four references. For each comparison, we compared a target return signal from one angle to references from every angular window for every target. If a reference from the correct target gave the smallest phase space radius, we recorded a correct identification; otherwise, we recorded an error. We repeated the identification process for composite references that spanned windows from 1 to 90°. The references did not overlap, so the total number of references ranged from 180 to 2.

Figure 4 shows the probability of making an error when deciding which of the four targets is present from the acoustic experimental data. The probability of error drops as the window width increases because using composite references for a large range of angles averages out noise and target alignment errors. The fact that the error probability drops as the window width increases also indicated that this target ID method is most sensitive to resonances in the target, because these resonances are independent of the aspect angle.

5 Conclusions

We were able to identify different targets based on the properties of their impulse response functions. The results show that this target ID method is similar to ID methods that use target resonances, but the current method uses long modulated pulses, allowing for time averaging to improve the signal to noise.

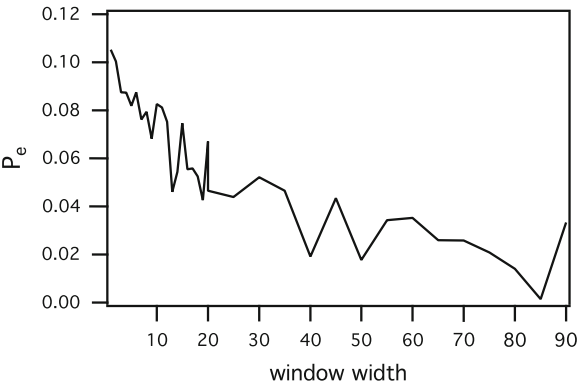

Fig. 4 Probability of making an error (P_e)when determining which of four targets was present, as reference window widths were increased from 1 to 90°. Target retruns from each individual angle were compared to composite references fitted over larger windows. The probability of error decreases as window width increases because the larger reference windows result in averaging of the reference which reduces noise and alignment errors.

Because of limits in our experimental system, the signals we used for training our method (the reference signals) were contaminated by noise. If we had low noise training data, this method should be able to yield a lower probability of error.

The theory behind this method depends on all signals coming from low dimensional dynamical systems, although the method will also work with randomly modulated signals, and random signals have an infinite number of dimensions. The random signal must be modulated onto a carrier in some way however, and while the global dimension of this carrier may be infinite, the local dimension is finite. so the target ID algorithm still works.

References

1. A.W. Rihaczek, S.J. Hershkowitz, *Theory and Practice of Radar Target Identification* (Artech House, Norwood, 2000)
2. A.J. Berni, Target identification by natural resonance estimation. Aerospace and electronic systems. IEEE Trans. AES **11**, 147–154 (1975)
3. E. Kennaugh, The K-pulse concept. IEEE Trans. Antennas propag. **29**, 327–331 (1981)
4. E. Rothwell, C. Kun-Mu, D. Nyquist, Extraction of the natural frequencies of a radar target from a measured response using E-pulse techniques. IEEE Trans. Antennas Propag. **35**, 715–720 (1987)
5. J.S. Bergin, P.M. Techau, J.E.D. Carlos, J.R. Guerci, in *Radar Waveform Optimization for Colored Noise Mitigation, IEEE Radar Conference*. IEEE, Alexandria, pp. 149–154 (2005)
6. S.U. Pillai, H.S. Oh, D.C. Youla, J.R. Guerci, Optimum transmit receiver design in the presence of signal-dependent interference and channel noise. IEEE Trans. Inf. Theory **46**, 577–584 (2000)
7. M. Vespe, C.J. Baker, H.D. Griffiths, Automatic target regognition using multi-diversity radar. Radar Sonar Navig. IET **1**, 470–478 (2007)

8. T.L. Carroll, Optimizing chaos-based signals for complex radar targets. Chaos **17**, 033103 (2007)
9. L.M. Pecora, T.L. Carroll, J.F. Heagy, Statistics for mathematical properties between time series embeddings. Phys. Rev. E **52**, 3420–3439 (1995)
10. F. Takens, in *Dynamical Systems and Turbulence*, eds. by D. Rand, L.-S. Young (Springer, Berlin, 1981)
11. T. Sauer, J.A. Yorke, M. Casdagli, Embedology. J. Stat. Phys. **65**, 579–616 (1991)
12. H.D.I. Abarbanel, R. Brown., J.J. Sidorowich, L.S. Tsmring, The analysis of observed chaotic data in physical systems. Rev. Modern Phys. **65**, 1331–1392 (1993)
13. L.M. Pecora, L. Moniz, J. Nichols, T.L. Carroll, A unified approach to attractor reconstruction. Chaos: an interdisciplinary. J. Nonlinear Sci. **17**, 013110–013119 (2007)
14. T.L. Carroll, F.J. Rachford, Using filtering effects to identify objects. Chaos: an interdisciplinary. J. Nonlinear Sci. **22**, 023107-9 (2012)
15. T.L. Carroll, Detecting variation in chaotic attractors. Chaos: an interdisciplinary. J. Nonlinear Sci. **21**, 023128-6 (2011)
16. M.B. Kennel, H.D.I. Abarbanel, False neighbors and false strands: a reliable minimum embedding dimension algorithm. Phys. Rev. E **66**, 026209 (2002)
17. A. Taflove, S.C. Hagness, *Computational Electrodynamics: The Finite Difference Time Domain Method* (Artech House, Norwood, 2005)

Effect of Voltage Oscillations on Response Properties in a Model of Sensory Hair Cell

Rami M. Amro and Alexander B. Neiman

Abstract Sensory hair cells in auditory and vestibular organs rely on active mechanisms to achieve high sensitivity and frequency selectivity. Recent experimental studies have documented self-sustained oscillations in hair cells of lower vertebrates on two distinct levels. First, the hair bundle can undergo spontaneous mechanical oscillations. Second, somatic electric voltage oscillations across the basolateral membrane of the hair cell have been observed. We develop a biophysical model of the bullfrog's saccular hair cell consisting of two compartments, mechanical and electrical, to study how the mechanical and the voltage oscillations interact to produce coherent self-sustained oscillations and how this interaction contributes to the overall sensitivity and selectivity of the hair cell. The model incorporates nonlinear mechanical stochastic hair bundle system coupled bi-directionally to a Hodgkin-Huxley type system describing somatic ionic currents. We isolate regions of coherent spontaneous oscillations in the parameter space of the model and then study how coupling between compartments affects sensitivity of the hair cell to external mechanical perturbations. We show that spontaneous electrical oscillations may enhance significantly the sensitivity and selectivity of the hair cell.

1 Introduction

Hair cells are peripheral sensory receptors in the inner ear of vertebrates which transduce mechanical vibrations to electrical signals [1, 2]. External mechanical perturbations are translated to electrical signals through the mechano-electrical transduction (MET) channels located in the stereocilia, apical projections of the cell immersed in

R. M. Amro (✉) · A. B. Neiman
Department of Physics and Astronomy, Ohio University, Athens, OH, 45701, USA
e-mail: ramiamro11@gmail.com

A. B. Neiman
e-mail: neimana@ohio.edu

V. In et al. (eds.), *International Conference on Theory and Application in Nonlinear Dynamics (ICAND 2012)*, Understanding Complex Systems,
DOI: 10.1007/978-3-319-02925-2_21,

potassium (K) rich endolymph. Stereocilia are arranged in the hair bundle in rows of increasing heights and linked by the so-called tip links. External mechanical perturbations deflect the hair bundle causing the tension in the tip links to change, which may elicit opening or closing of MET channels, mediating the influx of potassium and calcium ions to the cell and thus changing the cell's potential. Experimentally observed extreme sensitivity and frequency selectivity of hair cells suggested several mechanisms of active amplifications [1–3]. One of these mechanisms relies on active dynamics of the hair bundle which can be placed at the verge of dynamical instability, i.e. Andronov-Hopf bifurcation, providing the cell with high sensitivity, sharp frequency tuning curve and a compressive nonlinearity [4–6]. MET channels open in concert and exert forces on the hair bundle, the phenomenon known as gating compliance [7], resulting in a nonlinear force-displacement relation. In some hair cells the gating compliance may result in a differential negative stiffness of the hair bundle leading to its instability [8]. Combined with myosin-mediated adaptation [9, 10] this nonlinearity results in spontaneous mechanical hair bundle oscillatory motion. In particular, spontaneous oscillations of the hair bundle have been observed in many lower vertebrates such as amphibian sacculus, or turtle basilar paplia [11–15] and presumably responsible for the phenomenon of otoacoustic emissions in nonmammals [11, 12, 16]. Importantly, spontaneous hair bundle oscillations are essentially stochastic due to several thermal noise sources [17]. This natural stochasticity can be reduced in coupled hair bundles [18, 19].

Intriguingly, the same type of hair cells show spontaneous oscillations of the membrane potential. For example, several experimental groups reported on spontaneous voltage oscillations in saccular hair cells [20–23]. The functional role of these large-amplitude voltage oscillations is currently not known. One suggestion is that voltage oscillations provide additional feedback to the hair bundle dynamics which may help to reduce thermal fluctuations and thus to improve sensitivity of the hair cell [24]. Indeed earlier studies reported on reverse electro-mechanical transduction, providing evidence for bi-directional coupling between the hair bundle complex and the potential of the cell body [25]. Furthermore, transepithelial electrical stimulation of hair cells elicits the hair bundle motion [26]. Finally, a recent experimental study showed that somatic ionic conductances affect significantly the mechanical oscillations of hair bundles. [27].

In this paper we develop a model of sensory hair cell which includes mechanical and electrical compartments coupled bidirectionally. Sensitivity, frequency selectivity and compressive nonlinearity are three main features of the hair bundle dynamics [6]. We use the model to study how the coupling affects these three feature of the hair cell dynamics.

2 Two Compartmental Model of a Hair Cell

Our two compartmental system is based on previously developed models for the hair bundle mechanics and for the dynamics of the cell potential of the bullfrog's saccular hair cells. The coupling between the two compartments is bidirectional. The

Table 1 Parameters of the mechanical compartment

Symbol	Definition	value
λ	Drag coefficient of the hair bundle	2.8 μNs/m
λ_a	Effective friction coefficient of the molecular motors	10.0 μNs/m
K_{GS}	Gating spring stiffness	0.75 mN/m
K_{SP}	Stereocilia pivots stiffness	0.6 mN/m
D	Gating swing of MET channel	60.9 nm
T	Ambient temperature	300K
F_{max}	Maximal motors force	55 pN
S	Dimensionless Ca feedback strength	1.13
P_o	Open probability of MET channels	
N	Number of MET channels	50
ΔG	Energy change on MET channel opening	$10k_BT$

coupling from the mechanical to electrical compartment is due to direct mechano-electrical transduction, i.e. due to the MET current [28, 29]. The coupling from the electrical to mechanical compartment is mediated by the reverse electro-mechanical transduction whereby the cell voltage affects the calcium ions concentration near the myosin molecular motors controlling the adaptation rate of the hair bundle.

Several simple models were proposed to account for the active hair bundle motion including spontaneous mechanical oscillations in the bullforg's sacculus [14, 17, 30–33]. In this paper we use a model proposed in [17, 31]. The overdamped dynamics of the hair bundle are described by two stochastic differential equations: first for the position of the bundle tip, X and second for the displacement of the myosin motors, X_a along the stereocilia:

$$\begin{aligned}
\lambda\frac{dX}{dt} &= -K_{GS}(X - X_a - D\,P_o) - K_{SP}X + F_{ext}(t) + \sqrt{2k_BT\lambda}\eta(t),\\
\lambda_a\frac{dX_a}{dt} &= K_{GS}(X - X_a - D\,P_o) - F_{max}(1 - S\,P_o) + \sqrt{2k_BT\lambda_a}\eta_a(t),\\
P_o(X, X_a) &= \frac{1}{1 + A\,e^{-(X-X_a)K_{GS}D/(Nk_BT)}}, \quad A = e^{[\Delta G + K_{GS}D^2/(2N)]/(k_BT)}.
\end{aligned} \tag{1}$$

In Eq. (1) $\eta(t)$ and $\eta_a(t)$ are uncorrelated Gaussian white noise sources modeling thermal noise due to Brownian motion, MET channel cluttering and stochastic binding and unbinding of adaptation motors [17]. The external stimulus enters the model via the external force term $F_{ext}(t)$. Definition of parameters and their values are given in Table 1 and are essentially the same as used in [17, 18]. The control parameters of the hair bundle model are S and F_{max} which determine the strength of calcium (Ca) influence on adaptation motors and maximal force generated by the motors at stall when all MET channels are closed, respectively.

The dynamics of the cell's potential can be described by a Hodgkin-Huxley type system developed in [21–23]. We used a modified version of this model described in

details in [34]. The model includes 6 basolateral ionic currents and the MET current. The current balance equation is

$$C_{\mathrm{m}}\frac{dV}{dt} = -I_{\mathrm{K1}} - I_{\mathrm{BKS}} - I_{\mathrm{BKT}} - I_{\mathrm{DRK}} - I_{\mathrm{h}} - I_{\mathrm{Ca}} - I_{\mathrm{MET}}, \tag{2}$$

where I_{K1} is the inwardly rectifier potassium (K) current, I_{BKS} and I_{BKT} are Ca-activated steady and transient K currents, I_{h} is sodium / potassium h-type current, I_{DRK} is the delayed rectifier K current and I_{Ca} is the Ca current. The equation for the potential (2) is accompanied by equations for kinetics of ionic currents listed and for intracellular $[Ca^{2+}]$, totaling 12 differential equations. The detailed description of this system and parameters is provided in [34]. The control parameters of the electrical compartment are the maximal conductance of inwardly rectifier current, g_{K1}, and relative strength of Ca-activated currents, b_{K}. Depending on these two parameters, the electrical compartment shows rich variety of oscillatory patterns including quasi-periodic, bursting and chaotic oscillations [34]. By setting the fast activation variable for the inwardly rectifier current (I_{K1}) and $[Ca^{2+}]$ to their steady states we reduced the dimension of the electrical compartment by 2. We verified that this reduction did not change the voltage dynamics quantitatively.

Forward coupling from the mechanical to the electrical compartment is due to the MET current entering in Eq. (2),

$$I_{\mathrm{MET}} = g_{\mathrm{MET}} P_{\mathrm{o}}(X, X_{\mathrm{a}})(V(t) - E_{\mathrm{MET}}), \tag{3}$$

where $E_{\mathrm{MET}} = 0$ mV is the reversal potential potential and g_{MET} is the maximal value of the MET conductance, i.e. when all MET channels are open. The MET conductance g_{MET} thus serves as a "forward" coupling parameter. The dynamics of the hair bundle depend crucially on the concentration of Ca ions at the adaptation motors cite $[Ca^{2+}]_{\mathrm{M}}$, which is determined by the open probability of MET channels and by the potential of the cell V via electrodiffusion [14, 31]. For example, a decrease of the receptor potential V enhances the influx of Ca ions through MET channels resulting in increase of $[Ca^{2+}]_{\mathrm{M}}$ which in turn inhibits the motor activity. This backward "voltage to mechanics" coupling can be introduced via voltage-dependent calcium feedback parameter $S(V)$ in Eq.(1) [24],

$$S(V) = S_0 \frac{f(V)}{f(V_0)}, \quad f(V) = \frac{\varepsilon V}{1 - e^{\varepsilon V}}, \quad \varepsilon = 2q_e/(k_{\mathrm{B}}T),$$

where S_0 is a value of the feedback parameter S at a reference potential $V = V_0 = -55$ mV and q_e is the elementary charge. Since the voltage deviations are in the range -80 to -30 mV, $S(V)$ can be approximated by its first order Taylor expansion around the reference potential,

$$S(V) = S_0\,[1 + \alpha(V/V_0 - 1)]\,, \tag{4}$$

where we introduced the dimensionless parameter α controlling the strength of the backward coupling, such that $\alpha = 0$ corresponds to the hair bundle uncoupled from the variations of the receptor potential.

Two compartmental stochastic model composed of the hair bundle model (1) and of the Hodgkin-Huxley type model for the membrane potential (2) coupled via Eqs. (3) and (4) was studied numerically using the Euler-Maruyama method with the time step 0.1 ms. The control parameters of both compartments were chosen such that in the absence of coupling, stimulus and noise ($\alpha = 0$, $g_{\mathrm{MET}} = 0$, $F_{\mathrm{ext}} = 0$, $\eta = \eta_{\mathrm{a}} = 0$), the hair bundle and the voltage were at a stable equilibrium. In particular we fixed the parameters of the mechanical compartment at $(F_{\mathrm{max}}, S) = (55\ \mathrm{pN}, 1.13)$, and the parameters of the electrical compartment at $(b_{\mathrm{K}}, g_{\mathrm{K1}}) = (0.01, 1.0\ \mathrm{nS})$. The coupling strengths g_{MET} and α were then used as control parameters. Bifurcation analysis of equilibrium states of the deterministic model, i.e. stochastic terms η, $\eta_{\mathrm{a}} = 0$ in Eq. 1, was performed using CONTENT continuation software package [35]. We then explored spontaneous stochastic dynamics of the model versus the coupling strengths. In particular we calculated the power spectral density (PSD) of spontaneous hair bundle motion and then measured the quality factor Q of the main peak in the specrum and the mean amplitude of spontaneous oscillations as a function of the coupling strengths g_{MET} and α.

The sensitivity and frequency selectivity of the hair cell were estimated using periodic external force,

$$F_{\mathrm{ext}}(t) = F_0 \cos(2\pi f_{\mathrm{s}} t), \tag{5}$$

applied to the mechanical compartment (1). We calculated the time dependent averages of the hair bundle position, $\langle X(t) \rangle$ and of the membrane potential $\langle V(t) \rangle$ by averaging over 300 realizations of stochastic terms η and η_a during 500 periods of the external sinusoidal force. We then estimated the mechanical and electrical sensitivities as the ratios of the first Fourier harmonic of these averages, $\tilde{X}(f_{\mathrm{s}})$; $\tilde{V}(f_{\mathrm{s}})$, to the amplitude of the stimulus, F_0,

$$\chi_f(f_{\mathrm{s}}, F_0) = |\tilde{X}(f_{\mathrm{s}})|/F_0, \quad \chi_V(f_{\mathrm{s}}, F_0) = |\tilde{V}(f_{\mathrm{s}})|/F_0, \tag{6}$$

in units of nm/pN for the mechanical sensitivity χ_f, and mV/pN for the electrical sensitivity, χ_V.

3 Results and Discussion

In absence of coupling and noise the deterministic model is at a stable equilibrium, i.e. the mechanical compartment is at equilibrium with most of MET channels closed, $P_{\mathrm{o}} \approx 0.19$ and the electrical compartment is at $V = -53.5\ \mathrm{mV}$. With the increase of coupling, the equilibrium bifurcates to a limit cycle via the Andronov-Hopf (AH) bifurcation. On the parameter plane $(g_{\mathrm{MET}}, \alpha)$ the lines of the AH bifurcations isolate a region of spontaneous oscillations, shown in Fig. 1. In the region below the lower

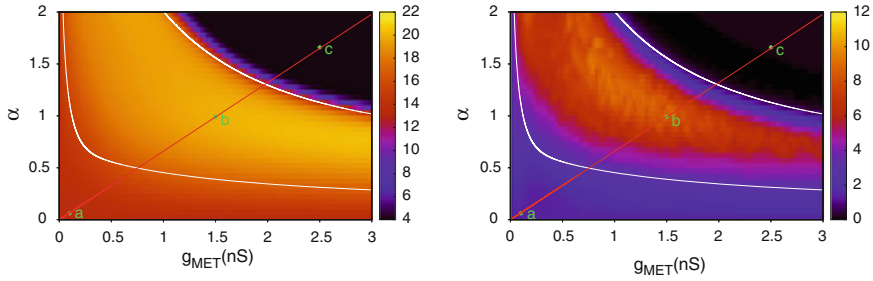

Fig. 1 Spontaneous dynamics of the hair cell model versus coupling strengths between mechanical and electrical compartments. *Left*: Amplidute of the hair bundle oscillationhs versus coupling strengths; the *color bar* in the *right* is in nm. *Right*: Quality factor Q of the main peak in the power spectral density of the hair bundle oscillation. On both panels the AH bifurcation lines of the deterministic system are shown by *white lines*. Points *a*, *b* and *c* indicate three different regions discussed in the text

AH bifurcation line, most of MET channels are closed, while in the region above the upper AH bifurcation line most of MET channels are open and the cell is depolarized. In the region between the AH bifurcation lines the deterministic model exhibits large-amplitude synchronous oscillations in mechanical and electrical compartments.
Thermal noise induces stochastic hair bundle oscillations even outside the deterministic oscillatory region. Figure 1 (left panel) shows that a region of large amplitude mechanical oscillations extends below the lower boundary of deterministic oscillatory region. Noise-induced bundle motion leads to opening of MET channels and since the Ca feedback is relatively weak below the lower AH bifurcation line, adaptation brings the bundle back to the equilibrium position allowing large-amplitude oscillation. On the contrary, above the upper boundary of deterministic oscillatory region large values of the backward coupling α lead to weak adaptation resulting in small-amplitude fluctuations of the hair bundle around the equilibrium with open MET channels. This is illustrated in Fig. 2 which shows the hair bundle displacement and the voltage traces at three points corresponding to three distinct regions on the parameter plane of the system (cf Fig. 1).

The coherence of spontaneous oscillations quantified with the quality factor, Q, of the main peak in the PSD of the hair bundle position, shows non-monotonous behavior being maximal at the center of the oscillatory region (point b in the right panel of Fig. 1). In the region below the lower AH line (point a in Figs. 1 and 2) the dynamics of the system is dominated by noise resulting in noisy oscillations around the equilibrium with broad peaks in PSDs at the natural frequency determined by the imaginary parts of the equilibrium's eigenvalues. In the deterministic oscillatory region (point b in Figs. 1 and 2) both compartments show synchronous and coherent oscillations with sharp peaks in PSDs. Finally, the region above the upper AH line (point c in Figs. 1 and 2) is characterized by overdamped small amplitude fluctuations with a low-frequency Lorentzian type PSD. The effect of the backward electro-mechanical

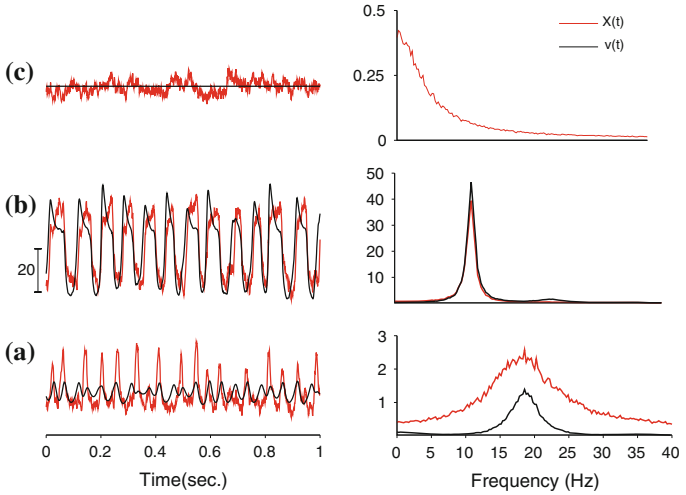

Fig. 2 Time series (*left*) and PSDs (*right*) of spontaneous mechanical oscillations (*red*, [nm]), and membrane potential (*black*, [mV]) for the points shown in Fig. 1. Units of PSDs are [nm^2/Hz] for the hair bundle displacement and [mV^2/Hz] for the membrane potential

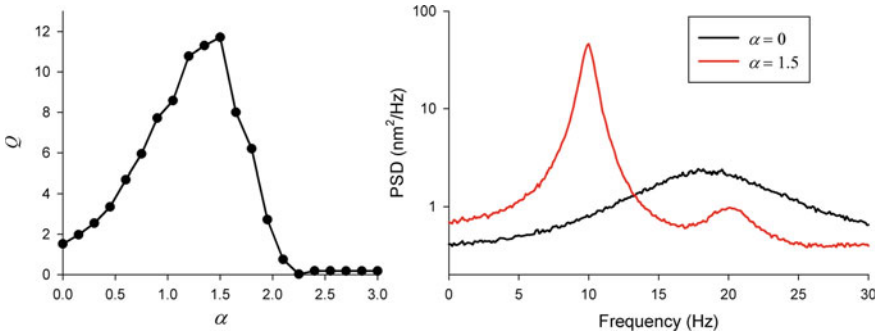

Fig. 3 Influence of the electrical compartment on the hair bundle oscillation. *Left*: Quality factor of the mechanical oscillation versus the backward coupling strength α for the fixed value of the MET conductance, $g_{\mathrm{MET}} = 1$ nS. *Right*: PSD of the hair bundle displacement for indicated values of α

coupling on the hair bundle dynamics is further illustrated in Fig. 3 showing that the coherence of spontaneous hair bundle oscillations is maximized by the backward coupling α.

Frequency response of mechanical and electrical compartments is shown in Fig. 4 for a weak mechanical sinusoidal stimulus (5). Sensitivity of mechanical and electrical compartments peaks at the frequency of spontaneous oscillations. Furthermore, the peak values of sensitivity is largest for the coupling strength corresponding to the most coherent spontaneous oscillations (cf Fig. 3, left panel). The sensitivity as a function of the stimulus strength shown in the lower panels of Fig. 4, demonstrates

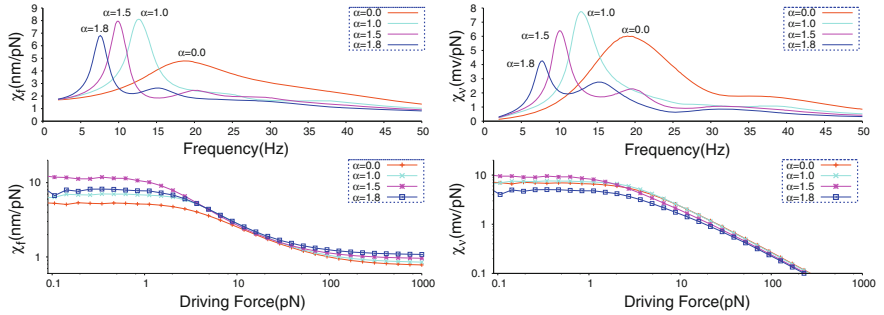

Fig. 4 Effect of the backward coupling on sensitivity of the hair cell model to external periodic force. *Left column* shows the mechanical sensitivity, i.e. the hair bundle sensitivity, χ_f. *Right column* shows the electrical sensitivity, χ_V. *Top panels* shows sensitivity versus stimulus frequency, f_s, for the fixed value of the stimulus amplitude $F_0 = 2$ pN and for indicated values of the backward coupling strength α. *Bottom panels* show the sensitivity versus stimulus amplitude, F_0. For indicated value of α the stimulus frequency was chosen to match the frequency of spontaneous oscillation. Direct mechano-electrical coupling strength was fixed at $g_{\mathrm{MET}} = 1$ nS

the phenomenon of compressive nonlinearity. Both compartments respond linearly to weak stimuli, while the sensitivity to stronger stimuli is suppressed. The differences in response properties appear for strong stimuli $F_0 > 100$ pN where the hair bundle starts to respond linearly again, while the sensitivity of the electrical compartment continues to decline. We note that similar effect was reported in [34] for voltage response where a linear model for the hair bundle was used. We also note that the backward coupling strength does not affect significantly the scaling of sensitivity with the stimulus amplitude.

The hair bundle sensitivity was studied for a wide range of forward and backward coupling strengths ($g_{\mathrm{MET}} \in [0, 3]$nS), ($\alpha \in [0, 2]$). For each values of g_{MET} and α we estimated the maximum sensitivity by varying the stimulus frequency f_s and then plotted this maximum value of sensitivity as a color-coded map. The resulting maximal sensitivity map is shown in Fig. 5, left panel. This map clearly shows the existence of optimal coupling strengths at which the hair cell is most sensitive to periodic perturbations. For a fixed value of the forward coupling strength $g_{\mathrm{MET}} = 1.0$ nS the sensitivity of the hair bundle peaks near $\alpha = 1.5$, shown on the right panel of Fig. 5, and corresponding well to the most coherent spontaneous oscillation (see Fig. 3).

4 Conclusions

The role of active processes in operational performance of sensory hair cells is a topic of intense current interest in sensory neuroscience [1–3, 36, 37]. In particular, the role of active hair bundle dynamics is a matter of debate [3, 6]. However,

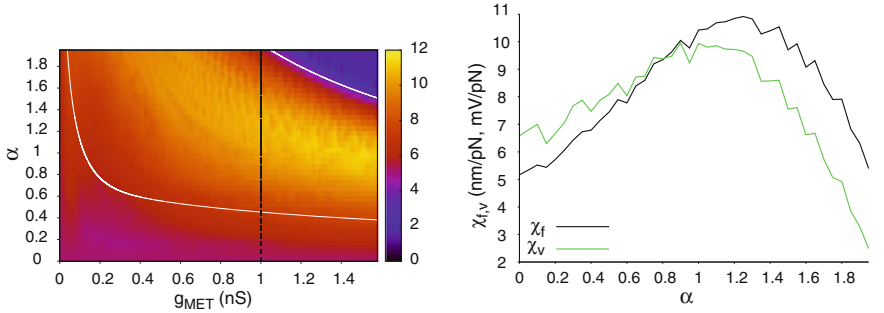

Fig. 5 Maximal sensitivity of the hair cell model to weak sinusoidal force, $F_0 = 1$ pN. *Left panel* shows maximal sensitivity of the hair bundle versus both forward (g_{MET}) and backward (α) coupling strengths. *Right panel* shows sensitivities of the hair bundle and membrane potential versus α for the fixed value $g_{\mathrm{MET}} = 1$ nS

hair cells in lower vertebrates demonstrate also spontaneous oscillations of somatic potential which presumably may affect mechanics of the hair bundle, or may be a result of bi-directional coupling of mechanical and electrical constituents of the hair cell. Unlike many previous modeling works which studied mechanical and electrical dynamics separately, we constructed a model incorporating nonlinear mechanical and electrical compartments coupled bi-directionally. We showed that spontaneous oscillations may arise due to bi-directional coupling even when uncoupled compartments are quiescent. The coherence of oscillations can be enhanced by tuning the coupling strengths between compartments resulting in enhanced sensitivity and sharper tuning to weak periodic mechanical stimulus. At the same time, the model shows other distinctive behaviors, such as compressive nonlinearity.

Acknowledgments We thank B. Lindner and A. Shilnikov for fruitful discussions. This work was supported in part by the Quantitative Biology Institute at Ohio University.

References

1. R. Fettiplace, C. Hackney, The sensory and motor roles of auditory hair cells. Nat. Rev. Neurosci. **7**(1), 19–29 (2006)
2. A. Hudspeth, Making an effort to listen: mechanical amplification in the ear. Neuron **59**(4), 530–545 (2008)
3. J. Ashmore, P. Avan, W. Brownell, P. Dallos, K. Dierkes, R. Fettiplace, K. Grosh, C. Hackney, A. Hudspeth, F. Jülicher, B. Lindner, P. Martin, J. Meaud, C. Petit, J. Sacchi, B. Canlon, The remarkable cochlear amplifier. Hear. Res. **266**, 1–17 (2010)
4. V. Eguiluz, M. Ospeck, Y. Choe, A. Hudspeth, M. Magnasco, Essential nonlinearities in hearing. Phys. Rev. Lett. **84**(22), 5232–5235 (2000)
5. P. Martin, A.J. Hudspeth, Active hair-bundle movements can amplify a hair cell's response to oscillatory mechanical stimuli. Proc. Natl. Acad. Sci. U.S.A. **96**, 14306–14311 (1999)
6. A.J. Hudspeth, F. Jülicher, P. Martin, A critique of the critical cochlea: Hopf-a bifurcation-is better than none. J. Neurophysiol. **104**(3), 1219–1229 (2010)

7. J. Howard, A. Hudspeth, Compliance of the hair bundle associated with gating of mechanoelectrical transduction channels in the bullfrog's saccular hair cell. Neuron **1**(3), 189–199 (1988)
8. P. Martin, A. Mehta, A. Hudspeth, Negative hair-bundle stiffness betrays a mechanism for mechanical amplification by the hair cell. Proc. Natl. Acad. Sci. U.S.A. **97**(22), 12026–12031 (2000)
9. R. Eatock, Adaptation in hair cells. Annu. Rev. Neurosci. **23**, 285–314 (2000)
10. R. Fettiplace, A. Ricci, Adaptation in auditory hair cells. Curr. Opin. Neurobiol. **13**(4), 446–451 (2003)
11. G.A. Manley, G.K. Yates, C. Kppl, Auditory peripheral tuning: evidence for a simple resonance phenomenon in the lizard tiliqua. Hear. Res. **33**(2), 181–189 (1988)
12. G.A. Manley, L. Gallo, Otoacoustic emissions, hair cells, and myosin motors. J. Acoust. Soc. Am. **102**(2 Pt 1), 1049–1055 (1997)
13. G.A. Manley, Evidence for an active process and a cochlear amplifier in nonmammals. J. Neurophysiol. **86**(2), 541–549 (2001)
14. P. Martin, D. Bozovic, Y. Choe, A. Hudspeth, Spontaneous oscillation by hair bundles of the bullfrog's sacculus. J. Neurosci. **23**(11), 4533–4548 (2003)
15. D. Ramunno-Johnson, C. Strimbu, L. Fredrickson, K. Arisaka, D. Bozovic, Distribution of frequencies of spontaneous oscillations in hair cells of the bullfrog sacculus. Biophys. J. **96**(3), 1159–1168 (2009). URL PM:19186151
16. M. Gelfand, O. Piro, M.O. Magnasco, Interactions between hair cells shape spontaneous otoacoustic emissions in a model of the tokay gecko's cochlea. PLoS One **5**(6), e11116 (2010). doi:10.1371/journal.pone.0011116
17. B. Nadrowski, P. Martin, F. Jülicher, Active hair-bundle motility harnesses noise to operate near an optimum of mechanosensitivity. Proc. Natl. Acad. Sci. U.S.A. **101**(33), 12195–12200 (2004)
18. K. Dierkes, B. Lindner, F. Jülicher, Enhancement of sensitivity gain and frequency tuning by coupling of active hair bundles. Proc. Natl. Acad. Sci. U.S.A. **105**(48), 18669–18674 (2008)
19. J. Barral, K. Dierkes, B. Lindner, F. Jülicher, P. Martin, Coupling a sensory hair-cell bundle to cyber clones enhances nonlinear amplification. Proc. Natl. Acad. Sci. U.S.A **107**(18), 8079–8084 (2010)
20. M. Ospeck, V.M. Eguluz, M.O. Magnasco, Evidence of a hopf bifurcation in frog hair cells. Biophys. J. **80**(6), 2597–2607 (2001)
21. L. Catacuzzeno, B. Fioretti, P. Perin, F. Franciolini, Spontaneous low-frequency voltage oscillations in frog saccular hair cells. J. Physiol. **561**, 685–701 (2004)
22. F. Jorgensen, A. Kroese, Ion channel regulation of the dynamical instability of the resting membrane potential in saccular hair cells of the green frog (rana esculenta). Acta Physiol. Scand. **185**(4), 271–290 (2005)
23. M. Rutherford, W. Roberts, Spikes and membrane potential oscillations in hair cells generate periodic afferent activity in the frog sacculus. J. Neurosci. **29**(32), 10025–10037 (2009)
24. L. Han, A. Neiman, Spontaneous oscillations, signal amplification, and synchronization in a model of active hair bundle mechanics. Phys. Rev. E. **81**, 041913 (2010)
25. W. Denk, W. Webb, Forward and reverse transduction at the limit of sensitivity studied by correlating electrical and mechanical fluctuations in frog saccular hair cells. Hear. Res. **60**(1), 89–102 (1992)
26. D. Bozovic, A. Hudspeth, Hair-bundle movements elicited by transepithelial electrical stimulation of hair cells in the sacculus of the bullfrog. Proc. Natl. Acad. Sci. U.S.A. **100**(3), 958–963 (2003)
27. D. Ramunno-Johnson, C.E. Strimbu, A. Kao, L.F. Hemsing, D. Bozovic, Effects of the somatic ion channels upon spontaneous mechanical oscillations in hair bundles of the inner ear. Hear. Res. **268**(1–2), 163–171 (2010)
28. T. Holton, A. Hudspeth, The transduction channel of hair cells from the bull-frog characterized by noise analysis. J. Physiol. **375**, 195–227 (1986)

29. J.O. Pickles, D.P. Corey, Mechanoelectrical transduction by hair cells. Trends Neurosci. **15**(7), 254–259 (1992)
30. Y. Choe, M. Magnasco, A. Hudspeth, A model for amplification of hair-bundle motion by cyclical binding of ca2+ to mechanoelectrical-transduction channels. Proc. Natl. Acad. Sci. U.S.A. **95**(26), 15321–15326 (1998)
31. J. Tinevez, F. Jülicher, P. Martin, Unifying the various incarnations of active hair-bundle motility by the vertebrate hair cell. Biophys. J. **93**(11), 4053–4067 (2007)
32. Y. Roongthumskul, L. Fredrickson-Hemsing, A. Kao, D. Bozovic, Multiple-timescale dynamics underlying spontaneous oscillations of saccular hair bundles. Biophys. J. **101**(3), 603–610 (2011)
33. D. Ó Maoiléidigh, E.M. Nicola, A.J. Hudspeth, The diverse effects of mechanical loading on active hair bundles. Proc. Natl. Acad. Sci. U.S.A. **109**(6), 1943–1948 (2012)
34. A.B. Neiman, K. Dierkes, B. Lindner, L. Han, A.L. Shilnikov, Spontaneous voltage oscillations and response dynamics of a hodgkin-huxley type model of sensory hair cells. J. Math. Neurosci. **1**(1), 11 (2011)
35. Y. Kuznetsov. http://www.staff.science.uu.nl/~kouzn101/CONTENT
36. R. Fettiplace, Defining features of the hair cell mechanoelectrical transducer channel. Pflugers Arch. **458**(6), 1115–1123 (2009). URL PM:19475417
37. J. Barral, P. Martin, The physical basis of active mechanosensitivity by the hair-cell bundle. Curr. Opin. Otolaryngol. Head Neck Surg. **19**(5), 369–375 (2011)

Low-Pass Filtering of Information in the Leaky Integrate-and-Fire Neuron Driven by White Noise

Benjamin Lindner

Abstract The question of how noisy spiking neurons respond to external time-dependent stimuli is a central topic in computational neuroscience. An important aspect of the neural information transmission is, whether neurons encode preferentially information about slow or about fast components of the stimulus (signal). A convenient way to quantify this is the spectral coherence function, that in some experimental data shows a global maximum at low frequencies (low-pass information filter), in some other cases has a maximum at higher frequencies (band-pass or high-pass information filter); information-filtering defined in this way is related but not identical to the usual filtering of spectral power. Here I demonstrate numerically that the leaky integrate-and-fire neuron driven by white noise (a stimulus without temporal correlations) acts as a low-pass information filter irrespective of the dynamical regime (fluctuation-driven and irregular or mean-driven and regular firing).

1 Introduction

Nerve cells in our brain transduce information about time-dependent stimuli like visual or auditory signals into sequences of stereotype action potentials called spike trains. An important aspect of neural information transmission is what are the most important features that are encoded in the neural sequence of action potentials. One important feature is the preferred frequency band in which neurons transmit information or, put differently, whether neurons encode preferentially slow or fast components of a time-dependent stimulus (signal). Experimentally one has seen both

B. Lindner (✉)
Bernstein Center for Computational Neuroscience Berlin, Philippstr. 13,
Haus 2, 10115 Berlin, Germany
e-mail: benjamin.lindner@physik.hu-berlin.de

B. Lindner
Physics Department, Humboldt University Berlin, Newtonstr. 15, 12489 Berlin, Germany

V. In et al. (eds.), *International Conference on Theory and Application in Nonlinear Dynamics (ICAND 2012)*, Understanding Complex Systems,
DOI: 10.1007/978-3-319-02925-2_22,

kinds of low-pass and high-pass filtering of information (not to be confused with the common filtering of signal power). This raises the question about the properties of neural dynamics or network properties that may lead to specific forms of information filtering.

Simple neuron models like the stochastic integrate-and-fire model are able to reproduce spiking statistics of cells in response to noisy currents to an astonishing degree of accuracy [1, 2]. Upon changing the mean and variance of the current injection, IF models display transitions between distinct firing regimes: pacemaker-like regular firing, the near-Poisson irregular firing with low rate, and the burst-like firing with a coefficient of variation (Cv) beyond unity [3–5]. In the so-called nonlinear IF model different response behavior with respect to additional stimulation is possible: from non-resonant purely noise-controlled response function of the perfect IF model to the resonances of the leaky, quadratic or exponential IF models [6, 7].

Despite all these differences for different nonlinearities of the model and despite the existence of distinct firing regimes, a previous study [7] suggested that IF models seem to share one property: they transmit most information about slow signal components. This can be seen by looking at the coherence as a function of frequency: it attains its global maximum at zero frequency. For the leaky IF model with selected parameters, this has been found numerically already in the early 1970's [8].

Here in this chapter, I discuss the coherence for the leaky IF model as a function of mean and intensity of its input fluctuations. It is shown that this model is a low-pass filter of information in the sense that the maximum of the coherence is at zero frequency. I also discuss how the half-width of the coherence behaves and how it compares to other characteristic frequencies of the system, namely, the inverse membrane-time constant and the firing rate of the model neuron. These results establish that for a white-noise driven leaky IF model a high-pass filtering of information is not possible. If the latter is observed in a real neuron, this tells us that most likely a more complicated dynamics than a one-dimensional IF model is involved.

2 Model and Measures of Interest

I consider a leaky integrate-and-fire (LIF) model with a noisy current input

$$\dot{v} = -v + \mu + \sqrt{2D_{\mathrm{bg}}}\xi_{\mathrm{bg}}(t) + \sqrt{2D_{\mathrm{st}}}\xi_{\mathrm{st}}(t), \tag{1}$$

which is complemented by a fire-and-reset rule: whenever $v(t)$ crosses the threshold v_T, a spike is registered and the voltage is reset to v_R and, after an absolute refractory period τ_{abs} has passed, released to evolve again according to the above equation. To reduce the number of free parameters, voltage is here defined as the deviation from the reset (implying $v_R = 0$) and is measured in multiples of the reset-threshold distance (implying $v_T = 1$); time is measured in multiples of the membrane-time constant (see [5] for details of the transformation from the model with

physical dimensions to the non-dimensional model considered here). Input parameters are the constant base current μ, the intensity D_{bg} of the background noise $\xi_{\mathrm{bg}}(t)$ (representing synaptic background fluctuations or channel noise), and the intensity D_{st} of the stimulus $\xi_{\mathrm{st}}(t)$. Both background noise and stimulus signal are assumed as Gaussian white noise with $\langle \xi_i(t)\xi_j(t')\rangle = \delta_{i,j}\delta(t-t')$ (where $i, j \in \{\mathrm{bg}, \mathrm{st}\}$).

The information transmission of this spiking model can be quantified by means of the spectral coherence function. To this end, one considers the Fourier transform in a time window $[0, T]$

$$\tilde{x}_T(\omega) = \int_0^T dt e^{i\omega t} x(t) \tag{2}$$

of the spike train

$$x(t) = \sum \delta(t - t_i) \tag{3}$$

where the t_i are the time instants of threshold crossings. The cross-spectrum of spike train and stimulus and the spike train power spectrum are defined as follows

$$S_{x,s}(\omega) = \lim_{T\to\infty} \frac{\langle \tilde{x}(\omega)\tilde{s}^*(\omega)\rangle}{T}, \quad S_{x,x}(\omega) = \lim_{T\to\infty} \frac{\langle \tilde{x}(\omega)\tilde{x}^*(\omega)\rangle}{T}. \tag{4}$$

The coherence function for the input signal and the output spike train is the squared correlation coefficient between input and output

$$C_{x,s} = \frac{|S_{x,s}(\omega)|^2}{S_{x,x}(\omega)S_{s,s}(\omega)} \tag{5}$$

and yields at each frequency a number between 0 and 1. Low or high information transmission in a certain frequency band is indicated by a coherence close to zero or one, respectively.

Generally, a system that shows under white-noise stimulation a coherence which decreases (increases) with frequency can be regarded as a low-pass (high-pass) filter of information. This kind of information filter is related but not identical with the commonly considered power filter. A linear bandpass-filter, for instance, driven by white background noise and a white noise stimulus would not act as an information filter—its coherence is simply flat. One formal reason for this is that the frequency dependences of cross-spectrum and power spectrum in Eq. (5) cancel out for a linear system. When both signal and noise pass through the same power filter, the filter cannot change the signal-to-noise ratio, which is what is essentially quantified by the coherence.

Despite the linearity of Eq. (1), the spiking LIF neuron model is *not* linear; it possesses the strong nonlinearity of the reset rule and thus we can expect that the LIF model performs one or the other kind of information filtering and that this information filter potentially depends on the firing regime that is set by the input parameters μ and

D. For the LIF driven by white Gaussian current noise, we fortunately know all the spectral functions of interest analytically. The cross-spectrum between input signal and output spike train is given by the product of input spectrum (just the constant $2D_{\rm st}$) and the complex rate-modulation factor, the so-called susceptibility [9, 10]

$$S_{x,s}(\omega) = \frac{2D_{\rm st}}{\sqrt{D}} \frac{r_0 i\omega}{i\omega - 1} \frac{\mathscr{D}_{i\omega-1}\left(\frac{\mu-v_T}{\sqrt{D}}\right) - e^{\Delta}\mathscr{D}_{i\omega-1}\left(\frac{\mu-v_R}{\sqrt{D}}\right)}{\mathscr{D}_{i\omega}\left(\frac{\mu-v_T}{\sqrt{D}}\right) - e^{\Delta}e^{i\omega\tau_{\rm abs}}\mathscr{D}_{i\omega}\left(\frac{\mu-v_R}{\sqrt{D}}\right)} \tag{6}$$

where

$$\Delta = \frac{v_R^2 - v_T^2 + 2\mu(v_T - v_R)}{4D}$$

and $\mathscr{D}_a(x)$ is the parabolic cylinder function [11]. The firing rate r_0 is given by

$$r_0 = \left[\tau_{\rm abs} + \sqrt{\pi}\int_{(\mu-v_T)/\sqrt{2D}}^{(\mu-v_R)/\sqrt{2D}} dz\, e^{z^2}\,\mathrm{erfc}(z)\right]^{-1}. \tag{7}$$

Alternative expressions for the susceptibility with vanishing refractory period have been derived by Brunel et al. (see [12] and References there in).

The power spectrum of the spike train is given by [3]

$$S_{x,x}(\omega) = r_0 \frac{\left|\mathscr{D}_{i\omega}\left(\frac{\mu-v_T}{\sqrt{D}}\right)\right|^2 - e^{2\Delta}\left|\mathscr{D}_{i\omega}\left(\frac{\mu-v_R}{\sqrt{D}}\right)\right|^2}{\left|\mathscr{D}_{i\omega}\left(\frac{\mu-v_T}{\sqrt{D}}\right) - e^{\Delta}e^{i\omega\tau_{\rm abs}}\mathscr{D}_{i\omega}\left(\frac{\mu-v_R}{\sqrt{D}}\right)\right|^2} \tag{8}$$

In both these expressions, $D = D_{\rm bg} + D_{\rm st}$ denotes the total noise intensity.

Combining Eqs. (6) and (8), the coherence of the LIF model reads:

$$C_{x,s} = \frac{2D_{\rm st}}{D}\frac{r_0\omega^2}{1+\omega^2} \frac{\left|\mathscr{D}_{i\omega-1}\left(\frac{\mu-v_T}{\sqrt{D}}\right) - e^{\Delta}\mathscr{D}_{i\omega-1}\left(\frac{\mu-v_R}{\sqrt{D}}\right)\right|^2}{\left|\mathscr{D}_{i\omega}\left(\frac{\mu-v_T}{\sqrt{D}}\right)\right|^2 - e^{2\Delta}\left|\mathscr{D}_{i\omega}\left(\frac{\mu-v_R}{\sqrt{D}}\right)\right|^2} \tag{9}$$

It can be seen that the absolute refractory period does enter this expression only via the firing rate and, hence, has no effect on the frequency dependence of the coherence. Increasing $\tau_{\rm abs}$ leads only to an overall reduction of the coherence. For this reason, we consider in the following the special case of a vanishing refractory period $\tau_{\rm abs} = 0$.

If we want to graphically illustrate the above results, this requires the numerical evaluation of the parabolic cylinder function at complex-valued index, a nontrivial task that can be achieved using software like Maple™ or Mathematica™. An alternative way to determine cross- and power spectra is the threshold-integration method

by Richardson [13], which can be easily implemented in common programming languages like C and can be readily extended to nonlinear IF models. In this work, I have mainly used the latter method but verified for selected parameter sets that this provides the same results as the explicit result evaluated in Maple16^{TM}.

Note that for fixed total noise intensity D the stimulus intensity D_{st} only scales the coherence function by a factor D_{st}/D . For this reason we set in the following $D = D_{st}$ implying $D_{bg} = 0$. With the same total noise intensity D, the coherence function with finite D_{bg} is obviously smaller than without intrinsic noise [8]. This is not in contradiction to the fact that the LIF displays stochastic resonance [9] because to see the latter phenomenon, we should keep the signal amplitude constant and vary the background noise intensity D_{bg}; in this case the total noise intensity is *not* fixed. Indeed, if $\mu < v_T$, the coherence at any frequency (proportional to the signal-to-noise ratio for periodic stimulation at this frequency) passes through a maximum as a function of D_{bg} [10].

3 Results

In Fig. 1 we show examples of power spectra, cross-spectra, and coherence functions for an LIF in the fluctuation-driven firing regime of high irregularity (a) and the mean-driven firing regime of rather regular firing pattern (b). For the setting in the fluctuation-driven regime, the steady state firing rate is $r_0 \approx 0.16$ and a coefficient of variation of the interspike interval is about $C_v \approx 0.835$ while for the parameters in Fig. 1b we have a higher firing rate $r_0 \approx 0.924$ and a considerably lower $C_v \approx 0.166$. Despite pronounced differences in the cross—and power spectra, that reflect differences in the spiking statistics and in the response to time-dependent signals, the

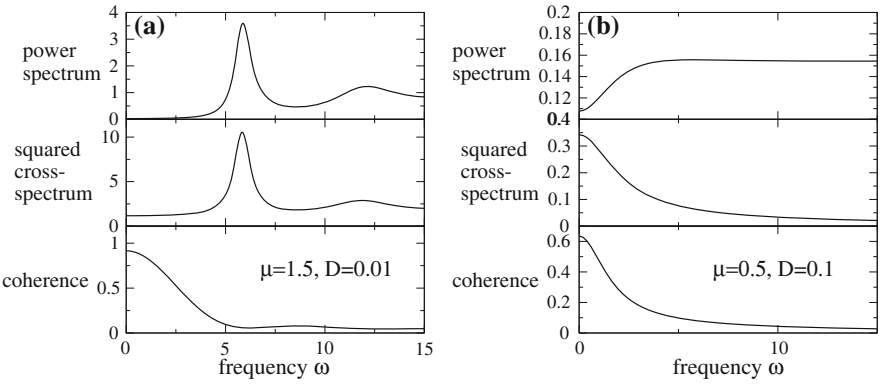

Fig. 1 Power spectrum (*top panel*), cross-spectrum (*mid panel*) and coherence as functions of frequency in the mean-driven regime (**a**) and the fluctuation driven regime (**b**) with mean input μ and total noise intensity as indicated in the figure.

coherence function in both cases attains its maximum at zero frequency and decays quite rapidly with increasing frequency.

The only qualitative difference occurs around the frequency comparable to the firing rate: the LIF in the regular (mean-driven) firing regime possesses a local *minimum* at this frequency, whereas the coherence of the LIF in the irregular (noise-induced or fluctuation-dominated) firing regime decays monotonically with frequency. Given that coherence has a global maximum around zero in both cases and given that the main share of information is transmitted in this low-frequency range, these difference appear as rather unimportant.

How can we quantify whether this low-pass behavior of the coherence is present for all combinations of base currents and noise intensities? To this end, we can consider a number of characteristics of the coherence function that are illustrated in Fig. 2.

We can first of all find the global maximum of the coherence curve as a function of frequency for various combinations of base current μ and noise (signal) intensity D. In the broad range of values considered, this yields always $\omega = 0$ as the frequency

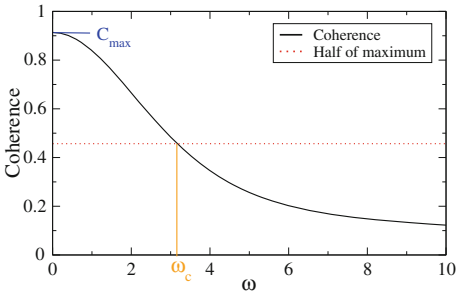

Fig. 2 Coherence function for $\mu = 1.2$ and $D = 0.1$. Indicated are the maximum, $C_{\max}$, the half value of the maximum (*dotted line*), and the frequency ω_c at which this half value is attained (*vertical line*)

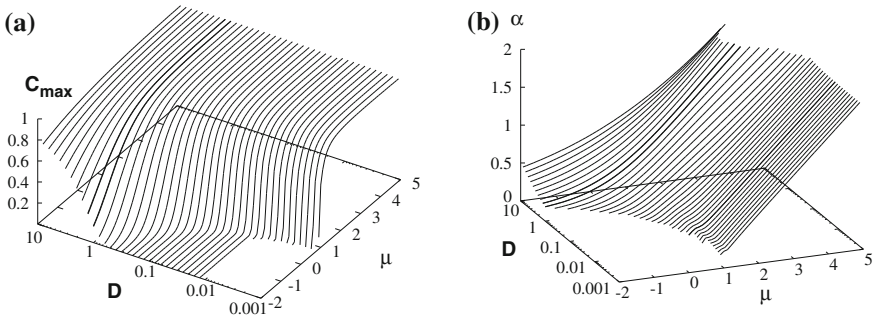

Fig. 3 The maximum (**a**) and the half-width (**b**) of the coherence between the driving noise and the output spike train as a function of the base current μ and the noise intensity D.

of this global maximum. In Fig. 3a, we show this maximum value of the coherence $C_{\max} = C_{xs}(\omega = 0)$ as a function of the base current μ and the noise intensity D. This value increases both with the noise intensity (here also the signal amplitude) and the base current. In the limit of large base current, the coherence approaches one which agrees with the limit for a perfect IF model, in which a leak term is absent. The main reason for this increase in the maximum value of the coherence is the increase in firing rate with growing base current - with an increasing number of spikes per unit time it becomes possible to encode an arbitrary slow stimulus (corresponding to the coherence at $\omega = 0$, i.e. its maximum) arbitrarily reliable. In the opposite limit of negative base current, the firing rate becomes exponentially small and thus the coherence is essentially zero unless a large noise intensity compensates for the decrease in base current.

As a measure of the bandwidth over which the LIF transmits the stimulus, I consider the (minimal) frequency ω_c at which the coherence attains half of its maximal value (cf. Fig. 2); ω_c is in the following referred to as the *half-width*. Also of interest is the ratio of this (cyclic) frequency to the frequency associated with the inverse membrane time constant (which we set to one):

$$\alpha = \frac{\omega_c}{2\pi}. \tag{10}$$

The parameter α will tell us whether the half-width is constrained by the inverse membrane time constant or not. In Fig. 3b α is plotted as a function of μ and D illustrating that for low firing rate (for $\mu < 1$ and small noise intensity D), the coherence halfwidth is smaller than the inverse membrane time constant, while at higher firing rate (in the mean-driven firing regime with $\mu > 1$) the information bandwidth is not limited by the membrane-time constant. In particular in this latter regime it is also instructive to compare ω_c to another typical frequency in the system, namely the firing rate:

$$\beta = \frac{\omega_c}{2\pi r_0}. \tag{11}$$

Because r_0 is also measured in multiples of the membrane time constant, the latter drops out of the ratio β.

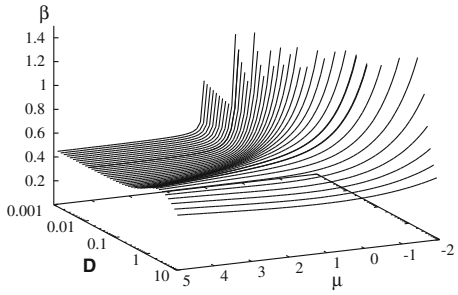

Fig. 4 Halfwidth normalized by the firing rate as a function of base current μ and noise intensity D

In Fig. 4 it becomes apparent that at high firing rate (large μ, small D), the halfwidth is determined mainly by the firing rate - the inverse membrane time constant does not play a role in this limit. There seems to be a saturation at about half of the width of the firing rate, i.e. frequencies sufficiently below the firing rate (smaller by a factor of two or three) are transmitted reliably ($C(\omega) > 0.5$). Expressed in multiples of the firing rate, the information bandwidth diverges in the opposite limit of vanishing firing rate. Here, however, one should keep in mind that in terms of the inverse membrane-time constant the halfwidth is still very small in this limit (cf. Fig. 3b).

4 Summary and Conclusions

In this chapter I have inspected the coherence function of a leaky integrate-and-fire neuron driven by white Gaussian noise. In accordance with previous findings at selected parameter sets [7] I have found that the LIF neuron acts as a low-pass filter on information about a time-dependent uncorrelated Gaussian stimulus for a broad range of input parameters. I have studied the magnitude and halfwidth of the coherence function. At low firing rate (subthreshold μ and small noise intensity D) the coherence is generally low and its half-width is constrained by the inverse membrane time constant (which was one in our units). At high firing rate (for suprathreshold $\mu > 1$), information transmission is high up to frequencies that are well below the firing rate; for large μ, the halfwidth seems to be given by $\omega_c \approx \pi r_0$.

Results from Ref. [7] indicate that low-pass information filtering is also prevailing in other integrate-and-fire models, as for instance, the perfect and the quadratic IF neurons. The bandwidth inspected here, however, may certainly differ. It is, for instance, known that the coherence of the perfect IF model at zero frequency is always one irrespective of the parameter values (similar to what seems to be the limit of the LIF model for $\mu \to \infty$). Furthermore, the halfwidth is solely controlled by the noise intensity [7]. The numerical methods by Richardson [13], which were applied here to the LIF can be also applied to the perfect and quadratic IF models as well as to the so-called exponential IF model [2, 6].

Desirable would be also to analytically study the coherence of a general nonlinear IF model at low frequencies: the conjecture of low-pass information filtering entails a negative curvature of the coherence at low frequencies that may be provable by perturbation methods. Unfortunately, this is already highly nontrivial for the LIF model for which we know the exact result for the coherence, namely, Eq. (9) but lack a simple small-frequency expansion that would permit to determine the sign of the curvature at $\omega = 0$.

The results achieved in this paper indicate that the LIF model is unable to reproduce cases of information highpass-filtering that have been observed in experiments. At the population level the coding by synchronous spikes provides a coherence function that is suppressed at low frequencies [14], an experimental observation that has been modeled and theoretically analyzed with populations of LIF neurons [15]. At the single-cell level possible candidates for information filtering are short-term synaptic

plasticity (however, see [16] but also [17]), spike-frequency adaptation [18], or subthreshold oscillations [19, 20]. Also the effect of temporally correlated background spiking [21] or synaptic filtering of uncorrelated input [22] will result in colored instead of white background noise and may thus lead to a decrease or increase of the coherence at low frequencies compared to the case of white noise. Filtering of information, regarded as a simple form of information processing, could thus assign (an additional) functional role to certain biophysical features of the neural dynamics.

Acknowledgments This research has been funded by the BMBF (FKZ: 01GQ1001A).

References

1. L. Badel, S. Lefort, R. Brette, C.C.H. Petersen, W. Gerstner, M.J.E. Richardson, Generalized integrate-and-fire models of neuronal activity approximate spike trains of a detailed model to a high degree of accuracy. J. Neurophysiol. **92**, 959 (2004)
2. L. Badel, S. Lefort, R. Brette, C.C.H. Petersen, W. Gerstner, M.J.E. Richardson, Dynamic I-V curves are reliable predictors of naturalistic pyramidal-neuron voltage traces. J. Neurophysiol. **99**, 656 (2008)
3. B. Lindner, L. Schimansky-Geier, A. Longtin, Maximizing spike train coherence or incoherence in the leaky integrate-and-fire model. Phys. Rev. E **66**, 031916 (2002)
4. A. N. Burkitt, A review of the integrate-and-fire neuron model: I. homogeneous synaptic input. Biol. Cyber. **95**(1) (2006)
5. R.D. Vilela, B. Lindner, Are the input parameters of white-noise-driven integrate & fire neurons uniquely determined by rate and CV? J. Theor. Biol. **257**, 90 (2009)
6. N. Fourcaud-Trocmé, D. Hansel, C. van Vreeswijk, N. Brunel, How spike generation mechanisms determine the neuronal response to fluctuating inputs. J. Neurosci. **23**, 11628 (2003)
7. R.D. Vilela, B. Lindner, A comparative study of three different integrate-and-fire neurons: spontaneous activity, dynamical response, and stimulus-induced correlation. Phys. Rev. E **80**, 031909 (2009)
8. R.B. Stein, A.S. French, A.V. Holden, The frequency response, coherence, and information capacity of two neuronal models. Biophys. J. **12**, 295 (1972)
9. B. Lindner, L. Schimansky-Geier, Transmission of noise coded versus additive signals through a neuronal ensemble. Phys. Rev. Lett. **86**, 2934 (2001)
10. B. Lindner, J. García-Ojalvo, A. Neiman, L. Schimansky-Geier, Effects of noise in excitable systems. Phys. Rep. **392**, 321 (2004)
11. M. Abramowitz, I.A. Stegun, *Handbook of Mathematical Functions* (Dover, New York, 1970)
12. N. Fourcaud, N. Brunel, Dynamics of the firing probability of noisy integrate-and-fire neurons. Neural Comp. **14**, 2057 (2002)
13. M. J. E. Richardson, Spike-train spectra and network response functions for non-linear integrate-and-fire neurons. Biol. Cybern. (to appear) **99**, 381–392 (2008)
14. J.W. Middleton, A. Longtin, J. Benda, L. Maler, Postsynaptic receptive field size and spike threshold determine encoding of high-frequency information via sensitivity to synchronous presynaptic activity. J. Neurophysiol. **101**, 1160 (2009)
15. N. Sharafi, J. Benda, B. Lindner, Information filtering by synchronous spikes in a neural population. J. Comp. Neurosci. **34**, 285 (2013)
16. B. Lindner, D. Gangloff, A. Longtin, J.E. Lewis, Broadband coding with dynamic synapses. J. Neurosci. **29**, 2076 (2009)
17. R. Rosenbaum, J. Rubin, B. Doiron, Short term synaptic depression imposes a frequency dependent filter on synaptic information transfer. PLoS Comput. Biol. **8**, e1002557 (2012)

18. J. Benda, A.V.M. Herz, A universal model for spike-frequency adaptation. Neural Comp. **15**, 2523 (2003)
19. M.J.E. Richardson, N. Brunel, V. Hakim, From subthreshold to firing-rate resonance. J. Neurophysiol. **89**, 2538 (2003)
20. T.A. Engel, L. Schimansky-Geier, A.V.M. Herz, S. Schreiber, I. Erchova, Subthreshold membrane-potential resonances shape spike-train patterns in the entorhinal cortex. J. Neurophysiol. **100**(3), 1576 (2008)
21. B. Lindner, Superposition of many independent spike trains is generally not a poisson process. Phys. Rev. E **73**, 022901 (2006)
22. N. Brunel, S. Sergi, Firing frequency of leaky integrate-and-fire neurons with synaptic current dynamics. J. Theor. Biol. **195**, 87 (1998)

Application of High Performance Computing for Simulating the Unstable Dynamics of Dilute Spark-Ignited Combustion

Charles E. A. Finney, Miroslav K. Stoyanov, Sreekanth Pannala, C. Stuart Daw, Robert M. Wagner, K. Dean Edwards, Clayton G. Webster and Johney B. Green

Abstract In collaboration with a major automotive manufacturer, we are using computational simulations of in-cylinder combustion to understand the multi-scale nonlinear physics of the dilute stability limit. Because some key features of dilute combustion can take thousands of successive cycles to develop, the computation time involved in using complex models to simulate these effects has limited industrys ability to exploit simulations in optimizing advanced engines. We describe a novel approach for utilizing parallel computations to reveal long-timescale features of dilute combustion without the need to simulate many successive engine cycles in series. Our approach relies on carefully guided, concurrent, single-cycle simulations to create metamodels that preserve the long-timescale features of interest. We use a simplified combustion model to develop and demonstrate our strategy for adaptively guiding the concurrent simulations to generate metamodels. We next will implement this strategy with higher-fidelity, multi-scale combustion models on large computing facilities to generate more refined metamodels. The refined metamodels can then be used to accelerate engine development because of their efficiency. Similar approaches might also be used for rapidly exploring the dynamics of other complex multi-scale systems that evolve with serial dependency on time.

1 Introduction

Gasoline-fueled internal combustion engines are by far the most widely used passenger car engine type in the U.S. Because of their performance, low cost and fuel flexibility, it is very likely that these engines will continue to play a dominant role for several decades [1, 2]. With anticipated changes in Corporate Average Fuel

C. E. A. Finney (✉) · M. K. Stoyanov · S. Pannala · C. S. Daw · R. M. Wagner · K. D. Edwards · C. G. Webster · J. B. Green
Oak Ridge National Laboratory, Oak Ridge, TN, 37831, USA
e-mail: finneyc@ornl.gov

V. In et al. (eds.), *International Conference on Theory and Application in Nonlinear Dynamics (ICAND 2012)*, Understanding Complex Systems,
DOI: 10.1007/978-3-319-02925-2_23,

Economy (CAFE) standards, automotive manufacturers are examining engine innovations such as dilute combustion, boosting and downsizing, and advanced fuel-injection concepts. The implementation of these technologies could help increase the energy efficiency of passenger vehicles and reduce U.S. dependence on petroleum.

Gasoline-fueled engines initiate combustion with an electric spark after air and fuel have been introduced and compressed in the cylinder. Combustion begins at the spark plug as a complex mixture of hot ionized gases and molecular free radicals and then propagates in a 3-dimensional flame front through the remaining unreacted gas mixture. The quality of the combustion (i.e., how much of the released energy is available to generate piston work and how many unwanted reaction byproducts are produced) depends on how fast and far the reaction front propagates in the highpressure and temperature environment before it extinguishes or the exhaust valve opens.

Recently, manufacturers have utilized charge dilution to increase fuel efficiency and reduce emissions. Charge dilution is accomplished by adding excess air or recirculated exhaust gas to the fuel-air mixture in the combustion chamber prior to ignition. The extra gas slows combustion and lowers peak temperature, resulting in less heat loss, higher piston work, and less nitrogen oxide formation. Up to a point, dilution can be beneficial, but when sufficiently high, flame initiation and propagation become unstable. As the stability limit is approached, complex combustion oscillations begin to grow rapidly. These oscillations are frequently referred to in the engine literature as cyclic dispersion, since they result in large combustion variations from one engine cycle (intake, compression, power, and exhaust piston strokes) to the next. The precise location of the stability limit depends on many different design and operating factors, so it is not usually possible to predict a priori where the limit will be for a given engine at any instance. This has forced engine manufacturers to adopt wide safety margins, thereby denying them the full benefit of charge dilution.

Engine manufacturers are now heavily investing in computational simulations to understand combustion instability. A major challenge is that many of the associated dynamical features are very subtle, span the entire 4D spatiotemporal space, and/or are infrequent. Some of the complexity is due to nonlinear feedback from prior engine cycles, so it is often necessary to simulate hundreds or thousands of sequential engine cycles in order to observe the important events. For experimental engine studies, recording thousands of consecutive cycles is a standard capability, but it is still not possible to get the 3D space distribution of all the relevant quantities. For detailed computational simulations that simultaneously account for multiple physical processes at different scales of space and time, the computational overhead and clock time required represent high costs. In addition, given the serial nature of cyclic dispersion, one cannot easily exploit the current generation of massively parallel computers. In this paper we describe efforts to develop a methodology for exploring the dilution stability limit that exploits the capabilities of detailed multiscale, multi-physics models and high-performance parallel computing. We expect

this methodology and the insights it generates will provide opportunities to accelerate development of more efficient gasoline engines.

Computer simulation of internal combustion engines has been studied for decades. The models used have ranged from very simple, zero- or first-order approximations with low accuracy but fast computational speed to very detailed, complex codes with high computational overhead. Typically, in models utilizing computational fluid dynamics (CFD), the primary objective has been to account for the interactions between the turbulent flow field and detailed chemical reactions and heat transport. Because of the computational cost and limited concurrency, such simulations have not been very useful for studying dynamics over many sequential cycles, (e.g., to view extreme, rare events).

Recently, some CFD models have incorporated large-eddy simulation (LES) to more accurately represent the links between turbulent mixing and combustion instability over a limited number (25–100) of successive engine cycles [3–5]. Such studies provide important insights into some aspects of dilute combustion instability, but they are not sufficient to understand the longer-timescale combustion oscillations. Also, they can only address limited parameter spaces, because very long run times (e.g., 30–40 h) are required to compute a single engine cycle on typical workstations (e.g., 32-core machines), translating to several months of computations for $\sim 10^2$ successive cycles. Direct scale-up of LES simulations to large numbers of processors (10^4) is not practical because of the small number of in-cylinder computational grid points (e.g., $\sim 10^6 - 10^7$), and the inter-processor communication time becomes overwhelmingly high as these problems are decomposed onto a large number of processors.

As described below, utilization of surrogate models or metamodels is an important part of our approach. Such models have been the subject of recent research, particularly in systems and controls settings [6–8]. Typically, these models are used to develop control strategies or to better understand the mechanisms behind important dynamic transitions [9]. We plan to use these models to construct sampling techniques so that we can perform several independent engine-cycle simulations to reconstruct the dynamics exhibited by many sequential cycle-to-cycle variations. These developments are an important basis in our efforts to understand and conceptualize the complex nature of engine combustion.

2 Technical Approach

2.1 Parallel Computation Methodology

We address the computational challenges of engine combustion simulation via a two-phase approach: (1) replacing simulations of many engine cycles with multiple concurrent single-cycle simulations to generate metamodels; and (2) utilizing the resulting metamodels for further studies of combustion instability in both serial and

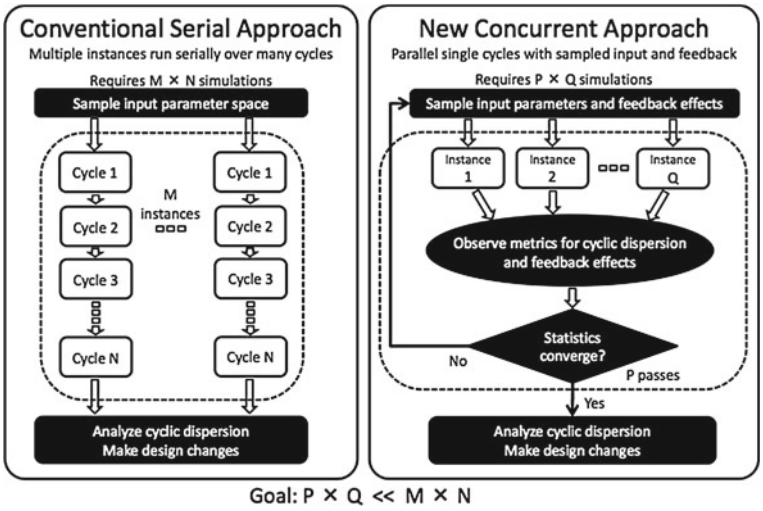

Fig. 1 The concurrent modeling strategy replaces serial combustion simulations over many engine cycles with multiple single-cycle simulations

massively parallel computations. The primary focus of this paper is to summarize recent progress toward the first phase, in which we have studied how to implement concurrent engine simulations in an adaptive manner to generate metamodels that accurately reflect the important dynamics. In the second phase, we will utilize the metamodels to rapidly explore much larger parameter spaces by utilizing the structure of the input-output response and concurrent single-cycle simulations than what would be possible with the current detailed combustion models used to simulate cycle-to- cycle variations in series.

Figure 1 compares our adaptive concurrent simulation strategy with traditional serial simulation. The key difference is that we substitute single-cycle engine simulations for long multi-cycle simulations. For each of the single-cycle simulations, we start with different values (chosen according to a sampling scheme) of model parameters and/or initial conditions. The resulting responses are then analyzed to find the parameters and initial conditions having the most significant impact on combustion stability. These parameters and conditions are then further explored adaptively to refine knowledge of their impact on combustion. In order to improve our adaptive metamodel-building algorithm and demonstrate the feasibility of this approach for engines, we initially employ a simplified engine combustion model (outlined in the next subsection) that is computationally inexpensive but still has the correct global dynamics. By using the simplified model to establish our basic methodology, we expect to reduce costs and maximize the efficient use computing resources. Further, we expect it to be more straightforward to demonstrate the accuracy of the initial metamodels compared with the simple model. Once our adaptive concurrent simulation strategy has been fully demonstrated with the simple combustion model, we

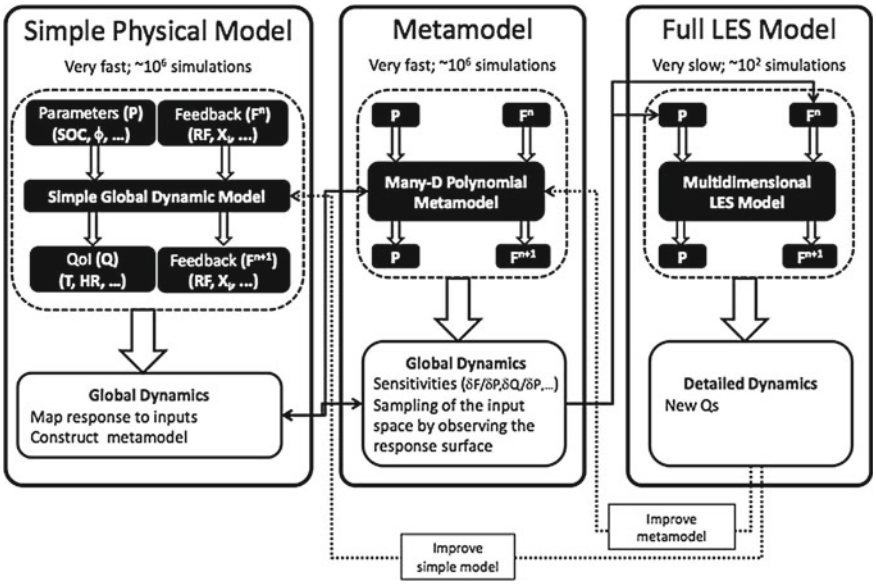

Fig. 2 The initial metamodels will be refined using simulations with more highly detailed physical models. Exploration of the detailed physical model response surface will be guided by the initial metamodels and make further use of concurrent adaptive simulation

plan to repeat the metamodel-building procedure with highly detailed CFD combustion models (see Fig. 2 for a conceptual schematic of implementation). These more detailed simulations will be carried out on massively parallel computers, using the advantages of parallel computation as much as possible. In the end, the ultimate objective is to create and use refined metamodels, which can better exploit parallel computational scaling, to more intensively explore the combustion instability hyperspace.

2.2 Simple Physical Combustion Model

The simple combustion model that we employ for developing our initial adaptive metamodel-generation scheme uses a lumped-physics approach to approximate propagating-flame combustion in a single-cylinder, four-stroke, spark-ignited internal combustion engine. We provide a brief description here to illustrate the major components of this model. Similar models have been widely studied and apply equally to EGR dilution.

We assume that a gaseous propane (C_3H_8) fuel is mixed with a set ratio of air, defined as the equivalence ratio (denoted φ, which here is defined as the actual fuel-air ratio divided by fuel-air ratio needed to exactly oxidize all the fuel; $\varphi < 1$ is fuel-lean), as the incoming charge. The assumed combustion stoichiometry is:

$$C_3H_8 + 5(O_2 + 3.76N_2) \rightarrow 3CO_2 + 4H_2O + 18.8N_2. \quad (1)$$

The cool intake charge is introduced into the engine cylinder and mixes with any hot exhaust gases from the previous cycle which did not get expelled from the cylinder during the exhaust stroke. The amount of the exhaust gas feeding forward to the next cycle is referred to as the residual fraction and typically ranges from 5 to 20 % in different operating modes. Residual gases are important because they change the initial conditions of the succeeding cycle and are one of the main drivers for cyclic dispersion; residual gas with unburned fuel changes the cylinder effective equivalence ratio away from the nominal value and thus affects combustion.

Once the intake valve closes, the mixture is compressed as the cylinder volume decreases as the piston travels toward its farthest range of motion (termed 'Top dead center'), and pressure and temperature rise. At a certain defined point near top dead center, combustion is initiated with energy input by a spark. In a simple model, the cumulative mass fraction of fuel which burns (MFB) follows a Wiebe exponential form [10]:

$$\mathrm{MFB}(\theta) = 1 - exp\left[-a \cdot \theta^{m+1}\right], \quad (2)$$

where a and m are shape factors, and θ is a normalized time term to complete combustion. In engines, it is useful to demark time by the angular crankshaft position, which rotates 720° in a four-stroke engine cycle. Figure 3 shows a representative form of the Wiebe function relating the mass fraction burned to the normalized combustion duration (on a crank-angle basis).

We also include a global energy balance over the cylinder that accounts for heat loss, friction, and piston work. During the power stroke, the charge continues to burn as prescribed by the Wiebe function. When the piston reaches a preset expansion angle, the exhaust valve opens and most of the hot cylinder contents leave the cylinder, except for the residual gases, whose composition and temperature depend on conditions at valve opening. The work delivered by the piston depends on combustion phasing, that is, the crank angle at which combustion initiates. If combustion is

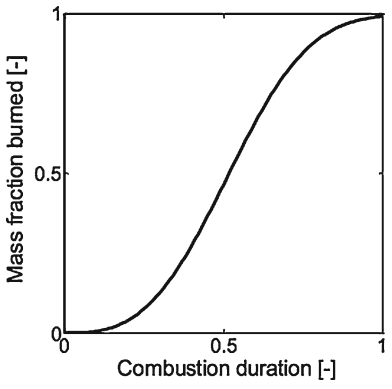

Fig. 3 Form of the Wiebe function at nominal values of $a = 5$ and $m = 2$

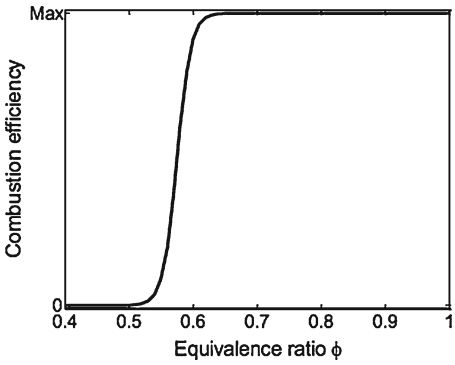

Fig. 4 Functional form of combustion efficiency with respect to equivalence ratio

too early (while the piston is still compressing the charge), very large pressures are produced, but work output is low. If combustion is initiated too late, both pressure and work are low. For this reason, phasing is treated as a model input parameter, and it is subject to some natural variations due to the cylinder conditions (e.g., chemistry, turbulence, etc.).

As noted in the Introduction, combustion becomes unstable as the fuel charge is diluted by excess air or recirculated exhaust gases. The net fraction of fuel consumed in each cycle is referred to as the combustion efficiency, and this drops off sharply when dilution reaches a certain critical level (see Fig. 4). The physics behind this behavior relates to the details of flame propagation and has been described in several ways, including percolation theory [10–12]. The sharpness of the transition is a strong contributor to combustion instability, and can lead to bifurcated cycle-to-cycle oscillations as dilution increases. For our simple model, we employ a simple functional form of the combustion efficiency with effective equivalence ratio that mimics the behavior seen in percolation models and also matches experimental observations.

Although the above model is relatively simple compared to detailed in-cylinder CFD models, it generates many key global combustion variables, including crank-angle-resolved fuel and oxygen concentrations, cylinder pressure, and temperature and integrated cycle-resolved variables including residual gas fraction and temperature, net piston work, and net fuel conversion. For this initial study, we chose net fuel conversion (expressed in terms of heat release) as a key indicator of combustion quality; this we term the quantity of interest. Depending on the particular needs, however, other relevant quantities of interest or a metric based on combinations of variables may be defined.

2.3 Adaptive Sampling Methodology

While direct Monte Carlo (MC) simulation lends itself to parallel computation, it is not an efficient way to explore the multi-dimensional response surface of complex models because it probes the hyperspace randomly. Furthermore, the MC approach

does not offer the ability to construct a surrogate approximation of the system with respect to the desired parameters. On the other hand, exhaustive combinatorial exploration of the surface (i.e., tensor product combinations of parameters) is also inefficient since the number of required simulations grows exponentially as dimension (number of parameters) increases. In this work, we efficiently explore the parameter space with use of adaptive sparse grid sampling, which chooses new simulation conditions as knowledge of the dynamics increases. Our initial goal is to identify the most efficient implementation using a simple model representation and then apply it to simulations with more detailed physical combustion systems to create refined metamodels.

Briefly, sparse grid sampling originated as an alternative quadrature technique used to approximate high-dimensional integrals [13], where linear combinations of only a few tensor product abscissas are chosen to maintain the asymptotic accuracy of the corresponding full tensor product approximation. Later, it was trivially extended to multi-dimensional interpolation, where hierarchical global Lagrange-type polynomials or local piecewise nodal polynomials are utilized [14, 15]. Moreover, adaptive refinement is achieved by setting a tolerance for the hierarchical surplus of the polynomial basis, which allows high-dimensional approximations in regions of interest [16–19].

For our purposes, we adaptively approximate the multidimensional model response surface by a sparse linear combination of simpler interpolating functions. However, due to the possible steep gradients and/or sharp transitions, we utilize a linear piecewise (local) polynomial basis rather than a global polynomial approach; extending the one-dimensional basis to a multi-dimensional sparse approximation is not trivial. In what follows, we use our implementation of the sparse grid adaptive algorithm 847 [20]. In the future, we intend to extend this approach to the even more efficient sparse grid adaptive wavelet method [19].

3 Discussion of Preliminary Results

For this first phase, we studied the simple physical model response at two nominal equivalence ratios, $\varphi = 0.8$ and 0.7. The behavior at $\varphi = 0.8$ is relatively simple, which unperturbed is a period-1 condition; for $\varphi = 0.7$, a period-2 condition is observed, as the critical transition point is approached with certain parametric variations. The parameter space is described by 8 variables relevant to the physical model: (1) the start of combustion (phasing); (2) a perturbation to the nominal fueling equivalence ratio; (3) a perturbation to the combustion rate parameter (m); (4, 5) coefficients (α and β) of the POD modes of the combustion chemistry; (6) the residual fraction; (7) the residual temperature; and (8) cylinder molar charge at intake valve closing. (Feedback variables include parameters 4–8.) Reasonable ranges of each parameter are defined, and a sampling grid is defined within a normalized range of each parameter according to the adaptive sparse-grid sampling scheme. The simple physical model exhibits very sharp changes in combustion with small parametric changes, and

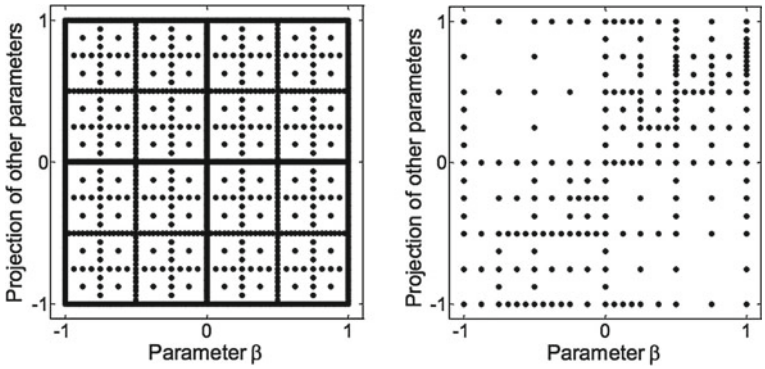

Fig. 5 2D projection of sparse grid using full (*left*) and adaptive (*right*) approach

hence we use a piecewise linear adaptive approximation of the response surface. For a two-dimensional projection of the problem, adaptive iteration allows us to achieve the same accuracy with only 210 adaptive points as opposed to 1537 full sparse grid points. In eight dimensions, the computational savings of using an adaptive approach is more than 10 times. For example, Fig. 5 depicts a map of sampling points over the normalized range of parameter variations. The adaptive sparse grid samples where most needed, while still maintaining accuracy, resulting in a significant reduction in the number of required sample points.

Using the adaptive sparse grid method with concurrent simulation of the simple physical model, we produced a metamodel which faithfully captures even the sharp nonlinear transitions of the simple model dynamics. Such faithful approximation is seen in Fig. 6, which displays the output of parameter β based on a 2D projection of the input parameters (as described above). The response surface matches that of the original model very well, with a few small wrinkles which are due to the piecewise linear nature of the basis functions.

The metamodel also approximates the dynamical behavior of the simple physical model faithfully. This is revealed in the different dynamical features visible at the two equivalence ratios of interest. These features are highlighted in Fig. 7, which compares symbol-sequence histograms generated by the simple physical and metamodels for consistent values of the input parameters at the nominal equivalence ratios of 0.8 and 0.7. The specific symbolization scheme used in this figure is based on partitioning the global combustion heat release into eight equiprobable regions (symbols), with each value on the horizontal axis representing a unique sequence of two successive symbols (with the sequence converted from octal to a decimal index); the vertical axis reflects the relative frequency of occurrence for each sequence. Such symbol statistics have proved to be useful for describing the noisy behavior of engine cyclic combustion variability [21].

In Fig. 7, the relatively flat histogram on the left (for $\varphi_0 = 0.8$) represents expected random variations about the equiprobable value of 1/64, which is consistent with

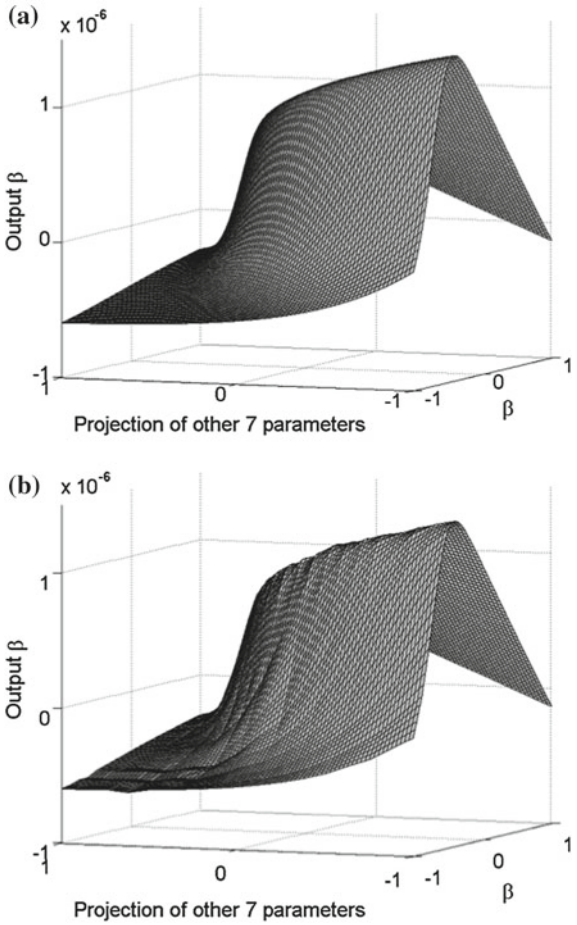

Fig. 6 Response of parameter β based on a 2D projection of parameters β and the other seven parameters, for the simple physical model (*top*) and the metamodel (*bottom*). The metamodel captures the sharpness of the surface, but because of the approximation scheme, the surface has very small wrinkles missing in the original model surface

noisy combustion variations around a fixed point. At increased dilution ($\varphi_0 = 0.7$ on the right), the sharp peaks at certain sequences reflect the deterministic feedback effects from residual gas in the simple physical model, which lead to large combustion oscillations.

4 Summary and Next Steps

We have described a methodology to explore the long-time-scale dynamics of a computationally expensive engine combustion model by using concurrent single-

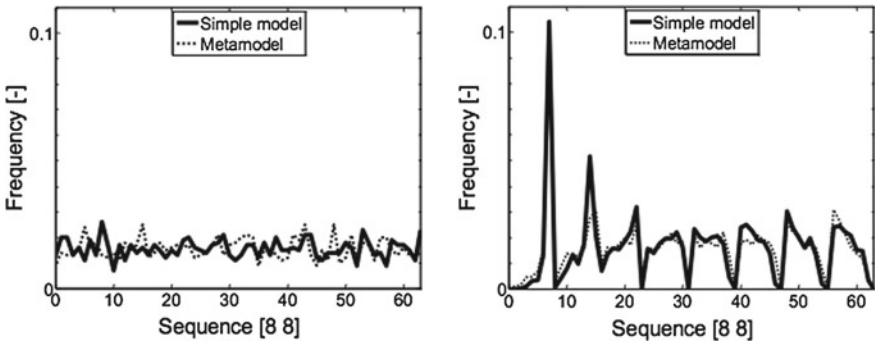

Fig. 7 Symbol-sequence histograms comparing simple and metamodel dynamics for equivalence ratio of 0.8 (*left*), dominated by stochastic variations, and 0.7 (*right*), dominated by deterministic effects

cycle simulations guided by adaptive sparse-grid sampling of the parameter hyperspace. We believe this methodology is especially suited for implementation on massively parallel computing architectures and will prove to be a significant advance over direct serial (in cycles) simulations with detailed multi-scale physical combustion models for studying rare and complex combustion instabilities.

Using a simple physical model which captures the global dynamical trends in observed engine behavior, we have applied the methodology to generate a combustion metamodel that appears to accurately mimic the nonlinear features of the simple physical model. With this metamodel, it is possible to very rapidly explore the long-timescale dynamics for a very large range of parametric variations. In addition, the metamodel structure is readily amenable to efficient scaling on massively parallel computing architectures (such as Titan at Oak Ridge National Laboratory, which has more than 300,000 CPU cores and over 18,000 GPUs).

In this next phase of this research, we will be implementing a limited number of high-fidelity LES simulations, with detailed combustion chemistry, on high performance computing facilities at the National Center for Computational Sciences. We will utilize the concurrent adaptive simulation methodology and the initially generated metamodels to guide the high-fidelity simulations to maximize the information produced. This information will, in turn, be used to construct more refined metamodels. With the latter, we will explore detailed questions posed by our industry collaborators regarding the fundamental nature of dilute combustion instability and how it can be controlled to meet fuel efficiency and emissions targets.

Acknowledgments This research was sponsored by the U.S. Department of Energy (DOE) under Contract DE-AC05-00OR22725 with the Oak Ridge National Laboratory, managed by UT-Battelle, LLC. The authors specifically thank Gurpreet Singh of the Office of Vehicle Technologies, DOE, for sponsoring this work.

References

1. U.S. Department of Enegy, *Report on the First Quadrennial* (Technology Review, September, 2011). 2011
2. U.S. Energy Information Administration. Annual Energy Outlook 2011 with Projections to 2035, (2011).
3. O. Vemorel, S. Richard, O. Colin, C. Angelberger, A. Benkenida, *Predicting cyclic variability in a 4valve SI engine using LES and the AVBP CFD code*. International Multidimensional Engine Modeling Users Group Meeting, Detroit, Michigan, USA, (2007).
4. B. Enaux, V. Granet, O. Vermorel, C. Lacour, C. Pera, C. Angelberger, LES study of cycle-to-cycle variations in a spark ignition engine. Proc. Combust. Inst. **33**(2), 3115–3122 (2011)
5. V. Granet, O. Vermorel, C. Lacour, B. Enaux, V. Dugue, T. Poinsot, Large-Eddy Simulation and experimental study of cycle-to-cycle variations of stable and unstable operating points in a spark ignition engine. Combust. Flame **159**(4), 1562–1575 (2012)
6. V.C.P. Chen, K.-L. Tsui, R.R. Barton, M. Meckesheimer, A review on design, modeling and applications of computer experiments. IIE Trans. **38**(4), 273–291 (2006)
7. G.G. Wang, S. Shan, Review of metamodeling techniques in support of engineering design optimization. ASME J. Mech. Des. **129**(4), 370–380 (2007)
8. T.W. Simpson, V. Toropov, V. Balabanov, F.A.C. Viana, Design and analysis of computer experiments in multidisciplinary design optimization: a review of how far we have come or not, in *proceedings of the 12th AIAA/ISSMO Multidisciplinary Analysis and Optimization Conference*, Victoria, BC, Canada, Paper No. AIAA 2008–5802, (2008)
9. Y. Kondo, K. Kaneko, S. Ishihara, Identifying dynamical systems with bifurcations from noisy partial observation. Preprint at http://arxiv.org/1208.4660 (2012)
10. J.I. Ghojel, Review of the development and applications of the Wiebe function: a tribute to the contribution of Ivan Wiebe to engine research. Int. J. Engine Res. **11**(4), 297–312 (2010)
11. I. Kul, D.L. Gnann, A.L. Beyerlein, D.D. Desmarteau, Lower flammability limit of difluoromethane and percolation theory. Int. J. Thermophys. **25**(4), 1085–1095 (2004)
12. I. Kul, C. Blaszkowski, Flammability studies of isomeric structures of ethane derivatives and percolation theory. Int. J. Thermophys. **28**(3), 906–917 (2007)
13. S.A. Smolyak, Quadrature and interpolation formulas for tensor products of certain classes of functions. Soviet Mathematics Doklady **4**, 240–243 (English translation) (1963)
14. M. Griebel, Adaptive sparse grid multilevel methods for elliptic PDEs based on finite differences. Computing **61**(2), 151–179 (1998)
15. F. Nobile, R. Tempone, C.G. Webster, An anisotropic sparse grid stochastic collocation method for partial differential equations with random input data. SIAM J. Numer. Anal. **46**(5), 2411–2442 (2008)
16. F. Nobile, R. Tempone, C.G. Webster, A sparse grid stochastic collocation method for partial differential equations with random input data. SIAM J. Numer. Anal. **46**(5), 2309–2345 (2008)
17. X. Ma, N. Zabaras. An adaptive hierarchical sparse grid collocation algorithm for the solution of stochastic differential equations. J. Comput. Phys. **228**(8) 3084–3113 (2009)
18. X. Ma, N. Zabaras, An adaptive high-dimensional stochastic model representation technique for the solution of stochastic partial differential equations. J. Comput. Phys. **229**(10), 3884–3915 (2010)
19. M. Gunzburger, C.G. Webster, G. Zhang, An adaptive wavelet stochastic collocation method for irregular solutions of partial differential equations with random input data. ORNL/TM-2012/186. To appear, SIAM J. Uncertainty Quantification (2012)
20. A. Klimke, B. Wohlmuth, Algorithm 847: spinterp: Piecewise multilinear hierarchical sparse grid interpolation in MATLAB. ACM Trans. Math. Softw. **31**(4), 561–579 (2005)
21. C.E.A. Finney, J.B. Green, C.S. Daw, Symbolic time-series analysis of engine combustion measurements. Society of Automotive Engineers Technical Paper 980624 (1998).

Investigating the Use of Manifold Embedding for Attractor Reconstruction from Time Series

Lucas A. Overbey and Colin C. Olson

Abstract Spatio-temporal analysis of a time series from a complex dynamical system often requires reconstruction of the state-space attractor from observations of a single state variable. The standard approach takes advantage of the Takens delay embedding theorem to obtain the reconstruction. We investigate here a modification which makes use of nonlinear spectral graph techniques for learning the underlying manifold from high-dimensional data. Specifically, we examine how well diffusion maps and locally-linear embedding recover system dynamics and their sensitivity to parameters. Analysis is conducted using individual observations of the chaotic Lorenz and Hénon attractors. We show that manifold embeddings, given selected parameter choices, can improve forecasting capability for chaotic time series.

1 Introduction

Many biological, environmental, and mechanical systems exhibit chaotic behavior [1–3]. Given limited observations of the system it is often useful to reconstruct the state space in order to better analyze its dynamics. Takens' seminal embedding theorem [4] provides a mechanism for unfolding the attractor from a single observed time series. Suppose we wish to characterize a system, represented by the multidimensional phase space that evolves such that $\mathbf{x}(n+1) = \mathbf{F}(\mathbf{x}(n))$, where $\mathbf{x}(n) = [x_1(n), x_2(n), \ldots, x_d(n)]$.

L. A. Overbey (✉)
SPAWAR Systems Center Atlantic, P.O. Box 190022, North Charleston, SC 29419-9022, USA
e-mail: lucas.overbey@navy.mil

C. C. Olson
Sotera Defense Solutions Inc, 2200 Defense Highway, Suite 405, Crofton, MD 21114-2929, USA
e-mail: colin.olson@gmail.com

V. In et al. (eds.), *International Conference on Theory and Application in Nonlinear Dynamics (ICAND 2012)*, Understanding Complex Systems,
DOI: 10.1007/978-3-319-02925-2_24,

Given an observation which is assumed to be a scalar projection of a system's dynamics, $s(n) = S(\mathbf{x}(n))$, Takens's theorem guarantees that we can construct a d_E-dimensional space that inherits many of the dynamical properties of the original d-dimensional system $\mathbf{X}$. The reconstruction unfolds the dynamics by taking time-delayed copies of the observation:

$$\mathbf{y}(n) = [s(n), s(n-T), \ldots, s(n-(d_E-1)T)], \tag{1}$$

where T is an integer multiple of the sampling time chosen such that the dynamics are optimally unfolded in a minimum number of allowable dimensions d_E.

Much work has focused on finding the delay T and dimension d_E that properly unfold the attractor without the complexity associated with unnecessarily large dimension [5–7]. However, construction of this state space does not necessarily provide enough information for a full dynamic analysis. For example, one may wish to forecast a chaotic system's future state given current observations. While the delay-reconstructed attractor provides the capability to produce other measures of the system dynamics, predictions are still inherently difficult because of the sensitivity to initial conditions exhibited by chaotic systems.

It may be constructive to investigate reconstructions that orient trajectories in phase space such that one can improve certain analyses. Broomhead and King [8] employed a singular-value decomposition (SVD) to map the time-delay embedding into a set of empirical orthogonal functions (EOFs) in $\mathbf{Y}$, weighted and ranked by their corresponding principal components (PCs). The PCs are found by projecting onto the principal axes of the d_E-dimensional ellipsoid that best fits the covariance of the data in $\mathbf{Y}$ in the least-squares sense. This idea has spawned the burgeoning field of singular spectrum analysis (SSA) [9, 10], which has proven useful for obtaining meaningful information about the spatial and temporal characteristics of the underlying system. The SSA construction is optimal when the underlying dynamics are linear. However, nonlinear processes will generally produce data lying on a curved manifold (representative of the state-space attractor), with non-Gaussian distributions unrepresentative of the ellipsoid used for identifying the PCs.

An alternative approach can be derived from static high-dimensional data analytics, where alternatives to PC analysis have been introduced to account for data lying on highly nonlinear manifolds. Many of these *manifold learning* approaches attempt to preserve local distance-based structures through spectral graph techniques, and have wide applicability in dimensionality reduction [11] and semi-supervised learning [12]. Recently, these techniques have begun to manifest in nonlinear time series analysis [13, 14], but their applicability is not fully understood. Giannakis and Majda [13] evaluated Laplacian eigenmaps as a technique for decomposing the state space analogous to SSA, but did not look at whether such techniques preserve system dynamics. Suetani and Akaho [14] attempt to employ ISOMAP as a dimensionality-reduction mechanism for a one-dimensional model embedded using a higher-dimensional delay-embedded observation.

Here, we use two manifold learning techniques, diffusion maps [15] and locally linear embedding (LLE) [16], to perform a nonlinear mapping of the reconstructed

state space that takes advantage of the actual nonlinear structure of attractor manifolds. We demonstrate that given the right manifold learning parameters, one can preserve the global invariant properties of the attractor. However, we find that for the purposes of time series forecasting, it may be advantageous to manipulate the manifold such that the global properties are not preserved; by, for example, embedding such that normally close but divergent trajectories are instead separated from each other such that selected near neighbors traverse similar paths through the state space. Results are shown for the chaotic Hénon map [17] and Lorenz system [2].

2 Manifold Embedding

Given the time-delayed embedding constructed as in Eq. (1), SSA involves an SVD decomposition,

$$\mathbf{Y} = \sum_{i=1}^{d_E} \mathbf{u}_i \sigma_i \mathbf{v}_i^{\top}, \qquad \sigma_i \geq 0, \tag{2}$$

where σ_i are the singular values and $\mathbf{u}_i$ and $\mathbf{v}_i$ are the left and right singular vectors, respectively. The weighted and ranked set of EOFs are:

$$\mathbf{E} = \sum_{i=1}^{d_E} \mathbf{v}_i \sigma_i . \tag{3}$$

This type of projection can yield poor representations if the underlying manifold is not linear [12, 15]. We utilize alternative decompositions based on manifold learning to account for nonlinear geometric structure in attractor manifolds. Given the context of nonlinear time series analysis based on a reconstructed phase space, we refer to these new approaches as *manifold embeddings*.

2.1 Locally Linear Embedding

LLE [16] is an unsupervised learning algorithm that computes neighborhood-preserving embeddings of high-dimensional or nonlinear inputs. By preserving linear reconstructions of local neighborhoods, LLE is able to learn the global structure of nonlinear manifolds. It has been applied to many machine learning problems including image and text classification. Typically, the LLE procedure involves a mapping of statically-generated high-dimensional data. Introducing this concept for a dynamics application, we describe the analogous procedure implemented on a time-delayed reconstruction of the state space $\mathbf{Y}$ (Eq. (1)). For each point on the reconstructed attractor, the κ nearest neighbors to that point are found based on geodesic distances.

LLE then computes weights W_{ij} by minimizing the cost function:

$$\gamma(W) = \sum_{i=1}^{N} |\mathbf{Y}_i - \sum_{j=1}^{\kappa} W_{ij}\mathbf{Y}_j|^2, \qquad \sum_{j=1}^{\kappa} W_{ij} = 1, \tag{4}$$

where N is the number of points on the attractor.

Next, the original attractor is mapped onto a new vector $\mathbf{Z}$ such that most of the data is represented in the first few dimensions. This mapping is done by minimizing the new cost function:

$$\Phi(\mathbf{Z}) = \sum_{i=1}^{N} |\mathbf{Z}_i - \sum_{j=1}^{\kappa} W_{ij}\mathbf{Z}_j|^2, \tag{5}$$

where the weights W_{ij} are now fixed and the coordinates $\mathbf{Z}$ are optimized. Equation (5) is minimized by solving a sparse $N \times N$ eigenvalue problem, whose eigenvectors provide an ordered set of orthogonal coordinates centered at the origin.

Thus, a manifold embedding using LLE will produce a ranked mapping of the reconstructed attractor that preserve local neighbor distances. Note that this is not guaranteed to preserve global invariants in the dynamics as the temporal relationship of points is not taken into account. Therefore, depending on the choice of neighborhood size κ, the manifold embedding based on LLE may result in dynamically different attractors.

2.2 Diffusion Maps

An alternative approach similarly seeks to reorganize data based on its underlying geometry such that local relationships between nearby points are preserved. However, diffusion maps [15] achieve this through a local similarity measure that represents a time-dependent diffusion process. Given a reconstructed attractor $\mathbf{Y}$, the connectivity of nearby points on the manifold can be expressed by a normalized likelihood function, $k(\mathbf{Y}_i, \mathbf{Y}_j)$, known as the diffusion kernel. The diffusion kernel is symmetric ($k(\mathbf{Y}_i, \mathbf{Y}_j) = k(\mathbf{Y}_j, \mathbf{Y}_i)$) and positivity preserving ($k(\mathbf{Y}_i, \mathbf{Y}_j) \geq 0$). A common choice is the Gaussian kernel,

$$k(\mathbf{Y}_i, \mathbf{Y}_j) = \exp\left(-\frac{|\mathbf{Y}_i - \mathbf{Y}_j|^2}{\sigma}\right). \tag{6}$$

Given the positivity preserving property, the connectivity can be related to the kernel function by

$$connectivity(\mathbf{Y}_i, \mathbf{Y}_j) = p(\mathbf{Y}_i, \mathbf{Y}_j) = \frac{1}{\nu_{\mathbf{Y}}} k(\mathbf{Y}_i, \mathbf{Y}_j), \tag{7}$$

where p can be viewed as the transition kernel of a Markov chain on $\mathbf{Y}$, and $P_{ij} = p(\mathbf{Y}_i, \mathbf{Y}_j)$ is the row-normalized diffusion matrix. $v_{\mathbf{Y}}$ here is a normalization constant. In terms of a random walk, P_{ij} represents the probability for a single step taken from i to j, and P_{ij}^t is the same probability over time t (or analogously, path length in a graph).

Next, we define the diffusion metric based on this structure, which measures the similarity between two points i and j in the observation space based on the probability of reaching point j from point i in t steps. The diffusion distance is

$$D_t(\mathbf{Y}_i, \mathbf{Y}_j)^2 = \sum_n |P_{ik}^t - P_{nj}^t|^2. \tag{8}$$

$D_t(\mathbf{Y}_i, \mathbf{Y}_j)$ is more robust to noise perturbation than several other mapping techniques, for example, those that involve geodesic distances, because it involves a summation over all paths of length t connecting $\mathbf{Y}_i$ to $\mathbf{Y}_j$. The diffusion distance in the state space $\mathbf{Y}$ becomes the Euclidean distance in the new diffusion space $\mathbf{Z}$. We can perform this mapping using an eigendecomposition of the diffusion matrix P_{ij}:

$$\begin{aligned} \mathbf{P} &= \mathbf{V}^{-1}\mathbf{K}, \\ \mathbf{Z} &= \sum_m^{d_E} \lambda_m^t \Psi_m, \end{aligned} \tag{9}$$

where $\mathbf{V}$ is the a diagonal matrix consisting of the row-sums of $\mathbf{K}$, λ_m are the eigenvalues, and Ψ_m are the eigenvectors.

Like LLE, the scale parameter (in this case σ for a Gaussian kernel) is critical to the character of the mapping. We are preserving diffusion distances which are based on random walks across not-necessarily temporally-correlated points. Again, global invariants of the dynamics are not guaranteed to be preserved. In the following sections, we investigate what embedding parameters will better preserve invariants and what parameter choices will produce the best results for a forecasting application.

2.3 Chaotic Attractor Embeddings

We illustrate these new embedding approaches by employing them on simulations of two well-known models capable of exhibiting chaos: the Hénon map and the Lorenz system. The Hénon map [17] is described by:

$$\begin{aligned} x_{n+1} &= y_n + 1 - ax_n^2, \\ y_{n+1} &= bx_n. \end{aligned} \tag{10}$$

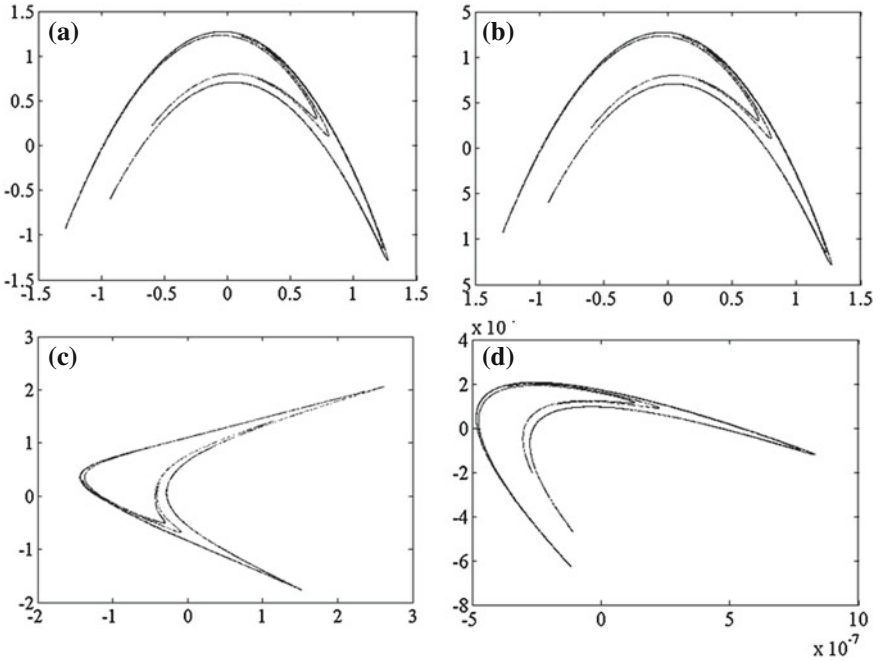

Fig. 1 Reconstructed canonical (chaotic) Hénon map attractor, using **a** delay embedding, **b** SVD embedding, **c** manifold embedding with LLE ($\kappa = 60$), and **d** manifold embedding with a diffusion map $\sigma = 200$

We utilize parameters $a = 1.4$ and $b = 0.3$ which yield chaotic dynamics. After removing transients, the time-delayed attractor is reconstructed using x_n as the observation. d_E is selected using the popular false nearest neighbors approach [6], and the delay T is chosen based on the average mutual information [5]. Note that while Broomhead and King [8] utilized a delay $T = 1$ to construct the embedding prior to performing SVD, we found that the "proper" delay as found by the mutual information performed better in our subsequent analyses in the remaining sections.

The reconstructions are shown in Fig. 1. SVD provides a linear transformation of the delay embedding, scaled by covariance ranks. LLE and diffusion map embeddings produce results somewhat akin to the SVD embedding in these examples. Here we chose large bandwidth parameters for both LLE (κ) and diffusion map (σ), such that global distances are better preserved in the mappings. LLE provides the least similar embedding.

We utilize a similar approach to embed and map the chaotic Lorenz ODE:

$$\begin{aligned} \dot{x} &= \sigma(y - x), \\ \dot{y} &= x(\rho - z) - y, \\ \dot{z} &= xy - \beta z, \end{aligned} \tag{11}$$

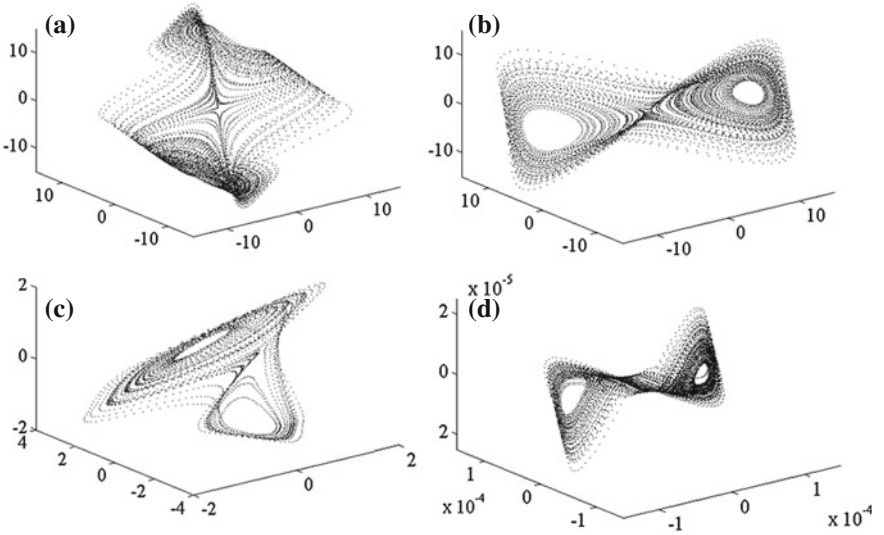

Fig. 2 Reconstructed chaotic Lorenz attractor, using **a** delay embedding, **b** SVD embedding, **c** manifold embedding with LLE ($\kappa = 60$), and **d** manifold embedding with a diffusion map $\sigma = 200$

where $\sigma = 10$, $\beta = 8/3$, and $\rho = 28$ for a chaotic regime as originally described by Lorenz [2]. We simulate the Lorenz using a step size $\Delta t = 0.1$. Removing transients and embedding x using a similar procedure to the Hénon map, the first three coordinates of the embeddings are shown in Fig. 2. Here, the SVD and diffusion map approaches produce visually similar results. The main difference between the two lies in the saddle point region of the Lorenz, where the diffusion map tends to squeeze the trajectories together in the first two coordinates resulting in a spiral trajectory in the third coordinate. The LLE projection is again the least similar and produces an asymmetric embedding between the two "butterfly wings" of the Lorenz. We conjecture that the large bandwidth of the diffusion map embedding leads to a fully populated adjacency matrix which better represents global dynamics in contrast to the banded (local) structure of the LLE adjacency matrix.

3 Global Dynamic Invariants

The goal of Takens' theorem [4] is to reconstruct the dynamics of the state space using only a single observed time series. This reconstruction conserves global invariant properties of the dynamics as long as a reliable embedding dimension d_E and time delay T are chosen. To test whether a selection of these properties are conserved through manifold embedding, we look at estimations of the Lyapunov spectrum [18] and correlation dimension [19].

3.1 Lyapunov Exponents and the Kaplan-Yorke Dimension

Lyapunov exponents (LEs) of a dynamical system describe the rate of separation of infinitesimally close trajectories in phase space. A chaotic system is typically characterized by at least one positive LE, with the sum of the exponents less than zero, thus conserving the dissipative nature of the system. A useful extension to the Lyapunov spectrum is the Kaplan-Yorke dimension [20], which provides an upper bound for the information dimension of the system. This measure is defined as:

$$D_{KY} = j + \sum_{i=1}^{j} \frac{\lambda_i}{|\lambda_{j+1}|}, \tag{12}$$

where λ_i are the LEs in descending order and j is the maximum integer such that the sum of the j largest exponents is non-negative.

To estimate the LEs and D_{KY} from a reconstructed phase space, we employ the method described by Sano and Sawada [21]. The process involves estimation of the flow operator A^n for a fiducial point $\mathbf{X}_n$ by comparing the t forward trajectories of its nearest neighbors, with a renormalization at each step n using the Gram-Schmidt procedure.

We compare the first λ_1 and D_{KY} for several different embedding approaches and parameter choices (Table 1). One can see that, given large enough bandwidth parameter choices for the manifold embedding methods, one can adequately maintain the properties of the Lyapunov spectra. Although not shown, it is also imperative to make proper d_E and T choices to preserve these properties for all listed approaches.

Table 1 λ_1, D_{KY}, and ν results for different embedding approaches

System	Embedding method	d_E	σ	K	λ_1	D_{KY}	ν
Hénon	System	2	–	–	0.418	1.26	1.21
Hénon	Delay emb	2	–	–	0.418	1.26	1.19
Hénon	SVD	2	–	–	0.420	1.27	1.20
Hénon	LLE	2	–	60	0.420	1.27	1.18
Hénon	Diff map	2	200	–	0.432	1.21	1.25
Lorenz	System	3	–	–	8.77E-3	2.07	2.04
Lorenz	Delay emb	4	–	–	9.07E-3	2.35	2.04
Lorenz	SVD	3	–	–	1.11E-2	2.16	2.12
Lorenz	LLE	3	–	60	1.12E-2	2.17	2.00
Lorenz	Diff map	3	200	–	1.11E-2	2.16	2.12
Lorenz	Diff map	3	1.0	–	9.86E-2	2.28	1.26

3.2 Correlation Dimension

Correlation dimension is an alternative measure of (fractal) dimensionality of strange attractors. For a phase space **X**, the correlation integral can be calculated by [19]:

$$C(\xi) = \lim_{n\to\infty} \frac{g}{N^2}, \tag{13}$$

where g is the number of pairs of points whose distance is less than ξ. For sufficiently large and evenly distributed points, the correlation integral (for small values of ξ) will take the form:

$$C(\xi) \sim \xi^{\nu}, \tag{14}$$

where ν is the correlation dimension. The results for correlation dimension in Table 1 are comparable to LE results, showing that one can maintain global invariants in the dynamics through manifold embedding, but again, care must be taken to ensure proper parameter choices.

4 Forecasting

Given the above results, one can make the case that manifold embeddings are capable of preserving the global dynamics given proper choices of embedding and manifold learning parameters. However, if one wished to calculate such global dynamic invariants, one could just as easily use the previous delay-embedding or SVD approaches and get comparable results. An interesting question is whether manifold embedding approaches can provide any analytic gains for forecasting where the state of the system will be at some future time.

A key problem with chaotic systems is their inherent unpredictability. We wish to see if we can achieve any gains in predictability through the use of a mapping that is structured based on the manifold itself. Here we will focus on manifold embedding with diffusion maps as they largely outperform LLE embeddings. Our forecasting evaluation involves a form of "self" prediction error. We ask, given an initial condition on a potentially noisy chaotic system, how well and how far ahead can we forecast where the system will be some time (prediction horizon) into the future. We begin by selecting a uniform subset of initial conditions (chosen as 0.1 % of the data [22]).We then time-evolve the nearest geometrical neighbors and the nearest point to the centroid of these neighbors some time Δt in the future. The centroid of the time-evolved neighbors represents a "prediction" of the time-evolved point. Therefore, we can assess how closely we correctly predicted this evolution by the Euclidean distance ε between the centroid and this point at time $t + \Delta t$. To account for the different sizes and potential dimensions of the attractors, we normalize the prediction errors by the size of the median distance on each attractor.

It may be the case that a manifold embedding that does not preserve the global invariant properties of the attractor may still yield better abilities for forecasting. In

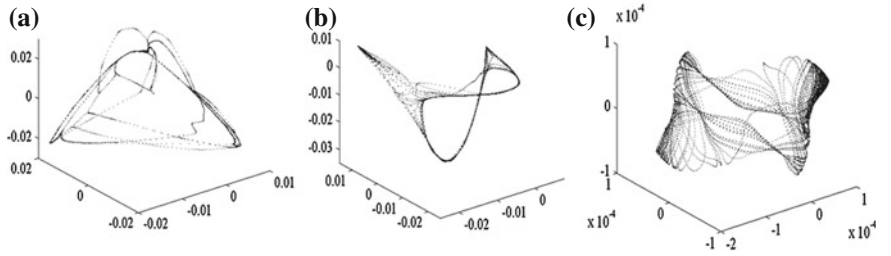

Fig. 3 First three coordinates of the Lorenz attractor using manifold embedding, diffusion map, with $d_E = 8$ and **a** $\sigma = 1$, **b** $\sigma = 8$, and **c** $\sigma = 200$. The threads of common trajectories on "spider webs" of the attractor in (**a**) typically provide better ability to forecast over short time scales, while global properties are better preserved in (**c**)

general, lower bandwidths will result in preservation of only local distances in the structure and allow more freedom in global distances to produce a transformation such that more of the manifold is unfolded in the first few coordinates. We visualize an example of this in Fig. 3. For smaller σ, the global structure of the attractor is not conserved but local trajectories are; thus, a "spider-web" or "cabling" effect occurs, where like trajectories are mapped very near each other in space and unlike trajectories are pushed away from each other. Unfortunately, similar yet divergent trajectories are also mapped near each other at positions corresponding with high sensitivities to initial conditions, e.g. saddle points. Depending on the balance between these competing effects, the trajectories of near neighbors may help improve predictability for this choice of σ.

Thus we consider a variety of different embedding dimension d_E and bandwidth σ choices for the diffusion map approach. We evaluated the chaotic Lorenz attractor described above, using $3 \leq d_E \leq 10$ and $1 \leq \sigma \leq 200$. A selection of these ε results are plotted as a function of prediction horizon Δt below (Fig. 4a). We compared a variety of nearest neighbor sizes in the prediction error calculation, and found the results to be fairly consistent. The results use 12 nearest neighbors.

A few observations are immediately apparent. First, the predictability tends to be better for a bandwidth of $\sigma = 1$ than for $\sigma = 200$. Although the higher bandwidth better preserves global dynamical properties, the local approach better separates the data into "threads" of common trajectories (Fig. 3a). Therefore, one can provide better forecasts using the lower bandwidth, especially at low prediction horizons. Note that as the prediction horizon increases, the high bandwidth case begins to outperform lower bandwidth cases. Interestingly, higher embedding dimension also tends to lead to better predictability. This is perhaps a result of the fact that manifold learning algorithms can preserve longer time scales in the dynamics when more time-delayed coordinates are present in the reconstructed attractor prior to the manifold mapping. However, as the dimension is increased, the choice of σ that leads to the best predictability may also change, as the size of the attractor will change with changes in dimension. Therefore, it may become difficult to determine what the ideal σ is for large d_E.

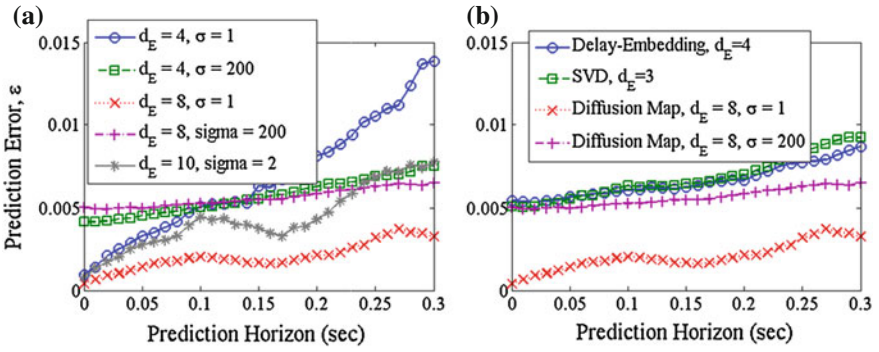

Fig. 4 Median prediction error ε as function of prediction horizon Δt for the Lorenz, using **a** manifold embedding with diffusion maps, varying d_E and σ and **b** proper delay-embedding and optimally-chosen SVD and diffusion map embeddings

To understand how manifold embedding performs compared to other embedding approaches, we show the prediction error for the typical delay embedding and for the best SVD embedding over the same range of d_E choices (Fig. 4b). For the Lorenz, a $d_E = 3$ produced the lowest ε for the SVD embedding, contrary to the manifold embedding approach, which yields better results at higher d_E.

Finally, we evaluate whether manifold embedding can still produce good forecasts in the presence of noise. To simulate noise, we apply additive Gaussian noise at a signal-to-noise ratio (SNR) of 20 and 10 dB to the time series, and perform the same embedding and prediction error approach as above (Fig. 5). The manifold embedding approach using diffusion maps performs comparatively even better relative to the other approaches than with no noise. These results are indicative of the diffusion mapping algorithm's robustness to noise perturbations [15].

5 Discussion

We have introduced the novel manifold embedding approach to attractor reconstruction from time series. The process involves a similar approach to embedding and mapping that SSA utilizes, but replacing SVD with manifold learning based algorithms. These approaches do not have the disadvantages in the presence of nonlinear attractor manifolds that SVD is vulnerable to. We have shown that these techniques, given proper parameter choices for embedding, can preserve the global dynamic properties of chaotic attractors. These global dynamic properties tend to be preserved using higher bandwidths in the manifold embedding algorithm, which is contrary to most applications of manifold learning [15] such as dimensionality reduction or semi-supervised learning. The need for these higher bandwidths is likely related to

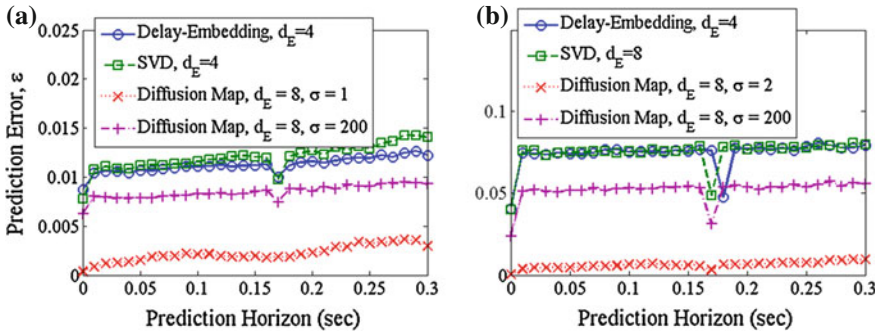

Fig. 5 Median prediction error ε as function of prediction horizon Δt for the Lorenz time series with additive noise, where **a** 20 dB SNR and **b** 10 dB SNR

the non-guaranteed preservation of global dynamics unless distances are preserved over a large enough range of data.

However, depending on the application, one may be more interested in short-time dynamics. In these scenarios, lower bandwidths can be advantageous. Because manifold embedding approaches rely on preservation of local distance structures in phase space, these dynamics can be better mapped to an underlying manifold in a new state space even when the global dynamics are not preserved. Thus, one can take advantage of these mappings to achieve better forecasts at short time scales than using either the traditional time-delay or SVD-based embeddings. A particular advantage of diffusion maps for manifold embedding is its robustness to noise. We show that diffusion map-based manifold embedding maintains high forecasting capability despite additive noise on a chaotic Lorenz time series.

References

1. L. Becks, F. Hilker, H. Malchow, K. Jurgens, H. Arndt, Experimental demonstration of chaos in a microbial food web. Nature Lett. **435**(30), 1226–1229 (2005)
2. E. Lorenz, Deterministic nonperiodic flow. J. Atmos. Sci. **20**(2), 130–141 (1963)
3. F. Moon, Fractal boundary for chaos in a two-state mechanical oscillator. Phys. Rev. Lett. **53**(10), 962–964 (1984)
4. F. Takens, Detecting strange attractors in turbulence, in *Dynamical Systems and Turbulence: Springer Lecture Notes in Mathematics*, ed. by D. Rand, L. Young (Springer, Berlin, 1981), pp. 366–381
5. A. Fraser, H. Swinney, Independent coordinates for strange attractors from mutual information. Phys. Rev. A **33**(2), 1134–1140 (1986)
6. M. Kennel, R. Brown, H. Abarbanel, Determining embedding dimension for phase-space reconstruction using a geometrical construction. Phys. Rev. A **45**(6), 3403–3411 (1992)
7. T. Sauer, J. Yorke, How many delay coordinates do you need? Int. J. Bifurcation Chaos **3**(3), 737–744 (1993)
8. D. Broomhead, G. King, Extracting qualitative dynamics from experimental data. Physica D **20**(23), 217236 (1986)

9. R. Vautard, M. Ghil, Singular spectrum analysis in nonlinear dynamics, with applications to paleoclimatic time series. Physica D **35**, 395–424 (1989)
10. N. Golyandina, V. Nekrutkin, A. Zhigljavsky, *Analysis of Time Series Structure: SSA and Related Techniques* (CRC, Boka Raton, 2001)
11. J. Lee, M. Verleysen, *Nonlinear Dimensionality Reduction* (Springer, New York, 2007)
12. M. Belkin, P. Niyogi, Semi-supervised learning on riemannian manifolds. Mach. Learn. **56**, 209–239 (2004)
13. D. Giannakis, A. Majda, Nonlinear laplacian spectral analysis for time series with intermittency and low-frequency variability. Proc. Nat. Acad. Sci. **109**(7), 2222–2227 (2012)
14. H. Suetani, S. Akaho, A ransac-based isomap for filiform manifolds in nonlinear dynamical systems -an application to chaos in a dripping faucet, in *ICANN*, pp. 277–284 (2011)
15. R. Coifman, S. Lafon, Nonlinear dimensionality reduction using locally linear embedding. Appl. Comput. Harmon. Anal. **21**(22), 530 (2006)
16. S. Roweis, L. Saul, Nonlinear dimensionality reduction using locally linear embedding. Science **290**(22)
17. M. Hénon, A two-dimensional mapping with a strange attractor. Commun. Math. Phys. **50**(1), 69–77 (1976)
18. J. Eckmann, D. Ruelle, Ergodic theory of chaos and strange attractors. Rev. Mod. Phys. **57**, 617 (1985)
19. P. Grassberger, I. Procaccia, Measuring the strangeness of strange attractors. Physica D **9**(1–2), 189–208 (1983)
20. J. Kaplan, J. Yorke, Chaotic behavior of multidimensional difference equations, in *Lecture Notes in Mathematics*, vol. 730, ed. by H. Peitgen, W. Walther (Springer, Berlin, 1979), pp. 204–227
21. M. Sano, Y. Sawada, Measurement of the lyapunov spectrum from a chaotic time series. Phys. Rev. Lett. **55**(10), 1082–1085 (1985)
22. L. Pecora, T. Carroll, Discontinuous and nondifferentiable functions and dimension increase induced by filtering chaotic data. Chaos **6**(3), 432–439 (1196)

The Dynamics of Coupled Spin-Torque Nano Oscillators: An Initial Exploration

J. Turtle, A. Palacios, V. In and P. Longhini

Abstract In this work we explore the use of Spin Torque Nano Oscillators (STNOs) to produce a spintronics voltage oscillator in the microwave range. STNOs are quite small—on the order of 10 nm—and frequency agile. However, experimental results to date have produced power outputs that are too small to be viable. We attempt to increase power output by investigating the dynamics of a system of electrically-coupled STNOs. To set the foundation for further analysis, we consider both Spherical and Complex Stereographic coordinates for the Landau-Lifshitz-Gilbert Equation with spin torque term. Both coordinate systems effectively reduce the equation of a single STNO from three dimensions to two. Further, the Complex Stereographic representation transforms the equation into a nearly polynomial form that may prove useful for advanced dynamics analysis. Qualitative bifurcation diagrams show a rich set of behaviors in the parallel and series coupled systems and serve to develop intuition in system dynamics.

1 Introduction

Spin Torque Nano Oscillators (STNO) are a ferromagnet-based electronics component. In certain steady-states, the magnetic moment precesses causing component resistance to oscillate [1]. Based on this oscillating resistance, an STNO can be utilized as a microwave-range voltage oscillator (see Fig. 1). STNOs offer many potential advantages over existing semi-conductor voltage oscillators including small physical size ($\sim$10 nm), a large tunable frequency range, and small output linewidths [2]. However, STNOs tested to date have yet to produce adequate power. STNOs need

J. Turtle · A. Palacios (✉) · V. In · P. Longhini
San Diego State University, San Diego, CA 2182, USA
e-mail: jturtle@rohan.sdsu.edu

A. Palacios
e-mail: apalacios@mail.sdsu.edu

V. In et al. (eds.), *International Conference on Theory and Application in Nonlinear Dynamics (ICAND 2012)*, Understanding Complex Systems,
DOI: 10.1007/978-3-319-02925-2_25,

to output at least 1 mW to be applicable [3]. The microwave power generated by an STNO was first measured in 2009 on the order of 100 nW [4]. STNOs cannot be made larger, so an obvious solution to increasing power is to couple multiple oscillators. However, in experiments it has proven difficult to synchronize even two STNOs [5]. Thus we have begun to study the dynamics of coupled STNOs to determine conditions for synchronization. In this article we report our initial findings starting with the model itself. We first explore alternate coordinate systems to reduce the dimension of the model and find a form that is more amenable to later analysis. Both spherical and complex stereographic coordinates are investigated. Next we vary the input current and numerically integrate until steady-state to create qualitative bifurcation diagrams. Bifurcation diagrams are generated for both parallel and series connected STNOs.

2 The Model

Magnetization in the free ferromagnetic layer is described by the Landau-Lifshitz equation with Gilbert damping and Slonczewski-Berger spin-torque term (LLGS) [6–10]

$$\frac{\mathrm{d}\mathbf{m}}{\mathrm{d}t} = \overbrace{-\gamma \mathbf{m} \times \mathbf{H}_{\mathrm{eff}}}^{\text{precession}} + \overbrace{\lambda \mathbf{m} \times \frac{\mathrm{d}\mathbf{m}}{\mathrm{d}t}}^{\text{damping}} - \overbrace{\gamma a\, g\left(P, \mathbf{m} \cdot \mathbf{S}_p\right) \mathbf{m} \times \left(\mathbf{m} \times \mathbf{S}_p\right)}^{\text{spin transfer torque}}, \quad (1)$$

where $\mathbf{m}$ represents the magnetization of the free ferromagnetic layer in Cartesian coordinates, γ is the gyromagnetic ratio and $\mathbf{H}_{\mathrm{eff}}$ is the effective field. λ serves as the magnitude of the damping term. In the spin torque term, a has units Oe and is proportional to the electrical current density [11]. g is a function of the polarization factor P, $\mathbf{m}$, and the fixed-layer magnetization direction $\mathbf{S}_p$. To determine the change of field direction with respect to time, we must consider three different classes of torques acting on the field direction $\mathbf{m}$: effective external magnetic field $\mathbf{H}_{\mathrm{eff}}$, damping λ, and spin transfer torque. $\mathbf{H}_{\mathrm{eff}}$ is the sum of several factors that can be effectively represented as external fields. The factors that we consider in this fashion are exchange, anisotropy and demagnetization. The actual external, or applied, field rounds out the sum

$$\mathbf{H}_{\mathrm{eff}} = \mathbf{H}_{\mathrm{exchange}} + \mathbf{H}_{\mathrm{anisotropy}} + \mathbf{H}_{\mathrm{demagnetization}} + \mathbf{H}_{\mathrm{applied}}.$$

We model the free layer as a single particle who's magnetization $\mathbf{m}$ represents the average of the layer. Thus there is no exchange with adjacent magnetic moments $\mathbf{H}_{\mathrm{exchange}} = \mathbf{0}$.

Spherical Coordinates

In Eq. (1), $\mathbf{m}$ has constant magnitude. We confine $\mathbf{m}$ to the surface of a unit sphere by choosing $\|\mathbf{m}\|_2 = \mathbf{1}$. Thus, spherical coordinates are a natural choice for $\mathbf{m}$ with the radius $\rho = 1$. In [12], Sun showed that Eq. (1) can be converted to

$$\begin{aligned}\frac{d\theta}{d\tau} = &-\alpha \sin\theta \cos\theta \\ &- h_p \left[(\sin\varphi + \alpha \cos\varphi) \sin\theta \cos\varphi\right] \\ &- h \left[\cos\varphi \sin\psi + \alpha \left(\sin\theta \cos\psi - \cos\theta \sin\varphi \sin\psi\right)\right] \\ &+ h_s \left[\alpha \cos\varphi \sin\phi + \sin\varphi \sin\phi \cos\theta - \cos\phi \sin\theta\right], \end{aligned} \tag{2}$$

$$\begin{aligned}\frac{d\varphi}{d\tau} = &-\cos\theta \\ &- h_p \left[(\cos\varphi \cos\theta - \alpha \sin\varphi) \cos\varphi\right] \\ &- h \left[\frac{\sin\theta \cos\psi - \cos\theta \sin\varphi \sin\psi - \alpha \cos\varphi \sin\psi}{\sin\theta}\right] \\ &+ h_s \left[\frac{\cos\varphi \sin\phi - \alpha \sin\varphi \sin\phi \cos\theta}{\sin\theta} + \alpha \cos\phi\right], \end{aligned}$$

where θ is the angle of inclination and φ is the azimuthal angle. These equations have been time-scaled by $\frac{\gamma h_k}{1+\lambda^2}$ (h_k is the magnitude of anisotropy) and parameters consolidated to: demagnetization magnitude h_p (yz-easy-plane), applied field magnitude h, applied field angle from z-axis ψ (confined to yz-plane), spin torque magnitude h_s, and spin torque angle from z-axis ϕ (also confined to yz-plane). Ultimately reducing the representation of the system from three dimensions to two.

Complex Stereographic Projection

A spherical surface can be projected onto a plane by using the complex variable ω and the following relationships:

$$\omega = \frac{m_x + i m_y}{1 + m_z} \quad \Rightarrow \quad \mathbf{m} = \begin{bmatrix} \dfrac{\omega + \bar{\omega}}{1 + |\omega|^2} \\ -i \dfrac{(\omega - \bar{\omega})}{1 + |\omega|^2} \\ \dfrac{1 - |\omega|^2}{1 + |\omega|^2} \end{bmatrix}. \tag{3}$$

Building on [11, 13], we reduce Eq. (1) to the form

$$\dot{\omega} = \frac{\gamma}{1 - i\lambda}\Bigg(- a\omega + ih_{a3}\omega + \frac{h_{a2}}{2}(1 + \omega^2) + im_{\parallel}\kappa\left[\cos\theta_{\parallel}\omega - \frac{1}{2}\sin\theta_{\parallel}\left(\mathrm{e}^{i\phi_{\parallel}} - \omega^2\mathrm{e}^{-i\phi_{\parallel}}\right)\right] - \frac{i4\pi S_o}{(1 + |\omega|^2)}\left[N_3(1 - |\omega|^2)\omega - \frac{N_1}{2}(1 - \omega^2 - |\omega|^2)\omega - \frac{N_2}{2}(1 + \omega^2 - |\omega|^2)\omega - \frac{(N_1 - N_2)}{2}\bar{\omega}\right]\Bigg), \tag{4}$$

where h_{a2} is the magnitude of the applied field in the y-direction and h_{a3} is the magnitudes of the applied field in the z-direction. κ is the anisotropy magnitude who's direction is determined by $\theta_{\parallel}$ and $\phi_{\parallel}$. The anisotropy is scaled by $m_{\parallel} = \mathbf{m} \cdot \mathbf{e}_{\parallel}$ where

$$\mathbf{e}_{\parallel} = \begin{bmatrix} \sin\theta_{\parallel}\cos\phi_{\parallel} \\ \sin\theta_{\parallel}\sin\phi_{\parallel} \\ \cos\theta_{\parallel} \end{bmatrix}.$$

S_0 is the saturation magnetization. Finally, $N_1 + N_2 + N_3 = 1$ and determine the effective demagnetization field resulting from the shape of the free layer. Now we have a two dimensional expression for the STNO that is close to polynomial form.

Coupling

Coupling is achieved by modeling a simple electrical circuit with STNOs arrayed in series or parallel. Figure 1 depicts the series configuration. The resistance of each STNO R_i is a function of the angle θ_i between M (fixed layer-green) and $\mathbf{m}$ (free layer-red):

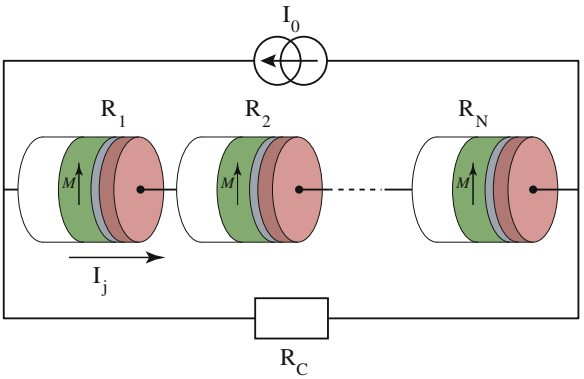

Fig. 1 Series arrayed STNOs with input current I_0 and output resistance R_c

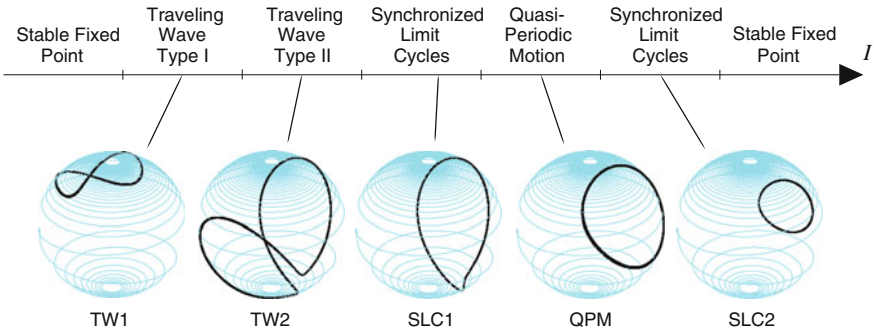

Fig. 2 Qualitative bifurcation diagram for 3 STNOs arranged in series and varying parameter $\boldsymbol{I}$ over the interval [0:3]

$$R_i = R_{0i} - \Delta R_i \cos\theta_i .$$

Here, R_0 is the median resistance of an STNO and ΔR is the maximum variance in resistance.

3 Numerical Exploration

Numeric simulations have revealed a rich variety of behaviors in a series-array of three STNOs. Figure 2 depicts a few example behaviors found by varying the current I. A high or low current simply causes all of the oscillators to converge to an equilibrium point. However, in the intermediate range there are multiple distinct regimes of oscillatory behavior. All numeric integrations in this diagram use the parameters: $\lambda = 0.1$, $h = 1$, $h_s = -1$, $h_p = 5$, $\phi = 0$, $\psi = \pi/4$, $R_0 = 2$, $\Delta R = 0.6$, $R_c = 50$.

Performing similar integrations for 3 STNOs coupled in parallel generates the qualitative bifurcation diagram in Fig. 3. As is seen, we find a region of oscillations in I bound on both sides by fixed points. Within the oscillatory region we discovered six distinct sub-regions. Three sub regions tend to synchronization, two show quasi-periodic motion, and one forms frequency synchronized orbits. All numeric integrations in this diagram use the parameters: $\lambda = 0.1$, $h = 1$, $h_s = -1$, $h_p = 5$, $\phi = 0$, $\psi = \pi/4$, $R_0 = 0.1$, $\Delta R = 0.03$, $R_c = 50$.

4 Remarks

The LLGS Eq. (1) is a nonlinear first-order ordinary differential equation confined to the unit sphere $\|\mathbf{m}\|_2 = 1$. We are able to reduce the dimension of a system of coupled STNOs by one-third using spherical or complex-stereographic coordinates.

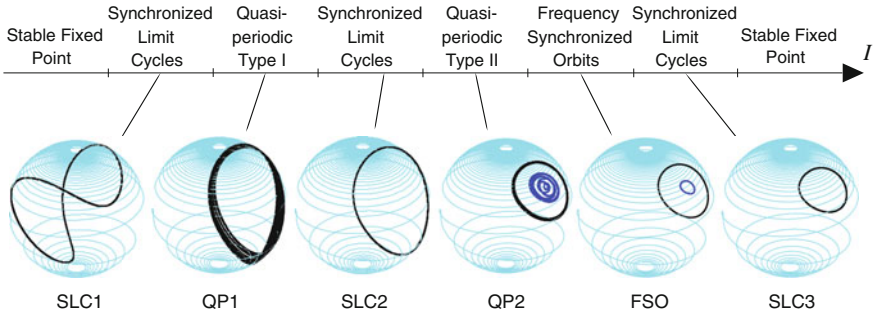

Fig. 3 Qualitative bifurcation diagram for 3 STNOs arranged in parallel and varying parameter ***I*** over the interval [0:7]

Not only does this increase the efficiency of numerics, but will also help in the future with a center manifold reduction. Furthermore, the form of the equations in complex stereographic coordinates is polynomial-like which may be helpful in future analysis.

In the series and parallel electric coupling scenarios, the system experiences all-to-all coupling or S_N symmetry. Most of the non-synchronous oscillating behaviors observed in Figs. 2 and 3 are consistent with $S_N \times S^1$ symmetry-breaking Hopf bifurcations. This leads us to believe that we can leverage the work of [14] to determine the existence and stability of non-synchronous oscillations.

References

1. A. Slavin, V. Tiberkevich, Nonlinear auto-oscillator theory of microwave generation by spin-polarized current. IEEE T. Magn. **45**(4), 1875–1918 (2009)
2. W. Rippard, M. Pufall, S. Russek, Comparison of frequency, linewidth, and output power in measurements of spin-transfer nanocontact oscillators. Phys. Rev. B **74**(22), 224, 409 (2006)
3. J. Persson, Y. Zhou, J. Akerman, Phase-locked spin torque oscillators: impact of device variability and time delay. J. Appl. Phys. **101**(9), 09A503–09A503 (2007)
4. A.E. Wickenden, C. Fazi, B. Huebschman, R. Kaul, A.C Perrella, W.H. Rippard, M.R. Pufall, Spin torque nano oscillators as potential tetrahertz (THz) communications devices. Tech. rep., DTIC Document (2009)
5. D. Li, Y. Zhou, C. Zhou, B. Hu, Global attractors and the difficulty of synchronizing serial spin-torque oscillators. Phys. Rev. B **82**(14), 140, 407 (2010)
6. L. Berger, Emission of spin waves by a magnetic multilayer traversed by a current. Phys. Rev. B **54**(13), 9353–9358 (1996). doi:10.1103/PhysRevB.54.9353
7. G. Bertotti, I. Mayergoyz, C. Serpico, Analytical solutions of landau-lifshitz equation for precessional dynamics. Phys. B **343**(1–4), 325–330 (2004)
8. M. dAquino, Nonlinear magnetization dynamics in thin-films and nanoparticles. Ph.D. thesis, Universitá degli Studi di Napoli Federico II, Naples (2004)
9. T. Gilbert, A phenomenological theory of damping in ferromagnetic materials. IEEE T. Magn. **40**(6), 3443–3449 (2004)
10. J.C. Slonczewski, Current-driven exitation of magnetic multilayers. J. Magn. Magn. Mater. **159**(1–2), L1–L7 (1996)

11. S. Murugesh, M. Lakshmanan, Spin-transfer torque induced reversal in magnetic domains. Chaos Solitons Fractals **41**, 2773–2781 (2009)
12. J.Z. Sun, Spin-current interaction with a monodomain magnetic body: a model study. Phys. Rev. B **62**, 570–578 (2000)
13. S. Murugesh, M. Lakshmanan, Bifurcation and chaos in spin-valve pillars in a periodic applied magnetic field. Chaos **19**, 043, 111 (2009)
14. A.P.S. Dias, A. Rodrigues, Hopf bifurcation with sn-symmetry. Nonlinearity **22**(3), 627 (2009)

Part II
Posters

Elaboration of a Multispecies Model of Solid Tumor Growth with Tumor-Host Interactions

A. Konstorum, S. A. Sprowl, A. D. Lander, M. L. Waterman and J. S. Lowengrub

Abstract There has been increasing evidence of the critical effects of microenvironmental influence on tumor growth and metastasis. In this report, we extend a multispecies continuum model of solid tumor growth to include interaction of the tumor with its microenvironment. This new model, which incorporates reported interactions between tumor- and stroma-derived chemical signals, predicts a nonlinear response to host factors: increased growth and asymmetry of the tumor at low levels of stromal fibroblast-produced Hepatocyte Growth Factor / Scatter Factor (HGF/SF), and reduced growth at high levels.We test the model predictions using colon cancer initiating cell (CCIC) spheroids grown in media in varying concentrations of HGF. The experiments show qualitatively similar behavior to the model predictions. We plan to use the experimental studies to calibrate the mathematical model, and to use the mathematical model to make predictions regarding tumor behavior in order to guide future experimental studies.

A. Konstorum (✉)
Department of Mathematics, UC, Irvine, USA
e-mail: akonstor@uci.edu

S.A. Sprowl · M.L. Waterman
Department of Microbiology and Molecular Genetics, UC, Irvine, USA
e-mail: ssprowl@uci.edu

M.L. Waterman
e-mail: marian.waterman@uci.edu

A.D. Lander
Department of Developmental and Cell Biologym, UC, Irvine, USA
e-mail: adlander@uci.edu

J.S. Lowengrub
Department of Mathematics, Department of Biomedical Engineering Center for Complex Biological Systems, UC, Irvine, USA
e-mail: lowengrb@math.uci.edu

V. In et al. (eds.), *International Conference on Theory and Application in Nonlinear Dynamics (ICAND 2012)*, Understanding Complex Systems,
DOI: 10.1007/978-3-319-02925-2_26,

1 Introduction

The importance of the microenvironment in tumor growth and metastasis has been established with a large body of research [1–6]. Nevertheless, the molecular interactions between tumor and stroma-resident cells, and the changes in both tissues that these interactions facilitate, are still under intense study, especially as it has become evident that pharmaceutical targeting of the tumor alone may not account for cancer promoting factors that are produced in the tumor microenvironment [7].

The purpose of this study is to extend a recently developed stem-cell based multispecies model of a solid tumor to include stromal interactions that are well corroborated by experimental data. Numerical analysis of the mathematical model allows us to examine, in silico, various scenarios of tumor-host interactions, and to compare our results against the experimental literature. Ultimately, we hope to use the model to make predictions about potential avenues for future research in malignancy, as well as pharmaceutical applications.

2 Background: A Mathematical Model of a Solid Tumor with Multiple Cell Types

A multispecies continuum model based on lineage dynamics of different tumor cell types has recently been developed by Youssefpour et al. [8]. As this model is extended here to incorporate tumor-host interactions, an overview of the model is necessary to understand the additions. Figure 1 summarizes the biological foundation of the model, while Fig. 2 summarizes the relevant equations.

3 Incorporating Host Effects

It has been shown in numerous studies that HGF production by cancer-associated fibroblasts in the stroma causes increased β-catenin localization in the nucleus of tumor cells near the tumor-host boundary, and additionally causes these cells to display properties of cancer stem cells such as increased migratory capacity and clonogenic potential [9, 10]. The effects of HGF can be attributed to binding of HGF to the c-Met receptor, which is expressed on tumor cells, and can result in a signaling cascade that ultimately leads to dissociation of β-catenin from its cytosolic partners and translocation into the nucleus where it can potentiate the canonical Wnt signal activity [11]. Based on these studies, we modify the equation for Wnt signaling, which represents the combined effects that promote Wnt signaling, such that concentration of HGF has a positive linear effect on Wnt signal production:

Elaboration of a multispecies model of solid tumor growth with tumor-host interactions.

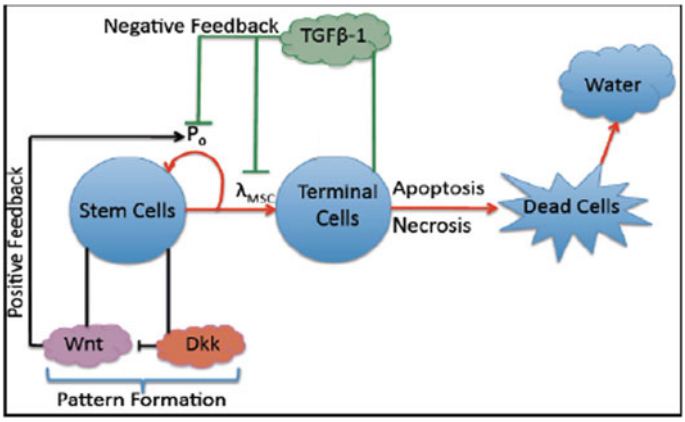

Fig. 1 A multispecies model of tumor signaling: Tumor tissue is composed of three cell types: cancer stem cells (CSCs), terminally differentiated cells (TCs), and dead cells (DCs). Stem cells have a probability of self renewal P_0, differentiate into TCs with probability $1 - P_0$, and divide at a rate λ_{MSC}. P_0 is promoted by Wnt (and other autocrine) signals produced by the stem cells, which are in turn inhibited by Dkk (and other) proteins, also produced by CSCs. TCs secrete proteins from the TGFβ superfamily that lower P_0 and λ_{MSC}. CSCs and TCs can become DCs by apoptosis or necrosis. Adapted from [8]

$$\frac{\partial C_{Wnt}}{\partial t} = \nabla \cdot (D_{Wnt} \nabla C_{Wnt}) + f\,(C_{Wnt}, C_{Dkk}) \tag{1}$$

$$f\,(C_{Wnt}, C_{Dkk}) = \nu_{PWnt} \frac{\lambda_{HGF} C_{HGF} + C_{Wnt}^2}{C_{Dkk}} C_0 \phi_{CSC} - \nu_{DWnt} C_{Wnt} + \mu_0 C_0\,(\phi_T - \phi_{DC})\,, \tag{2}$$

where the HGF-induced production of Wnt signaling is modeled in the first term of the right-hand side of Eq. (2). Creating a model for HGF concentration is a more difficult matter, as there have been far fewer studies on the molecular basis for changes in HGF production by cancer-associated stromal cells. There have been many studies that have shown a direct effect of cancer cells on HGF production via their secretion of growth factors and cytokines such as TNFα, bFGF, and PDGF that bind to the EGF receptor on stromal cells and cause upregulation of HGF production [2, 12]. Thus, we cannot currently specify whether the stem cells preferentially release these growth factors and if increased β-catenin localization (via HGF signaling) results in an increased release of these factors from neighboring tumor cells, which would indicate a positive feedback mechanism. With the data available, we model a positive effect of growth factors from viable tumor tissue on HGF production in the stroma. Additionally, there is substantial evidence that TGFb is a negative regulator of HGF production in stromal cells, and thus we include its inhibitory effect in the model (2):

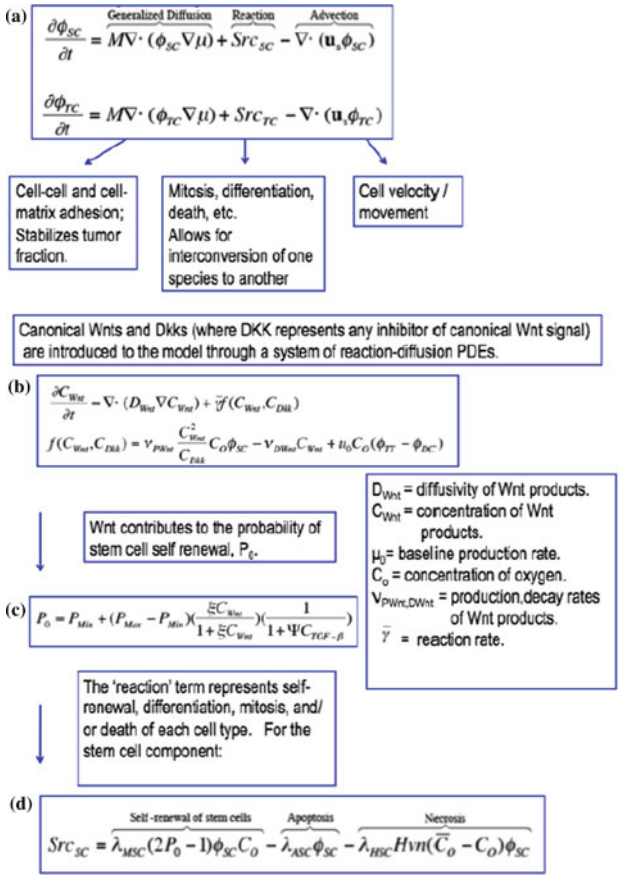

Fig. 2 Modeling the multispecies tumor: A brief outline of the model is given here. For a more detailed description, see [8]. The functions ϕ_{SC}, ϕ_{TC} (shown) and ϕ_{DC}, ϕ_W, ϕ_H (not shown) represent the local fractions of CSC, TC, and DC populations in lineage and the water and host cells, respectively. The sum of the volume fractions equals 1. **a** For each cell type, the conservation equation is posed, where $J = -M\phi\nabla\mu$ is a generalized flux (or cellular diffusion), Src is the mass-exchange term, and us is the mass-averaged velocity of the solid components, assumed to satisfy Darcys law and is given by $\nabla \cdot u_s = Src_{SC} + Src_{TC} + Src_{DC}$. Cells are assumed to move with the mass-averaged velocity. For$J = -M\phi\nabla\mu$, M is the mobility and μ is the chemical potential, which is proportional to the variational derivative of the adhesion energy. The flux is derived from an adhesion energy that accounts for interactions among the cells. **b** We account for a self-renewal promoter, such as Wnt, which increases the self-renewal fraction of CSCs, and an inhibitor of the self-renewal promoter, such as Dkk, using a generalized Geierer-Meinhardt-Turing system of reaction-diffusion equations. Both are only produced by CSCs, and Wnt diffusion range is assumed to be shorter than that of Dkk. **c** CSC self-renewal fraction, P_0 is positively regulated by Wnt and negatively regulated by TGFβ with ξ and Ψ the feedback response of the CSCs to the respective proteins. **d** Source term for CSCs. Proportion of CSCs are increased by mitosis rate of CSCs, λ_{MSC}, that are self-renewing, and is dependent on C_0, the local concentration of oxygen and nutrients. $Hvn(x)$ denotes the Heaviside function, which is equal to 1 when $x > 0$ and 0 otherwise. $\bar{C}_0$ denotes the minimum level of oxygen and nutrients required for cell viability. Src_{TC} and Src_{DC} are modeled analogously

$$\frac{\partial C_{HGF}}{\partial t} = \nu_{PHGF} \frac{C_{GF}}{\xi + \lambda_{TGF\beta} C_{TGF\beta}} C_0 \phi_H + \overbrace{\eta_0 C_0 \phi_0}^{\text{HGF background production rate}} - \overbrace{\nu_{DHGF} C_{CHGF}}^{\text{HGF decay/ binding rate}} + \nabla \cdot (D_{HGF} \nabla C_{HGF}), \quad (3)$$

where the inhibition by TGFb and promotion by tumor-produced growth factors is modeled in the first term of the right-hand side of Eq. (3).

As discussed above, HGF-promoting growth factors are released by tumor cells, but it is not known whether the production of these growth factors is different in stem and differentiated cells. Thus, we allow for the production rate of growth factors to be different for each of the cell types:

$$\frac{\partial C_{HGF}}{\partial t} = \nabla \cdot (D_{GF} \nabla C_{GF}) + \overbrace{C_0 \left(\nu_{GFS} \phi_{CSC} + \nu_{GFT} \phi_{TF}\right)}^{\text{Growth Factor production rate}} - \overbrace{\nu_{DFG} C_{GF}}^{\text{Growth Factor decay / binding rate}} \quad (4)$$

We refer the reader to Table 1 for description of the variable and parameter symbols.

4 Numerical and Experimental Methods

For the nondimensionalization and numerical implementation, we followed a previously published numerical method, which we briefly describe here [8]. An adaptive finite difference-nonlinear multi grid method [13, 14] was used to solve the governing equations efficiently. For reasons described in [8, 13], we solved for $\phi_T = \phi_{CSC} + \phi_{TC} + \phi_{DC}$. To remove a high-order time step constraint incurred by an explicit method, we used an implicit 2nd order accurate time discretization of Crank-Nicholson type, and spatial derivatives were discretized using 2nd order accurate central difference approximations. In regions of large gradients, block structured Cartesian refinement was used to provide enhanced local resolution.

In the experiments, colon cancer initiating cells (CCICs) were cultured as spheroids in ultra-low attachment flasks (Corning) using DMEM/F12 50:50 supplemented with N2, B12, EGF, bFGF, heparin, sodium pyruvate, and penicillin/ streptomycin [15]. Unlike typical cell lines, CCICs are multipotent and capable of regenerating heterogeneous tumors with characteristics analogous to those found in primary tumors, from which they are derived [15, 16]. CCICs were trypsinized using a no-serum trypsin inhibitor. Single cells were counted and plated in 96 well ultra-low attachment plates (Corning) using the previously mentioned media with or without HGF at various concentrations. CCICs were imaged at 10x resolution once each day. Cell clusters were observed for sphere morphology and size. Sphere size was determined by outlining the major sphere boundary (excluding scattered or shed cells) using ImageJ. Average volume increase over day 3 from three experimental trials was calculated in order to allow the spheroids 72 hours to adapt to new media.

Variable or parameter	Description	Value	Reference and / or rationale (if not in text)
ϕ_H	stromal fraction (=1-ϕ_T)		
C_{HGF}	concentration of HGF		
C_{GF}	concentration of HGF- promoting factors		
D_{GF}	diffusion coefficient for GF	1.0	[17, 18]
D_{HGF}	diffusion coefficient for HGF	0.1	Set to a value lower than for GF due to higher molecular weight of HGF and necessity for HGF to be processed by molecules in ECM before it can bind to c-MET [19].
λ_{HGF}	strength of Wnt induction by HGF	1.0	Optimal reference data not available, plan to calibratein future experiments.
$\lambda_{TGF\beta}$	inhibitory effect of TGFb on HGF production	1.0	[20]
η_0	background HGF production rate by non-cancer associated stromal cells	0.0001	Set to a value significantly lower than GF-induced production levels [21].
$\nu_{PHGF,DHGF}$	induction, decay rates of HGF	0.1, 1.0	[12, 19]
$\nu_{GFS,GFT}$	production rates of GF modeled by stem and differentiated cells, respectively	0.1, 0.1; 10,10	Varies widely by cell type [22]. Here, at low and high levels. Levels set to be equal in both conditions since differential production rate information not available.

5 Results

Numerical results from incorporation of low HGF signal, created by a lower production rate of growth factors ($\nu_{GFS,GFT} = 0.1$) resulted in increased tumor asymmetry, instability, and volume when compared to the no host simulation (Fig. 3a, b; No host and Host: low HGF categories). By increasing growth factor production rate ($\nu_{GFS,GFT} = 10$), maximal HGF levels at the tumor-host boundary were increased approximately 100-fold (Fig. 3c), and resulted in a nonlinear growth response to HGF, namely at higher HGF levels, the tumor had greater symmetry and lower growth rate than at low HGF (Fig. 3, Host: high HGF category).

Experiments were performed to corroborate results of the model with primary colon cancer initiating cell (CCIC) spheroids grown in increasing concentration of HGF. Spheroids are a relevant model for tumor growth since they can be used to examine 3-dimensional properties of growing tissues, which more closely resemble in vivo tumors than 2-dimensional culture models (23). The experimental results show increasing spheroid growth rate with increasing concentration of HGF up to 100 ng/ml, but decreased growth and asymmetry at 250 ng/ml as compared to lower levels of HGF (Fig. 4), which is qualitatively consistent with the model predictions.

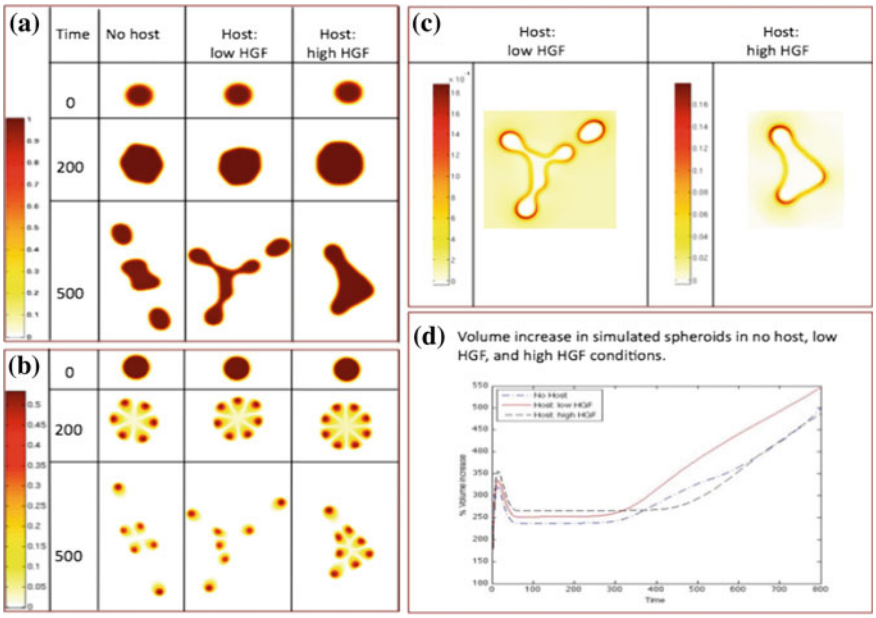

Fig. 3 Simulation results of tumor-host model: Visualization of numerical results of the mathematical formulation for incorporation of host factors (HGF) at low and high levels into a multispecies model for **a** total tumor, **b** stem cell fraction, and **c** HGF concentration (note difference in scale). **d** Tumor volume is increased in low HGF environment, but decreases in increased concentration of HGF

6 Discussion

We have created a mathematical model for tumor-host interactions by incorporating chemical interactions between host and tumor tissues into a multispecies continuum model of tumor growth. Our theoretical results at low HGF indicate a good match to the literature, namely that inclusion of host interactions increased tumor growth rate and dispersion, as well as stem cell concentration at the tumor-host boundary, over the no host model. The non-monotonic response is due to decrease in heterogeneity of cell species at the tumor-host boundary resulting from an increased concentration of stem cells in that region. This leads to more uniform growth, ie. less branching over time than what is found in the low HGF model. Indeed, it has recently been shown that at high concentrations of HGF, myogenic stem cells become quiescent, while at lower concentrations, they proliferate and differentiate [23].

While our model matches experimental observations qualitatively, our ultimate goal is to create an experimentallycalibrated mathematical model that can be used, in conjunction with experimental verification, to make testable predictions about tumor behavior in various conditions, including presence of stroma and subsequent therapy. To this end, we have begun an experimental collaboration using tumor spheroids

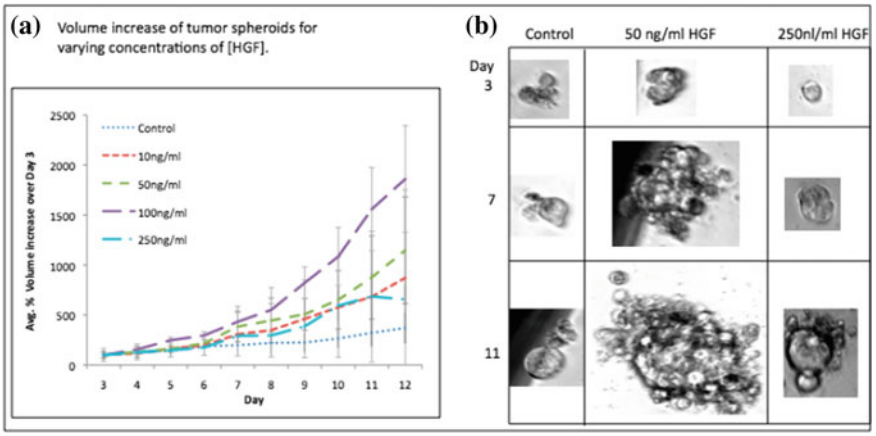

Fig. 4 Tumor spheroid culture with increasing [HGF]: CCIC tumor spheroids were grown in media with increasing concentration of HGF. **a** Average volume increase (from day 3) of three experimental trials / day. **b** Sample images from spheroids grown in control (left column), +50 ng/ml HGF media (*center column*), and +250 ng/ml HGF media (*right column*)

developed with the CCIC cell line [15, 16]. While the current experiments did not include feedback from tumor onto stroma, but only addition of HGF at increasing concentrations in the media, there is still strong resemblance of the model to the experiment as the interactions in the model serve to increase the effective HGF at the tumor-host boundary, which is mimicked by higher concentrations in the experimental media. The experimental observations show both an increase in tumor area and increased asymmetry and dispersiveness of the tumor at lower concentrations of HGF, and a slower growth rate and higher tumor symmetry at high levels of HGF (Fig. 4), indicating similarity of outcomes between the model and experiment.

Work is currently in progress to calibrate our numerical model to the experimental system by matching the growth parameters and timescale of the experimental system, removing feedback to stroma, and incorporating the nonlinear effect of HGF at higher concentrations on tumor growth. The framework of the calibrated model remains the same as to what is presented in this paper.

In parallel, the experimental system is also being developed to include a co-culture with stroma and staining for stem and other cell types in order to better match our current model, which is more closely aligned with the in vivo dynamics of HGF action on tumor growth. Furthermore, we plan to incorporate, into both the numerical and experimental system, the following: quantification and modeling of cell spread, tumor angiogenesis, and macrophage involvement in tumor growth. Our long-term goal is to build a predictive model that can be efficiently used to better understand tumor physiology and response to treatment.

Acknowledgments The authors would like to thank the National Institutes of Health and the National Cancer Institute for funding through grants 1RC2CA148493-01 and P30CA062203 for

the Chao Comprehensive Cancer Center at UC Irvine. In addition, we acknowledge partial support from NIH grant P50GM76516 for a Center of Excellence in Systems Biology at UC Irvine. Further, AK gratefully acknowledges support from National Institutes for BioImaging and Bioengineering, JSL for support from the National Science Foundation, Division of Mathematical Sciences, and MLW for support from NIH grants CA096878 and CA108697.

References

1. T. Borovski, E. De Sousa, F. Melo, L. Vermeulen, J.P. Medema, Feb 2011 Cancer Res. **71**(3), 634–639 (2011)
2. K. Matsumoto, T. Nakamura, Int. J. Cancer **119**(3), 477–483 (2006)
3. D. Hanahan, R.A. Weinberg, Cell **144**(5), 646–674 (2011)
4. A. Orimo, R.A. Weinberg, Cell Cycle **5**(15), 1597601 (2006)
5. K. Pietras, A. Ostman, Exp. Cell Res. **316**(8), 132431 (2011)
6. D. Hanahan, L.M. Coussens, Cancer Cell **21**(3), 30922 (2012)
7. P.A. Kenny, G.Y. Lee, M.J. Bissell, Front Biosci **12**(3468), 74 (2007)
8. H. Youssefpour, X. Li, A.D. Lander, J.S. Lowengrub, J. Theor. Biol. **304**(39), 59 (Jul 2012)
9. L. Vermeulen, E. De Sousa, F. Melo, M. van derHeijden, K. Cameron, J.H. deJong, T. Borovski, J.B. Tuynman, M. Todaro, C. Merz, H. Rodermond, M.R. Sprick, K. Kemper, D.J. Richel, G. Stassi, J.P. Medema, Nat. Cell Biol. **12**(5), 468–476 (2010)
10. A. Kaminski, J.C. Hahne, E.-M. Haddouti, A. Florin, A. Wellmann, N. Wernert, Int. J .Mol. Med. **18**(5), 941–950 (2006)
11. G. Banumathy, P. Cairns, Cancer Biol. Ther. **10**(7), 658–664 (2010)
12. A. De Luca, M. Gallo, D. Aldinucci, D. Ribatti, L.D. Lamura, A. Alessio, R. De Filippi, A. Pinto, N. Normanno, J. Cell Physiol. **226**(8), 21318 (2011)
13. S.M. Wise, J.S. Lowengrub, H.B. Frieboes, V. Cristini, J. Theor. Biol. **253**(3), 52443 (2008)
14. S.M. Wise, J. Sci. Comput. **44**(1), 38–68 (2010)
15. S.S. Sikandar, K.T. Pate, S. Anderson, D. Dizon, R.A. Edwards, M.L. Waterman, S.M. Lipkin, Cancer Res. **70**(4), 146978 (2010)
16. L. Ricci-Vitiani, D.G. Lombardi, E. Pilozzi, M. Biffoni, M. Todaro, C. Peschle, R. De Maria, Nature **445**(7123), 1115 (2007)
17. N. Quarto, F.P. Finger, D.B. Rifkin, J. Cell Physiol. **147**(2), 3118 (1991)
18. D.F. Bowen-Pope, R. Ross, Clin. Endocrinol. Metab. **13**(1), 191–205 (1984)
19. O. Holmes, S. Pillozzi, J.A. Deakin, F. Carafoli, L. Kemp, P.J.G. Butler, M. Lyon, E. Gherardi, J. Mol. Biol. **367**(2), 395–408 (2007)
20. K. Matsumoto, H. Tajima, H. Okazaki, T. Nakamura, J. Biol. Chem. **267**(35), 2491720 (1992)
21. S.-W. Tyan, W.-H. Kuo, C.-K. Huang, C.-C. Pan, J.-Y. Shew, K.-J. Chang, E.Y.-H.P. Lee, W.-H. Lee, PLoS One **6**(1), e15313 (2011)
22. T. Nakamura, K. Matsumoto, A. Kiritoshi, Y. Tano, T. Nakamura, Cancer Res. **57**(15), 330513 (1997)
23. M. Yamada, R. Tatsumi, K. Yamanouchi, T. Hosoyama, S.-i. Shiratsuchi, A. Sato, W. Mizunoya, Y. Ikeuchi, M. Furuse, R.E. Allen, Am. J. Physiol. Cell Physiol. **298**(3), C46576 (2010)

Resistive Switching Assisted by Noise

G. A. Patterson, P. I. Fierens and D. F. Grosz

Abstract We extend results by Stotland and Di Ventra [1] on the phenomenon of resistive switching aided by noise. We further the analysis of the mechanism underlying the beneficial role of noise and study the Electrical Pulse Induced Resistance (EPIR) ratio dependence with noise power. In the case of internal noise we find an optimal range where the EPIR ratio is both maximized and independent of the preceding resistive state. However, when external noise is considered, no beneficial effect is observed.

1 Introduction

In this work, we study a passive device called *memristor* which was proposed by Chua [2] and has been modeled and extensively studied by, e.g., Strukov et al. [3]. A memristor is a two-terminal device with the property that its resistance changes according with the electric charge that has flowed across it. The model in Ref. [3] reproduces, in a qualitative way, the resistive switching behavior of compounds such as TiO_2. It consists of two resistors in series whose equivalent resistance depends on the dopant concentration, and it is described by a simple nonlinear dynamic equation.

The effect of resistive switching has been experimentally studied in many materials, such as simple oxides, and in more complex compounds such as manganites and cuprates, among others [4, 5]. Results are usually reported as current-voltage hysteretic curves, or as the resulting resistance versus the externally applied field. One possible application of this phenomenon is in the design of non-volatile memories.

G. A. Patterson (✉)
Facultad de Ciencias Exactas y Naturales, Universidad de Buenos Aires, Buenos Aires, Argentina
e-mail: german@df.uba.ar

P. I. Fierens · D. F. Grosz
Instituto Tecnológico de Buenos Aires (ITBA) and Consejo Nacional de Investigaciones Científicas y Técnicas (CONICET), Buenos Aires, Argentina

V. In et al. (eds.), *International Conference on Theory and Application in Nonlinear Dynamics (ICAND 2012)*, Understanding Complex Systems,
DOI: 10.1007/978-3-319-02925-2_27,

Over the past decade extensive research was conducted in this direction by studying different properties, such as, retention times, temperature dependence, pulsing protocols, *etc*. In order to quantify the switching performance, the EPIR ratio is defined as $(R_h - R_l)/R_l$, where R_h and R_l are the high and low non-volatile resistive states after input pulsing, respectively. A higher EPIR ratio is desirable in order to attain a larger contrast between resistive states.

In this work we extend results by Stotland and Di Ventra [1] where the addition of white Gaussian noise to Strukov's equations was studied, showing that there is an optimal noise intensity that maximizes the contrast between high and low resistive states. They considered internal noise, inherent to the sample dynamics, and also suggested that the same results could be obtained if external noise was taken into account.

The paper is organized as follows: In Sect. 2 we review the model proposed by Strukov et al. and introduce the stochastic model. In Sect. 3 we show results of the stochastic model, and in Sect. 4 we present our conclusions.

2 Resistive Switching Model and Dynamics

Strukov et al. [3] introduced a model of a memristor consisting of a sample of length L divided into two doped/undoped regions with oxygen vacancies. Figure 1 shows a schematic of the sample model, where z marks the boundary between both regions. The memristive system is described by

$$\begin{aligned} V(t) &= R(z)I(t)\,, \\ \frac{dz}{dt} &= f(z, I)\,, \end{aligned} \tag{1}$$

where $V(t)$ is the potential difference across the sample, $I(t)$ is the current, and R is the sample resistance. Each region has a resistance that depends on the doping level. The net sample resistance is thus modeled as the resulting in-series resistance, and

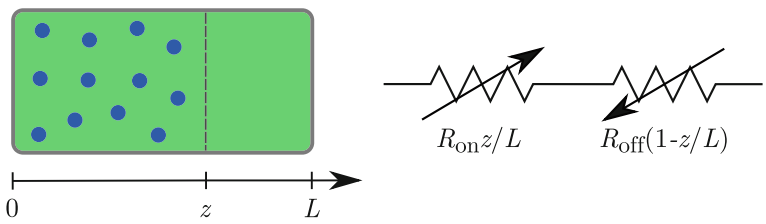

Fig. 1 The *memristor* model consists of a sample divided into two doped/undoped regions with oxygen vacancies. The position z of the boundary between both regions determines the net resistance of the sample

is given by

$$R(z) = R_{off} - (R_{off} - R_{on})z/L \ , \tag{2}$$

where $R_{off} > R_{on}$ are the extreme possible values of resistance. The motion of the boundary is determined by the drift of vacancies produced by an external field and is given by (see, e.g., [3, 6])

$$\frac{dz}{dt} = \frac{\mu R_{on}}{L} F(z) I(t) \ , \tag{3}$$

where μ is the average dopant mobility. The window function $F(z) = 1 - (2z/L - 1)^2$ is introduced to account for experimentally observed nonlinearities and also enforces that z remains within the interval $(0, L)$ [3, 7].

Linearization of Eq. (2) around the two fixed points at $z = 0$ and $z = L$ leads to first order differential equations [8]

$$\begin{aligned} \frac{dz}{dt} &\approx \frac{4\mu R_{on} V(t)}{L^2 R_{off}} z \ , \\ \frac{dz}{dt} &\approx -\frac{4\mu V(t)}{L^2}(z - L) \ . \end{aligned} \tag{4}$$

Note that, since $R_{on}/R_{off} < 1$, the boundary moves faster when it is close to the fixed point at $z = L$ than at $z = 0$.

For convenience, we rewrite Eq. (3) in a dimensionless form as

$$\frac{dx}{d\tau} = \frac{F(x)}{1 - \Delta R x} v(\tau) \ , \tag{5}$$

where $\Delta R = (R_{off} - R_{on})/R_{off}$, $x = z/L$, $\tau = \mu A(1 - \Delta R)t/L^2$, $v(\tau) = V(t)/A$, and A is the amplitude of the external applied field in volts.

We considered the influence of both internal and external white Gaussian noise, the internal noise affects the velocity of the internal state variable x, while external noise is added to the input signal v.

3 Results and Discussion

The externally applied field consisted of a sequence of pulses $+1 \rightarrow 0 \rightarrow -1 \rightarrow 0$ repeated 5 times. The pulsewidth was 2, $\Delta R = 0.75$ and the resistance was computed during the last repetition. We solved Eq. (5) for the time evolution of the resistance for each noise realization and intensity. In Fig. 2 the EPIR ratio is shown as a function of the noise intensity Γ. The initial conditions are $x_0 = 0.9$ (circles) and $x_0 = 0.1$ (squares). The same behavior is observed for both initial conditions, namely the EPIR ratio increases with noise until it reaches a maximum at $\Gamma \approx 10^{-7}$. A second

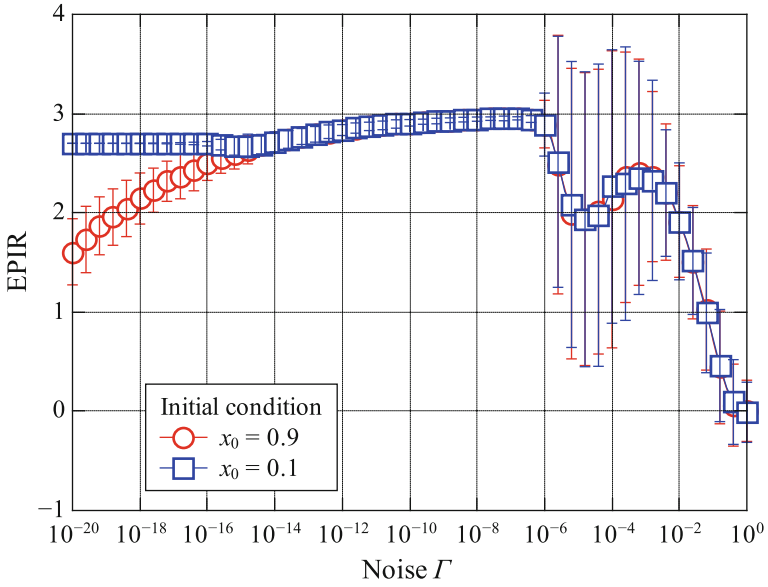

Fig. 2 EPIR ratio versus internal noise intensity averaged over 1000 realizations. Two maxima at $\Gamma \approx 10^{-7}, 10^{-3}$ are observed. Error bars are taken as one standard deviation. Note the erratic behavior for $\Gamma \gtrsim 10^{-6}$

peak is observed at $\Gamma \approx 10^{-3}$ but with a large standard deviation caused by the strong noise at that point. It is important to note that from Fig. 2 the EPIR ratio is nearly independent of the initial condition and that standard deviations are small for $\Gamma \in \left[10^{-15}, 10^{-7}\right]$.

One of the effects of noise is to help the boundary between the doped/undoped regions in the sample to escape from $x = 0, 1$. Eq. (4) suggest that the first maximum is reached when noise helps the boundary to escape from the border at $x = 1$. Since the boundary moves slower at $x = 0$, a stronger noise intensity is required to detach it, thus leading to a second maximum.

When external noise was considered, we did not find a noise intensity that maximizes the EPIR ratio. In Fig. 3 results are shown for the same set of parameters and initial conditions used before. In this case the window function effectively reduces the contribution of noise close to the sample borders. However, when the noise intensity is strong enough to counteract the window effect, the motion of the boundary is erratic, leading to a large standard deviation, and the EPIR ratio depends strongly on the initial condition.

In Fig. 4 the time evolution of the boundary is shown *vs*. noise intensity. In this case, the applied sequence was $+1 \rightarrow -1 \rightarrow +1 \rightarrow -1$, the pulsewidth was 2, and the initial condition was $x = 0.9$. We found a relation between the position reached by the boundary at the end of the first pulse, x_n—marked with circles in Fig. 4—and noise intensity: $1 - x_n \propto \sqrt{\Gamma}$.

Phase space trajectories are shown in Fig. 5 for the noiseless and internal noise ($\Gamma = 10^{-10}$ and 10^{-2}) cases. The applied signal is $v(\tau) = \sin(\omega\tau)$, the initial position is $x_0 = 0.9$, and the angular frequency $\omega = 1$. In the noiseless case,[1] the trajectory is a small closed loop. The boundary starts the motion from x_0 towards $x = 1$. At time $\tau = \pi/\omega$, the velocity is zero and the applied field is reversed. Then it increases and the boundary moves in the opposite direction until it reaches the initial state at $\tau = 2\pi/\omega$. Larger loops are obtained when considering a moderately strong internal noise in the system. In this case, at time $\tau = \pi/\omega$ the velocity differs from zero as can be seen in Fig. 4. In fact, if noise is turned off, for instance at $(\tau_{off}, x_{off} = 0.9)$ as shown in Fig. 5, the motion will remain in the orbit determined by the new initial conditions (τ_{off}, x_{off}) and deterministic Eq. (5). This way we see that noise has an important effect only when the boundary is close to the sample borders. At these points, in the case of internal noise, the velocity is strongly dependent on the noise intensity and leads to different trajectories. In the case of external noise, the window function reduces the influence of noise and no significant effect is observed.

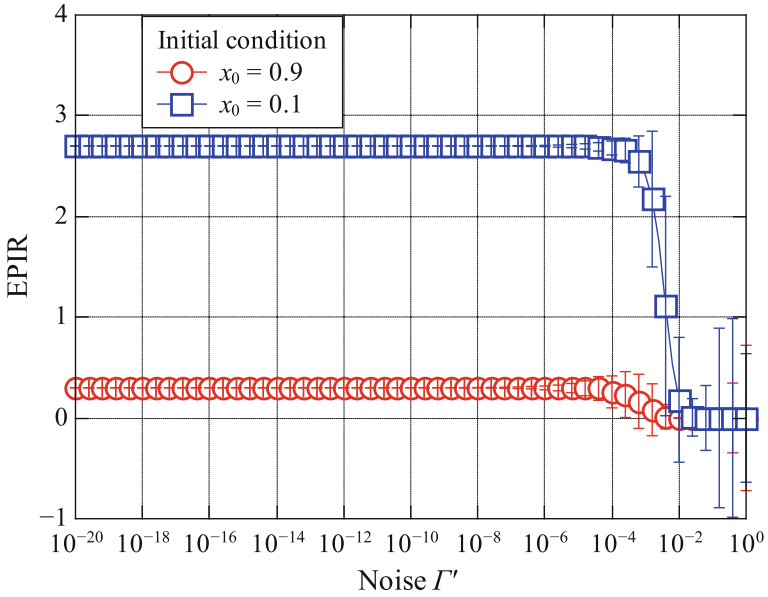

Fig. 3 EPIR ratio versus external noise intensity averaged over 1,000 realizations. No maxima are observed and the EPIR ratio degrades for noise intensities $\Gamma' \gtrsim 10^{-5}$

[1] The deterministic position of the boundary as a function of time can be obtained by direct integration of Eq. (5) and shown to be periodic with period $2/\omega$.

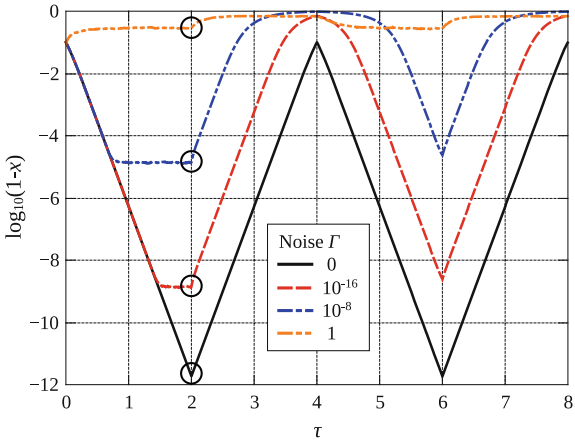

Fig. 4 Average boundary time evolution versus noise intensity. Positions after the first pulse (marked with circles) are noise dependent, leading to a new dynamic condition

4 Conclusions

In summary, we presented results on the phenomenon of resistive switching under the influence of noise. On the one hand, we found that, when internal noise is considered, there is a range of noise intensities where the EPIR ratio is maximized and independent of the initial conditions. On the other hand, external noise only has the effect of degrading the EPIR ratio since strong intensities are needed to counteract the window-function effect. Moreover, we showed that, when the boundary is close to the borders of the sample, its velocity is strongly influenced by noise. We believe

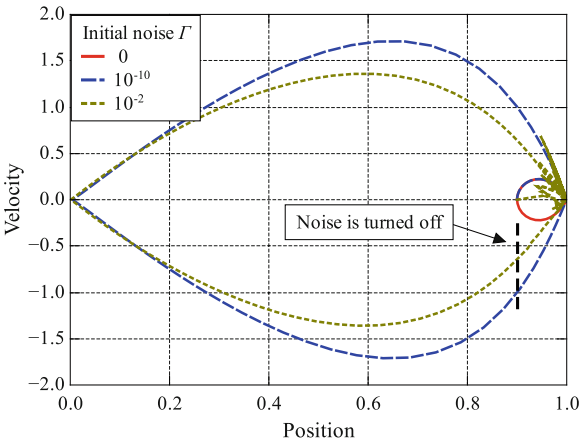

Fig. 5 Phase space trajectories for three different initial noise intensities. When the trajectories cross $x = 0.9$ after the first voltage reversal the noise is turned off

these results may be of relevance in systems where the large scale of electronic integration renders the effect of noise unavoidable.

Acknowledgments We gratefully acknowledge financial support from ANPCyT under project PICT-2010 # 121.

References

1. A. Stotland, M. Di Ventra, Phys. Rev. E **85**, 011116 (2012)
2. L. Chua, IEEE Trans. Circuit Theory **18**, 507–519 (1971)
3. D.B. Strukov et al., Nature **453**, 80–83 (2008)
4. A. Sawa, Mater. Today **11**, 28 (2008)
5. R. Waser, M. Aono, Nat. Mater. **6**, 833 (2007)
6. J. Blanc, D.L. Staebler, Phys. Rev. B **4**, 3548 (1971)
7. Y.N. Joglekar, S.J. Wolf, Eur. J. Phys. **30**, 661 (2009)
8. S.H. Strogatz, *Nonlinear Dynamics and Chaos* (Perseus Books, New York, 1994)

Topology Independent SIS Process: Theory and Application

Igor Tomovski, Igor Trpevski and Ljupčo Kocarev

Abstract Following the nonlinear dynamical system (NLDS) approach, we model and analyze a SIS type of spreading process on complex networks. The model is characterized by a special form of contact dynamics for which the term "acquisition exclusivity" is being used. Assuming statistical independence of joint events in the analysis, which is a valid approximation under several constrains, an analytic solution is obtained for the probabilities that network nodes are infected at an instance in time. Furthermore this solution is topologically independent. It is argued that there are two reasons why the studied setting should be considered valid from an engineering viewpoint. First, the studied process (under certain constrains) may be used as mechanism for controlled spreading of useful content in a network. Second, the SIS spreading process is characterized by high epidemic threshold. Therefore "acquisition exclusivity" should be considered as a mechanism for eradication of viral infections from networks.

1 Introduction

In this paper spreading process of SIS type, taking place on networks characterized by *acquisition exclusivity*, is being analyzed. We use the term *acquisition exclusivity* to refer to a special form of network contact dynamics, where at each instance a node contacts and acquires some form of material from exactly one of its neighbors, chosen randomly. Similar settings may be found in the literature in the analysis of certain social phenomena, for example the so called *Voter model* [1]. Our interest

I. Tomovski (✉) · I. Trpevski · L. Kocarev
Macedonian Academy of Sciences and Arts, bul. Krste Misirkov,
1000 Skopje, Macedonia
e-mail: igor@manu.edu.mk
e-mail: igortrpevski@cs.manu.edu.mk
e-mail: lkocarev@ucsd.edu

V. In et al. (eds.), *International Conference on Theory and Application in Nonlinear Dynamics (ICAND 2012)*, Understanding Complex Systems,
DOI: 10.1007/978-3-319-02925-2_28,

on the subject is primarily from an engineering view point. We show that, under the circumstances analyzed in the paper, the studied setting can be used as a basis for development of applications for controlled spreading of content.

On the other hand, analysis showed that this form of network contact dynamics significantly increases the epidemic threshold for the SIS spreading process. Since the SIS model is a good representative of re-occurring spreading processes, this finding may be further generalized to other similar models as well. In that sense, we suggest that *acquisition exclusivity* could be considered as tool for virus eradication from complex networks and used as an alternative contact dynamics in engineering networks, when an epidemics occurs.

In the analysis of the process, we adopt the nonlinear dynamical system approach (NLDS) introduced by Wang et al. [2] and Chakrabarti et al. [3]. Statistical independence of joint events (the point estimate approximation [3]) is taken into account. This approach, as shown in the original papers [2, 3], as well as similar and follow-up works [4–6] is valid in networks with regular node dynamics. Numerical simulations indicated that in networks characterized by *acquisition exclusivity*, the assumption is valid under several constraints. First, a large minimal node degree is required. This prerequisite is usually met when the process is studied on social networks. One may argue that in the near future this constraint will be fulfilled for a number of technical networks, primarily wireless networks, as well as those where the cost per link is relatively low. Good example are sensor networks, where already large minimal node degree is recommended [7]. In addition, in practical applications, one may consider taking relatively large values for the infection rate $\beta \to 1$. Under these assumptions, it is shown that the analyzed spreading process is analytically solvable, i.e. an analytical solution for the nodes status probabilities may be found. Furthermore, the obtained results indicate that, under the circumstances, the analyzed spreading process is topology independent.

2 Description of the Analyzed Process

We consider a network described with the adjacency matrix $\mathbf{A} = [a_{ij}]$, that is unweighed, connected and bidirectional, i.e. $\mathbf{A}$ is symmetric and irreducible. Let $p(i \leftarrow j), i \neq j = \overline{1, N}$ represent the contact probabilities, i.e. the probability that node i will contact and, possibly, acquire some form of spreading content from node j, at each instance . Contact probabilities satisfy the following relations: $p(i \leftarrow j) > 0$, if $a_{ij} = 1$, and $p(i \leftarrow j) = 0$ otherwise, and in general $p(i \leftarrow j) \neq p(j \leftarrow i)$. Due to *acquisition exclusivity* $\sum_{j=\overline{1,N}} p(i \leftarrow j) = 1$. We call matrix $\mathbf{B} = [b_{ij}]$, such that $b_{ij} = p(i \leftarrow j)a_{ij}$, contact matrix. It is obvious that $\mathbf{B}$ is irreducible and asymmetric, satisfying $\sum_{j=\overline{1,N}} b_{ij} = 1$.

Adopting the *NLDS* approach presented in [2, 3] and assuming that no instantaneous reinfection may occur within one time step, the SIS process taking place on networks characterized by "acquisition exclusivity" may be described with the following set of probability difference equations:

$$p_i^I(t+1) = (1 - p_i^I(t)) \sum_{j=1}^{N} \beta b_{ij} p_j^I(t) + (1-\delta) p_i^I(t), \tag{1}$$

where $p_i^I(t)$, $i = \overline{1, N}$ denotes the probability that node i is infected at time t. Parameter β, usually referred to as the "infection rate", is the probability that a susceptible node connected to an infected one will become infected itself, while δ the probability that an infected node will become susceptible again, both within one time step.

Two fixed points of the system (1) are obvious: $p_1^I = p_2^I = ... = p_N^I = p^I = 0$ and $p_1^I = p_2^I = ... = p_N^I = p^I = 1 - \frac{\delta}{\beta}$. The second has no meaning if $\frac{\delta}{\beta} > 1$.

The obtained fixed points, so far, only indicate potential system (network-spreading process) behavior. In what follows, we present two Theorems that state that the obtained fixed points, under the given circumstances, are the only valid attractors of the system (1), for different parametric regions.

Theorem 1 *For $\delta > \beta$ the system described with the set of equations (1) is globally (on $[0, 1]^N$) asymptotically stable (the origin is a globally asymptotically stable fixed point).*

Theorem 2 *For $\beta > \delta$, the point $p^I = (p_1^I, p_2^I, ..., p_N^I) \in [0, 1]^N$, such that $p_1^I = p_2^I = ... = p_N^I = p^I = 1 - \frac{\delta}{\beta}$, is globally asymptotically stable fixed point for the system (1).*

The proofs of both Theorems, especially Theorem 2, require thrall mathematical analysis, as well as introduction of several Lemmas. Due to space restriction, they are omitted in this text and will be presented elsewhere .

From the previous discussion, we may define the average number of infected nodes in the network, $N_I = \lim_{t\to\infty} \sum_{i=\overline{1,N}} p_i^I(t)$, for different parametric regions:

$$N_I = \begin{cases} 0, & \frac{\delta}{\beta} > 1 \\ (1 - \frac{\delta}{\beta})N, & \frac{\delta}{\beta} < 1 \end{cases},$$

with N being the number of nodes in the graph. As one may notice, the obtained result for the average number of nodes that are infected, does not depend on the network topology, but only on the parameters that describe the infection process (β and δ).

3 Numerical Simulations and Analyzes

In order to check the validity of the analytic results presented in the previous section, as well as to investigate the regions in which they adequately mimic the reality, stochastic simulations were performed and the results were compared with those an-

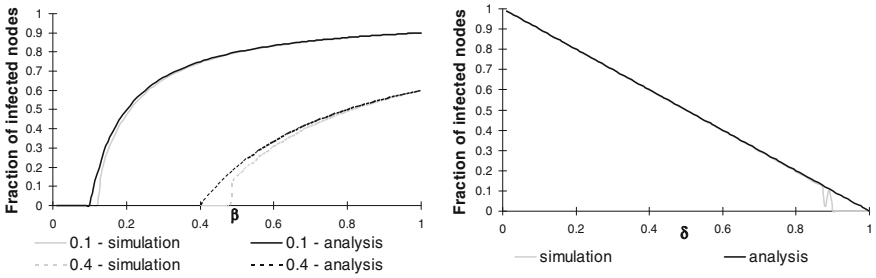

Fig. 1 Fraction of infected nodes for the SIS type process occurring on the Barabási-Albert network with $m_0 = 8$ and $m = 7$: *Left*, as a function of β for $\delta = 0.1$ (*black* full line-analytic result, *gray* full line-simulation); $\delta = 0.4$ (*black dashed line*-analytic result, *gray dashed line*-simulation); *Right* as a function of δ for $\beta = 1$ (*black* line-analytic result, *gray* line-simulation)

alytically obtained. The simulations were performed on Barabási-Albert graphs [8], where the minimal node degree was altered by changing the parameter m. In the simulations, connection probabilities $p(i \leftarrow j)$ were chosen randomly for each existing link.

The stochastic simulations were performed as follows: first the system network-infection, starting from arbitrary initial conditions, was iterated for 2,000 time steps in order to reach the stationary regime. Then, the system was further iterated for another 8,000 time steps, after which the results were averaged. The simulations were repeated several times for different values of the parameters β and δ. The results of the analysis for one of the used networks are presented in Fig. 1.

Several conclusions were derived from the analysis. First, the validity of the analytical results increases as the minimal node degree in the network increases. Second, there is a good degree of accuracy for large β/δ ratios. Finally, the accuracy is further increased when larger values of β are considered.

4 Application

The results from both the analysis and the numerical simulations indicate that under several assumptions, an application for controlled spreading of content may be developed, based on the principles described in this paper. The application will form a virtual network that will function in acquisition exclusivity contact mode. A minimal value of the node degree will be pre-determined for each node; however, users (nodes) will be able to freely increase the number of personal contacts. The useful content will spread through the network as a SIS type of process with β close to '1'. Parameter δ will be a controlled variable which will determine the number of users that will possess the information at an instance in time.

The SIS process taking place on networks that work in "acquisition exclusivity" mode of contact dynamics is characterized with an epidemic threshold $\beta = \delta$ (as well as the *contact process* [9, 10]). This is significantly higher threshold value, than

the one for the SIS infection occurring on networks with regular contact dynamics ($\frac{\beta}{\delta} = \frac{1}{\lambda_{1_A}}$ [2, 3, 6, 11]). In that sense, we suggest that acquisition exclusivity may be used as an engineering solution for virus eradication from complex networks. Following mechanism of action might be considered: when infection occurs, the network is switched to acquisition exclusivity mode of work and once the infection is eradicated, the network is switched back to normal regime.

For $\beta > \delta$, acquisition exclusivity might be insufficient to complete infection eradication by itself. In this case some form of additional measures as node immunization or vaccination [12–16] should be considered as well; however, acquisition exclusivity will severely reduce the costs of the additional protective measures.

5 Conclusion

We examine a SIS type of spreading processes that takes place on networks characterized by acquisition exclusivity type of contact dynamics. It is suggested that the process, under the imposed restrictions, is analytically solvable with respect to the status probabilities of nodes, while the obtained results are topology independent. This could be used as a basis for development of practical applications for controlled spreading of certain useful content. With respect to the epidemic threshold that characterizes the process on the observed networks, we suggest that acquisition exclusivity, implemented as an alternative to regular contact dynamics, may be taken into account as a practical and cost effective method for infection eradication in complex networks.

Acknowledgments We thank ONR Global (grant N62909-10-1-7074) and Macedonian Ministry of Education and Science (grant Annotated graphs in System Biology) for partial support [17].

References

1. K. Suchecki, V. M. Eguiluz, M. San Miguel, Voter model dynamics in complex networks: Role of dimensionality, disorder, and degree distribution. Phys. Rev. E **72**(3), 036132/1–036132/8 (2005)
2. Y. Wang, D. Chakrabarti, C. Wang, C. Faloutsos, Epidemic Spreading in Real Networks: an Eigenvalue Viewpoint, in *Proceedings of the 22nd International Symposium on Reliable Distributed Systems (IEEE SRDS03)*, Florence, 6–8 October 2003, pp. 25–34
3. D. Chakrabarti, Y. Wang, C. Wang, J. Leskovec, C. Faloutsos, Epidemic thresholds in real networks. ACM Trans. Inf. Syst. Secur. **10**(4), 13:1–13:26 (2008)
4. D. Smilkov, L. Kocarev, Influence of the network topology on epidemic spreading. Phys. Rev. E **85**(1), 016114/1–016114/10 (2012)
5. I. Tomovski, L. Kocarev, Simple algorithm for virus spreading control on complex networks. IEEE Trans. Circuits Syst. I Regul. Pap. **59**(4), 763–771 (2012)
6. P. Van Mieghem, J. Omic, R. Kooij, Virus spread in networks. IEEE/ACM Trans. Netw. **17**(1), 1–14 (2009)

7. S. Poduri, G.S. Sukhatme, Constrained coverage for mobile sensor networks, in *Proceedings of IEEE International Conference on Robotics and Automation—ICRA 04*, vol. 1, New Orleans, 24 April–1 May 2004, pp. 165–172
8. R. Albert, A.-L. Barabasi, Statistical mechanics of complex networks. Rev. Mod. Phys. **74**, 47–97 (2002)
9. S. Gomez, A. Arenas, J. Borge-Holthoefer, S. Meloni, Y. Moreno, Discrete-time Markov chain approach to contact-based disease spreading in complex networks. Eur. Phys. Lett. **89**(3), 38009/p1–38009/p6 (2010)
10. S. Gomez, A. Arenas, J. Borge-Holthoefer, S. Meloni, Y. Moreno, Probabilistic framework for epidemic spreading in complex networks. Int. J. Complex Syst. Sci. **1**, 47–51 (2011)
11. A. Ganesh, L. Massoulie, D. Towsley, The effect of network topology on the spread of epidemics, in *Proceedings of IEEE Infocom*, vol. 2, Miami, 13–17 March 2005, pp. 1455–1466
12. R. Pastor-Satorras, A. Vespignani, Immunization of complex networks. Phys. Rev. E **65**(3), 036104/1–036104/8 (2002)
13. L.B. Shaw, I.B. Schwartz, Enhanced vaccine control of epidemics in adaptive networks. Phys. Rev. E **81**(4), 046120/1–046120/5 (2010)
14. Y. Wan, S. Roy, A. Saberi, Network design problems for controlling virus spread, in *Proceedings of 46th IEEE Conference on Decision and Control*, New Orleans, 12–14 December 2007, pp. 3925–3932
15. Y. Wan, S. Roy, A. Saberi, Designing spatially-heterogeneous strategies for control of virus spread. IET Syst. Biol. **2**(4), 184–201 (2008)
16. L. Yongfeng, C. Jingan, The effect of constant and pulse vaccination on SIS epidemic models incorporating media coverage. Commun. Nonlinear. Sci. Numer. Simulat. **14**(5), 2353–2365 (2009)
17. I. Tomovski, I. Trpevski and L. Kocarev, Topology Independent SIS Processes: an engineering viewpoint. Commun. Nonlinear. Sci. Numer. Simulat. **19**(3), 627–637 (2014)

The Role of Duty Cycle in a Three Cell Central Pattern Generator

Jeremy Wojcik, Robert Clewley and Andrey Shilnikov

Abstract We describe a novel computational approach to reduce detailed models of central pattern generation to an equationless mapping that can be studied geometrically. Changes in model parameters, coupling properties, or external inputs produce qualitative changes in the mapping. These changes uncover possible biophysical mechanisms for control and modulation of rhythmic activity. Our analysis does not require knowledge of the equations that model the system, and so provides a powerful new approach to studying detailed models, applicable to a variety of biological phenomena beyond motor control. We demonstrate our technique on a motif of three reciprocally inhibitory cells that is able to produce multiple patterns of bursting rhythms. In particular, we examine the qualitative geometric structure of two-dimensional maps for phase lag between the cells.

1 Introduction

A central pattern generator (CPG) is a neural microcircuit comprised of cells whose synergetic interactions, without a sensory input, can produce rhythmic bursting patterns that determine motor behaviors of an animal, such as heart beat, respiration, and locomotion [1, 2]. A multifunctional CPG can exhibit distinct rhythmic behaviors depending on input conditions: for example, switching between trot and gallop gaits in many mammals [3] or between swimming and crawling in leeches [4, 5]. Although

J. Wojcik (✉) · R. Clewley · A. Shilnikov
Neuroscience Institute and Department of Mathematics and Statistics,
Georgia State University, PO Box 5030, Atlanta, GA 30303, USA
e-mail: jwojcik1@gsu.edu

R. Clewley
e-mail: rclewley@gsu.edu

A. Shilnikov
e-mail: ashilnikov@gsu.edu

V. In et al. (eds.), *International Conference on Theory and Application in Nonlinear Dynamics (ICAND 2012)*, Understanding Complex Systems,
DOI: 10.1007/978-3-319-02925-2_29,

such circuits are mostly hypothetical in the central nervous system of mammals, they have been located in many fish and invertebrates and in the spinal cord or peripheral nervous systems of mammals.

Switching between motor rhythms in a multifunctional CPG is attributed to switching between corresponding oscillatory attractors [5]. A key scientific issue is how modulation and control can switch the system between states, and how the CPG achieves robustness to noise and heterogeneity. Theoretically, the problem is therefore how to obtain parsimonious answers to the scientific questions through mathematical analysis and simulation of these models. A common approach has been to first reduce each neuron's activity to a one- or two-dimensional return map using, for example, phase resetting techniques, and then to compose these maps to form an approximate representation of the cycle-to-cycle network activity [6, 7]. Instead, we directly analyze a single return map induced by the full dynamics of a biophysical network CPG model. This map will be defined qualitatively through numerical simulations and does not require knowledge of explicit phase equations for the underlying network model. This makes our technique applicable to a wide range of detailed (high-dimensional) models of rhythmic activity in biological networks, especially those that are not easily reduced to low-dimensional systems of equations by explicit means.

Elemental circuit configurations for CPG models are often reduced to three oscillators but their components are typically anatomically and physiologically diverse [8–11]. We consider a model of endogenously bursting neurons coupled in a ring [12] using fast reciprocal synaptic inhibition modeled by fast threshold modulation [13]. The neurons are 3-dimensional reduced models of leech heart interneurons, as defined in ref. [14]. We demonstrate that the duty cycle of bursting, the fraction of the burst period in which the cell bursts, is a physiologically relevant order parameter that can be used to control switching between outcomes.

2 Qualitative Analysis of Phase-Lag Maps

We examine polyrhythmic outcomes of the motif for *short* (∼20 %), *medium* (∼50 %), and *long* (∼80 %) bursting duty cycles. For this we computationally derive return maps for phase lags $\Delta\phi_{21}$ and $\Delta\phi_{31}$ between burst onsets in cell 2 (green) and cell 3 (red) relative to the reference cell 1 (blue) (Fig. 1). As the period of network oscillation changes through time, we define the phase between cells to be relative to the time interval between which the voltage V_1 of cell 1 increases through a threshold of -40 mV. We define $\Delta\phi_{i1}^{(n)} \in [0, 1)$ as the phase lag between the nth consecutive burst onsets in cells 1 and i. As the network evolves from an initial state, the relative phases of each oscillator on each subsequent cycle n generate a sequence $\{\Delta\phi_{31}^{(n)}, \Delta\phi_{21}^{(n)}\}$, which we plot within the unit square; for convenience the iterates are joined with lines to preserve cycle ordering in the phase lag maps (Figs. 2, 3). Thus, the original, continuous-time 9D system is reduced to a 2D stroboscopic

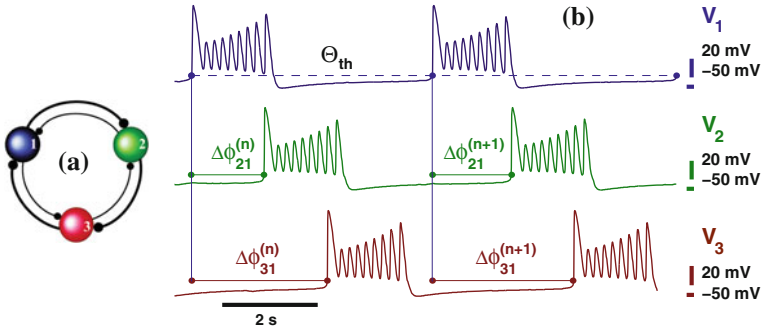

Fig. 1 Voltage traces: the phase (mod 1) of reference cell 1 (*blue*) is reset when V_1 reaches $\Theta_{\text{th}} = -40\,\text{mV}$. The time between burst onsets in cell 2 (*green*) and 3 (*red*) determine a sequence of phase lags $\{\Delta\phi_{21}^{(n)}, \Delta\phi_{31}^{(n)}\}$ normalized to the varying recurrence times of cell 1

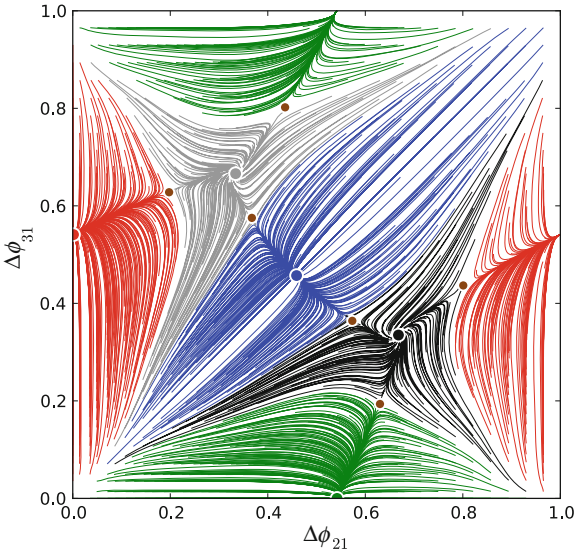

Fig. 2 Phase-lag map for the homogeneous, medium bursting motif at $V_{\text{K2}}^{\text{shift}} = -21.0\,\text{mV}$, showing five phase-locked (fixed point) attractors: *red* at $\sim \left(0, \frac{1}{2}\right)$, *green* $\left(\frac{1}{2}, 0\right)$, *blue* $\left(\frac{1}{2}, \frac{1}{2}\right)$, *black* $\left(\frac{2}{3}, \frac{1}{3}\right)$ and *gray* $\left(\frac{1}{3}, \frac{2}{3}\right)$, whose basins are separated by six saddles (*brown dots*)

return map for the phase lags defined on a torus $[0, 1) \times [0, 1)$, with $\Delta\phi_{i1}$ mod 1. The maps are not derived as explicit equations, but instead are tabulated on a 40×40 (or more) grid of initial points whose iterates comprehensively reveal the underlying vector field. We then study the geometric properties of the maps. In particular, we can locate equilibrium points of the maps, which we refer to as fixed points (FPs). We evaluate the stability of these objects and characterize bifurcations by using the methods of the qualitative theory of dynamical systems.

Figure 2 shows the $(\Delta\phi_{31}, \Delta\phi_{21})$ phase-lag map for the homogeneous, medium bursting motif when $V_{\mathrm{K2}}^{\mathrm{shift}} = -21.0\,\mathrm{mV}$. The map possesses five stable FPs (color-coded dots) corresponding to the coexisting phase-locked bursting patterns: red at $(\left(\Delta\phi_{21} \approx 0,\ \Delta\phi_{31} \approx \frac{1}{2}\right)$, green $\left(\frac{1}{2}, 0\right)$, blue $\left(\frac{1}{2}, \frac{1}{2}\right)$, black $\left(\frac{2}{3}, \frac{1}{3}\right)$ and gray $\left(\frac{1}{3}, \frac{2}{3}\right)$. The attraction basins of these points are divided by separatrices (incoming and outgoing sets) of six saddle points (brown dots). The saddles separate the basins of attraction of the 5 fixed points which correspond to phase locked states.

The outcome of the homogeneous motif depends on the initial phase distributions of the cells. When the cells are about to burst together, their initial phases are near the origin in the phase plane. In this case, any of the five rhythmic pattern outcomes has a chance of occurring (Fig. 2). Each rhythm is robust, so well chosen perturbations are needed to switch the motif between rhythms. An efficient and easy way to perturb an inhibitory motif is to apply an appropriately-timed hyperpolarizing pulse to the targeted cell [12, 15]. Figure 4 demonstrates the approach for the homogeneous motif. The phase-lag maps create a guide for where and how long a hyperpolarizing pulse is needed to switch between rhythms. For example, if we begin at the FP $\left(\frac{1}{2}, \frac{1}{2}\right)$ and perturb cell 2 (green) we change the phase-lags $\Delta\phi_{21}$ and $\Delta\phi_{31}$. This changes the position on the phase lag diagram and moves the phase point into the basin of attraction of another rhythm, as in Fig. 1.

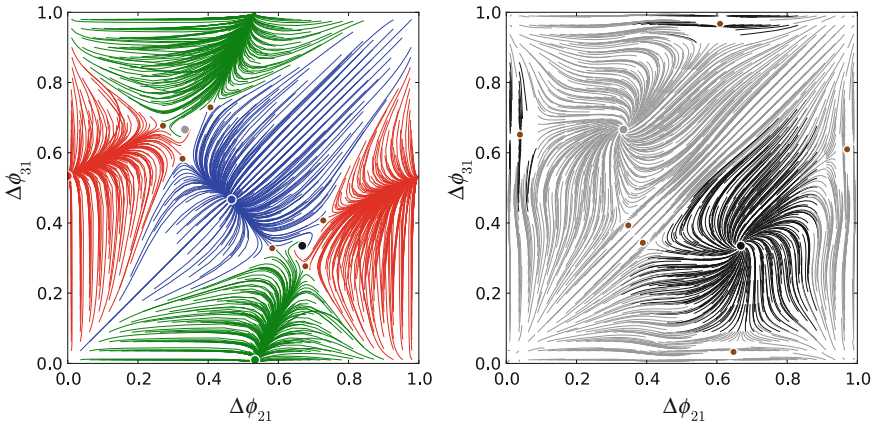

Fig. 3 Homogeneous phase-lag mapping for $V_{\mathrm{K2}}^{\mathrm{shift}} = -18.95\,\mathrm{mV}$ motif at $V_{\mathrm{K2}}^{\mathrm{shift}} = -18.95\,\mathrm{mV}$, showing three attractors (*blue, red*, and *green dots*). Each corresponds to an anti-phase rhythm where one cell bursts solo followed by synchronized bursts in the other two cells. The fixed points for counter-clockwise and clockwise traveling waves (*black dots*) are unstable. *Right* Phase-lag map for the homogeneous, long bursting motif at $V_{\mathrm{K2}}^{\mathrm{shift}} = -22.5\,\mathrm{mV}$, revealing two equally dominant rhythmic attractors: at $\left(\frac{1}{3}, \frac{2}{3}\right)$ and at $\left(\frac{2}{3}, \frac{1}{3}\right)$

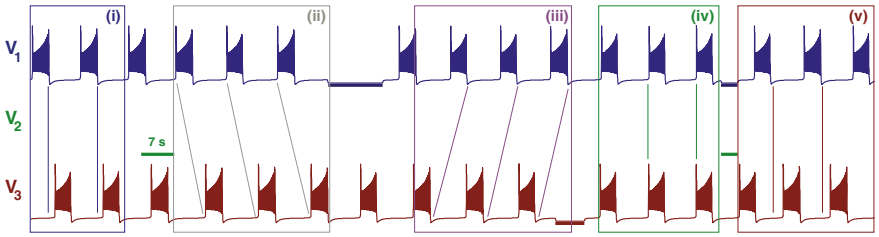

Fig. 4 Five types of robust bursting rhythms in the medium-length bursting motif, using $g_{\text{syn}} = 5 \cdot 10^{-3}$ (increased from its nominal value to illustrate stable states without long transients). Appropriately-timed inhibitory pulses (horizontal bars) temporarily suppress the targeted cells and switch between the rhythms. Episode (*i*) shows the $\left(\frac{1}{2}, \frac{1}{2}\right)$ FP interrupted by a pulse to cell 2. On release of cell 2 from suppression, the clockwise $\left(\frac{1}{3}, \frac{2}{3}\right)$ FP is observed. After cell 1 is temporarily suppressed, the counter-clockwise $\left(\frac{2}{3}, \frac{1}{3}\right)$ FP is observed in episode (*iii*). A pulse releasing cell 3 from inhibition then makes cell 2 lead in the $\left(0, \frac{1}{2}\right)$ rhythm of episode (*iv*). After cells 1 and 2 have been simultaneously hyperpolarized, cell 3 leads the motif in the $\left(\frac{1}{2}, 0\right)$ in the last episode (*v*) of the voltage trace

3 Duty Cycle is an Order Parameter of the Network

The duty cycle (DC) of bursting oscillations is the fraction of the burst period in which the cell is spiking (Fig. 1), and is a property known to affect the synchronization properties of coupled bursters [15]. DC can be measured experimentally from voltage traces in neural dynamics. In this study, we control DC through the intrinsic parameter $V_{\text{K2}}^{\text{shift}}$, which measures the deviation from the experimentally identified voltage value at which the slow K^+ current is half-activated [14]. DC depends monotonically on $V_{\text{K2}}^{\text{shift}}$. As the activation kinetics of this current are shifted to depolarized voltages, the cells produce first short, then medium, and then long burst trains before transitioning to continuous spiking. We consider weak inhibitory coupling determined by the maximal conductance g_{syn}, which is set at $5 \cdot 10^{-4}$ nS in the homogeneous case.

Comparison of the maps for the homogeneous motifs in cases of medium (Fig. 2), short (Fig. 3, left) and long (Fig. 3, right) bursting demonstrates that the DC is an order parameter for such configurations. As such, short bursting (DC $\sim$ 20%) makes both traveling waves impossible because the corresponding FPs exist but are unstable. In contrast, for long bursting (DC $\sim$ 80%), these patterns equally dominate the dynamics by narrowing the attractor basin of the other FPs—shrinking the range of phases that can lead to alternative patterns.

4 Summary

In this work we presented a simple network motif of three bursting cells reciprocally coupled by fast inhibitory synapses in a ring. We showed that the model can generate multiple, coexisting rhythms, selected by the initial conditions of the

cells. We characterized the essential temporal properties of the coupled system by measuring just two differences ("lags") in the phase between the three oscillators along simulated orbits. By systematic variation of the initial conditions, the computational exploration of the possible rhythmic outcomes led to a reduction of the original 9D system of differential equations to a graphical and equationless representation of the 2D mapping of cycle-to-cycle phase lags. Crucially, a feature of this reduction is that explicit equations were replaced by a qualitative portrait of the maps. Nonetheless, the geometric properties of the maps, and how they change as model parameters are varied, can be understood through standard qualitative techniques of dynamical systems theory. In particular, the rhythmic patterns of the motif correspond to fixed and periodic attractors of the maps. The basins of attraction for the rhythms are separated by phase thresholds known as saddles.

The power of our technique is that it avoids the need for equations, and as such makes few assumptions about the nature of the models of the coupled oscillators making up the motif or their detailed form of coupling. For instance, the models may be high-dimensional and possess multiple time scales. In order to define the phase lags, we only assume that the cells burst regularly. In principle, our technique can be generalized to a larger number of cells. Problems of human visualization of higher-dimensional phase-lag maps notwithstanding, the concepts of fixed points and periodic orbits carry through to higher dimensions.

We discovered that the primary "order parameter" determining the pattern outcomes is the duty cycle of bursting: short bursting promotes anti-phase rhythms, while long bursts will self-arrange into one of two traveling wave patterns typical of unidirectionally-coupled inhibitory rings. The dynamics of the motif with medium-length duty cycle is richer due to the existence of five competing rhythmic outcomes. We therefore hypothesize a possible biophysical control mechanism for switching between CPG patterns: common inhibition or excitation to the circuit, which varies the duty cycle of all cells simultaneously. For complete details see [16, 17] and references therein.

References

1. E. Marder, R.L. Calabrese, Principles of rhythmic motor pattern generation. Physiol. Rev. **76**, 687–717 (1996)
2. F. Skinner, N. Kopell, E. Marder, Mechanisms for oscillation and frequency control in networks of mutually inhibitory relaxation oscillators. J. Comput. Neurosci. **1**, 69–97 (1994)
3. A. Selverston, *Model Neural Networks and Behavior* (Plenum Press, New York, 1985)
4. K.L. Briggman, W.B. Kristan, Multifunctional pattern generating circuits. Annu. Rev. Neurosci. **31**, 271–294 (2008)
5. W.B. Kristan, R.L. Calabrese, W.O. Friesen, Neuronal basis of leech behaviors. Prog. Neurobiol. **76**, 279–327 (2005)
6. C.C. Canavier, D.A. Baxter, J.W. Clark, J.H. Byrne, Control of multistability in ring circuits of oscillators. Biol. Cybern. **80**, 87–102 (1999)
7. G.B. Ermentrout, K. Kopell, Fine structure of neural spiking and synchronization in the presence of conduction delays. Proc. Natl. Acad. Sci. USA **95**, 1259–1264 (1998)

8. R. Milo, et al., Science **298**, 824–827 (2002)
9. A. Prinz, D. Bucher, E. Marder, Similar network activity from disparate circuit parameters. Nat. Neurosci. **7**(12), 1345–1352 (2004)
10. M.I. Rabinovich, P. Varona, A.I. Selverston, H.D. Abarbanel, Dynamical principles in neuroscience. Rev. Modern. Phys. **78**(4), 1213–1265 (2006)
11. O. Sporns, R. Kötter, Motifs in brain networks. PLoS Biol. **2**(11), 1910–1918 (2004)
12. A. Shilnikov, R. Gordon, I. Belykh, Polyrhythmic synchronization in bursting network motif. Chaos **18**, 037120 (2008)
13. N. Kopell, D. Somers, Rapid synchronization through fast threshold modulation. Biol. Cybern. **68**(5), 393–407 (1993)
14. A. Shilnikov, G. Cymbalyuk, Transition between tonic-spiking and bursting in a neuron model via the blue-sky catastrophe. Phys. Rev. Lett. **94**, 048101-4 (2005)
15. I. Belykh, A. Shilnikov, When weak inhibition synchronizes strongly desynchronizing networks of bursting neurons. Phys. Rev. Lett. **101**, 078102-4 (2008)
16. J. Wojcik, A.L. Shilnikov, Order parameter for bursting polyrhythms in multifunctional central pattern generators. Phys. Rev. E **83**, 056209-6 (2011)
17. J. Wojcik, Neural Cartography: Computer Assisted Poincaré Return Mappings for Biological Oscillations Mathematics Dissertations. Paper 10. http://digitalarchive.gsu.edu/math_diss/10 (2012)

On the Approach of Ensemble of Interacting Imperfect Models

Miroslav Mirchev and Ljupco Kocarev

Abstract Several approaches of ensemble of interacting imperfect models combined based on observed data either by adaptive synchronization, optimized couplings or weighted combining have been recently proposed. In this study we further examine the weighted combining method using the Hindmarsh-Rose (HR) neuron model and the different outcomes that we can expect. We generate data with an HR model usually referred as 'truth' and use the data to train an ensemble of HR models with perturbed parameter values, so that together they mimic the truth. The results show that the weights of the ensemble can be learned using data from a truth HR model exhibiting bursting, in order to represent the same bursting behavior as well as other behaviors such as spiking and random bursting.

1 Introduction

The idea of combining individual models in order to gain improved estimates and predictions is widely present in many areas and has been explored for solving different kinds of problems [1]. In the recent period several ensembles of imperfect models which interactively communicate have been studied, particularly toward application to climate predictions. In [2, 3] an ensemble of coupled models was proposed which adaptively synchronizes with the observed data. Another approach was explored in [4] where the coupling coefficients can be learned from observed data by cost function

M. Mirchev (✉)
Dipartimento di Elettronica e Telecomunicazioni ,Politecnico di Torino, Duca degli Abruzzi 24, 10129 Turin, Italy
e-mail: miroslav.mirchev@polito.it

L. Kocarev
Macedonian Academy of Sciences and Arts, Skopje, Macedonia and BioCircuits Institute, University of California, San Diego, La Jolla, CA 92093-0402, USA
e-mail: lkocarev@ucsd.edu

V. In et al. (eds.), *International Conference on Theory and Application in Nonlinear Dynamics (ICAND 2012)*, Understanding Complex Systems,
DOI: 10.1007/978-3-319-02925-2_30,

minimization. Both analyzes assume a 'truth' model generating data and imperfect models obtained by perturbing the 'true' parameters. These analyzes show that the interactive ensembles represent the truth better than the models individually or their average. The approach from [4] has been further studied in [5] in respect to shorter amount of observed data, larger differences between the individual models, negative and larger values of the coupling coefficients and certain modifications to the learning procedure. In [6] it was observed that large coupling coefficients actually lead to a model with dynamics which is a convex combination of the individual models and therefore this combination could be learned directly.

In this paper we further study the weighted combining method using the Hindmarsh-Rose (HR) neuron model [7]. As truth we use a HR model exhibiting bursting and we train a weighted ensemble of imperfect HR models with perturbed parameter values. The ensemble can then be used to mimic any future behavior of the truth. In Sect. 2 we briefly describe the weighted combining method and the Hindmarsh-Rose model. Some numerical results are presented in Sect. 3, while Sect. 4 concludes the paper.

2 Ensemble of Interacting Hindmarsh-Rose Models

The methods of interactive ensembles of models have been previously mostly applied to systems with dimensions of similar time-scale. In this study we use the HR model [7] which exhibits fast-slow dynamics, i.e. some state variables change at a slower rate than the others. The model has been developed to be a simplified qualitative representation of a neuron's behavior and its equations of motion are

$$\begin{aligned} \dot{x} &= y - a * x^3 + bx^2 + I - z \\ \dot{y} &= c - dx^2 - y \\ \dot{z} &= r(s(x - x_1) - z), \end{aligned} \tag{1}$$

where x represents the membrane potential, y is a recovery variable, z is a slowly varying adaptation current, I is an external current and a, b, c, d, r, s and x_1 are parameters. With the change of the external current and the parameters the model can exhibit regular bursting, spiking and random bursting as well as individual spikes and bursts.

We assume that as truth (T) we have one Hindmarsh-Rose (HR) model and there are M imperfect models obtained by perturbing at most P parameters in each equation. We use a weighted ensemble, as in [6], in which the i-th component of the dynamics f_m^i of each model m is included by weight w_m^i, so the equation of motion of each ensemble component is defined as

$$\dot{x_e}^i = \sum_m w_m^i f_m^i(\mathbf{x_e}) \tag{2}$$

An error can be defined for each component i and each model m as the deference between the true state change and the state change of model m initialized from the truth state. The overall sum-squared-error per component is a quadratic function of the weights which in turn can be minimized directly [6], or the derivatives of the error with respect to the weights can be equalized to zero and then least squares can be applied. Alternatively, a learning procedure similar to the one described in [4] could be considered.

In our case the ensemble can be rewritten in the form of Eq. (1), so that for each ensemble parameter p_e, $p_e = \sum_m w_m^i p_m$. If the weights are constrained to form an affine combination per component ($\sum_m w_m^i = 1$) the unperturbed parameters of the ensemble will become equal to the truth, while to have a perturbed ensemble parameter equal to a truth parameter p_T, the constraint $\sum_m w_m^i p_m = p_T$ needs to be satisfied. Thus, if $P + 1 \leq M$ the system of equations relating the weights per component is not overdetermined and we could have an exact solution. If the weights are further constrained to positive values, so they form a convex combination ($w_m^i > 0$ and $\sum_m w_m^i = 1$), to have an exact solution the truth parameters should be in the range between the perturbed parameters. Otherwise, if these conditions are not satisfied or the models structurally differ from the truth, the optimization could provide a set of weights as well as possible.

3 Numerical Analyzes

We assume that as truth we have a time series of 10,000 time units of data obtained by integrating an HR model with time step 0.01. These data are generated by a model exhibiting bursting ($a = 1$, $b = 3$, $c = 1$, $d = 5$, $r = 0.001$, $s = 4$ and $I = 2$), so that the system visits diverse areas of the three dimensional ($D = 3$) phase space, but alternatives could be explored and the applied external current I could be also varied. We add a small amount of Gaussian noise to the observed data and as the noise level becomes higher, longer series of observed data are required to accurately capture the truth behavior.

The ensemble consists of three imperfect models ($M = 3$) differing from the truth by up to 30 % in a, b, c, d, s and x_1, so that there are two parameter perturbations per equation ($P = 2$) and only r remains unchanged. It can be noticed on Fig. 1, as expected [1, 6], that a uniformly weighted ensemble mimics the truth better than the individual models. Therefore, the goal is to find a set of weights of the dynamics of the individual models which would represent the truth as best as possible.

We search for an optimal set of weights by applying quadratic programming with weights constrained to form a convex combination per component as in [6], but if a good solution can not be found the constraints could be relaxed, however, in our case a solution was found with the given constraints. As a next step we evaluate the obtained ensemble by making $N = 1000$ test runs of both the truth and the ensemble. At each run the ensemble is initialized from a different truth state with excluded transient dynamics and added noise. Then both the ensemble and the truth are integrated forward for 10,000 time units.

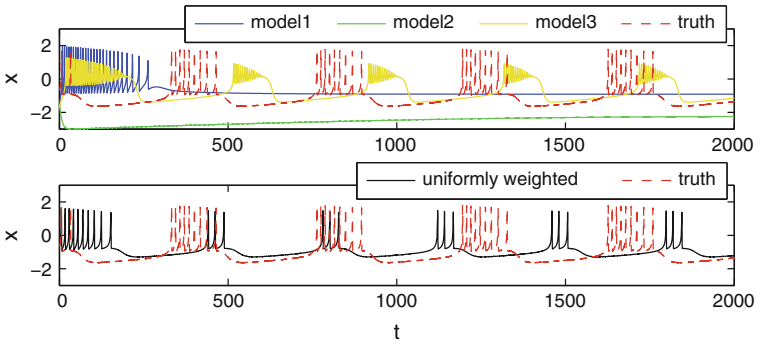

Fig. 1 The membrane potential (x) of a bursting HR model (truth) and three other models with perturbed parameters

Besides examining the bursting behavior, we are also interested if the obtained ensemble can mimic the truth if there is a change in I ($I = 4$) so the truth exhibits spiking and furthermore if there is change in both r and I ($I = 3.25$, $r = 0.005$) so the truth exhibits random bursting, i.e. the number of spikes in each burst is random. In this way the ensemble is confronted to a behavior different than the one used to learn the weights.

There are different ways to estimate the predictive power of the trained ensemble. One way to compare pairs of neurons is to calculate the correlation between the output signals, though, many other approaches exist [8]. To quantify the quality of the predictions at each time step we calculate an average correlation coefficient (r) as an average of the component-pairwise Pearson correlation coefficients between the ensemble (x_e) and the truth (T)

$$r = \frac{1}{D}\sum_{i=1}^{D}\frac{\sum_{j=1}^{N}(x_{e_j}^i - \overline{x_e^i})(T_j^i - \overline{T^i})}{\sqrt{\sum_{j=1}^{N}(x_{e_j}^i - \overline{x_e^i})^2 \sum_{j=1}^{N}(T_j^i - \overline{T^i})^2}} \tag{3}$$

The average correlation coefficient is shown on Fig. 2 for the three considered behaviors, while Fig. 3 shows a single prediction of the x variable. It can be noticed that in bursting the correlation decreases slowly during the period of examination with small variations and the single prediction also shows that the ensemble follows the truth behavior. In random bursting the correlation is relatively high (>0.6) during the first 180 time units and drops to zero after 300 time units, though, the ensemble still mimics the truth behavior.

On the other hand, in spiking the correlation drops bellow 0.6 after the first 20 time units. Afterward, the correlation periodically rises to high values corresponding to a periodic matching of the spikes and drops bellow zero when the spikes mismatch is largest. It was observed that the largest mismatch is in the z variable and after the initialization the ensemble goes through a short transient period after which the

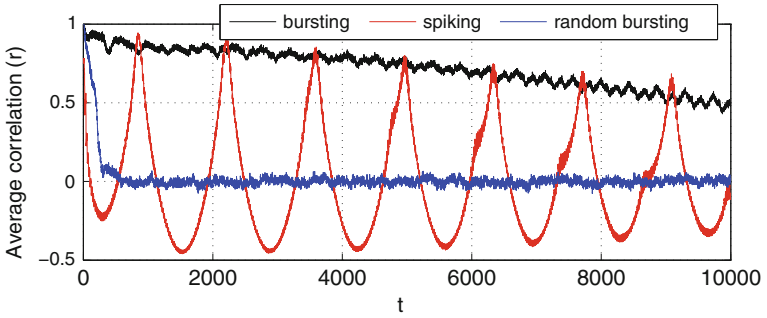

Fig. 2 The average correlation (r) between the model and the truth for an HR model in bursting, spiking and random bursting behavior based on 1,000 test runs of 10,000 time units

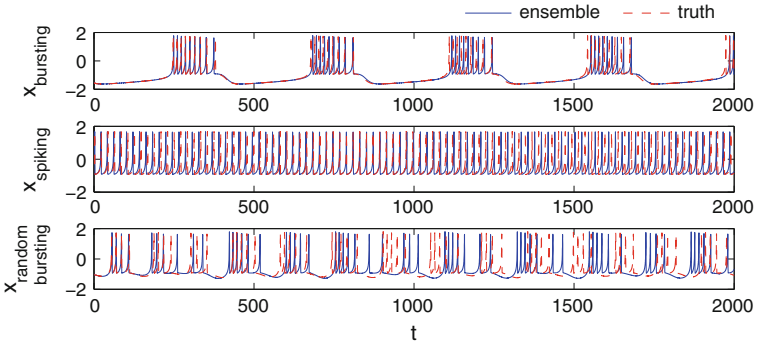

Fig. 3 A single prediction run of x in bursting, spiking and random bursting behavior

Table 1 Means (μ), standard deviations (σ) and covariances of the truth and the ensemble based on 1,000 test runs for bursting (burst.), spiking (spik.) and random bursting (r.burst.) behaviors

	μ_x	μ_y	μ_z	σ_x	σ_y	σ_z	cov_{xy}	cov_{xz}	cov_{yz}
Truth burst.	−1.120	−6.876	1.919	0.566	3.992	0.116	1.7649	0.0034	0.0268
Ensemble burst.	−1.120	−6.858	1.921	0.564	3.983	0.117	1.7596	0.0034	0.0299
Truth spik.	−0.595	−2.257	4.018	0.545	1.283	0.005	0.1998	0.0000	−0.0042
Ensemble spik.	−0.591	−2.194	4.033	0.537	1.248	0.005	0.1911	0.0000	−0.0041
Truth r.burst.	−0.800	−3.481	3.200	0.506	1.752	0.115	0.4809	0.0033	0.0343
Ensemble r.burst.	−0.798	−3.453	3.207	0.503	1.803	0.124	0.4957	0.0039	0.0483

spiking rate becomes more similar to the true. Therefore, it can be argued that after this transient period the ensemble misses or adds one spike per each correlation drop bellow zero, which can be also noticed at Fig. 3. We should note that attempts to train the ensemble with the truth exhibiting spiking resulted in less accurate predictions than using bursting data.

As previously studied in [4, 5], the characteristics of the long term behavior of the observed process are also of interest. Therefore, in Table 1 the summary statistics (mean values, standard deviations and covariances) based on the 1,000 test runs of the truth and the ensemble are presented and it can be seen that the given characteristics of the truth are well preserved by the ensemble.

4 Conclusions

We have studied the weighted ensemble of interacting models and its different possible solutions using the Hindmarsh-Rose (HR) neuron model which have fast and slow dynamics. It was shown that by observing an HR model exhibiting bursting a weighted ensemble can be trained to capture the same behavior. Moreover, the same ensemble is also capable to mimic future spiking and random bursting behaviors.

During the optimization the weights were strictly constrained to form a convex combination per component, however, in other circumstances these constraints could be relaxed if necessary. One possible alternative is regularizing the problem to make small positive weights preferable while still allowing negative weights if required. The analyzed method worked well with small amount of noise but for higher noise levels data should be observed over a longer period or alternative learning strategies could be considered.

Acknowledgments This work was partially supported by project EC Grant #266722.

References

1. C.M. Bishop, *Pattern Recognition and Machine Learning (Information Science and Statistics)* (Springer, Secaucus, 2006)
2. G. Duane, J. Tribbia, B. Kirtman, Consensus on long-range prediction by adaptive synchronization of models, in *EGU General Assembly Conference Abstracts*, ed. by D.N. Arabelos, C.C. Tscherning, pp. 13324, April 2009
3. G. Duane, Synchronicity from synchronized chaos. Arxiv.org/abs/1101.2213. (Submitted 2011)
4. L.A. van der Berge, F.M. Selten, W. Wiegerinck, G.S. Duane, A multi-model ensemble method that combines imperfect models through learning. Earth Syst. Dyn. **2**(1), 161–177 (2011)
5. M. Mirchev, G.S. Duane, W.K.S. Tang, L. Kocarev, Improved modeling by coupling imperfect models. Commun. Nonlinear Sci. Numer. Simul. **17**(7), 2741–2751 (2012)
6. W. Wiegerinck, F.M. Selten, Supermodeling: combining imperfect models through learning, in *NIPS Workshop on Machine Learning for Sustainability (MLSUST)*, 2011
7. J.L. Hindmarsh, R.M. Rose, A model of neuronal bursting using three coupled first order differential equations. Proc. Roy. Soc. Lond. Ser. B. Biol. Sci. **221**(1222), 87–102 (1984)
8. M.R. Cohen, A. Kohn, Measuring and interpreting neuronal correlations. Nat. Neurosci. **14**, 811–819 (2011)

Synchronization in Coupled MEMS Resonators

Suketu Naik and Takashi Hikihara

Abstract In this paper, the experimental results of a MEMS resonator with hard-spring response are shown. Under specific excitation conditions, the resonator shows an extension of the hysteresis during upsweep and downsweep of the excitation frequency. The extension of the hysteresis can be tuned by changing the excitation voltage. Sensitivity in regards to change in excitation conditions including ac voltage, dc bias, and pressure is demonstrated. Furthermore a unidirectionally coupled system consisting of the above nonlinear resonators is also characterized.

1 Introduction

Micromechanical devices provide ample opportunities to explore rich dynamical behaviors including synchronization. MEMS devices can exhibit many nonlinear behaviors including the hard-spring effect and the soft-spring effect. Along with ac excitation voltage and bias, actuation mechanisms such as parallel plate comb-drive or laterally driven comb-drive determine whether soft-spring or hard-spring behavior is exhibited. Furthermore a closed-loop coupled nonlinear system can offer additional advantages including self-excited oscillations and synchronization to an excitation signal. In this paper the experimental results of synchronization in an electronically coupled system of Micro Electro Mechanical System (MEMS) resonators with hysteresis in frequency-domain are entailed.

S. Naik (✉)
SSC-Pacific, 53560 Hull Street, San Diego, CA 92152, USA
e-mail: suketunaik@gmail.com

T. Hikihara
Department of Electrical Engineering, Kyoto University, Katsura, Nishikyo, Kyoto 615–8510, Japan
e-mail: hikihara.takashi.2n@kyoto-u.ac.jp

V. In et al. (eds.), *International Conference on Theory and Application in Nonlinear Dynamics (ICAND 2012)*, Understanding Complex Systems,
DOI: 10.1007/978-3-319-02925-2_31,

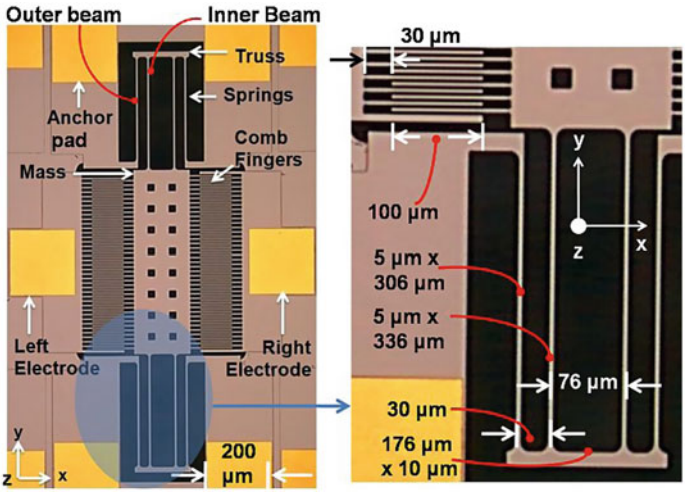

Fig. 1 Comb-drive resonator fabricated in SOIMUMPs process: note the difference between the lengths of the inner beam and outer beam within a pair of folded beams

2 Single Nonlinear Resonator

Figure 1 illustrates a laterally driven comb-drive resonator that was fabricated in SOIMUMPs process [1]. The resonator consists of a perforated mass suspended by folded springs. The springs are attached to the truss. The device is designed to be symmetric in x and y axes to provide stable oscillations. Usually the device is biased at a dc voltage. By applying ac voltage between the comb fingers attached to the mass and the fixed electrode (either left or right electrode in Fig. 1), a time varying electrostatic force is generated which makes the mass vibrate in the x-direction. Typically the motional current, which is proportional to the change in the capacitance between the comb fingers and the excitation voltage, is measured. The vibration in this type of resonator will be only in the x-direction due to two design features: folded flexure and thickness of the structure. These features reduce the axial stress and restrict the out-of-plane movement thereby minimizing unstable and unwanted vibrations in the other axes [2]. Also small dimples were placed to avoid the stiction between the long comb-fingers with small gap.

2.1 Design and Fabrication

The devices were fabricated in a SOIMUMPs process. SOIMUMPs is a simple Silicon-On-Insulator (SOI) patterning and etching process offered by Memscap, Inc. The end result is a 25 µm thick doped Silicon as the structural layer which is patterned and etched on a 400 µm thick Silicon substrate with 2 µm thick Oxide as the insulating

layer [1]. The substrate underneath the structure is completely removed in a back-etch which reduces parasitic capacitances and damping. The Pad Metal layer is used for the bond-pads for excitation and detection. The folded beam design reduces axial stress components present in a single beam and extends the stroke in the intended direction of motion. Each end of the folded beam pair (total of four pairs) is free to expand and contract in all directions. The resonating mass is suspended by flexures on four sides; the total stiffness of the entire structure in a given direction can be verified by running a modal analysis in FEA software. The frequency associated with the fundamental mode is 9681.43 Hz. The truss reduces motion in the y-axis in this mode. The analysis of the other modes reveals that the frequencies corresponding to the other two modes are farther away from the fundamental frequency. These two frequencies are due to the torsional and lateral modes that can be present in the suspension beams. Springs are made to be long and narrow and are terminated with fillets to minimize breakage. The design presented in this chapter is comprised of the folded beams with outer fold. The inner beams were designed to be slightly longer than the outer beams as shown in Fig. 1. This creates a ratio between the inner beam (IB) and outer beam (OB) and introduces an asymmetry. With $L_{OB} = 306\,\mu m$ and $L_{IB} = 336\,\mu m$, $k_{OB}/k_{IB} = L_{IB}^3/L_{OB}^3 = 1.32$.

2.2 Nonlinearity

Nonlinearity in the MEMS devices can appear due to large vibrations, residual stress, variation in the individual elements, contact with other elements, circuit elements, and/or a combination of all of the above. Typically the nonlinearity in MEMS is categorized as soft-spring effect and hard-spring effect. In the soft-spring effect the springs soften, that is the restoring force decreases as the displacement increases. On the other hand the hard-spring effect is characterized by an increase in the restoring force with increasing displacement. The actuation mechanism plays a major role in which type of behavior is exhibited. For example, parallel plate actuation generates a strong dependence on the bias in the applied force value; it effects the linear spring constant term by reducing it. At high dc bias the effective linear spring constant term becomes negative and the device exhibits soft-spring effect. On the other hand, hard-spring behavior can occur in a laterally driven comb-drive when it is driven by large force. In either case, the primary cause of the nonlinearity is the deformation of material. Usually linear displacement occurs in the first lateral mode when small force is applied at the tip of the beam. In this mode, the springs go through large deformation in the presence of a large force which can result in the nonlinear restoring force.

3 Experimental Results

Measurements were performed on Agilent 4,294A impedance analyzer on resonators fabricated on separate dies and single die. The left electrode was connected to the high port, the anchor pad (resonating structure) was connected to the low port, and

the right electrode was connected to the ground. From the equivalent circuit model of a resonator, the impedance analyzer can display the real part containing a purely mechanical term plus an offset attributed by a purely capacitive term and the imaginary part containing purely capacitive terms. In the linear operation, the quality factor Q was measured as 4,640, 5,540, 4,026 for three different resonators on separate dies. For this measurement, the resonators were excited with a dc bias of 20 V, an ac amplitude of 25 mV, and the pressure inside the vacuum chamber was set to 30 Pa.

3.1 Change in Excitation Conditions

In this section, the frequency responses of the resonator while changing excitation conditions including ac voltage, bias, and pressure are briefly discussed.

AC Voltage

Figure 2 shows the upsweep frequency responses of the resonator. For the purpose of clarity, the downsweep responses are not shown. However it was observed that less than 5 Hz variation existed during the downsweep in all three resonators. As shown in Fig. 2, the resonators show a typical hard-spring response up to a certain value of the ac voltage after which the response extends to a higher value of frequency. As shown in Fig. 2a, the approximate value of the ac excitation amplitude at which the extension occurs is 170 mV. The frequency at which the extension in a given resonator occurs at higher excitation amplitudes is nearly identical, as was observed in all resonators. Another important observation is that during the upsweep, the resonators show slight ringing in the middle of the curve as shown in Fig. 2a. The resonator seems to have gone through more bifurcations which help continue the upsweep response. The springs can maintain a stable vibration up to only a certain frequency, after which it drops to a lower value such that the restoring force in the springs can maintain an equilibrium with the excitation force. Also note that within the extended hysteresis region the coexistence of two vibrational amplitudes indicates a better control and predictability for switching the resonator between the two states. However the mechanism for the extended hysteresis (see Sect. 3.2) depends on the interplay between outer beam and inner beam which should be carefully controlled. This feature is crucial in facilitating multiple bifurcations in the resonator and thereby extending the response. It is worthy to note that by increasing ac voltage, the folded beam pairs exhibit large displacement which leads to large deformation as the beams harden. Hence the overall nonlinear spring constant increases when ac voltage is increased and as a result the responses *do not overlap* before the extended region for small values of ac voltage.

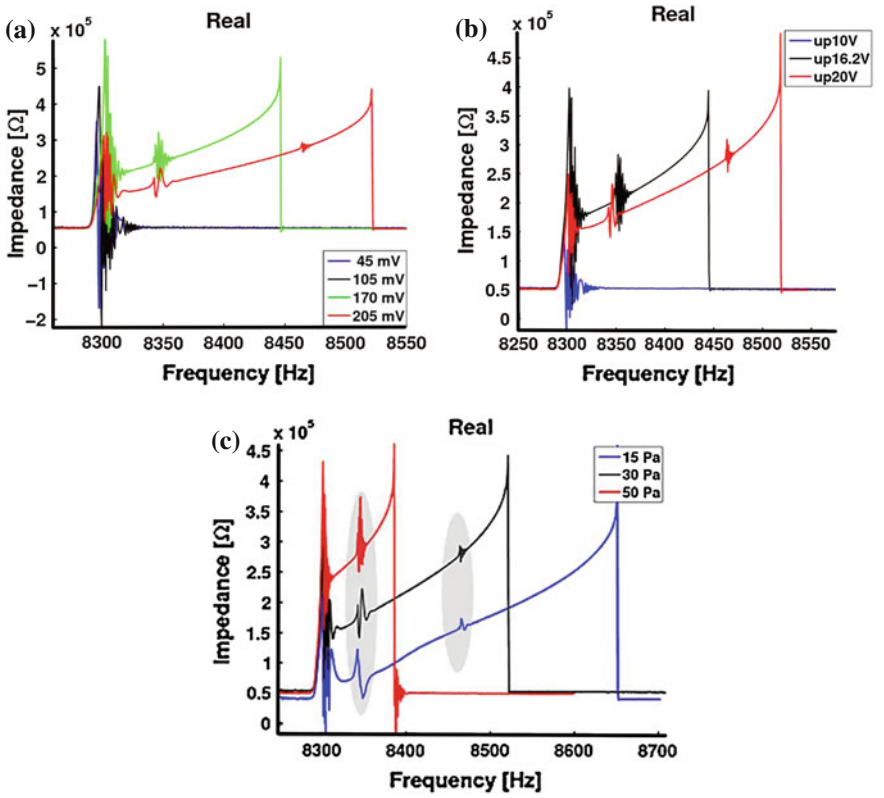

Fig. 2 Change in excitation conditions (note that downsweep responses are not shown for clarity and only the real parts of the frequency responses are shown to illustrate the mechanical behavior): **a** ac amplitude = [45, 105, 170, 205 mV], bias = 20 V, and pressure = 30 Pa, **b** bias = [10, 16.2, 20 V], ac amplitude = 205 mV, and pressure = 30 Pa, **c** pressure = [15, 30, 50 Pa] with ac excitation amplitude = 205 mV and bias = 20 V

Bias

While changing the bias, the behavior is qualitatively similar as shown in Fig. 2b. Here the electrostatic force increases significantly while incrementing the bias voltage. This is due to an increase in the steady-state capacitance between the comb fingers. The resonators display the nonlinear resonance at a low bias value. Also it is important to note that the extension of the hysteresis depends more on the bias voltage than the ac excitation amplitude. For example, a high ac excitation amplitude with a low bias does not always induce the extended hysteresis. As mentioned in the previous section, the frequency at which the extension occurs was observed to be identical while increasing the bias value. The effect of increasing bias is that it changes the equilibrium position of the resonator around which the folded beam pairsresonate in

the presence of the ac voltage. Hence the change in dc does not significantly increase the overall nonlinear spring constant which results in *overlapping* of the frequency response in the lower frequency range.

Pressure

The effect of changing pressure is that it influences the molecular resonance in the material and as a result the motional resistance exhibited by the device increases with an increase in the pressure. For example, the experiments conducted on a device in the air showed only the linear resonance due to high damping. Bias > 60 V and ac amplitude = 1 V were required to produce any motion in the device. In air the device was not tested at an excitation value higher than the above value lest it may break. Hence a clear nonlinear resonance and extension of the hysteresis were not observed. However in the vacuum starting at 100 Pa, the devices exhibited a distinct nonlinear resonance similar to the one shown in previous sections due to the low damping. To compare the influence of pressure and the damping, devices were tested at 50, 30 and 15 Pa. Figure 2c shows that at all pressure values, the nonlinear resonance occurs at approximately the same frequency point. This type of ringing was observed more or less in all resonators. Note that this behavior may have been induced by additional bifurcations. The mechanism behind these bifurcations can be attributed to the interaction of the outer beams with the inner beams thereby sustaining the vibrations. Finally it is important to note that while varying the pressure, the temperature change inside the chamber was not monitored or considered. Temperature can affect the molecular resistance and the damping such that some of the qualitative behavior would change.

3.2 Mechanism for the Extended Nonlinear Resonance

The causes of the nonlinear behavior shown in the above sections are as follows. As the structure resonates, the inner beams and outer beams shown in Fig. 1 expand and compress together (vice versa in the other direction). Normally this helps extend the linear range of the resonator. Also the compliance in the truss can partially relieve the axial compression. However the long and narrow beams can be axially loaded when they experience a large electrostatic force during the peak resonance [2]. As a result the inner beams develop higher modes of vibration due to high tensile force to maintain equilibrium. Additionally the outer beams are designed to be stiffer than the inner beams with a ratio of 1.32; hence they tend to compress less. This type of nonuniform stress distribution in the inner and outer beams can cause more hardening. Also note the location of the four beams on the truss; the distance between the inner and outer beam in a given pair and the distance between two given pairs are not equal. Additionally the outer beams can also be axially loaded and can exhibit a higher mode of vibration as a result of the nonuniform expansion and contraction.

All these conditions can cause the mass to sustain the vibrations as the frequency is swept past the resonance frequency and as a result the extension of hysteresis can occur. The mechanism behind hysteresis and extended hysteresis has already been discussed in detail in one of our papers [3].

4 Coupled Resonators

The coupled experiment was performed by using three resonators on a single die (referred to as Res 1, Res 2, Res 3 from now on). The test die was attached by non-conductive epoxy in the center of the device PCB and devices were wire-bonded to the pcb traces using gold wires with diameter $= 25\,\mu$m. The motional current produced by the device was read off the anchor pad. The substrate, the pcb, and the vacuum chamber were also grounded to reduce parasitic capacitances. The experiments were conducted on a motion resistant test-bench to dampen the ambient vibrations. The three resonators on a single die were coupled together by discrete electronics such that they form a closed-loop system, i.e. $1 \rightarrow 2 \rightarrow 3 \rightarrow 1$.

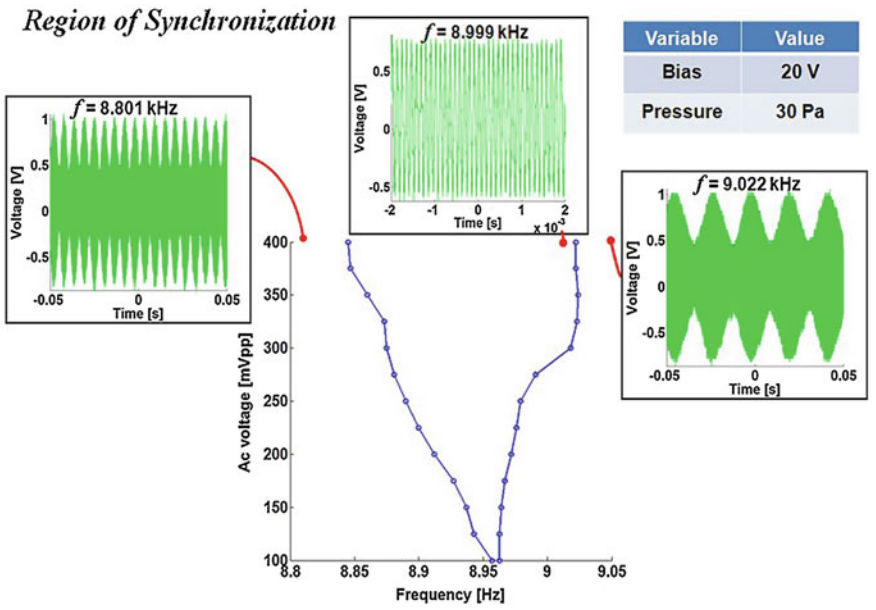

Fig. 3 The coupled system with a priori in-phase vibrations in the presence of ac excitation signal: region of synchronization is shown where x-axis denotes the frequency of the excitation signal and y-axis denotes the peak-to-peak voltage level of excitation signal. Outside of the sync region, the oscillations are quasiperiodic as shown in the insets

4.1 Self Excitations

In this experiment the devices were biased using a dc power supply. As mentioned previously, the bias voltage plays a role of shifting the equilibrium position of the resonator. If a resonator is in steady-state and the bias is applied suddenly, the resonator changes its steady-state or the equilibrium value (in the single well potential) after some transient behavior induced by the noise in the circuit. Hence without the bias the initial positions of the resonators are identical before applying an excitation signal. [1] The output of a given resonator was fed to current-to-voltage (I-V) converter which was connected to an amplifier with a variable gain which can tune the overall coupling strength between the resonators. The output of the coupling amplifier was then connected to the next element in the ring. Next a bias of 20 V was applied simultaneously on all the resonators. After that, the resonators were self-excited by adjusting the gains of the coupling amplifiers. The inherent noise vibrations in the circuit components act as the excitation signals to the resonators. The noise induced vibrations are amplified by the coupling amplifiers. In this way the noise is fed from the one element to the next element in the loop and thus each element drives the other element with this noise. As the noise in the system traverses around the loop, the resonators start to vibrate first arbitrarily and then by responding to the mechanism of self-organized synchronization induced by the coupling strengths past the critical values. Eventually at a sufficiently large vibration the resonators fully synchronize with each other, as a result as the signal-to-noise ratio gets higher and stable sinusoidal vibrations emerge depending on the coupling strengths. The shared frequency of oscillation is approximately 9 kHz and the amplitude levels are 2.12 V for Res 1, 0.68 for Res 2, and 1.86 V for Res 3. While tuning the coupling strengths, a narrow range of frequencies was observed in which stable vibrations occur. The frequency and the amplitude of the vibrations increase as the coupling strengths are carefully matched and increased. Other combinations of the coupling produce unstable (quasiperiodic) vibrations.

4.2 Synchronization with the AC Excitation Signal

In this experiment, the ac excitation with dc bias was connected to the input ports of the coupled system via a bias-tee network. The 1:1 region of synchronization is shown in Fig. 3, inside which the frequency of the coupled system was observed to be the same as the excitation frequency. Unstable (quasiperiodic) oscillations were observed outside of the boundaries. It was observed that the region of synchronization can shrink, widen, or shift by changing coupling strengths which impact the self-excited frequencies and the amplitude levels. The influence of large nonlinearity is also evident by the curved boundaries. For excitation amplitude less than 100 mV,

[1] Here we assume that the fabrication process has no/very little effect on the initial positions of the resonators.

the vibrations were observed to be unstable with substantial quasiperiodicity. It is possible for this region to be closed depending on damping and the noise in the circuit. For example, at the pressure of 15 Pa the same coupled system shows a wider area below 100 mV.

5 Summary

In this paper, the experimental results of nonlinear MEMS resonators were reported. It was shown that the variation in the excitation voltage affects the frequency response significantly. An extension of the hysteresis and thus an enlargement of usable amplitude bandwidth were observed. The unidirectionally coupled system exhibited stable self-excited oscillations depending on the coupling strengths and it also synchronized to the excitation signal. The experimental study shown in this paper indicates that the coupled system has a strong potential as a sensor depending on the applications.

Acknowledgments This work was supported in part by Global Center of Excellence (GCOE) program at Kyoto University, Kyoto Environmental Nanotechnology Cluster, Regional Innovation Cluster Program 2010, and Ministry of Education, Culture, Sports, Science and Technology (MEXT). The authors would like to acknowledge valuable help and advice from Dr. Patrick Longhini (SSC-Pacific), Dr. Huy Vu (San Diego State University), Dr. Antonio Palacios (San Diego State University), and Dr. Visarath In (SSC-Pacific).

References

1. A. Cowen, G. Hames, D. Monk, S. Wilcenski, B. Hardy, *Soimumps Design Handbook Revision 6.0* (MEMSCAP Inc., Durham, 2009)
2. C. Acar, A. Shkel, *MEMS Vibratory Gyroscopes* (Springer Science+Business Media, New York, 2009)
3. S. Naik, T. Hikihara, Characterization of a mems resonator with extended hysteresis. IEICE Electron. Expr. **8**(5), 291–298 (2011)